


Springer Optimization and Its Applications 200

Giorgio Fasano
János D. Pintér *Editors*

Modeling and Optimization in Space Engineering

New Concepts and Approaches

 Springer

Springer Optimization and Its Applications

Volume 200

Series Editors

Panos M. Pardalos , *University of Florida*

My T. Thai , *University of Florida*

Honorary Editor

Ding-Zhu Du, *University of Texas at Dallas*

Advisory Editors

Roman V. Belavkin, *Middlesex University*

John R. Birge, *University of Chicago*

Sergiy Butenko, *Texas A&M University*

Vipin Kumar, *University of Minnesota*

Anna Nagurney, *University of Massachusetts Amherst*

Jun Pei, *Hefei University of Technology*

Oleg Prokopyev, *University of Pittsburgh*

Steffen Rebennack, *Karlsruhe Institute of Technology*

Mauricio Resende, *Amazon*

Tamás Terlaky, *Lehigh University*

Van Vu, *Yale University*

Michael N. Vrahatis, *University of Patras*

Guoliang Xue, *Arizona State University*

Yinyu Ye, *Stanford University*

Aims and Scope

Optimization has continued to expand in all directions at an astonishing rate. New algorithmic and theoretical techniques are continually developing and the diffusion into other disciplines is proceeding at a rapid pace, with a spot light on machine learning, artificial intelligence, and quantum computing. Our knowledge of all aspects of the field has grown even more profound. At the same time, one of the most striking trends in optimization is the constantly increasing emphasis on the interdisciplinary nature of the field. Optimization has been a basic tool in areas not limited to applied mathematics, engineering, medicine, economics, computer science, operations research, and other sciences.

The series **Springer Optimization and Its Applications (SOIA)** aims to publish state-of-the-art expository works (monographs, contributed volumes, textbooks, handbooks) that focus on theory, methods, and applications of optimization. Topics covered include, but are not limited to, nonlinear optimization, combinatorial optimization, continuous optimization, stochastic optimization, Bayesian optimization, optimal control, discrete optimization, multi-objective optimization, and more. New to the series portfolio include Works at the intersection of optimization and machine learning, artificial intelligence, and quantum computing.

Volumes from this series are indexed by Web of Science, zbMATH, Mathematical Reviews, and SCOPUS.

Giorgio Fasano • János D. Pintér
Editors

Modeling and Optimization in Space Engineering

New Concepts and Approaches

 Springer

Editors

Giorgio Fasano
Thales Alenia Space
Turin, Italy

János D. Pintér
Department of Management Science and
Information Systems
Rutgers Business School - New Brunswick
Campus, Rutgers University
Piscataway, NJ, USA

ISSN 1931-6828

ISSN 1931-6836 (electronic)

Springer Optimization and Its Applications

ISBN 978-3-031-24811-5

ISBN 978-3-031-24812-2 (eBook)

<https://doi.org/10.1007/978-3-031-24812-2>

Mathematics Subject Classification: 37N05, 37N40, 49-06, 65K05, 70M20, 90Bxx, 90-08, 90C11, 90C26, 90C29, 90C30, 05B40, 68T01, 68T05, 68T20, 68T37, 68T40

© The Editor(s) (if applicable) and The Author(s), under exclusive license to Springer Nature Switzerland AG 2023

This work is subject to copyright. All rights are solely and exclusively licensed by the Publisher, whether the whole or part of the material is concerned, specifically the rights of translation, reprinting, reuse of illustrations, recitation, broadcasting, reproduction on microfilms or in any other physical way, and transmission or information storage and retrieval, electronic adaptation, computer software, or by similar or dissimilar methodology now known or hereafter developed.

The use of general descriptive names, registered names, trademarks, service marks, etc. in this publication does not imply, even in the absence of a specific statement, that such names are exempt from the relevant protective laws and regulations and therefore free for general use.

The publisher, the authors, and the editors are safe to assume that the advice and information in this book are believed to be true and accurate at the date of publication. Neither the publisher nor the authors or the editors give a warranty, expressed or implied, with respect to the material contained herein or for any errors or omissions that may have been made. The publisher remains neutral with regard to jurisdictional claims in published maps and institutional affiliations.

This Springer imprint is published by the registered company Springer Nature Switzerland AG
The registered company address is: Gewerbestrasse 11, 6330 Cham, Switzerland

Preface

Space engineering projects frequently require the analysis, modeling, and solution of advanced optimization problems. The primary concern of the earliest topical studies was the viability of missions to accomplish. Optimization was aimed at mission analysis, with specific attention to safety and technical feasibility. Therefore, space engineering projects required the analysis of mission trajectories, with paramount consideration given to crew protection and then to the optimization of fuel consumption.

More recently, commercial interests and cost-efficiency aspects related to space projects have become increasingly important. A well-known example is the continuing operation of the International Space Station.

For current and forthcoming space engineering projects, today's higher environmental awareness imposes mission constraints that in the past were completely or almost neglected. The ambitious goals of planned interplanetary explorations – specifically including manned missions – will require advanced analytical approaches to guarantee safety, to maximize the performance of the systems adopted, and to make use of mission resources as efficiently as possible.

While the quality of the decisions required by space engineering projects has been increasing, we have also witnessed continuing innovation regarding theoretical advances and ready-to-use decision support tools for such applications. The results of scientific innovation, modeling, and algorithmic developments are enhanced by today's advanced computational modeling and optimization environments. Since the earliest space engineering applications, the solution to increasingly hard optimization problems has become necessary. Earlier numerical optimization approaches were limited to handling *linear* or *convex nonlinear continuous* models, as well as *integer linear* or *mixed integer-continuous linear* optimization problems. (For clarity, we note here that *integer linear* optimization problems are already *non-convex*, but their handling can be based on classical approaches.) More recent advances in the area of optimization enable the handling of *continuous and mixed integer non-convex* problem formulations. This development enables the solution of often more realistic – but, as a rule, significantly harder – optimization problems.

The present volume consists of 14 contributed chapters. These chapters are written by leading experts who offer in-depth discussions of the mathematical modeling and algorithmic aspects of tackling a range of space engineering applications. Next, we present a brief summary of the topics discussed in the book, citing all chapters by the alphabetical order of the contributing (first) authors.

Advances in the Control Propellant Minimization for the Next Generation Gravity Mission, by Alberto Anselmi, Stefano Cesare, Sabrina Dionisio, Giorgio Fasano, and Luca Massotti, discusses the advancement of previous work by the same authors, dedicated to the problem of minimizing the control propellant in the future Next Generation Gravity Mission. The research presented here focuses on the optimal position and orientation of the thrusters installed on board in the presence of control requirements.

Transition of Two-Dimensional Quasi-periodic Invariant Tori in the Real-Ephemeris Model of the Earth-Moon System, by Nicola Baresi, focuses on the advanced concept of quasi-periodic invariant tori, currently representing a cutting-edge topic in astrodynamics. Modern numerical continuation techniques for generating two-dimensional invariant tori in the elliptical restricted three-body problem of the Earth-Moon system are introduced. The upcoming Lunar Orbital Platform Gateway serves as reference to demonstrate the applicability of the methodology.

Hypersonic Point-to-Point Travel for the Common Man, by Carlos Bislip and Erwin Mooij, explores the possibility of identifying, for a chosen route and reference vehicle, a set of parameters guaranteeing the admissible conditions for “common” (not specifically selected) individuals. An advanced *ad hoc* optimization approach is introduced. Evolutionary procedures are adopted, including the multi-objective evolutionary algorithm, based on decomposition with differential evolution. The Sanger II spaceplane and the associated Hypersonic ORbital Upper Stage (HORUS) have been taken as a reference. The results obtained in terms of optimal trajectory show the efficiency of the approach proposed.

The necessity of measuring the position and attitude of a target object almost instantaneously frequently occurs in aerospace engineering. *Bifocal Metrology Applications in Space Engineering*, by Fulvio Bresciani, Giorgio Fasano, and Janos D. Pinter, proposes a conceptually simple, yet innovative optical approach based on a compact bifocal projective system and a target identifier consisting of light spots. The chapter addresses the relevant mathematical aspects, with a special focus on measurement error analysis and two optimization problems concerning system sizing and light spot shaping, respectively. A real-world application is briefly introduced.

A Revisited Analysis of the Radioisotope Sail and Its Possible Application to Relativistic Spaceflight, by Luca Derosa, addresses the concept of radioisotope sail with potential application to relativistic space missions. Mathematical models, based on the special theory of relativity, are considered with reference to different relativistic spaceflight profiles. A case study, concerning the hypothetical use of a radioisotope sail as the propulsion system for a mission to Pluto, is presented, comparing the performances of the proposed technology with classical systems.

This work provides an inspiring summary of a so far little-investigated topic, i.e., space propulsion by virtue of radioactive materials.

The EXTREMA project (Engineering Extremely Rare Events in Astrodynamics for Deep-Space Missions in Autonomy) addresses a paradigm shift regarding deep-space guidance, navigation, and control. *The ERC-Funded EXTREMA Project: Achieving Self-Driving Interplanetary CubeSats*, by Gianfranco Di Domenico, Eleonora Andreis, Andrea Carlo Morelli, Gianmario Merisio, Vittorio Franzese, Carmine Giordano, Alessandro Morselli, Paolo Panicucci, Fabio Ferrari, and Francesco Topputo, proposes CubeSats (square-shaped miniaturized satellites) with autonomous maneuvering capabilities. This chapter presents an overview of EXTREMA, highlighting the relevant approaches, methodologies, and objectives. Expected outcomes and impact on future space exploration scenarios are also discussed.

Data Reduction for Optimizing the Attitude Control Dispatch in a Spacecraft, by Christophe Durand, Giorgio Fasano, and Andrea Forestieri, originates from a dedicated attitude control dispatch study discussed in another chapter of this volume by Anselmi *et al.* The control dispatch optimization approach is based on a time discretization of the mission scenarios to consider. The chapter proposes an *ad hoc* clustering methodology, in order to make the relevant optimization problem computationally tractable. The k-means and k-medoids methods are considered together with the Davies-Bouldin index and other evaluation criteria. An experimental analysis is performed for a specific case study.

Second Order Sufficient Conditions of Strong Minimality with applications to Orbital Transfers, by Leonardo Mazzini, offers a contribution to the topic of indirect methods for optimal control. It studies second-order extended sufficiency conditions, applicable without strict Legendre conditions and without local controllability assumptions, also in the frame of saturated and bang-bang control. A procedure to maximize the interval where the sufficient conditions can be applied using a Riccati matrix equation is introduced and compared with the classic conjugate point condition. Applications to finite and infinite thrust orbital transfer cases are presented.

Evolutionary Optimisation of a Flexible-Launcher Simple Adaptive Control System, by Erwin Mooij, proposes the application of a simple adaptive approach to the pitch control of a conventional, flexible launcher. An *ad hoc* evolutionary optimization algorithm is introduced: it is based on a floating-point representation of the design parameters, stochastic universal sampling selection, arithmetic crossover, non-uniform mutation, and Pareto ranking. The simultaneous minimization of the state deviation and the control effort is attained, while the oscillation of the control has been used as optimization criterion. A dedicated simulation study demonstrates the efficiency of the approach proposed.

Optimization and Solution Approaches in Utilizing Wireless Sensor Networks for Exploring Moon Planets and Space, by Ömer Özkan, reviews wireless sensor networking (WSN) applications in space, to explore the Moon, planets, and associated moons, or asteroids. The detectable physical data include, but are not limited, to temperature, pressure, radiation, seismic conditions, optical parameters,

and gas composition. An overall optimization point of view is adopted to maximize the performances of the WSNs considered.

Near-Optimal Guidance and Pulse-Modulated Reduced-Attitude Control for Orbit Injection, by Mauro Pontani, Andrea Pianalto, Stefano Carletta, and Paolo Teofilatto, investigates a new guidance, control, and actuation architecture for upper-stage orbit injection maneuvers. The proposed explicit near-optimal guidance algorithm is based on the local projection of the position and velocity variables and on the real-time solution of the associated minimum-time problem. A new nonlinear reduced attitude control algorithm is introduced, and the overall dynamics of the upper stage is modeled using Kane's method. An upper stage, with realistic propulsion parameters selected for numerical testing, demonstrates the effectiveness of the approach proposed, via dedicated Monte Carlo simulations.

A Pareto Front Numerical Reconstruction Strategy Applied to a Satellite System Conceptual Design, by Gustavo J. Santos, Sebastian Giusti, and Roberto Alonso, proposes an efficient approach for satellite system design, based on multi-objective parametric optimization. The objectives considered at system design level are usually conflicting. For instance, the overall performance has to be maximized, while (also) minimizing the total mass or volume. The overall global optimization approach proposed leverages the direct numerical simulation of the optimization problem and addresses the estimation of the optimal Pareto frontier. A case study, consisting of a low orbit satellite, is analyzed, comparing the approach proposed with a genetic algorithm-based multi-objective optimization procedure.

Time-Varying Lyapunov Control Laws with Enhanced Estimation of Distribution Algorithm for Low-Thrust Trajectory Design, by Abolfazl Shirazi, Harry Holt, Roberto Armellin, and Nicola Baresi, investigates the general problem of optimal design of space trajectories via an enhanced optimization algorithm, within the framework of Estimation of Distribution Algorithms (EDAs), incorporated with Lyapunov and Q-law feedback control methods. Real-world case studies, relevant to Earth-orbiting satellites, are analyzed in the chapter, illustrating the potential of the approach proposed.

In the life of a spacecraft, the launch and early operational phase are among the most critical, because of the high level of uncertainty present. *Indirect Optimization of Robust Orbit Transfer Considering Thruster Underperformance*, by Francesco Simeoni, Lorenzo Casalino, and Antonio Amelio, proposes an efficient indirect optimization method to determine robust control laws, taking into account the possibility of dramatic thruster underperformance. The insertion of a spacecraft in a highly elliptic orbit with multiple apogee burns is considered a case study analyzing the effect of non-nominal thrust in the first apogee maneuver.

This book will be of interest for researchers and practitioners working in the field of space engineering. Since it offers an in-depth exposition of the mathematical modeling, algorithmic and numerical solution aspects of the topics covered, the book will be useful also for aerospace engineering graduate and post-graduate students who wish to expand upon their knowledge, by studying real-world applications and challenges that they will meet in their professional work. The contributed chapters are mainly focused on space engineering practice. With this

aspect in mind, researchers and practitioners in mathematical systems modeling, operations research, optimization, and optimal control will also benefit from the case studies presented in this work.

The model development and optimization approaches discussed in the book can be extended also toward other application areas that are not directly related to space engineering. Hence, this book can be a useful reference to assist the development of new modeling and optimization applications. Readers will obtain a broad overview of some of the most challenging space engineering operational scenarios of today and tomorrow: this will be useful for managers in the aerospace field, as well as in other industrial sectors.

Acknowledgments

First and foremost, we wish to thank all contributing authors for their high-quality work, and for their efforts to make the publication of this volume possible. We are grateful to our colleagues who assisted us with peer reviews of the contributed chapters. We also wish to thank Elizabeth Loew and the entire publication team of Springer for their devoted work that has led to the publication of this book.

GF thanks also Walter Cugno and Roberto Angelini of Thales Alenia Space (Turin, Italy) for their support of the research and development activities related to modelling and optimization addressing a range of space engineering applications.

Giorgio Fasano and János D. Pintér

Contents

Advances in the Control Propellant Minimization for the Next Generation Gravity Mission	1
Alberto Anselmi, Stefano Cesare, Sabrina Dionisio, Giorgio Fasano, and Luca Massotti	
Transition of Two-Dimensional Quasi-periodic Invariant Tori in the Real-Ephemeris Model of the Earth–Moon System	33
Nicola Baresi	
Hypersonic Point-to-Point Travel for the Common Man	61
Carlos Bislip and Erwin Mooij	
Bifocal Metrology Applications in Space Engineering	95
Fulvio Bresciani, Giorgio Fasano, and János D. Pintér	
A Revisited Analysis of the Radioisotope Sail and Its Possible Application to Relativistic Spaceflight	123
Luca Derosa	
The ERC-Funded EXTREMA Project: Achieving Self-Driving Interplanetary CubeSats	167
Gianfranco Di Domenico, Eleonora Andreis, Andrea Carlo Morelli, Gianmario Merisio, Vittorio Franzese, Carmine Giordano, Alessandro Morselli, Paolo Panicucci, Fabio Ferrari, and Francesco Topputo	
Data Reduction for Optimizing the Attitude Control Dispatch in a Spacecraft	201
Christophe Durand, Giorgio Fasano, and Andrea Forestieri	
Second-order Sufficient Conditions of Strong Minimality with applications to Orbital Transfers	221
Leonardo Mazzini	

Evolutionary Optimisation of a Flexible-Launcher Simple Adaptive Control System 251
Erwin Mooij

Optimization and Solution Approaches in Utilizing Wireless Sensor Networks for Exploring Moon, Planets, and Space 285
Omer Ozkan

Near-Optimal Guidance and Pulse-Modulated Reduced-Attitude Control for Orbit Injection 301
Mauro Pontani, Andrea Pianalto, Stefano Carletta, and Paolo Teofilatto

A Pareto Front Numerical Reconstruction Strategy Applied to a Satellite System Conceptual Design 331
Gustavo J. Santos, Sebastián M. Giusti, and Roberto Alonso

Indirect Optimization of Robust Orbit Transfer Considering Thruster Underperformance 349
Francesco Simeoni, Lorenzo Casalino, and Antonio Amelio

Time-Varying Lyapunov Control Laws with Enhanced Estimation of Distribution Algorithm for Low-Thrust Trajectory Design 377
Abolfazl Shirazi, Harry Holt, Roberto Armellin, and Nicola Baresi

About the Editors

Giorgio Fasano is a researcher and practitioner at Thales Alenia Space, with nearly four decades of experience in the field of optimization and a broad range of space engineering applications. He holds an M.Sc. degree in Mathematics. He is a Fellow of the Institute of Mathematics and its Applications (IMA, UK), with the designation of Chartered Mathematician; he is also a Chartered Scientist (Science Council, UK). His interests include mathematical modeling, operations research, mixed integer programming, global optimization, and optimal control. He is the author of *Solving Non-standard Packing Problems by Global Optimization and Heuristics* (Springer, 2014) and co-editor of *Operations Research in Space and Air* (Ciriani *et al.*, Kluwer Academic Publishers, 2003). He is also the author of numerous other peer-reviewed research publications.

János D. Pintér is a researcher, educator, and practitioner with nearly five decades of experience in the broad area of systems modeling, analytics, and optimization, with a special emphasis on algorithm and software development for nonlinear optimization. He holds M.Sc., Ph.D., and D.Sc. degrees in Mathematics. So far, he has authored and edited ten books, including the award-winning monograph *Global Optimization in Action* (Kluwer Academic Publishers, 1996; Springer, 2013). He is also author or co-author of more than 200 book chapters, journal articles, research reports, book reviews, and software reviews. Dr. Pintér has been a member and officer of international professional organizations including the societies CORS, EUROPT, HORS, and INFORMS. He has also been serving for extensive periods of time on the editorial board of international professional journals. Dr. Pintér is the principal developer of a range of nonlinear optimization software products. In 2020, he joined the Department of Management Science and Information Systems at Rutgers University, where he teaches a range of business analytics/operations research topics.

In addition to the current volume, Fasano and Pintér are co-editors of the following works.

Modeling and Optimization in Space Engineering, Springer, 2013.

Optimized Packings with Applications, Springer, 2015.

Space Engineering – Modeling and Optimization with Case Studies, Springer, 2016.

Modeling and Optimization in Space Engineering – State of the Art and New Challenges, Springer, 2019.

Advances in the Control Propellant Minimization for the Next Generation Gravity Mission



Alberto Anselmi, Stefano Cesare, Sabrina Dionisio, Giorgio Fasano, and Luca Massotti

List of Acronyms

AOCS	Attitude and Orbit Control System
CoM	Centres of Mass
DCT	Drag Compensation Thruster
DFACS	Drag Free and Attitude Control System
DoF	Degrees of Freedom
E2E	End-to-End simulator
ESA	European Space Agency
FCT	Fine Control Thruster
GO	Global Optimization
GOCE	Gravity field and Ocean Circulation Explorer
GRACE	Gravity Recovery and Climate Experiment
LAGEOS	Laser Geodynamics Satellite
LL-SST	Low-Low Satellite-to-Satellite Tracking
MBW	Measurement Bandwidth
MILP	Mixed Integer Linear Programming
NGGM	Next Generation Gravity Mission
NLPN	Non-Linear Programming
POD	Precise Orbit Determination
RC	Repeat Cycle
SD	Spectral Density

A. Anselmi (✉) · S. Cesare · S. Dionisio · G. Fasano
Thales Alenia Space, Turin, Italy
e-mail: anselmi121@gmail.com; stefano.cesare@thalesalieniaspace.com;
sabrina.dionisio@thalesalieniaspace.com; giorgio.fasano@thalesalieniaspace.com

L. Massotti
European Space Agency, ESTEC, Noordwijk, The Netherlands
e-mail: luca.massotti@esa.int

SSD Satellite-to-Satellite Distance
SST Satellite-to-Satellite Tracking

1 Introduction

The optimization problem described in this chapter arose within the preliminary (Phase 0) studies of the Next Generation Gravity Mission (NGGM), a candidate project of the European Space Agency (ESA) dedicated to high-quality measurement of the temporal variations of the Earth's gravity field by pairs of satellites flying in formation in Low Earth Orbit (LEO). Currently, a version of the NGGM is being addressed as part of the ESA-NASA cooperation in the frame of the MAGIC (Mass Change and Geosciences International Constellation) project. The design of the MAGIC mission occurs under different assumptions than those taken into consideration in this paper. Up-to-date information about the mission is provided in [1, 2].

This chapter extends and enhances earlier research documented in a previous paper [3]. The mission scenario assumed in [3] and in the present work is as follows. The NGGM satellite pair will measure the gravity gradient signal between two satellites flying in loose formation at about 100 km mutual distance, in high/medium-inclination, low-altitude orbits, by means of a laser interferometer (Laser Tracking Instrument). Geodetic-quality Global Navigation Satellite System (GNSS) receivers and high-precision accelerometers mounted on each satellite make up the rest of the payload complement. The basic NGGM formation consists of two satellite pairs, each arranged in a "pearl-string" formation (i.e., flying along the same trajectory), one pair in near-polar (89°) orbit and another in medium-inclination (at minimum 65°) orbit. The mission aims at enabling long-term monitoring of the temporal variations of Earth's gravity field at relatively high temporal (down to 3 days) and increased spatial resolutions (up to 100 km) at longer time intervals, optimizing the spatial sampling for multiple temporal resolutions [1]. The fundamental observable is the variation of the distance between the two satellites in each pair, measured by a laser interferometer [4]. As a necessary complement, accelerometers measure the non-gravitational accelerations, to be separated from the gravity signal in the data processing. The mission product is the data set of positions and ambient accelerations, collected on board each spacecraft pair over a life of 7 years at minimum 10 Hz rate.

Each NGGM spacecraft, as conceived in the Phase 0 studies, consists of a modified LEO platform providing the spacecraft services and accommodating a thermally stabilized payload bay hosting the laser metrology and accelerometer elements on a high-stability structure. A 10-mN class thruster (drag compensation thruster, DCT) provides orbit maintenance/formation control and drag control in the direction of motion. In addition, a functionally redundant set of 1-mN class thrusters (fine control thruster, FCT) provides acceleration control (orbit maintenance/formation control as well as attitude/drag control) in the cross-axes. The type, number, and configuration of the FCTs impose major challenges to the

spacecraft and mission design. In the following, the FCTs will also be denoted as mini-thrusters or, when no ambiguity can occur, simply as thrusters.

The thruster set must provide tiny forces, equal and opposite to the ambient forces due to the residual air drag, with high dynamic range, high resolution, low noise, fast response time, and low propellant consumption, such as to make a long duration mission practical. Early trade-off studies established electric thrusters as the preferred candidate actuators. Given the thruster characteristics, an optimized design of the control system is fundamental to making the mission feasible.

The general problem is defined as follows: design a system of N thrusters, with N as small as possible, including redundancy to failure of any one thruster and power processing unit, capable of matching the environmental forces with conservative margins, over a long-duration mission, subject to global constraints (maximum power available at any time; maximum portable propellant mass) and to technological limits (min/max thrust and total impulse per thruster).

For obvious reasons, the general problem cannot be solved for any ambient acceleration environment; the solution must be tailored to a specific mission. A prerequisite is a detailed software model of the interaction of the spacecraft with the air particles, in the given orbit, with account taken of multiple causes of uncertainty of the air density, including the epoch, given the dependence of the density on the solar cycle. Once the spacecraft model is established, the control problem can be addressed.

It is assumed that the on-board controller receives at any given instant sufficient measurements of the forces and torques acting on the spacecraft, and a suitable algorithm exists that can dispatch individual commands to each of the N thrusters such that the sum total of the forces and torques dispatched matches the ambient forces and torques within a given tolerance. The problem is then to find the thruster layout (number, position, and orientation) that minimizes an objective function under given additional constraints. Normally the objective function is the total mass of propellant consumed over the lifetime and the most important constraint is the thrust range of the thrusters. For physical reasons N is equal or greater than 8 and the position of the thrusters is highly constrained by the spacecraft configuration, leaving few practical options open. The main variables to be decided are the $2N$ angles defining the orientation in space of the thruster lines of force.

The problem is solved progressively. A number of time profiles of the forces and torques is generated, representative of the foreseeable external conditions (chiefly the solar flux driving the atmospheric density at the selected mean altitude). The time profiles comprise a large fraction of the mission time (order of 1 year) sampled at a small time step (few seconds). First, a small set of representative control instances is selected by a clustering algorithm and the problem is solved for this reduced set. The obtained thruster positions are fixed. Then, given the N thrusters at the selected positions, the optimal orientations are found by solving the full optimization problem with the orientation angles as variables. This overall process can be repeated until a satisfactory solution is found.

The optimal thruster plant found in this way is then tested, by means of a dedicated simulation environment (E2E simulator, see [5]) against the full 7-year

time series of the perturbations under a range of solar flux conditions. Occasionally, the thruster plant may fail to cope with an instantaneous force/torque realization. Usually these cases are sparse and the controller can handle them without impact. The number of such failures is taken as an index of the quality of the solution.

The problem and the solution assuming no thruster failures are illustrated in [3]. A realistic system must offer redundancy as well, i.e., the ability to carry on with the mission without impairment in case of failure. The usual “cold redundancy” solution (two identical thruster branches, one working and one idle, the idle branch replacing completely the one in use when a thruster fails) is not practical for electric propulsion when many thrusters are involved. Therefore, one looks for a solution with 1 or 2 extra thrusters which can replace any one of the original sets. The main objective of the new research documented in this chapter was to solve the optimization problem including this type of redundancy. The focus of the new research also included a more realistic account taken of the technological constraints (dynamic range, total impulse) applicable to the candidate thruster types under consideration for the NGGM.

Section 2 discusses the relevant control problem. Section 3 outlines the thruster layout optimization problem as considered in the dedicated research and presents the state-of-the-art analysis, including notably the approach to the redundancy problem and the solutions found. Section 4 investigates the impacts of the layout solutions obtained on the real-world mission scenarios. Finally, Section 5 draws the conclusions and outlines some potential avenues for future research.

2 The Control Problem

To accomplish its scientific objectives, each NGGM satellite shall be designed with the special concern of minimizing the relevant disturbance to the payload. To this purpose, each satellite shall be endowed with a dedicated control system capable of carrying out several tasks in close coordination, as illustrated below.

- Orbit altitude control

As the planned average orbit altitude is subject to decay, it must be constantly monitored and maintained. Therefore, the control system must properly keep the orbits for all the cycles involved around their nominal values.

- Formation control

The satellite-to-satellite distance must be bounded around the initial parameters through a continuous control action that must not interfere with the scientific measurements.

- Non-gravitational acceleration control (drag-free control)

It is necessary to reduce the non-gravitational acceleration acting on each satellite to a level (to optimize the accelerometer sensitivity as close as possible to its intrinsic noise) where the measurement errors, arising from the coupling of the accelerometer imperfections with the residual accelerations, are compatible with the mission performance. The drag-free control must properly be coordinated

with the orbit altitude control and the formation control. In particular, the forces exerted by the drag-free control must not act in opposition to those applied to the satellite to maintain the orbit altitude and the formation geometry.

- Satellite-to-satellite line pointing control

The alignment between the beam of the laser interferometer and the satellite-to-satellite line must be controlled and constantly maintained within the tight requested bounds.

The overall control design considered in this chapter is essentially the same as that discussed in the previous paper [3]. An extended thruster layout optimization, however, has been carried out to obtain a highly efficient non-fully-redundant solution (i.e., where the redundant thrusters are fewer than the nominal ones).

With this perspective, the thruster layout has been refined to account for:

- Possible differences in the force/torque demand profiles between the two satellites of the pair
- Different thrust force/torque profiles corresponding to different atmospheric density conditions
- The thrust authority required by the other AOCs modes and in case of contingencies.

The above points have been considered focusing mainly on the aspects illustrated here below:

- The mission duration was reduced to 7 years (from 11, as supposed in the previous studies). This, in principle, leads to a reduction of the overall fuel consumption.
- The current limiting factors consist of the admitted thruster range, the power demand, and the thruster lifetime.

In the all-electric design of Phase 0, to perform the orbit corrections relevant to the launcher injection errors and to guarantee safe collision avoidance manoeuvres, the maximum thrust of the DCT must be advantageously exploited. It is assumed not to exceed 15 mN in order to be compatible with the electric power availability.

In summary, for the thruster layout optimization process the following assumptions were made for the control force/torque time-dependent data:

- The orbit altitude is 345 km and the inclination 66° for minimum, mean, and maximum atmospheric density conditions.
- Fusion of time-dependent data between the leader and follower satellites is performed to obtain two satellites with the same thruster layout configuration, allowing in-orbit interchangeability of the leader-follower roles.
- Time-dependent data include the initial transient phase of the formation control to account for stronger force/torque requests w.r.t. the science steady state phase (in the previous studies, the maximum force along the longitudinal axes was assumed to be 20 mN, while in the present work it is 15 mN corresponding to the on-board available power); the inclusion of the transient phases has the specific

purpose of assessing the control authority in terms of forces/torques during the orbital manoeuvres, e.g., of an along-track orbital correction/change.

- The DCT misalignment is 0.1° at 3σ truncated Gaussian.
- No support from the magnetic torquer equipment to exert the torque control is considered for the science phases, but for the transient phases only.
- An overall time of approximately 2.5 months is simulated for the science phase, plus 1 month for the formation transient phase, with a sampling every 400 s (25,000 samples for each atmospheric density condition).

Figures 1 and 2 show the time-dependent forces and torques acting on the leader satellite in case of maximum atmospheric density conditions. The effects of the

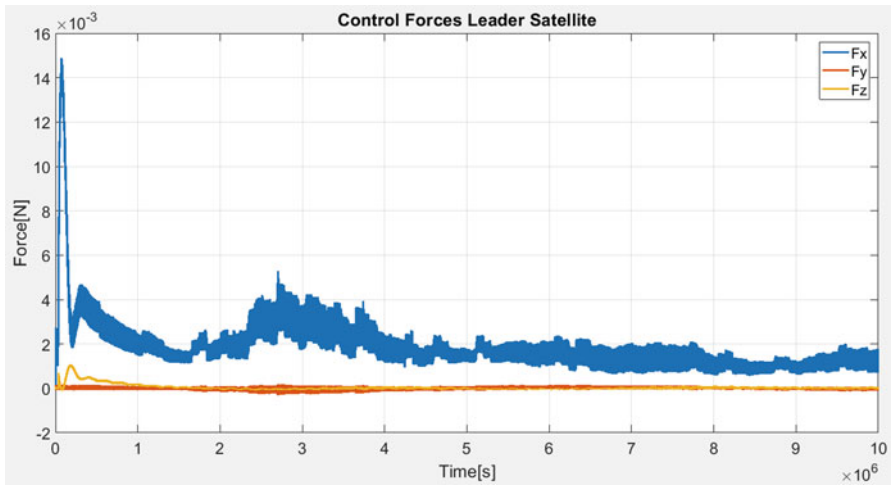


Fig. 1 Non-gravitational forces acting on the leader satellite – maximum atmospheric density

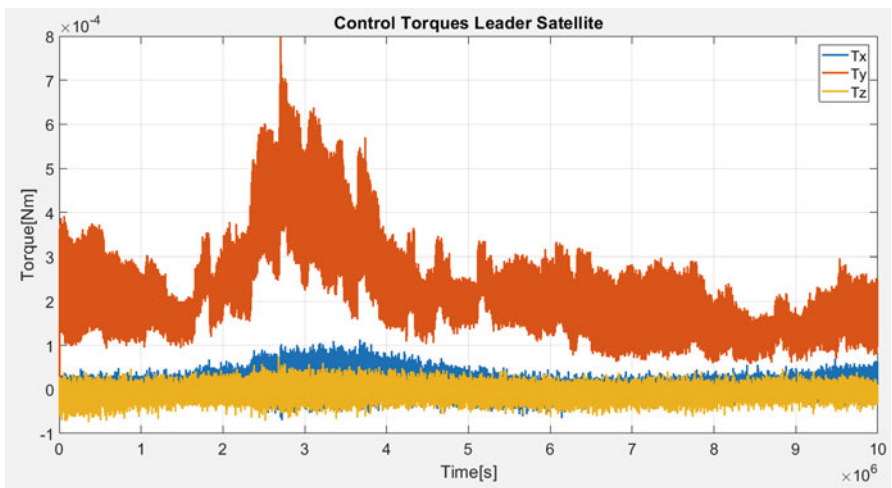


Fig. 2 Torques acting on the leader satellite – maximum atmospheric density

transient phase corresponding to the formation control associated to an orbital correction/change are visible at the beginning of the series in Fig. 1.

3 Thruster Layout Optimization

This section is dedicated to the thruster layout analysis. The relevant problem is stated and the overall approach outlined. Two case studies are overviewed with the main purpose of illustrating the focus of the analysis carried out.

3.1 Problem Statement and Overall Approach

The analysis performed by the authors in the preceding NGGM studies showed the importance of determining an ad hoc (mini-)thruster layout in order to minimize the overall control propellant during the whole mission. In all these former studies, it was implicitly assumed that the thrusters involved were able to work as planned with no breakdown. In addition to what was investigated previously, here the occurrence of possible thruster failures is considered. More precisely, it is assumed that any one of these thrusters can stop working at any phase of the mission. The present study has the further ambition of managing this single-failure issue by avoiding “cold redundancy”. The idea of a straightforward duplication of any (optimal) thruster layout in the no-failure hypothesis would actually be impractical (specifically for an all-electric propulsion design). To this purpose, a number of redundant thrusters are included.

A possible alternative to the approach here proposed could consider a larger number of nominal thrusters, always available if necessary (except in the case of failure), and no redundant thrusters. Although quite suggestive, this option is not discussed here, representing a possible subject of future research.

The overall optimization framework relevant to the approach followed here consists in guaranteeing the mission feasibility, while minimizing the propellant consumption compatible with the minimum number of thrusters involved. Thruster position and orientation are in general changed, whenever opportune, to set up a new configuration including both nominal and redundant thrusters. Each redundant thruster in the new optimal solution is able to replace (at least partially) more than one of the nominal ones (in order to avoid total duplication).

The situation where no failure affects any nominal thruster (during the whole mission) is referred to in the following as *nominal operational scenario*. *Failure operational scenario #* refers to the situation in which nominal thruster # has failed, all the others remaining operational. The general optimization criterion, consisting in the minimum propellant consumption, may thus assume the following diverse specific connotations:

- Minimum propellant consumption, considering exclusively the nominal operational scenario.

- Minimum propellant consumption considering all possible operational scenarios (i.e., nominal and all failure scenarios).
- Weighted combinations of the above criteria.

As anticipated, the configuration concerning both the nominal and redundant thrusters is assumed to be fixed during the whole mission. Therefore, the positions and orientations of all the thrusters encompassed are parameters to be determined (once and for all) in the design phase. The primary scope of the analysis described here consists, as a matter of fact, in finding the most appropriate values for these parameters, in accordance with the given mission requirements and the specific optimization criterion selected. In addition, this analysis also aims at identifying possible drawbacks and even bottlenecks relevant to the thruster typology and relative sizing.

The approach followed by the authors both in this and the previous studies, albeit general, is deemed particularly suitable when cutting-edge electric propulsion technology is involved as in the present case. The optimization methodology conceived with this perspective (see [6, 7]) adopts mathematical models and algorithms based on global optimization (GO, see, e.g., [8, 9]), mixed integer linear/non-linear programming (MILP/MINLP, see, e.g., [9, 10]), as well as ad hoc heuristics.

To outline the problem in question also from a mathematical point of view, the interval $[0, T]$ is first introduced. It expresses the given timeframe over which the relevant analysis has to be fulfilled. As the two satellites involved in this work are supposed to be identical, the entire control dispatch analysis can simply focus on a generic spacecraft which can stand for both. This is ideally represented by a dynamic system S , assumed to be a rigid body. An appropriate S -based orthogonal reference frame (O, x, y, z) , denoted as the main reference frame, is defined (the x axis is longitudinal). The entire interval $[0, T]$ is then discretized into a set of sub-intervals, of duration Δ each, delimited by the $N_I + 1$ instants $i \in \{0, 1, \dots, N_I\} = I$. At each instant i a force $\mathbf{F}_i = (F_{xi}, F_{yi}, F_{zi})$ and a torque $\mathbf{T}_i = (T_{xi}, T_{yi}, T_{zi})$, representing the overall control request (determined by the on-board control system), have to be exerted on the system (constantly) during the relative time sub-interval Δ , through the available thrusters.

In light of the above, two major issues, referred to as *nominal* and *redundancy* problems, respectively, arise. The analysis of the former (inclusive of sensitivity aspects) can actually provide a preliminary understanding for the layout to reshape, including, for instance, an estimate of the number of nominal thrusters to adopt, as well as insights on possible operational criticalities. The two problems are stated here below:

- Nominal problem (P_N)

A (suitable) number of (nominal) thrusters have to be selected with given technical features (not necessarily identical) to provide the force \mathbf{F}_i and torque \mathbf{T}_i as requested at each instant i over the whole time frame $[0, T]$. Their positions/orientations are determined in order to satisfy the mission requirements, as

well as the optimization criterion adopted (clearly, a comprehensive dedicated analysis could contemplate more than one possible choice).

- Redundancy problem (P_R)

Extension of the nominal problem, where a single nominal thruster (not known a priori) is assumed to be non-operative for the whole mission (as the worst case has to be considered). Redundant thrusters are introduced to overcome the potential single-failure event, while optimizing the selected performance criterion (considering different criteria, as appropriate).

The P_N mathematical formulation is not reported here, being simply a sub-case of the P_R one. The overall (discretized) model of the redundancy problem (P_R), in consideration of the above assumptions, is outlined herein. In this formulation the possible contribution of the DCT thruster is not considered for the sake of simplicity (its inclusion is straightforward). The following basic and additional constraints (expressed by a compact formalism and allowing for a slight abuse of notation) are encompassed.

Basic constraints:

$$\forall \alpha \in O_S \forall i \in I \quad \begin{pmatrix} v & \hat{v} \\ p \times v & \hat{p} \times \hat{v} \end{pmatrix} \begin{pmatrix} u_{1\alpha i} \\ \dots \\ u_{r\alpha i} \\ \dots \\ u_{N_A\alpha i} \\ \dots \\ \hat{u}_{1\alpha i} \\ \dots \\ \hat{u}_{\hat{r}\alpha i} \\ \dots \\ \hat{u}_{\hat{N}_{\hat{A}}\alpha i} \end{pmatrix} = \begin{pmatrix} F_{\alpha i} \\ T_{\alpha i} \end{pmatrix}, \quad (1)$$

$$\forall r \in A \quad \|v_r\| = 1, \quad (2-1)$$

$$\forall \hat{r} \in \hat{A} \quad \|\hat{v}_{\hat{r}}\| = 1, \quad (2-2)$$

$$\forall r \in A \forall \alpha \in O_S \forall i \in I \quad u_{r\alpha i} \in [\underline{U}_r, \overline{U}_r], \quad (3-1)$$

$$\forall \hat{r} \in \hat{A} \forall \alpha \in O_S \forall i \in I \quad \hat{u}_{\hat{r}\alpha i} \in [\underline{\hat{U}}_{\hat{r}}, \overline{\hat{U}}_{\hat{r}}], \quad (3-2)$$

$$\forall r \in A \quad p_r D_{pr}, \quad (4-1)$$

$$\forall \hat{r} \in \hat{A} \quad \hat{\mathbf{p}}_{\hat{r}} \in \hat{D}_{\hat{p}\hat{r}}, \quad (4-2)$$

$$\forall r \in A \quad \mathbf{v}_r \in D_{vr}, \quad (5-1)$$

$$\forall \hat{r} \in \hat{A} \quad \hat{\mathbf{v}}_{\hat{r}} \in \hat{D}_{\hat{v}\hat{r}}. \quad (5-2)$$

The notations here adopted are explicated in the following.

- *Nominal thrusters:*

$A = \{1, \dots, r, \dots, N_A\}$ is the set of (nominal) thrusters;

$O_S = \{0, \dots, \alpha, \dots, N_A\}$ is the set of (nominal and failure) operational scenarios;

$\mathbf{p}_r = (x_r, y_r, z_r)$ is, for each thruster r , the unit vector representing its position;

$\mathbf{v}_r = (v_{rx}, v_{ry}, v_{rz})$ is, for each thruster r , the unit vector representing its orientation;

v is the (sub-)matrix whose columns are the (column) vectors $(v_{rx}, v_{ry}, v_{rz})^T$, i.e.,

$$v = \left((v_{1x}, v_{1y}, v_{1z})^T, \dots, (v_{rx}, v_{ry}, v_{rz})^T, \dots, (v_{N_Ax}, v_{N_Ay}, v_{N_Az})^T \right);$$

$\mathbf{p}_r \times \mathbf{v}_r = (q_{rx}, q_{ry}, q_{rz})$ is, for each thruster r , the cross product of \mathbf{p}_r and \mathbf{v}_r ;

$p \times v$ is the (sub-)matrix whose columns are the column vectors $(q_{rx}, q_{ry}, q_{rz})^T$, i.e.,

$$p \times v = \left((q_{1x}, q_{1y}, q_{1z})^T, \dots, (q_{rx}, q_{ry}, q_{rz})^T, \dots, (q_{N_Ax}, q_{N_Ay}, q_{N_Az})^T \right);$$

$u_{r\alpha i}$ is, for each thruster r , the (Euclidean) norm $\|\mathbf{F}_{r\alpha i}\|$ of the force exerted by r in operational scenario α at instant i , i.e., $\mathbf{F}_{r\alpha i} = u_{r\alpha i} \mathbf{v}_r$;

$\underline{U}_r, \overline{U}_r$ are, for each thruster r , the lower and upper limits (imposed on the force norms $u_{r\alpha i}$ (depending on the specific technical characteristics of the thrusters));

$D_{pr} \subset R^3$ is, for each thruster r , a compact domain delimiting the admissible positions (in compliance with the given geometrical/operational requirements);

$D_{vr} \subset R^3$ is, for each thruster r , a compact domain delimiting the admissible orientations (in compliance with the given geometrical/operational requirements);

- *Redundant thrusters:*

All the above notations relevant to the nominal thrusters are directly carried over the redundant simply by introducing the hat symbol ($\hat{\cdot}$), e.g., \hat{r} is the index

associated with the generic redundant thruster and $\hat{A} = \{1, \dots, \hat{r}, \dots, N_{\hat{A}}\}$ is the corresponding set.

- *Forces and torques:*

$F_{\alpha i} = (F_{x\alpha i}, F_{y\alpha i}, F_{z\alpha i})^T$ is the overall force (represented as a column vector), requested by the controller (from the thrusters) in operational scenario α at instant i ;

$T_{\alpha i} = (T_{x\alpha i}, T_{y\alpha i}, T_{z\alpha i})^T$ is the overall torque (represented as a column vector), requested by the controller (from the thrusters) in operational scenario α at instant i .

Constraints (1) represent the control dispatch equations; (2-1) and (2-2) are normalization conditions defining the orientation unit vectors. The following additional constraints, optional depending on the specific analysis focus, can be included.

Additional constraints:

$$\forall r \in A \forall \alpha \in O_s \forall i \in \{0, 1, \dots, N_I - 1\} \quad |u_{r\alpha(i+1)} - u_{r\alpha i}| \leq L_r, \quad (6-1)$$

$$\forall \hat{r} \in \hat{A} \forall \alpha \in O_s \forall i \in \{0, 1, \dots, N_I - 1\} \quad |\hat{u}_{\hat{r}\alpha(i+1)} - \hat{u}_{\hat{r}\alpha i}| \leq \hat{L}_{\hat{r}}, \quad (6-2)$$

$$\forall r \in A \forall \alpha \in O_s \quad \sum_{i \in I} u_{r\alpha i} \leq \frac{J_r}{\Delta}, \quad (7-1)$$

$$\forall \hat{r} \in \hat{A} \forall \alpha \in O_s \quad \sum_{i \in I} \hat{u}_{\hat{r}\alpha i} \leq \frac{J_{\hat{r}}}{\Delta}. \quad (7-2)$$

Here, L_r is a (positive) constant limiting the increments/decrements of the force exerted by each thruster r in any two subsequent instants of any operational scenario α (this constraint can be set, for instance, when adopting electric propulsion to take into account the given response time requirements); for each thruster r J_r is an upper bound on the total impulse admissible during any one operational scenario α . An analogous meaning is given to the terms relative to the redundant thrusters.

The general optimization objective, representing the propellant consumption minimization, is expressed as below:

$$\min \left\{ \sum_{r \in A} f_r(u_{r\alpha i}) + W_S \left(\sum_{r \in A} f_r(u_{r\alpha i}) + \sum_{\hat{r} \in \hat{A}} \hat{f}_{\hat{r}}(\hat{u}_{\hat{r}\alpha i}) \right) \right\}, \quad (8)$$

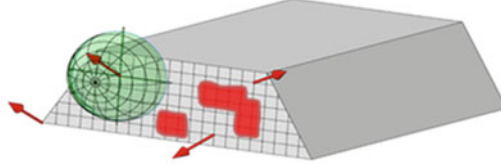


Fig. 3 Example of discretized positions (with forbidden zones in red), some thruster orientation vectors (red arrows), and an orientation semi-sphere (centred in one node of the grid)

where, for each thruster r , $f_r(u_{r\alpha i})$ is the propellant consumption function (shaped on the thruster characteristics and depending on the magnitude of the force exerted) in operational scenario α at instant i ; W_S is an appropriate optimization weight ($W_S \geq 0$ and $W_S = 0$ when only the propellant consumption of the nominal operational scenario is minimized). Analogous notations are assumed for the terms corresponding to the redundant thrusters (where $\hat{u}_{\hat{r}\alpha i} = 0$ for $\alpha = 0$).

In the present study (as well as in the previous ones), the domains D_{pr} are grids of admissible (discretized) positions with holes representing forbidden zones. These grids are virtually placed on the frontal or rear surfaces of the spacecraft. The domains D_{vr} consist of semi-spheres each one centred in a node of the grids. Figure 3 shows an example of a grid (with holes) of admissible positions on the rear surface of a spacecraft and an orientation semi-sphere (associated with a grid node).

The above specification for the D_{vr} domains can simply be obtained by replacing the general conditions (5-1) and (5-2) with the following:

$$\forall r \in A \quad \underline{V}_r \leq (v_{rx}, v_{ry}, v_{rz})^T \leq \overline{V}_r, \quad (9-1)$$

$$\forall \hat{r} \in \hat{A} \quad \hat{\underline{V}}_{\hat{r}} \leq (\hat{v}_{rx}, \hat{v}_{ry}, \hat{v}_{rz})^T \leq \hat{\overline{V}}_{\hat{r}}. \quad (9-2)$$

Here, $\underline{V}_r = (0, -1, -1)$ or $\underline{V}_r = (-1, -1, -1)$ depending on the surface involved (i.e., the former if thruster r is placed on the frontal, the latter if on the rear); this is analogous for the corresponding upper limit, i.e., $\overline{V}_r = (1, 1, 1)$ or $\overline{V}_r = (0, 1, 1)$. The same notations are adopted concerning the general redundant thruster \hat{r} . As is gathered, actually the semi-spheres in question are determined by the intersection of constraints (2-1) and (9-1), or (2-2) and (9-2), respectively. In the study discussed here (as well as in the previous ones), expression (8) has been linearized as follows:

$$\min \left\{ \sum_{\substack{r \in A \\ \alpha = 0 \\ i \in I}} K_r u_{rai} + W_S \left(\sum_{\substack{r \in A \\ \alpha \in O_S, \alpha \neq 0 \\ i \in I}} K_r u_{rai} + \sum_{\substack{\hat{r} \in \hat{A} \\ \alpha \in O_S, \alpha \neq 0 \\ i \in I}} \hat{K}_{\hat{r}} \hat{u}_{\hat{r}\alpha i} \right) \right\}, \quad (10)$$

with $K_r, \hat{K}_{\hat{r}} > 0$ (for an in-depth discussion on the general expression (8) see [11]).

As pointed out in [3], the problem P_N is NP-hard. This is more the case for P_R and, hence, in general it is deemed to be extremely challenging to undertake tout court by any global optimization approach. The overall heuristic (recursive) methodology, purposely conceived [12], has therefore the purpose of finding satisfactory solutions, albeit non-proven optimal. It is actualized by means of a dedicated mathematical library, consisting of the following modules:

- Preliminary solution (PS)
- Preliminary solution optimization (PSO)
- Overall solution assessment (OSA)

The PS module performs a search for preliminary (roughly approximate) solutions to a simplified version of the problem (P_R). For this purpose, a subset $\underline{I} \subset I$ of instants is selected a priori (by means of clustering techniques) as representative of the whole operational scenario associated with the entire set I (for an in-depth discussion of this aspect see [7]). This module has the main purpose of determining, for each nominal/redundant thruster, the position, as well as the octant (of the corresponding semi-sphere) in which the force unit vector is supposed to be oriented.

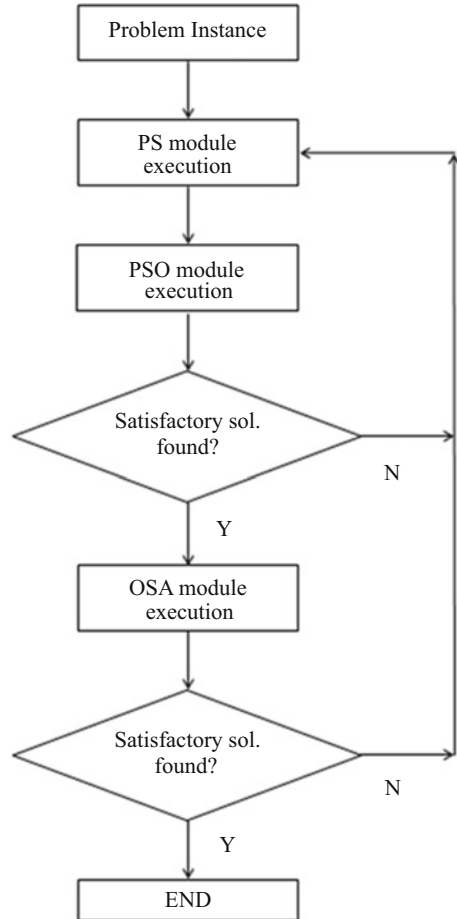
The PSO module is aimed at refining the PS solution. The thruster positions deriving from the PS module are fixed, while an approximate orientation within the selected octants is determined for the force unit vector of each thruster. For the PSO module, also a subset $\underline{I}' \subset I$ ($|\underline{I}| \leq |\underline{I}'|$) of representative instants is considered.

The OSA module has first the task (OSA-1) of assessing the solution obtained by the PSO module over the whole set of instants I (or a subset $I'' \subset I$, $|\underline{I}'| \leq |\underline{I}''|$). Furthermore, this module performs local optimization to improve the PSO solution (OSA-2), suggesting the positions of additional redundant thrusters, if necessary (OSA-3).

Backward iterations can be performed whenever deemed appropriate and the solution process reactivated. The overall logic, in its basic conception, is illustrated by Fig. 4. Different paths of the optimization process define specific solution strategies. Relevant examples are:

- PS + PSO + OSA - 2(+OSA - 1);
- PS + OSA - 3 + OSA - 2(+OSA - 1)

Fig. 4 Basic logic of the solution process



existing preliminary P_N solution (e.g., from previous analyses) + OSA-3 + OSA-2 (+ OSA-1);

PS + OSA - 2 + PSO + OSA - 2 (+OSA - 1).

3.2 Case Studies

At this stage of the project, a major concern consisted in limiting the overall number of thrusters (nominal and redundant) as much as possible. From previous research it had resulted that at least eight thrusters were necessary to solve the nominal problem (P_N) satisfactorily. Additionally, it had been shown that eight nominal thrusters with only one redundant were not able to yield acceptable solutions to the redundancy

problem (P_R) in practice. The challenge thus became that of envisioning a solution with eight nominal thrusters and two redundant thrusters. In this perspective, considering the extremely restrictive operational framework assumed, even close-to-feasible solutions were admitted. To this purpose, a relaxation of Eq. (1) was adopted as described in the following.

Considering the redundancy problem (P_R) in question, an *infeasible instant* occurs when one (or more) of the control dispatch Eq. (1) for forces and torques is not satisfied. Therefore, even one of these equations, in any single instant, can become a stumbling block for the whole solution. This can simply be avoided by introducing in each equation an error variable. These error variables are denoted (for each axis x, y, z and each instant i) as $\varepsilon_{Fxi}, \varepsilon_{Fyi}, \varepsilon_{Fzi}$ and $\varepsilon_{Txi}, \varepsilon_{Tyi}, \varepsilon_{Tzi}$ for the forces and torques, respectively. All these variables have lower and upper bounds (of equal magnitude), i.e., $\forall i \ \varepsilon_{Fi} = (\varepsilon_{Fxi}, \varepsilon_{Fyi}, \varepsilon_{Fzi})^T \in [-E_F, E_F]$ and $\forall i \ \varepsilon_{Ti} = (\varepsilon_{Txi}, \varepsilon_{Tyi}, \varepsilon_{Tzi})^T \in [-E_T, E_T]$, where $E_F, E_T > 0$ are the admitted tolerances. Equation (1) is hence substituted by the expressions below:

$$\forall \alpha \in O_S \forall i \in I \quad \begin{pmatrix} v & \hat{v} \\ p \times v & \hat{p} \times \hat{v} \end{pmatrix} \begin{pmatrix} u_{1\alpha i} \\ \dots \\ u_{r\alpha i} \\ \dots \\ u_{N_A\alpha i} \\ \dots \\ \hat{u}_{1\alpha i} \\ \dots \\ \hat{u}_{\hat{r}\alpha i} \\ \dots \\ \hat{u}_{\hat{N}_A\alpha i} \end{pmatrix} = \begin{pmatrix} T_{\alpha i} + \varepsilon_{Fi} \\ T_{\alpha i} + \varepsilon_{Ti} \end{pmatrix} \quad (11)$$

(also in this case, the possible contribution of the DCT thruster is neglected).

A solution that minimizes the sum of infeasibilities is obtained by minimizing the sum of the error variables (with suitable weights). The relevant optimization objective is:

$$\varepsilon = \sum_{O_S, i} [|\varepsilon_{Fxi}| + |\varepsilon_{Fyi}| + |\varepsilon_{Fzi}| + W_\varepsilon (|\varepsilon_{Txi}| + |\varepsilon_{Tyi}| + |\varepsilon_{Tzi}|)], \quad (12)$$

where W_ε is an appropriate constant with physical dimension L^{-1} . This is actually the approach adopted for the OSA module in the feasibility analysis reported in this section (where W_ε has a unit of m^{-1}). The optimization objective of the previous modules (i.e., PS and PSO) is instead the minimization of the overall propellant consumption (adopting objective function (10) with $W_S = 1$), as in the basic formulation (with no relaxation for Eq. (1)). The utilization of two redundant thrusters significantly reduces the number of infeasible instants with

respect to the previous option with a single redundant thruster only. Nonetheless, these infeasibilities are not totally absent in the final solutions found. The two case studies are described in Sects. 3.2.1 and 3.2.2.

In both, an average orbit of 345 km is considered. Three different atmospheric density conditions are examined, i.e., minimum, mean, and maximum. The DCT thrust level ranges from 0.6 to 15 mN and it is supposed to be always active except for the science phase in minimum atmospheric density conditions. The default lower limit for the force of the FCT thrusters (only for the redundant or both nominal and redundant) is relaxed (from 0.05 to 0 mN). This relaxation has the purpose of detecting possible operational scenarios during which the deactivation of the corresponding thrusters, resulting mostly inactive in the solution, could be profitably imposed. The maximum admissible thrust for both the nominal and redundant thrusters is 1 mN. The selected (sub-)set $s(I, I', I'')$ of the representative instants consist of ~300 elements for both the PS and PSO modules, and ~1500 for the OSA module. All the results reported in the following refer to those obtained with the OSA module (final solution).

In this analysis, the science phases are distinguished from the transient ones, i.e., those occurring after the orbital manoeuvres when the control system acts to attain a new steady state. Although the leader and follower satellites are assumed to be identical from a design point of view, their operational conditions (e.g., their attitude) are different in terms of overall force and torque requested at each instant. The relevant results are however very similar, therefore, in the following, only the leader satellite is considered (in both case studies). The analysis here discussed mostly addresses the following aspects for the different mission phases/operational scenarios:

- The total impulse exerted by each thruster
- The forces (over time) exerted by each thruster
- The errors (w.r.t. the infeasibility instants)
- The utilization of each thruster, in each instant, with forces exerted below the (actual) lower limit (i.e., 0.05 mN)

In general, an ideal solution is expected to feature: a uniform distribution of the impulses, forces, and torques exerted by the thrusters (both nominal and redundant) in each phase; no infeasibility instants; either thrusters totally inactive (i.e., 0% of usage) or fully active (i.e., 100% of usage) in each phase/operational scenario; no thrust saturation occurring (i.e., no forces exerted by the thrusters reach the given upper limit of 1 mN).

An overall assessment of the results obtained with the analysis reported herein is provided in Sect. 4. The overall layout optimization approach discussed so far actually entails a number of approximations due to the significant difficulty of the problem. A further dedicated analysis based on an advanced dynamic simulation represents therefore the ultimate step of the study in question. The actual mathematical models of the on-board control system are adopted for this purpose, replacing in particular the set of instants I with the actual control steps. In Sects.

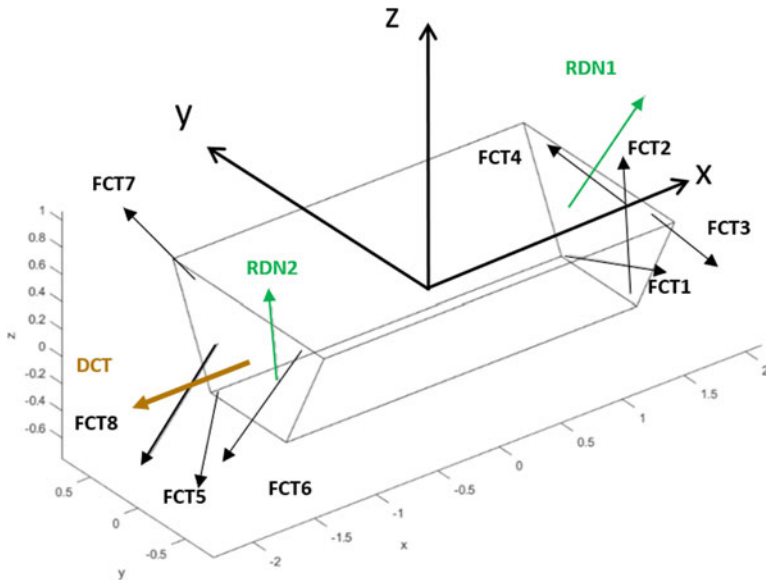


Fig. 5 Case study 1 solution thruster layout

3.2.1 and 3.2.2, only a (very) limited part of the results obtained are reported. An exposition of the ultimate outcomes relevant to the dynamic simulation analysis carried out is provided in Sect. 4.

3.2.1 Case Study 1

In this case study, the minimum thrust for the nominal thrusters (when active) is 0.05 mN, while, for the redundant thrusters, this limitation is reduced to 0 mN. Figure 5 provides a graphical view of the solution obtained.

Figure 6 illustrates the total impulse provided by the nominal and redundant thrusters of the leader satellite for the science phase in minimum atmospheric density conditions for the nominal operational scenario. Figure 7 illustrates the total impulse provided by the nominal and redundant thrusters of the leader satellite for the science phase in minimum atmospheric density conditions for the failure scenarios 1–4 (corresponding to the frontal nominal thrusters).

The total impulse figures, when projected over the total time span of 7 years, are compatible with the upper limit <120 kNs assumed for the thruster technology. Figure 8 illustrates the forces (mN) over time (s) provided by the nominal and redundant thrusters of the leader satellite for the science phase in mean atmospheric density conditions for the nominal operational scenario.

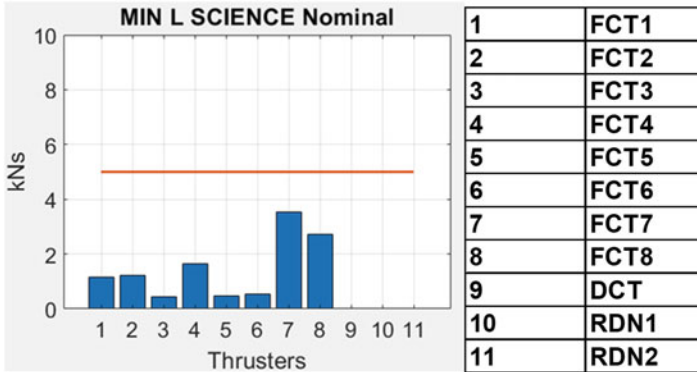


Fig. 6 Total impulse (kNs) in 3.5 months, science phase, minimum atmospheric density, nominal operational scenario

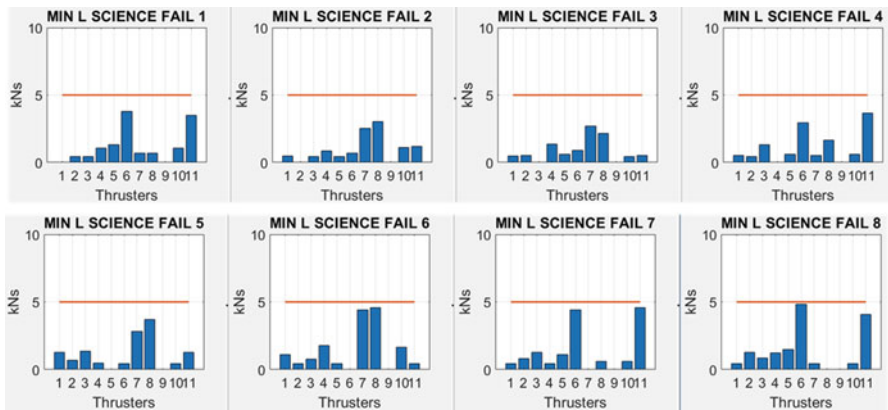


Fig. 7 Total impulse (kNs) in 3.5 months, science phase, minimum atmospheric density, failure operational scenarios

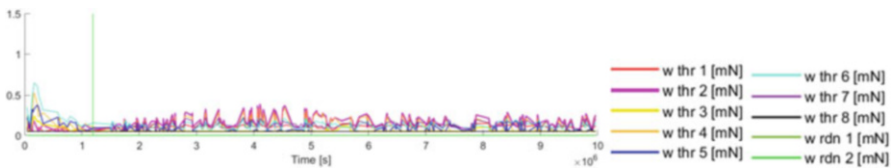


Fig. 8 Forces (mN) over time (s), transient/science phases, mean atmospheric density, nominal operational scenario

Figure 9 illustrates the time profile of the forces provided by the nominal and redundant thrusters of the leader satellite for the science phase in mean atmospheric density conditions for the failure scenarios 1–4 (front thrusters).

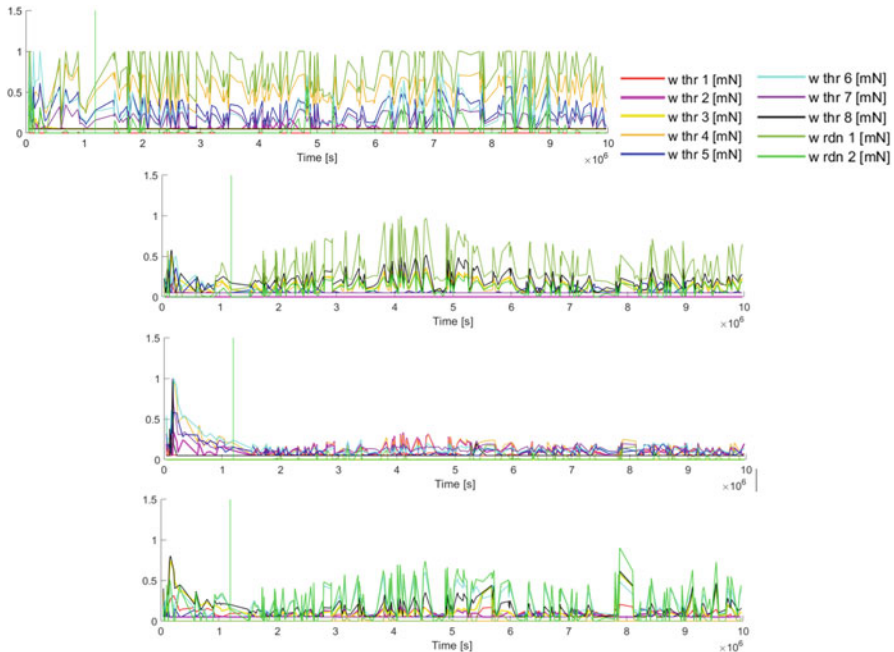


Fig. 9 Forces (mN) over time (s), transient/science phases, mean atmospheric density, failure operational scenarios 1–4 (in order from top to bottom)

The time profile of failure scenario 1 (top plot of Fig. 9) shows saturation of some thrusters which reach the assumed upper limit of 1 mN. This is an unwanted effect and it is treated further on (case study 2). Figure 10 shows the profiles corresponding to failure of thrusters 5–8 (rear thrusters).

Figure 11 illustrates the force (mN) over time (s) provided by the DCT thruster of the leader satellite for both the transient and science phases in maximum atmospheric density conditions, for the nominal operational scenario. This also indicates that other solutions can be explored for the DCT, like a cluster of thrusters of smaller class for drag compensation purposes in science phase, and a cluster of impulsive thrusters of larger class for operations, initial formation acquisition, and CAM (collision avoidance manoeuvre).

Tables 1 and 2 report the average error magnitudes with respect to the forces and torques in the (relaxed) control dispatch Eq. (11), and the corresponding atmosphere conditions (Min, Mean, Max), for the transient and science phases.

Figures 12, 13 and 14 show examples of “infeasibility” occurring when the calculated force and torque components to be dispatched cannot be met by the system:

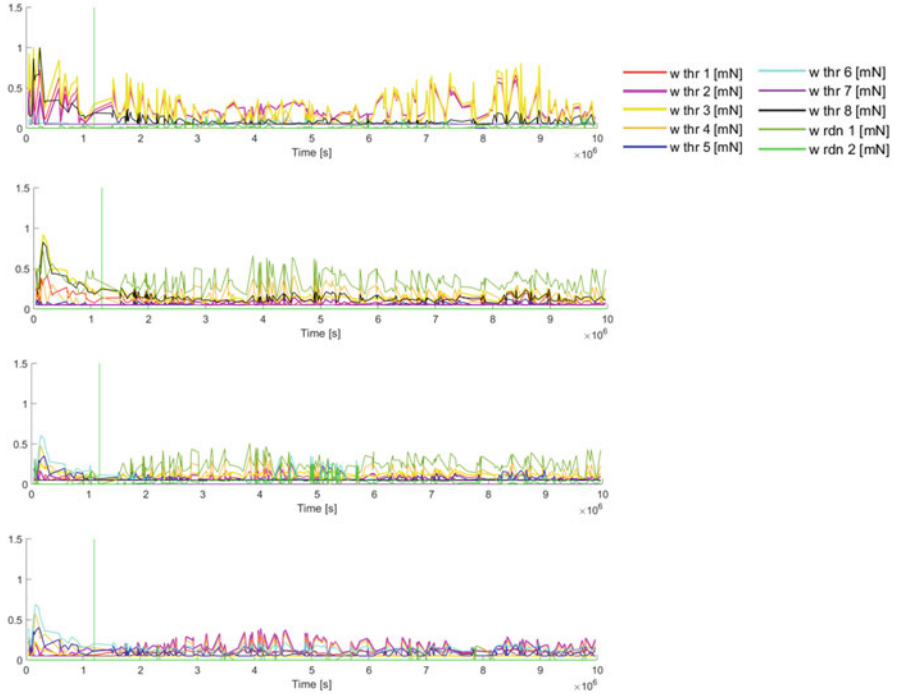


Fig. 10 Forces (mN) over time (s), transient/science phases, mean atmospheric density, failure operational scenarios 5–8 (in order from top to bottom)

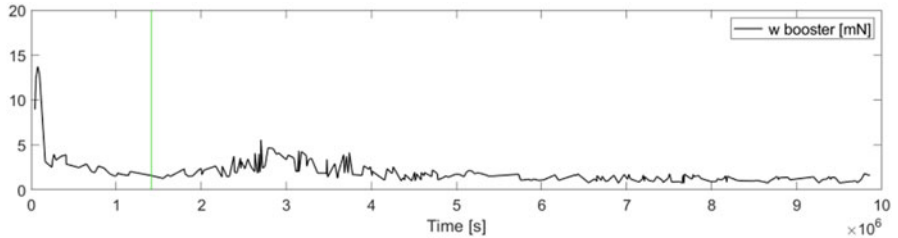


Fig. 11 DCT force (mN) over time (s), transient/science phases, maximum atmospheric density

- In minimum atmospheric density conditions, failure operational scenario 8, some F_y components are above the requested values (5 infeasibilities out of about 1500 representative instants).
- In mean atmospheric density conditions, failure operational scenario 5, one F_y component is below the requested value.
- In maximum atmospheric density conditions, failure operational scenario 2, some F_y components are above the requested values (5 infeasibilities).

Table 1 Number of infeasible instances and error magnitude found in the 8 failure scenarios with the 3 atmosphere conditions – transient phase

	Atmosphere	Component	Number of infeasible instances	Average error magnitude (mN or mNm)
Failure_scen_1			0	
Failure_scen_2			0	
Failure_scen_3	Min	F_y	2	0.00033
Failure_scen_4	Min	$F_y F_z T_x$	1	0.00442
			1	0.00183
			1	0.00005
Failure_scen_5	Max	F_y	2	0.00054
Failure_scen_6	Min	T_x	6	0.00201
Failure_scen_7			0	
Failure_scen_8			0	
TOTAL			13	

Table 2 Number of infeasible instances and error magnitude found in the 8 failure scenarios with the 3 atmosphere conditions – science phase

	Atmosphere	Component	Number of infeasible instances	Average error magnitude (mN or mNm)
Failure_scen_1	Max	F_y	2	0.00021
Failure_scen_2	Max	F_y	5	0.00228
Failure_scen_3			0	
Failure_scen_4	Max	F_y	7	0.00051
Failure_scen_5	Mean	F_y	1	0.00053
Failure_scen_6	Min	F_y	1	0.00002
	Max	F_y	1	0.000005
Failure_scen_7	Min	$F_x F_y$	1	0.00006
			1	0.00037
Failure_scen_8	Min	F_y	5	0.00147
TOTAL			24	

Note that one or more infeasibility only indicates that the problem as a whole admits no solution. The value provided in output does not give any information. The solver arbitrarily decides whether the value provided as output is above or below the request.

Summarizing, case study 1 significantly improved the corresponding solutions obtained in the previous studies involving fewer than two redundant thrusters. Infeasibility errors are few and sparse and their magnitude is very small (order of a few μN or μNm). They almost always occur in the components of the force and torque of the smallest magnitude, F_y and T_x . The global error, as expressed by objective function (12), is also small: its value, resulting from the optimization

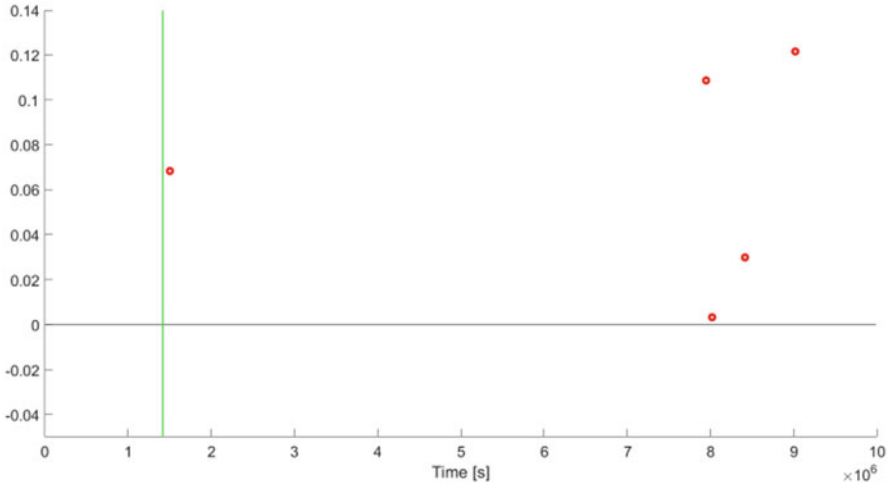


Fig. 12 Minimum atmospheric density case, transient/science phases, failure operational scenario 8 F_y components (mN) above the requested values

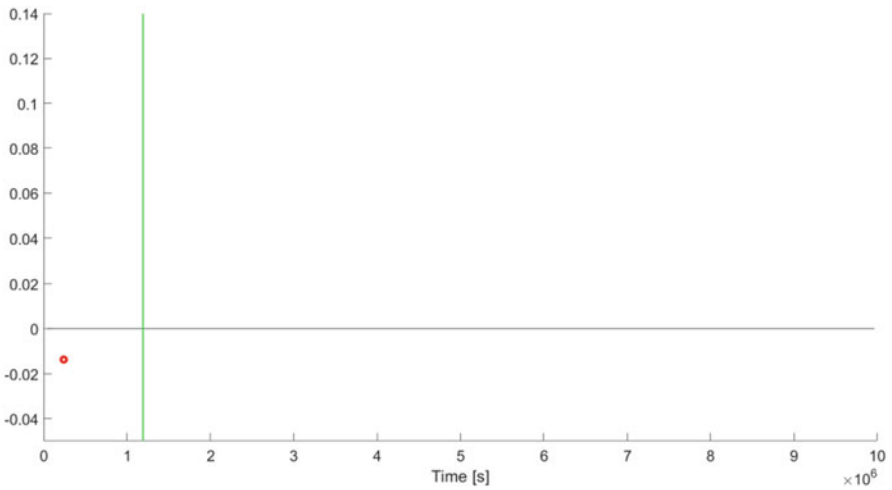


Fig. 13 Mean atmospheric density case, transient/science phases, failure operational scenario 5, F_y component (mN) below the requested value

process, amounts to 2.4 mN (w.r.t. ~ 1500 instants). Potential directions for further improvement were investigated in case study 2.

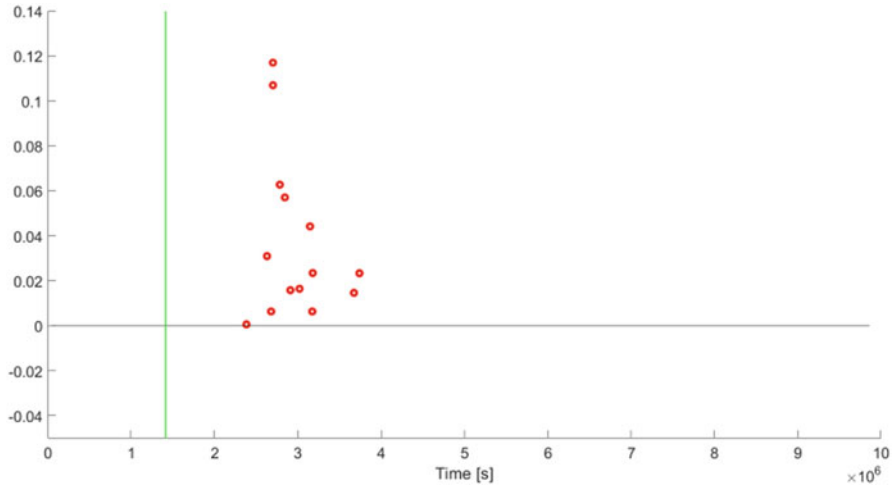


Fig. 14 Maximum atmospheric density case, transient/science phases, failure operational scenario 2, F_y components (mN) above the requested values

3.2.2 Case Study 2

Case study 2 was dedicated to assessing the effect on the solutions of the assumed thrust levels and the error tolerances. In case study 2, a further relaxation relative to the minimum admissible thrust is introduced by assuming that it is 0 mN also for the nominal thrusters. As in the solution discussed above, the leader and follower satellites show only negligible differences in their behaviours. In particular, the thruster utilization is very similar. The same positions utilized in case study 1 have been adopted for case study 2 as well. The obtained orientations result in being essentially unvaried.

The overall error (see objective function (12)) amounts to 0.08 mN (w.r.t. ~1500 instants, neglecting all errors ≤ 0.000009 mN for the forces and ≤ 0.000009 mNm for the torques). In minimum atmospheric density conditions, errors occur exclusively in the transient phase, for the sole failure operational scenarios 3, 4, and 6, where $0 \leq T_x \leq 0.0009$ mNm. No error occurs in mean atmospheric conditions while in maximum atmospheric density conditions, errors appear exclusively in the science phase for the sole failure operational scenarios 1 and 2, where $0 \leq F_y \leq 0.00009$ mN. In this case study, the prevalent errors are also associated with F_y and T_x .

Similar to case study 1, the maximum atmospheric density conditions have no critical impact on the overall feasibility. The results of the feasibility analysis carried out for case study 2 have been extended by a dedicated sensitivity analysis. The relevant outcomes are discussed herein, focusing separately on the following aspects:

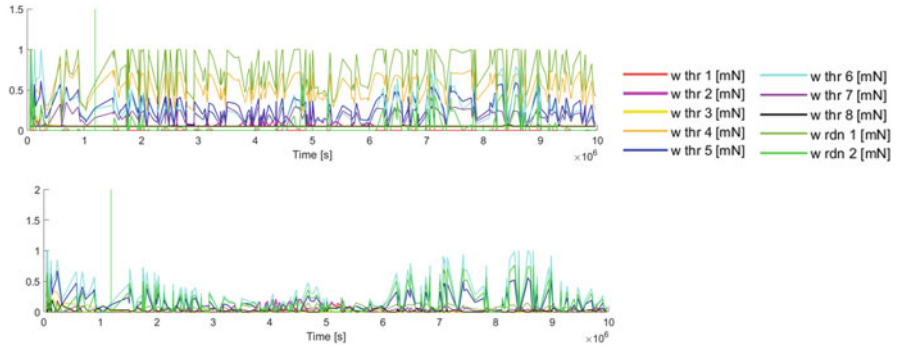


Fig. 15 Overall error relaxation solution (on top) vs that corresponding to case study 1. Forces (mN), minimum atmospheric density, failure operational scenario 1

- Overall error relaxation (w.r.t. the minimum value obtained) and fuel consumption minimization.
- Minimum/maximum thrust limit relaxation.

Recalling that in this case study the minimum overall error obtained is 0.08 mN, the following relaxation is introduced:

$$\varepsilon = \sum_{O_{S,i}} [|\varepsilon_{F_{xi}}| + |\varepsilon_{F_{yi}}| + |\varepsilon_{F_{zi}}| + W_\varepsilon (|\varepsilon_{T_{xi}}| + |\varepsilon_{T_{yi}}| + |\varepsilon_{T_{zi}}|)] \leq 0.09 \text{ mN.}$$

With this additional inequality, the original problem P_R is solved by considering the minimization objective expression (10). While the consequent overall error increment is as a matter of fact irrelevant from a practical point of view, the above relaxation yields a reduction of approximately 5.2% of the total fuel consumption (w.r.t. to the corresponding feasibility problem).

Another improvement obtained by this approach (w.r.t. case study 1 and the original version of case study 2) concerns thrust saturation. Figure 15 compares, for mean atmospheric conditions and for failure operational scenario 1, the solution obtained in case study 2 (considering the overall error relaxation) with that of case study 1. This shows that the thrust saturation problem was an effect of a too tight error tolerance.

As anticipated, the second part of the sensitivity analysis carried out for case study 2 considers the potential advantages deriving from the relaxation of the lower and upper limits on the force associated with the (nominal and redundant) thrusters. The precise purpose is that of identifying the “cost”, in terms of thrust range extension, to attain full feasibility (i.e., solutions with zero total error).

As a first result, no fully feasible solution can be found with a maximum thrust < 1.1 mN (albeit with a minimum thrust of 0 mN for both the nominal and redundant thrusters). Thrust ranges allowing full feasibility are reported in Table 3.

Table 3 Thrust ranges allowing full feasibility

Thrust range	Lower thrust limit (mN)	Upper thrust limit (mN)
(1)	0.014	1.2
(2)	0.026	1.3
(3)	0.036	1.4
(4)	0.05	1.535

The above results suggest that the presence of a thrust minimum limit >0 mN renders the control dispatch problem very demanding. Fully feasible solutions can be obtained by relaxing both limits (0.05 mN, 1 mN), as in ranges (1), (2), and (3), or the upper limit only, as in (4). As can be observed, an extension of the upper limit can compensate for the presence of lower limits (>0 mN). Range (4) clearly shows that the cost (in terms of upper limit extension) to obtain an overall error exactly equal to zero (with the lower limit of 0.05 mN) is very high and therefore not justifiable from a practical and technological point of view.

3.2.3 General Remarks

Some general remarks on the results of study cases 1 and 2 follow. Further insight is provided in Sect. 4 aimed at discussing the analysis based on the dynamic simulation.

- In contrast to the previous studies, here the activation of the DCT thruster, both in minimum and mean atmospheric density conditions, proves to be significantly advantageous. This has been possible because its thrust lower limit in the present analysis has been reduced from 1 to 0.6 mN. This apparently slight modification actually allows reducing the inclination of the rear (nominal and redundant) thrusters with respect to the x axis and, consequently, an increased possibility to exploit their thrust in the y and z axis directions.
- A significant overall error reduction ($\sim 90\%$) with respect to the solutions of the previous studies has been obtained. The thrust lower-limit relaxation (from 0.05 to 0 mN) has proven to be useful in identifying advantageous thruster switch-offs. A dedicated analysis is recommended for future developments.
- A limited relaxation with respect to the overall error (e.g., from 0.08 to 0.09 mN) can provide appreciable fuel consumption reduction.
- A relaxation of the thrust upper limit, for both the nominal and redundant thrusters (e.g., from 1 to 1.4 mN) is recommended.
- The presence of a minimum thrust limit (>0 mN) has a strong impact on the overall fuel consumption.

4 Satellite Control Simulation and Mission Performance

The two layout solutions found and described in Sect. 3.2.1 (Case 1) and Sect. 3.2.2 (Case 2) are reproduced in Fig. 16. It is apparent that the two cases have very similar thruster inclinations. Consequently, both solutions turn out to have similar total impulses and show similar robustness of the control problem.

The two layout solutions were evaluated on the complete 3.5-month time series sampled at a 400 s, from which the 1500 representative instants had been selected. This verification was done considering the following thruster ranges:

- FCT 50–1000 μN
- DCT 0.6–15 mN

and all possible thruster failure scenarios.

Similar behaviour as found in the case studies (1 and 2) was found in the complete simulation. Both solutions only sporadically exceed the tolerable error bounds. In particular, Case 1 is affected by a few errors in F_y (the control force along the y axis), see Fig. 17. Case 2 is affected by a lower total number of errors, but these involve both the control force along the y axis (F_y) and the control torque with respect to the x axis (T_x), see Fig. 18.

The Case 1 layout was subjected to a dedicated verification by the E2E simulator. Figure 19 shows a sample of the results.

The full simulation confirmed that the sporadic “infeasible” instants do not affect the controls, which are robust to such occurrences. Further refinement of the algorithms and procedures will minimize or completely eliminate such defects.

On a functional level, we find that the total impulse per thruster is often a reliable indicator of which thrusters will be active in each case of failure. Actually, in some cases, by switching off one thruster, the propellant usage may be considerably reduced without affecting the overall performance. As an example, Fig. 19 shows the effect of the failure of thruster 8 in minimum atmospheric density conditions. By switching off the front redundant thruster RDN1 and activating the DCT thruster, the

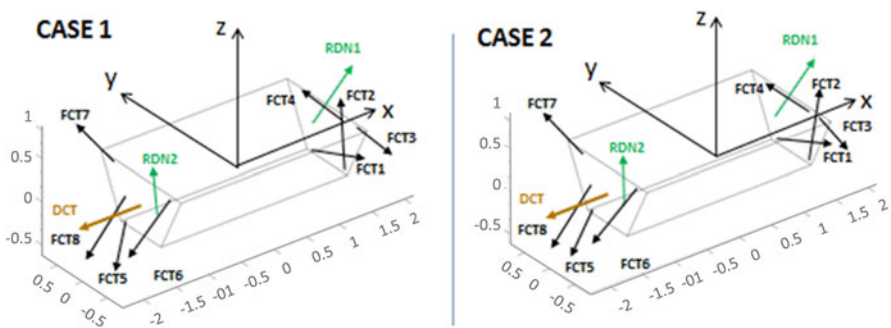


Fig. 16 Case 1 and Case 2 thruster layouts

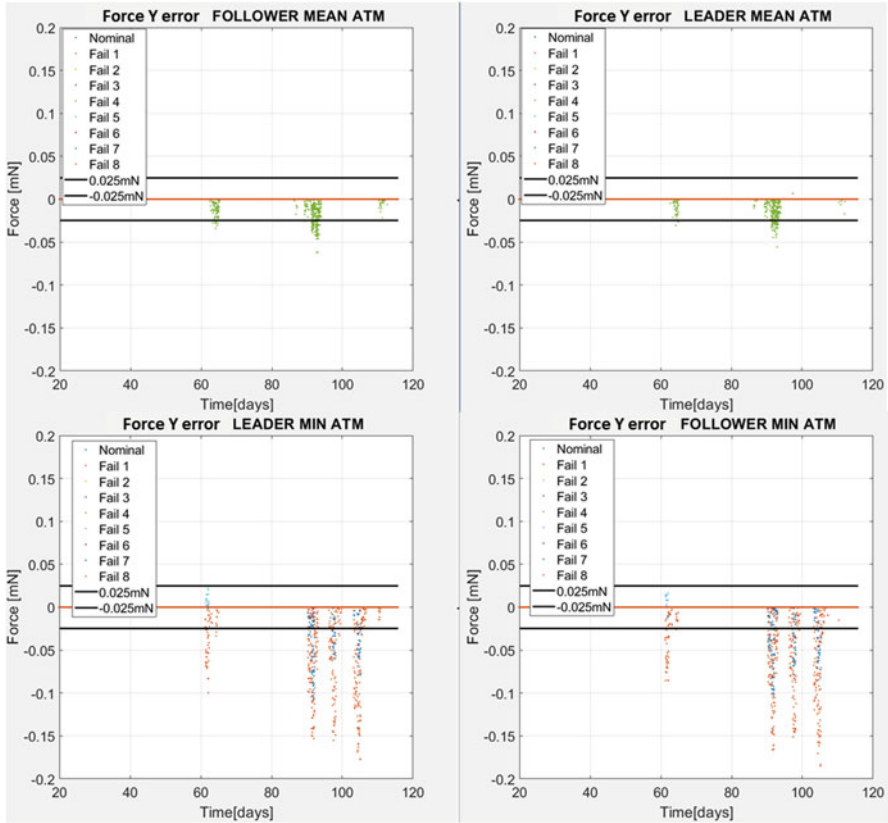


Fig. 17 Case 1 (sporadic) errors w.r.t. F_y

overall thruster usage is kept under the expected limits and the residual errors are completely eliminated. Therefore, this leads to a more robust solution.

Given defined mission parameters, all failure scenarios can be studied in advance, and a dedicated strategy – which nominal thrusters shall be kept on and which redundant thrusters shall be switched on – can be defined for each failure case.

5 Concluding Remarks and Future Developments

The general problem addressed in this paper was to design a thruster system able to control all linear and angular degrees of freedom of an NGGM satellite, affected by air drag, subject to a minimum-propellant criterion and to constraints as to the number, location, orientation, and thrust range of the actuators. In a first phase, documented in [3], the problem was solved under idealized conditions:

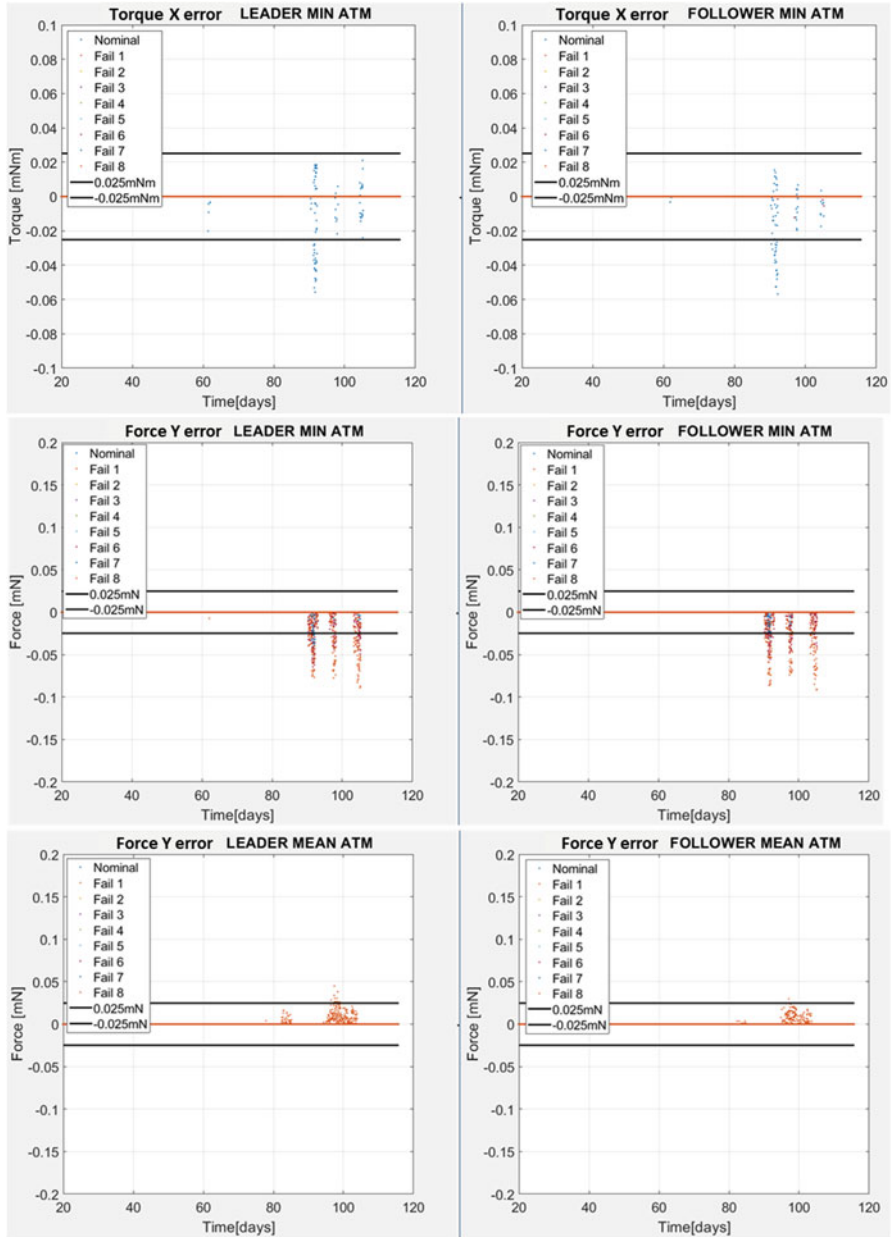


Fig. 18 Case 2 (sporadic) errors w.r.t. T_x and F_y

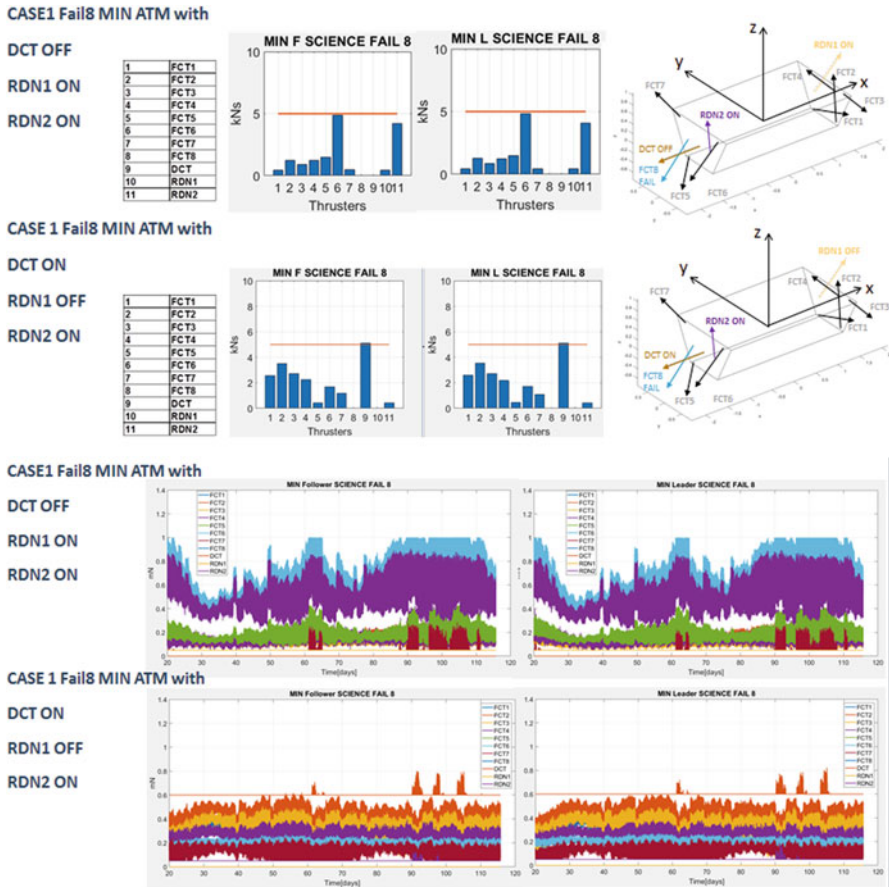


Fig. 19 Example of thruster switch-off: failure scenario in mean atmospheric density

no redundancy and no special limits to the applicable thrust ranges. Under very conservative assumptions as to the air drag environment, it was shown that this “nominal” problem (no redundancy considered) may be solved by a set of 8 mini-thrusters (FCT, 1-mN class), located on the forward and aft sides of the spacecraft, plus 1 larger thruster (DCT, 10-mN class) on the aft side.

In a second phase, illustrated here, the redundancy problem was addressed. On board resource constraints forbid simple duplication of the complete electric thruster plant as is implemented in conventional thruster systems; therefore, functional redundancy was sought, i.e., the minimum number of extra thrusters able to replace any one of the nominal sets. Moreover, thrust range constraints were introduced including a minimum thrust level of $50\mu\text{N}$ and a ratio of maximum-to-minimum thrust level not greater than about 20. Under the same drag environment assumptions, a fully single-failure-tolerant solution was found using two extra FCT

thrusters, one on the forward and one on the aft side (the DCT was assumed to be simply duplicated, as in the GOCE design).

The problem is formulated as an optimization problem with constraints and solved by a dedicated algorithm [6, 12]. Occasionally and rarely, one of the equations may not have a solution. This was shown to occur for very small values of the commanded thrust and the addition of a tolerance variable solves the problem. The overall control design was shown to be robust to such occurrences. The solutions found are very sensitive to the allowable thrust range assumed for the thrusters. Both the lower limit and the upper limit can significantly affect the solutions.

Two thruster types, DCT and FCT, were assumed, reflecting the non-symmetry of the drag environment (the force in the direction of motion being generally at least one order of magnitude larger than the side forces) leading to two different implementations. However, DCT and FCT may blend into one if the environment is very mild (high altitude and/or very low solar activity). In [3], the lower limit of the DCT thrust was assumed to be 1 mN and the DCT was turned off in low and moderate atmosphere conditions (when 1 mN is too large w.r.t. the ambient forces). In this new study, the lower limit was reduced to 0.6 mN and this was enough to make the use of DCT profitable even with low ambient forces, for the specific worst-case altitude at the lower bound of the admissible orbit range.

A sensitivity analysis showed that a lower limit of the FCT thrust $\neq 0$ has a large impact on the propellant consumption, and that increasing the upper limit above 1 mN reduces the errors considerably. These results give important inputs to the technological developments that will determine which thrust limits and range may be efficiently implemented in a given thruster type.

Many avenues remain open for further research into the electric thruster layout optimization problem, including:

- Introducing constraints on the instantaneous electric power consumed by the thruster plant;
- Introducing an upper limit to the total impulse available to each thruster;
- Assessing “hot” vs “cold” redundancy (e.g., 10 FCT thrusters active from the start, with tolerance of 1 or 2 failures, instead of 8 active plus 2 extra thrusters activated when a failure occurs).

References

1. Haagmans R., Siemes C., Massotti L., Carraz O., Silvestrin P. ESA's Next-Generation Gravity Mission Concepts. *Rendiconti Accademia Nazionale dei Lincei, January 2020*, Springer, DOI: <https://doi.org/10.1007/s12210-020-00875-0> (2020)
2. Massotti L., Siemes C., March G., Haagmans R., Silvestrin P. Next Generation Gravity Mission Elements of the Mass Change and Geoscience International Constellation: From Orbit Selection to Instrument and Mission Design. *Remote Sens.* **2021**, *13*, 3935. <https://doi.org/10.3390/rs13193935> (2021)

3. Anselmi, A., Cesare, S., Dionisio, S., Fasano, G., Massotti, L. Control propellant minimization for the Next Generation Gravity Mission. In: Fasano, G., Pintér, J.D., Eds., *Modeling and Optimization in Space Engineering – State of the Art and New Challenges*. Springer (2019)
4. Nicklaus, K., Cesare, S., Dahl, C., Massotti, L., Bonino, L., Mottini, S., Pisani, M., Silvestrin, P. Laser metrology concept consolidation for NGGM. *CEAS Space J.* 2020, 12, 313–330, doi:<https://doi.org/10.1007/s12567-020-00324-6> (2020)
5. Dionisio, S., Anselmi, A., Bonino, L., Cesare, S., Massotti, L., Silvestrin, P. The Next Generation Gravity Mission challenges, consolidation of the system concepts and technological innovations, Space Ops Conference, Marseille, France 28 May – 1 June (2018)
6. Fasano, G. Dynamic System Control Dispatch: A Global Optimization Approach. In: Fasano, G., Pintér, J.D., Eds., *Modeling and Optimization in Space Engineering – State of the Art and New Challenges*. Springer (2019)
7. Durand, C., Fasano, G., Forestieri, A. Data Reduction for Optimizing the Attitude Control Dispatch in a Spacecraft. In: Fasano, G., J.D. Pintér, Eds, *Modeling and Optimization in Space Engineering – New Concepts and Approaches*. Springer (2022)
8. Horst, R., Pardalos, P.M., Thoai, N.V. *Introduction to Global Optimization*, Second Edition. Kluwer Academic Publishers (2000)
9. Pintér, J.D. *Global Optimization in Action – Continuous and Lipschitz Optimization: Algorithms, Implementations and Applications*. Springer (1996)
10. Sahinidis, N.V. *Mixed-integer nonlinear programming 2018*. *Optimization and Engineering*, volume 20, pages 301–306 (2019)
11. Fasano, G., Pintér, J.D. Efficient Piecewise Linearization for a Class of Non-convex Optimization Problems: Comparative Results and Extensions. In: Pintér, J.D., Terlaky, T., Eds, *Modeling and Optimization: Theory and Applications*. MOPTA 2017. Springer Proceedings in Mathematics & Statistics, vol 279. Springer, Cham. https://doi.org/10.1007/978-3-030-12119-8_3 (2019)
12. Fasano, G. NGGM Thruster Redundancy Management TN22, Thales Alenia Space April (2021)

Transition of Two-Dimensional Quasi-periodic Invariant Tori in the Real-Ephemeris Model of the Earth–Moon System



Nicola Baresi

1 Introduction

Since the ground-breaking discovery that water ice may be found near permanently shadowed regions at the lunar poles [1–3], private companies and governmental entities have turned their attention toward our natural companion. Nowadays, the Moon is no longer considered as political “high-ground,” but rather as a scientifically exciting, elusive, and potentially profitable neighbor that will soon be visited by an increasing number of satellite missions [4].

One of the most ambitious prospects is the Lunar Orbital Platform Gateway (LOPG), a cislunar outpost that will contribute to land the first female astronaut on the surface of the Moon by the end of this decade [5]. The LOPG would provide scientists and engineers with crucial information on how to sustain the human presence beyond low-Earth orbit regardless of reduced gravity, space radiation, and scarce resources.

The candidate orbits of the gateway have been down-selected after extensive trade-off analyses that considered key mission design components such as direct access to the lunar surface, good coverage, communication budgets, “cheap” transfer opportunities, and solar eclipses [6]. It was found that the (2:9) and (1:4) synodic resonant southern Near Rectilinear Halo Orbits (NRHO)s offer the best trade-off performance against the different mission design requirements derived for a safe return to the lunar surface. These candidate trajectories belong to the L_1 and L_2 halo families of the Circular Restricted Three-Body Problem (CRTBP) [7]. However—differently from the majority of halo orbits—NRHOs are found to be

N. Baresi (✉)
Surrey Space Centre, Guildford, UK
e-mail: n.baresi@surrey.ac.uk

nearly unstable and relatively close to the lunar surface (periapsis altitude below 5000 km).

Of particular interest to the astrodynamics community are NRHO trajectories whose period is a rational fraction of the Sun–Earth–Moon synodic month (i.e., the time required by the Moon to return to its original angular separation with respect to the Earth–Sun direction). By choosing appropriate initial conditions, it can be demonstrated that solar eclipses due to the Moon and Earth can be either minimized or totally avoided [8, 9]. It follows that a spacecraft mission, launched in a proper synodic resonant NRHO and at the appropriate timing, can be operated for its entire life cycle without fear for solar power shortages. This feature has been observed even when the synodic resonant orbit is continued in the real-ephemeris model of the Earth–Moon system [9, 10]. However, it remains uncertain whether this is applicable to all of the synodic resonant orbits within the NRHO subfamily, as well as if transitioning to the full-ephemeris model of the Earth–Moon system would not reduce the perilune altitude of the candidate orbit to crash-threatening values. Finding answers to these questions requires astrodynamics researchers to delve into higher fidelity models of the Earth–Moon system, thereby replacing the continuum of periodic orbits with a Cantor set of two- or higher-dimensional Quasi-Periodic invariant Tori (QPT) [11].

Research on QPT has gained momentum over the past few years. Since the pioneering work by Castellá and Jorba [12], astrodynamics practitioners have consolidated numerical procedures that enable fast and robust computation of entire families of two-dimensional QPT [13]. Gómez and Mondelo have first calculated the Fourier coefficients of quasi-periodic Lissajous and halo orbits in the CRTBP based on the invariant curves of stroboscopic mappings [14]. Olikara and Scheeres modified this approach to operate directly on phase space coordinates and generalize the algorithm to other systems and orbit families [15]. The resulting procedure, hereby referred to as GMOS, calculates families of quasi-periodic invariant tori by solving a two-point boundary value problem (TPBVP) for the invariant curves of a stroboscopic map [13]. This technique represents an accurate and self-contained alternative with respect to the methodologies of Schilder et al. and Kolemen et al., which calculate either invariant tori of flows (via finite differences) or invariant curves of Poincaré mappings [16, 17]. More recently, McCarthy, Rosales, Henry, and Villegas-Pinto have applied the GMOS algorithm to calculate quasi-periodic invariant tori and their whiskers either in the Sun–Earth–Moon bicircular model or in the circular-elliptic version of it [18–21]. This was done in parallel to the work of Haro and De la Llave and Kumar and Anderson, who have recently proposed and advanced an interesting alternative based on the parametrization method [22, 23].

Regardless of the numerical procedures adopted in the researches above, access to quasi-periodic solutions of non-integrable problems enables a better understanding of key astrodynamics models such as the Earth–Moon CRTBP and Elliptic Restricted Three-Body Problem (ERTBP) [24, 25]. Both of these systems are crucial in planning and designing spacecraft missions to the Moon, as seen in the mission analyses and design of the LOPG and upcoming lunar CubeSats [26–29].

This chapter overviews modern astrodynamics techniques for the numerical calculation and continuation of two-dimensional invariant tori. Furthermore, it expands on two-dimensional torus maps that can be used to visualize key orbital parameters and dynamical quantities aiding with the trajectory design process. A systematic procedure to transition of quasi-periodic trajectories in the real-ephemeris model of the Earth–Moon system is finally proposed building on zero-radial-velocity curves that can be extracted from the aforementioned torus maps.

The applications of this approach are twofold: one can either generate real-ephemeris orbits from CRTBP resident objects (e.g., large two-dimensional invariant tori that can be found in the center manifolds of periodic orbits) or provide higher quality initial guesses for trajectory optimization algorithms aimed at researching real-ephemeris substitutes of CRTBP orbits. This chapter prioritizes the second application by first calculating dynamical substitutes of LOPG in the Earth–Moon ERTBP model and later transitioning these candidate quasi-periodic trajectories in the real-ephemeris model of the Earth–Moon system. More details on these dynamical models and numerical techniques can be found in the following sections.

2 Dynamical Models

This section introduces the dynamical models used for this chapter’s analyses. First, the equations of the ERTBP are derived and analyzed in terms of pulsating normalized coordinates. Second, the general N-body problem of the Sun–Earth–Moon spacecraft system is described and considered for the real-ephemeris model adopted in this research.

2.1 ERTBP

Consider the motion of a spacecraft subject to the gravitational attraction of the Earth and the Moon. It is assumed that the mass of the spacecraft does not perturb the motion of the two primaries, as well as that the Moon orbits the Earth in an eccentric orbit with semi-major axis $a = 384,400$ km and eccentricity $e = 0.054$.

The equations of motion of the satellite can be derived with respect to a rotating coordinate frame centered on the Moon and such that the \hat{x} -axis is constantly aligned with the Earth–Moon direction, \hat{z} is parallel to the orbital angular momentum of the Moon, and $\hat{y} = \hat{z} \times \hat{x}$ completes the right-handed triad. Such a rotating reference frame \mathcal{S} is hereby referred to as “synodic” and an illustration of it is provided in Fig. 1.

Next, pulsating coordinates and a change of independent variable are introduced so as to further simplify the expressions of the spacecraft dynamics. Let \mathbf{r} and \mathbf{v} be the position and synodic velocity vectors of the spacecraft as seen with respect to the Moon such that

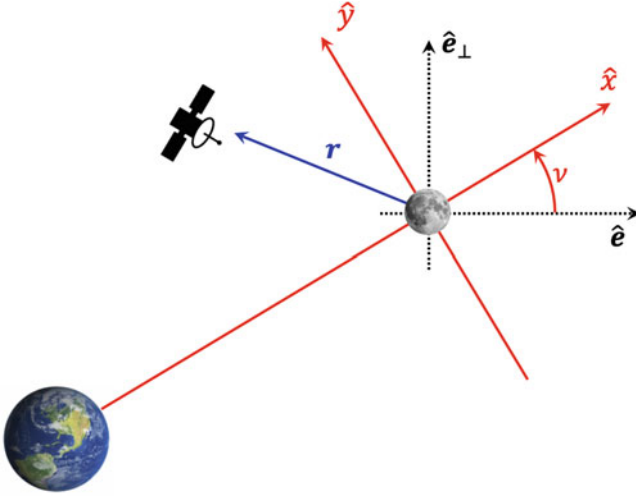


Fig. 1 Earth–Moon synodic frame as seen from the perifocal frame of the Earth–Moon system

$$\tilde{\mathbf{r}} = \gamma \mathbf{r}/p, \quad \tilde{\mathbf{v}} = \gamma' \mathbf{r}/p + \gamma \mathbf{v}/(p\omega) \quad (1)$$

may be defined as the pulsating position and velocity vectors of the satellite, respectively. A convenient and invertible linear transformation can be defined between the two coordinate sets via

$$\tilde{\mathbf{X}} = \begin{bmatrix} \frac{\gamma}{p} I_3 & 0_3 \\ \frac{\gamma'}{p} I_3 & \frac{\gamma}{p\omega} I_3 \end{bmatrix} \mathbf{X}, \quad \mathbf{X} = \begin{bmatrix} \frac{p}{\omega} I_3 & 0_3 \\ -\frac{\omega p \gamma'}{\gamma^2} I_3 & \frac{p\omega}{\gamma} I_3 \end{bmatrix} \tilde{\mathbf{X}}, \quad (2)$$

where $\mathbf{X} = [\mathbf{r}^T, \mathbf{v}^T]^T$, $\tilde{\mathbf{X}} = [\tilde{\mathbf{r}}^T, \tilde{\mathbf{v}}^T]^T$, $\gamma = 1 + e \cos \nu$, $\gamma' = d\gamma/d\nu = -e \sin \nu$, I_3 is the three-by-three identity matrix, 0_3 is the zero three-by-three matrix, and ν is the true anomaly of the Moon. The time rate of change of ν is defined as

$$\omega = \frac{d\nu}{dt} = n \frac{\gamma^2}{(1 - e^2)^{3/2}}, \quad (3a)$$

whereas

$$n = \sqrt{(\mu_m + \mu_\oplus)/a^3}, \quad (3b)$$

$$p = a(1 - e^2) \quad (3c)$$

stand for the Moon's mean motion and semi-parameter, respectively. It is highlighted that $\tilde{\mathbf{v}}$ describes the true anomaly rate of change of $\tilde{\mathbf{r}}$ as seen with respect to the Moon-centered synodic frame, i.e., $\tilde{\mathbf{v}} = \tilde{\mathbf{r}}' = d\tilde{\mathbf{r}}/d\nu$, with $\mu_{\oplus} = 398600.4354 \text{ km}^3/\text{s}^2$ and $\mu_m = 4902.8001 \text{ km}^3/\text{s}^2$ as the Earth's and Moon's gravitational parameters, respectively.

Using pulsating coordinates, the true anomaly rate of change of $\tilde{\mathbf{r}}$ and $\tilde{\mathbf{v}}$ may be recast as the system of first-order ordinary differential equations given by

$$\tilde{\mathbf{X}}' = \mathbf{f}(\nu, \tilde{\mathbf{X}}, \mathbf{p}) := \begin{cases} \tilde{\mathbf{v}}, \\ \frac{\mathbf{g}(\tilde{\mathbf{r}})}{\gamma} - \left([Z][Z] + e \frac{\cos \nu}{\gamma} [I_3] \right) \tilde{\mathbf{r}} - 2 [Z] \tilde{\mathbf{v}}, \end{cases} \quad (4)$$

where $(-)'$ denotes differentiation with respect to the Moon's true anomaly in the synodic frame and

$$[Z] = \begin{bmatrix} 0 & -1 & 0 \\ 1 & 0 & 0 \\ 0 & 0 & 0 \end{bmatrix}. \quad (5a)$$

Furthermore,

$$\mathbf{g}(\tilde{\mathbf{r}}) = -\frac{\mu}{\tilde{r}^3} \tilde{\mathbf{r}} - \frac{(1-\mu)}{\tilde{r}_{\oplus}^3} \tilde{\mathbf{r}}_{\oplus} + \frac{(1-\mu)}{\tilde{r}_{m\oplus}^3} \tilde{\mathbf{r}}_{m\oplus}, \quad (5b)$$

where $\mu = \mu_m/(\mu_m + \mu_{\oplus}) = 0.012$ is the mass ratio parameter of the Earth–Moon system, and $\tilde{\mathbf{r}}_{\oplus}$ and $\tilde{\mathbf{r}}_{m\oplus}$ are the position vectors of the spacecraft and the Moon as seen from the Earth.

In what follows, the vectorial quantities $\tilde{\mathbf{X}}$ and \mathbf{p} are used to denote the state and parameter vectors of the system (4), whereas $\tilde{r}_{\oplus} = \|\tilde{\mathbf{r}}_{\oplus}\|$ and $\tilde{r}_{m\oplus} = \|\tilde{\mathbf{r}}_{m\oplus}\|$ stand for the norm of the $\tilde{\mathbf{r}}_{\oplus}$ and $\tilde{\mathbf{r}}_{m\oplus}$, respectively. Introducing $\tilde{\mathbf{r}} = [\tilde{x}, \tilde{y}, \tilde{z}]^T$ and $\tilde{\mathbf{v}} = [\tilde{u}, \tilde{v}, \tilde{w}]^T$ as the components of the position and velocity vectors of the spacecraft as seen from the Moon in the synodic pulsating reference frame, one finds that the components of $\tilde{\mathbf{r}}_{\oplus}$ and $\tilde{\mathbf{r}}_{m\oplus}$ in the same coordinate system are given by

$$\tilde{\mathbf{r}}_{\oplus} = \begin{bmatrix} \tilde{x} + 1 \\ \tilde{y} \\ \tilde{z} \end{bmatrix}, \quad \tilde{\mathbf{r}}_{m\oplus} = \begin{bmatrix} 1 \\ 0 \\ 0 \end{bmatrix}. \quad (6)$$

It is worth noting that the equations of motion (4) reduce to the equations of the CRTBP as soon as e is set to zero and length and time units are chosen such that $a = n = 1$. This property is hereby exploited to generate periodic orbits in the circular restricted three-body problem of the Earth–Moon system and implement homotopy continuation procedures aimed at calculating quasi-periodic dynamical

substitutes in the ERTBP problem. These ERTBP trajectories are later utilized to produce full-ephemeris orbits in the high-fidelity dynamics of Sect. 2.2.

2.2 Full Ephemeris

While the gravitational attraction of the Earth and the Moon is the dominating forces acting on a spacecraft in the cislunar and circumlunar environment, other forces and dynamical perturbations do have a non-negligible impact on its orbital propagation. In particular, both the Sun and the non-spherical shape of the Moon should be taken into account while trying to capture the dynamical evolution of satellites in libration point orbits. Additionally, the motion of the Moon about the Earth is far from being Keplerian as demonstrated by the plots of Fig. 2, in which the time histories of the Moon's orbit elements as seen from the Earth are shown.

For all these reasons, the real dynamics of a spacecraft can be best approximated with a *full-ephemeris* model in which the location of the Sun, the Earth, and the Moon is given by precomputed orbit files obtained from high-fidelity propagations [30]. These orbit files can be downloaded from NASA's NAIF webpage and imported into software development platforms such as MATLAB using ad hoc libraries and code packages [31, 32].

Given the locations of the three celestial objects, the equations of motion of the satellite can be rewritten in a Moon-centered inertial frame \mathcal{I} such as ECLIPJ2000 and propagated according to the dynamics

$$\dot{\mathbf{Y}} = \mathbf{f}(\mathbf{Y}) = \begin{cases} \mathbf{V}, \\ \nabla\mathcal{U} - \mu_{\oplus} \left(\frac{\mathbf{r}_{\oplus}}{r_{\oplus}^3} - \frac{\mathbf{r}_{m\oplus}}{r_{m\oplus}^3} \right) - \mu_{\odot} \left(\frac{\mathbf{r}_{\odot}}{r_{\odot}^3} - \frac{\mathbf{r}_{m\odot}}{r_{m\odot}^3} \right), \end{cases} \quad (7)$$

where $(\dot{})$ denotes differentiation with respect to time in the inertial frame, $\mathbf{Y} = [\mathbf{r}^T, \mathbf{V}^T]^T$, \mathbf{V} is the inertial velocity of the spacecraft, μ_{\odot} is the gravitational parameter of the Sun, and \mathbf{r}_{\odot} and $\mathbf{r}_{m\odot}$ are the relative position vector of the spacecraft and the Moon as seen from the Sun, respectively. The symbol $\nabla\mathcal{U}$ denotes the gradient of the Moon's gravitational potential, namely [33]

$$\mathcal{U} = \frac{\mu_m}{r_m} \sum_{l=0}^2 \sum_{m=0}^l \left(\frac{R_m}{r_m} \right)^l \mathcal{P}_m^l(\sin\theta) [C_{l,m} \cos(m\lambda) + S_{l,m} \sin(m\lambda)], \quad (8)$$

where $R_m = 1737.1$ km is the equatorial radius of the Moon, \mathcal{P}_m^l are the associated Legendre polynomials of order l and degree m , θ is the spacecraft's latitude, and λ is its longitude. $C_{l,m}$ and $S_{l,m}$ are the Moon's Stokes' coefficients, and their values can be found online as estimated by the NASA's GRAIL mission [34]. In what follows, the gravitational potential of the Moon is truncated after the eighth

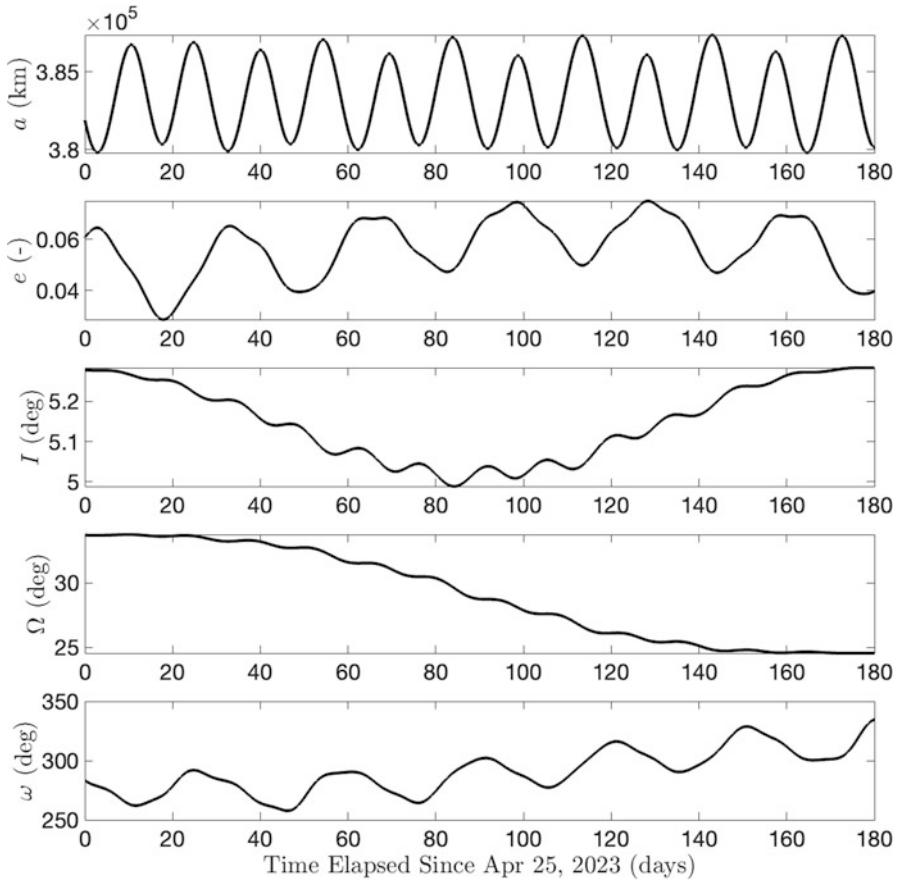


Fig. 2 Time history of the Moon's orbit elements from Apr 25, 2023 00:00:00 (UTC)

order and degree due to a necessary compromise between computational runtime and numerical accuracy. Additional orders and degrees can be included if needed without affecting the proposed methodologies and continuation strategies.

Finally, it is worth noting that a mapping between inertial and synodic coordinates can be established once the position and velocity vectors of the Moon are known:

$$\mathbf{Y} = \begin{bmatrix} [\mathcal{I}\mathcal{S}] & 0_3 \\ [\mathcal{I}\mathcal{S}][\tilde{\boldsymbol{\omega}}] & [\mathcal{I}\mathcal{S}] \end{bmatrix} \mathbf{X}, \quad (9)$$

where $\boldsymbol{\omega} = [\omega_x \ \omega_y \ \omega_z]^T$ is the angular velocity vector of the synodic frame, \mathcal{S} , as seen from the ECLIPJ2000 frame, \mathcal{I} , and

$$[\tilde{\omega}] = \begin{bmatrix} 0 & -\omega_z & \omega_y \\ \omega_z & 0 & -\omega_x \\ -\omega_y & \omega_x & 0 \end{bmatrix}, \quad [TS] = \begin{bmatrix} \mathbf{r}_{m\oplus} & \frac{\mathbf{h}_{m\oplus} \times \mathbf{r}_{m\oplus}}{\|\mathbf{h}_{m\oplus} \times \mathbf{r}_{m\oplus}\|} & \frac{\mathbf{h}_{m\oplus}}{h_{m\oplus}} \\ r_{m\oplus} & & h_{m\oplus} \end{bmatrix}. \quad (10)$$

In Eq. (10), $\mathbf{h}_{m\oplus} = \mathbf{r}_{m\oplus} \times \mathbf{V}_{m\oplus}$ is the specific angular momentum vector of the Moon as seen from the Earth, whereas ω_x , ω_y , and ω_z are the components of the angular velocity vector obtained via SPICE and its dynamic frame definitions. Given ω , Eq. (9) can also be combined with Eq. (2) in order to yield a bijective transformation between pulsating and inertial coordinates. Such a transformation will be proven useful when converting ERTBP states on the surface of two-dimensional invariant tori to inertial Cartesian coordinates for full-ephemeris optimization.

3 Quasi-periodic Orbits in ERTBP

Computing a quasi-periodic invariant torus requires finding a diffeomorphism $\mathbf{u}(\theta) : \mathbb{T}^d \rightarrow \mathcal{T} \in \mathbb{R}^n$ such that motion on the surface of \mathcal{T} can be characterized by d incommensurate frequencies $\omega = \dot{\theta} \in \mathbb{R}^d$ [35]. Indeed, T -periodic orbits can be considered as one-dimensional invariant tori ($d = 1$), whereby $\theta = \theta_0$ represents the phase angle and $\omega_0 = 2\pi/T$ is the orbital frequency. Adding an extra angular coordinate leads to a two-dimensional invariant torus such as the one portrayed in Fig. 3 and so forth.

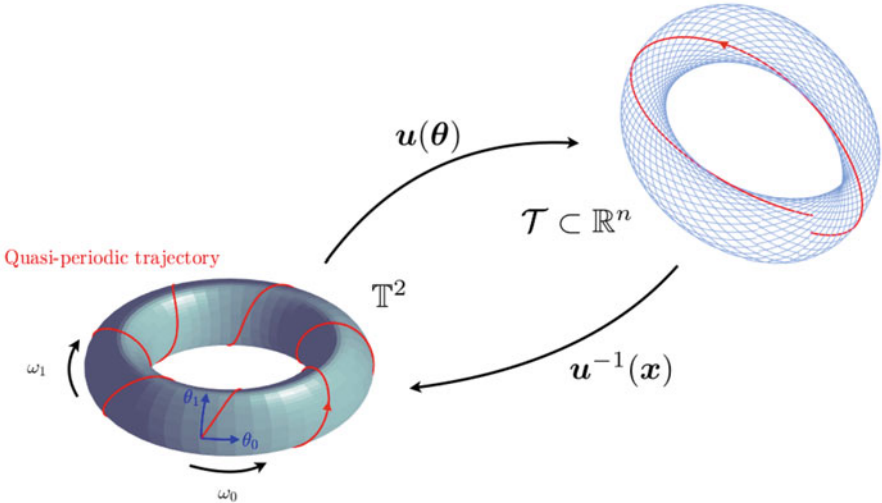


Fig. 3 Two-dimensional invariant torus in both torus and phase spaces

Since the frequencies of a torus are incommensurate by definition, quasi-periodic trajectories on its surface will densely cover the manifold as time grows to infinity. Furthermore, after a full revolution in the “toroidal” direction θ_0 , it is expected that the remaining $d - 1$ angular quantities would rotate by $\boldsymbol{\rho} = 2\pi [\omega_1/\omega_0, \dots, \omega_{d-1}/\omega_0]^T$ in their corresponding angular domains. The quantity $\boldsymbol{\rho}$ is known in the literature as the rotation number or vector of the torus depending on whether d is equal to or greater than 2. Given $\mathbf{u}(\cdot)$, T , and $\boldsymbol{\rho}$, motion on the surface of the manifold can be fully determined.

For the purposes of this chapter, two-dimensional invariant tori that substitute one-dimensional CRTBP periodic orbits in the higher fidelity model of the Earth–Moon ERTBP are considered. These manifolds are computed by means of a numerical continuation procedure that calculates invariant curves of stroboscopic mappings as illustrated in Ref. [11, 13, 36]. A summary of the key passages required for its implementation is offered in the following subsection.

3.1 The GMOS Algorithm

The GMOS algorithm enables fast and robust calculation of two-dimensional invariant tori by integrating groups of candidate quasi-periodic trajectories over one full toroidal period. The images of this stroboscopic mapping are later rotated to undo the effects of the “poloidal” rotation in θ_1 and to construct a system of nonlinear equations that can be solved via Newton’s method.

To illustrate the GMOS approach, let $\varphi_T(\cdot) : \mathbb{R}^n \rightarrow \mathbb{R}^n$ be the solution flow of Eq. (4) integrated over some time T . Such a mapping is usually referred to as the stroboscopic mapping, and it comes with interesting dynamical properties when applied to quasi-periodic trajectories on the surface of a two-dimensional invariant torus. Indeed, given any arbitrary initial condition $\tilde{\mathbf{X}}_0 = \mathbf{u}(\theta_0, \theta_1) \in \mathcal{T}$, it is expected that, after some time $T = 2\pi/\omega_0$,

$$\varphi_T(\mathbf{u}(\theta_0, \theta_1)) = \mathbf{u}(\theta_0, \theta_1 + \boldsymbol{\rho}), \quad (11)$$

as it follows from the boundary conditions $\mathbf{u}(\theta_i + 2\pi, \cdot) = \mathbf{u}(\theta_i, \cdot)$. This implies that the one-dimensional curve $\mathcal{C}(\cdot) := \mathbf{u}(\theta_0, \cdot)$ would be invariant for the stroboscopic mapping φ_T .

Additionally, starting from Eq. (11) and regardless of the initial values of θ_0 and θ_1 , it is possible to introduce a rotation operator $R_{-\boldsymbol{\rho}}$ such that

$$R_{-\boldsymbol{\rho}}[\varphi_T(\mathbf{u}(\theta_0, \theta_1))] - \mathbf{u}(\theta_0, \theta_1) = \mathbf{0}, \quad \forall \theta_0, \theta_1. \quad (12)$$

To import Eq. (12) into a computer environment, consider N equally distributed points along the θ_1 direction in torus coordinates, such that

$$\mathbf{Z}_0 = \left[\mathbf{u}(\theta_0, 0)^T, \mathbf{u}\left(\theta_0, \frac{2\pi}{N}\right)^T, \dots, \mathbf{u}\left(\theta_0, \frac{2\pi(N-1)}{N}\right)^T \right]^T \quad (13)$$

would denote the collection of N candidate quasi-periodic trajectories' initial conditions in phase space coordinates. After time $T = 2\pi/\omega_0$, the images of the stroboscopic mapping $\varphi_T(\mathbf{u}(\theta_0, \cdot))$ may be combined to form

$$\mathbf{Z}_T = \left[\mathbf{u}(\theta_0, \rho)^T, \mathbf{u}\left(\theta_0, \frac{2\pi}{N} + \rho\right)^T, \dots, \mathbf{u}\left(\theta_0, \frac{2\pi(N-1)}{N} + \rho\right)^T \right]^T, \quad (14)$$

a new collection of states that can be used to approximate the one-dimensional curve $\mathcal{C} \in \mathbb{R}^n$. Starting from \mathbf{Z}_T , the Fourier coefficients of \mathcal{C} can be retrieved via the Discrete Fourier Transform (DFT) [37]:

$$\hat{\mathbf{u}}_T[k] = \sum_{n=0}^{N-1} \mathbf{u}\left(\theta_0, \frac{2\pi n}{N} + \rho\right) e^{-2\pi j(nk/N)}. \quad (15)$$

Similarly, any point on \mathcal{C} can be approximated using the inverse operation

$$\mathbf{u}(\theta_0, \theta_1) = \frac{1}{N} \sum_{k=0}^{N-1} \hat{\mathbf{u}}_T[k] e^{jk\theta_1}, \quad (16)$$

including

$$\begin{aligned} R_{-\rho}[\mathbf{u}(\theta_0, \theta_1)] &= \mathbf{u}(\theta_0, \theta_1 - \rho), \\ &= \frac{1}{N} \sum_{k=0}^{N-1} \hat{\mathbf{u}}_T[k] e^{jk(\theta_1 - \rho)}, \\ &= \frac{1}{N} \sum_{k=0}^{N-1} \hat{\mathbf{u}}'_T[k] e^{jk\theta_1}. \end{aligned} \quad (17)$$

Equation (17) demonstrates the effects of the rotation operator $R_{-\rho}$, which acts on the Fourier coefficients of \mathcal{C} in order to rotate the ensemble of the N equally spaced points \mathbf{Z}_T by an angular quantity $-\rho$.

Perhaps, Eq. (17) is better understood in matrix form via

$$[R_{-\rho}] = [D^{-1}][Q_{-\rho}][D], \quad (18)$$

where $[D]$ and $[D^{-1}]$ are the Discrete and Inverse Discrete Fourier transform, rewritten in matrix form, and $[Q_{-\rho}]$ is a diagonal matrix that rotates the Fourier coefficients $\hat{\mathbf{u}}_T[k]$ by $e^{-jk\rho}$ [13]. Combined with Eqs. (13) and (14), Eq. (18) yields

a set of $n \times N$ constraints that must be satisfied by any collection of N equally spaced points \mathbf{Z}_0 on any arbitrary invariant curve \mathcal{C} of φ_T :

$$\mathbf{G}(\boldsymbol{\zeta}) := [R_{-\rho}] \mathbf{Z}_T - \mathbf{Z}_0 = \mathbf{0}. \quad (19)$$

To solve for the unknown variables $\boldsymbol{\zeta} = [\mathbf{Z}_0^T, T, \rho]^T$, Eq. (19) is usually augmented with phase conditions, $p(\boldsymbol{\zeta})$, and parametrization equations, $q(\boldsymbol{\zeta}, s)$, that enable the system

$$\mathbf{H}(\boldsymbol{\zeta}, s) := \begin{bmatrix} \mathbf{G}(\boldsymbol{\zeta}) \\ p(\boldsymbol{\zeta}) \\ q(\boldsymbol{\zeta}, s) \end{bmatrix} \quad (20)$$

to satisfy the hypotheses of the Implicit Function Theorem (IFT) [38]. In particular, given an initial solution, $\boldsymbol{\zeta}_0$, obtained for an initial continuation parameter, s_0 , the existence and uniqueness of a smooth family branch of solutions $\boldsymbol{\zeta}(s)$, such that

- $\mathbf{H}(\boldsymbol{\zeta}(s), s) = \mathbf{0}$, $\forall s$ near s_0
- $\boldsymbol{\zeta}(s_0) = \boldsymbol{\zeta}_0$

can be guaranteed as long as

- $\nabla_{\boldsymbol{\zeta}} \mathbf{H}(\boldsymbol{\zeta}_0, s_0)$ is nonsingular.
- \mathbf{H} and $\mathbf{H}_{\boldsymbol{\zeta}}$ are smooth near $\boldsymbol{\zeta}_0$.

Under the umbrella of the IFT, the equations of the GMOS algorithm can be embedded into a predictor–corrector procedure that enables marching along different family branches of non-integrable dynamical systems. The problem, for the purposes of this chapter, is that the initial solutions, $\boldsymbol{\zeta}_0$, are typically provided in the lower fidelity model of the CRTBP.

To mitigate this issue and develop a self-contained robust numerical continuation procedure, the vector of unknown variables is augmented in order to include the eccentricity of the Earth–Moon system as a psuedo-homotopy continuation parameter. That is, $\boldsymbol{\zeta} = [\mathbf{Z}_0^T, T, \rho, e]^T$. The additional variable in $\boldsymbol{\zeta}$ slightly complicates the expressions of the Jacobian matrix of $\mathbf{H}(\boldsymbol{\zeta}(s), s)$ but nevertheless allows one to *grow* the original periodic orbit into its corresponding quasi-periodic dynamical substitutes for different values of e .

To complete the numerical setup of the GMOS algorithm and produce some examples, recall that ERTBP quasi-periodic invariant tori are known to live in one-parameter families of solutions that essentially replace the original continuum of CRTBP periodic orbits [39]. In practice, following the addition of the Moon’s eccentricity, one phase condition and two parametrization equations should be sufficient to correctly identify unique QPT members within their corresponding family branches. Indeed, the second of the two angular quantities is often matched to the independent variable of the problem— ν in the ERTBP case—implying $\omega_1 = 1$ [11]. Quantitatively, this trick removes ρ from the unknown variables as

$\rho = 2\pi\omega_1/\omega_0 = T$. Then, $\boldsymbol{\zeta} = [\mathbf{Z}_0^T, T, e]^T$. Furthermore, the fact that v is also appearing explicitly in the equations of motion prevents ambiguities in the allocation of the \tilde{X}_0 points along the \mathcal{C} curve, thus removing the need for a second phase condition in the poloidal direction of the manifold.

As for the remaining phase condition and parametrizing equation, these are typically provided by [11, 36]

$$p(\boldsymbol{\zeta}) := \frac{1}{N} [\mathbf{Z}_0(s) - \mathbf{Z}_0(s_0)]^T \frac{\partial \mathbf{Z}_0}{\partial \theta_0}(s_0), \quad (21)$$

$$q_1(\boldsymbol{\zeta}, s) := T(s) - T^* \quad (22)$$

and pseudo-arclength continuation [38]

$$\begin{aligned} q_2(\boldsymbol{\zeta}, s) := & \frac{1}{N} [\mathbf{Z}_0(s) - \mathbf{Z}_0(s_0)]^T \frac{\partial \mathbf{Z}_0}{\partial s}(s_0) + \dots \\ & + [T(s) - T(s_0)] \frac{\partial T}{\partial s}(s_0) + [e(s) - e(s_0)] \frac{\partial e}{\partial s}(s_0) + \delta s, \end{aligned} \quad (23)$$

respectively, with $\delta s = (s - s_0)$, and

$$\frac{\partial \mathbf{Z}_0}{\partial \theta_0}(s_0) = \frac{2\pi}{T(s_0)} \left(\mathbf{F}(v, \mathbf{Z}_0(s_0), e(s_0)) - \frac{\partial \mathbf{Z}_0}{\partial \theta_1}(s_0) \right), \quad (24)$$

as demonstrated in Ref. [15]. In Eq.(24), $\mathbf{F}(v, \mathbf{Z}_0(s_0), e(s_0))$ stands for the collection of the N vector fields $\mathbf{f}(v + 2\pi(i-1)/N, \tilde{X}_i, \mathbf{p})$, $i = 0, \dots, N-1$, evaluated for each of the N quasi-periodic trajectories $\tilde{X}_i = \mathbf{u}(\theta_0, \theta_{1,i})$, whereas $\frac{\partial \mathbf{Z}_0}{\partial \theta_1}(s_0)$ stands for the partial derivatives of \mathbf{Z}_0 along the θ_1 direction. These partial derivatives can be calculated via the DFT of \mathbf{Z}_0 as

$$\frac{\partial \mathbf{Z}_0}{\partial \theta_1}(s_0) = [D^{-1}][\partial_{-\rho}][D]\mathbf{Z}_0, \quad (25)$$

where $[\partial_{-\rho}]$ is a diagonal matrix that multiplies the Fourier coefficients $\hat{\mathbf{u}}_T[k]$ by a quantity $j k$. In contrast, $\left[\frac{\partial \mathbf{Z}_0}{\partial s}\right]$, $\left[\frac{\partial T}{\partial s}\right]$, and $\left[\frac{\partial e}{\partial s}\right]$ stand for the components of the family tangent $\left[\frac{\partial \boldsymbol{\zeta}}{\partial s}\right]$, which can be approximated via the secant method by comparison between two adjacent solutions [38]:

$$\left[\frac{\partial \boldsymbol{\zeta}}{\partial s}\right](s_0) = \frac{\boldsymbol{\zeta}(s_0) - \boldsymbol{\zeta}(s_{-1})}{\|\boldsymbol{\zeta}(s_0) - \boldsymbol{\zeta}(s_{-1})\|}, \quad (26)$$

Note that $\mathbf{Z}_0(s_0)$, $\frac{\partial \mathbf{Z}_0}{\partial \theta_0}(s_0)$, $\frac{\partial \mathbf{Z}_0}{\partial \theta_1}(s_0)$, $\frac{\partial \mathbf{Z}_0}{\partial s}(s_0)$, $\frac{\partial T}{\partial s}(s_0)$, and $\frac{\partial e}{\partial s}(s_0)$ are all evaluated at the known solution ζ_0 and therefore can be kept constant throughout the numerical solution of Eq. (20). The same holds true for the desired longitudinal frequency of the manifold, i.e., the T^* quantity appearing in Eq. (22). This value is usually set equal to the period of the initiating CRTBP periodic orbit in order to ensure that the calculated two-dimensional tori are indeed the dynamical substitutes of the candidate trajectory.

At last, Newton's method can be finally implemented in order to update the values of $\zeta = [\mathbf{Z}_0^T, T, e]^T$ until $\|\mathbf{H}(\zeta, s)\|$ is lower than a given threshold, e.g., 10^{-10} . The update equation at the k th iteration reads as

$$\zeta^{(k+1)} = \zeta^{(k)} - \left[\nabla_{\zeta} \mathbf{H}(\zeta^{(k)}, s) \right]^{\dagger} \mathbf{H}(\zeta^{(k)}, s), \quad (27)$$

where $[\cdot]^{\dagger}$ denotes the left pseudo-inverse of $\nabla_{\zeta} \mathbf{H}(\zeta^{(k)}, s)$, the non-square Jacobian matrix of $\mathbf{H}(\zeta^{(k)}, s)$. A summary of the GMOS algorithm is disclosed in Algorithm 1, along with a table of the GMOS user-defined parameters utilized in this research (Table 1).

3.2 Initial Guess Generation

As stated in Algorithm 1, the GMOS algorithm can be properly initialized with appropriate values of ζ_0 , $\frac{\partial \mathbf{Z}_0}{\partial \theta_0}(s_0)$, $\frac{\partial \zeta}{\partial s}(s_0)$. All of these quantities can be retrieved from the CRTBP if any candidate periodic orbit is seen as the overlap of N identical quasi-periodic trajectories in the Earth–Moon ERTBP with $e = 0$. Accordingly, let X_0 be the initial conditions of a periodic orbit in the Earth–Moon CRTBP with period T . The vector of initial conditions can be repeated N times, where N is the number of quasi-periodic trajectories chosen to represent an invariant curve \mathcal{C} of the stroboscopic mapping $\varphi_T(X_0)$:

$$\mathbf{Z}_0 = [\mathbf{X}_0^T, \mathbf{X}_0^T, \dots, \mathbf{X}_0^T]^T \in \mathbb{R}^{6N}. \quad (28)$$

Table 1 GMOS user-defined parameters utilized in this chapter

Parameter	Value	Meaning
N_{QPT}	100	Max. number of family members to be computed
MaxIter	10	Max. number of iterations for the corrector step
Tol	10^{-10}	Convergence tolerance
N	201	No. of quasi-periodic trajectories
δs	10^{-4}	Initial continuation step length

Algorithm 1 GMOS algorithm

Given $s_0 = 0$, $\delta s = 10^{-4}$, ζ_0 , $\frac{\partial \zeta}{\partial s}(s_0)$, $\frac{\partial \mathbf{Z}_0}{\partial \theta_0}(s_0)$,

for $i = 1:N_{QPT}$ **do**

Predictor:

$$\zeta^{(1)} = \zeta_0 + \delta s \left[\frac{\partial \zeta_0}{\partial s} \right]$$

Corrector:

for $k = 1:\text{MaxIter}$ **do**

Calculate $\mathbf{H}(\zeta^{(k)}, s)$, $\nabla_{\zeta} \mathbf{H}(\zeta^{(k)}, s)$

if $\|\mathbf{H}(\zeta, s)\| \leq \text{Tot}$ **then**

Family member has been computed!

Calculate New Family Tangent:

$$\frac{\partial \zeta}{\partial s} = (\zeta^{(k)} - \zeta_0) / \|\zeta^{(k)} - \zeta_0\|;$$

Store s , $\zeta^{(k)}$, $\frac{\partial \zeta}{\partial s}$;

Set $s_0 = s$, $\zeta_0 = \zeta^{(k)}$, $\frac{\partial \zeta}{\partial s}(s_0) = \frac{\partial \zeta}{\partial s}$;

Update partial derivatives with respect to θ_0 :

$$\frac{\partial \mathbf{Z}_0}{\partial \theta_1}(s_0) = [D^{-1}][\partial_{-\rho}][D]\mathbf{Z}_0;$$

$$\frac{\partial \mathbf{Z}_0}{\partial \theta_0}(s_0) = \frac{2\pi}{T(s_0)} \left(\mathbf{F}(\mathbf{Z}_0(s_0)) - \frac{\partial \mathbf{Z}_0}{\partial \theta_1}(s_0) \right);$$

Calculate new continuation step length δs ;

Break; # Move to next family member

else

end

$$\zeta^{(k+1)} = \zeta^{(k)} - [\nabla_{\zeta} \mathbf{H}(\zeta^{(k)}, s)]^{\dagger} \mathbf{H}(\zeta^{(k)}, s);$$

end if

end for

if $k == \text{MaxIter}$ **then**

Differential Corrector has not converged!

Return; # Quit numerical continuation

end if

end for

The vector of initial conditions can be processed via the DFT in order to estimate $\frac{\partial \mathbf{Z}_0}{\partial \theta_0}(s_0)$. Furthermore, it can be integrated under the augmented dynamical systems $\mathbf{F}(v, \mathbf{Z}, 0)$ over time T and utilized to construct $\nabla_{\zeta} \mathbf{h}(\zeta_0, s_0)$, where $\zeta_0 = [\mathbf{Z}_0^T, T, 0]^T$, and

$$\mathbf{h}(\boldsymbol{\zeta}_0, s_0) := \begin{bmatrix} \mathbf{G}(\boldsymbol{\zeta}) \\ p(\boldsymbol{\zeta}) \\ q_1(\boldsymbol{\zeta}, s) \end{bmatrix} = \mathbf{0}. \tag{29}$$

Deprived of the pseudo-arclength continuation equation (23), the system (29) is satisfied by each quasi-periodic invariant torus of any family branch. It follows that a Singular Value Decomposition (SVD) of $\nabla_{\boldsymbol{\zeta}} \mathbf{h}(\boldsymbol{\zeta}_0, s_0)$ should not only demonstrate this singularity but also provide users with an accurate approximation of the family tangent $\frac{\partial \boldsymbol{\zeta}}{\partial s}$ evaluated in $\boldsymbol{\zeta}_0$. Figure 4 displays the initial (2:9) and (1:4) CRTBP periodic orbits along with their initial family tangents obtained via the proposed SVD-based procedure.

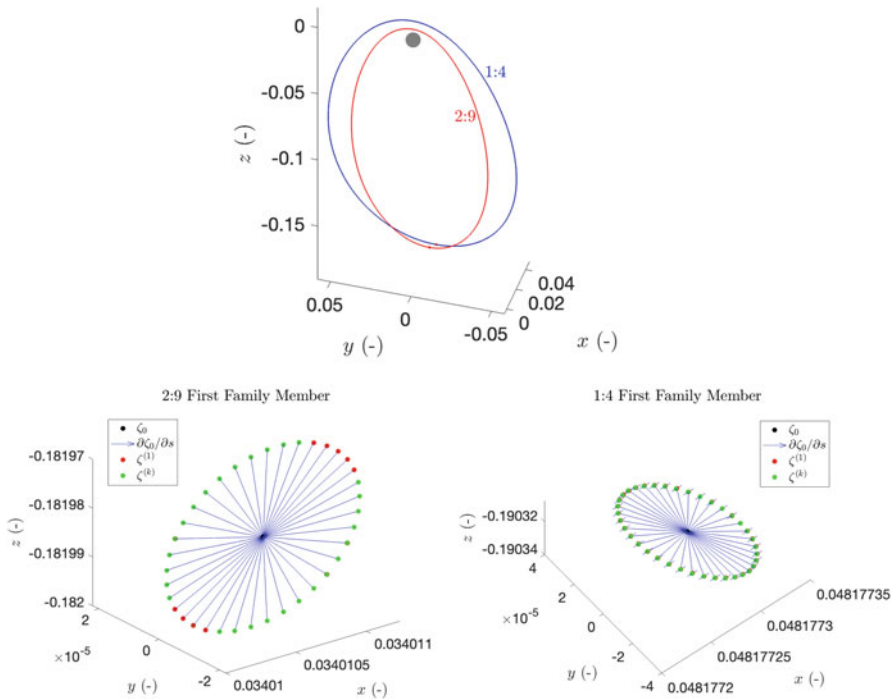


Fig. 4 (Top) 2:9 and 1:4 synodic resonant orbits in the CRTBP model. (Bottom) ERTBP initial guesses along with their corresponding family tangents

3.3 Numerical Continuation

Starting from the initial values of ζ_0 , $\frac{\partial \mathbf{Z}_0}{\partial \theta_0}(s_0)$, $\frac{\partial \zeta}{\partial s}(s_0)$ obtained as in Sect. 3.2, the GMOS algorithm can be iterated over a user-defined maximum number of N_{QPT} family members and stopped prematurely as soon as the algorithm no longer converges or the value of the eccentricity exceeds the Moon’s average value of $e = 0.054$. Figures 5 and 6 illustrate some of the quasi-periodic invariant tori obtained throughout the numerical continuation procedure for different values of e . The (2:9) and (1:4) family members obtained for $e = 0.054$ are further analyzed and manipulated in the following subsection.

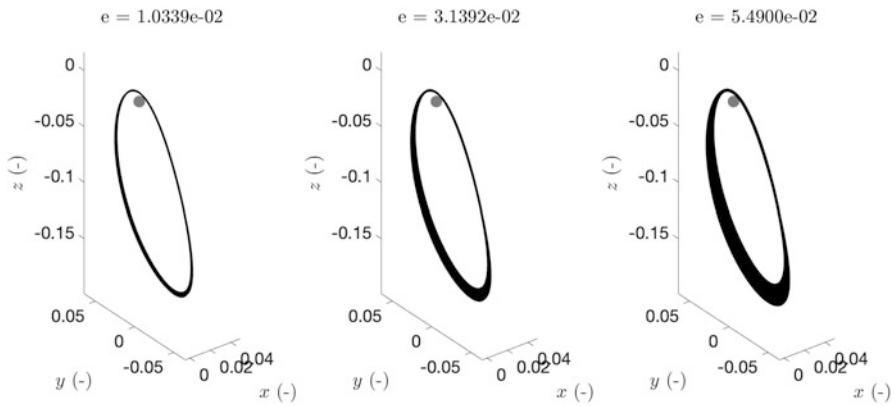


Fig. 5 Homotopy continuation of the 2:9 ERTBP dynamical substitute

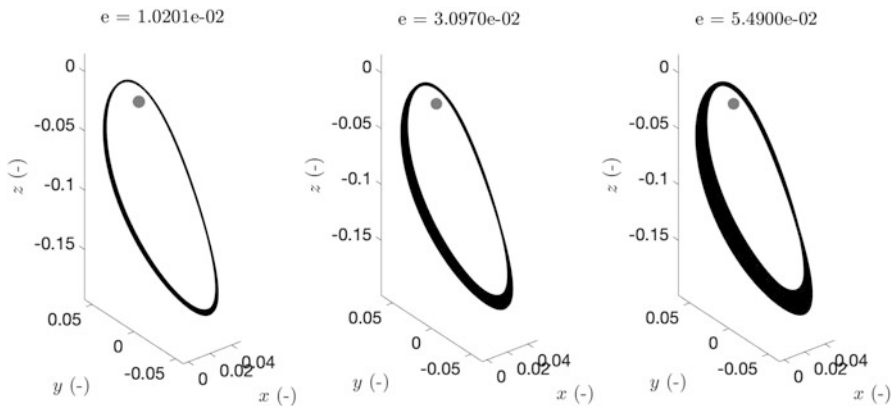


Fig. 6 Homotopy continuation of the 1:4 ERTBP dynamical substitute

3.4 Post-processing and Torus Maps

Having completed the homotopy continuation from $e = 0$ to $e = 0.054$ and obtained two-dimensional invariant substitutes for the LPOG candidate orbits, trajectories on the surface of these two-dimensional invariant tori can be immediately generated via

$$\begin{cases} \theta_0(v) = \theta_0(v_0) + \omega_0(v - v_0), \\ \theta_1(v) = \theta_1(v_0) + v, \end{cases} \quad (30)$$

where $\omega_0 = 2\pi/T$. Considering the simplicity of Eq. (30), it is tempting to exploit the diffeomorphism that maps trajectories in \mathbb{R}^6 onto trajectories in torus coordinates and vice versa in order to visualize key dynamical quantities across the surface of the torus as well as generate initial guesses for full-ephemeris optimizations. These *torus maps* can be generated by integrating the output of the GMOS algorithm over one stroboscopic time and store the Cartesian coordinates of the quasi-periodic trajectories over a uniform grid of points in $\mathbb{T}^2 : [0, 2\pi) \times [0, 2\pi)$. This approach works as follows.

First, observe that each of the quasi-periodic orbit initial conditions in \mathbf{Z}_0 can be associated with the torus initial coordinates $\theta_0(v_0) = 0$ and $\theta_1(v_0) = 2\pi(i - 1)/N$, $\forall i = 0, 1, \dots, N - 1$, as illustrated in Eq. (13). Second, one can integrate \mathbf{Z}_0 according to the augmented dynamics $\mathbf{F}(v, \mathbf{Z}, e)$ and collect the images of the stroboscopic mapping $\mathbf{Z}_i = \Psi_{v_i}(\mathbf{Z}_0)$ for any arbitrary value of $v \in [0, T]$, where Ψ_v is the now solution flow of $\mathbf{F}(v, \mathbf{Z}, e)$ over time v . At each $v = v_i = iT/M$, $i = 0, \dots, M - 1$, one can rotate the Fourier coefficients of \mathbf{Z}_i by a quantity $-v_i$ and obtain the values of the N quasi-periodic trajectories in correspondence with $\theta_{1,i} = 2\pi(i - 1)/N$, $i = 0, 1, \dots, N - 1$. After one stroboscopic time T , the images of the stroboscopic mapping overlap with the initial conditions of the quasi-periodic torus as prescribed by Eq. (12).

Shown in Figs. 7 and 8 are the (2:9) and (1:4) dynamical substitutes along with their corresponding radial velocity curves obtained in MATLAB using the torus map pseudo-code of Algorithm 2 with $M = 1000$ and $N = 37$. Also shown in Figs. 7 and 8 are representative quasi-periodic trajectories initialized in $\theta_0(v_0) = \theta_1(v_0) = 0$ and integrated over several stroboscopic times. The zero-radial velocity curves corresponding to the perilunes and apolunes of the quasi-periodic trajectories are highlighted in magenta so as to emphasize the difference with respect to the periodic orbit case, in which the points of zero-radial velocity are constantly aligned with the Earth–Moon direction ($\theta_0 = 0$ and $\theta_0 = \pi$ for the apolune and perilune points, respectively).

It is also worth noting that the zero-radial velocity contours can be easily extracted from the MATLAB `contourf` command in order to calculate spline coefficients for the apolune and perilune curves. These spline coefficients can be later passed to `ode` event functions that detect intersections with arbitrary quasi-periodic trajectories along the two-dimensional invariant manifold. This passage

Algorithm 2 Torus map generation

Given \mathbf{Z}_0 , T , e , $d = 6$, M , and N

Create uniform grid of true anomaly values:

$$v_i = iT/M, i = 0, \dots, M$$

Integrate augmented dynamics $\mathbf{F}(v, \mathbf{Z}, e)$ over $v \in [0, T]$

Store or Interpolate \mathbf{Z}_i values at v_i points.

Initialize two-dimensional array $\mathbf{Q} \in \mathbb{R}^{dN \times M}$:

$\mathbf{Q} = \text{zeros}(d*N, M)$;

for $i = 0:M-1$ **do**

 Rotate states on stroboscopic curves:

$$\mathbf{Q}(:, i+1) = R_{-v_i}[\mathbf{Z}_i] = \left[\mathbf{u}(\theta_0^i, 0)^T, \dots, \mathbf{u}\left(\theta_0^i, \frac{2\pi(N-1)}{N}\right)^T \right]^T$$

end for

Copy first column and first d -rows of \mathbf{Q} to enforce periodicity at the boundaries of contour plots and cover entire $(0, 2\pi) \times (0, 2\pi)$ domain:

$\mathbf{Q} = [\mathbf{Q}, \mathbf{Q}(:, 1)]$;

$\mathbf{Q} = [\mathbf{Q}; \mathbf{Q}(1:d, :)]$;

Calculate dynamical quantity of interest in $u(\theta_0^i, \theta_1^j)$:

for $i = 0:M$ **do**

for $j = 0:N$ **do**

$q(j+1, i+1) = q_{i,j}(\mathbf{Q}(d*j+1:d*(j+1), i+1))$

end for

end for

Example Torus Map

tht0 = linspace(0, 2*pi, M+1);

tht1 = linspace(0, 2*pi, N+1);

[THT0, THT1] = meshgrid(tht0, tht1)

figure(), contourf(THT0, THT1, q)

Extract q_value contour:

$[C, h] = \text{contour}(THT0, THT1, q, [q_value, q_value])$

is key as it enables the fast and reliable calculation of good initial guesses for quasi-periodic trajectories in the full-ephemeris model of the Earth–Moon system. It also works for arbitrary propagation times and hyperbolic QPT, whereby numerical integration errors can cause trajectories to diverge and escape along the unstable manifold direction. An overview of the transition to full-ephemeris approach is offered in the next section.

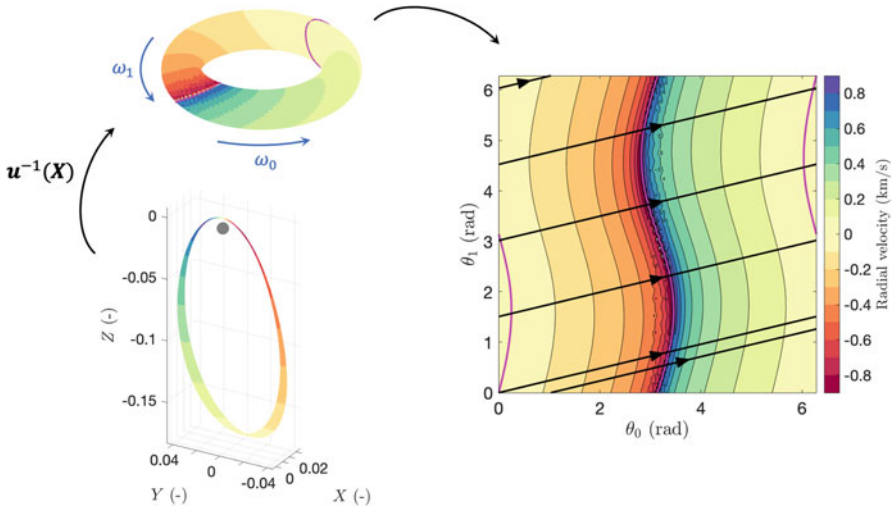


Fig. 7 2:9 dynamical substitute along with its radial velocity torus map. The magenta lines denote the zero-radial velocity curves found in correspondence with the perilune and apolune points along the manifold

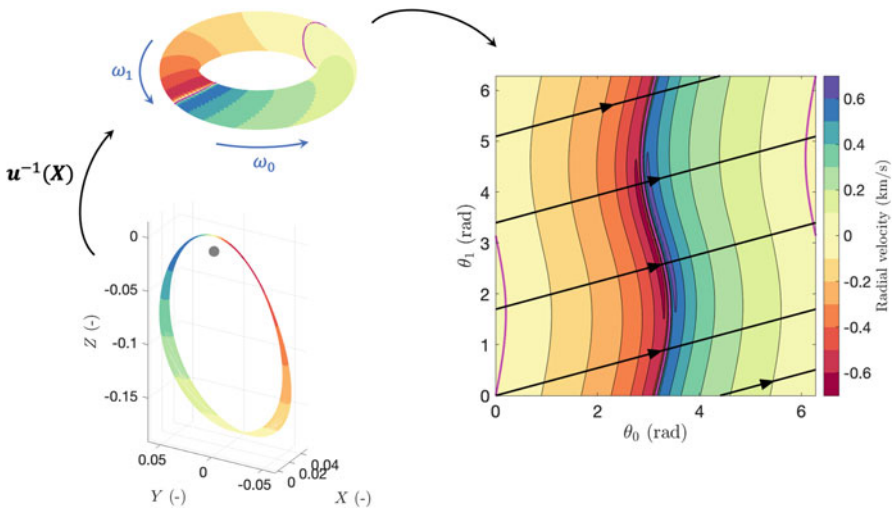


Fig. 8 1:4 dynamical substitute along with its radial velocity torus map. The magenta lines denote the zero-radial velocity curves found in correspondence with the perilune and apolune points along the manifold

4 Transition to Full-Ephemeris Model

This section deals with the transition of candidate quasi-periodic trajectories into the full-ephemeris model of the Earth–Moon system. A freeware trajectory

software developed by Stefano Campagnola and his team has been adopted for the calculations [40]. jTOP, as it is called, takes as an input discrete points along a candidate trajectory, their epochs in UTC time coordinates, along with forward and backward propagation times between consecutive nodes. Internally, the software propagates the states of the trajectory forward and backward in time, possibly in a higher fidelity dynamical model, so as to evaluate the residuals in both time and Cartesian coordinates at user-defined patching points. These residuals and their partial derivatives are later passed to SNOPT, a shareware trajectory optimization procedure [41], which nullifies their values in both the space and time domains while adjusting the nodes, epochs, and forward and backward propagation times of the candidate trajectory. Figure 9 illustrates the concept of the jTOP approach for three consecutive nodes along a candidate quasi-periodic trajectory.

For the purposes of this chapter, initial nodes, epochs, and forward and backward propagation times are generated in the ERTBP model of the Earth–Moon system starting from the two-dimensional torus maps of Sect. 3.4. Each of the nodes is later propagated using the full-ephemeris dynamics of Eq. (7), as seen in the Moon-centered ECLIPJ2000 reference frame. The dynamical model includes the gravitational influence of a spherical Sun and Earth, as well as an 8×8 spherical harmonics expansion of the Moon’s gravity field. The epoch of the first apolune point is arbitrarily set to 25 Apr 2023, 00:00:00 (UTC), whereas the full-ephemeris trajectory is evaluated over one year. One additional revolution is appended before and after the first and last apolune points so as to robustify the SNOPT convergence and avoid undesirable *edge effects* during the nominal duration of the orbit [42]. These and other considerations affect the creation and optimization of the full-ephemeris first guess as highlighted in the following subsections.

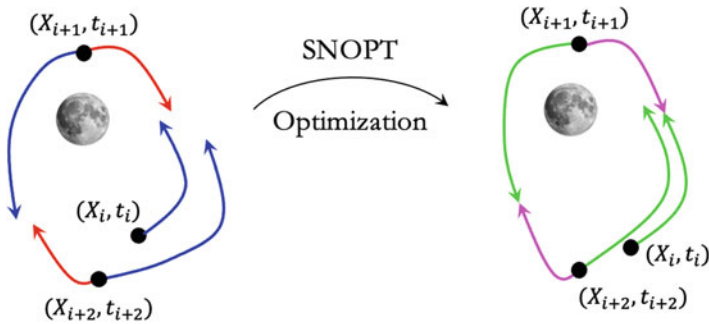


Fig. 9 Conceptual illustration of the jTOP transition to full-ephemeris strategy

4.1 First-Guess Generation

Once the epoch of the initial apolune point has been arbitrarily chosen, the initial value of the Moon’s true anomaly can be easily calculated using SPICE ephemerides files available in jTOP. Given ν^* , a horizontal line can be drawn in the torus maps of Figs. 7 or 8, recalling that the poloidal angular coordinate of the torus, θ_1 , was indeed identified with the true anomaly of the Earth–Moon system (Sect. 3.2). The intersection of this horizontal line with the magenta curves of Figs. 7 and 8 locates an initial apolune point for the full-ephemeris initial guess. It also provides mission designers with the initial conditions of the desired quasi-periodic trajectory in torus coordinates: $\theta_{0,0}$ and $\theta_{1,0} = \nu^*$.

Starting from the initial torus coordinates and $t_0 = 0$ —the time elapsed since the arbitrarily chosen epoch—it is possible to integrate the augmented torus dynamics

$$\begin{cases} \frac{d\theta_0}{d\nu} = \omega_0, \\ \frac{d\theta_1}{d\nu} = 1, \\ \frac{dt}{d\nu} = \frac{(1 - e^2)^{3/2}}{n \gamma^2} \end{cases} \quad (31)$$

and record the exact torus coordinates and time elapsed between consecutive zero-radial velocity curve crossings. The crossings are detected in MATLAB using `ode` event functions that have access to the spline coefficients of the magenta lines of Fig. 7 and 8. The “events” detected over one year for the (2:9) and (1:4) ERTBP tori are summarized in Fig. 10 along with two extra nodes at the beginning and end of the initial guess that provide SNOPT with additional flexibility in manipulating the full-ephemeris orbit. A total of $121 + 4$ and $107 + 4$ nodes have been registered for the two synodic resonant orbits considered in this chapter. Each of these nodes contains the torus coordinates at the apolune and perilune curve crossings, as well as the time elapsed since the first apolune epoch.

By means of the diffeomorphism \mathbf{u} , obtained using the GMOS algorithm of Sect. 3.1, each of the torus coordinate pairs can be mapped into position and velocity vector coordinates in pulsating normalized units. These pulsating normalized coordinates can be rotated in the ECLIPJ2000 frame using Eq. (9) along with the reference frame transformations available in SPICE (and, by extension, jTOP). In parallel, the time elapsed since the beginning of the simulation can be added to the ephemeris time of the arbitrarily chosen epoch, thereby creating an initial value for the candidate nodes’ time stamps. Obtaining an initial guess for the forward and backward propagation times between consecutive nodes is now trivial, as the difference between adjacent epochs can be calculated and divided by two. The only quantities left are the backward and forward propagation times of the first and last nodes, respectively, which can be conveniently set to 0. Passing these values to jTOP yields the full-ephemeris initial guesses depicted in Fig. 11, as seen from a Moon-

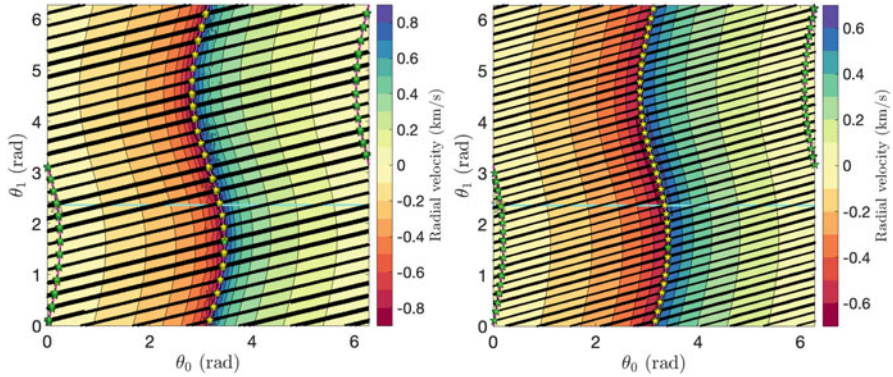


Fig. 10 Full-ephemeris first-guess generation using the (2:9) (left) and (1:4) (right) ERTBP dynamical substitute torus maps. The cyan line indicates the location of the Moon's true anomaly at epoch

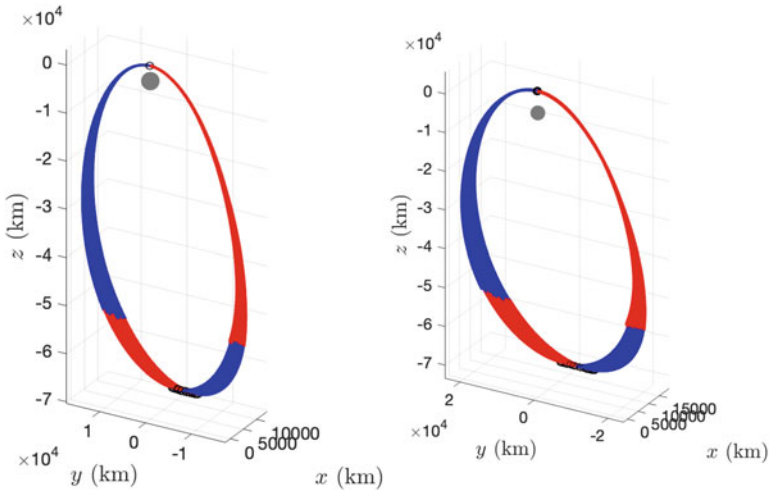


Fig. 11 left) (2:9) and right) (1:4) full-ephemeris initial guesses as seen in a Moon-centered synodic frame after propagation in jTOP. Trajectory legs in blue denote forwardly propagated orbits, whereas red points stand for backwardly propagated ones

centered synodic frame. It can be verified that the residuals at the patching points are generally nonzero due to the higher fidelity dynamics being integrated between the different nodes. Nevertheless, the structure of the quasi-periodic torus seems to be preserved, and it can be fully optimized using the numerical procedure of the following subsection.

4.2 SNOPT Optimization

At last, the full-ephemeris initial guesses for the (2:9) and (1:4) LOPG baseline trajectories can be optimized in jTOP using an embedded interface with the SNOPT optimizer. The goal of this trajectory optimization step is to minimize the ΔV consumption at the patching points obtained after forward and backward propagation of the candidate nodes. While minimizing the ΔV discrepancies at the patching points, the optimizer seeks to satisfy a list of nonlinear constraints that ensure the continuity in both the time and position coordinates. The apsidal nature of the full-ephemeris nodes is hereby preserved by adding additional constraints to nullify the dot products between the position and velocity vectors of the candidate trajectory at the apolune and perilune points. Furthermore, if the magnitude of the ΔV difference at any of the patching point is found to be less than 1 mm/s^2 , the ΔV error of the patching point is removed from the cost function and replaced by a nonlinear constraint that ensures continuity in the velocity coordinates as well.

Ideally, by the end of the optimization procedure, all of the patching points should be continuous in the time, position, and velocity domains with a zero cost function being passed to the SNOPT optimizer. In such a situation, the software seeks for a feasible solution that satisfies all of the nonlinear requirements. It is at this stage that the set of nonlinear constraints is augmented in order to guarantee that the epoch of the first apolune point would remain close to the arbitrarily chosen one. In addition, the location of the perilune points is confined within a box of $\pm 5000 \text{ km}$ and $\pm 3000 \text{ km}$ in the x - and z -coordinates of the initial perilune points, respectively. These additional constraints facilitate the convergence onto the desired full-ephemeris quasi-periodic trajectory by preventing the optimized SNOPT solution to diverge far from the original quasi-periodic trajectories. Furthermore, crashes against the surface of the Moon are avoided by means of inequality constraints that calculate the altitude of the trajectory at the perilune points and prevent it from being less than 50 km from the surface of the planetary satellite.

The output of the trajectory optimization procedure is depicted in Figs. 12 and 13, respectively. It can be verified that the size and shapes of the final orbits are indeed very similar to the candidate initial guesses obtained with the two-dimensional tori of Sec. 3.1. Each of these candidate trajectories can be now converted into a `.bsp` file using the publicly available `mkspk` executable for more in-depth analyses and scientific investigations [32].

5 Conclusions

This chapter overviews modern astrodynamics techniques for the numerical calculation of two-dimensional quasi-periodic invariant tori. An algorithm, based on the invariant curves of stroboscopic mapping, has been implemented and adopted from the literature in order to calculate dynamical substitutes of synodic resonant

Fig. 12 Final (2:9) full-ephemeris orbit as seen in a Moon-centered synodic frame after optimization in jTOP. Trajectory legs in green denote forwardly propagated orbits, whereas magenta points stand for backwardly propagated ones

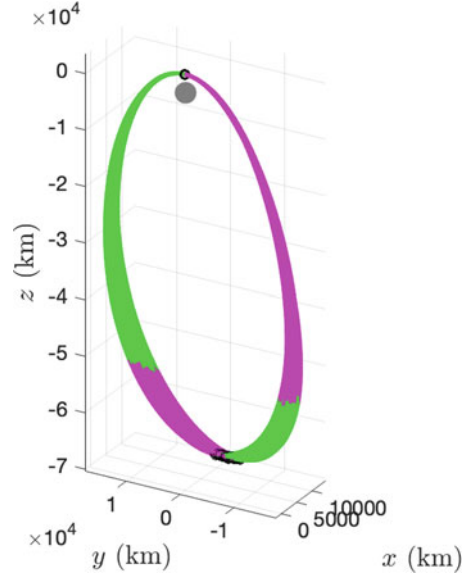
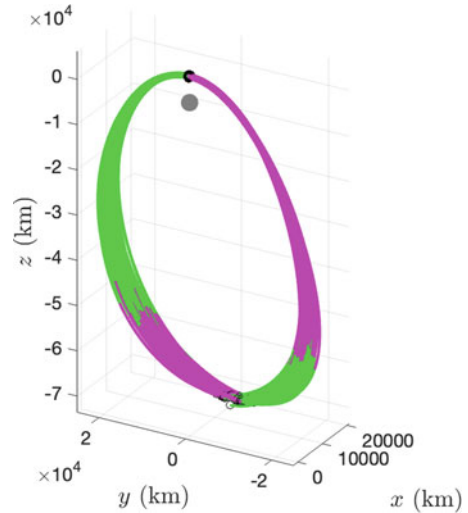


Fig. 13 Final (1:4) full-ephemeris orbit as seen in a Moon-centered synodic frame after optimization in jTOP. Trajectory legs in green denote forwardly propagated orbits, whereas magenta points stand for backwardly propagated ones



near rectilinear halo orbits around the Moon. More specifically, the (2:9) and (1:4) NRHOs have been considered as the baselined trajectories of the LOPG.

It has been found that the original CRTBP periodic orbits can be safely continued in the ERTBP of the Earth–Moon system via a pseudo-homotopy continuation strategy that grows the eccentricity of the two primaries up to $e = 0.0549$. The obtained two-dimensional invariant tori are later processed a posteriori using two-dimensional contour plots that can help illustrate key dynamical quantities (e.g., the lunar altitude), as well as locate zero-radial velocity curves on the surface of

the manifold. By extracting the spline coefficients of these curves, reliable initial guesses for transitioning the candidate solutions in the real-ephemeris model of the Earth–Moon systems can be generated. This process is demonstrated in jTOP, a trajectory optimization package that minimizes residuals between forwardly and backwardly propagated legs at orbit-specific patching points.

References

1. William C Feldman, Sylvestre Maurice, David Jeffery Lawrence, Robert C Little, SL Lawson, O Gasnault, Roger C Wiens, Bruce L Barraclough, Richard C Elphic, Thomas H Prettyman, et al. Evidence for water ice near the lunar poles. *Journal of Geophysical Research: Planets*, 106(E10):23231–23251, 2001.
2. R Sridharan, SM Ahmed, Tirtha Pratim Das, P Sreelatha, P Pradeepkumar, Neha Naik, and Gogulapati Supriya. ‘Direct’ evidence for water (H₂O) in the sunlit lunar ambience from CHACE on MIP of Chandrayaan I. *Planetary and Space Science*, 58(6):947–950, 2010.
3. Shuai Li, Paul G Lucey, Ralph E Milliken, Paul O Hayne, Elizabeth Fisher, Jean-Pierre Williams, Dana M Hurley, and Richard C Elphic. Direct evidence of surface exposed water ice in the lunar polar regions. *Proceedings of the National Academy of Sciences*, 115(36):8907–8912, 2018.
4. Leonard David. *Moon Rush: The New Space Race*. National Geographic Books, 2019.
5. Diane Davis, Sagar Bhatt, Kathleen Howell, Jiann-Woei Jang, Ryan Whitley, Fred Clark, Davide Guzzetti, Emily Zimovan, and Gregg Barton. Orbit maintenance and navigation of human spacecraft at cislunar near rectilinear halo orbits. In *27th AAS/AIAA Space Flight Mechanics Meeting, San Antonio, Texas, February 5–9, 2017*. American Astronautical Society, 2017.
6. David E Lee. White paper: gateway destination orbit model: a continuous 15 year NRHO reference trajectory. Technical report, 2019.
7. KC Howell and JV Breakwell. Almost rectilinear halo orbits. *Celestial mechanics*, 32(1):29–52, 1984.
8. Emily M Zimovan-Spreen, Kathleen C Howell, and Diane C Davis. Near rectilinear halo orbits and nearby higher-period dynamical structures: orbital stability and resonance properties. *Celestial Mechanics and Dynamical Astronomy*, 132(5):1–25, 2020.
9. Takuya Chikazawa, Nicola Baresi, Stefano Campagnola, Naoya Ozaki, and Yasuhiro Kawakatsu. Minimizing eclipses via synodic resonant orbits with applications to EQUULEUS and MMX. *Acta Astronautica*, 180:679–692, 2021.
10. Emily M Zimovan, Kathleen C Howell, and Diane C Davis. Near rectilinear halo orbits and their application in cis-lunar space. In *3rd IAA Conference on Dynamics and Control of Space Systems, Moscow, Russia*, volume 20, 2017.
11. Zubin P Olikara. *Computation of quasi-periodic tori and heteroclinic connections in astrodynamics using collocation techniques*. PhD thesis, University of Colorado at Boulder, 2016.
12. Enric Castella and Àngel Jorba. On the vertical families of two-dimensional tori near the triangular points of the bicircular problem. *Celestial Mechanics and Dynamical Astronomy*, 76(1):35–54, 2000.
13. Nicola Baresi, Zubin P Olikara, and Daniel J Scheeres. Fully numerical methods for continuing families of quasi-periodic invariant tori in astrodynamics. *The Journal of the Astronautical Sciences*, 65(2):157–182, 2018.
14. G. Gómez, W S Koon, Martin W Lo, Jerrold E Marsden, Josep Masdemont, and Shane D Ross. Connecting orbits and invariant manifolds in the spatial restricted three-body problem. *Nonlinearity*, 17:1571–1606, 2004.

15. Zubin P. Olikara and Daniel J Scheeres. Numerical Method for Computing Quasi-periodic Orbits and Their Stability in the Restricted Three-Body Problem. *Advances in Astronautical Sciences*, 145:911–930, 2012.
16. Frank Schilder, Hinke M. Osinga, and Werner Vogt. Continuation of Quasi-periodic Invariant Tori. *SIAM Journal on Applied Dynamical Systems*, 4(3):459–488, Jan 2005.
17. Egemen Kolemen, N. Jeremy Kasdin, and Pini Gurfil. Multiple Poincaré sections method for finding the quasiperiodic orbits of the restricted three body problem. *Celestial Mechanics and Dynamical Astronomy*, 112(1):47–74, Jan 2012.
18. Brian P McCarthy and Kathleen C Howell. Leveraging quasi-periodic orbits for trajectory design in cislunar space. *Astrodynamics*, 5(2):139–165, 2021.
19. José J Rosales, Angel Jorba, and Marc Jorba-Cuscó. Families of halo-like invariant tori around l_2 in the Earth–Moon Bicircular Problem. *Celestial Mechanics and Dynamical Astronomy*, 133(4):1–30, 2021.
20. Damennick Henry and Daniel J Scheeres. Transfers between intersecting quasiperiodic tori. In *Paper AAS 20-588 presented at the 2020 Astrodynamics Specialist Conference*, 2020.
21. Daniel Villegas-Pinto, Nicola Baresi, Slim Locoche, and Daniel Hestroffer. Quasi-periodic near-rectilinear halo orbits in the circular-elliptic restricted four-body problem. In *Paper presented at the 2021 AAS/AIAA Astrodynamics Specialist Conference*, 2021.
22. A. Haro and R. de la Llave. A Parameterization Method for the Computation of Invariant Tori and Their Whiskers in Quasi-Periodic Maps: Explorations and Mechanisms for the Breakdown of Hyperbolicity. *SIAM Journal on Applied Dynamical Systems*, 6(1):142–207, 2007.
23. Bhanu Kumar, Rodney L Anderson, and Rafael de la Llave. Rapid and accurate computation of whiskered tori and their manifolds near resonances in periodically perturbed planar circular restricted 3-body problems. *arXiv preprint arXiv:2105.11100*, 2021.
24. Victory Szebehely. *Theory of Orbit*. Elsevier, 1967.
25. R A Broucke. Stability of periodic orbits in the elliptic, restricted three-body problem. *AIAA Journal*, 7(6):1003–1009, 1969.
26. Barbara A Cohen, Paul Ottinger Hayne, Benjamin T Greenhagen, and David A Paige. Lunar flashlight: Exploration and science at the moon with a 6u CubeSat. In *AGU Fall Meeting Abstracts*, volume 2015, pages EP52B–07, 2015.
27. Ana M Cipriano, Diogene A Dei Tos, and Francesco Topputo. Orbit design for LUMIO: The lunar meteoroid impacts observer. *Frontiers in Astronomy and Space Sciences*, 5:29, 2018.
28. Stefano Campagnola, Javier Hernando-Ayuso, Kota Kakihara, Yosuke Kawabata, Takuya Chikazawa, Ryu Funase, Naoya Ozaki, Nicola Baresi, Tatsuaki Hashimoto, Yasuhiro Kawakatsu, et al. Mission analysis for the em-1 CubeSats EQUULEUS and OMOTENASHI. *IEEE Aerospace and Electronic Systems Magazine*, 34(4):38–44, 2019.
29. James Pezent, Rohan Sood, and Andrew Heaton. High-fidelity contingency trajectory design and analysis for NASA’s near-earth asteroid (NEA) scout solar sail mission. *Acta Astronautica*, 159:385–396, 2019.
30. Jeffrey S Parker and Rodney L Anderson. *Low-energy lunar trajectory design*, volume 12. John Wiley & Sons, 2014.
31. Charles H Acton Jr. Ancillary data services of NASA’s navigation and ancillary information facility. *Planetary and Space Science*, 44(1):65–70, 1996.
32. Charles Acton, Nathaniel Bachman, Boris Semenov, and Edward Wright. A look towards the future in the handling of space science mission geometry. *Planetary and Space Science*, 150:9–12, 2018.
33. David A Vallado. *Fundamentals of astrodynamics and applications*, volume 12. Springer Science & Business Media, 2001.
34. Alex S Konopliv, Ryan S Park, Dah-Ning Yuan, Sami W Asmar, Michael M Watkins, James G Williams, Eugene Fahnestock, Gerhard Kruizinga, Meegyeong Paik, Dmitry Strelakov, et al. High-resolution lunar gravity fields from the grail primary and extended missions. *Geophysical Research Letters*, 41(5):1452–1458, 2014.
35. Hendrik W Broer, George B Huitema, and Mikhail B Sevryuk. *Quasi-periodic motions in families of dynamical systems: order amidst chaos*. Springer, 2009.

36. Nicola Baresi. *Spacecraft formation flight on quasi-periodic invariant tori*. PhD thesis, University of Colorado at Boulder, 2017.
37. John P Boyd. *Chebyshev and Fourier spectral methods*. Courier Corporation, 2001.
38. Rüdiger Seydel. *Practical Bifurcation and Stability Analysis*. Springer Science & Business Media, 2009.
39. Angel Jorba and Jordi Villanueva. On the persistence of lower dimensional invariant tori under quasi-periodic perturbations. *Journal of Nonlinear Science*, 7(5):427–473, 1997.
40. Stefano Campagnola, Naoya Ozaki, Yoshihide Sugimoto, Chit Hong Yam, Hongru Chen, Yosuke Kawabata, Satoshi Ogura, Bruno Sarli, Yasuhiro Kawakatsu, Ryu Funase, et al. Low-thrust trajectory design and operations of Procyon, the first deep-space micro-spacecraft. In *25th International Symposium on Space Flight Dynamics*, volume 7. German Aerospace Center (DLR) Munich, Germany, 2015.
41. Philip E Gill, Walter Murray, and Michael A Saunders. SNOPT: An SQP algorithm for large-scale constrained optimization. *SIAM review*, 47(1):99–131, 2005.
42. Kenshiro Oguri, Kenta Oshima, Stefano Campagnola, Kota Kakihara, Naoya Ozaki, Nicola Baresi, Yasuhiro Kawakatsu, and Ryu Funase. Equuleus trajectory design. *The Journal of the Astronautical Sciences*, 67(3):950–976, 2020.

Hypersonic Point-to-Point Travel for the Common Man



Carlos Bislip and Erwin Mooij

1 Introduction

Hypersonic travel has historically been experienced exclusively by healthy and heavily trained individuals. The increased accelerations experienced are known to cause a variety of effects on human physiology, ranging from heavy breathing and discomfort to gravity-induced loss of consciousness (G-LOC). Furthermore, high speed travel has not been technologically feasible, nor economically viable for the population at large. However, advancements in both computational and rocket technology have shown glimpses of a broader cross section of the population being able to participate in what is known as *space tourism*. However, medical screenings and prior training, if not required, are strongly suggested.

The commercial aviation industry has advanced to the point where, for the most part, only individuals susceptible to lower ambient pressures are recommended to avoid travel. Though during a typical flight there are moments where the accelerations are larger than those experienced while at sea level and constant velocity, the portion of the population that cannot travel on an aircraft is effectively negligible. This mass availability is essential for cost reduction and economies of scale, both of which are key factors relevant to commercial airlines. Hence, even if hypersonic travel were technically feasible to the point that it became commonplace, it is reasonable to believe that without the inclusion of a significant portion of the population, any endeavour would most certainly remain economically out of reach for the common individual.

This chapter aims to delineate a framework in which the design space is explored with the goal of identifying a trajectory with hypersonic velocities, for a specified

C. Bislip · E. Mooij (✉)

Faculty of Aerospace Engineering, Delft University of Technology, Delft, The Netherlands
e-mail: e.mooij@tudelft.nl

route and vehicular configuration, where individuals could travel without health screenings and prior training. This effectively translates to a trajectory where the mechanical loads experienced by the passengers are analogous to those experienced while at sea level and constant velocity or a maximum total mechanical load of $1 g_0$. However, due to the nature of the vehicle selected and the calculation of the g_0 -loads, the $1 g_0$ maximum is in effect an *increase* to values experienced while at sea level and constant velocity. To identify such a trajectory, a three degrees-of-freedom translational simulator is built in C++ with TU Delft Astrodynamics Toolbox (Tudat) and Parallel Global Multi-objective Optimiser (PaGMO) libraries. Tudat is an open-source C++ package that contains a set of publicly available libraries¹ of mathematical tools, environmental models, numerical integrators, and interpolators (linear and cube spline). PaGMO is ‘*an optimisation framework developed within the Advanced Concepts Team of the European Space Agency (ESA)*’.² It is an open-source software written in C++ that enables automatic parallelisation of its optimisers and includes evolutionary algorithms that can be used with multiple objectives, such as NSGA-II and MOEA/D (DE) [1–3].

The simulator, presented in Sect. 2, employed an open-loop guidance system with idealised navigation and control systems, where node control is the control method [4, 5]. For use with the evolutionary algorithms, the decision vector parameters are presented in Sect. 3, while the fitness vector components are discussed in Sect. 4. As the design space is not well understood, it is unknown how effective these available evolutionary algorithms would be. Hence, the extensive design space exploration discussed in Sect. 5 is performed to inform the selection of a genetic algorithm, an objective function case, and a given number of independent variables.

Finally, in Sect. 6, the trajectory optimisation will be performed via two approaches. One approach performs separate optimisations for each phase, denoted throughout as *decoupled*. Within the decoupled approach, the descent phase is performed for a variety of starting points. The ascent phase optimisation is then linked to its corresponding decoupled descent phase, with the goal of producing a linkable trajectory. The alternate approach combines the ascent and descent phases into one large problem, denoted throughout as *coupled*. A sub-optimal trajectory is found and used as a reference for localised optimisation, followed by a detailed analysis. Concluding remarks and suggestions for further study are given in Sect. 7.

2 Simulation Model

The most relevant components of the simulation model are sequentially discussed. These include the reference vehicle and mission in Sects. 2.1 and 2.2. This is followed by a summary of the simulated flight dynamics and aerodynamic heating in

¹ <https://github.com/Tudat>, accessed on 20-Mar-2022.

² <https://esa.github.io/pagmo2>, accessed on 20-Mar-2022.

Sects. 2.3 and 2.4. Finally, a key discussion about the vehicle’s guidance is presented in Sect. 2.5. It is important to note that though not presented nor discussed, the simulation model has been successfully validated against known reference missions.

2.1 Reference Vehicle

The reference vehicle is the second stage of the Sanger II system [7]. Though the first stage was not intended for passenger transport, it did consider an optional second stage for this express purpose. Known as the Hypersonic ORbital Upper Stage (HORUS), the second stage would be air launched with the goal of reaching orbit. The HORUS stage design experienced a series of versions. Of these, the most relevant are the HORUS-2B and HORUS-3B.

The HORUS-2B, which provides the overall geometric features shown in Fig. 1a, was a manned winged reusable vehicle with a crew of 2–4 and a small cargo payload. In this configuration, the vehicle would provide Space Station support, which was at the time estimated to be at an orbit with an altitude of 450 km at an

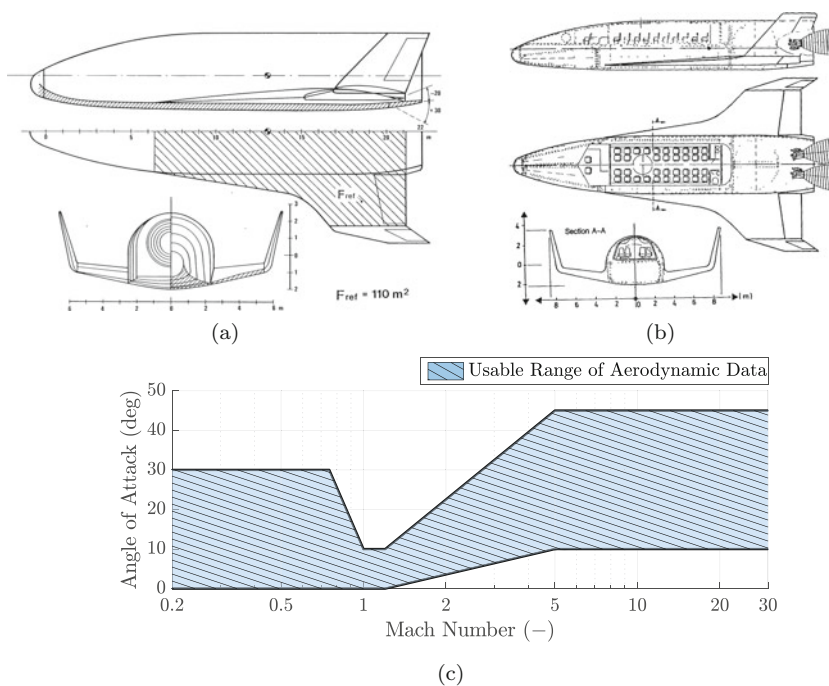


Fig. 1 DLR’s HORUS cross section, passenger concept, and trimmable envelope [7, 8, 10]. (a) HORUS-2B cross section. (b) Passenger HORUS-3B conceptual design. (c) Trimmable aerodynamic envelope

Table 1 HORUS characteristics [7, 8]

Description	Units	Value
MBB ATC-700 Engine	–	2
Max engine thrust (T_{\max})	kN	700
Specific impulse	s	472
Propellant mass	kg	65,000
Max payload mass	kg	7000
Re-entry mass	kg	26,029
I_{xx}	kg·m ²	119,000
I_{yy}	kg·m ²	769,000
I_{zz}	kg·m ²	806,000

inclination of 28.5° . As the HORUS-3B, shown in Fig. 1b, the vehicle would be capable of cabin modifications that would facilitate accommodating 36 passengers for the explicit purpose of space tourism. This version had a complete propulsion system with 65 Mg of propellant and 2 rocket engines. Each engine had a thrust of 700 kN and a specific impulse I_{sp} of 472 s [7].

The HORUS-3B engine characteristics will be used with the HORUS-2B aerodynamic database provided by MBB [8] and discretised by Mooij [9]. The vehicle's trimmable envelope is illustrated in Fig. 1c, whereas Table 1 presents a summary of the vehicle's characteristics.

2.2 Reference Mission

The reference mission to simulate will begin post-separation of the second stage at an altitude h_0 of 35 km and a velocity of Mach 6.6 with an initial heading χ_0 to the destination. The reference origin is the Koninklijke Luchthaven Schiphol (Amsterdam Airport Schiphol), and the reference destination is Washington Dulles International Airport. The simulation is terminated upon reaching the terminal area defined by a distance of 0.75° from the reference destination coordinates. At this distance, the Terminal Area Energy Management (TAEM) system would guide the system in the final phases of its flight, analogous to the Space Shuttle's Orbiter [15]. This is beyond the scope of the present work. A great circle is created by the reference origin and destination to define the trajectory's initial angular distance-to-go $\theta_{ToGo,0}$, equal to about 55.82° .

2.3 Flight Dynamics

The translational equations of motion of the system are defined by the gravitational force, the aerodynamic forces, and the resultant of all thrust forces. These forces are all defined in their own reference frames, which requires them to be transformed

to the inertial frame, \mathcal{F}_I , through a corresponding rotation matrix \mathbf{C} . The rotation matrix convention is such that the left arrow symbol \leftarrow indicates the direction of rotation. For example, $\mathbf{C}_{I \leftarrow A}$ would rotate a vector from the aerodynamic frame \mathcal{F}_A to the inertial frame \mathcal{F}_I .

$$\frac{d\mathbf{V}_I}{dt} = [\ddot{x}_I, \ddot{y}_I, \ddot{z}_I]^T = \frac{1}{m} (\mathbf{F}_{g,I} + \mathbf{F}_{A,I} + \mathbf{F}_{T,I}) \quad (1a)$$

$$= \frac{1}{m} (\mathbf{C}_{I \leftarrow V} \mathbf{F}_{g,V} + \mathbf{C}_{I \leftarrow A} \mathbf{F}_{A,A} + \mathbf{C}_{I \leftarrow B} \mathbf{F}_{T,B}) \quad (1b)$$

$$\frac{d\mathbf{r}_{cm,I}}{dt} = [\dot{x}_I, \dot{y}_I, \dot{z}_I]^T = \mathbf{V}_I \quad (2)$$

Though the force terms are each subsequently discussed in more detail, the final set of equations can then be put together as shown in Eqs. (1a) and (2). Equation (1a) expresses the time rate of change of the vehicle's inertial frame velocity \mathbf{V}_I in Cartesian coordinates yielding the vehicle's inertial frame acceleration, also in Cartesian coordinates. This acceleration, expressed as the second time derivative of position (i.e. \ddot{x}_I , \ddot{y}_I , and \ddot{z}_I), is in turn equal to the sum of inertial frame forces divided by the mass m . Similarly, Eq. (2) expresses the time derivative of the position of the vehicle's inertial frame centre of mass $\mathbf{r}_{cm,I}$ in Cartesian coordinates yielding the vehicle's inertial frame velocity \mathbf{V}_I , also in Cartesian coordinates and as the first time derivative of position (i.e. \dot{x}_I , \dot{y}_I , and \dot{z}_I).

The gravitational acceleration can be defined with first-order approximations, such as the Earth's flattening. The Earth's flattening can be mostly accounted for with the J_2 zonal harmonic and equivalent to $1.082626523 \times 10^{-3}$ [11]. To include these effects, the gravitational acceleration is defined with spherical coordinates in the vertical frame, \mathcal{F}_V .

$$\mathbf{F}_{g,V} = m \mathbf{g}_V = m [g_n, 0, g_d]^T \quad (3)$$

$$g_n = -3J_2 \frac{\mu}{r^2} \left(\frac{R_E}{r} \right)^2 \sin \delta \cos \delta \quad (4)$$

$$g_d = \frac{\mu}{r^2} \left[1 - \frac{3}{2} J_2 \left(\frac{R_E}{r} \right)^2 (3 \sin^2 \delta - 1) \right] \quad (5)$$

The gravitational force the Earth imposes on an object is shown in Eq. (3). In Eqs. (4) and (5), μ is the Earth's gravitational parameter equal to $398600.440 \text{ km}^3/\text{s}^2$, g_n is the gravitational acceleration in the north direction, and g_d is downwards along the radial direction. Furthermore, r is the radial distance of the reference vehicle to the centre of the Earth and δ is the geocentric latitude. The dependency on longitude is not present due to an assumed rotational symmetry of the central mass M of the Earth [11, 12].

The aerodynamic drag, D , side force, S , and lift, L , are a function of velocity V , angle of attack α , and sideslip angle β . These terms are defined in the aerodynamic frame based on airspeed. Though defined in the airspeed frame $\mathcal{F}_{A,A}$, they must be used in the groundspeed frame $\mathcal{F}_{A,G}$. However, since wind effects are not considered, they may be used as is to calculate the vehicle's dynamic pressure $\bar{q} = \frac{1}{2}\rho V^2$ (where ρ is the local density) and the aerodynamic coefficients for drag C_D , side force C_S , and lift C_L .

$$\mathbf{F}_{A,A} = -[D, S, L]^T = -\bar{q}S_{ref}[C_D, C_S, C_L]^T \quad (6)$$

Equation (6) presents the relevant expression for the aerodynamic forces. As side forces are not considered, through the assumption of $\beta = 0$, only the drag and lift coefficients C_D and C_L are determined from the aerodynamic database. They are, however, a function of the vehicle's Mach number M , angle of attack, body flap deflection angle δ_b , and elevon deflection angle δ_{el} . The deflection angles are determined to maintain a trimmed flight.

Regarding the thrust force term, the vehicle is modelled to have a single commanded thrust force $T_c = \xi T_{\max}$ that is applied through the \hat{x} -axis of the body frame, \mathcal{F}_B . The commanded thrust force is the combined value of the maximum available thrust from the rocket engines and a throttle setting ξ , which will be explained further in Sect. 2.5.

$$\mathbf{F}_{T,B} = [T_c, 0, 0]^T \quad (7)$$

2.4 Aerodynamic Heating

The heat input will be evaluated with a simplified expression known as the *Chapman Equation* [13]. The expression evaluates the convective heat flux per unit area at the stagnation point of the vehicle's nose, which has a known radius R_N .

$$q_c = C\rho^n V^m \left(1 - \frac{T_w}{T_{wad}}\right) \quad (8)$$

$$q_{rad} = \varepsilon\sigma T_w^4 = q_c \quad (9)$$

$$T_w = \sqrt[4]{\frac{q_c}{\varepsilon\sigma}} \quad (10)$$

Equation (8) is the hot-wall generalised form of Chapman's Equation, where $n = 0.5$, $m = 3.15$, and $C = 1.83 \times 10^{-8} R_N^{-0.5}$. The ratio of wall temperatures (T_w and T_{wad}) is determined by assuming thermal equilibrium and equating Eq. (8) with the radiative heat flux, as shown in Eq. (9). This requires an iterative process with an initial assumed value of either q_c or T_w and sequentially updating each other

until convergence [14]. In Eq. (10), ε is the surface emissivity and σ is the *Stefan-Boltzmann constant*. Following simplified and effective methods, the integrated heat load will be determined as the numerical integral of the heat flux q_c .

2.5 Guidance

Typical control methods used in aerospace applications use some form of feedback to apply control corrections about a known reference value (see Fig. 2). However, the current problem does not have known reference values for any control parameter. Additionally, the ideal controller is to have an instantaneous effect on command settings and aerodynamic trim. These considerations give reason to the use of node control, which utilises a set of control nodes to relate control parameters to an arbitrary independent variable. The control parameters are defined at each control node and interpolated at all other points. This brings forth the issues of identifying the number of control nodes, their relative locations, the independent variable, and the interpolation method.

The number of control nodes and their relative locations have a direct and significant effect on the design space and the resulting trajectory. Regarding the design space, a control node requires the definition of each applicable control parameter. A maximum of three control parameters are to be on either ascent or descent: angle of attack α , bank angle σ , and throttle setting ξ . These parameters, being defined at each control node, then require an associated value in the independent variable space.

Figure 3 illustrates the time histories of a series of variables for a typical coupled trajectory that could be considered as candidates for the independent variable. The general expectation of the independent variable is to be well behaved and monotonically increasing/decreasing. The overall purpose of this desired behaviour is to minimise oscillations (well behaved) and avoid ambiguities (monotonic) in the evaluation of the control parameters. In relation to the application in the problem, it is also known that a significant amount of energy must be steadily dissipated to

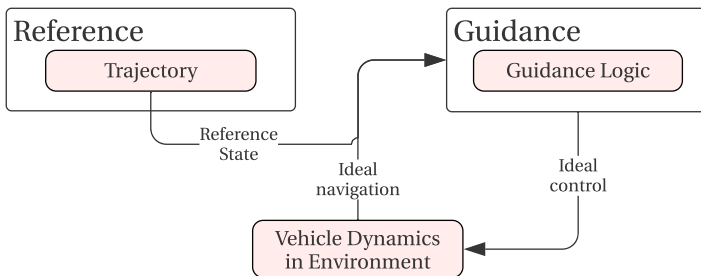


Fig. 2 Pseudo open-loop GNC system with ideal navigation module and ideal control module

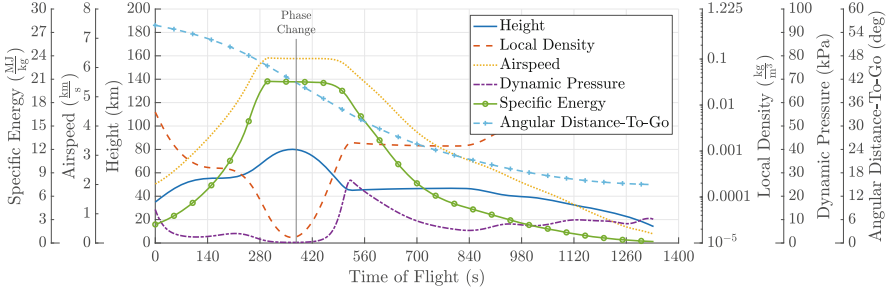


Fig. 3 Typical coupled trajectory time histories of candidate control node independent variables

maintain a reduced increase in g_0 -loads. This requires the independent variable to be dynamic enough to change the control parameters as needed yet sufficiently stable as to not generate sudden changes nor oscillations.

The Space Shuttle’s Orbiter landing guidance system, also known as the TAEM system, used the concept of *energy height* [15]. The successful Orbiter landings indicate that this concept indeed satisfies the requirements, particularly due to the combination of the vehicle’s height and velocity into a single value. Furthermore, the expression may also be known as specific energy, effectively removing any mass term from the relation. The formulation, based on a flat Earth, has clear differences from the expression that corresponds to a spherical Earth. However, the normalised distributions of the separate formulations, as implemented within any particular trajectory, will be equivalent. The variable’s utility with node control, as applied to re-entry vehicles, has been previously demonstrated by Mooij and Hänninen [4], Dijkstra et al. [5], and Hess and Mooij [6].

$$\hat{E} = \frac{E}{E_{\max}} = \frac{1}{E_{\max}} \left(g_0 h + \frac{1}{2} V^2 \right) \quad (11)$$

The maximum specific energy, E_{\max} in Eq. (11), is determined with the maximum height h_{\max} and maximum airspeed V_{\max} parameters defined in Sect. 3. Though these could be coupled into a single optimisation parameter encompassing the entire range generated by the separate parameters, it was chosen to not do so to allow an additional degree of freedom. Naturally, since E_{\max} is effectively an optimisation parameter that is defined prior to the evaluation of the trajectory and is also taken as the reference value, the useful range of values will also be affected. If at any point a trajectory’s scaled specific energy goes beyond 1, all evaluated control parameters would remain at their corresponding value of a scaled specific energy value of 1.

Figure 4 illustrates the scaling transformation on the specific energy time history of a typical trajectory, where the maximum scaled specific energy $\hat{E}_{\max, \text{actual}}$ evaluates to a value of 0.93. It is important to note that E_{\max} is set with initialised values and is not influenced from the trajectory’s values. Initial and final specific

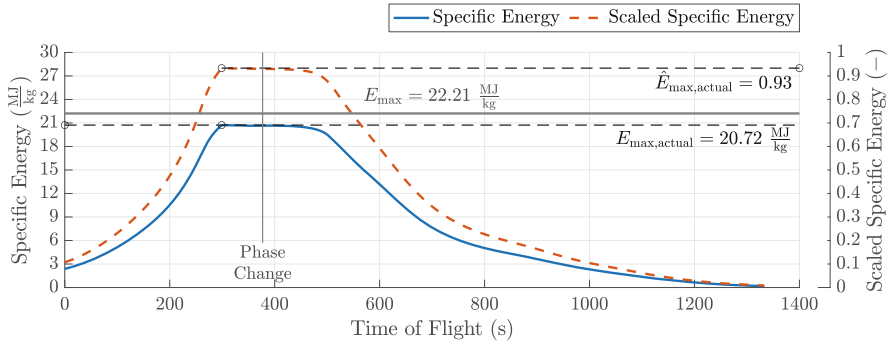


Fig. 4 Illustration of scaling $E \rightarrow \hat{E}$ [$h_{\max} \approx 119$ km, $V_{\max} \approx 6.5$ $\frac{\text{km}}{\text{s}}$]

Table 2 Nominal initial and final specific energy state source parameters

Description	Units	Initial	Final
Mach	–	6.6	2.5
Height	km	35.0	25.0
Specific energy	MJ/kg	2.38	0.518
Scaled specific energy ^a	–	0.107	0.023

^a Based on sample data from Fig. 4

energy states need not be fixed either; if fixed, four parameters are removed from the design space. The relevant values are presented in Table 2, where Mach numbers are converted to velocity with the NRLMSISE-00 atmospheric model. The sample scaled specific energy values used a scaling factor of $E_{\max} = 22.21 \frac{\text{MJ}}{\text{kg}}$, as shown in Fig. 4.

The previous work by Dijkstra et al. [5] concluded the Non-Uniform Independent Node (NUIN) method to be applicable for trajectory optimisation. Its implementation requires $n - 1$ initial values in the range of $[0, 1]$ for n nodes. These values are then cumulatively summed per each control node i in a node location vector, which is then scaled by the maximum value (the total sum). This procedure implicitly generates the control node intervals and ensures all node locations are within $[0, 1]$

$$\mathbf{x} = [x_1, x_2, \dots, x_{n-1}] \in [0, 1] \tag{12}$$

$$x_{\text{node},i} = \begin{cases} 0 & \text{if } i = 1 \\ \sum_{j=2}^i x_{j-1} & \text{if } i > 1 \end{cases} \tag{13}$$

$$\hat{x}_{\text{node},i} = \frac{x_{\text{node},i}}{x_{\text{node},n}} \tag{14}$$

$$\hat{E}_{\text{node,mapped},i} = (\hat{E}_{\max} - \hat{E}_{\min}) \hat{x}_{\text{node},i} + \hat{E}_{\min} \tag{15}$$

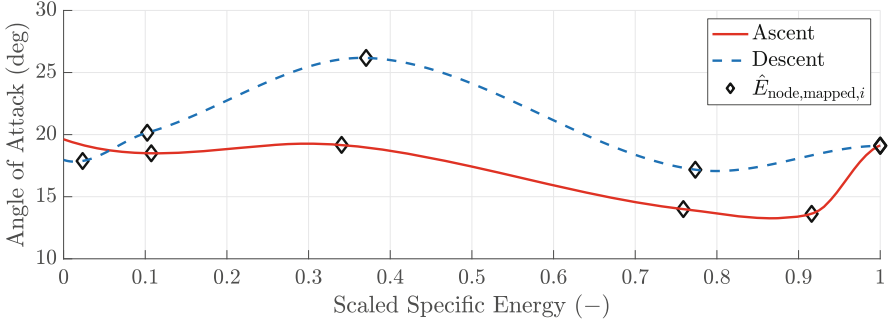


Fig. 5 Node mapping to the energy domain is followed by the application of guidance matrix values and the implementation of Hermite interpolation

$$\hat{E}_{\min} = \begin{cases} \hat{E}_{\text{initial}} & \text{if ascent} \\ \hat{E}_{\text{final}} & \text{if descent} \end{cases} \quad (16)$$

$$\mathbf{\Gamma} = \begin{bmatrix} \hat{E}_{\min} & \alpha_1 & \sigma_1 & \xi_1 \\ \hat{E}_2 & \alpha_2 & \sigma_2 & \xi_2 \\ \vdots & \vdots & \vdots & \vdots \\ \hat{E}_{n-1} & \alpha_{n-1} & \sigma_{n-1} & \xi_{n-1} \\ \hat{E}_{\max} & \alpha_n & \sigma_n & \xi_n \end{bmatrix} \quad (17)$$

The process is illustrated by evaluating Eqs. (12) through (14), followed by mapping the node locations to the energy domain through Eq. (15). The resulting guidance matrix $\mathbf{\Gamma}$ for each phase will then contain the nodal scaled specific energy as it is related to each control parameter initialisation. Equation (17) shows the structure of the guidance matrix created for each trajectory phase, where \hat{E}_{\max} is defined by Eq. (16).

As a piecewise polynomial, high degree polynomials could induce large oscillations (commonly referred to as *Runge's Phenomenon*). Figure 5 illustrates that this issue will be addressed by implementing cubic Hermite interpolators with smooth and continuous first derivatives at the endpoints, as developed by Han and Guo [16].

2.5.1 Skip Suppression

During descent, the flight-path angle will be controlled to ensure that the vehicle does not bounce back out of the atmosphere or experience excessive skipping. This is achieved by elaborating further on the derivation presented by Vinh et al. [17], followed by setting flight-path angle rate $\dot{\gamma} = 0$ if the flight-path angle $\gamma \geq 0$ and identifying the corresponding values of the remaining parameters. Neither thrust

vector control (TVC), such as gimbaling, nor side forces are included. These considerations allow for the derivation of an expression from which the bank angle can be determined. However, this bank angle may be different from the operational parameter that would be determined via node control.

$$\begin{aligned} \cos \sigma_{ss} = & \frac{m}{L + T_c \sin \alpha} (g_d \cos \gamma - g_n \sin \gamma \cos \chi \cdots \\ & \cdots - \omega_E^2 r \cos \delta (\cos \delta \cos \gamma + \sin \gamma \sin \delta \cos \chi) \cdots \\ & \cdots - \frac{V^2}{r} \cos \gamma - 2\omega_E V \cos \delta \sin \chi) \end{aligned} \quad (18)$$

$$\sigma_c = \begin{cases} \text{if descent \& } \rho > \rho_{\min} & \begin{cases} \sigma & \text{if } \gamma < 0.0 \\ \sigma_{ss} & \text{if } \gamma \geq 0.0 \end{cases} \\ \text{otherwise} & 0.0 \end{cases} \quad (19)$$

The resulting expression based on the Vinh et al. [17] derivation is shown in Eq. (18). The skip suppression bank angle σ_{ss} is shown to be a function of previously discussed forces, such as lift L , thrust T_c , and gravity in its components g_n and g_d . Additional required parameters are the vehicle's mass m , airspeed V , angle of attack α , flight-path angle γ , heading angle χ , geocentric latitude δ , and radial distance r from the Earth's centre. Finally, though potentially having negligible effects, the Earth's angular speed ω_E of $7.2921150 \times 10^{-5} \frac{\text{rad}}{\text{s}}$ is largely included for completion.

Equation (19), on the other hand, introduces the commanded bank angle logic. The expression shows that the bank angle will be fixed to zero during the ascent phase. During the decent phase, banking of any kind will be commanded if a minimum local density is being met. The said banking will be determined by node control if the flight-path angle γ is lower than zero or by skip suppression with Eq. (18) if the flight-path angle γ is non-negative.

2.5.2 Lateral Guidance

During descent, the vehicle will use the angle of attack to dissipate excess energy and the bank angle to ensure that a path that continuously decreases in altitude. Though a mild slip is not expected to be problematic, the oscillatory behaviour could also bring about undesired oscillatory evaluations of the guidance variables. Regardless, these considerations would not guide the vehicle towards its intended destination.

The vehicle's lateral guidance is implemented by restricting the heading error χ_e with a so-called heading error dead-band $\chi_{e,db}$ and a *bank reversal*. The heading error dead-band $\chi_{e,db}$ is taken to be a function of angular distance-to-go θ_{ToGo} from the intended target. The bank reversal is a sign change of the bank angle that occurs

if the magnitude of the heading error continues to increase beyond its corresponding dead-band. However, the goal is to reach the TAEM, which would allow the lateral guidance to aim at any point on the boundary of the TAEM. This creates a moving target that is bound by tangential great circles generated from the vehicle's location.

Figure 6 illustrates the arbitrary location of the vehicle at point A and the central target at point B . The circle around B represents the TAEM region, which is tangent to the great circles that originate from A at T_1 and T_2 . The heading angles required to follow the great circles would define χ_{T_1} and χ_{T_2} , and any heading angle within these bounds would indicate that the vehicle is aiming towards the TAEM region.

$$\chi_e = \begin{cases} 0 & \text{if } \chi_{T_1} \leq \chi \leq \chi_{T_2} \\ \chi - \chi_{T_1} & \text{if } |\chi - \chi_{T_1}| < |\chi - \chi_{T_2}| \\ \chi - \chi_{T_2} & \text{if } |\chi - \chi_{T_2}| < |\chi - \chi_{T_1}| \end{cases} \quad (20)$$

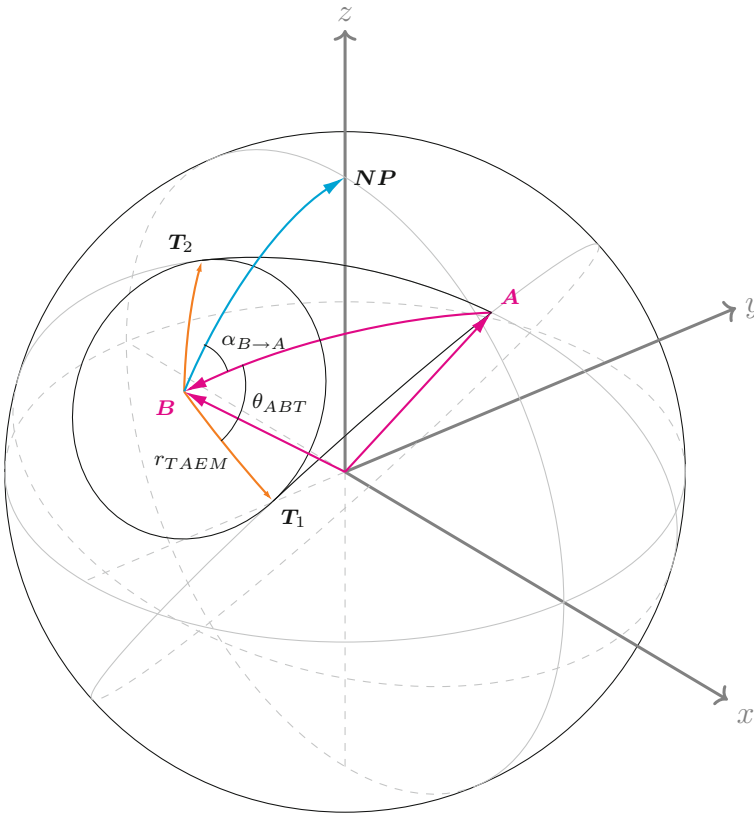


Fig. 6 Geometry for deriving the heading to tangent points on an arbitrary circle on the surface of a sphere

Equation (20) shows that a heading error only occurs when the vehicle is not aiming towards the TAEM region. To identify these bounds, the internal angles θ_{ABT_1} and θ_{ABT_2} are identified by using the modified Gram–Schmidt procedure. Vector algebra and Cartesian coordinates are used through the implementation of the procedure outlined below.

$$U_1 = A - \left(\frac{A \cdot \hat{B}}{\hat{B} \cdot \hat{B}} \right) \cdot \hat{B} \quad (21)$$

$$\hat{U}_1 = \frac{U_1}{\|U_1\|} \quad (22)$$

$$\hat{B} = \frac{B}{\|B\|} \quad (23)$$

$$\theta_{ABT_1} = \theta_{ABT_2} = \theta_{ABT} = \arccos \left[\frac{(A \cdot B) \tan r_{TAEM}}{A \cdot \hat{U}_1} \right] \quad (24)$$

$$\alpha_{B \rightarrow T_{1,2}} = \alpha_{B \rightarrow A} \pm \theta_{ABT} \quad (25)$$

Equations (21) through (23) facilitate the calculation of the internal angle θ_{ABT} with Eq.(24). In this equation, r_{TAEM} is the radius of the TAEM region and effectively the distance from point B at which the tangent points are located. To then identify the coordinates of the tangent points, the azimuth $\alpha_{B \rightarrow A}$ from the central target (point B) to the vehicle (point A) is first determined. Equation (25) is then used to calculate the heading $\alpha_{B \rightarrow T_{1,2}}$ to tangent points T_1 and T_2 . Once the coordinates of T_1 and T_2 are known, the bounding heading angles of the vehicle (χ_{T_1} and χ_{T_2}) and the corresponding dynamic target angular distance-to-go $\theta_{ToGo,dyn}$ are calculated. In the event that $\chi_e = 0$, as determined with Eq. (20), the vehicle would have a heading angle that aims towards the TAEM region. In this case, a similar approach is used to determine the coordinates of the TAEM boundary intersection point, which then allows for the calculation of the angular distance $\theta_{ToGo,dyn}$.

3 The Decision Vector

The approach to the current problem will be to structure the decision vector into two sets of optimisation parameters: *non-nodal* and *nodal* parameters. Both sets are a function of the trajectory phase to be evaluated, especially when comparing coupled and decoupled decision vectors.

All parameters not associated with node control are shown in Table 3. Their associated exploration bounds are provided for each trajectory type. From these non-nodal parameters, the additional mass $m_{\text{additional}}$, the phase termination distance ratio ζ , and the decoupled descent distance-to-go ratio $\hat{\theta}_{ToGo,i}$ warrant additional context.

Table 3 Non-nodal parameters and exploration bounds

Description	Parameter	Units	Exploration bounds					
			Ascent		Descent		Coupled	
			Lower	Upper	Lower	Upper	Lower	Upper
Initial flight-path angle	γ_0	deg	1.5	8.0	-89.9	0.0	1.5	8.0
Maximum airspeed	V_{\max}	km/s	a		3.0	7.0	3.0	7.0
Maximum height	h_{\max}	km	a		70.0	200.0	70.0	200.0
Additional mass	$m_{\text{additional}}$	Mg	a		0.0	30.0	0.0	30.0
Phase termination distance ratio	ζ	-	a		-		0.1	0.7
Ascent optimisation airspeed	$V_{f,\text{ascent}}$	km/s	a		-		-	
Ascent optimisation height	$h_{f,\text{ascent}}$	km	a		-		-	
Final ascent flight-path angle	γ_f	deg	a		-		-	
Initial distance-to-go ratio ^b	$\hat{\theta}_{T_oG_o,i}$	-	-	-	0.3	0.9	-	-
Descent optimisation airspeed	$V_{0,\text{descent}}$	km/s	-		0.75	7.0	-	
Descent Optimisation Height	$h_{0,\text{descent}}$	km	-		35.0	200.0	-	

^a Fixed to corresponding linking value determined by decoupled descent optimisation

^b Will be evaluated at fixed intervals of 0.15

Though nominal operations of the reference vehicle would have taken it to orbit, the current implementation not only limits the total mechanical loads but might also require longer operations within a thicker atmosphere. The possibility of increased propellant mass is then considered by also increasing the vehicle's dry mass as a function of the additional mass parameter.

$$m_{\text{dry,actual}} = m_{\text{dry}} \left[1 + 0.3 \left(\frac{m_{\text{additional}}}{m_0} \right) \right] \quad (26)$$

The phase termination distance ratio ζ is used during the ascent phase as a necessary condition before terminating. It means that a portion of the initial central target angular distance-to-go $\theta_{T_oG_o,0}$ must be travelled before the next phase can commence. This translates to the minimum angular distance required θ_{required} , which is the minimum angular distance to travel from the destination coordinates.

$$\zeta = \left(\frac{\theta_{\text{required}}}{\theta_{T_oG_o,0}} \right) \quad (27)$$

The initial decoupled descent distance-to-go ratio $\hat{\theta}_{T_oG_o,i}$ parameter is only used for a decoupled descent phase to fix the initial location of the vehicle with respect to the central target. The initial angular distance-to-go $\theta_{T_oG_o,i}$ is then the angular distance from the central target at which the simulation begins.

$$\hat{\theta}_{T_oG_o,i} = \left(\frac{\theta_{T_oG_o,i}}{\theta_{T_oG_o,0}} \right) \quad (28)$$

Table 4 Nodal parameters and exploration bounds

Description	Parameter	Units	Decoupled				Coupled			
			Ascent		Descent		Ascent		Descent	
			Lower	Upper	Lower	Upper	Lower	Upper	Lower	Upper
Angle of attack	θ	deg	10.0	20.0	0.2	50	10.0	20.0	0.0	50
Bank angle	σ	deg	-		0.0	89.0	-		0.0	89.0
Throttle setting	ξ	-	0.2	1.0	-		0.2	1.0	0.2	1.0

Table 5 Phase termination conditions

Description	Parameter	Units	Condition	
			Ascent	Descent
Ascent phase termination ^a	Eq. (29)	-	TRUE	-
Minimum allowable mach number	M_{min}	-	-	1.05
Minimum allowable height	h_{min}	km	$\frac{9}{10} h_0$	10.0
Minimum angular distance from central target	$\theta_{ToGo,min}$	deg	0.75	
Change in Angular distance from central target ^b	$\Delta\theta_{ToGo}$	deg	>0	

^a Not applicable to decoupled ascent trajectories

^b Used to indicate that the vehicle is travelling away from the central target

Table 4 presents the nodal parameters along with their general bounds as they are used in both decoupled and coupled evaluations. Though they are similar, the distinction lies in the idea that in a decoupled descent phase it is assumed that there is no more propellant mass available, whereas a coupled descent phase may still have leftover propellant from its coupled ascent phase.

Table 5 presents the phase termination conditions required throughout the evaluation of any decision vector. The table first references the necessary condition for a phase change in either a coupled trajectory or the ascent phase of a decoupled trajectory type.

$$(\hat{\theta}_{ToGo} \geq \zeta) \wedge (\gamma \leq 0) \wedge (\dot{\gamma} \leq 0) \rightarrow \text{Terminate ascent phase} \tag{29}$$

Equation (29) shows that a combination of three conditionals must be simultaneously met. The first condition being that $\hat{\theta}_{ToGo}$ must be equal or greater than ζ , which is the phase termination distance ratio defined in Eq. (27). This means that the vehicle must have first travelled a minimum distance before allowing a phase change. The second and third conditionals indicate that the vehicle’s flight-path angle, γ , and corresponding rate, $\dot{\gamma}$, must both be equal to or lesser than zero. These mean that the vehicle must aim towards the Earth’s surface without levelling back to a horizontal flight.

The lowest Mach number the descent phase will evaluate, M_{min} , is due to the reference vehicle’s aerodynamic database not being defined for subsonic velocities. The lowest possible heights are included to terminate ascent phases that neither maintain nor increase the vehicle’s height and to terminate descent phases that have

descended far beyond the height required for nominal TAEM interface conditions (see Table 2 for more details).

4 The Fitness Vector

The evolutionary algorithms available within PaGMO use a combination of objective functions, equality constraints, and inequality constraints to define an individual's fitness. For simplicity, the current implementation will focus on the objective functions determined by calculating a series of cost functions, constraint violations, and penalties that must be minimised. The corresponding expressions are computed according to the nature of the variables in question. Each value is scaled by a relevant limiting value, yielding a series of non-dimensional values, which can then be summed in different combinations for the fitness vector.

The costs have been defined to minimise the total angular distance-to-go, the total propellant mass, and the integrated heat load.

$$C_{\theta_{ToGo}} = 100\hat{\theta}_{ToGo,f} = 100 \left(\frac{\theta_{ToGo,f}}{\theta_{ToGo,0}} \right) \quad (30)$$

$$C_{mass} = 100 \left(\frac{m_{dry,actual} - m_{dry}}{m_{dry}} \right) + \frac{|V_0 - V_{max,actual,a}|}{I_{sp}g_0 \ln(m_{0,actual}/m_{f,a})} \quad (31)$$

$$C_Q = \frac{1}{t_{tof}q_{c,a}} \sum^N q_c(t) \Delta t \quad (32)$$

Constraint violations are used for all constrained variables, such as the g -load, dynamic pressure, bending moment, and nose-cone stagnation heat flux. These constraints, summarised in Table 6, would produce a violation only if the variable in question goes beyond the imposed constraint. The generic form is given by

Table 6 Summary of operational constraints

Description	Symbol	Units	Value	Source
Total g_0 -Load	n_a	g_0	1.0	Current study
Dynamic pressure	\bar{q}_a	kPa	25.0	a
Bending moment	$(\bar{q}\alpha)_a$	kPa·deg	250.0	a
Stagnation heat flux	$q_{c,a}$	kW/m ²	700.0	a
Directional jerk ^b	j_a	m/s ³	2.0 ^b	c

^a See Dirkx and Mooij [18]

^b Secondary constraint, not enforced

^c See ISO [19]

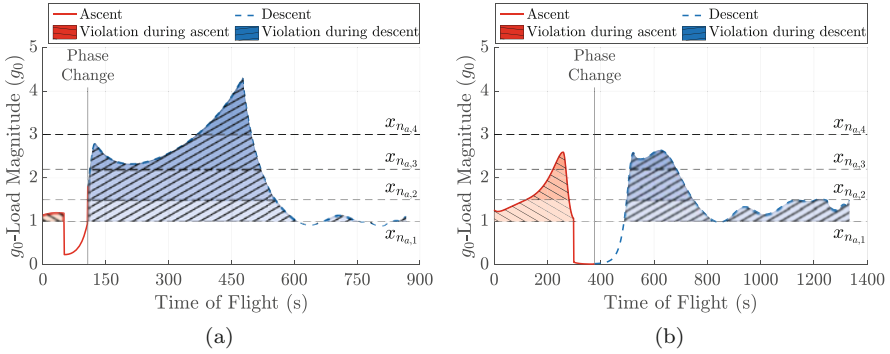


Fig. 7 Sample data for computation of constraint violations. (a) High peak low duration violation. (b) Low peak long duration violation

$$V_c = \frac{x_{\max} - x_c}{x_c} + \frac{\sum_{i=1}^n (x_i - x_c) \Delta t}{t_{tof} \cdot x_c} \quad (33)$$

where the first term in Eq. (33) corresponds to the effect of the maximum constraint violation. The second term corresponds to the effect of the magnitude of each individual violation along with its duration throughout the trajectory, i.e., the area bounded by the portions of the curve that are beyond the constraint and the constraint line. Furthermore, Eq. (33) will be applied separately to each trajectory phase due to the difference in expected dynamics and operating parameters.

Figure 7 illustrates the combined effects of the duration of a phase, the overall trends, and the constraints being imposed, as expected from Eq. (33). Figure 7a shows how increased values can have a persistent effect that may be reduced by a low duration, whereas Fig. 7b shows how lower values can have a more significant resulting effect if prolonged throughout the trajectory. It is also possible to see the difference in relative calculation throughout each trajectory phase, accentuating the importance of calculating separate values for each phase.

Additional penalties are incurred for undesired trajectory characteristics. These include flight-path angles that have the ‘wrong sign’ during each phase and non-monotonic scaled specific energy profiles. The rationale for the flight-path angles is to avoid opposing changes in elevation during each trajectory phase, while the monotonically increasing/decreasing profiles would ensure unique evaluations of the guidance variables determined through node control.

$$P_\gamma = \frac{1}{360} \left| \left(x_{\max} + \frac{\sum_{i=1}^n x_i \Delta t}{t_{tof}} \right) \right| \begin{cases} \text{if ascent,} & \forall x < 0 \\ \text{if descent,} & \forall x > 0 \end{cases} \quad (34)$$

$$P_{\hat{E}} = \sum_{i=2}^n |x_i - x_{i-1}| \begin{cases} \text{if ascent,} & x_i < x_{i-1} \\ \text{if descent,} & x_i > x_{i-1} \end{cases} \quad (35)$$

Simply put, during ascent, it is desired to have non-negative flight-path angles and a monotonically increasing scaled specific energy profile, while during descent it is desired to have non-positive flight-path angles and a monotonically decreasing scaled specific energy profile. These characteristics can be determined from the conditionals in Eqs. (34) and (35).

$$P_{E_{f,a}} = 10 \frac{|E_{0,d} - E_{f,a}|}{E_{0,d}} \quad (36)$$

$$P_{\gamma_{f,a}} = 10 \frac{|\gamma_{0,d} - \gamma_{f,a}|}{\gamma_{0,d}} \quad (37)$$

Additional penalties are imposed on decoupled ascent trajectories. Shown in Eqs. (36) and (37), these are intended to connect the final specific energy and flight-path angle of the ascent phase to target values corresponding to initial values of the descent phase.

5 Design Space Exploration

The design space is understood to be prohibitively large, as it is not possible to evaluate all combinations within a parameter set. Furthermore, the problem is not well understood given that this particular implementation of the reference vehicle has not been previously evaluated. Thus, a variety of Monte-Carlo evaluations were initially performed to guide the selection of individuals for the initial populations and to inform the ranges of the decision vector parameters. This exercise was done in an effort to improve the effectiveness of the optimisation process of both the design space exploration and the trajectory optimisation itself.

Figure 8 shows the results of a Monte-Carlo evaluation. This test was completed for an unconstrained run of a coupled trajectory type, a population of 100,000 individuals with five (5) control nodes, which were randomly selected from a uniform distribution with a given random seed. The propagation/guidance step sizes of 1 s were selected to reduce the computational load while remaining within the vehicle's validated performance capabilities.

Figure 8a shows a distribution of values whose ranges for the maximum body frame mechanical load are significantly higher than desired (much greater than 1 g_0) while also remaining far from the intended target. In fact, the figure shows a high concentration of individuals with n_{\max} of about 5 g_0 that reached a minimum angular distance from the central target of about 48°. This observation is confirmed by the top left chart of the violation histograms shown in Fig. 8b, further illustrating the low probability of randomly identifying feasible individuals.

A design space exploration is performed to evaluate the effectiveness of a variety of optimisation approaches. This will be done by evaluating various of the optimisers available in PaGMO with a series of combinations of initial population

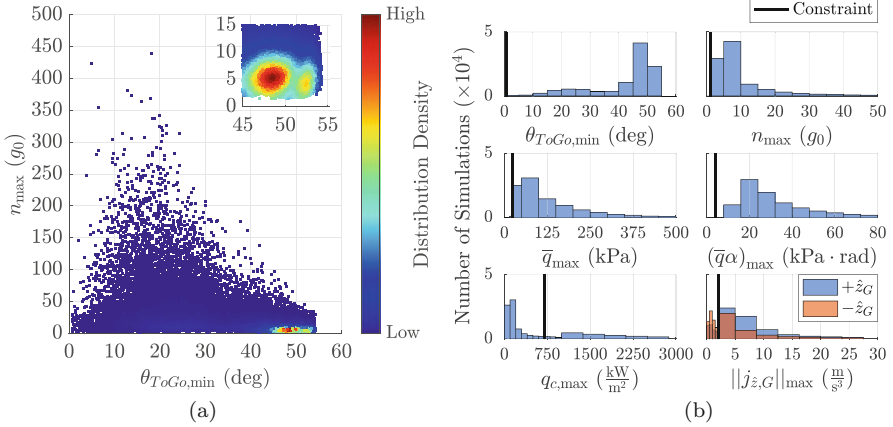


Fig. 8 Uniformly distributed random individuals with initial random seed 1 and 5 control nodes. (a) Variable comparison. (b) Violation histogram

Table 7 Fitness vector terms per objective function case (OFC)

Term	Eq.	Type	Objective function case														
			A	B	C	D	E	F	G	H	I	J	K	L	M ^a	N	
Angular distance-to-go	(30)	C	x	x	x	x	x	x	x	x	x	x	x	x	x	x	x
Fuel mass	(31)	C										x					x
Heat load	(32)	C									x	x				x	x
Total g_0 -Load	(33)	V		x	x	x	x	x	x	x	x	x					
Dynamic pressure	(33)	V			x	x	x	x	x	x	x	x					
Bending moment	(33)	V				x	x	x	x	x	x						
Heat flux	(33)	V					x	x	x	x	x						
Flight-path angle	(34)	P						x	x	x	x		x				
Monotonic energy state	(35)	P							x	x	x						
Grouping 1 ^b	–	V										x	x	x	x	x	x
Grouping 2 ^c	–	P												x	x	x	x
Decoupled ascent $E_{f,a}$	(36)	P ^d	x	x	x	x	x	x	x	x	x	x	x	x	x	x	x
Decoupled ascent $\gamma_{f,a}$	(37)	P ^d	x	x	x	x	x	x	x	x	x	x	x	x	x	x	x

Term Types: Cost (C), Constraint Violation (V), and Penalty (P)

^a OFC-M.1 augments the total g_0 -load violation by a factor of 10

^b Grouping 1 is composed of all V-type terms

^c Grouping 2 is composed of all P-type terms

^d Applied when linking decoupled phases

sources, a number of control nodes, initial random seed initialisers, objective function cases, single- vs multi-objective, and constrained vs unconstrained. The objective function cases are defined in Table 7, where they are composed of different combinations of the costs, constraint violations, and penalties introduced in Sect. 4.

Table 8 Design space exploration factors to investigate

Factor	Options
Number of nodes	[5, 6, 7]
PRNG seed initialiser	[234998684, 88236, 5927502]
Initial populations	PRNG vs. Individual ranking
Number of objectives	Single vs. Multi/many
Constraint Type	Unconstrained vs. Constrained
Optimization algorithm	NSGA-II, MOEA/D (DE), IHS
Objective function case	OFC-A to OFC-N (Table 7)

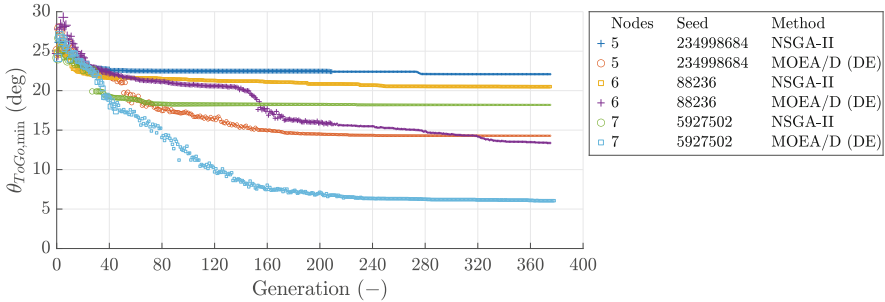


Fig. 9 Generational history of $\theta_{ToGo,min}$ for an unconstrained single-objective coupled (ascent phase only), OFC-A, and initial population sourced from fitness vector ranking

With the factors presented in Table 8, the design space exploration optimisations had a maximum number of generations of $N_{max} = 500$ with a minimum equal to 75% of the maximum. Within the 75% and 100%, the optimisation continued until the change of the population’s average fitness was negligible.

Figure 9 and Table 9 present an excerpt of the variety of summarising tools created to analyse the data. Figure 9 shows the generational history of $\theta_{ToGo,min}$ corresponding to the population’s top individual for a variety of factors and an OFC-A. It is possible to observe how, with this particular set of cases, NSGA-II [1] had an overall tendency to converge to a much higher $\theta_{ToGo,min}$, whereas MOEA/D (DE) [2] was able to reach lower values. Within MOEA/D (DE), it is also possible to see reduced $\theta_{ToGo,min}$ as the number of control nodes increased. Additionally, the MOEA/D (DE) profiles show signs of increased diversity as the overall $\theta_{ToGo,min}$ is reduced. This can be observed by the ‘noise’ as the overall trends continue to decrease the $\theta_{ToGo,min}$. Table 9 presents a summary of the minimum values of the constrained variables for various objective function cases with the MOEA/D (DE) genetic algorithm. The colour coding corresponds to the number of nodes that produced the minimum value.

It is clear that the numerous evaluations resulting from the combination of factors being investigated (see Table 8) yield a dataset from which drawing conclusions becomes a challenge. As a result, key indicators were used to draw conclusions due to the overall complexity of the data. Among them was the consistency of satisfying

Table 9 Coupled ascent phase constrained multi-objective: MOEA/D (DE). Population sourced from fitness vector ranking

MOEA/D (DE)														
Objective Function Case		B	C	D	E	F	G	H	I	J	K	L	M	N
$\sigma_{ fitness }$	5	19.02	9.11	18.32	20.09	498.6	16.66	13.82	926.0	277.2	441.0	8.68	330.8	567.8
	6	18.90	13.15	14.71	16.76	18.52	16.52	760.1	344.5	13.19	16.40	19.42	907.8	406.8
	7	10.70	23.27	22.10	12.63	17.33	398.3	1269	1210	13.23	19.48	16.18	14.54	17.24
Variable	S.F.	Scaled variable minimum per objective function case												
$\theta_{T \rightarrow G_0}$	deg	3.37	1.01	1.00	1.02	1.10	3.59	1.17	8.31	3.40	4.00	2.20	1.27	1.46
n	g_0	1.55	1.67	1.53	1.17	1.11	1.24	1.56	1.44	1.12	1.00	1.61	1.17	1.18
\bar{q}	kPa	14.3	1.00	1.09	1.03	1.00	1.00	1.19	1.00	1.00	1.00	1.00	1.00	1.00
$\bar{q}\alpha$	kPa·rad	2.83	1.65	1.69	1.56	1.60	1.47	1.76	1.64	1.35	1.41	1.42	1.00	1.26
q_c	kW/m ²	118.4	11.13	12.72	12.27	5.29	6.85	6.85	2.56	5.67	2.31	2.51	6.44	1.00
Q	MJ/m ²	21.73	17.96	23.26	32.40	7.83	10.03	3.95	4.38	6.02	9.98	2.22	9.12	1.00
$\sigma_{ fitness }$ = Fitness magnitude standard deviation		Variable minimum as achieved by												
S.F. = Scaling Factor = Variable minimum among all objective function cases		<div style="display: flex; justify-content: space-around; align-items: center;"> = 5 nodes = 6 nodes = 7 nodes </div>												

Table 10 Trajectory optimisation input parameters

Parameter	Selection
Population size	100
Population source	Fitness vector ranking
Max. generations	3000 \rightarrow 100
Control nodes	7
Objective type	Multiple
Objective function case	OFC-N ^a
Optimising Algorithm	MOEA/D (DE)
Time steps ($\Delta t_p \Delta t_g$)	1s \rightarrow 0.05s 1s \rightarrow 0.1s

Arrow (\rightarrow): general then localised optimisation

^a Parallel evaluation will be done with OFC-I

constraints with the recurrence of low maximum values, reduced dimensionality in both decision vector and fitness vector space, and the population's diversity.

Table 10 presents a summary of the resulting optimization primary parameters to be used for the optimisation of both coupled and decoupled trajectories. From these parameters, the maximum number of generations and the propagation and guidance time steps (Δt_p and Δt_g) show two sets, corresponding to the initial optimisation and a localised refined optimisation.

6 Trajectory Optimisation

The trajectory optimisation was performed with two separate approaches. The decoupled approach, presented in Sect. 6.1, begins with the parallel evaluation of a descent phase optimisation with five different starting points defined by $\hat{\theta}_{ToGo,i}$. The initial conditions of these evaluations are then analysed with the purpose of extracting terminal state target values for ascent phase optimisations. These evaluations are then intended to be linked such that a continuous trajectory would then be generated. Details and analysis are presented throughout the section leading to the conclusion that a continuous trajectory was not found.

Section 6.2, on the other hand, presents the coupled approach, where a general optimisation is performed and then followed by a localised optimisation. The section then discusses the resulting sub-optimal individual found from the approach.

6.1 Decoupled Approach

Following the parameter bounds introduced in Table 3 and the optimisation parameters detailed in Table 10, the decoupled approach begins by evaluating the descent phase at five different decoupled descent distance-to-go ratios. These evaluations

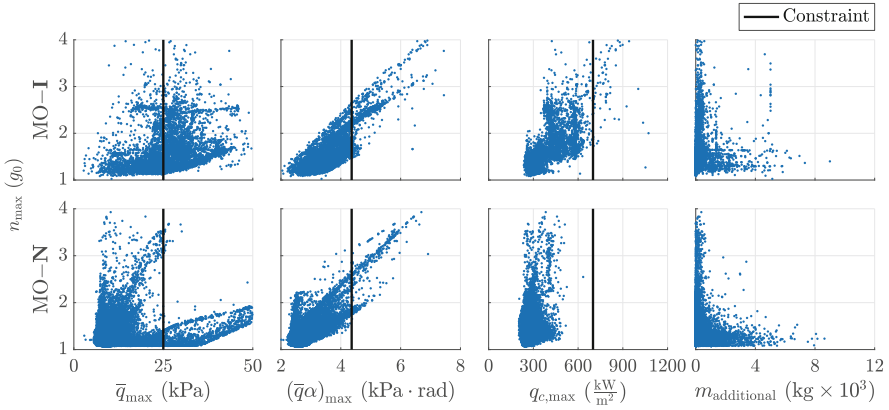


Fig. 10 Decoupled descent single- and multi-objective (SO & MO) variable comparisons at TAEM for OFC-I and OFC-N with $\hat{\theta}_{ToGo,i} = 0.30$

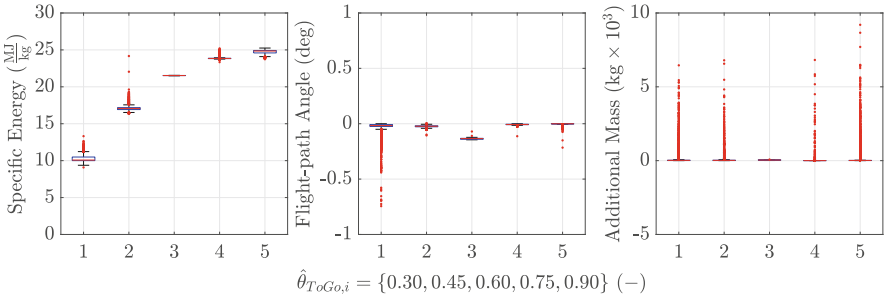


Fig. 11 Boxplots of phase change values of filtered individuals for all $\hat{\theta}_{ToGo,i}$

were initialised with $\hat{\theta}_{ToGo,i} = \{0.30, 0.45, 0.60, 0.75, 0.90\}$ and yielded numerous individuals that satisfied most of the operational constraints shown in Table 6.

Figure 10 shows the maximum g_0 -load throughout the decoupled decent phase compared to the maximum values for dynamic pressure, bending moment, and stagnation heat flux. These point clouds show the resulting individuals throughout all generations that have reached the TAEM. As calculated, a significant portion of the population was close to the $1-g_0$ constraint. Similar distributions were observed for all other $\hat{\theta}_{ToGo,i}$, though with reduced total populations as $\hat{\theta}_{ToGo,i}$ increased. This was to be expected as larger $\hat{\theta}_{ToGo,i}$ mean larger initial angular distances-to-go at the start of the decoupled descent phase.

The selection criteria from all individuals that reached the TAEM include the satisfaction of all constraints presented in Table 6 with the distinction of $n_{max} \leq 1.15 g_0$. The initial specific energy $E_{0,d}$, initial flight-path angles $\gamma_{0,d}$, and additional mass of the individuals selected from the decoupled descent phase are presented in Fig. 11.

The figure shows the distribution of the values as boxplots for each $\hat{\theta}_{ToGo,i}$. These boxplots illustrate the distribution of data through its quartiles, where outliers are depicted at red discrete points beyond the black lines. The 25th and 75th percentiles are, respectively, illustrated by the lower and upper bounds of each blue box, and the sample's median (50th percentile) is shown as the single red line within each box.

The distributions show an increase of the initial specific energy as $\hat{\theta}_{ToGo,i}$ increases, which is to be expected. Curiously, the case of $\hat{\theta}_{ToGo,i} = 0.60$ yielded values that were within the trend yet with an increasingly small spread, indicating a significantly small population compared to the other cases. A possible explanation would be need for additional generations to increase the total individuals found.

The initial decoupled descent flight-path angles were observed to have a trend towards zero. Though the parameter's upper bound was fixed at $\gamma_{0,d,max} = 0$, there were clear outliers, especially for the case of $\hat{\theta}_{ToGo,i} = 0.30$. These outliers can be explained by the understanding that the closer the vehicle is to the TAEM, the lower the need for an extended downrange, hence the possibility of a more negative initial flight-path angle. Additional to the outliers, the case of $\hat{\theta}_{ToGo,i} = 0.60$ shows a median lower than -0.1 deg. However, all values are within a relatively close distance from zero, which would be compatible with the goal of minimising mechanical loads throughout the trajectory.

All decoupled decent cases had a tendency to minimise the additional mass to the point of being borderline negligible. Since the effect of the additional mass parameter on the decoupled descent cases was to increase the total dry mass of the vehicle, there was a possibility that the parameter was unnecessarily limiting the optimisation. Understanding that there was a minimum dry mass (nominal dry mass of the vehicle), this driver to have almost negligible additional mass opened up the possibility of the optimiser driving the system to a configuration that carried the nominal fuel mass or less. However, the spread of outliers indicates a possibility of potential individuals with additional mass. This led to the definition of three mass cases for the decoupled ascent optimisation: minimised additional mass, nominal fuel mass, and minimised fuel mass.

The median values of the selected initial decoupled descent specific energy and flight-path angle ($E_{0,d}$ and $\gamma_{0,d}$) were then taken as optimisation targets for the final state of the decoupled ascent phase as $E_{f,a}$ and $\gamma_{f,a}$, along with the values of the corresponding trajectory linking parameters introduced in Table 3. The optimisation parameters for the decoupled ascent phase were the same as for the decoupled descent, shown in Table 10. Once evaluated, the selection criteria for all mass cases required a relaxed maximum n_{max} of $1.50 g_0$. This was due to the lack of individuals that had reached their corresponding transition point ($\hat{\theta}_{ToGo} = \hat{\theta}_{ToGo,i}$) with tighter constraints.

The distributions of specific energy at the end the decoupled ascent phase ($\hat{\theta}_{ToGo} = \hat{\theta}_{ToGo,i}$) are shown in the left plot of Fig. 12, with ascent optimisation targets as black lines. The most significant observation is that none of the distributions reached the targeted specific energy levels. Most of the distributions followed

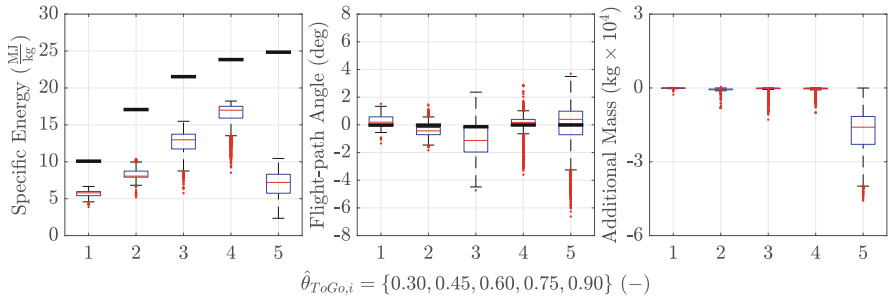


Fig. 12 Decoupled ascent transition point boxplots of filtered individuals for various $\hat{\theta}_{ToGo,i}$ for minimised fuel mass and $n_{max} \leq 1.50 g_0$. Ascent optimisation targets shown in black lines

the decreasing trend of the target energy levels as $\hat{\theta}_{ToGo,i}$ decreased. However, the case of $\hat{\theta}_{ToGo,i} = 0.90$ was not only significantly lower than the required target but it did not follow the decreasing trend. It is understood that this phenomenon occurs due to the selection of the individuals with a reduced n_{max} that have reached $\hat{\theta}_{ToGo} = 0.90$, while they have not had the temporal nor spatial opportunity, or need, to convert the propellant mass’ energy into kinetic and potential energy. Simply put, the vehicle reaches the phase transition point too fast without the need to consume more propellant. Though it is clear that there could be a larger conversion of energy within the relatively short distance, especially with the available propellant, it is expected that the g_0 -loads would be significantly larger. This ultimately would exclude these individuals from the distributions of interest. Regarding the transition point flight-path angles, the largest variation was brought about by $\hat{\theta}_{ToGo,i} = 0.90$, also pointing to the difficulty of identifying individuals that can reach the required specific energy levels without extreme n_{max} values. Though not illustrated, all mass cases showed an overall tendency towards the nominal mass configuration, which shows a preference of a lighter vehicle to reduce the maximum g_0 -loads during the ascent phase.

From these distributions, it can be said that the decoupled ascent optimisation process successfully drives the populations to the desired phase transition point ($\hat{\theta}_{ToGo} = \hat{\theta}_{ToGo,i}$) yet is unable to produce the specific energy targets required by the decoupled descent optimisation with reduced n_{max} . Though the actual fuel consumption and time histories are not discussed, the fact remains that the current decoupling of the search space drives the descent phase optimisation into a region of the design space that does not intersect with the region where the decoupled ascent phase optimisation yields lower n_{max} values. This is a reasonable conclusion, given that the decoupled descent optimisation does not have a strong link to the decoupled ascent phase optimisation. Hence, a functional relationship is not available with which the optimisation process can guide the populations towards regions that are intersecting. As such, a linkable decoupled trajectory was not identified.

6.2 Coupled Approach

The coupled approached optimisation was performed according to the optimisation parameters shown in Table 10. Figure 13 shows the maximum g_0 -load throughout the entire trajectory compared to the maximum values for dynamic pressure, bending moment, and stagnation heat flux. These point clouds show the resulting individuals throughout all generations that have reached the TAEM. The lower row shows that with OFC-N the maximum dynamic pressures satisfied the constraint with sufficient margin, unlike the corresponding decoupled descent phase. The maximum bending moments had a spread across the constraint line that was skewed towards satisfying the constraint, and unlike the decoupled decent phase, the heat flux had a larger concentration around the constraint line. Unlike with the decoupled approach, the separate phases of the coupled approach did not produce trajectories with max g_0 -loads approaching values as close to 1 g_0 .

A sub-optimal individual was identified from the point clouds, as shown in Fig. 14 with the red dot. This value, denoted as $n_{\max,\min}$ for the minimum of the maximum g_0 -loads, was found to be 1.19 g_0 . When comparing the relative location of the red dot within the distributions of each of the variables shown in Fig. 14, the maximum bending moment is approximate to its median, whereas the maximum heat flux is closer to the left tail of the distribution. The additional mass, however, is at approximately 5500 kg and towards the right tail of the distribution.

To further drive the loads towards the constraint of 1 g_0 , the sub-optimal point was then used as a reference for local optimisation. The decision vector was expanded by 1-, 2-, 5-, and 10%, and a Monte-Carlo test was performed with 5000 individuals and refined time steps of $\Delta t_p = 0.05$ s and $\Delta t_g = 0.1$ s. Not only did this not drive the $n_{\max,\min}$ of the population closer to the constraint, but many individuals did not reach the TAEM. This may imply that the optimisation process had already

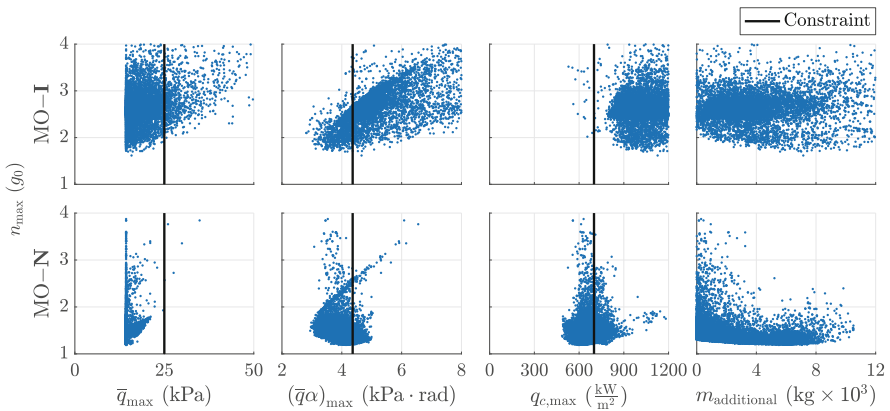


Fig. 13 Coupled trajectory single- and multi-objective (SO & MO) variable comparisons at TAEM for OFC-I and OFC-N

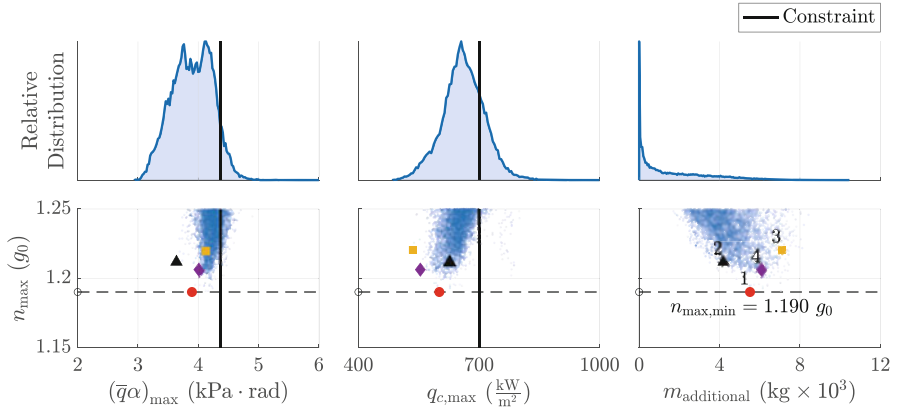


Fig. 14 Identification of sub-optimal and reference individuals used for localised global optimisation

converged to a small region and/or the result of the tests were a replication of the observations from the initial Monte-Carlo design space exploration with 100,000 individuals. This led to the localised optimisation of the population to be with the same global optimisation method (MOEA/D (DE)), albeit with a reduced design space.

The objective function cases evaluated were OFC-N and OFC-M.1. The selection of OFC-N was to maintain continuity with the initial evaluation. The $n_{\max} - m_{\text{additional}}$ Pareto front showed a well-behaved trend where an increase in $m_{\text{additional}}$ indicated a possible reduction in n_{\max} . This led to the creation and selection of OFC-M.1, where the mass cost is no longer included and the total g_0 -load constraint violation was increased by an order of magnitude.

The reference points were selected along the $n_{\max} - (\bar{q}\alpha)_{\max}$ and $n_{\max} - q_{c,\max}$ Pareto fronts. Including $n_{\max,\min}$, a total of four points were selected, as shown in Fig. 14 by the numeric labels in the bottom right panel. Each case had a set of parameter bounds created by expanding the decision vector of each individual identified in Fig. 14. A decision vector expansion of 5% was chosen because it brought about the most individuals to the TAEM with the localised Monte-Carlo tests. However, the $m_{\text{additional}}$ was arbitrarily defined to have a range of [4000, 15,000] kg. The initial populations used to seed the localised global optimisation were determined by identifying the individuals that produced the lowest 100 n_{\max} from the general global optimisation. The maximum number of generations was set to 100.

Figure 15 illustrates the variable comparisons of all individuals that reached the TAEM for two cases. The relevant reference individual is identified in the top left corner of the first panel of each row, and its corresponding placement in each panel is identified by the intersection of the dashed lines. OFC-N is presented in green asterisks and OFC-M.1 is presented as dark red squares. It is possible to see in the figure how each objective function case drives the populations in different

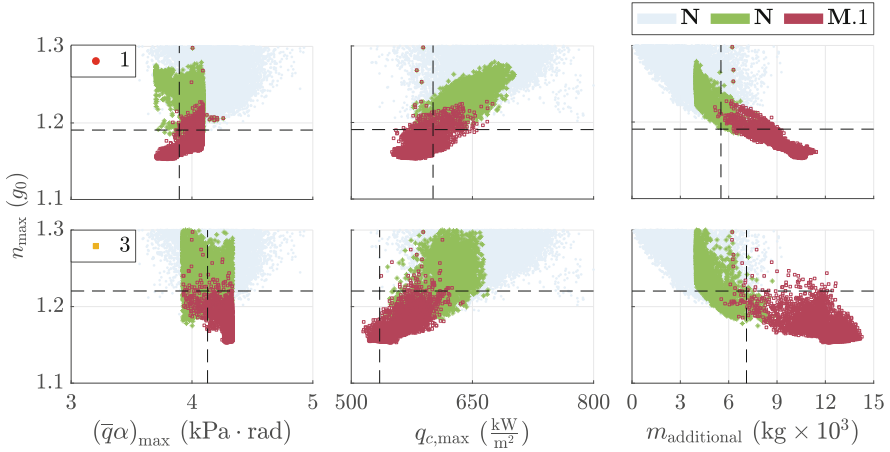


Fig. 15 Localised multi-objective optimisation variable comparisons for OFC-N and OFC-M.1

directions. OFC-N did not significantly drive n_{\max} values closer to $1 g_0$. It can also be seen that this case had a clear tendency of minimising $m_{\text{additional}}$, as it drove the populations towards the lower bound of 4000 kg. OFC-M.1, on the other hand, was able to drive n_{\max} values further towards the $1 g_0$ constraint. However, this was achieved at the expense of significantly increasing $m_{\text{additional}}$.

The $n_{\max} - m_{\text{additional}}$ front was chosen for further analysis. The selection was based on the relatively well-behaved curve and the fact that $m_{\text{additional}}$ is a known input parameter. The improvement on n_{\max} can be clearly visualised in Fig. 16, where all localised global optimisation populations are aggregated over the general TAEM population. The figure shows the distributions of each objective function case for $m_{\text{additional}}$ in the top panel and for n_{\max} on the right panel. The additional mass distributions for OFC-N (blue and green areas) show a trend towards their minimum bounds (0 kg and 4000 kg). The distribution of OFC-M.1 (red area) has a large spread with a larger proportion around 10,500 kg. The corresponding distributions for n_{\max} show that only OFC-M.1 was able to drive the population towards a lower n_{\max} . The lowest value is identified as n_{\max, \min_2} with the second red dot and a value of $1.152 g_0$. It is also possible to see that $m_{\text{additional}}$ values larger than 10,500 kg only increased n_{\max} , suggesting that further improvement in this relation was no longer possible. In short, though there is a clear improvement in n_{\max} , the difference is effectively negligible and comes at the need of a significantly higher additional mass.

Three Pareto fronts are also shown in Fig. 16. Though the left portions of the Pareto fronts were from the initial optimisation, it can be seen that as the additional mass increased, the Pareto points were increasingly selected from the local optimisations. Visual comparisons of their decision vectors, trajectory data, and variable time histories showed relatively small differences for the individuals near n_{\max, \min_2} . In fact, other than for $m_{\text{additional}}$, the decision vectors showed characteristics of

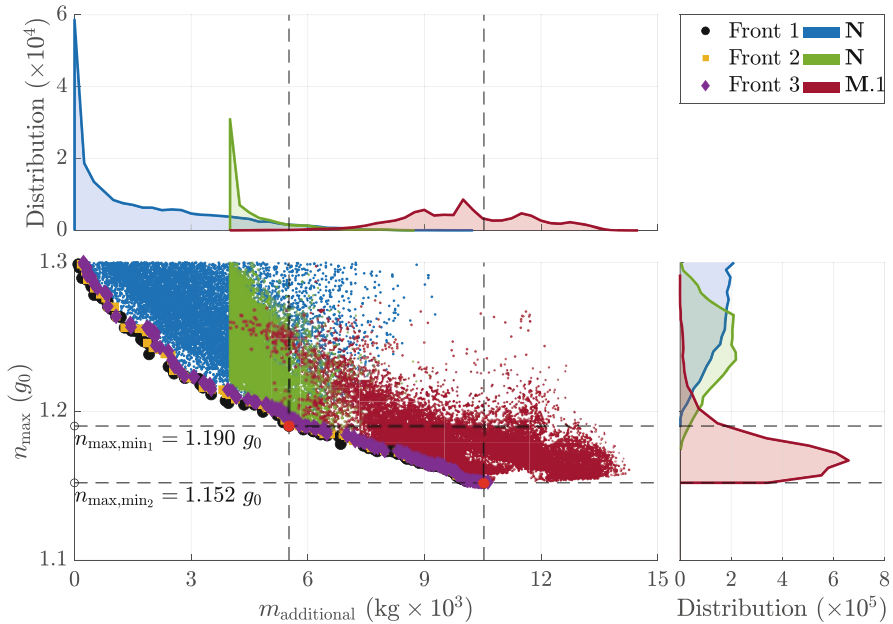


Fig. 16 Pareto front of maximum g_0 -load vs. additional mass, including general (OFC-N) and local optimisations (OFC-N and OFC-M.1)

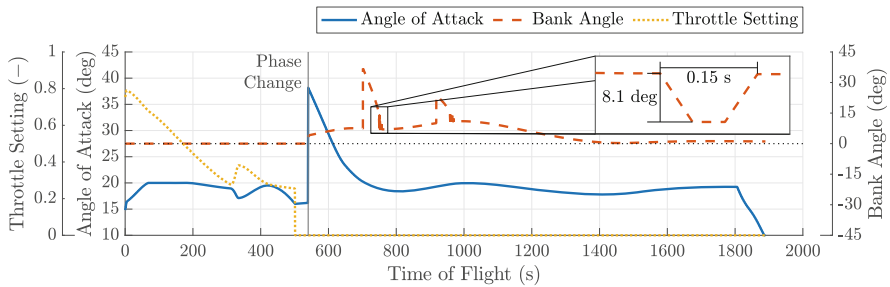


Fig. 17 ‘Best’ individual time history: control variables

clustering. However, as a sensitivity analysis has not been completed by modelling realistic uncertainties, it is unclear how deviations from the clusters may affect the resulting trajectories.

Figure 17 shows the time histories of the control variables. Angle of attack, shown in solid blue, presents a saturated segment during the ascent phase, a significant spike during the phase change that is eased off during the initial descent and a steep decrease at the end. The steep decrease at the end is a result of the vehicle’s aerodynamic envelope at lower Mach numbers (see Fig. 1c). The bank angle, shown in the dashed red line, is zero during the ascent phase and positive

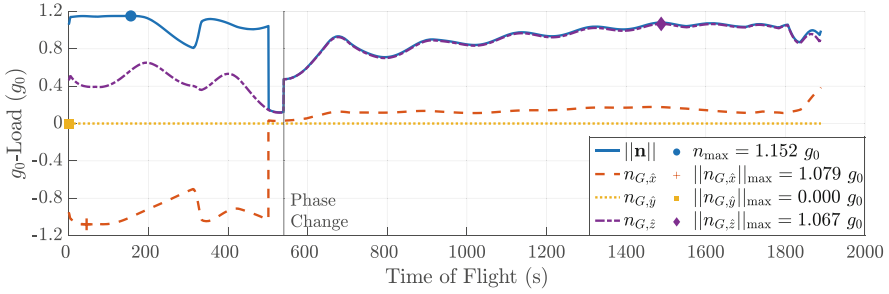


Fig. 18 ‘Best’ individual time history: g_0 -loads

during the descent phase. This particular profile implies that the vehicle did not perform a bank reversal. Additionally, there are two spikes with certain oscillations occurring as they revert to the lower trend. The large spikes are the result of the skip suppression, where the bank angle required to avoid skipping is commanded if $\gamma \geq 0$ and $\dot{\gamma} \geq 0$. The oscillations are the natural consequence of the vehicle’s flight-path angle and its time rate of change as the trajectory maintains a horizontal or slightly negative path. However, the largest oscillation, shown on the inset, is relatively short-lived. Though the values have an effect on the calculated trajectory, these oscillations would not be feasibly executed if a controlled flight is performed. The throttle setting, shown as the yellow dotted line, has an initial decreasing trend that is shortly interrupted and then continues to decrease. The throttle setting then has a sudden reduction to zero, engine shut-off, prior to terminating the ascent phase. This confirms the hypothesis about thrust being present exclusively during the ascent phase. As the ascent phase extracts the fuel mass’s energy, it is also expected that higher mechanical loads would be experienced by passengers during the initial phase of the coupled trajectory.

The overall decreasing trend of the throttle setting works in concert with the angle of attack in maintaining a relatively low g_0 -load. Figure 18 illustrates the g_0 -load magnitude and its components in the passenger frame, \mathcal{F}_G . The figure also shows the points of maximum absolute values. The g_0 -load magnitude, shown in solid blue, presents the maximum value of $1.152 g_0$. Prior to that point, there is a relatively constant line. However, these values are due to an exchange in component distribution along the $\mathcal{F}_{G,\hat{x}}$ and $\mathcal{F}_{G,\hat{z}}$ axes. The value has a short decrease and goes below $1 g_0$ during a pull-up manoeuver where the angle of attack and throttle setting both decrease. However, when they increase again, the total g_0 -load increases to over $1 g_0$. The value then shows a short undulation before having a sharp decrease prior to the phase change. Once in the descent phase, the total g_0 -load has a step increase to about $0.5 g_0$ prior to showing an undulating trend that eventually goes above $1 g_0$ for almost the remainder of the trajectory. This undulation along $\mathcal{F}_{G,\hat{z}}$ can be traced to the vehicle’s height, flight-path angle, and flight-path angle rate (all during descent). Throughout the trajectory, the $\mathcal{F}_{G,\hat{x}}$ axis dominates during the ascent phase, while the $\mathcal{F}_{G,\hat{z}}$ axis dominates during the descent phase. In fact, the

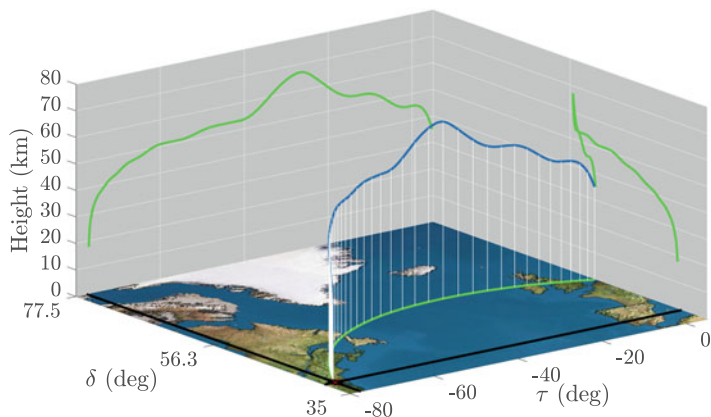


Fig. 19 ‘Best’ individual height over planar trajectory

maximum absolute value of the ascent phase corresponds to $n_{G,\hat{x}} = -1.079 g_0$ (red cross on red dashed line), while for the descent phase it corresponds to $n_{G,\hat{z}} = 1.067 g_0$ (purple diamond on purple semi-dashed line). These directional maxima are not entirely sustained as they occur within flight segments that are within clear violation of the $1 g_0$ constraint. The extended exposure during ascent lasts about 160 s and about 400 s during descent.

The vehicle’s trajectory is shown in Fig. 19, with its height over a planar trajectory. Of note is the geographic path of the ground track, where the ascent phase occurs above the region associated with the United Kingdom and the descent phase occurs largely above the northeastern coast of the USA. Furthermore, the lack of bank reversals can be seen as the vehicle aims to the circle defined by the TAEM. Though not shown, numerous other trajectories presented similar characteristics.

7 Concluding Remarks

The overall exercise could be described in four main segments: development of a trajectory simulator with the identification of key generalised parameters; objective function case definition with a variety of costs, constraint violations, and penalties; design space exploration with different factors, dimensionality considerations, and objective function cases; and trajectory optimisation execution with subsequent localised exploitation.

The key generalised parameters used in the trajectory simulator allowed for the evaluation of ascent and descent profiles with different expected dynamics, albeit at the expense of increased dimensionality. Similarly, though defining the objective functions and their combinations required a certain degree of creativity, it was ultimately their influence on the optimisation that was of both concern and interest.

The design space exploration executed was an important step in the process. Though the number of factors investigated brought forth a complex dataset, it did allow for an improved understanding of the capabilities and limitations of the factors as applied to the current problem. Visualising and summarising the exploration data with the ultimate goal of identifying preferred factors for trajectory optimisation is a challenging task that must be done with care and caution. However, the conclusions drawn from the observations are understood to shed light on the problem and provide a reference for future studies. These include the implementation of node control, objective function case, and the optimisation algorithm selected.

The execution of the trajectory optimisation follows relatively easily once an increased confidence in the understanding of the design space is acquired. In fact, this understanding can be used to further exploit the design space, as performed with the localised global optimisation with the *coupled* phase approach. It was possible to see the $n_{\max} - m_{\text{additional}}$ front required a significant increase in additional mass to reduce the n_{\max} . This is understood to be a natural consequence of the decreasing throttling required to sufficiently accelerate the vehicle to reach the TAEM while minimising the n_{\max} experienced throughout the trajectory (i.e. longer thrust time with variable mass flow rate).

That being so, the *decoupled* phase approach was unable to generate linkable trajectories, which is understood to have been due to the optimiser driving the populations of the separate optimisations to regions that did not intersect. Though the reason may be due to a lack of sufficient implicit linking qualities or the decoupling rationale, it may also be due to the ranges of parameter bounds and the selection of the objective function case.

Overall, the problem structure is understood to drive a given population towards characteristics of interest if sufficient phase coupling is considered. That is to say that though phase decoupling may be initially preferred due to a reduced design space, the complex non-linear dynamics of the problem may still require the evaluation of coupled phases if conditions cannot be ensured for decoupling.

Ultimately, though the *coupled* approach did require a significant increase in additional mass for the chosen route and vehicle, the result does indicate the possibility of using the approach to identify a set of parameters that could drive the optimal design of a vehicular configuration and associated route such that an individual could participate in hypersonic travel without health screenings.

Among the recommendations to further study are the augmentation of the equations of motion and GNC module to consider a more realistic flight; the evaluation of alternate optimisers; other vehicular configurations and propulsive systems and the inclusion of no-fly zones.

References

1. Deb, K. and Pratap, A. and Agarwal, S. and Meyarivan, T., "A Fast and Elitist Multiobjective Genetic Algorithm: NSGA-II", *IEEE Transactions on Evolutionary Computation*, Vol. 6, No. 2, pp. 182–197, 2002.

2. Zhang, Q. and Li, H., "MOEA/D: A Multiobjective Evolutionary Algorithm Based on Decomposition", *IEEE Transactions on Evolutionary Computation*, Vol. 11, No. 2, pp. 712–731, 2007.
3. Biscani, F. and Izzo, D. and Yam, C. H., "A Global Optimisation Toolbox for Massively Parallel Engineering Optimisation", *ArXiv e-prints*, 2010.
4. Mooij, E. and Hänninen, P.G., "Distributed Global Trajectory Optimization of a Moderate Lift-to-Drag Re-Entry Vehicle", *AIAA Guidance, Navigation, and Control Conference*, 2009.
5. Dijkstra, M. and Mooij, E. and Sudmeijer, K., "Trajectory Optimization to Support the Study of Hypersonic Aerothermodynamic Phenomena", *AIAA Atmospheric Flight Mechanics (AFM) Conference, Guidance, Navigation, and Control and Co-located Conferences*, 2013.
6. Hess, Jaimy and Mooij, Erwin, "Node Control and Numerical Optimization of Aerogravity-Assist Trajectories", *AIAA Atmospheric Flight Mechanics Conference*, 2017.
7. Koelle, D. E. and Kuczera, H., "Sänger II, an advanced launcher system for Europe", *Acta Astronautica*, Vol. 19, No. 1, pp. 63–72, 1989.
8. MBB, "Study on Re-entry Guidance and Control - Final Report, Vol. 2, Reference Vehicle Definition and Orbital Constraints", *MBB Space Communication and Propulsion Systems Division*, TN-ESA 6718/85-1, Rev. A. 1988.
9. Mooij, E., "The HORUS-2B Reference Vehicle", *Delft University of Technology*, Memorandum M-682, 1995.
10. Koelle, D. E. and Kuczera, H., "Sänger Space Transportation System - Progress Report", *41st International Astronautical Congress, International Astronautical Congress (IAF)*, IAF-90-175. 1990.
11. Yoder, C. F., "Astrometric and Geodetic Properties of Earth and the Solar System", *Global Earth Physics: A Handbook of Physical Constants*, AGU Reference Shelf 1, American Geophysical Union, 1995.
12. Regan, F. J. and Anandakrishnan, S. M., "Dynamics of Atmospheric Re-Entry", 1st ed, *AIAA, AIAA Education Series*, 1993.
13. Chapman, D. R., "An Approximate Analytical Method for Studying Entry into Planetary Atmospheres", *NACA - Scientific and Technical Information Division*, NACA-TN-4276, 1958.
14. Tauber, M. E. and Menees, G. P. and Edelman, H.G., "Aerothermodynamics of Transatmospheric Vehicles", *Journal of Aircraft*, Vol. 24, No. 9, pp. 594–602, 1987.
15. Moore, T. E., "Space Shuttle Entry Terminal Area Energy Management", *Washington, DC: National Aeronautics and Space Administration, Lyndon B. Johnson Space Center*, NASA Technical Memorandum 104744 1991.
16. Han, X. and Guo, X., "Cubic Hermite interpolation with minimal derivative oscillation", *Journal of Computational and Applied Mathematics*, Vol. 331, pp. 82–87, 2018.
17. Vinh, N. X. and Busemann, A. and Culp, R. D., "Hypersonic Planetary Entry Flight Mechanics", *The University of Michigan Press*, 1980.
18. Dirkx, D. and Mooij, E., "Optimization of entry-vehicle shapes during conceptual design", *Acta Astronautica*, Vol. 94, No. 1, pp. 198–214, 2014.
19. ISO, "Measurement of ride quality - Part 1: Lifts (elevators)", *International Organization for Standardization*, ISO 18738-1:2012(en), 2012.

Bifocal Metrology Applications in Space Engineering



Fulvio Bresciani, Giorgio Fasano, and János D. Pintér

1 Introduction

This chapter discusses a novel approach aimed at determining the relative attitude and position of objects. Such metrological scenarios frequently arise in applications that include robotics (collaborative robots, robotic arm control), military applications, and aeronautics (target configuration). One of the significant aeronautical applications is the autonomous landing control system for aircraft. This application is relevant, e.g., in radar-silence conditions, for the landing of ultralight aircraft, for drones in tracks without a control tower, and for aircraft carriers. Figure 1 illustrates the landing of an aircraft on an aircraft carrier, indicating the optical head (OH), and the target.

This metrological aspect is becoming increasingly important also in space engineering: consult Bresciani [1]. To accomplish the task, the technology has to provide quick and reliable measurements of the attitude and position of a spacecraft with respect to the other(s). Several examples of real-world space engineering applications entailing this advanced capability are briefly reviewed next.

The vision system of the STRONG satellite of the European Space Agency (ESA) represents a significant example. It has the scope of determining the line of sight and the range of the relative position between two or more satellites. A second

F. Bresciani (✉) · G. Fasano
Thales Alenia Space, Turin, Italy
e-mail: fulvio.bresciani@thalesaleniaspace.com; giorgio.fasano@thalesaleniaspace.com
<https://www.thalesgroup.com/en>

J. D. Pintér
Department of Management Science and Information Systems, Rutgers Business School - New Brunswick Campus, Rutgers University, Piscataway, NJ, USA
e-mail: jpinter@business.rutgers.edu



Fig. 1 Aircraft landing on an aircraft carrier

example of interest concerns PROBA-3, ESA's first precision formation flying mission. A pair of satellites fly together maintaining a fixed configuration as a "large rigid structure" in space to investigate formation-flying technologies. Conceptually, the PROBA-3 mission consists of two independent, three-axis stabilized mini satellites flying in a formation with relative position control accuracy of less than 1 mm, see Fig. 2. The two mini satellites are referred to as Coronagraph SpaceCraft (CSC) with metric dimensions of $1.1 \times 1.8 \times 1.7 \text{ m}^3$, and Occulter SpaceCraft (OSC) with dimensions of $0.9 \times 1.4 \times 0.9 \text{ m}^3$. The paired satellites jointly form a 150-meter-long solar coronagraph to study the Sun's faint corona more closely to the solar rim than has ever been achieved before.

A further noteworthy example is the Magsat program, a joint project by the National Aeronautics and Space Administration (NASA) and the United States Geological Survey (USGS) to measure near-earth magnetic fields on a global basis. The spacecraft consisted of two distinct parts, see Fig. 3: the instrument module that contains a vector and a scalar magnetometer, in addition to its unique basis apparatus; and the base module that contains the data-handling, power, communication, command, and attitude-control subsystems to support the instrument module. The magnetometers were deployed after launch, using a deployable scissor boom, to a position of 6 m behind the spacecraft. At this distance, the influence of magnetic materials from the instrument and base module was less than 1 nanotesla. The directional accuracy of the vector magnetometer was required to be of 20 arc seconds in all three axes (coordinates). The related error allocation analysis determined that the attitude control subsystem was required to yield an accuracy of 7 arc seconds per axis to meet the overall system requirements. The performance

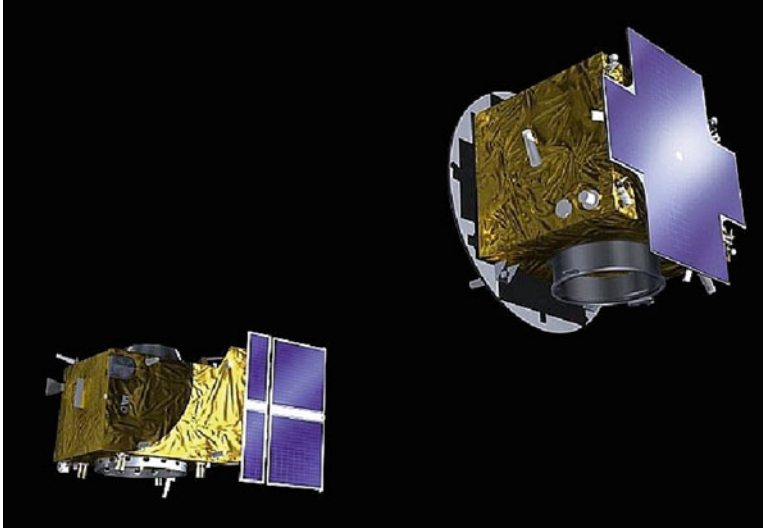


Fig. 2 PROBA-3 CSC (left) and OSC (right). (Credits: ESA)

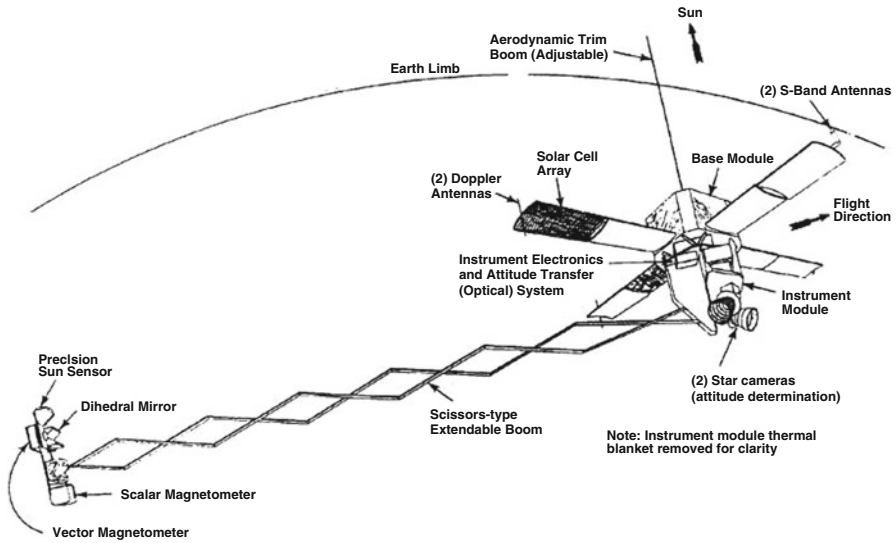


Fig. 3 Magsat orbital configuration. (Credits: NASA)

goal was set to 1 arc second for pitch and yaw, and 5 arc seconds for twist (roll). The pitch-yaw acquisition range required was $\pm 0.5^\circ$ as a goal, with a precision range over ± 3 arc minutes. The twist system required a precision range of $\pm 0.08^\circ$ over the pitch-yaw precision range. Moreover, the dynamic range in the magnetometer platform displacement motion was set to $\pm 0.25^\circ$ in any transverse direction.

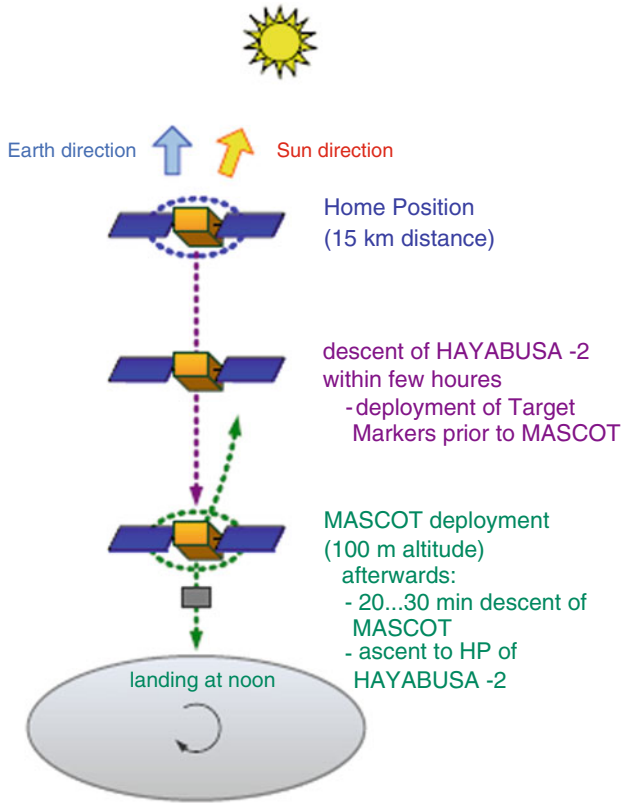


Fig. 4 HAYABUSA-2 deployment phase (left) and MASCOT separation (right). (Credits: JAXA)

Another interesting application is represented by HAYABUSA-2, an asteroid exploration mission by the Japanese Space Exploration Agency (JAXA), aimed at studying Asteroid 1999 JU3. The spacecraft deploys the MASCOT lander built in Europe for an in situ study of surface composition and properties, see Fig. 4. The landing site is selected prior to the MASCOT deployment by evaluating the global asteroid map, but restricted to the illuminated asteroid side. During a sampling “dress rehearsal” maneuver, the main spacecraft descends from its home position (HP) to an altitude of approximately 100 m and deploys the lander by initializing a proper Δv through the separation mechanism. The lander then freefalls to the surface, while HAYABUSA-2 ascends back to its HP located at a distance of 15 km. During the first phase, after being released, MASCOT reaches the asteroid. Here, the metrological aspects are particularly demanding due to the requested accuracy. Similar scenarios occur, e.g., in active debris removal, object rendezvous, and formation-flying.

The OCSD (Optical Communications and Sensor Demonstration) program is the first in a new series of six NASA-managed demonstration missions adopting

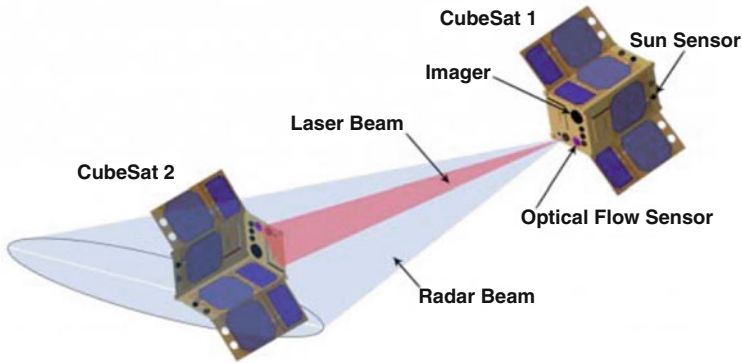
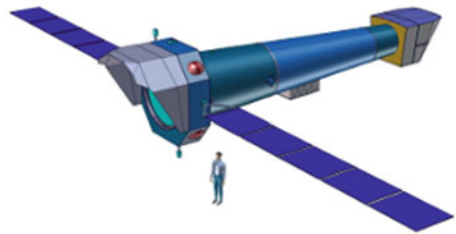


Fig. 5 Two CubeSats in close proximity operations. (Credits: Aerospace Corp)

Fig. 6 Athena telescope.
(Credits: ESA Concurrent Design Facility)



CubeSat to test technologies that enable new uses of these miniature satellites, measuring approximately $10 \times 10 \times 10 \text{ cm}^3$. The first mission is a technical demonstration of the various systems testing the laser communication terminal. The next two satellites will be deployed as a pair to demonstrate the ability to maneuver small spacecraft in close proximity (approximately 200 m) to one another using low-cost sensors and a novel water propulsion, see Fig. 5. This technology can enhance the ability of small spacecraft to work in coordination with other satellites to explore asteroids, planets, and moons, as well as inspecting other spacecraft.

The Athena (Advanced Telescope for High-ENERgy Astrophysics) mission of ESA, see <https://sci.esa.int/web/athena>, is selected in this chapter as a specific case study for the innovative metrological approach proposed. Athena is based on an X-ray telescope (see Fig. 6) designed to address the Cosmic Vision science theme “The Hot and Energetic Universe.” This satellite will utilize a telescope with a 12-m focal length and two primary instruments: the high-resolution X-ray Integral Field Unit (X-IFU) and the Wide Field Imager (WFI) featuring a moderate resolution and a large field of view. The high-precision measurement of the telescope line of sight (LoS) internal misalignments is crucial. The on-board metrological instrument is expected to be placed as close as possible to the node and focal plane center of the telescope mirror to detect at a very high precision the errors in the LoS vector, due to inevitable thermal distortions.

Metrological problems of the type illustrated above are usually tackled by adopting very complex systems that often use different technologies in parallel: for optical metrology, consult, e.g., Tyson [13] and Yoshizawa [14]. The most frequently used metrological solutions considered in space applications include the Universal Lateral and Longitudinal Integrated Sensor (ULLIS), Hexa-Dimensional Optical Metrology (HDOM), ATV Videometer, and Rendezvous Laser Vision System (RELAVIS).

- The Universal Lateral and Longitudinal Integrated Sensor (ULLIS) is a sensor composed of a detector, an optical system, and an electronic unit on one side, in addition to a set of retroreflectors on the other side. This device has the capability to measure both the lateral and longitudinal positions of one side with respect to the other.
- The Hexa-Dimensional Optical Metrology (HDOM) is a metrological system aimed at providing the 3D-position and 3D-attitude of one side with respect to the reference frame of another side.
- The ATV Videometer is a metrological system based on visual techniques utilized to support the docking of the Automated Transfer Vehicle (ATV, ESA) to the International Space Station (ISS).
- The Rendezvous Laser Vision System (RELAVIS) is a system designed to support autonomous space operations. RELAVIS provides accurate detection, tracking, and estimation of spacecraft for rendezvous-docking operations, satellite inspection, and servicing operations.

A promising alternative approach is based on the innovative bifocal concept, see Bresciani and Musso [2–4]. This system is characterized by a double optical train, which yields information about position and attitude of an object with respect to another, for all six degrees of freedom. It covers a variable range of possible distances, i.e., from ten meters to tens of kilometers, depending on the application and measurement purpose. In the specific case of space engineering (the application field considered in this chapter), the bifocal metrological systems can provide precise information about the mutual position and attitude of two spacecraft in a short, medium, and far range involving only one sensor and covering either fine or coarse accuracies. In fact, the bifocal metrology is the first optical projective system able to tackle six degrees of freedom metrological scenarios that adopts a single sensor. A simple analytical algorithm solves the related six degrees of freedom problem without the need for high computing power. The optical system is very simple and compact: in addition to the light target, composed by only three Light Emitted Diodes (LEDs), has no particular complexity in terms of volume accommodation, technological developments, space qualifications, and on-ground characterization. All the components of this metrological system can be selected among the already space-qualified items.

These key aspects of the bifocal metrology with respect to the existing metrologies make the new approach suitable for a wide range of space applications: rendezvous and docking, co-orbiting satellites, large space instruments based on formation flying technology, extendable structures, and CubeSat networks.

The remainder of this chapter is structured as follows. Section 2 presents the bifocal system concept. Section 3 is dedicated to the mathematical aspects, concerning the projected image generation, the inverse problem of reconstructing the target position and attitude by the projected image measurement, the analytical solution, and the relative error analysis. Section 4 discusses two optimization problems regarding the bifocal system sizing and the light spot shaping, respectively. A real-world application is illustrated in Sect. 5, and conclusions are presented in Sect. 6.

2 Bifocal System Concept

The bifocal system discussed here consists of the following components:

- A light target consisting of three LEDs placed at the vertices of an isosceles triangle.
- A two-channel optical head (each channel with its own focal length) that focuses the light target image on an image sensor.

The working principle of the system is shown in Fig. 7, when two spacecrafts denoted by S1 and S2 are considered. The optical head consisting of the optical trains OT1 and OT2 is installed on S1, and the three LEDs are positioned on S2.

The joint presence of two focal lengths allows using the device as a single focal metrology system with different operative ranges (coarse metrology) or as a metrology system with a better accuracy than a classical projection metrology

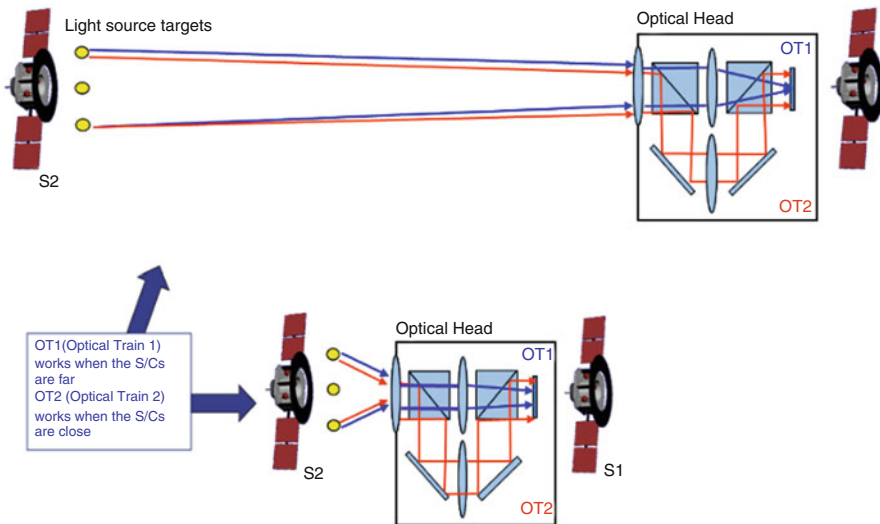


Fig. 7 Bifocal system: basic concept

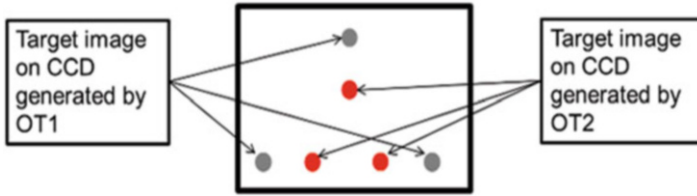


Fig. 8 CCD target image projection

system (fine metrology). When the spacecrafts are either far or close, a coarse measurement can be performed. When both target images are projected on the image sensor (charged coupled device, CCD) a refined measurement can be carried out: see Fig. 8.

Considering the target light spots (three for each optical channel) on the projected image plane, through a simple mathematical algorithm requiring little computing power, it is possible to determine the position and attitude accurately (considering six degrees of freedom, including the roll, pitch, and yaw angles), with respect to the optical head.

3 Mathematical Model

In this section, the analytical computation of position and attitude of a generic target with respect to all the six degrees of freedom using a bifocal optical system is described: for further details, consult Bresciani and Musso [2–4].

3.1 3D-Transformation Matrix

Consider an orthogonal right-handed 3D-coordinate system with origin O and axes x , y , and z . Angular rotations around the axes x , y , and z can be represented by the following rotation matrices, see, e.g., Ghali [6]:

$$R_x(\theta) = \begin{bmatrix} 1 & 0 & 0 & 0 \\ 0 & \cos \theta & \sin \theta & 0 \\ 0 & -\sin \theta & \cos \theta & 0 \\ 0 & 0 & 0 & 1 \end{bmatrix}, \quad (1-1)$$

$$R_y(\beta) = \begin{bmatrix} \cos \beta & 0 & -\sin \beta & 0 \\ 0 & 1 & 0 & 0 \\ \sin \beta & 0 & \cos \beta & 0 \\ 0 & 0 & 0 & 1 \end{bmatrix}, \tag{1-2}$$

$$R_z(\gamma) = \begin{bmatrix} \cos \gamma & \sin \gamma & 0 & 0 \\ -\sin \gamma & \cos \gamma & 0 & 0 \\ 0 & 0 & 1 & 0 \\ 0 & 0 & 0 & 1 \end{bmatrix}, \tag{1-3}$$

where θ , β , and γ are the rotation angles with respect to x , y , and z .

The 3D-translation matrix is defined by

$$T_{xyz}(\Delta x, \Delta y, \Delta z) = \begin{bmatrix} 1 & 0 & 0 & 0 \\ 0 & 1 & 0 & 0 \\ 0 & 0 & 1 & 0 \\ \Delta x & \Delta y & \Delta z & 1 \end{bmatrix}, \tag{2}$$

where Δx , Δy , and Δz are the displacements along the axes x , y , and z , respectively.

Rotations and translations are applied to a point with coordinates (X, Y, Z) by the following transformation:

$$\begin{aligned} [X', Y', Z', 1] &= [X, Y, Z, 1] R_x(\theta) R_y(\beta) R_z(\gamma) T_{xyz}(\Delta x, \Delta y, \Delta z) \\ &= [X, Y, Z, 1] M(\theta, \beta, \gamma, \Delta x, \Delta y, \Delta z) \end{aligned} \tag{3}$$

Here (X, Y, Z) is the original point, and (X', Y', Z') is the point after the roto-translation shown above. The matrix $M(\theta, \beta, \gamma, \Delta x, \Delta y, \Delta z) = R_x(\theta) R_y(\beta) R_z(\gamma) T_{xyz}(\Delta x, \Delta y, \Delta z)$ can be expressed as

$$M(\theta, \beta, \gamma, \Delta x, \Delta y, \Delta z) = \begin{bmatrix} \cos \gamma \cos \beta & \sin \gamma \cos \beta & -\sin \beta & 0 \\ \sin \theta \sin \beta \cos \gamma - \sin \gamma \cos \theta & \sin \gamma \sin \beta \sin \theta + \cos \gamma \cos \theta & \sin \theta \cos \beta & 0 \\ \cos \theta \sin \beta \cos \gamma - \sin \gamma \sin \theta & \sin \gamma \sin \beta \cos \theta - \cos \gamma \sin \theta & \cos \theta \cos \beta & 0 \\ \Delta x & \Delta y & \Delta z & 1 \end{bmatrix} \tag{4}$$

Hence, the explicit form of Eq. (3) is

$$[X', Y', Z', 1] = [X, Y, Z, 1] \begin{bmatrix} \cos \gamma \cos \beta & \sin \gamma \cos \beta & -\sin \beta & 0 \\ \sin \theta \sin \beta \cos \gamma - \sin \gamma \cos \theta & \sin \gamma \sin \beta \sin \theta + \cos \gamma \cos \theta & \sin \theta \cos \beta & 0 \\ \cos \theta \sin \beta \cos \gamma - \sin \gamma \sin \theta & \sin \gamma \sin \beta \cos \theta - \cos \gamma \sin \theta & \cos \theta \cos \beta & 0 \\ \Delta x & \Delta y & \Delta z & 1 \end{bmatrix} \tag{5}$$

The transformation shown above is used as a basic underlying concept for the optical application discussed in this chapter. Prior to introducing the bifocal

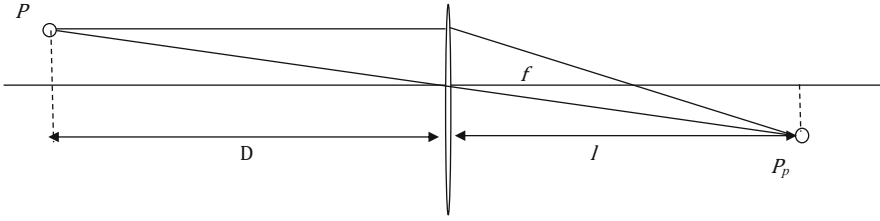


Fig. 9 Mono-focal projective system

approach, the mono-focal case is outlined, consisting of a simple optical projective system. In this scenario, the relationship between the object P and its projected image P_p is illustrated in Fig. 9.

In Fig. 9, D is the horizontal distance between the target point P and the lens utilized, while l is the horizontal distance between the lens center and the projection P_p . The distance between the lens focus and the projection is denoted by f . The axes x and y of the right-handed reference frame (x, y, z) considered here lie on the projection plane (y is the vertical axis); the axis z (oriented toward the target point P) is parallel to D and l . The following expression holds:

$$P_p(X_P, Y_P, Z_P) = P_p\left(\frac{lX}{D}, \frac{lY}{D}, 0\right) \tag{6}$$

where (X, Y, Z) are the coordinates of the target point P .

Considering the relation (6), Eq. (5) links the image point $P_p(X_P, Y_P, Z_P)$ and the corresponding $P'_p(X'_P, Y'_P, Z'_P)$ obtained by the rotations $\theta, \beta,$ and γ and the displacements $\Delta x, \Delta y,$ and Δz along the axes. The following equation holds:

$$\begin{bmatrix} X'_P \\ Y'_P \\ 0 \\ \frac{l}{D} \end{bmatrix} = \frac{l}{D} [X, Y, 0, 1] \begin{bmatrix} \cos \gamma \cos \beta & \sin \gamma \cos \beta & -\sin \beta & 0 \\ \sin \theta \sin \beta \cos \gamma - \sin \gamma \cos \theta & \sin \gamma \sin \beta \sin \theta + \cos \gamma \cos \theta & \sin \theta \cos \beta & 0 \\ \cos \theta \sin \beta \cos \gamma - \sin \gamma \sin \theta & \sin \gamma \sin \beta \cos \theta - \cos \gamma \sin \theta & \cos \theta \cos \beta & 0 \\ \Delta x & \Delta y & \Delta z & 1 \end{bmatrix} \tag{7}$$

3.2 Bifocal Problem Statement

The bifocal system discussed in this chapter is depicted schematically by Fig. 10. Here A is the target and B details the positions of the three light sources $P_1(X_1, Y_1, Z_1), P_2(X_2, Y_2, Z_2), P_3(X_3, Y_3, Z_3)$ selected as the target. C represents the bifocal optical system as a whole (optical head), consisting of two equal-size lenses and

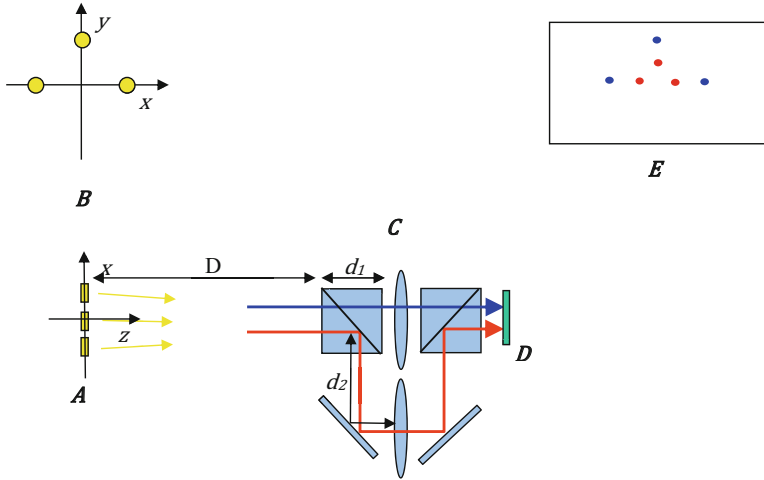


Fig. 10 Schematic representation of a bifocal system

four mirrors. **D** and **E** are the perpendicular and parallel views, respectively, of the image plane.

The bifocal system is, in fact, a combination of two mono-focal systems involving lenses 1 and 2, with l_1 and l_2 as the corresponding internal optical lengths. The two generated images (colored in blue and red for lenses 1 and 2) have the magnitudes $M(f_1)$ and $M(f_2)$, depending on the focal distances f_1 and f_2 , respectively. The two associated sets of projected points, generated by the target three (light-)points for lenses 1 and 2 are denoted by $P_{1p1}(X_{1p1}, Y_{1p1}, Z_{1p1})$, $P_{2p1}(X_{2p1}, Y_{2p1}, Z_{2p1})$, $P_{3p1}(X_{3p1}, Y_{3p1}, Z_{3p1})$, and $P_{1p2}(X_{1p2}, Y_{1p2}, Z_{1p2})$, $P_{2p2}(X_{2p2}, Y_{2p2}, Z_{2p2})$, $P_{3p2}(X_{3p2}, Y_{3p2}, Z_{3p2})$.

The general bifocal problem consists of determining the position and attitude of a target (identified by three light sources) with respect to a given initial condition, by measuring the positions of the corresponding projected six points generated by the bifocal system. Specifically, it is assumed that the initial positions of the three target (light-)points $P_1(X_1, Y_1, Z_1)$, $P_2(X_2, Y_2, Z_2)$, $P_3(X_3, Y_3, Z_3)$ are known with respect to the assigned reference frame (associated with the bifocal optical head), as well as their projected images $P_{1p1}(X_{1p1}, Y_{1p1}, Z_{1p1})$, $P_{2p1}(X_{2p1}, Y_{2p1}, Z_{2p1})$, $P_{3p1}(X_{3p1}, Y_{3p1}, Z_{3p1})$, and $P_{1p2}(X_{1p2}, Y_{1p2}, Z_{1p2})$, $P_{2p2}(X_{2p2}, Y_{2p2}, Z_{2p2})$, $P_{3p2}(X_{3p2}, Y_{3p2}, Z_{3p2})$, generated by lenses 1 and 2. After rotations θ , β , and γ of the target (around the axes x , y , and z , respectively), and displacements Δx , Δy , and Δz of the target along the axes x , y , and z , the projected points $P'_{1p1}(X'_{1p1}, Y'_{1p1}, Z'_{1p1})$, $P'_{2p1}(X'_{2p1}, Y'_{2p1}, Z'_{2p1})$, $P'_{3p1}(X'_{3p1}, Y'_{3p1}, Z'_{3p1})$, generated by lens 1, are correlated with the corresponding initial projected points $P_{1p1}(X_{1p1}, Y_{1p1}, Z_{1p1})$, $P_{2p1}(X_{2p1}, Y_{2p1}, Z_{2p1})$, $P_{3p1}(X_{3p1}, Y_{3p1}, Z_{3p1})$, generated by lens 1, by three equations having the general form of Eq. (5). Similarly, three equations of the general form of Eq. (5) relate the new projected points $P'_{1p2}(X'_{1p2}, Y'_{1p2}, Z'_{1p2})$, $P'_{2p2}(X'_{2p2}, Y'_{2p2}, Z'_{2p2})$, $P'_{3p2}(X'_{3p2},$

Y'_{3p2}, Z'_{3p2}), generated by lens 2, with the corresponding initial projected images $P_{1p1}(X_{1p1}, Y_{1p1}, Z_{1p1}), P_{2p1}(X_{2p1}, Y_{2p1}, Z_{2p1}), P_{3p1}(X_{3p1}, Y_{3p1}, Z_{3p1})$ generated by lens 2.

In general, a roto-translation of the target $\theta, \beta, \gamma, \Delta x, \Delta y,$ and Δz (with respect to the known initial condition) can be expressed by a system of six equations of the form of Eq. (5), each corresponding to one of the projected points $P'_{1p1}(X'_{1p1}, Y'_{1p1}, Z'_{1p1}), P'_{2p1}(X'_{2p1}, Y'_{2p1}, Z'_{2p1}), P'_{3p1}(X'_{3p1}, Y'_{3p1}, Z'_{3p1}), P'_{1p2}(X'_{1p2}, Y'_{1p2}, Z'_{1p2}), P'_{2p2}(X'_{2p2}, Y'_{2p2}, Z'_{2p2}),$ and $P'_{3p2}(X'_{3p2}, Y'_{3p2}, Z'_{3p2})$. The bifocal problem consists of inverting this system of equations so that the new configuration of the target (with respect to the initial condition), expressed by $\theta, \beta, \gamma, \Delta x, \Delta y,$ and Δz can be derived by the direct measurements of the projected points shown above: here we assume that $P_{1p1}(X_{1p1}, Y_{1p1}, Z_{1p1}), P_{2p1}(X_{2p1}, Y_{2p1}, Z_{2p1}),$ and $P_{3p1}(X_{3p1}, Y_{3p1}, Z_{3p1})$ are known.

3.3 Mathematical Solution

In order to solve the inverted system of equations introduced in Sect. 3.2, as per the initial conditions, the three target light-points are specified with respect to the optical head reference frame as follows:

$$\begin{aligned} P_1(X_1, Y_1, Z_1) &= (X_0, 0, 0), \\ P_2(X_2, Y_2, Z_2) &= (-X_0, 0, 0), \\ P_3(X_3, Y_3, Z_3) &= (0, Y_0, 0). \end{aligned}$$

As shown above, P_1 and P_2 are placed (symmetrically) along the x -axis at a distance X_0 from the origin, while P_3 is on the y -axis at a distance Y_0 from the origin. Since P_1 and P_2 are not affected by rotations around the x axis, Eq. (5) can be applied to both corresponding projected points, obtained either by lens 1 or 2, by adopting the simplifying condition $\theta = 0$. This yields the following specific equations for the projections P'_{1p1} and P'_{2p1} :

$$\left[X'_{1p1}, Y'_{1p1}, 0, \frac{l_1}{D+d_1} \right] = \frac{l_1}{D+d_1} [X_0, 0, 0, 1] \begin{bmatrix} \cos \gamma \cos \beta & \sin \gamma \cos \beta & -\sin \beta & 0 \\ -\sin \gamma & \cos \gamma & 0 & 0 \\ \sin \beta \cos \gamma & \sin \gamma \sin \beta & \cos \beta & 0 \\ \Delta x & \Delta y & \Delta z & 1 \end{bmatrix}, \quad (8-1)$$

$$\left[X'_{2p1}, Y'_{2p1}, 0, \frac{l_1}{D+d_1} \right] = \frac{l_1}{D+d_1} [-X_0, 0, 0, 1] \begin{bmatrix} \cos \gamma \cos \beta & \sin \gamma \cos \beta & -\sin \beta & 0 \\ -\sin \gamma & \cos \gamma & 0 & 0 \\ \sin \beta \cos \gamma & \sin \gamma \sin \beta & \cos \beta & 0 \\ \Delta x & \Delta y & \Delta z & 1 \end{bmatrix}, \quad (8-2)$$

where $D + d_1$ is the working distance of lens 1. After algebraic manipulations that are omitted, the following equations are obtained:

$$\Delta X'_{12p1} = \frac{2l_1}{D + d_1} X_0 \cos \gamma \cos \beta, \quad (9-1)$$

$$\Delta Y'_{12p1} = \frac{2l_1}{D + d_1} X_0 \sin \gamma \cos \beta, \quad (9-2)$$

where $\Delta X'_{12p1} \equiv X'_{1p1} - X'_{2p1}$ and $\Delta Y'_{12p1} \equiv Y'_{1p1} - Y'_{2p1}$. Further technical details concerning the mathematical formulation outlined here are presented by Bresciani and Musso [2–4].

Operating exactly the same way as lens 1, for lens 2 analogous equations are obtained:

$$\Delta X'_{12p2} = \frac{2l_2}{D + d_2} X_0 \cos \gamma \cos \beta, \quad (10-1)$$

$$\Delta Y'_{12p2} = \frac{2l_2}{D + d_2} X_0 \sin \gamma \cos \beta, \quad (10-2)$$

where $\Delta X'_{12p2} = X'_{1p2} - X'_{2p2}$ and $\Delta Y'_{12p2} = Y'_{1p2} - Y'_{2p2}$.

Combining (9-1), (9-2), (10-1), and (10-2) yields the following relations:

$$\gamma = a \tan \left(\frac{\Delta Y'_{12p1}}{\Delta X'_{12p1}} \right), \quad (11)$$

$$D = \frac{l_1 d_2 \Delta X'_{12p2} - l_2 d_1 \Delta X'_{12p1}}{l_1 \Delta X'_{12p1} - l_2 \Delta X'_{12p2}}, \quad (12)$$

$$\beta = a \cos \left(\frac{\Delta X'_{12p1} (D + d_1)}{2l_1 X_0 \cos \left(a \tan \left(\frac{\Delta Y'_{12p1}}{\Delta X'_{12p1}} \right) \right)} \right). \quad (13)$$

Additionally, by (8-1), (8-2), (11), (12), and (13), the displacements Δx and Δy can be expressed, respectively, as follows:

$$\Delta x = X'_{1p1} \frac{D + d_1}{l_1} - X_0 \cos \gamma \cos \beta \quad (14)$$

$$\Delta y = Y'_{1p1} \frac{D + d_1}{l_1} - Y_0 \cos \gamma \cos \beta \quad (15)$$

Applying Eq. (5) to the projected point P'_{3p1} (generated by lens 1), the following equations hold:

$$X'_{3p1} = \frac{l_1 Y_0}{D + d_1} \left(\sin \vartheta \sin \beta \cos \gamma - \sin \gamma \cos \vartheta + \frac{\Delta x}{Y_0} \right), \quad (16-1)$$

$$Y'_{3p1} = \frac{l_1 Y_0}{D + d_1} \left(\sin \vartheta \sin \beta \sin \gamma + \cos \gamma \cos \vartheta + \frac{\Delta y}{Y_0} \right). \quad (16-2)$$

Finally, ϑ can be derived by (16-1) and (16-2), giving rise to the following expressions:

$$\vartheta = a \sin \left(\frac{B}{\sin \beta} \right), \quad (17)$$

$$B = \frac{\left(X'_{3p1} Y_0 - \Delta x Q \right) \cos \gamma + \left(Y'_{3p1} Y_0 - \Delta y Q \right) \sin \gamma}{Q Y_0},$$

$$Q = \frac{l_1 Y_0}{D + d_1}.$$

To summarize the above discussion, the solutions obtained in this section for the inverted system introduced in Sect. 3.2 are represented by relations (11), (12), (13), (14), (15), and (17). The following obvious conditions are postulated:

$$\gamma \in \left] -\frac{\pi}{2}, \frac{\pi}{2} \right[\quad \Delta X_{12p1} \neq 0, \quad (18)$$

$$l_1 \Delta X'_{12p1} - l_2 \Delta X'_{12p2} \neq 0 \quad \left(\frac{X'_{1p1}}{l_2} \neq \frac{X'_{1p2}}{l_1} \right), \quad (19)$$

$$\beta \in]0, \pi[, \quad (20)$$

$$\vartheta \in \left[-\frac{\pi}{2}, \frac{\pi}{2} \right]. \quad (21)$$

It is understood that $X_0 > 0$, $Y_0 > 0$, $l_2 > l_1 \neq 0$, $d_2 > d_1 \neq 0$. It should be also noted that, due to the construction of the bifocal system, the following relations hold:

$$\Delta X'_{12p1} \neq 0, \frac{l_1 d_2 \Delta X'_{12p2} - l_2 d_1 \Delta X'_{12p1}}{l_1 \Delta X'_{12p1} - l_2 \Delta X'_{12p2}} > 0, \text{ and } l_1 \Delta X'_{12p1} - l_2 \Delta X'_{12p2} \neq 0.$$

During the algebraic manipulation carried out to obtain expression (13), it has been implicitly assumed that $-1 \leq \frac{\Delta X'_{12p1}(D+d_1)}{2l_1 X_0 \cos \gamma} \leq 1$. Therefore, expression (13) is well defined for all given values of $\Delta X'_{12p1}$ and $\Delta Y'_{12p1}$ (recall also that, by (18), $\gamma \neq \pm \frac{\pi}{2}$). Analogous considerations hold for (17) by (20). Note additionally that the existence conditions for γ can be extended considering the whole angle $[0, 2\pi]$ provided that it is possible to identify, each time, the specific sub-intervals involved (e.g., $\gamma \in]-\frac{\pi}{2}, \frac{\pi}{2}[$ or $\gamma \in]\frac{\pi}{2}, \frac{3\pi}{2}[$). In any case, the conditions $\gamma \neq \pm \frac{\pi}{2}$ and $\gamma \neq \frac{3\pi}{2}$ must be satisfied. Analogous considerations hold for β , while no extension for ϑ would be of use.

3.4 Error Analysis

This section studies the impact of measurement errors, relative to the image-points, on the computation of the position and attitude of the target (by the inverse equation system corresponding to (11), (12), (13), (14), (15), and (17)). More precisely, taking a worst-case perspective, the maximum error for the terms ϑ , β , γ , D , Δx , and Δy is estimated, assuming that the absolute value of the measurement error associated with the variables X'_{1p1} , Y'_{1p1} , X'_{2p1} , Y'_{2p1} , Y'_{3p1} , X'_{1p2} , and X'_{2p2} is less than a given E . The distance D is deemed to represent the most critical aspect, especially when large distances are involved. The maximum error $|\varepsilon_D|_{\max}$ with respect to the distance D is briefly discussed next.

Considering Eq. (12), the error $|\varepsilon_D|$ with respect to the actual distance D is expressed as follows:

$$|\varepsilon_D| = \left| \frac{l_1 d_2 \Delta X'_{12p2} - l_2 d_1 \Delta X'_{12p1} + l_1 d_2 \varepsilon'_{12p2} - l_2 d_1 \varepsilon'_{12p1}}{l_1 \Delta X'_{12p1} - l_2 \Delta X'_{12p2} + l_1 \varepsilon'_{12p1} - l_2 \varepsilon'_{12p2}} - D \right|, \tag{22}$$

where ε'_{12p1} and ε'_{12p2} represent the measurement errors corresponding to $\Delta X'_{12p1}$ and $\Delta X'_{12p2}$, respectively. Depending on the specific technology adopted, with the estimated maximum error E , the following bounds are considered:

$$\left| \varepsilon'_{12p1} \right| \leq E, \tag{23-1}$$

$$\left| \varepsilon'_{12p2} \right| \leq E. \tag{23-2}$$

Since $\frac{l_1 d_2 \Delta X'_{12p2} - l_2 d_1 \Delta X'_{12p1}}{l_1 \Delta X'_{12p1} - l_2 \Delta X'_{12p2}} = D$ ($D \geq 0$), and $l_1 \Delta X'_{12p1} - l_2 \Delta X'_{12p2} < 0$ ($l_2 > l_1$ and $\Delta X'_{12p2} > \Delta X'_{12p1}$ due to the way the optical system is constructed), the following relation holds:

$$|\varepsilon_D|_{\max} = \max_{\vartheta, \beta, \gamma, \Delta x, \Delta y, \varepsilon'_{12p1}, \varepsilon'_{12p2}} \left| \frac{l_1 d_2 \Delta X'_{12p2} - l_2 d_1 \Delta X'_{12p1} + l_1 d_2 \varepsilon'_{12p2} - l_2 d_1 \varepsilon'_{12p1}}{l_1 \Delta X'_{12p1} - l_2 \Delta X'_{12p2} + l_1 \varepsilon'_{12p1} - l_2 \varepsilon'_{12p2}} - D \right|, \quad (24)$$

where $\vartheta, \beta, \gamma, \Delta x, \Delta y$ vary within given intervals (delimiting the roto-translations to consider). To find a first approximation $\left| \tilde{\varepsilon}_D \right|_{\max}$ for (24) (by involving a reduced number of variables), the following terms are introduced:

$$\eta_D^- = \max_{\vartheta, \beta, \gamma, \Delta x, \Delta y, \Delta z} \left\{ D - \frac{l_1 d_2 \Delta X'_{12p2} - l_2 d_1 \Delta X'_{12p1} + l_1 d_2 E + l_2 d_1 E}{l_1 \Delta X'_{12p1} - l_2 \Delta X'_{12p2} - l_1 E - l_2 E} \right\}, \quad (25-1)$$

$$\eta_D^+ = \max_{\vartheta, \beta, \gamma, \Delta x, \Delta y, \Delta z} \left\{ \frac{l_1 d_2 \Delta X'_{12p2} - l_2 d_1 \Delta X'_{12p1} - l_1 d_2 E - l_2 d_1 E}{l_1 \Delta X'_{12p1} - l_2 \Delta X'_{12p2} + l_1 E + l_2 E} - D \right\}. \quad (25-2)$$

Here we assume $\frac{l_1 d_2 \Delta X'_{12p2} - l_2 d_1 \Delta X'_{12p1} + l_1 d_2 E + l_2 d_1 E}{l_1 \Delta X'_{12p1} - l_2 \Delta X'_{12p2} - l_1 E - l_2 E} > 0$, and $\frac{l_1 d_2 \Delta X'_{12p2} - l_2 d_1 \Delta X'_{12p1} - l_1 d_2 E - l_2 d_1 E}{l_1 \Delta X'_{12p1} - l_2 \Delta X'_{12p2} + l_1 E + l_2 E} > 0$. The approximate term $\left| \tilde{\varepsilon}_D \right|_{\max}$ ($\left| \tilde{\varepsilon}_D \right|_{\max} > |\varepsilon_D|_{\max}$) is thus expressed as

$$\left| \tilde{\varepsilon}_D \right|_{\max} = \max \{ \eta_D^-, \eta_D^+ \}. \quad (26)$$

Let us remark that more than one single critical roto-translation in (24) or (26) could occur that gives rise to the maximum error: for example, due to symmetrical conditions. The issue of identifying the whole set of critical roto-translations is not trivial, and it is not considered in this chapter: it could be the subject of further research.

4 Optimization Aspects

Mathematical optimization models have been introduced in Sect. 3.4 concerning the error analysis of the studied optical system. There, a worst-case approach is adopted to estimate the maximum possible error with respect to the distance D (due to measurement errors relative to the projection differences $\Delta X'_{12p1}$ and $\Delta X'_{12p1}$

associated with lenses 1 and 2, respectively). In this section, two optimization problems are discussed with the scope of maximizing the overall performances of the bifocal system illustrated in this chapter. The first optimization problem, discussed in Sect. 4.1, is aimed at finding the size of the optical head so that the error with respect to distance D becomes as small as possible.

The second optimization problem concerns the specific features of the light spots utilized as the target image for the bifocal system. In fact, the light spots are not idealized geometrical points (as assumed in the mathematical formulation of Sect. 3), but they have an actual size. Therefore, each light spot is identified as a surface by the image sensor (CCD). In general, the light energy intensity on this surface does not have a uniform distribution. The concept of light spot centroid is introduced to represent the distribution of the light energy intensity on the light spot surface. This concept is the equivalent to the center of mass for a mass distribution in a geometric domain. Each light spot centroid is identified with one of the three single light points utilized by the bifocal system, to determine the roto-translation of the whole target as discussed in Sect. 3. In general, a roto-translation of the target yields a variation in the light energy intensity distribution on the surface of each light spot. The position of each light spot centroid typically varies as well with respect to the CCD. This centroid displacement is thus due to not only the actual roto-translation of the whole target, but also to the change in the light energy intensity distribution on the light spot surface. Therefore, the centroid displacement on each light spot surface, obtained after a roto-translation of the target, also depends on the light energy intensity distribution of the spot before the roto-translation. If the roto-translations of the target are limited with respect to the initial (nominal) condition, then the light energy intensity distribution of each light spot in the nominal condition can be properly shaped a priori, to minimize the centroid displacement. Consequently, under these proximity conditions, the precision of the bifocal metrological approach is maximized. This optimization aspect is discussed in Sect. 4.2.

4.1 System Sizing Optimization

The maximum error $|\varepsilon_D|_{\max}$ related to the distance D , as expressed by (24) depends implicitly also on the following parameters that characterize the bifocal system: d_1, d_2 (corresponding to $D + d_1, D + d_2$ working distances of lenses 1 and 2, respectively), l_1, l_2 (internal optical lengths of lenses 1 and 2, respectively), and f_1, f_2 (focal distances of lens 1 and 2, respectively). These parameters can vary within their ranges: $d_1 \in [\underline{D}_1, \overline{D}_1]$, $d_2 \in [\underline{D}_2, \overline{D}_2]$, $l_1 \in [\underline{L}_1, \overline{L}_1]$, $l_2 \in [\underline{L}_2, \overline{L}_2]$, $f_1 \in [\underline{F}_1, \overline{F}_1]$, $f_2 \in [\underline{F}_2, \overline{F}_2]$, where $\underline{D}_1, \underline{D}_2, \underline{L}_1, \underline{L}_2, \underline{F}_1, \underline{F}_2$ and $\overline{D}_1, \overline{D}_2, \overline{L}_1, \overline{L}_2, \overline{F}_1, \overline{F}_2$ are the lower and upper technological bounds. Next, the following *minimax* optimization problem is considered:

$$|\overline{\varepsilon_D}|_{\min} = \min_{d_1, d_2, l_1, l_2, f_1, f_2} \left\{ \max_{\vartheta, \beta, \gamma, \Delta x, \Delta y, \varepsilon'_{12p1}, \varepsilon'_{12p2}} \left| \frac{l_1 d_2 \Delta X'_{12p2} - l_2 d_1 \Delta X'_{12p1} + l_1 d_2 \varepsilon'_{12p2} - l_2 d_1 \varepsilon'_{12p1}}{l_1 \Delta X'_{12p1} - l_2 \Delta X'_{12p2} + l_1 \varepsilon'_{12p1} - l_2 \varepsilon'_{12p2}} - D \right| \right\}. \quad (27)$$

Here, $|\overline{\varepsilon_D}|_{\min}$ is the minimum error related to the distance D , with respect to the parameters d_1 , d_2 , l_1 , l_2 , f_1 , and f_2 , in the worst case as expressed by (24). Considering the difficulty of this optimization problem, especially if a global optimization point of view is adopted (see, e.g., [5, 8, 11]), the variables ϑ , β , γ , Δx , Δy , ε'_{12p1} , ε'_{12p2} , and ε'_{12p2} can be fixed in (27) at the values obtained by solving optimization problem (24). This implies that problem (27) can be simplified as follows:

$$|\overline{\varepsilon_D}|_{\min} = \min_{d_1, d_2, l_1, l_2, f_1, f_2} \left\{ \left| \frac{l_1 d_2 \Delta X'_{12p2} - l_2 d_1 \Delta X'_{12p1} + l_1 d_2 \varepsilon'_{12p2} - l_2 d_1 \varepsilon'_{12p1}}{l_1 \Delta X'_{12p1} - l_2 \Delta X'_{12p2} + l_1 \varepsilon'_{12p1} - l_2 \varepsilon'_{12p2}} - D \right| \right\}, \quad (28)$$

where only d_1 , d_2 , l_1 , l_2 , f_1 , f_2 are considered as variables, while $\Delta X'_{12p2}$, $\Delta X'_{12p1}$, ε'_{12p2} , ε'_{12p1} take instead the values corresponding to the worst-case solution provided by (24). In this framework it is implicitly assumed that exclusively the critical roto-translation corresponding to the solution obtained for (24) is considered. If the number of critical roto-translations providing the same error $|\varepsilon_D|_{\max}$ as the solution of (24) is available, then it is possible to properly extend optimization problem (28) in order to consider all of these. For this purpose, the error

$$(|\overline{\varepsilon_D}|)_{\alpha} = \left| \frac{l_1 d_2 \Delta X'_{12p2} - l_2 d_1 \Delta X'_{12p1} + l_1 d_2 \varepsilon'_{12p2} - l_2 d_1 \varepsilon'_{12p1}}{l_1 \Delta X'_{12p1} - l_2 \Delta X'_{12p2} + l_1 \varepsilon'_{12p1} - l_2 \varepsilon'_{12p2}} - D \right|_{\alpha}$$

can be associated with each critical roto-translation solution α (fixing the corresponding values ϑ , β , γ , Δx , Δy , ε'_{12p1} , ε'_{12p2} obtained from (24)). The extended optimization problem can be then expressed as $\min_{d_1, d_2, l_1, l_2, f_1, f_2} \sum_{\alpha} (|\overline{\varepsilon_D}|)_{\alpha}$.

4.2 Light Spot Optimization

In this section, first we recall the concept of light spot centroid: then the spot optimization model is formulated. As we pointed out, the concept of centroid in optical metrology is analogous to that of the center of mass relative to a continuous mass distribution within a given domain. As is known, this is formulated as follows:

$$u_c = \frac{\int_S u_{\beta} \rho(u) du}{\int_S \rho(u) du}. \quad (29)$$

Here, u_c is the center of mass, in the three-dimensional case u_{β} with $\beta = 1, 2, 3$ are the coordinates in the given reference frame, S is the continuous domain,

and $\rho(u)$ is the associated density function. In the optical context, an analogous expression holds, when the mass density is replaced by the light energy intensity $I(u)$. Regarding the discretized image created on the CCD, the following two-dimensional light intensity centroid is introduced:

$$X_c = \frac{\sum_{i,j} X_{ij} I(X_{ij}, Y_{ij})}{I_T}, \quad Y_c = \frac{\sum_{i,j} Y_{ij} I(X_{ij}, Y_{ij})}{I_T}. \tag{30}$$

Here, $(X_{ij}, Y_{ij}) \in \mathbb{N}_0 \times \mathbb{N}_0$ (denoting non-negative integer coordinates) are the points (pixels) representing the CCD (discretized) domain with respect to a given orthogonal reference frame (O, X, Y) associated with the CCD. The integer-valued function $I(X_{ij}, Y_{ij}) \in \mathbb{N}$ is the light energy intensity. Without loss of generality, it is assumed that $(X_{00}, Y_{00}) = (0, 0)$, and that $X_{ij}, Y_{ij} \geq 0$ holds for all pairs i, j . Any roto-translation of a target (consisting of light spots) generates, in general, a displacement in the corresponding light spot centroids. Therefore, considering a general light spot, the relative centroid displacement with respect to the CCD reference frame coordinates is expressed as follows:

$$\Delta X_c = \left| \frac{\sum_{ij} X_{ij} I_{ij} - \sum_{ij} X_{ij} I'_{ij}}{I_T} \right|, \quad \Delta Y_c = \left| \frac{\sum_{ij} Y_{ij} I_{ij} - \sum_{ij} Y_{ij} I'_{ij}}{I_T} \right|. \tag{31}$$

Here, I_{ij} and I'_{ij} represent (with a simplified notation) the intensities $I(X_{ij}, Y_{ij})$ and $I'(X_{ij}, Y_{ij})$ before and after the centroid displacement, respectively. Moreover, $I_T \equiv \sum I_{ij}$ with the intensity conservation condition shown below:

$$\sum_{ij} I_{ij} = \sum_{ij} I'_{ij}. \tag{32}$$

Therefore, the overall Euclidean centroid displacement is

$$\Delta_c = \frac{1}{I_T} \sqrt{\Delta X_c^2 + \Delta Y_c^2}. \tag{33}$$

In the following, it is assumed that the light spots corresponding to the initial target position and attitude with respect to the bifocal system can be generated so that their intensity distributions are identical to each other. Therefore, the optimization problem discussed here focuses on a single light spot. Its initial intensity distribution $w(X_{ij}, Y_{ij}) \in \mathbb{N}$, expressed in bit units and referred to in the following as the nominal state, is considered together with a changed state $w'(X_{ij}, Y_{ij}) \in \mathbb{N}$ (also expressed in bit units). In the following, these notations are simplified as w_{ij} and w'_{ij} . The changed state w'_{ij} corresponds to an overall intensity distribution variation, considered as representative of the perturbations of the nominal light spot in a limited neighborhood of the initial conditions.

The objective of the optimization approach proposed is to determine an intensity distribution w_{ij} for the nominal light spot to minimize the overall centroid displacement, as expressed by (33) corresponding to the perturbed intensity state w'_{ij} . Moreover, we want to determine the intensity distribution w_{ij} so that it is highly “regular,” symmetrical with respect to the centroid and strongly concentrated around it (while vanishing as more external areas are reached). The function $w'_{ij} = f_{ij}(w_{ij}, \vartheta, \beta, \gamma, \Delta x, \Delta y, \Delta z)$ that, for each (X_{ij}, Y_{ij}) , associates the perturbed intensity w'_{ij} with the nominal intensity w_{ij} and the general roto-translation $\vartheta, \beta, \gamma, \Delta x, \Delta y, \Delta z$ (recall Sect. 3) is very difficult to express mathematically.

Observe that considering all possible perturbations $(\vartheta, \beta, \gamma, \Delta x, \Delta y, \Delta z)$ in a limited neighborhood of the nominal condition (corresponding to $\vartheta = 0, \beta = 0, \gamma = 0, \Delta x = 0, \Delta y = 0, \Delta z = 0$) would lead to a challenging *minimax* problem. These aspects are therefore omitted in the model discussed here, providing instead a simplified approximate formulation of the problem. This model is expressed in terms of mixed integer linear programming (MILP), consult, e.g., Hillier [7], Minoux [9], and Nemhauser [10]. The convention of using capital letters for constants and lower-case letters for variables is adopted henceforth.

A discretized domain (sub-domain of the CCD containing the light spot) is described by the integer coordinates (X_{ij}, Y_{ij}) assuming that $i \in [0, N], j \in [0, N]$, and N is an even integer. The perturbed intensity distribution w'_{ij} is supposed to be determined by imposing that $\forall i, j \quad |w_{ij} - w'_{ij}| \leq \overline{\Delta W}$ and $\sum_{ij} |w_{ij} - w'_{ij}| = P_T$, with $\overline{\Delta W}$ and P_T as appropriately chosen positive constants, in addition to the total intensity conservation Eq. (32) applied to w_{ij} and w'_{ij} , i.e., $\sum_{ij} w = \sum_{ij} w'_{ij}$. All this is, as a matter of fact, just a simplifying trick to avoid the non-trivial challenge of expressing the actual function $w'_{ij} = f_{ij}(w_{ij}, \vartheta, \beta, \gamma, \Delta x, \Delta y, \Delta z)$ explicitly, as well as of dealing with a far more challenging *minimax* problem. The resulting formulation is therefore a surrogate model, defined in order to provide approximate practical solutions, while removing excessive complexity.

Following this approach, in addition to the intensity conservation condition (32), we assume that it is possible to choose $\overline{\Delta W}$ and P_T so that the conditions listed above can realistically condition the intensity distributions w'_{ij} as approximately representative of all considered perturbations. In this perspective, these conditions, acting on the intensity variations both at a pixel and at an overall level, can be interpreted as a relaxation of the constraint $w'_{ij} = f_{ij}(w_{ij}, \vartheta, \beta, \gamma, \Delta x, \Delta y, \Delta z)$ and a significant simplification of the original *minimax* problem. The values for $\overline{\Delta W}$ and P_T have to be estimated a priori, and this necessarily entails some arbitrariness. For instance, these parameters could be chosen bearing in mind the most critical or the most frequent cases. In general, different estimations lead to diverse solutions for the intensity distribution w_{ij} of the nominal light spot. The alternative solutions obtained can be compared to each other, to select (by means of dedicated numerical simulations) the most suitable scenario from a practical point of view.

Considering all aspects stated above, the simplified model is formulated next, explaining step by step the meaning of the expressions involved. First, the binary variables $\sigma_{ij} \in \{0, 1\}$, $\delta_{ij}^- \in \{0, 1\}$, and $\delta_{ij}^+ \in \{0, 1\}$ are defined as follows:

$$\begin{aligned} \sigma_{ij} &= 1 \text{ if pixel } (i, j) \text{ is active (i.e., } w_{ij} > 0) \\ \sigma_{ij} &= 0 \text{ otherwise,} \end{aligned}$$

$$\begin{aligned} \delta_{ij}^- &= 1 \text{ if } w_{ij} > w'_{ij}, \\ \delta_{ij}^- &= 0 \text{ otherwise,} \end{aligned}$$

$$\begin{aligned} \delta_{ij}^+ &= 1 \text{ if } w_{ij} < w'_{ij}, \\ \delta_{ij}^+ &= 0 \text{ otherwise.} \end{aligned}$$

Here $w_{ij}, w'_{ij} \in \mathbb{N}_0$.

The variables $d_{ij}^- \in \mathbb{N}_0$ and $d_{ij}^+ \in \mathbb{N}_0$ are defined next as follows:

$$\begin{aligned} d_{ij}^- &= w_{ij} - w'_{ij} \text{ if } w_{ij} > w'_{ij}, \\ d_{ij}^- &= 0 \quad \text{otherwise,} \end{aligned}$$

$$\begin{aligned} d_{ij}^+ &= w'_{ij} - w_{ij} \text{ if } w_{ij} < w'_{ij}, \\ d_{ij}^+ &= 0 \quad \text{otherwise.} \end{aligned}$$

The variables $\sigma_{ij}, \delta_{ij}^-, \delta_{ij}^+, d_{ij}^-$, and d_{ij}^+ are interrelated as shown below:

$$\forall i, j \quad \delta_{ij}^- + \delta_{ij}^+ \leq \sigma_{ij}, \tag{34}$$

$$\forall i, j \quad d_{ij}^- \geq \underline{\Delta W} \delta_{ij}^-, \tag{35-1}$$

$$\forall i, j \quad d_{ij}^+ \geq \underline{\Delta W} \delta_{ij}^+, \tag{35-2}$$

$$\forall i, j \quad d_{ij}^- \leq \overline{\Delta W} \delta_{ij}^-, \tag{36-1}$$

$$\forall i, j \quad d_{ij}^+ \leq \overline{\Delta W} \delta_{ij}^+. \tag{36-2}$$

Here the positive integers $\underline{\Delta W}$ and $\overline{\Delta W}$ represent the minimum and maximum admissible intensity change, expressed in bit units, for each active pixel (i, j) . The lower bounds (35-1) and (35-2) are introduced to easily realize detectable changes in the intensity distribution w'_{ij} . The following lower and upper bounds hold for both the nominal and perturbed states w_{ij} and w'_{ij} , respectively, in each active pixel:

$$\forall i, j \quad w_{ij} - d_{ij}^- \geq \underline{W}\sigma_{ij}, \quad (37-1)$$

$$\forall i, j \quad w_{ij} + d_{ij}^+ \leq \overline{W}\sigma_{ij}. \quad (37-2)$$

Here the positive integers \underline{W} and \overline{W} represent the minimum and maximum admissible intensity associated with each pixel (i, j) . From (37-1) and (37-2) it can also be observed that all active pixels in the nominal condition coincide with the active pixels of the perturbed state: this way, the overall shape of the light spot remains unaltered.

The next condition represents the overall intensity perturbation imposed, expressed again in bit units:

$$\sum_{ij} (d_{ij}^- + d_{ij}^+) = P_T \quad (38)$$

Here P_T is a positive integer.

The overall intensity (W_T) conservation condition, involving both the nominal and the perturbed states w_{ij} and w'_{ij} , is formulated as:

$$W_T = \sum_{ij} w_{ij} = \sum_{ij} w'_{ij}. \quad (39)$$

As a reasonable general condition, the intensity distribution w_{ij} is expected to approximate a bell-shaped continuous function with compact support. (For a similar shape, one can think of an appropriately truncated normal distribution.) The conditions introduced next pursue this overall shape by regularity and symmetry criteria. Specifically, the conditions given below determine a monotonically increasing or decreasing trend, with respect to the central pixel (\hat{i}, \hat{j}) for the nominal intensity distribution w_{ij} :

$$\forall i, j \mid i < \hat{i} - 1 \quad w_{ij} + \underline{DW}\sigma_{ij} \leq w_{i+1,j}, \quad (40-1)$$

$$\forall j \quad w_{\hat{i}-1,j} \leq w_{\hat{i},j}, \quad (40-2)$$

$$\forall j \quad w_{\hat{i}+1,j} \leq w_{\hat{i},j}, \quad (40-3)$$

$$\forall i, j \mid i > \hat{i} + 1 \quad w_{ij} - \underline{DW}\sigma_{ij} \geq w_{i+1,j}, \quad (40-4)$$

$$\forall i, j \mid j < \hat{j} - 1 \quad w_{ij} + \underline{DW}\sigma_{ij} \leq w_{i,j-1}, \quad (40-5)$$

$$\forall i \quad w_{i,\hat{j}-1} \leq w_{i\hat{j}}, \quad (40-6)$$

$$\forall i \quad w_{i,\hat{j}+1} \leq w_{i\hat{j}}, \quad (40-7)$$

$$\forall i, j \mid j > \hat{j} + 1 \quad w_{ij} - \underline{DW}\sigma_{ij} \geq w_{i,j+1}. \quad (40-8)$$

Here, $\hat{i}, \hat{j} = \frac{N}{2}$, and the positive integer \underline{DW} is the minimum intensity increment/decrement (expressed in bit units) corresponding to two adjacent indices $i, i + 1$ or $j, j + 1$, except for the indices immediately adjacent to \hat{i} and \hat{j} . The following ‘‘Lipschitzian’’ conditions are further imposed to the nominal intensity distribution w_{ij} to prevent sudden increments/decrements in adjacent indices:

$$\forall i, j \mid i < \hat{i} \quad w_{i+1,j} - w_{ij} \leq \overline{DW}, \quad (41-1)$$

$$\forall i, j \mid i > \hat{i} \quad w_{ij} - w_{i+1,j} \leq \overline{DW}, \quad (41-2)$$

$$\forall i, j \mid j < \hat{j} \quad w_{i,j+1} - w_{ij} \leq \overline{DW}, \quad (41-3)$$

$$\forall i, j \mid j > \hat{j} \quad w_{ij} - w_{i,j+1} \leq \overline{DW}, \quad (41-4)$$

where \overline{DW} is an appropriate bound, compliant with the given technological restrictions.

Several ‘‘weak’’ symmetry conditions are introduced additionally, to induce a desired overall trend of the nominal intensity distribution $w_{i,j}$. Their formulation is shown below:

$$\forall j \quad w_{0j} = w_{Nj}, \quad (42-1)$$

$$\forall j \quad w_{\hat{i}-1,j} = w_{\hat{i}+1,j}, \quad (42-2)$$

$$\forall j \quad \sum_{i < \hat{i}} w_{ij} = \sum_{i > \hat{i}} w_{ij}, \quad (42-3)$$

$$\forall i \quad w_{i0} = w_{iN}, \quad (42-4)$$

$$\forall i \quad w_{i, \hat{j}-1} = w_{i, \hat{j}+1}, \quad (42-5)$$

$$\forall i \quad \sum_{j < \hat{j}} w_{ij} = \sum_{j > \hat{j}} w_{ij}. \quad (42-6)$$

To consider realistic scenarios, it can be further imposed that all the pixels corresponding to non-decreasing intensity with respect to the nominal distribution (i.e., $w'_{ij} \geq w_{ij}$) delimit convex areas of the domain (X_{ij}, Y_{ij}) . For example, additional conditions such as $\forall i, j \quad \sum_{\bar{i} > i, j} d_{ij}^- \leq N^2 (1 - \delta_{ij}^+)$ can be introduced. These conditions express the property that from a certain index i (not determined a priori) all subsequent pixels with index $\bar{i} > i$ have a non-decreasing intensity and vice versa. (However, these aspects are not discussed in this chapter.)

Since in any real context the intensity is expected to be maximal in a central area of the spot, this criterion is selected as the optimization objective. The overall centroid displacement is instead bounded by the following inequalities:

$$\frac{\sum_{ij} X_{ij} w_{ij} - \sum_{ij} X_{ij} w'_{ij}}{W_T} \leq \bar{\Delta}_C, \quad (43-1)$$

$$\frac{\sum_{ij} Y_{ij} w_{ij} - \sum_{ij} Y_{ij} w'_{ij}}{W_T} \leq \bar{\Delta}_C, \quad (43-2)$$

Here $\bar{\Delta}_C$ is an appropriate estimation of the maximum acceptable displacement for the centroid. Finally, the following optimization criterion is introduced:

$$\max \sum_{(i,j) \in A_C} w_{ij}. \quad (44)$$

where A_C represents a proper central area.

It can be observed that the model solutions are necessarily related to the choice of the parameters $\overline{\Delta W}$ and P_T , assumed to represent the specific case under study. As anticipated, a number of different choices can be compared to select the most suitable option from a practical point of view. This approach could however be significantly improved by adopting a multi-scenario optimization point of view. In this perspective, instead of $\overline{\Delta W}$ and P_T a set of parameters $\overline{\Delta W}_\alpha$ and $P_{T\alpha}$ ($\alpha = 1, \dots, N_S$) are considered. A perturbed intensity $w'_{ij\alpha}$ is associated with the corresponding parameters $\overline{\Delta W}_\alpha$ and $P_{T\alpha}$, and the whole model is extended by properly replicating and readjusting the conditions and the objective function involved. However, this aspect – as a possible topic of future research – is not investigated here.

5 An Illustrative Case Study

As mentioned in Sect. 1, the bifocal system has recently been considered for possible utilization for the Athena satellite. The case study is only briefly outlined here, omitting (for confidentiality reasons) most of the technical details.

The two instruments, high-resolution X-ray Integral Field Unit (X-IFU) and Wide Field Imager (WFI) mentioned in Sect. 1, are accommodated within the Focal Plane Module (FPM). The Mirror Assembly Module (MAM) is placed at an assigned distance (12 m) from the FPM. Since the telescope line of sight is determined by the telescope mirror position and attitude, the on-board metrology is aimed at supporting the active control of the MAM focal point position with respect to the FPM instruments. The proposed design for the bifocal metrology on board Athena considers:

- The bifocal optical head mounted on the MAM and aligned with it
- One light target on each instrument

The overall light target is essentially composed by three LEDs defining an isosceles triangle. With reference to this specific case study, three main aspects have been investigated in depth (by applying the concepts discussed in Sects. 3.4, 4.1 and 4.2):

- Error analysis for the measured distance between the MAM focal point position and the FPM instruments
- Optimal system sizing
- Light spot optimization

Fig. 11 Case study: nominal intensity distribution example 1

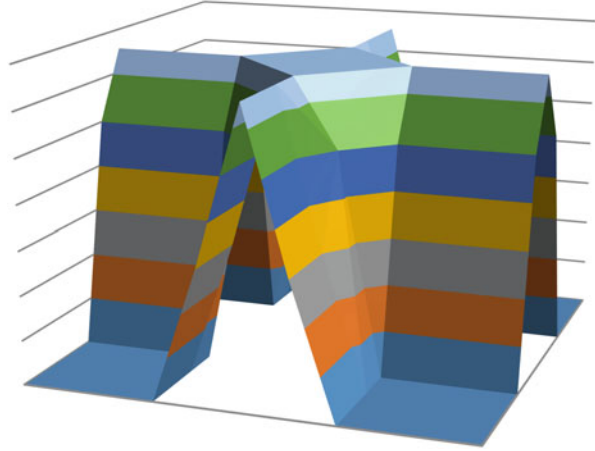
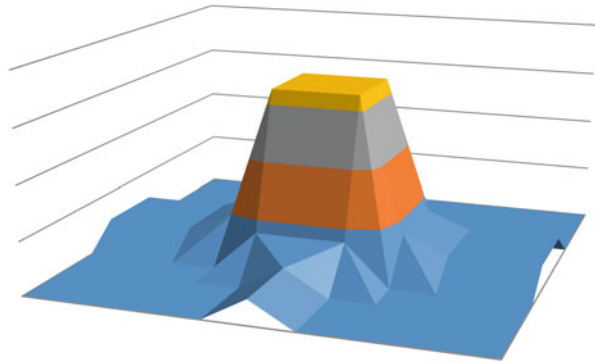


Fig. 12 Case study: nominal intensity distribution example 2



The optimization models considered for both error analysis and system sizing have been solved by the global-local nonlinear optimization software package LGO [12]. Again, technical details are not reported here for confidentiality reasons. As a main result, a trade-off concerning the optimal focal distances f_1 and f_2 has been made. On the one hand, these terms should be close to each other ($f_1 \sim f_2$) and as large as possible, compatibly with the maximum admissible dimension of the optical head. On the other hand, a small difference between f_1 and f_2 can give rise to possible partial overlapping between the light spot projections on the CCD.

The MILP model adopted for the light spot optimization has been solved by the IBM ILOG CPLEX solver (version 12.3). Several possible solutions have been considered. Figures 11 and 12 illustrate two examples of optimal nominal light spots obtained for the case study (the physical units have been omitted for confidentiality reasons).

6 Concluding Remarks

The work presented here discusses an innovative metrological approach, based on a recently patented bifocal optical system [2–4]. This system is aimed at measuring the position and attitude of a target item, identified by means of three light spots, almost instantaneously and with high precision. The approach proposed is simple and efficient: here it is discussed in relation to advanced space engineering applications, but not limited to these.

In this chapter, the concept of the bifocal optical system is discussed in depth, investigating some mathematical aspects relevant to the overall methodology adopted, including error analysis, system sizing optimization, and light spot optimization. Finally, a real-world case study is highlighted.

Future research can be aimed at advancements in relation to both the error analysis and system sizing optimization problems discussed here. In this perspective, enhancements of the global optimization approach followed aimed at improving the global search can be expected. Concerning the light spot optimization problem, to extend solution adaptability and reliability, the corresponding MILP model could be considered in a multi-scenario optimization approach.

References

1. Bresciani, F. (2016) An innovative bifocal metrology system for aerospace applications. *Journal of Instrumentation*, Vol. 11, 4th International Conference Frontiers in Diagnostics Fix Technologies (ICFDT4).
2. Bresciani F., Musso, F. (2015) Projective optical metrology system for determining attitude and position. IT007-BIS EP2508427 (Patent granted in EP and USA).
3. Bresciani, F., Musso, F. (2016) Coarse and fine projective optical metrology system IT007 EP2508428 (Patent granted in EP and USA).
4. Bresciani, F., Musso, F. (2017) Projective optical metrology system. IT008 EP2677338 (Patent granted in EP and USA).
5. Floudas, C.A. and Pardalos P.M., Eds. (2001) *Encyclopedia of Optimization*. Kluwer Academic Publishers, Dordrecht, The Netherlands.
6. Ghali, S. (2008) *Introduction to Geometric Computing*. Springer Science + Business Media, New York.
7. Hillier, F.S. and Lieberman, G.J. (2001) *Introduction to Operations Research*. McGraw-Hill, New York.
8. Liberti, L., Maculan, N., (Eds.) (2005) *Global Optimization: From Theory to Implementation*. Springer Science + Business Media, New York.
9. Minoux, M. (1986) *Mathematical Programming: Theory and Algorithms*. John Wiley & Sons, Paris.
10. Nemhauser, G.L., Wolsey, L.A. (1988) *Integer and Combinatorial Optimization*. Wiley, New York.
11. Pintér, J.D. (1996) *Global Optimization in Action*. Kluwer Academic Publishers, Dordrecht, The Netherlands. Available from Springer Science + Business Media, New York.
12. Pintér, J.D. (2015) *LGO – A Model Development and Solver System for Global-Local Nonlinear Optimization. User’s Guide*. PCS Inc., Canada.

13. Tyson, R.K. (2010) *Principles of Adaptive Optics*. Taylor & Francis Group (3rd ed.). CRC Press, Boca Raton, FL.
14. Yoshizawa, T. (Ed.). (2015) *Handbook of Optical Metrology. Principles and Applications*. Taylor & Francis Group (2nd ed.). CRC Press, Boca Raton, FL.

A Revisited Analysis of the Radioisotope Sail and Its Possible Application to Relativistic Spaceflight



Luca Derosa

1 Introduction

The radioisotope sail as a propulsion system has already been preliminarily described in previous works, as in [1–3], but in the author's opinion it is possible to enrich what has already been done.

The study was conducted within the framework of the Special Theory of Relativity as the performance level achievable by the propulsion system is not known a priori, not only in this first study but also in subsequent ones which will tend to make it obtain even better results and therefore potentially suitable for the relativistic context.

Specifically, in this study:

- We have defined the mathematical models of different possible spaceflight profiles under relativistic conditions, also considering specific profiles never previously studied
- We have defined the mathematical models of the radioisotope sail, obtaining every formula for the case of single decay, double decay, and decay chain related to alpha decay, and therefore showing a novel treatment not present in literature
- We analyzed the possible compatibility between the behavior of the radioisotope sail and the flight profiles studied, showing novel considerations
- We calculated the hypothetical performance of this propulsion system for a mission to Pluto

L. Derosa (✉)
iMEX.A, Torino, Italy
e-mail: luca.derosa@imexa.it

The study was conducted in the context of the Special Relativity, in order to provide a useful mathematical tool in the event that humanity in the future will be able to fly at relativistic speeds.

2 Fundamentals of Relativistic Spaceflight

In this section we report the main expressions of spaceflight in relativistic conditions, in the framework of the Special Theory of Relativity.

2.1 Rocket Equation

We can derive the rocket equation, the most significant equation of the space engineering, in two different forms: the classical version still used today as a reference base in all space missions and the relativistic version useful for future missions at speeds that are not negligible compared to that of light.

2.1.1 Classical Rocket Equation or Tsiolkovsky Equation

We consider at time t a spacecraft with velocity V and mass m .

Then we consider at time $t + dt$ that the same spacecraft ejects a mass m_p at the velocity w_e (i.e., the *exhaust velocity*), relative to the spacecraft itself, and consequently the latter assumes a velocity equal to $V + dV$ and a mass equal to $m - dm_p$.

We can write the momentum of the whole system (spacecraft) at time t :

$$q_0 = m \cdot V \quad (1)$$

and at the time $t + dt$ (spacecraft + ejected mass):

$$q_1 = (m - dm_p) \cdot (V + dV) + dm_p \cdot (V - w_e) \quad (2)$$

Considering the conservation of momentum, we have that $q_0 = q_1$, and after a few simple steps we can derive the thrust T :

$$m \cdot \frac{dV}{dt} = \frac{dm_p}{dt} \cdot w_e \rightarrow \dot{m}_p \cdot w_e = T \quad (3)$$

From that formula we can integrate in t , between an initial instant and a final instant, and obtain a possible formulation of *Tsiolkovsky equation*:

$$\Delta V = w_e \cdot \ln \frac{m_i}{m_f} \quad (4)$$

If we consider the specific impulse, defined as:

$$I_{sp} = \frac{T}{\dot{m}_p \cdot g_0} = \frac{w_e}{g_0} \quad (5)$$

we can yield the Tsiolkovsky equation in a different formulation:

$$\Delta V = g_0 \cdot I_{sp} \cdot \ln \frac{m_i}{m_f} \quad (6)$$

We can also rewrite the equation in other different ways:

$$m_f = m_i \cdot e^{-\frac{\Delta V}{w_e}} = m_i \cdot e^{-\frac{\Delta V}{g_0 \cdot I_{sp}}} \quad (7)$$

2.1.2 Relativistic Rocket Equation or Ackeret Equation

In this section we can study the behavior of a spacecraft flying at relativistic speed, in order to derive the corresponding rocket equation by following one of the many possible ways.

With respect to a coordinate reference system (a reference system at rest, compared to the spacecraft) we can write:

$$d(m \cdot V) - w_e \cdot dm_p = 0 \quad (8)$$

and for the law of conservation of mass-energy:

$$dm + dm_p = 0 \rightarrow dm = -dm_p \quad (9)$$

From (8) and (9) one then finds:

$$d(m \cdot V) + w_e \cdot dm = 0 \rightarrow (V + w_e) \cdot dm + m \cdot dV = 0 \quad (10)$$

Remembering the link in Relativity between the rest mass m' (or proper mass) and the relativistic mass m (or coordinate mass), using c to represent the speed of light in vacuum:

$$m = \frac{m'}{\sqrt{1 - \frac{V^2}{c^2}}} \quad (11)$$

and the law of relativistic velocity addition applied to the exhaust velocity (w_e in the coordinate reference system and w_e' in the proper reference system, i.e., a reference system that moves together with the spacecraft):

$$w_e' = \frac{V + w_e}{1 + \frac{V \cdot w_e}{c^2}} \quad (12)$$

we can insert them in Eq. (10), considering w_e' a constant value (fundamental requirement for the relativistic rocket), and after a few simple steps we can obtain a formulation of *Ackeret equation*:

$$\Delta V = c \cdot \frac{1 - \left(\frac{m_f'}{m_i'}\right)^{\frac{2 \cdot w_e'}{c}}}{1 + \left(\frac{m_f'}{m_i'}\right)^{\frac{2 \cdot w_e'}{c}}} \quad (13)$$

It is possible to see the explicit derivation of the Ackeret equation in many texts, following as many different approaches, including for example the Robert Forward's well-known AIAA publication "A Transparent Derivation of the Relativistic Rocket Equation [1]."

We can rewrite the last equation introducing the specific impulse:

$$\Delta V = c \cdot \frac{1 - \left(\frac{m_f'}{m_i'}\right)^{\frac{2 \cdot g_0 \cdot I_{sp}'}{c}}}{1 + \left(\frac{m_f'}{m_i'}\right)^{\frac{2 \cdot g_0 \cdot I_{sp}'}{c}}} \quad (14)$$

Another way to write the Ackeret equation is with hyperbolic functions:

$$\Delta V = c \cdot \tanh\left(\frac{w_e'}{c} \cdot \ln \frac{m_i'}{m_f'}\right) \text{ or } \Delta V = c \cdot \tanh\left(\frac{g_0 \cdot I_{sp}'}{c} \cdot \ln \frac{m_i'}{m_f'}\right) \quad (15)$$

2.2 Relativistic Spaceflight Profiles

In this section we present the analysis results of the most important flight profiles in relativistic conditions. In all cases we assume w_e' as a constant.

2.2.1 Uniform Linear Motion

In relativity like in classical physics the simplest type of motion is the uniform linear one.

We assume the coordinate velocity V as a constant, then we can calculate the relation between the proper time τ and the coordinate time t :

$$dt = \frac{d\tau}{\sqrt{1 - \frac{V^2}{c^2}}} \rightarrow t(\tau) = \frac{\tau}{\sqrt{1 - \frac{V^2}{c^2}}} \quad (16)$$

and the inverse relation is:

$$\tau(t) = \sqrt{1 - \frac{V^2}{c^2}} t \quad (17)$$

The value of coordinate space is:

$$V = \frac{dx}{dt} \rightarrow x(t) = V t \quad (18)$$

or as a function of τ is:

$$x(\tau) = V \frac{\tau}{\sqrt{1 - \frac{V^2}{c^2}}} \quad (19)$$

The inverse relation of the last two are, respectively:

$$t(x) = \frac{x}{V} \quad (20)$$

$$\tau(x) = \frac{x}{V} \sqrt{1 - \frac{V^2}{c^2}} \quad (21)$$

2.2.2 Hyperbolic Motion

For a generic motion, from the scalar form of the relativistic second law of motion we have:

$$T = \frac{d(m V)}{dt} \quad (22)$$

and if we explicitly derive it we obtain:

$$T = \frac{dm}{dt} V + m a \quad (23)$$

where T is the thrust applied to the spacecraft, a is the coordinate acceleration expressed by dV/dt , and m is the coordinate mass.

We can replace the expression of proper mass in Eq. (23) and solve it with respect to the coordinate acceleration to have:

$$a(t) = \frac{dV}{dt} = \frac{T(t)}{m'(t)} \left(1 - \frac{V(t)^2}{c^2} \right)^{3/2} \quad (24)$$

If we integrate and solve it with respect to V we obtain:

$$V(t) = \frac{T(t) t}{m'(t)} \frac{1}{\sqrt{1 + \left(\frac{T(t) t}{m'(t) c} \right)^2}} \quad (25)$$

To derive the specific characteristics of the hyperbolic motion, we assume that the proper acceleration is constant and equal to $a' = T/m'$. So we can rewrite the last two equations as follows:

$$a(t) = a' \left(1 - \frac{V(t)^2}{c^2} \right)^{3/2} \quad (26)$$

$$V(t) = \frac{a' t}{\sqrt{1 + \left(\frac{a' t}{c} \right)^2}} \quad (27)$$

We can invert the last relation to yield:

$$t(V) = \frac{V}{a' \cdot \sqrt{1 - \frac{V^2}{c^2}}} \quad (28)$$

and rewrite the coordinate acceleration as follows:

$$a(t) = \frac{a'}{\left[1 + \left(\frac{a' t}{c} \right)^2 \right]^{3/2}} \quad (29)$$

We can introduce the well-known relation:

$$T(\tau) = w_e' \cdot \dot{m}'(\tau) \quad (30)$$

where \dot{m}' is the mass flow rate with respect to the proper reference frame, and we obtain:

$$\frac{dV}{d\tau} \frac{d\tau}{dt} = \frac{w_e' \cdot \dot{m}'}{m'} \left(1 - \frac{V^2}{c^2}\right)^{3/2} \rightarrow \frac{dV}{d\tau} \sqrt{1 - \frac{V^2}{c^2}} = \frac{w_e' \cdot \dot{m}'}{m'} \left(1 - \frac{V^2}{c^2}\right)^{3/2} \quad (31)$$

that after integration gives the aforementioned Ackeret equation (here we define a generic expression, function of the proper time):

$$V(\tau) = c \cdot \frac{1 - \left(\frac{m'(\tau)}{m'(0)}\right)^{\frac{2 \cdot w_e'}{c}}}{1 + \left(\frac{m'(\tau)}{m'(0)}\right)^{\frac{2 \cdot w_e'}{c}}} \text{ or } V(\tau) = c \cdot \tanh \left[\frac{w_e'}{c} \cdot \ln \left(\frac{m'(0)}{m'(\tau)} \right) \right] \quad (32)$$

Following a few simple steps, we can rewrite the Ackeret equation as an explicit function of the proper acceleration:

$$V(\tau) = c \cdot \frac{1 - e^{\frac{2 \cdot a' \cdot \tau}{c}}}{1 + e^{\frac{2 \cdot a' \cdot \tau}{c}}} \text{ or } V(\tau) = c \cdot \tanh \left(\frac{a' \tau}{c} \right) \quad (33)$$

that can be inverted to yield:

$$\tau(V) = \frac{c}{a'} \cdot \operatorname{artanh} \left(\frac{V}{c} \right) \quad (34)$$

We can also get proper mass as an explicit function of proper time:

$$m'(\tau) = m'(0) \cdot e^{-\frac{a' \tau}{w_e'}} \quad (35)$$

And, consequently, the mass flow rate:

$$\dot{m}'(\tau) = -\frac{dm'(\tau)}{d\tau} = \frac{m'(0) a'}{w_e'} \cdot e^{-\frac{a' \tau}{w_e'}} \rightarrow \dot{m}'(\tau) = \dot{m}'(0) \cdot e^{-\frac{a' \tau}{w_e'}} \quad (36)$$

being $\dot{m}'(0) = (m'(0) \cdot a) / w_e'$ and consequently $a' = (w_e' \cdot \dot{m}'(0)) / m'(0)$.

Since $V(t) = dx(t)/dt$ we can obtain the following expressions:

$$x(t) = \frac{c^2}{a'} \left[\sqrt{1 + \left(\frac{a' t}{c} \right)^2} - 1 \right] \quad (37)$$

$$t(x) = \frac{c}{a'} \sqrt{\left(1 + \frac{a' x}{c^2} \right)^2 - 1} \quad (38)$$

We can also obtain the relation between proper time and coordinate time:

$$\tau(t) = \frac{c}{a'} \operatorname{arsinh}\left(\frac{a' t}{c}\right) \text{ or } \tau(t) = \frac{c}{a'} \ln \left[\sqrt{1 + \left(\frac{a' t}{c}\right)^2} + \frac{a' t}{c} \right] \quad (39)$$

$$t(\tau) = \frac{c}{a'} \sinh\left(\frac{a' \tau}{c}\right) \quad (40)$$

Thanks to the last expressions we can find the relation between space travelled and proper time:

$$x(\tau) = \frac{c^2}{a'} \left[\cosh\left(\frac{a' \tau}{c}\right) - 1 \right] \quad (41)$$

and between coordinate acceleration and proper time:

$$a(\tau) = \frac{a'}{\left[1 + \sinh^2\left(\frac{a' \tau}{c}\right)\right]^{3/2}} \quad (42)$$

Finally, we can obtain the following expressions about space travelled:

$$\tau(x) = \frac{c}{a'} \operatorname{acosh}\left(1 + \frac{a' x}{c^2}\right) \quad (43)$$

$$V(x) = c \cdot \sqrt{1 - \frac{1}{\left(1 + \frac{a' x}{c^2}\right)^2}} \quad (44)$$

$$x(V) = \frac{c^2}{a'} \frac{\left[1 - \sqrt{1 - \frac{V^2}{c^2}}\right]}{\sqrt{1 - \frac{V^2}{c^2}}} \quad (45)$$

2.2.3 Constant Thrust Motion – Exhaust Velocity $w_e' \neq c$

In this case we assume the thrust is constant, so mass flow rate must be constant as well:

$$\dot{m}' = \frac{T}{w_e'} = \text{constant} \quad (46)$$

and, as a consequence, we can recalculate some quantities already defined.

The first quantity we can calculate is the proper mass in terms of proper time as follows:

$$\dot{m}' = -\frac{dm'(\tau)}{d\tau} \rightarrow m'(\tau) = m'(0) - \frac{T}{w_{e'}} \cdot \tau \quad (47)$$

from which one gets the definition of the proper acceleration as a function of the proper time:

$$a'(\tau) = \frac{T}{m'(\tau)} = \frac{T}{m'(0) - \frac{T}{w_{e'}} \cdot \tau} \quad (48)$$

As done in the previous section, we can refer to the relation (31) that in this case becomes:

$$\frac{dV}{d\tau} \sqrt{1 - \frac{V^2}{c^2}} = \frac{T}{m'(0) - \frac{T}{w_{e'}} \cdot \tau} \left(1 - \frac{V^2}{c^2}\right)^{3/2} \quad (49)$$

that after integration yields the Ackeret equation:

$$V(\tau) = c \cdot \frac{1 - \left(1 - \frac{T \cdot \tau}{m'(0) \cdot w_{e'}}\right)^{\frac{2 \cdot w_{e'}}{c}}}{1 + \left(1 - \frac{T \cdot \tau}{m'(0) \cdot w_{e'}}\right)^{\frac{2 \cdot w_{e'}}{c}}} \quad (50)$$

or proper time as a function of velocity, inverting it:

$$\tau(V) = \frac{m'(0) \cdot w_{e'}}{T} \left[1 - \left(\frac{c - V}{c + V}\right)^{\frac{c}{2 \cdot w_{e'}}} \right] \quad (51)$$

It is impossible to analytically calculate the other remaining quantities, so the only way is the numerical approach.

2.2.4 Constant Thrust Motion – Exhaust Velocity $w_{e'} = c$

If we study the particular case where $w_{e'} = c$, i.e., the case when the particles emitted are photons, we can explicitly calculate almost all quantities unlike the previous case.

First of all we rewrite the expressions already seen in the previous section (Ackeret equation is also valid for massless particles):

$$\dot{m}' = \frac{T}{c} = \text{constant} \quad (52)$$

$$m'(\tau) = m'(0) - \frac{T}{c} \cdot \tau \quad (53)$$

$$a'(\tau) = \frac{T}{m'(0) - \frac{T}{c} \cdot \tau} \quad (54)$$

$$V(\tau) = c \cdot \frac{1 - \left(1 - \frac{T \cdot \tau}{m'(0) \cdot c}\right)^2}{1 + \left(1 - \frac{T \cdot \tau}{m'(0) \cdot c}\right)^2} \quad (55)$$

$$\tau(V) = \frac{m'(0) c}{T} \left[1 - \sqrt{\frac{c - V}{c + V}} \right] \quad (56)$$

Now we can obtain the relation between the proper time and the coordinate time:

$$t(\tau) = \frac{2 m'(0) c T \tau - T^2 \tau^2 + 2 m'(0)^2 c^2 \ln \left(\frac{m'(0) c}{m'(0) c - T \tau} \right)}{4 m'(0) c T} \quad (57)$$

and the inverse relation:

$$\tau(t) = \frac{m'(0) c}{T} \left[1 - \sqrt{W \left(e^{\frac{m'(0) c - 4 T t}{m'(0) c}} \right)} \right] \quad (58)$$

where W is the *Lambert W-function* (also called *Omega function*), i.e., the inverse function of $f(W) = W \cdot e^W$. Even for every number x we have $x = W(x) \cdot e^{W(x)}$.

Thanks to the last expressions we can find the relations between velocity and coordinate time:

$$V(t) = c \cdot \frac{1 - W \left(e^{\frac{m'(0) c - 4 T t}{m'(0) c}} \right)}{1 + W \left(e^{\frac{m'(0) c - 4 T t}{m'(0) c}} \right)} \quad (59)$$

$$t(V) = \frac{m'(0) \cdot c}{4 T} \left[\frac{2 V}{c + V} - \ln \left(\frac{c - V}{c + V} \right) \right] \tag{60}$$

and between coordinate acceleration and time (coordinate and proper):

$$a(t) = \frac{8 T W \left(e^{\frac{m'(0) c - 4 T t}{m'(0) c}} \right)}{m'(0) \left[1 + W \left(e^{\frac{m'(0) c - 4 T t}{m'(0) c}} \right) \right]^3} \tag{61}$$

$$a(\tau) = \frac{8 T m'(0)^3 c^4 [m'(0) c - T \tau]^2}{[2 m'(0)^2 c^2 - 2 m'(0) c T \tau + T^2 \tau^2]^3} \tag{62}$$

If we want to calculate the relation between coordinate distance x and the proper time, before doing so we need to define the following expression:

$$V(\tau) = \frac{dx}{d\tau} \frac{d\tau}{dt} \tag{63}$$

and consequently, we have to integrate:

$$\int_0^x dx = \int_0^\tau V(\tau) \frac{d\tau}{dt} d\tau \tag{64}$$

The solution is:

$$x(\tau) = \frac{-2 m'(0) c T \tau + T^2 \tau^2 + 2 m'(0)^2 c^2 \ln \left(\frac{m'(0) c}{m'(0) c - T \tau} \right)}{4 m'(0) T} \tag{65}$$

and the inverse relation is:

$$\tau(x) = \frac{m'(0) c}{T} \frac{\sqrt{-\frac{1}{W \left(-e^{-\frac{4 T x + m'(0) c^2}{m'(0) c^2}} \right)} - 1}}{\sqrt{-\frac{1}{W \left(-e^{-\frac{4 T x + m'(0) c^2}{m'(0) c^2}} \right)}}} \tag{66}$$

The last formula can also be written in an alternative form:

$$\tau(x) = \frac{m'(0) c}{T} \cdot \left[-\exp \left(-\frac{4 T x + m'(0) c^2 + m'(0) c^2 W \left(-\exp \left(-\frac{4 T x + m'(0) c^2}{m'(0) c^2} \right) \right)}{2 m'(0) c^2} \right) + 1 \right] \quad (67)$$

It is possible to yield the relation between x and t :

$$x(t) = \frac{c}{2 T} \left[2 T t - m'(0) c + m'(0) c W \left(e^{\frac{m'(0) c - 4 T t}{m'(0) c}} \right) \right] \quad (68)$$

and between velocity and space (direct and inverse relation):

$$V(x) = c \cdot \frac{1 + W \left(-e^{-\frac{4 T x + m'(0) c^2}{m'(0) c^2}} \right)}{1 - W \left(-e^{-\frac{4 T x + m'(0) c^2}{m'(0) c^2}} \right)} \quad (69)$$

$$x(V) = -\frac{m'(0) c^2}{4 T} \left[\frac{2 V}{c + V} + \ln \left(\frac{c - V}{c + V} \right) \right] \quad (70)$$

2.2.5 Negative Exponential Acceleration Motion

In this case we assume a negative exponential trend of the mass flow rate and the thrust, which are, respectively:

$$\dot{m}'(\tau) = K_1 \cdot e^{-K_2 \tau} \quad (71)$$

$$T(\tau) = w_e' \cdot \dot{m}'(\tau) = w_e' \cdot K_1 \cdot e^{-K_2 \tau} \quad (72)$$

where K_1 and K_2 are coefficients that characterize every specific negative exponential trend.

We can obtain the negative exponential trend of proper mass in terms of proper time as follows:

$$m'(\tau) = m'(0) - \frac{K_1}{K_2} \left(1 - e^{-K_2 \tau} \right) \quad (73)$$

and also the proper acceleration behavior that turns out to be of a negative exponential type (this trend gives the name to this motion):

$$a'(\tau) = \frac{w_e' \cdot K_1 \cdot e^{-K_2 \tau}}{m'(0) - \frac{K_1}{K_2} (1 - e^{-K_2 \tau})} \quad (74)$$

As previously done, we can refer to the relation (31) that in this case becomes:

$$\frac{dV}{d\tau} \sqrt{1 - \frac{V^2}{c^2}} = \frac{w_e' \cdot K_1 \cdot e^{-K_2 \tau}}{m'(0) - \frac{K_1}{K_2} (1 - e^{-K_2 \tau})} \left(1 - \frac{V^2}{c^2}\right)^{3/2} \quad (75)$$

that after integration yields the Ackeret equation:

$$V(\tau) = c \cdot \frac{1 - \left[1 - \frac{K_1 \cdot (1 - e^{-K_2 \tau})}{K_2 \cdot m'(0)}\right]^{\frac{2 \cdot w_e'}{c}}}{1 + \left[1 - \frac{K_1 \cdot (1 - e^{-K_2 \tau})}{K_2 \cdot m'(0)}\right]^{\frac{2 \cdot w_e'}{c}}} \quad (76)$$

or proper time as a function of velocity, inverting it:

$$\tau(V) = -\ln \left[1 + \frac{K_2}{K_1} m'(0) \left(\left(\frac{c - V}{c + V}\right)^{\frac{c}{2 w_e'}} - 1\right)\right] \quad (77)$$

It is impossible to analytically calculate the other remaining quantities, so the only way is the numerical approach.

2.2.6 Characteristic Formulas of All Profiles Studied

In this section we collect all the formulas derived in the previous sections for every type of motion studied (we exclude here the uniform linear motion only, since its simplicity), in order to have the possibility to compare them with each other with a single glance (Table 1).

We can also graphically represent some of the relations expressed in Table 1 (Figs. 1, 2, and 3), to show more clearly their behavior, considering equal initial proper acceleration $a'(0)$ and initial proper mass $m'(0)$.

The behavior of mass flow rate is similar to the thrust, so we can avoid drawing it.

3 Fundamentals of Radioactive Decay

Every radioactive material, i.e., unstable, naturally emits particles at relativistic speeds. This phenomenon is called radioactive decay.

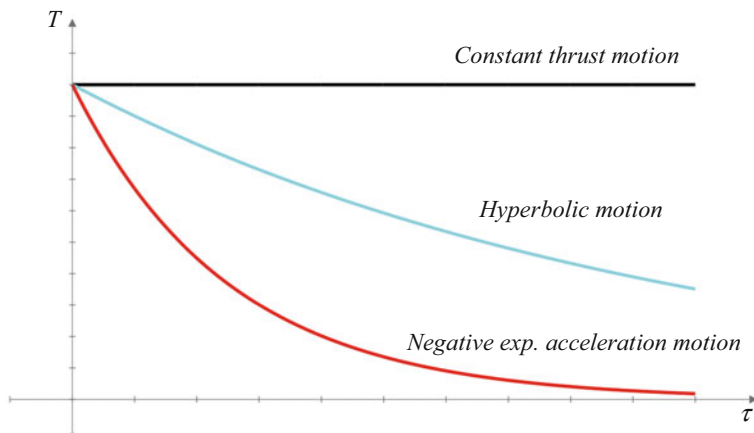


Fig. 1 Qualitative comparison between the behavior of thrust T for constant thrust motion (black line), hyperbolic motion (light blue line), and negative exponential acceleration motion (red line)

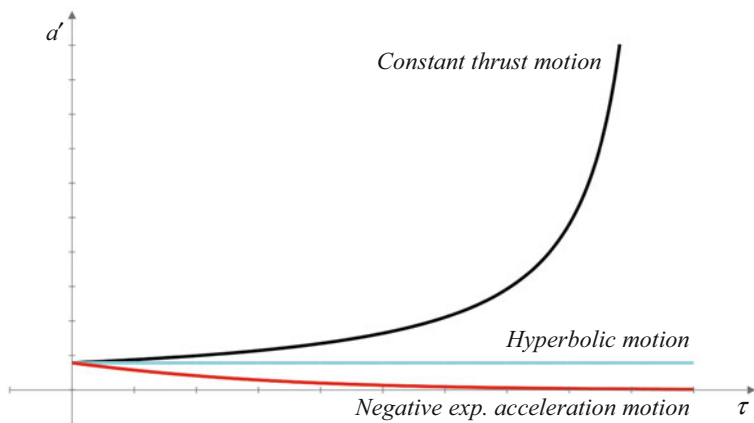


Fig. 2 Qualitative comparison between the behavior of proper acceleration a' for constant thrust motion (black line), hyperbolic motion (light blue line), and negative exponential acceleration motion (red line)

Due to the particles emitted, the initial material is transformed into a different material. The new material obtained can be stable, i.e., unable to transform itself further, or it can be unstable too and continue in a subsequent decay. In the latter case we speak of a decay chain.

The particles emitted constitute the so-called ionizing radiation and are different according to the type of radioactive material under examination. These include beta minus particles β^- (electrons), beta plus particles β^+ (positrons), alpha α^{2+} (doubly ionized helium), and gamma rays γ . They can be ejected from the material in any direction, which cannot be defined a priori.

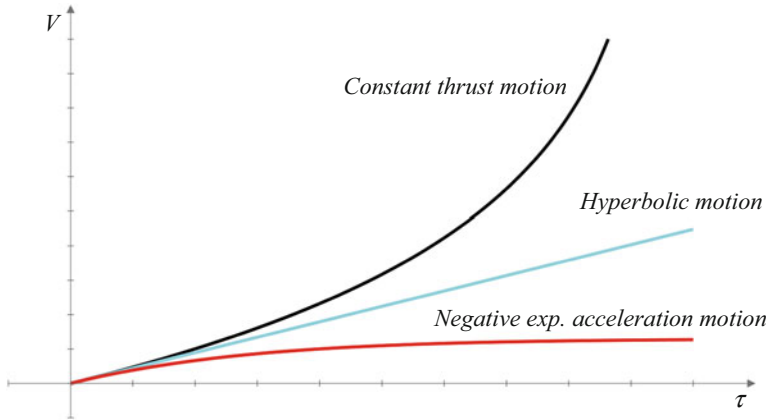


Fig. 3 Qualitative comparison between the behavior of velocity V for constant thrust motion (black line), hyperbolic motion (light blue line), and negative exponential acceleration motion (red line)

Radioactive decay is a natural phenomenon that does not need to be started, but equally it cannot be accelerated, slowed down, or stopped (some research groups have actually modified the decay rate, but the variations are currently numerically negligible for the purposes discussed here). Furthermore, a secondary effect of the decay is the heating of the material in which it occurs.

Radioactive decay takes place according to the so-called radioactive decay law, which states that the probability per unit time that a nucleus will decay is constant, independent of time. This constant is called the decay constant and is denoted by λ . In other words, the radioactive decay law states that the number of particles emitted by each material decreases over time, more or less quickly depending on the material itself, while the average speed of the particles remains unchanged.

In view of using radiation for propulsive purposes, we can make some initial considerations.

Alpha particles are potentially suitable for propelling a spacecraft: they have a high momentum, thanks to their electric charge they can be deflected by an appropriate magnetic field, in order to direct them in the desired direction (opposite to flight direction), and they can be shielded very easily to protect the spacecraft. However, the ease of absorption is also a problem, as a part of particles can be reabsorbed by the same material that emitted them. To try to exploit at least half of such particles it is necessary to hypothesize the use of an extremely thin sail, so that “only” half of the particles emitted are reabsorbed by the material of the sail and the other half is expelled.

Gamma rays are neutral and have a penetration power too high so we cannot deflect them in the desired direction and cannot exploit their energy to thrust the spacecraft.

Table 1 Characteristic formulas of spaceflight profiles

	Hyperbolic motion	Constant thrust motion	$w_e' \neq c$	$w_e' = c$	Negative exponential acceleration motion
$T(\tau)$	$d' \cdot m'(0) \cdot e^{-\frac{d' \cdot \tau}{w_e}}$	$w_e' \cdot \dot{m}' = \text{const}$	$w_e' \cdot \dot{m}' = \text{const}$	$c \cdot \dot{m}' = \text{const}$	$w_e' \cdot K_1 \cdot e^{-K_2 \tau}$
$\dot{m}'(\tau)$	$\dot{m}'(0) \cdot e^{-\frac{d' \cdot \tau}{w_e}}$	$\frac{T}{w_e} = \text{const}$	$\frac{T}{w_e} = \text{const}$	$\frac{T}{c} = \text{const}$	$K_1 \cdot e^{-K_2 \tau}$
$m'(\tau)$	$m'(0) \cdot e^{-\frac{d' \cdot \tau}{w_e}}$	$m'(0) - \frac{T}{w_e} \cdot \tau$	$m'(0) - \frac{T}{w_e} \cdot \tau$	$m'(0) - \frac{T}{c} \cdot \tau$	$m'(0) - \frac{K_1}{K_2} (1 - e^{-K_2 \tau})$
$a'(\tau)$	$\frac{w_e \cdot \dot{m}'(0)}{m'(0)} = \text{const}$	$\frac{T}{m'(0) - \frac{T}{w_e} \cdot \tau}$	$\frac{T}{m'(0) - \frac{T}{w_e} \cdot \tau}$	$\frac{T}{m'(0) - \frac{T}{c} \cdot \tau}$	$\frac{w_e' \cdot K_1 \cdot e^{-K_2 \tau}}{m'(0) - \frac{K_1}{K_2} (1 - e^{-K_2 \tau})}$
$a(\tau)$	$\frac{d'}{\left[1 + \sinh^2\left(\frac{d' \cdot \tau}{c}\right)\right]^{3/2}}$	Numerical	Numerical	$\frac{8 T m'(0)^3 \cdot d' \left[\frac{m'(0) \cdot c - 4 T \tau}{m'(0) \cdot c} \right]^2}{\left[2 m'(0)^2 \cdot c^2 - 2 m'(0) \cdot c T \tau + T^2 \tau^2 \right]^3}$	Numerical
$a(t)$	$\frac{d'}{\left[1 + \left(\frac{d' \cdot t}{c}\right)^2\right]^{3/2}}$	Numerical	Numerical	$\frac{8 T W \left(e^{\frac{m'(0) \cdot c - 4 T t}{m'(0) \cdot c}} \right)}{m'(0) \left[1 + W \left(e^{\frac{m'(0) \cdot c - 4 T t}{m'(0) \cdot c}} \right) \right]^3}$	Numerical
$V(\tau)$	$c \cdot \tanh\left(\frac{d' \cdot \tau}{c}\right)$	$c \cdot \frac{1 - \left(1 - \frac{T \cdot \tau}{m'(0) \cdot w_e}\right) \frac{2 \cdot w_e'}{c}}{1 + \left(1 - \frac{T \cdot \tau}{m'(0) \cdot w_e}\right) \frac{2 \cdot w_e'}{c}}$	$c \cdot \frac{1 - \left(1 - \frac{T \cdot \tau}{m'(0) \cdot c}\right) \frac{2}{1 + \left(1 - \frac{T \cdot \tau}{m'(0) \cdot c}\right) \frac{2}{c}}}{1 + \left(1 - \frac{T \cdot \tau}{m'(0) \cdot c}\right) \frac{2}{c}}$	$c \cdot \frac{1 - \left(1 - \frac{T \cdot \tau}{m'(0) \cdot c}\right) \frac{2}{1 + \left(1 - \frac{T \cdot \tau}{m'(0) \cdot c}\right) \frac{2}{c}}}{1 + \left(1 - \frac{T \cdot \tau}{m'(0) \cdot c}\right) \frac{2}{c}}$	$c \cdot \frac{1 - \left[1 - \frac{K_1 (1 - e^{-K_2 \tau})}{K_2 m'(0)} \right] \frac{2 \cdot w_e'}{c}}{1 + \left[1 - \frac{K_1 (1 - e^{-K_2 \tau})}{K_2 m'(0)} \right] \frac{2 \cdot w_e'}{c}}$
$V(t)$	$\frac{d' \cdot t}{\sqrt{1 + \left(\frac{d' \cdot t}{c}\right)^2}}$	Numerical	Numerical	$c \cdot \frac{1 - W \left(e^{\frac{m'(0) \cdot c - 4 T t}{m'(0) \cdot c}} \right)}{1 + W \left(e^{\frac{m'(0) \cdot c - 4 T t}{m'(0) \cdot c}} \right)}$	Numerical
$\tau(V)$	$\frac{c}{d'} \operatorname{artanh}\left(\frac{V}{c}\right)$	$\frac{m'(0) \cdot w_e'}{T} \left[1 - \left(\frac{c-V}{c+V}\right) \frac{2 \cdot w_e'}{c} \right]$	$\frac{m'(0) \cdot c}{T} \left[1 - \sqrt{\frac{c-V}{c+V}} \right]$	$\frac{m'(0) \cdot c}{T} \left[1 - \sqrt{\frac{c-V}{c+V}} \right]$	$-\ln \left[1 + \frac{K_2}{K_1} m'(0) \left(\left(\frac{c-V}{c+V}\right) \frac{2 \cdot w_e'}{c} - 1 \right) \right]$
$t(V)$	$\frac{V}{d' \cdot \sqrt{1 - \frac{V^2}{c^2}}}$	Numerical	Numerical	$\frac{m'(0) \cdot c}{4 T} \left[\frac{2 V}{c+V} - \ln \left(\frac{c-V}{c+V} \right) \right]$	Numerical

$\tau(t)$	$\frac{c}{a'} \operatorname{arsinh}\left(\frac{a't}{c}\right)$	Numerical	$\frac{m'(0) c}{T} \left[1 - \sqrt{W\left(e^{\frac{m'(0) c - 4 T t}{m'(0) c}}\right)} \right]$	Numerical
$t(\tau)$	$\frac{c}{a'} \sinh\left(\frac{a'\tau}{c}\right)$	Numerical	$\frac{2 m'(0) c T \tau - T^2 \tau^2 + 2 m'(0)^2 c^2 \ln\left(\frac{m'(0) c}{m'(0) c - T \tau}\right)}{4 m'(0) c T}$	Numerical
$\tau(x)$	$\frac{c}{a'} \operatorname{arcosh}\left(1 + \frac{a'x}{c^2}\right)$	Numerical	$\frac{m'(0) c}{T} \sqrt{\frac{1 - \frac{W\left(-\frac{4 T x + m'(0) c^2}{m'(0) c^2}\right)}{-e}}{1 - \frac{W\left(-\frac{4 T x + m'(0) c^2}{m'(0) c^2}\right)}{-e}}}$	Numerical
$t(x)$	$\frac{c}{a'} \sqrt{\left(1 + \frac{a'x}{c^2}\right)^2 - 1}$	Numerical	Numerical	Numerical
$x(\tau)$	$\frac{c^2}{a'} \left[\cosh\left(\frac{a'\tau}{c}\right) - 1 \right]$	Numerical	$\frac{-2 m'(0) c T \tau + T^2 \tau^2 + 2 m'(0)^2 c^2 \ln\left(\frac{m'(0) c}{m'(0) c - T \tau}\right)}{4 m'(0) T}$	Numerical
$x(t)$	$\frac{c^2}{a'} \left[\sqrt{1 + \left(\frac{a't}{c}\right)^2} - 1 \right]$	Numerical	$\frac{c}{2T} \left[2 T t - m'(0) c + m'(0) c W\left(e^{\frac{m'(0) c - 4 T t}{m'(0) c}}\right) \right]$	Numerical
$V(x)$	$c \cdot \sqrt{1 - \frac{1}{\left(1 + \frac{a'x}{c^2}\right)^2}}$	Numerical	$c \cdot \frac{1+W\left(-\frac{4 T x + m'(0) c^2}{m'(0) c^2}\right)}{1-W\left(-\frac{4 T x + m'(0) c^2}{m'(0) c^2}\right)}$	Numerical
$x(V)$	$\frac{c^2}{a'} \left[\frac{1 - \sqrt{1 - \frac{V^2}{c^2}}}{\sqrt{1 - \frac{V^2}{c^2}}} \right]$	Numerical	$-\frac{m'(0) c^2}{4 T} \left[\frac{2 V}{c+V} + \ln\left(\frac{c-V}{c+V}\right) \right]$	Numerical

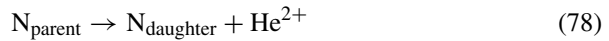
Beta minus particles could be suitable to thrust a spacecraft because they can be deflected by a magnetic field in the desired direction and they have a penetration power intermediate, so they escape from a thin plate but at the same time we can easily shield the spacecraft from them. However, they have a small momentum, due to their very small mass, and therefore the thrust generated could be negligible.

Beta plus particles have a tendency to react very easily with the same material that emitted them, through the annihilation process, making them very difficult to use for propulsive purposes.

Following these considerations, among the possible types of decay we assume to consider only alpha type.

3.1 Alpha Decay

In alpha decay a nuclide (called *parent*) emits a helium nucleus (doubly ionized helium), and is transformed into another nuclide (called *daughter*) with an atomic number (number of protons) decreased by 2 and a mass number (sum of protons and neutrons) decreased by 4:



If the daughter nuclide is stable the process stops, otherwise the daughter nuclide generates a second decay and so on until a stable nuclide is obtained.

It is important to stress that the decays that occur along a chain, which began with alpha decay, are not necessarily all of the alpha type. But in this study we consider for simplicity that they are so.

The energy Q released in alpha decay is equal to the difference in mass energy between the parent nuclide and the final products, and appears as kinetic energy of the latter. We can write:

$$Q = [m_1 - (m_2 + m_e)] \cdot c^2 = E_{k,2} + E_k \quad (79)$$

where m_1 , m_2 , and m_e are, respectively, the masses of the parent, daughter, and emitted particle (alpha particle), and $E_{k,2}$ and E_k are the kinetic energies of the daughter and emitted particle.

Assuming the parent nuclide is at rest, the daughter must recoil in the opposite direction to the alpha particle, and with the same momentum:

$$m_2 w_D = m_e w_e \quad (80)$$

where w_D and w_e are, respectively, the speeds of the daughter and emitted particle.

If we calculate the ratio between their kinetic energies we have:

$$\frac{E_{k,2}}{E_k} = \frac{\frac{1}{2} m_2 w_D^2}{\frac{1}{2} m_e w_e^2} = \frac{(m_2 w_D)^2 \cdot m_e}{(m_e w_e)^2 \cdot m_2} = \frac{m_e}{m_2} \quad (81)$$

then we can then derive the relation:

$$Q = E_k \left(1 + \frac{m_e}{m_2} \right) \quad (82)$$

4 Radioisotope Sail as Propulsion System

We investigated the possible application of a radioisotope sail as space propulsion system, in particular considering the use of only radioactive material emitting alpha particles along the considerations done in the previous section.

In the following sections we will describe a simplified configuration to indicate the main characteristic elements of the system and we will report the mathematical model defined for different types of alpha decay (single or multiple decay).

4.1 Configuration

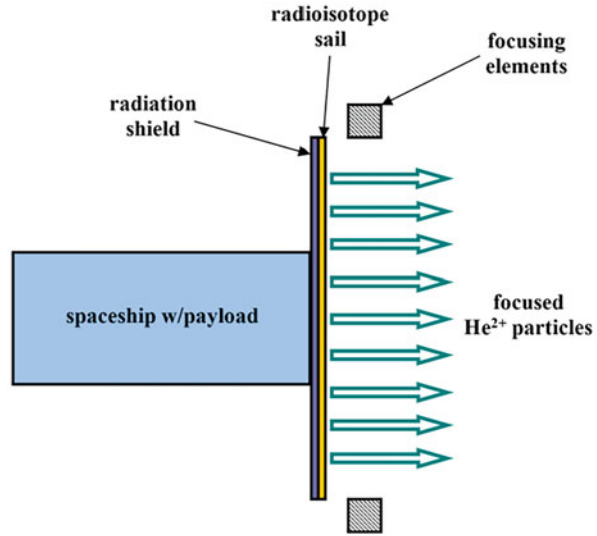
In defining a very simplified scheme (see Fig. 4), useful for a first approach to the topic, we indicate the main elements that can constitute the radioisotope sail propulsion system:

- *Radioisotope sail* – it is made of a radioactive material characterized by alpha decay (single or multiple decay) and emitting alpha particles which generate the wanted thrust.
- *Radiation shield* – it shields the spaceship by radiations (in the case of alpha particles only, it can be made of a very lightweight material).
- *Focusing elements* – they redirect the radiation emitted by the sail using suitable magnetic fields in order to focus it in a single direction opposite to the flight direction.

Furthermore, it is necessary to introduce some characteristic quantities of the hypothetical spacecraft useful for the study:

- Propellant mass M_{prop} , i.e., the mass of the propellant used for propulsion (in this case radioisotope material)
- Dry mass M_{dry} , i.e., the sum of spacecraft mass and payload mass, excluding propellant mass only

Fig. 4 Simplified scheme of a radioisotope sail propulsion system



- Spacecraft mass, i.e., the mass of structures, mechanisms, subsystems, radiation shields, focusing elements, etc.
- Payload mass, e.g., the mass of scientific instruments, experiments, astronauts, and everything that justified the spaceflight
- Total mass M_t , i.e., the launch mass ($=M_{\text{dry}} + M_{\text{prop}}$)

All mass quantities are considered in the proper reference frame.

Considering the simple configuration presented, we can therefore report the results of the physical-mathematical study of the propulsion system in a first version that can be improved in future studies.

Note

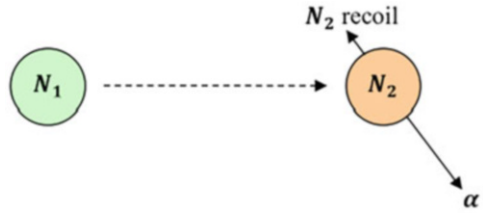
To make expressions more readable, from the following section onward, the quotes ' for the quantities referring to the proper reference system will not be shown (but they will be in any case defined at the terminology level, to avoid misunderstanding).

4.2 Single Decay Mathematical Model

The simplest case that can be studied is the single decay: a radioactive nuclide N_1 decays in a stable nuclide N_2 emitting at least one particle. In particular in this study we take into consideration an alpha particle α at high energies. In the Fig. 5 is shown a simple scheme of the decay process.

To derive behavior and performance of radioisotope sails, we have to set up the following mathematical model using well-known formulas of nuclear physics and special relativity.

Fig. 5 Single alpha decay scheme



The first step is to assign the following characteristics of the radioactive material:

- Atomic mass m_1 of the parent nuclide N_1
- Atomic mass m_2 of the stable daughter nuclide N_2
- Rest mass of emitted particle m_e (i.e., helium nucleus in this study) during the decay from N_1 to N_2
- Half-life $\tau_{1/2}$ of the nuclide N_1
- Decay energy Q (value known from literature) released during the decay from N_1 to N_2

Above and following quantities are defined in the proper reference frames.

4.2.1 Decay Characteristics

The first quantity calculated is the decay constant:

$$\lambda = \frac{\ln 2}{\tau_{1/2}} \tag{83}$$

and, knowing the decay energy Q , we can also yield the kinetic energy E_k of emitted alpha particle inverting the relation (82):

$$E_k = \frac{Q}{1 + \frac{m_e}{m_2}} \tag{84}$$

4.2.2 Dynamical Characteristics and Masses

Knowing E_k we can calculate the following quantities:

- Average momentum $p \cdot c$ of emitted particles (it is usually multiplied by c to give results in MeV), considering the recoil of N_2

$$p \cdot c = \sqrt{E_k^2 + 2 \cdot E_k \cdot m_e \cdot c^2} \tag{85}$$

or in a more classical way we can have p alone

$$p = \frac{\sqrt{E_k^2 + 2 \cdot E_k \cdot m_e \cdot c^2}}{c} \quad (86)$$

- Average gamma factor γ of emitted particles

$$\gamma = 1 + \frac{E_k}{m_e \cdot c^2} \quad (87)$$

- Average speed w_e of emitted particles

$$w_e = c \cdot \sqrt{1 - \frac{1}{\gamma^2}} \quad (88)$$

- Average specific impulse I_{sp} of emitted particles

$$I_{sp} = \frac{w_e}{g_0} \rightarrow I_{sp} = \frac{c}{g_0} \cdot \sqrt{1 - \frac{1}{\gamma^2}} \quad (89)$$

It is also necessary to calculate some quantities related to the mass.

First of all, we can calculate the number of atoms of nuclide N_1 at time zero as:

$$N_1(0) = N_0 = \frac{M_{prop,0}}{m_1} \quad (90)$$

where $M_{prop,0}$ is the propellant mass at initial time $\tau = 0$.

Then the following important quantities can be calculated:

- Number of atoms of the nuclide N_1 as a function of proper time (taking into account the number of nuclides already decayed into N_2)

$$N_1(\tau) = N_0 \cdot e^{-\lambda \cdot \tau} \quad (91)$$

- Number of atoms of the stable nuclide N_2 as a function of proper time, that it is also equal to the number of alpha particles generated N_e

$$N_2(\tau) = N_0 - N_1(\tau) = N_0 \cdot (1 - e^{-\lambda \cdot \tau}) = N_e(\tau) \quad (92)$$

- Lost mass M_{lost} as a function of proper time, equal to the sum of the masses lost during decay

$$M_{lost}(\tau) = m_e \cdot N_2(\tau) = m_e \cdot N_0 \cdot (1 - e^{-\lambda \cdot \tau}) \quad (93)$$

- Propellant mass M_{prop} as a function of proper time

$$M_{\text{prop}}(\tau) = M_{\text{prop},0} - m_e \cdot N_0 \cdot (1 - e^{-\lambda \cdot \tau}) \quad (94)$$

$$= m_1 \cdot N_0 - m_e \cdot N_0 \cdot (1 - e^{-\lambda \cdot \tau}) \quad (95)$$

$$= N_0 \cdot [m_1 - m_e \cdot (1 - e^{-\lambda \cdot \tau})] \quad (96)$$

- Total mass M_t as a function of proper time

$$M_t(\tau) = M_t(0) - m_e \cdot N_0 \cdot (1 - e^{-\lambda \cdot \tau}) \quad (97)$$

$$= M_{\text{dry}} + M_{\text{prop},0} - m_e \cdot N_0 \cdot (1 - e^{-\lambda \cdot \tau}) \quad (98)$$

$$= M_{\text{dry}} + N_0 \cdot [m_1 - m_e \cdot (1 - e^{-\lambda \cdot \tau})] \quad (99)$$

- Mass flow rate $\dot{m}(\tau)$ as a function of proper time

$$\dot{m}(\tau) = \frac{dM_{\text{lost}}(\tau)}{d\tau} = -\frac{dM_t(\tau)}{d\tau} = m_e \cdot N_0 \cdot \lambda \cdot e^{-\lambda \cdot \tau} \quad (100)$$

that can be rewritten as:

$$\dot{m}(\tau) = m_e \cdot \dot{N}(\tau) \quad (101)$$

if we define $\dot{N}(\tau)$ as the particle flow rate:

$$\dot{N}(\tau) = \frac{dN_e(\tau)}{d\tau} = N_0 \cdot \lambda \cdot e^{-\lambda \cdot \tau} \quad (102)$$

4.2.3 Propulsion Performance

It is possible to calculate the thrust provided by the radioisotope sail, as a function of proper time, using the well-known formula coming from space propulsion theory:

$$T(\tau) = w_e \cdot \dot{m}(\tau) = w_e \cdot m_e \cdot N_0 \cdot \lambda \cdot e^{-\lambda \cdot \tau} \quad (103)$$

We can notice that thrust trend is negative exponential and we stress that for the sake of simplicity has not been introduced a correction coefficient that takes into account the geometric losses due to the expulsion directions of the alpha particles (which can be expelled in any direction with equal probability). The absence of this correction is however acceptable as the geometric losses are compensated by the configuration of the propulsion system which involves the use of focusing elements, hypothesized precisely to reduce these losses to a minimum.

We can also calculate the total impulse:

$$I_t(\tau) = \int_0^\tau T(\tau) d\tau = w_e \cdot m_e \cdot N_0 \cdot (1 - e^{-\lambda \cdot \tau}) \quad (104)$$

To find achievable ΔV (in the case of relativistic flight) as a function of proper time, it is necessary to use the *Ackeret equation* already seen:

$$\Delta V(\tau) = c \cdot \frac{1 - \left(\frac{M_t(\tau)}{M_t(0)}\right)^{\frac{2 \cdot w_e}{c}}}{1 + \left(\frac{M_t(\tau)}{M_t(0)}\right)^{\frac{2 \cdot w_e}{c}}} = \quad (105)$$

$$= c \cdot \frac{1 - \left(\frac{M_t(0) - m_e \cdot N_0 \cdot (1 - e^{-\lambda \cdot \tau})}{M_t(0)}\right)^{\frac{2 \cdot w_e}{c}}}{1 + \left(\frac{M_t(0) - m_e \cdot N_0 \cdot (1 - e^{-\lambda \cdot \tau})}{M_t(0)}\right)^{\frac{2 \cdot w_e}{c}}} \quad (106)$$

or in a different form:

$$\Delta V(\tau) = c \cdot \tanh\left(\frac{w_e}{c} \cdot \ln \frac{M_t(0)}{M_t(\tau)}\right) \quad (107)$$

$$= c \cdot \tanh\left(\frac{w_e}{c} \cdot \ln \frac{M_t(0)}{M_t(0) - m_e \cdot N_0 \cdot (1 - e^{-\lambda \cdot \tau})}\right) \quad (108)$$

Finally, it is possible to calculate the proper acceleration:

$$a(\tau) = \frac{T(\tau)}{M_t(\tau)} = \frac{w_e \cdot m_e \cdot N_0 \cdot \lambda \cdot e^{-\lambda \cdot \tau}}{M_t(0) - m_e \cdot N_0 \cdot (1 - e^{-\lambda \cdot \tau})} \quad (109)$$

Note

As already said in the Chap. 3 of this paper, alpha particles are easily reabsorbed by sail material itself. It is therefore necessary to hypothesize the use of a very thin layer of radioactive material, to limit this problem as much as possible.

However, we must take into account that half of the particles emitted by the sail will go in the flight direction (forward direction) and will be absorbed by the protective shield, while the other half will go in the opposite direction (rearward direction) and generate thrust. The alpha particles ejected in the rearward direction in a preliminary and approximate way will all be considered effective, thanks to the presence of the focusing elements.

We can therefore introduce a corrective coefficient that takes this problem into account, reducing the effective value of M_{lost} by 50% and consequently the other quantities connected to it: \dot{m} , T , I_t , ΔV , and a .

4.2.4 Compatibility with Negative Exponential Acceleration Motion

The proper acceleration shown in the relation (109) is clearly time depending, in particular it is decreasing following a trend that is of a negative exponential type.

Thus, a single decay radioisotope sail follows exactly the negative exponential proper acceleration motion described in Sect. 2.2.5, and it is then not compatible with the other trends seen (e.g., hyperbolic motion).

4.3 Double Decay Mathematical Model

In this second case there is a radioactive nuclide N_1 which decays in a daughter radioactive nuclide N_2 emitting one alpha particle at high energies, and later the nuclide N_2 decays, emitting the same kind of particle, in a stable nuclide N_3 , granddaughter of N_1 . In Fig. 6 is shown a simple scheme of the decay process.

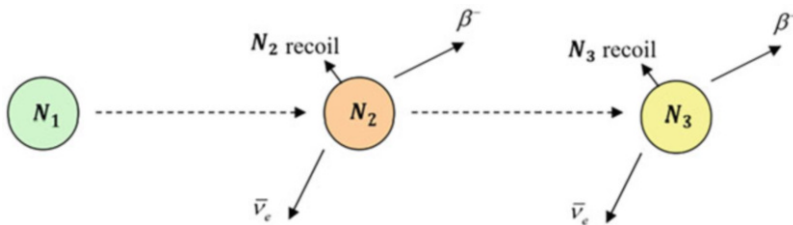


Fig. 6 Double alpha decay scheme

The first step is to assign the following characteristics of the radioactive material:

- Atomic mass m_1 of the parent nuclide N_1
- Atomic mass m_2 of the daughter nuclide N_2
- Atomic mass m_3 of the stable granddaughter nuclide N_3
- Rest mass of emitted particle m_e during the decay from N_1 to N_2 and from N_2 to N_3
- Half-life $\tau_{1/2, 1}$ of the nuclide N_1
- Half-life $\tau_{1/2, 2}$ of the nuclide N_2
- Decay energy Q_1 released during the decay from N_1 to N_2
- Decay energy Q_2 released during the decay from N_2 to N_3

Above and following quantities are defined in the proper reference frames.

4.3.1 Decay Characteristics

The first quantities calculated are the decay constants of N_1 to N_2 :

$$\lambda_1 = \frac{\ln 2}{\tau_{1/2,1}} \quad (110)$$

$$\lambda_2 = \frac{\ln 2}{\tau_{1/2,2}} \quad (111)$$

and, knowing the decay energy Q , we can also define the average kinetic energy E_k of each emitted particle, considering the recoil in each step of decay chain:

$$E_{k,1} = \frac{Q_1}{1 + \frac{m_e}{m_2}} \quad (112)$$

$$E_{k,2} = \frac{Q_2}{1 + \frac{m_e}{m_3}} \quad (113)$$

4.3.2 Dynamical Characteristics and Masses

Knowing E_k we can calculate the following quantities:

- Average momentum $p \cdot c$ of emitted particles

$$p_1 \cdot c = \sqrt{E_{k,1}^2 + 2 \cdot E_{k,1} \cdot m_e \cdot c^2} \quad (114)$$

$$p_2 \cdot c = \sqrt{E_{k,2}^2 + 2 \cdot E_{k,2} \cdot m_e \cdot c^2} \tag{115}$$

or in a more classical way we can have p alone

$$p_1 = \frac{\sqrt{E_{k,1}^2 + 2 \cdot E_{k,1} \cdot m_e \cdot c^2}}{c} \tag{116}$$

$$p_2 = \frac{\sqrt{E_{k,2}^2 + 2 \cdot E_{k,2} \cdot m_e \cdot c^2}}{c} \tag{117}$$

- Average gamma factor γ of emitted particles

$$\gamma_1 = 1 + \frac{E_{k,1}}{m_e \cdot c^2} \tag{118}$$

$$\gamma_2 = 1 + \frac{E_{k,2}}{m_e \cdot c^2} \tag{119}$$

- Average speed w_e of emitted particles

$$w_{e,1} = c \cdot \sqrt{1 - \frac{1}{\gamma_1^2}} \tag{120}$$

$$w_{e,2} = c \cdot \sqrt{1 - \frac{1}{\gamma_2^2}} \tag{121}$$

- Instantaneous average speed of all emitted particles, defined using alpha particle flow rates of the first and second steps of decay chain

$$w_{e,ave}(\tau) = \frac{w_{e,1} \cdot \dot{N}_{e,1}(\tau) + w_{e,2} \cdot \dot{N}_{e,2}(\tau)}{\dot{N}_{e,1}(\tau) + \dot{N}_{e,2}(\tau)} \tag{122}$$

where $\dot{N}_{e,1}(\tau)$ is the particle flow rate emitted in the first decay and $\dot{N}_{e,2}(\tau)$ is the particle flow rate emitted in the second decay

- Integral average speed of all emitted particles in the proper time interval τ considered, since the instantaneous average speed changes in time

$$\bar{w}_e = \frac{1}{\tau} \int_0^\tau w_{e,ave}(\tau) d\tau \tag{123}$$

- Instantaneous average specific impulse I_{sp} for the whole system

$$I_{\text{sp}}(\tau) = \frac{w_{e,\text{ave}}(\tau)}{g_0} = \frac{1}{g_0} \cdot \frac{w_{e,1} \cdot \dot{N}_{e,1}(\tau) + w_{e,2} \cdot \dot{N}_{e,2}(\tau)}{\dot{N}_{e,1}(\tau) + \dot{N}_{e,2}(\tau)} \quad (124)$$

- Integral average specific impulse in the proper time interval τ considered, since the instantaneous average specific impulse changes in time

$$\bar{I}_{\text{sp}} = \frac{\bar{w}_e}{g_0} = \frac{1}{g_0 \cdot \tau} \int_0^\tau w_{e,\text{ave}}(\tau) d\tau \quad (125)$$

It is also necessary to calculate some quantities related to the mass.

First of all, we can calculate the number of atoms of nuclide N_1 at time zero as:

$$N_1(0) = N_0 = \frac{M_{\text{prop},0}}{m_1} \quad (126)$$

Then the following important quantities can be calculated:

- Number of atoms of the nuclide N_1 as a function of proper time (taking into account the number of nuclides decayed into N_2)

$$N_1(\tau) = N_0 \cdot e^{-\lambda_1 \cdot \tau} \quad (127)$$

- Number of atoms of the nuclide N_2 as a function of proper time (taking into account also the number of nuclides decayed into N_3)

$$N_2(\tau) = N_0 \cdot \frac{\lambda_1}{\lambda_2 - \lambda_1} \cdot (e^{-\lambda_1 \cdot \tau} - e^{-\lambda_2 \cdot \tau}) \quad (128)$$

- Number of atoms of the nuclide N_{2t} generated from N_1 as a function of proper time, that it is also equal to the number of alpha particles generated in the first decay $N_{e,1}(\tau)$

$$N_{2t}(\tau) = N_0 - N_1(\tau) = N_0 \cdot (1 - e^{-\lambda_1 \cdot \tau}) = N_{e,1}(\tau) \quad (129)$$

- Number of atoms of the stable nuclide N_3 as a function of proper time, that it is also equal to the number of alpha particles generated in the second decay $N_{e,2}(\tau)$

$$N_3(\tau) = N_0 - N_1(\tau) - N_2(\tau) = N_{2t}(\tau) - N_2(\tau) \quad (130)$$

$$= N_0 \cdot \left(1 - \frac{\lambda_2}{\lambda_2 - \lambda_1} \cdot e^{-\lambda_1 \cdot \tau} + \frac{\lambda_1}{\lambda_2 - \lambda_1} \cdot e^{-\lambda_2 \cdot \tau} \right) = N_{e,2}(\tau) \quad (131)$$

We can now explicitly calculate the particle flow rates $\dot{N}_{e,1}(\tau)$ and $\dot{N}_{e,2}(\tau)$ as follows:

$$\dot{N}_{e,1}(\tau) = \frac{dN_{e,1}(\tau)}{d\tau} = N_0 \cdot \lambda_1 \cdot e^{-\lambda_1 \cdot \tau} \quad (132)$$

$$\dot{N}_{e,2}(\tau) = \frac{dN_{e,2}(\tau)}{d\tau} = N_0 \cdot \frac{\lambda_1 \cdot \lambda_2}{\lambda_2 - \lambda_1} \cdot (e^{-\lambda_1 \cdot \tau} - e^{-\lambda_2 \cdot \tau}) \quad (133)$$

and thanks to these two relations, we can also explicitly yield the instantaneous average speed of Eq. (122)

$$w_{e,ave}(\tau) = \frac{w_{e,1} + w_{e,2} \cdot \frac{\lambda_2}{\lambda_2 - \lambda_1} \cdot (1 - e^{(\lambda_1 - \lambda_2) \cdot \tau})}{1 + \frac{\lambda_2}{\lambda_2 - \lambda_1} \cdot (1 - e^{(\lambda_1 - \lambda_2) \cdot \tau})} \quad (134)$$

the integral average speed of Eq. (123)

$$\bar{w}_e = \frac{w_{e,1} - w_{e,2}}{(2 \cdot \lambda_2 - \lambda_1) \cdot \tau} \cdot \ln \frac{\lambda_1 + \lambda_2 \cdot (e^{(\lambda_1 - \lambda_2) \cdot \tau} - 2)}{\lambda_1 - \lambda_2} + \frac{\lambda_2 \cdot w_{e,2} - (\lambda_1 - \lambda_2) \cdot w_{e,1}}{2 \cdot \lambda_2 - \lambda_1} \quad (135)$$

the instantaneous average specific impulse of Eq. (124)

$$I_{sp}(\tau) = \frac{1}{g_0} \cdot \frac{w_{e,1} + w_{e,2} \cdot \frac{\lambda_2}{\lambda_2 - \lambda_1} \cdot (1 - e^{(\lambda_1 - \lambda_2) \cdot \tau})}{1 + \frac{\lambda_2}{\lambda_2 - \lambda_1} \cdot (1 - e^{(\lambda_1 - \lambda_2) \cdot \tau})} \quad (136)$$

and the integral average specific impulse of Eq. (125)

$$\bar{I}_{sp} = \frac{w_{e,1} - w_{e,2}}{g_0 \cdot (2 \cdot \lambda_2 - \lambda_1) \cdot \tau} \cdot \ln \frac{\lambda_1 + \lambda_2 \cdot (e^{(\lambda_1 - \lambda_2) \cdot \tau} - 2)}{\lambda_1 - \lambda_2} + \frac{\lambda_2 \cdot w_{e,2} - (\lambda_1 - \lambda_2) \cdot w_{e,1}}{g_0 \cdot (2 \cdot \lambda_2 - \lambda_1)} \quad (137)$$

- Lost mass M_{lost} as a function of proper time, equal to the sum of the masses lost of the first and the second decays

$$M_{lost}(\tau) = M_{lost,1}(\tau) + M_{lost,2}(\tau) = m_e \cdot (N_{2t}(\tau) + N_3(\tau)) \quad (138)$$

$$= m_e \cdot N_0 \cdot \left(2 - \frac{2 \cdot \lambda_2 - \lambda_1}{\lambda_2 - \lambda_1} \cdot e^{-\lambda_1 \cdot \tau} + \frac{\lambda_1}{\lambda_2 - \lambda_1} \cdot e^{-\lambda_2 \cdot \tau} \right) \quad (139)$$

- Propellant mass M_{prop} as a function of proper time

$$M_{prop}(\tau) = M_{prop,0} - M_{lost}(\tau) \quad (140)$$

$$= m_1 \cdot N_0 - m_e \cdot N_0 \cdot \left[2 - \frac{2 \cdot \lambda_2 - \lambda_1}{\lambda_2 - \lambda_1} \cdot e^{-\lambda_1 \cdot \tau} + \frac{\lambda_1}{\lambda_2 - \lambda_1} \cdot e^{-\lambda_2 \cdot \tau} \right] = \quad (141)$$

$$= N_0 \cdot \left\{ m_1 - m_e \cdot \left[2 - \frac{2 \cdot \lambda_2 - \lambda_1}{\lambda_2 - \lambda_1} \cdot e^{-\lambda_1 \cdot \tau} + \frac{\lambda_1}{\lambda_2 - \lambda_1} \cdot e^{-\lambda_2 \cdot \tau} \right] \right\} \quad (142)$$

- Total mass M_t as a function of proper time

$$M_t(\tau) = M_{\text{dry}} + M_{\text{prop}}(\tau) \quad (143)$$

$$= M_{\text{dry}} + N_0 \cdot \left\{ m_1 - m_e \cdot \left[2 - \frac{2 \cdot \lambda_2 - \lambda_1}{\lambda_2 - \lambda_1} \cdot e^{-\lambda_1 \cdot \tau} + \frac{\lambda_1}{\lambda_2 - \lambda_1} \cdot e^{-\lambda_2 \cdot \tau} \right] \right\} \quad (144)$$

- Total mass flow rate $\dot{m}(\tau)$, sum of the mass flow rates of particles emitted both in the first and the second decay, as a function of proper time

$$\dot{m}(\tau) = \frac{dM_{\text{lost}}(\tau)}{d\tau} = -\frac{dM_t(\tau)}{d\tau} \quad (145)$$

$$= m_e \cdot N_0 \cdot \frac{\lambda_1}{\lambda_2 - \lambda_1} \cdot \left[(2 \cdot \lambda_2 - \lambda_1) \cdot e^{-\lambda_1 \cdot \tau} - \lambda_2 \cdot e^{-\lambda_2 \cdot \tau} \right] \quad (146)$$

where the mass flow rate of alpha particles emitted in the first decay is

$$\dot{m}_1(\tau) = m_e \cdot N_0 \cdot \lambda_1 \cdot e^{-\lambda_1 \cdot \tau} \quad (147)$$

and the mass flow rate of alpha particles emitted in the second decay is

$$\dot{m}_2(\tau) = m_e \cdot N_0 \cdot \frac{\lambda_1 \cdot \lambda_2}{\lambda_2 - \lambda_1} \cdot (e^{-\lambda_1 \cdot \tau} - e^{-\lambda_2 \cdot \tau}) \quad (148)$$

4.3.3 Propulsion Performance

It is possible to calculate the thrust provided by the radioisotope sail, as a function of proper time, using the instantaneous average speed:

$$T(\tau) = w_{e,\text{ave}}(\tau) \cdot \dot{m}_e(\tau) = w_{e,1} \cdot \dot{m}_1(\tau) + w_{e,2} \cdot \dot{m}_2(\tau) \quad (149)$$

$$= \left[w_{e,1} + w_{e,2} \cdot \frac{\lambda_2}{\lambda_2 - \lambda_1} \cdot \left(1 - e^{(\lambda_1 - \lambda_2) \cdot \tau} \right) \right] \cdot m_e \cdot N_0 \cdot \lambda_1 \cdot e^{-\lambda_1 \cdot \tau} \quad (150)$$

We can also find the total impulse:

$$I_t(\tau) = \int_0^\tau T(\tau) d\tau = \int_0^\tau (w_{e,1} \cdot \dot{m}_1(\tau) + w_{e,2} \cdot \dot{m}_2(\tau)) d\tau \quad (151)$$

$$= m_e \cdot N_0 \cdot \left\{ w_{e,1} (1 - e^{-\lambda_1 \cdot \tau}) + \frac{w_{e,2}}{\lambda_2 - \lambda_1} [\lambda_2 (1 - e^{-\lambda_1 \cdot \tau}) - \lambda_1 (1 - e^{-\lambda_2 \cdot \tau})] \right\} \quad (152)$$

To find achievable ΔV (in the case of relativistic flight) as a function of proper time the *Ackeret equation* is necessary, using the integral average speed calculated in the same proper time interval (since Ackeret equation requires constant exhaust speed and using this average value we can simulate this condition):

$$\Delta V(\tau) = c \cdot \frac{1 - \left(\frac{M_t(\tau)}{M_t(0)} \right)^{\frac{2 \cdot \bar{w}_e}{c}}}{1 + \left(\frac{M_t(\tau)}{M_t(0)} \right)^{\frac{2 \cdot \bar{w}_e}{c}}} \quad (153)$$

$$= c \cdot \frac{1 - \left(\frac{M_{\text{dry}} + N_0 \cdot \left\{ m_1 - m_e \cdot \left[2 - \frac{2 \cdot \lambda_2 - \lambda_1}{\lambda_2 - \lambda_1} \cdot e^{-\lambda_1 \cdot \tau} + \frac{\lambda_1}{\lambda_2 - \lambda_1} \cdot e^{-\lambda_2 \cdot \tau} \right] \right\}}{M_{\text{dry}} + N_0 \cdot m_1} \right)^{\frac{2 \cdot \bar{w}_e}{c}}}{1 + \left(\frac{M_{\text{dry}} + N_0 \cdot \left\{ m_1 - m_e \cdot \left[2 - \frac{2 \cdot \lambda_2 - \lambda_1}{\lambda_2 - \lambda_1} \cdot e^{-\lambda_1 \cdot \tau} + \frac{\lambda_1}{\lambda_2 - \lambda_1} \cdot e^{-\lambda_2 \cdot \tau} \right] \right\}}{M_{\text{dry}} + N_0 \cdot m_1} \right)^{\frac{2 \cdot \bar{w}_e}{c}}} \quad (154)$$

or in a different form:

$$\Delta V(\tau) = c \cdot \tanh \left(\frac{\bar{w}_e}{c} \cdot \ln \frac{M_t(0)}{M_t(\tau)} \right) \quad (155)$$

$$= c \cdot \tanh \left(\frac{\bar{w}_e}{c} \cdot \ln \frac{M_{\text{dry}} + N_0 \cdot m_1}{M_{\text{dry}} + N_0 \cdot \left\{ m_1 - m_e \cdot \left[2 - \frac{2 \cdot \lambda_2 - \lambda_1}{\lambda_2 - \lambda_1} \cdot e^{-\lambda_1 \cdot \tau} + \frac{\lambda_1}{\lambda_2 - \lambda_1} \cdot e^{-\lambda_2 \cdot \tau} \right] \right\}} \right) \quad (156)$$

We do not use the explicit expression of the integral average speed \bar{w}_e in order not to compromise the readability of the last formulas.

Finally, it is possible to calculate the proper acceleration:

$$a(\tau) = \frac{T(\tau)}{M_t(\tau)} = \frac{\left[w_{e,1} + w_{e,2} \cdot \frac{\lambda_2}{\lambda_2 - \lambda_1} \cdot (1 - e^{(\lambda_1 - \lambda_2) \cdot \tau}) \right] \cdot m_e \cdot N_0 \cdot \lambda_1 \cdot e^{-\lambda_1 \cdot \tau}}{M_{\text{dry}} + N_0 \cdot \left\{ m_1 - m_e \cdot \left[2 - \frac{2 \cdot \lambda_2 - \lambda_1}{\lambda_2 - \lambda_1} \cdot e^{-\lambda_1 \cdot \tau} + \frac{\lambda_1}{\lambda_2 - \lambda_1} \cdot e^{-\lambda_2 \cdot \tau} \right] \right\}} \quad (157)$$

The proper acceleration expression is of the same type of that indicated in Sect. 2.2.5, which therefore appears to be the reference motion also for the radioisotope sail with double decay.

4.4 Generalized Mathematical Model for Any Decay Chain

After having studied the two most common and simple cases of decay, single and double, we define a generalized mathematical model suitable for any decay chain, but in any case, considering only the decay with the formation of alpha particles.

The first step consists of assigning the following characteristics of the radioactive material, considering i a positive integer:

- Atomic mass m_i of a generic parent nuclide N_i
- Atomic mass m_{i+1} of a generic daughter nuclide N_{i+1}
- Atomic mass m_1 of the initial parent nuclide N_1
- Atomic mass m_n of the final stable nuclide N_n
- Rest mass of each emitted particle m_e
- Half-life $\tau_{1/2, i}$ of the nuclide N_i
- Decay energy Q_i released during the decay from N_i to N_{i+1}
- Last step of the decay chain n

4.4.1 Decay Characteristics

The first quantity calculated is the decay constant of each nuclide:

$$\lambda_i = \frac{\ln 2}{\tau_{1/2, i}} \quad (158)$$

and, knowing the decay energy Q_i , we can also define the average kinetic energy $E_{k, i}$ of emitted alpha particle:

$$E_{k, i} = \frac{Q_i}{1 + \frac{m_e}{m_{i+1}}} \quad (159)$$

4.4.2 Dynamical Characteristics and Masses

Knowing $E_{k, i}$ we can calculate the following quantities:

- Average momentum $p_i \cdot c$ of emitted particles (it is usually multiplied by c to give results in MeV)

$$p_i \cdot c = \sqrt{E_{k,i}^2 + 2 \cdot E_{k,i} \cdot m_e \cdot c^2} \quad (160)$$

or in a more classical way we can have p alone

$$p_i = \frac{\sqrt{E_{k,i}^2 + 2 \cdot E_{k,i} \cdot m_e \cdot c^2}}{c} \quad (161)$$

- Average gamma factors γ_i of emitted particles

$$\gamma_i = 1 + \frac{E_{k,i}}{m_e \cdot c^2} \quad (162)$$

- Average speeds w_e, i of emitted particles

$$w_{e,i} = c \cdot \sqrt{1 - \frac{1}{\gamma_i^2}} \quad (163)$$

- Instantaneous average speed w_e , ave of all emitted particles

$$w_{e,ave}(\tau) = \frac{\sum_{i=1}^{n-1} (w_{e,i} \cdot \dot{N}_{e,i}(\tau))}{\sum_{i=1}^{n-1} \dot{N}_{e,i}(\tau)} \quad (164)$$

- Integral average speed \bar{w}_e of all emitted particles in the proper time interval τ considered

$$\bar{w}_e = \frac{1}{\tau} \int_0^\tau \frac{\sum_{i=1}^{n-1} (w_{e,i} \cdot \dot{N}_{e,i}(\tau))}{\sum_{i=1}^{n-1} \dot{N}_{e,i}(\tau)} d\tau \quad (165)$$

- Instantaneous average specific impulse I_{sp} for the whole system

$$I_{sp}(\tau) = \frac{1}{g_0} \cdot \frac{\sum_{i=1}^{n-1} (w_{e,i} \cdot \dot{N}_{e,i}(\tau))}{\sum_{i=1}^{n-1} \dot{N}_{e,i}(\tau)} \quad (166)$$

- Integral average specific impulse in the proper time interval τ considered, since the instantaneous average specific impulse changes in time

$$\bar{I}_{sp} = \frac{\bar{w}_e}{g_0} = \frac{1}{g_0 \cdot \tau} \int_0^\tau \frac{\sum_{i=1}^{n-1} (w_{e,i} \cdot \dot{N}_{e,i}(\tau))}{\sum_{i=1}^{n-1} \dot{N}_{e,i}(\tau)} d\tau \quad (167)$$

As in the previous section, we can calculate the number of atoms of nuclide N_1 at time zero as:

$$N_1(0) = N_0 = \frac{M_{\text{prop},0}}{m_1} \quad (168)$$

Then the following important quantities can be calculated:

- Number of atoms of the nuclide N_i (taking into account the number of nuclides N_i already decayed into N_{i+1}), as described by *Bateman equation*

$$N_i(\tau) = \begin{cases} N_0 \cdot e^{-\lambda_1 \cdot \tau} & i = 1 \\ N_0 \cdot \prod_{r=1}^{i-1} \lambda_r \cdot \left(\sum_{r=1}^i C_r e^{-\lambda_r \cdot \tau} \right) & i > 1 \end{cases} \quad (169)$$

where $C_r = 1 / \left[\prod_{s=1, s \neq r}^i (\lambda_s - \lambda_r) \right]$

- Number of emitted particles generated in the i -th decay or the total number of nuclides N_{i+1} generated from N_i (from here we consider only the case of $i > 1$)

$$N_{e,i}(\tau) = N_0 - \sum_{g=1}^i N_g(\tau) \quad (170)$$

$$N_{e,i}(\tau) = N_0 \left(1 - \sum_{g=1}^i \left(\prod_{r=1}^{g-1} \lambda_r \cdot \left(\sum_{r=1}^g C_r e^{-\lambda_r \cdot \tau} \right) \right) \right) \quad (171)$$

We can also calculate the particle flow rates as

$$\dot{N}_{e,i}(\tau) = \frac{dN_{e,i}(\tau)}{d\tau} = - \sum_{g=1}^i \frac{dN_g(\tau)}{d\tau} \quad (172)$$

$$= N_0 \cdot \sum_{g=1}^i \left(\prod_{r=1}^{g-1} \lambda_r \cdot \left(\sum_{r=1}^g C_r \lambda_r e^{-\lambda_r \cdot \tau} \right) \right) \quad (173)$$

and thanks to that relation, we can also yield an explicit version of the instantaneous average speed of Eq. (165)

$$w_{e,\text{ave}}(\tau) = \frac{\sum_{i=1}^{n-1} \left\{ w_{e,i} \cdot \left[\sum_{g=1}^i \left(\prod_{r=1}^{g-1} \lambda_r \cdot \left(\sum_{r=1}^g C_r \lambda_r e^{-\lambda_r \cdot \tau} \right) \right) \right] \right\}}{\sum_{i=1}^{n-1} \left[\sum_{g=1}^i \left(\prod_{r=1}^{g-1} \lambda_r \cdot \left(\sum_{r=1}^g C_r \lambda_r e^{-\lambda_r \cdot \tau} \right) \right) \right]} \quad (174)$$

and of the instantaneous average specific impulse of Eq. (167)

$$I_{\text{sp}}(\tau) = \frac{1}{g_0} \cdot \frac{\sum_{i=1}^{n-1} \left\{ w_{e,i} \cdot \left[\sum_{g=1}^i \left(\prod_{r=1}^{g-1} \lambda_r \cdot \left(\sum_{r=1}^g C_r \lambda_r e^{-\lambda_r \cdot \tau} \right) \right) \right] \right\}}{\sum_{i=1}^{n-1} \left[\sum_{g=1}^i \left(\prod_{r=1}^{g-1} \lambda_r \cdot \left(\sum_{r=1}^g C_r \lambda_r e^{-\lambda_r \cdot \tau} \right) \right) \right]} \quad (175)$$

We cannot explicitly derive the integral average speed and the integral average specific impulse.

- Lost mass M_{lost} as a function of proper time, equal to the sum of the all masses lost

$$M_{\text{lost}}(\tau) = \sum_{i=1}^{n-1} M_{\text{lost},i}(\tau) = \sum_{i=1}^{n-1} (m_e \cdot N_{e,i}(\tau)) \quad (176)$$

$$= m_e \cdot N_0 \cdot \sum_{i=1}^{n-1} \left(1 - \sum_{g=1}^i \left(\prod_{r=1}^{g-1} \lambda_r \cdot \left(\sum_{r=1}^g C_r e^{-\lambda_r \cdot \tau} \right) \right) \right) \quad (177)$$

- Propellant mass M_{prop} as a function of proper time

$$M_{\text{prop}}(\tau) = M_{\text{prop},0} - M_{\text{lost}}(\tau) \quad (178)$$

$$= N_0 \cdot \left(m_1 - m_e \cdot \sum_{i=1}^{n-1} \left(1 - \sum_{g=1}^i \left(\prod_{r=1}^{g-1} \lambda_r \cdot \left(\sum_{r=1}^g C_r e^{-\lambda_r \cdot \tau} \right) \right) \right) \right) \quad (179)$$

- Total mass M_t as a function of proper time

$$M_t(\tau) = M_{\text{dry}} + M_{\text{prop}}(\tau) \quad (180)$$

$$= M_{\text{dry}} + N_0 \cdot \left(m_1 - m_e \cdot \sum_{i=1}^{n-1} \left(1 - \sum_{g=1}^i \left(\prod_{r=1}^{g-1} \lambda_r \cdot \left(\sum_{r=1}^g C_r e^{-\lambda_r \cdot \tau} \right) \right) \right) \right) \quad (181)$$

- Total mass flow rate $\dot{m}(\tau)$, sum of all mass flow rates, as a function of proper time

$$\dot{m}(\tau) = \frac{dM_{\text{lost}}(\tau)}{d\tau} = -\frac{dM_t(\tau)}{d\tau} \quad (182)$$

$$= m_e \cdot N_0 \cdot \sum_{i=1}^{n-1} \left(\sum_{g=1}^i \left(\prod_{r=1}^{g-1} \lambda_r \cdot \left(\sum_{r=1}^g C_r \lambda_r e^{-\lambda_r \cdot \tau} \right) \right) \right) \quad (183)$$

From this relation we can yield the mass flow rate of alpha particles emitted in the i -th decay as

$$\dot{m}_i(\tau) = m_e \cdot N_0 \cdot \sum_{g=1}^i \left(\prod_{r=1}^{g-1} \lambda_r \cdot \left(\sum_{r=1}^g C_r \lambda_r e^{-\lambda_r \cdot \tau} \right) \right) \quad (184)$$

4.4.3 Propulsion Performance

It is possible to calculate the thrust provided by the radioisotope sail, as a function of proper time:

$$T(\tau) = w_{e,ave}(\tau) \cdot \dot{m}(\tau) = \sum_{i=1}^{n-1} (w_{e,i} \cdot \dot{m}_i(\tau)) \quad (185)$$

$$= m_e \cdot N_0 \cdot \sum_{i=1}^{n-1} \left\{ w_{e,i} \cdot \left[\sum_{g=1}^i \left(\prod_{r=1}^{g-1} \lambda_r \cdot \left(\sum_{r=1}^g C_r \lambda_r e^{-\lambda_r \cdot \tau} \right) \right) \right] \right\} \quad (186)$$

We can also obtain the total impulse:

$$I_t(\tau) = \int_0^\tau T(\tau) d\tau = \int_0^\tau \sum_{i=1}^{n-1} (w_{e,i} \cdot \dot{m}_i(\tau)) d\tau \quad (187)$$

$$= \sum_{i=1}^{n-1} w_{e,i} \int_0^\tau \dot{m}_i(\tau) d\tau = \sum_{i=1}^{n-1} w_{e,i} M_{lost,i}(\tau) \quad (188)$$

$$= m_e \cdot N_0 \cdot \sum_{i=1}^{n-1} w_{e,i} \left(1 - \sum_{g=1}^i \left(\prod_{r=1}^{g-1} \lambda_r \cdot \left(\sum_{r=1}^g C_r e^{-\lambda_r \cdot \tau} \right) \right) \right) \quad (189)$$

To find achievable ΔV (in the case of relativistic flight) as a function of proper time the *Ackeret equation* is necessary, using the integral average speed calculated in the same proper time interval:

$$\Delta V(\tau) = c \cdot \frac{1 - \left(\frac{M_t(\tau)}{M_t(0)} \right)^{\frac{2 \cdot \bar{w}_e}{c}}}{1 + \left(\frac{M_t(\tau)}{M_t(0)} \right)^{\frac{2 \cdot \bar{w}_e}{c}}} \quad (190)$$

$$= c \cdot \frac{1 - \left(\frac{M_{dry} + N_0 \cdot \left(m_1 - m_e \cdot \sum_{i=1}^{n-1} \left(1 - \sum_{g=1}^i \left(\prod_{r=1}^{g-1} \lambda_r \cdot \left(\sum_{r=1}^g C_r e^{-\lambda_r \cdot \tau} \right) \right) \right) \right)}{M_{dry} + N_0 \cdot m_1} \right)^{\frac{2 \cdot \bar{w}_e}{c}}}{1 + \left(\frac{M_{dry} + N_0 \cdot \left(m_1 - m_e \cdot \sum_{i=1}^{n-1} \left(1 - \sum_{g=1}^i \left(\prod_{r=1}^{g-1} \lambda_r \cdot \left(\sum_{r=1}^g C_r e^{-\lambda_r \cdot \tau} \right) \right) \right) \right)}{M_{dry} + N_0 \cdot m_1} \right)^{\frac{2 \cdot \bar{w}_e}{c}}} \quad (191)$$

or in a different form:

$$\Delta V (\tau) = c \cdot \tanh \left(\frac{\bar{w}_e}{c} \cdot \ln \frac{M_i(0)}{M_i(\tau)} \right) \tag{192}$$

$$= c \cdot \tanh \left(\frac{\bar{w}_e}{c} \cdot \ln \frac{M_{\text{dry}} + N_0 \cdot m_1}{M_{\text{dry}} + N_0 \cdot \left(m_1 - m_e \cdot \sum_{i=1}^{n-1} \left(1 - \sum_{g=1}^i \left(\prod_{r=1}^{g-1} \lambda_r \cdot \left(\sum_{r=1}^g C_r e^{-\lambda_r \cdot \tau} \right) \right) \right) \right) \right) \right) \tag{193}$$

Finally, it is possible to calculate the proper acceleration:

$$a(\tau) = \frac{T(\tau)}{M_i(\tau)} = \frac{m_e \cdot N_0 \cdot \sum_{i=1}^{n-1} \left\{ w_{e,i} \cdot \left[\sum_{g=1}^i \left(\prod_{r=1}^{g-1} \lambda_r \cdot \left(\sum_{r=1}^g C_r \lambda_r e^{-\lambda_r \cdot \tau} \right) \right) \right] \right\}}{M_{\text{dry}} + N_0 \cdot \left(m_1 - m_e \cdot \sum_{i=1}^{n-1} \left(1 - \sum_{g=1}^i \left(\prod_{r=1}^{g-1} \lambda_r \cdot \left(\sum_{r=1}^g C_r e^{-\lambda_r \cdot \tau} \right) \right) \right) \right) } \tag{194}$$

The proper acceleration expression is of the same type of that indicated in Sect. 2.2.5, which therefore appears to be the reference motion for the radioisotope sail in general.

4.5 Example of Application

We suppose to use a radioisotope sail as the main propulsion system for a robotic mission to Pluto, in two different cases: single alpha decay and double alpha decay.

We suppose to send *New Horizons* spacecraft, assuming to replace only the propulsion system, in order to be able to compare the performance between the real NASA mission and this hypothetical as well as simplified one. In this first study we are neglecting problems related to launch of radioactive materials, storage of radioactive materials, limited availability or production difficulties of radioactive materials, inability to delay the decay start before launch (here we considered that the start of the decay coincided with the start of the spacecraft’s flight, already in terrestrial parking orbit), focusing system, etc.

The main data of NASA mission and spacecraft were:

- $M_{\text{dry}} = 401 \text{ kg}$
- $M_{\text{prop},0} = 77 \text{ kg}$
- $M_{\text{tot}}(0) = 478 \text{ kg}$
- $D_{\text{pluto}} = 32 \text{ AU} = 4.79 \cdot 10^9 \text{ km}$
- $\tau_f = 9.5 \text{ y}$

where τ_f is the total time to fly from the Earth to Pluto (mission time).

In this study we assume to carry onboard the same quantity of propellant as *New Horizons* mission, i.e., 77 kg. This mass is equivalent to a sail of more than 60 m², if we consider a thickness of less than 0.1 mm and the materials listed in the following tables.

4.5.1 Pluto Mission with a Single Decay Radioisotope Sail

In the first part of the study we hypothesized the use of radioactive materials characterized exclusively by single alpha decay, thus ignoring any subsequent steps in the chain. In Table 2 are collected all the results obtained thanks to the expressions seen in the previous sections and corresponding to this first configuration (single decay).

We can see that, with the simplified assumptions made, it is theoretically possible to achieve better results than *New Horizons* mission in terms of flight time.

4.5.2 Pluto Mission with a Double Decay Radioisotope Sail

In the second part of the study we hypothesized the use of radioactive materials characterized by double alpha decay, thus ignoring any subsequent steps in the chain. In Table 3 are collected all the corresponding results.

We can see that the double decay configuration allows to further improve theoretical performance.

5 Conclusions

The radioisotope sail represents a propulsion system with interesting potential.

As demonstrated in this study, from a theoretical point of view and considering a series of simplifying hypotheses, the achievable performances are high in comparison with the classical propulsion systems for exploration within the Solar System.

The achievable speeds do not, however, allow to consider, in this phase of the study, the use of such a propulsion system for relativistic interstellar missions. In the best case of those studied, it would take thousands of years to reach the Alpha Centauri System. Future studies will tell whether it is possible to optimize the system to a level that makes such journeys plausible or whether it is appropriate to focus on less ambitious use.

It is certainly necessary to deepen the study by expanding the mathematical models to the more generic case of a decay chain in which the emitted particles can be both alpha and beta minus, and optimizing the choice of the best performing radioactive material among all those possible. In addition, various additional factors will have to be considered, including the (pejorative) effects due to geometric losses; the design, possible consumption and performance of the particle focusing system; the difficulties related to the procurement, production, storage and handling of radioactive materials; the condition for which the decay cannot be considered incipient when the spacecraft arrives in the parking orbit, but must necessarily be considered already started; natural heating due to decay and the possible positive contribution of thermal radiation to propulsion.

Table 2 Numerical results for an Earth–Pluto mission, with radioisotope sail under single alpha decay conditions

	Th – 227 ↓	Ra – 223 ↓	Ac – 225 ↓
Single alpha decay	Ra – 223	Rn – 219	Fr – 221
m_1	$3.77 \cdot 10^{-25}$ kg	$3.70 \cdot 10^{-25}$ kg	$3.74 \cdot 10^{-25}$ kg
m_2	$3.70 \cdot 10^{-25}$ kg	$3.64 \cdot 10^{-25}$ kg	$3.67 \cdot 10^{-25}$ kg
$\tau_{1/2}$	18.72 d	11.43 d	10.0 d
λ	$4.286 \cdot 10^{-7}$ 1/s	$7.019 \cdot 10^{-7}$ 1/s	$8.023 \cdot 10^{-7}$ 1/s
Q	6146.43 keV	5978.99 keV	5935.10 keV
E_k	$9.85 \cdot 10^{-13}$ J	$9.58 \cdot 10^{-13}$ J	$9.51 \cdot 10^{-13}$ J
	$9.67 \cdot 10^{-13}$ J	$9.41 \cdot 10^{-13}$ J	$9.34 \cdot 10^{-13}$ J
w_e	17043 km/s	16808 km/s	16747 km/s
I_{sp}	5.69 % c	5.61 % c	5.59 % c
M_{lost}	$1.74 \cdot 10^6$ s	$1.71 \cdot 10^6$ s	$1.71 \cdot 10^6$ s
$T(0)$	0.68 kg	0.69 kg	0.68 kg
$T(\tau_f)$	4.96 N	8.15 N	9.20 N
$a(0)$	~0 mN	~0 mN	~0 mN
$a(\tau_f)$	$1.04 \cdot 10^{-2}$ m/s ²	$1.70 \cdot 10^{-2}$ m/s ²	$1.92 \cdot 10^{-2}$ m/s ²
$\Delta V(\tau_f)$	~0 m/s ²	~0 m/s ²	~0 m/s ²
	24.21 km/s	24.31 km/s	24.00 km/s
	0.008 % c	0.008 % c	0.008 % c
τ_f	6.3 y	6.3 y	6.4 y

(continued)

Table 2 (continued)

	Po – 210 ↓	Th – 228 ↓	Po – 208 ↓
Single alpha decay	Pb – 206	Ra – 224	Pb – 204
m_1	$3.49 \cdot 10^{-25}$ kg	$3.79 \cdot 10^{-25}$ kg	$3.45 \cdot 10^{-25}$ kg
m_2	$3.42 \cdot 10^{-25}$ kg	$3.72 \cdot 10^{-25}$ kg	$3.39 \cdot 10^{-25}$ kg
$\tau_{1/2}$	138.3736 d	1.9126 y	2.898 y
λ	$5.798 \cdot 10^{-8}$ 1/s	$1.148 \cdot 10^{-8}$ 1/s	$7.579 \cdot 10^{-9}$ 1/s
Q	5407.45 keV	5520.08 keV	5215.5 keV
E_k	$8.66 \cdot 10^{-13}$ J	$8.84 \cdot 10^{-13}$ J	$8.36 \cdot 10^{-13}$ J
	$8.50 \cdot 10^{-13}$ J	$8.69 \cdot 10^{-13}$ J	$8.20 \cdot 10^{-13}$ J
w_e	15,977 km/s	16,154 km/s	15,690 km/s
I_{sp}	5.33 % c	5.39 % c	5.23 % c
M_{lost}	$1.63 \cdot 10^6$ s	$1.65 \cdot 10^6$ s	$1.60 \cdot 10^6$ s
$T(0)$	0.73 kg	0.65 kg	0.67 kg
$T(\tau_f)$	0.68 N	0.13 N	0.09 N
$a(0)$	~0 mN	4 mN	8 mN
$a(\tau_f)$	$0.14 \cdot 10^{-2}$ m/s ²	$0.03 \cdot 10^{-2}$ m/s ²	$0.02 \cdot 10^{-2}$ m/s ²
$\Delta V(\tau_f)$	~0 m/s ²	~0 m/s ²	~0 m/s ²
	24.54 km/s	22.85 km/s	22.13 km/s
	0.008 % c	0.007 % c	0.007 % c
τ_f	6.7 y	9.3 y	10.0 y

The first line indicates the radioactive materials considered (each with parent nuclide and daughter nuclide)

Table 3 Numerical results for an Earth–Pluto mission, with radioisotope sail under double alpha decay conditions

	Ac – 225 ↓ Fr – 221 ↓ At – 217	Th – 227 ↓ Ra – 223 ↓ Rn – 219	Th – 228 ↓ Ra – 224 ↓ Rn – 220
Double alpha decay			
m_1	$3.74 \cdot 10^{-25}$ kg	$3.77 \cdot 10^{-25}$ kg	$3.79 \cdot 10^{-25}$ kg
m_2	$3.67 \cdot 10^{-25}$ kg	$3.70 \cdot 10^{-25}$ kg	$3.72 \cdot 10^{-25}$ kg
m_3	$3.60 \cdot 10^{-25}$ kg	$3.64 \cdot 10^{-25}$ kg	$3.64 \cdot 10^{-25}$ kg
$\tau_{1/2,1}$	10.0 d	18.72 d	1.9126 y
$\tau_{1/2,2}$	4.79 min	11.43 d	3.631 d
λ_1	$8.023 \cdot 10^{-7}$ 1/s	$4.286 \cdot 10^{-7}$ 1/s	$1.148 \cdot 10^{-8}$ 1/s
λ_2	$2.412 \cdot 10^{-3}$ 1/s	$7.019 \cdot 10^{-7}$ 1/s	$2.209 \cdot 10^{-6}$ 1/s
Q_1	5935.10 keV $9.51 \cdot 10^{-13}$ J	6146.43 keV $9.85 \cdot 10^{-13}$ J	5520.08 keV $8.84 \cdot 10^{-13}$ J
Q_2	6457.80 keV $1.03 \cdot 10^{-12}$ J	5978.99 keV $9.58 \cdot 10^{-13}$ J	5788.85 keV $9.27 \cdot 10^{-13}$ J
$E_{k,1}$	$9.34 \cdot 10^{-13}$ J	$9.67 \cdot 10^{-13}$ J	$8.69 \cdot 10^{-13}$ J
$E_{k,2}$	$1.02 \cdot 10^{-12}$ J	$9.41 \cdot 10^{-13}$ J	$9.11 \cdot 10^{-13}$ J

(continued)

Table 3 (continued)

	Ac - 225 ↓ Fr - 221 ↓ At - 217	Th - 227 ↓ Ra - 223 ↓ Rn - 219	Th - 228 ↓ Ra - 224 ↓ Rn - 220
Double alpha decay	16,747 km/s 5.59 % c	17,043 km/s 5.69 % c	16,154 km/s 5.39 % c
$w_e, 1$	17,464 km/s 5.83 % c	16,808 km/s 5.61 % c	16,539 km/s 5.52 % c
$w_e, 2$	17,106 km/s 5.71 % c	16,877 km/s 5.63 % c	16,347 km/s 5.45 % c
\bar{w}_e			
\bar{T}_{sp}	$1.74 \cdot 10^6$ s	$1.72 \cdot 10^6$ s	$1.67 \cdot 10^6$ s
M_{lost}	1.37 kg	1.36 kg	1.18 kg
$T(0)$	9,20 N	4,96 N	0.13 N
$T(\tau_f)$	-0 mN	-0 mN	32 mN
$a(0)$	$1.92 \cdot 10^{-2}$ m/s ²	$1.04 \cdot 10^{-2}$ m/s ²	$0.03 \cdot 10^{-2}$ m/s ²
$a(\tau_f)$	-0 m/s ²	-0 m/s ²	-0 m/s ²
$\Delta V(\tau_f)$	49,07 km/s 0.016 % c	47,99 km/s 0.016 % c	40,38 km/s 0.013 % c
τ_f	3.1 y	3.3 y	5.7 y

The first line indicates the radioactive materials considered (each with parent nuclide, daughter nuclide, and granddaughter nuclide)

References

1. R. L. Forward, Radioisotope Sails for Deep Space Propulsion and Electrical Power, 31st AIAA, ASME, SAE and ASEE, Joint Propulsions Conference and Exhibit, AIAA-1995-2593
2. A. Bolonkin, Radioisotope Space Sail and Electro-Generator, 41st AIAA, ASME, SAE and ASEE, Joint Propulsions Conference and Exhibit, AIAA-2005-4225
3. Z. Wenwu, L. Zhen, Y. Yang, D. Shiyu: Revisiting Alpha decay-Based Near-Light-Speed Particle Propulsion. *Applied Radiation and Isotopes*, 114, 14–18 (2016)

The ERC-Funded EXTREMA Project: Achieving Self-Driving Interplanetary CubeSats



**Gianfranco Di Domenico, Eleonora Andreis, Andrea Carlo Morelli,
Gianmario Merisio, Vittorio Franzese, Carmine Giordano,
Alessandro Morselli, Paolo Panicucci, Fabio Ferrari, and Francesco Topputo**

1 Introduction

Since the beginning of the space era, interplanetary probes have commonly been operated from ground. Operations are conducted by flight control and involve performing a number of routine tasks, mainly of scientific, systems engineering, and flight-related nature. Governing the space flight consists of determining the spacecraft position, planning its trajectory, and controlling its motion. Accordingly, these activities are known as a whole as Guidance, Navigation and Control (GNC).

The EXTREMA project (Engineering Extremely Rare Events in Astrodynamics for Deep-Space Missions in Autonomy) aims toward a paradigm shift on how deep-space GNC is performed, enabling CubeSats with autonomous capabilities. The project has received a consolidator grant from the European Research Council (ERC), a prestigious acknowledgment that funds cutting-edge research in Europe.

This chapter is intended to give an overview of EXTREMA, highlighting the approaches, methodologies, and objectives; moreover, the expected results, outcomes, and impact on future space exploration scenarios are also discussed.

1.1 Framing

The space sector is experiencing a flourishing growth. Space economy is booming. Integrated space-based services will soon benefit mankind at unprecedented levels.

G. Di Domenico (✉) · E. Andreis · A. C. Morelli · G. Merisio · V. Franzese · C. Giordano ·
A. Morselli · P. Panicucci · F. Ferrari · F. Topputo
Politecnico di Milano, Milano, Italy
e-mail: gianfranco.didomenico@polimi.it

Private companies are establishing several artificial constellations composed of thousands of satellites. Space tourism is progressively becoming reality. The momentum characterizing the near-Earth space will soon affect outer space as well. At this pace, a multitude of miniaturized probes will soon pervade the inner solar system. The abundantly variegated minor bodies (asteroids and comets) will be the destination of numerous missions. Rocky planets will feature networks of artificial satellites to support science and operations. A shift from space exploration to systematic space exploitation will take place due to the steady reduction of natural resources on the Earth. All in all, evidence is mounting that the near future will be characterized by a large number of deep-space missions.

Deep-space GNC is the subject of EXTREMA. The acute increase of deep-space missions will shortly lead to saturation of ground-based facilities. State-of-the-art operations require dedicated teams and infrastructures, which is expensive. The rapid proliferation of deep-space assets induces a dramatic urgency of granting autonomy to space probes. At the actual pace, human-in-the-loop, flight-related operations for deep-space missions will soon become unsustainable. Autonomous deep-space GNC is the gateway for a sustainable exploration and exploitation of the outer space. This involves a significant paradigm shift:

? Research Question

To what extent can we navigate the solar system free of human supervision?

EXTREMA addresses the research question above, by challenging the current paradigm under which spacecraft are piloted in interplanetary space. In this perspective, self-driving spacecraft become the main focus: machines that can travel in deep space and reach their destination in a totally autonomous fashion. These systems are used to engineer ballistic capture (BC), an extremely rare event in astrodynamics that is characterized by high sensitivity, thereby proving the effectiveness of autonomy in a complex scenario. Validating this technology will be a step toward uncharted territories in space exploration: missions will no longer be limited by our capability to operate spacecraft. Space and ground systems will be unchained. It will be a disruptive innovation in access to outer space, especially when combined with system miniaturization. CubeSats, nanosatellites made of cubic modular units (10 cm edge and 1.3 kg mass [1]), have granted research institutions and small companies access to the near-Earth space, once a prerogative of few large agencies.

Although the success of CubeSats for the Earth observation is unquestionable, deep-space exploration is still dominated by conventional monolithic spacecraft. Several technological gaps prevent realizing interplanetary CubeSats: with their minute budgets, power production, communication, micro propulsion, attitude pointing, orbit control, and radiation shielding become extremely challenging. However, the recent success of the two MarCO CubeSats [2] indicates that inter-

planetary CubeSats are bound to thrive in the near future. Nevertheless, it can be proven that the overall cost for interplanetary missions scales with the system mass, except for what concerns operations: under the current paradigm, operating a 1-kg spacecraft requires the same effort as operating a 1-ton one. Self-driving interplanetary CubeSats have the potential to demolish this last barrier, favoring full mission scalability. A reduced effort required for operation will further lower the overall mission cost, making it even easier for small institutions to access outer space. Interplanetary CubeSats have been envisaged either as payloads of flagship missions or as stand-alone systems. The former are released in situ by a mothership, while the latter must undertake a deep-space cruise. Stand-alone interplanetary CubeSats are considered in EXTREMA, as they are more amenable to the conceived experiments. Moreover, in their role as technological demonstrators, self-driving interplanetary CubeSats will represent a milestone toward autonomous GNC of larger platforms. Due to their limited resources and large distances, leading to low data rates and communication delays, self-driving capability in deep-space cruise for CubeSats is imperative. This leads to postulate EXTREMA's research hypothesis:

Enable deep-space limited-budget spacecraft to determine their position using information embedded in the environment, plan their trajectory using on-board available computational resources, and govern their motion using on-board low-thrust propulsion, for the whole duration of an interplanetary mission.

The hypothesis denotes that the spacecraft has to:

- (a) Infer information from the surrounding environment and analyze them to determine the position
- (b) Generate a plan for the trajectory that reaches the target mission destination
- (c) Execute the plan and correct for possible deviations arising from unmodeled disturbances

It is assumed that the three actions are executed recursively during the cruise, until the mission destination is reached. The conceptual logic of the research hypothesis introduces two actors: the spacecraft and the environment. They interact by virtue of the information inferred by the former and through its dynamics, which in turn alters their relationship. This paradigm is challenging because the deep-space environment is scarce of information, and the spacecraft has limited control authority. The logic is executed in a totally autonomous fashion; no intervention from ground is contemplated in the research hypothesis.

1.2 State of the Art

EXTREMA is a research project of intra-disciplinary nature. Various fields of space engineering are examined under the same umbrella in order to answer the research question. Particularly involved are the spacecraft guidance, navigation, and control, as well as the BC, a phenomenon of highly nonlinear astrodynamics that is proposed to allow limited-control spacecraft to enter a temporary orbit about a planet.

1.2.1 Guidance

Guidance design is the process of determining the trajectory connecting two points. The nominal solution is usually found by solving a trajectory optimization problem since one wants to minimize, e.g., the propellant spent or the time of flight. Designing the guidance can take days, if not months [3]; the solution has to be validated against system and mission constraints before being flown. The guidance is always found on ground. As is, it is one of those operations that requires a significant human intervention. Any algorithm deficiency or solution non-compliance is taken care of by the operator. Performing this task on board poses a significant challenge: the solution has to be found in near real time and with limited computing power.

Depending on the propulsion technology, the guidance considers either *impulsive* or *continuous* maneuvers. The former originate from high-thrust chemical propulsion, and the latter stems from low-thrust electric propulsion. The two models lead to different optimization schemes. Nonlinear programming problems are faced in high-thrust propulsion [4, 5], where one solves for a finite number of unknowns. Nonlinear optimal control problems are treated in low-thrust propulsion [6, 7], the solution being infinite-dimensional. The hypothesis in EXTREMA involves using low-thrust propulsion, which is more efficient when maneuvering in deep space (impulses are instead desirable when imparted near major bodies). Therefore, the focus is on automating the search for continuous steering laws by using the available on-board computing power.

Metaheuristics methods (global optimization algorithms that employ heuristic rules [8, 9]) and indirect methods (based on the calculus of variations [10, 11]) are not suitable for on-board applications; they suffer from high sensitivity to initial guesses. Although improvements have been proposed, e.g., through smoothing [12, 13] and initialization techniques [14, 15] or by adding a migration scheme [16] and scaling factors [17], the convergence issues remain unsolved. Direct methods transform a continuous problem into a discrete one. They result in computationally expensive large-scale problems [18, 19] and cannot be handled on board. However, due to their robustness, some studies refined the discretization techniques [20, 21] and applied convex [22, 23] and differential dynamic programming [24, 25] to lower the computational burden. Feedback-driven Lyapunov-based methods are computationally affordable. Effort has been put to improve their general non-

optimality by including additional constraints [26] and optimizing parameters [27, 28]. Recent approaches use artificial intelligence to design robust, but less optimal and less flexible on-board guidance schemes [29–31]. Yet, none of the existing methods guarantees convergence, which is crucial in EXTREMA.

1.2.2 Navigation

Navigation is the process of determining the spacecraft orbit in space. Traditional navigation techniques for the Earth-orbiting satellites and deep-space probes rely on radiometric tracking and ground-based orbit determination. Radiometric observables (two-way ranging and range rate) yield position accuracies in the order of meters in a low-Earth orbit and kilometers in deep space [32]. The drawback of using traditional radiometric-based navigation is in their interaction with ground. This is unavoidable and yields large costs.

The vision in EXTREMA predicts a large number of spacecraft wandering in the solar system. In this scenario, radiometric navigation is not an option: ground-based facilities can track a few spacecraft per time and will be congested soon. Moreover, the research involves using limited-budget systems, which brings in low data rates. On-board autonomous navigation detaches the spacecraft from ground control. Consistently with the hypothesis, the focus is on those methods capable of analyzing the information inherent in the environment to extract the spacecraft position. Optical navigation is the key to guaranteeing these features.

Optical navigation exploits images to reconstruct the observation geometry between the spacecraft and the observed celestial object. In close proximity to asteroids or moons, features like craters are used to estimate an observer position [33]. Landmarks are associated with sharp variations in image brightness [34, 35] (e.g., shadowing due to a crater’s rim). The image can be further processed with ellipse fitting methods to retrieve the craters’ geometry [36]. This is correlated to the object surface map via template matching to estimate the observer position [37]. At mid-range to an ellipsoidal celestial object, when its full shape is visible in an image (e.g., the Moon), its contour can be resolved via edge detection algorithms and used for relative navigation [38, 39]. The object size and shape in the image are linked to the actual ones to estimate the relative camera-to-object range, while the object position in the image is related to the actual camera-to-object line of sight [40, 41]. For the deep-space case, methods able to extract the line-of-sight directions to some visible moons or planets, detected via centroid finding algorithms [42], can be used to feed triangulation schemes [43, 44]. In all cases, state filtering is required to estimate the actual spacecraft orbit based on past measurements [45].

1.2.3 Control

Trajectory control handles the deviations of the actual spacecraft trajectory from the one planned. In space flight, this discrepancy is mainly due to unmodeled

perturbations, uncertain initial state, and thrust magnitude/pointing errors. Owing to their permanent and unpredictable nature, closed-loop trajectory control is applied routinely. The aim is either to cancel the anomalies in order to adhere to the nominal solution (trajectory tracking) or to recompute the baseline at regular intervals starting from the off-nominal state (closed-loop guidance). Like guidance, spacecraft trajectory control is always performed on ground.

The most classic and robust way to perform trajectory tracking consists of linearizing the equations of motion about the nominal solutions [46]. Although solid, this method is suboptimal and neglects nonlinearities [47]. Classical tracking techniques include neighboring optimal control (NOC) and model predictive control (MPC). NOC finds the feedback control corrections to obtain locally optimal paths [48], while MPC corrects a finite-horizon control profile based on the predicted and desired output [49].

Nevertheless, for a near real-time implementation, the sustainability of numerical computations is paramount. Several techniques have been developed to reduce the computational burden [50, 51]. Machine learning-based applications have recently been proposed for spacecraft guidance and control [29]. Deep learning techniques have been used for on-board guidance and control; the key is to learn a large dataset of optimal state–control pairs computed offline [52]. Reinforcement learning has also been applied to design and train controllers for proximity motion [53] and fuel-optimal pinpoint landing [54].

1.2.4 Ballistic Capture

BC is a process through which a spacecraft can approach a planet and enter a temporary orbit about it without requiring maneuvers in between. The mechanism arises when at least two gravitational pulls are considered. As such, one must go beyond the classic Keplerian decomposition of the solar system to infer these solutions. BC was discovered in the attempt to reduce the propellant required to reach the Moon [55]; its effectiveness was proven in the rescue of Hiten [56].

The method based on stable sets [57] allows extracting BC orbits with prescribed features [58]. BC is very rare: it occurs 1 out of 10,000 times when performing grid sampling [59]. In EXTREMA, BC is used because it is a desirable solution for limited-control platforms, which cannot afford to enter into orbits about a planet because they lack significant orbit control. For years it was thought that BC could not occur about inner planets. In [60], it was shown that BC orbits at Mars exist, and they are cheaper, safer, and more flexible than the classical maneuvers. The key is to accomplish low-thrust orbits culminating in BC, as shown in Fig. 1. A mechanism similar to BC has been observed in the motion of natural objects [61–63].

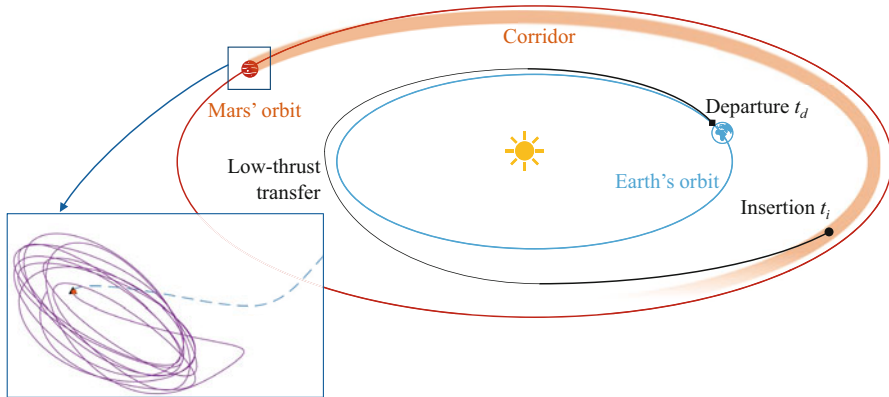


Fig. 1 Earth–Mars low-thrust transfer culminating in ballistic capture at Mars

1.3 The EXTREMA Project

The challenge set in EXTREMA is ambitious. Freeing deep-space probes from human control will determine a significant reduction of the overall operation costs. The goal is to put an end to the supervision in the cruise phase and let the spacecraft reach autonomously its final destination. Because the focus is on interplanetary CubeSats, proving the research hypothesis will guarantee the sustainability of deep-space missions at moderate costs.

The challenges and innovative nature of EXTREMA are summarized in the following key aspects:

- (a) Determining the spacecraft position in deep space has always relied on radiometric tracking from ground. Spacecraft have never been conceded the possibility to determine their position in autonomy. To do so with no contacts, one has to be able to extract information from the surrounding environment.
- (b) The scarce number of high-cost deep-space probes has imposed a highly cautious operations approach. With their number increasing, their size reducing, and in turn their cost lowering, one has to take more risks when operating deep-space probes.
- (c) Orbits about a planet are achieved with large propulsive maneuvers. Proving the feasibility of ballistic capture allows systems characterized by low or no control to enter a temporary orbit about a planet, which is not currently possible.

A comprehensive overview of EXTREMA is given in Fig. 2. The project is supported by three pillars, each one designed to answer an Operational Research Question (ORQ):

1. **Pillar 1** deals with autonomous navigation and aims to develop algorithms and techniques to reconstruct the state of the spacecraft through optical navigation.

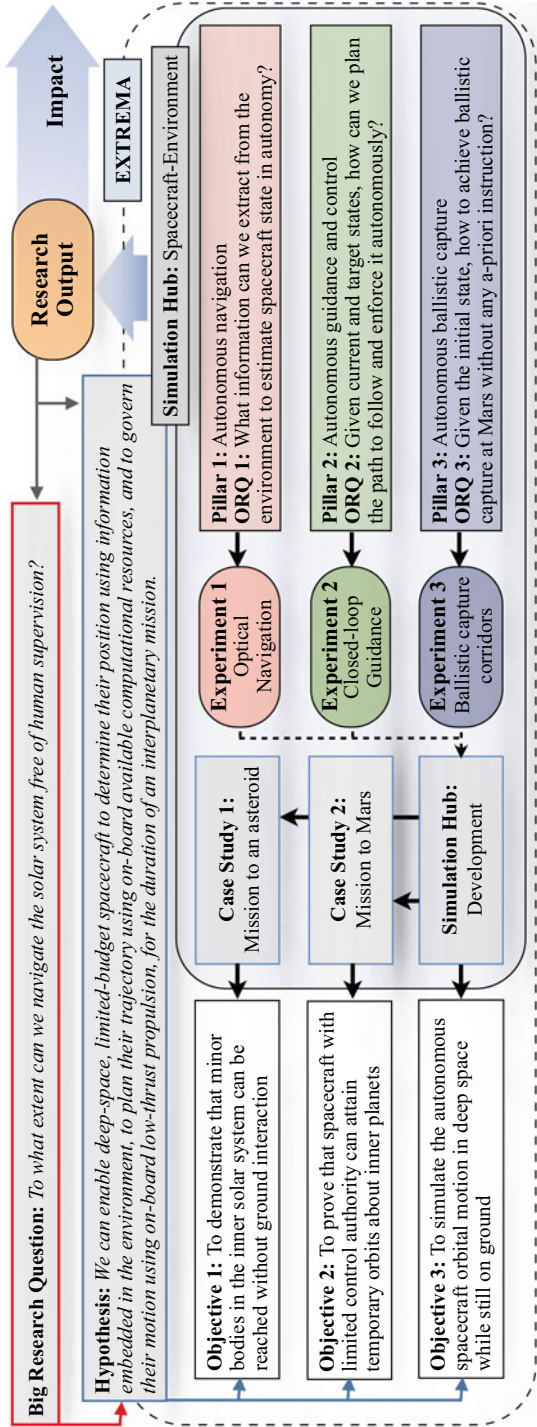


Fig. 2 Overview of the EXTREMA project objectives and structure

2. **Pillar 2** deals with autonomous guidance and control and aims to develop state-of-the-art trajectory computing algorithms under a closed-loop guidance paradigm, in which a new trajectory is recomputed on board whenever required.
3. **Pillar 3** faces autonomous BC and aims to validate the previous algorithms in a complex scenario that is also appealing for CubeSats missions.

Three experiments are foreseen, one within each pillar. The experiments will produce intermediate results and are instrumental for the EXTREMA Simulation Hub (ESH). The ESH is an integrated infrastructure to carry on dynamic simulations of the spacecraft–environment interaction, allowing high-fidelity testing of deep-space autonomous GNC systems for CubeSats.

2 Methodology

In this section, an overview of the methodology that will be employed in EXTREMA to attain its objectives and answer the ORQs and the main research questions is provided.

2.1 *Autonomous Navigation*

Optical navigation relies on image processing to extract relevant information about the external environment and the probe position. The current trend in space community is to enable optical navigation in proximity with uncooperative objects [64, 65] and with irregular small bodies [66, 67]; EXTREMA wants to depart from the state of the art and, in particular, extend it to deep space.

When in deep space, a spacecraft camera working in the visible band can observe stars, planets, and minor bodies. The geometry of the stars is fixed in common mission time frames; this enables a robust and reliable attitude estimation [68, 69]. Instead, planets and minor bodies move at shorter time scales: while the inertial geometry of a known object is a predictable function of the epoch, its apparent geometry depends also on the observer location. Therefore, planets and minor bodies can be thought of as light beacons that can be exploited to solve for the observer position [70, 71]. This leads to the first EXTREMA ORQ:

? Operative Research Question 1

What information can we extract from the environment to estimate the spacecraft state in autonomy?

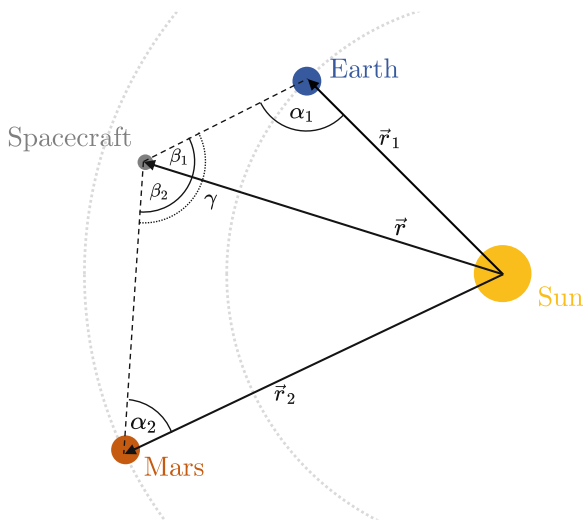


Fig. 3 Example of triangulation schemes. The geometry of the problem allows for the reconstruction of the spacecraft state in the solar system

It is possible to determine the spacecraft trajectory by acquiring and tracking the line-of-sight directions to the visible planets and minor bodies, whose motion is known via ephemeris models. The line-of-sight directions are given to a navigation filter to triangulate the spacecraft orbit, provided that the attitude is estimated from star asterisms (Fig. 3). This method is completely autonomous because:

- The ephemerides of the major planets and the minor bodies in the solar system are stored on board and accessed to retrieve the inertial states of the light beacons.
- The line-of-sight directions to non-stellar objects are acquired by cameras working in the visible band (e.g., star trackers) and determined via image processing algorithms already used in space (e.g., centroid finding algorithm [42, 69, 72]).
- The spacecraft trajectory is estimated via on-board navigation filtering with triangulation embedded methods [73].

The accuracy of the deep-space optical navigation depends on the accuracy of the inertial line-of-sight directions to the navigation beacons. These directions are affected by:

- Image processing errors.** When an image containing a light beacon is acquired, it is processed via centroid finding algorithms: a region of interest binds the light dot in the image and its center of brightness is computed, thus introducing a shift with respect to the real beacon location.
- Camera performances.** Optical techniques work better with high-resolution cameras, narrow fields of view, and sensible limit magnitudes, as these can

detect more objects and with higher accuracy with respect to the less performing sensors. Because of that, high-performance sensors provide better attitude and line-of-sight estimates. Unfortunately, such equipment is not always available on space assets, especially when dealing with CubeSat missions characterized by low budgets.

- (c) **Uncertainties in attitude estimation mounting errors.** These introduce errors when transforming the line-of-sight directions from the sensors to the inertial frames.

These aspects can heavily affect navigation performances. The assessment of their influence on the navigation is done within a hardware-in-the-loop (HIL) experiment, described in Sect. 3.1.

2.2 *Autonomous Guidance and Control*

The Guidance and Control (GC) process aims to determine the optimal transfer trajectory to reach the target point by responding to any deviation from the nominal trajectory with a proper guidance and control plan. It therefore requires the knowledge of the current spacecraft position and velocity, which is the output of the navigation. The low-thrust trajectory design is complex, time-consuming, and computationally expensive since the GC scheme must also fulfill all trajectory constraints and keep the spacecraft within the operational envelope.

One of the EXTREMA objectives is to enable new capabilities in the area of GC, with the goal of automatizing the process by identifying algorithms suitable for on-board use, without the intervention of ground operators. We can therefore state the second EXTREMA ORQ:

? **Operative Research Question 2**

Given current and target states, how can we plan the path to follow and enforce it autonomously?

Currently, the operator has to monitor the GC and manually take appropriate actions in case of deviations from the nominal trajectory. On the contrary, on-board computation of guidance and control exposes the mission to risks as the following three requirements must be fulfilled [74] :

- (a) **Robustness.** On-board GC must guarantee convergence, in the sense that a feasible solution must be obtainable at any instant. This is crucial for autonomous GC as algorithm deficiencies cannot be tolerated.
- (b) **Computational efficiency.** GC must be compatible with available on-board computational resources. This is a major problem as GC planning is complex,

and traditional techniques require a considerable amount of computing power, requiring the employment of on-ground computing resources.

- (c) **Optimality.** A cost function is to be minimized, usually the fuel consumption. This is essential for small satellite deep-space missions due to their structurally limited propellant budgets.

The most common state-of-the-art methods used to solve the low-thrust space trajectory optimization problem have been mentioned and briefly described in Sect. 1.2.1. Here, we focus on the approach that has been selected to be a candidate for autonomous spacecraft guidance. Convex Programming (CP) [75] is a direct optimization method particularly suited for real-time applications since it requires little computational effort [76]. The GC system will trigger the CP method to generate new reference trajectories when off-nominal conditions are detected or the deviation is beyond a predefined tolerance. However, the low-thrust minimum-fuel problem is non-convex. For this reason, in order to be solved by means of convex optimization algorithms, some convexification techniques must be employed to obtain an equivalent convex problem. The original problem is eventually solved through iterative strategies that solve a sequence of convexified problems, as Sequential Convex Programming [77]. These techniques will be adapted to the EXTREMA project to obtain a Deep-Space Closed-Loop Guidance (DSCLG) algorithm.

The aim of EXTREMA is to demonstrate the feasibility of autonomous CubeSats, and therefore the guidance and control scheme will be validated with a dedicated experiment, as described in Sect. 3.2. Given initial and target states, the reference trajectory and the corresponding control profile are generated by an Single-Board Computer (SBC) with characteristics in line with those of actual on-board computers (OBCs) and actuated with a physical engine whose force output is recorded by a set of force transducer before being fed to a high-fidelity numerical propagator.

2.3 *Autonomous Ballistic Capture*

BC mechanism is suited for limited-control platforms, which cannot afford to enter into orbits about a planet because of the lack of proper means.

In Pillar 3, the object of study is how a spacecraft can attain BC in autonomy. The spacecraft assumed already in deep space has to acquire BC at Mars without relying on any information provided from ground. Mars is chosen without loss of generality due to its relevance in long-term exploration. This leads to the third operative research question:

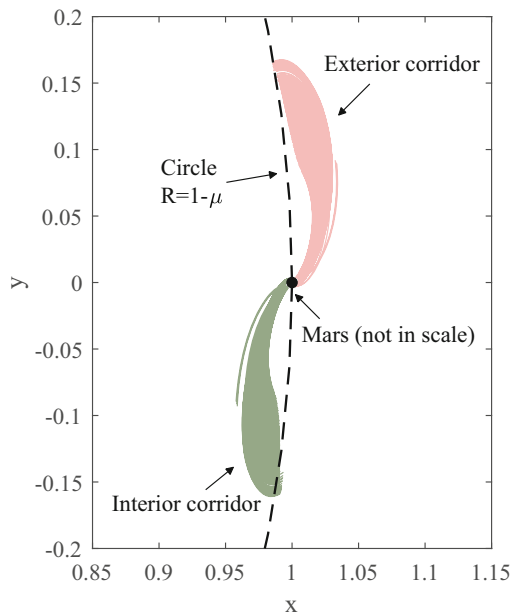
Operative Research Question 3

Given the initial state, how can we achieve ballistic capture at Mars without any a priori instruction?

BC is an event that occurs on extremely rare occasions and requires acquiring a proper state (position and velocity) far away from the target planet [60]. Massive numerical simulations are required to find the specific conditions that support capture. In the method shown in [57], stable sets are computed via grid sampling and propagation. Millions of initial conditions are integrated and classified according to the orbits they generate. The initial conditions that grant capture define a capture set, which in turn is used to find the capture corridors [78]: these are streams of orbits that can be targeted far away from the planet and that guarantee BC (interior and exterior corridors are shown in Fig. 4).

The method based on stable sets is preferred due to its versatility: it works for any model, energy, and epoch [59]. The key is to grant the spacecraft the capability to manipulate the stable sets in order to self-compute BC corridors. Nevertheless, stable set computation on board is not an option. Moreover, these sets depend on both capture epoch and osculating eccentricity, so they cannot be computed once for all [57]. Thus, the challenge is to develop and validate an algorithm compatible with the on-board resources.

Fig. 4 BC corridors from capture epoch t_0 to $t_0 - 600$ days. Interior and exterior corridors are colored in pink and green, respectively. Trajectories are represented in nondimensional coordinates in the roto-pulsating frame



The proposed strategy is based on the offline computation of a catalog of stable sets, computed for a predefined grid of values of (1) Mars true anomaly (which can be linked with the position of Mars on its orbit and thus to the epoch of the first close encounter), (2) the osculating eccentricity of the orbit at the first encounter, and (3) the number of post-capture revolutions. The offline simulations will be carried out using the GRavity Tidal Slide (GRATIS) software. GRATIS implements a high-fidelity model of a three-dimensional full-ephemeris restricted n-body problem, including non-spherical gravity terms as well as solar radiation pressure [79].

Once the stable set catalog is computed, it will be stored on the same breadboard used in the experiment introduced in the previous sections. Because this process may require significant amount of storage, the boundaries of stable sets will be extracted and stored. These are the only elements that matter when manipulating the sets. Therefore, a propagation scheme for the integration of the capture trajectories compatible with the computational performances of the breadboard will be developed. The epochs not covered by the catalog are retrieved through a multi-dimensional interpolation like the ones implemented in [80]. In this way, the spacecraft will be granted the possibility of self-computing the capture corridors for any arrival epoch.

The validation will involve the experimental setup described in Sect. 3.2, with the exception that the guidance and control algorithms will be upgraded to manage target points defined on a moving manifold. This will be done by adding terminal constraints expressed as a time-varying vector-valued function.

3 Modeling

In order to test and validate the outcomes of the three pillars, proper modeling of the phenomena and systems characterizing the interplanetary transfer must be performed. This is not a trivial task, as these are characterized by strong interactions between physical domains and involve sub-phenomena acting at very different scales.

Historically, the modeling of interplanetary transfers has heavily relied on mathematical approximations, system decoupling, and numerical and computational tools to build models for predicting and analyzing the evolution of the quantities of interest. Statistical approaches have been employed to guarantee the robustness of the outcomes against effects not included in the original models.

Given the advances in the capabilities of micro-computing and technologies for embedded systems, a different kind of models, mixing numerical tools with physical implementations of the systems of interest, emerged. Depending on which parts of the systems were physically represented, these have been named hardware-in-the-loop (HIL), processor-in-the-loop (PIL), or even human-in-the-loop simulations. The advantages of such approaches can be seen in terms of:

- (a) **Simulation fidelity**, as the approximations brought by numerical models of physical elements do not introduce errors in the simulations
- (b) **Resources required**, as it is possible to relieve the numerical integrators from the need to propagate the evolution of physical systems; this benefits, in particular, those simulations involving phenomena happening at very different time scales
- (c) **Simulation flexibility**, as it is possible to obtain a faithful simulation of harsh environment and phenomena employing tailored sets of sensors and actuators, without leaving the safety of the lab environment

In the past years, multiple frameworks for HIL simulations have been proposed. However, they all were characterized by a single critical drawback that would make them unsuitable for deep-space applications. As the evolution of physical models is subject to certain time scales, the synchronization of the virtual part of the model with the physical one hinders all the speed advantages brought by numerical simulation: no matter how powerful the computing platform is; since they need inputs from the real world to go on with the simulation, they are bounded to the time scale of the physical models. As interplanetary transfers are usually long-lasting, this means that a single simulation could span months, if not years: this would make the development and testing of the models a task spanning decades.

Luckily, this issue can be cleverly avoided by employing particular mathematical tools. In particular, the dynamic similarity, already known in simulation engineering for applications related to aerodynamics [81], fluid dynamics [82], electronics, [83], and hydraulics [84], can be exploited for deep-space simulations too. The idea is to map the original system, represented by the original spacecraft and the original environment as they are in the real world, to a faster-evolving system, linked to the original by a set of definite mathematical relationships involving the quantities of interest (Fig. 5). The simulation models can mimic the behavior of the scaled system, benefiting from shorter simulation times and keeping all the advantages brought by HIL simulations.

Moreover, by manipulating the mapping-defining parameters, it is possible to tailor the simulation to better comply with the availability of resources in the lab environment. For instance, as it will be better described in Sect. 3.2, it will be possible to map an ion engine characterized by high exhaust velocities (and low-thrust values, requiring precision measuring equipment to be properly read) to a simpler cold gas thruster, guaranteeing at the same time high levels of fidelity.

3.1 Modeling of Optical Navigation Systems

EXTREMA will assess the accuracy of the deep-space optical navigation method through hardware-in-the-loop simulations using analogs of both the CubeSat and the environment. This is to perform verification and validation of navigation algorithms developed for autonomous deep-space operations with an optical facility. This is

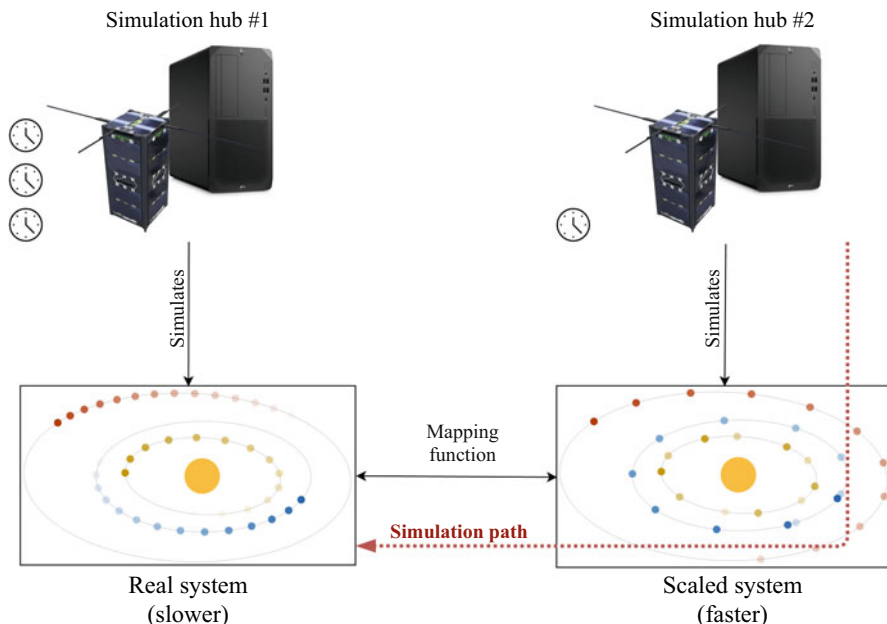


Fig. 5 Conceptual scheme of the mapping approach. The information on the original system is retrieved from the simulations performed on the scaled one through a defined mapping function, following the simulation path highlighted in red

achieved during ground testing by providing the OBC high-fidelity images as if they were taken in space.

The main components of the optical facility, shown in Fig. 6, are:

- (a) A high-fidelity deep-space scene renderer, capable of producing an image given the information on the spacecraft state, i.e., position, velocity, and orientation
- (b) A high-resolution screen to stimulate the camera with rendered images
- (c) A system of lenses that makes sure that the observed objects are seen as if they were at an infinite distance
- (d) An optical camera consistent with the ones carried on board the CubeSats
- (e) A processing unit that receives the raw image as taken by the camera and processes it to perform both image processing, i.e., the beacon line-of-sight extraction, and filtering

The camera, the system of lenses, and the screen are mounted on an optical breadboard and placed in a dark box. To ensure the developed algorithm is as general as possible and robust to different hardware, the facility employs a lens system that is able to adapt the light cast from the screen to different cameras and fields of view.

The optical facility is used as a means to perform validation and verification of the navigation within a HIL Experiment: EXTREMA Experiment 1.

Experiment 1

Experiment 1 will embed on a computing board the image processing and navigation algorithms to process images taken with the camera mounted on the optical facility.

The breadboard is an industrial Single-Board Computer (SBC), e.g., 64-bit ARM, equipped with a CPU that is representative of the typical on-board CubeSat processors. The data interface between the camera and the SBC will have bandwidths comparable to the ones typical of CubeSats' data buses.

During its operations, the true spacecraft state is provided to the renderer which produces an image of the deep-space sky as observed by a flying camera. The image is then projected on a high-resolution screen to stimulate the laboratory camera which is mounted on its support. The spacecraft camera, which has been previously calibrated with respect to the screen and the optical breadboard, observes the screen and acquires images of the environment through the lenses system to reproduce the same conditions in space. Then, the taken image is sent to the SBC which estimates the spacecraft attitude from star asterisms, identifies the planets in the images, extracts its line of sight, and performs navigation by providing this information to the navigation filter. Finally, the navigation error statistics and its robustness are assessed by comparison between the true spacecraft state used to render the image.

Experiment 1 will be executed in three steps:

- (a) First, the aforementioned image processing and navigation algorithms will be developed. This includes the robust attitude determination, the autonomous planet identification in the images, their line-of-sight extraction, and the implementation of *ad hoc* navigation filters.
- (b) The optical facility will be designed, integrated, and tested. This includes the selection of the components to reduce collimation errors, limit the facility mass and size, and design a flexible hardware system for different camera and simulation conditions. Furthermore, a dedicated calibration procedure will be developed to correct misalignments and distortions due to mounting and optical devices.
- (c) Once the optical navigation algorithm is developed, the experimental facility of Pillar 1 has to be designed, integrated, and tested. A static test will be performed to quantify the position error; a dynamic test with a given spacecraft orbit will be needed to assess the filter performances.

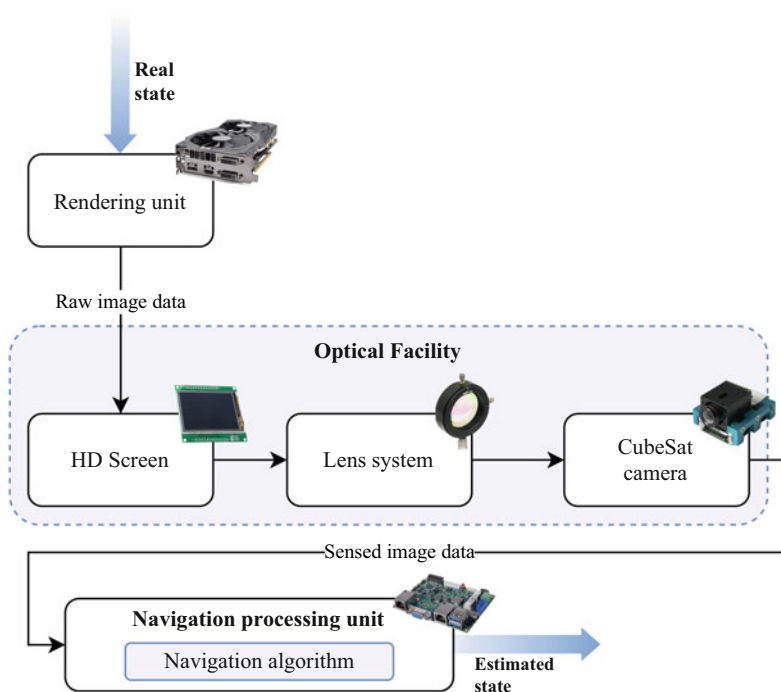


Fig. 6 Logic of the Optical Facility to test the navigation algorithms

Experiment 1 will not only validate the proposed deep-space optical navigation and assess its feasibility but also enable to understand its robustness. Moreover, Experiment 1 is a building block for the EXTREMA Simulation Hub (Sect. 4.1).

3.2 Modeling of Low-Thrust Propulsion Systems

The thruster test bench is used to validate the GC algorithm for self-driving deep-space CubeSats. As outlined in Sect. 2.2, the thrust facility shall model the real actuation of a low-thrust propulsion system, measure the produced thrust, and feed the measurement to a high-fidelity numerical propagator.

It is worth noting that a true real-time simulation would require an extremely long time: an interplanetary transfer requires many months or even years. EXTREMA aims at exploiting a scaled model of the system, correlating the results to the original one thereafter. Through a mapping between the original system and a fast-evolving one, it will be possible to execute the simulations on shorter time frames, lasting a few hours or days.

Employing the accelerating framework also brings a significant advantage in terms of experiment feasibility. Indeed, applying the mathematical relationships governing the dynamic similarity results in higher thrust levels in the lab environment: this frees the experiment from the employment of complex, expensive electrical engines that also require ad hoc setups to be operated (i.e., vacuum chambers or bulky pipes to avoid the interaction of the plume with the surroundings) and ultra-high-accuracy measurement rigs to sense the tiny thrust force output. It is instead possible to tailor the scaling parameters to adapt the *scaled thruster* to the technological limits and safety requirements of the lab environment.

Currently, no traditional engine can guarantee both high levels of thrust and reduced fuel mass consumption. However, by properly fixing its remaining degrees of freedom, the accelerating framework allows lowering the requirements on the specific impulse of the thrusters, mapping a high-efficient low-thrust ion engine to a higher-thrust technology with lower efficiency levels, like a cold gas thruster. While this translates in levels of fuel mass consumption that cannot comply with a CubeSat, these can be achieved with simple laboratory equipment such as pressurized tanks or supply pipes. By selecting compressed air as fuel, even the need for tanks is removed, since it is possible to directly compress the surrounding air with a mechanical compressor and regulate it with a tailored pipeline before feeding the fuel to the thruster.

Of course, the feeding system and the thrusting test bench shall take into account the fundamental differences in the typical thrust profiles of ion and cold gas thrusters. While the dynamic similarity allows to freely choose the thrust level and the specific impulse of the thruster, additional requirements on multiple parameters and characteristics of the thrust profile — like rising and fall times, oscillations, and stability of response — cannot be avoided nor neglected, calling for a careful design of the thrust test bench.

Experiment 2

The functional layout of Experiment 2 is represented in Fig. 7. The current state (estimated by the navigation algorithm) and target state, together with the propagated state (assumed as ground truth), are fed as inputs to the guidance and control algorithm, which is installed on a single-board computer. The output of the GC scheme is used to actuate the cold gas thruster that is installed on the thruster test bench. The produced force is measured by the load cell and then transmitted to the orbital propagator.

The thrust test bench is composed of three parts:

1. The thrust balance, where the thruster and the load cell are positioned
2. The pneumatics feeding line, which provides the required pressure level to the thruster
3. The single-board computer, which computes the optimized trajectory, applies the scaling, and actuates the thruster by acting on the solenoid valve and pressure regulators

The thrust balance is installed on a laboratory workbench and has a vertical layout, with the thrust force that acts vertically from bottom to top. A hole on the worktop increases the distance between the thruster outlet and the underlying lower surface, reducing all possible interferences due to turbulence. The two main drivers of this design choice are:

- (a) The magnitude of the scaled thrust forces, which is of the order of a few Newtons instead of the mN or μN of a low-thrust engine
- (b) The simpler calibration process with respect to the horizontal or torsional thrust balances

More accurate and precise models of thrust balance, like the torsional and horizontal thrust balance, exist and are usually employed for accurate measurement of the performances of low-thrust engines [85]. Anyway, their calibration and setup are much more complex, and additional care must be taken in the preparation of the experiment. Additionally, they often require amplification mechanisms [86], which might also introduce nonlinear effects if the force variation throughout the execution of the experiment varies and gets close to the full scale of the force sensor.

The described setup shall, therefore, guarantee the repeatability and high fidelity of measurements. This is a key aspect in the EXTREMA simulations: an interplanetary or deep-space transfer employs multiple thrust arcs, which are in turn interrupted by multiple navigation sessions. Therefore, multiple activations of the cold gas thruster are needed, and it will not be advisable to perform intermediate calibrations during the execution of a simulation. The simpler design shall therefore guarantee an easier setup and smoother execution of the experiment.

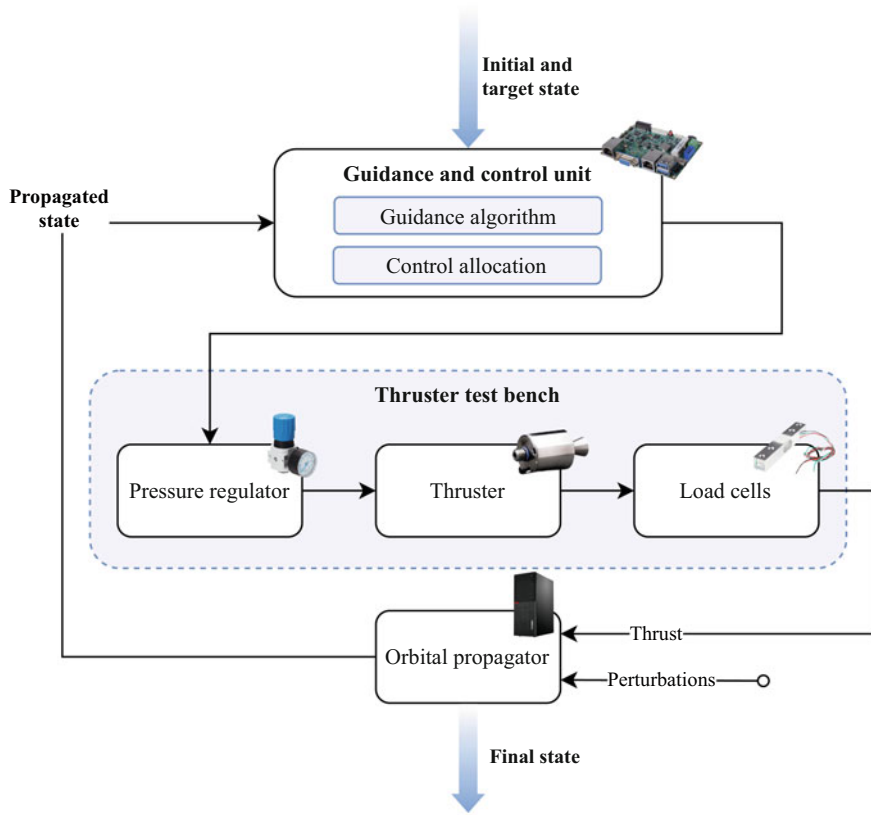


Fig. 7 Logic of the thrust test bench to test the robustness of guidance algorithms

Experiment 2 will be executed in three steps:

1. First, the DSCLG algorithm will be developed. It will be a computationally inexpensive and robust algorithm suitable for on-board applications.
2. The thrust facility will be designed, integrated, and tested. At first, pneumatic components will be selected, the support structure will be designed and optimized, and finally, the focus will be on the design of the nozzle. Once the structure weight is known, the load cell will be selected and integrated. The second step will be concluded by the definition of a calibration procedure and testing of the facility.
3. The third step aims at integrating the outcome of the previous ones: the guidance algorithm will be deployed on the SBC, which will also actuate the scaled thruster. Functional tests will be performed to assess the actuation errors, and fine-tuning will be performed to guarantee that these will be within the expected operational thruster misperformance.

Experiment 2 will validate the Guidance and Control scheme and assess its robustness. Experiment 2 is also a building block for the EXTREMA Simulation Hub (Sect. 4.1).

4 Integrated Simulation of Interplanetary Transfers

In this section, an approach to integrate the outcomes from the previously described experiment will be explained, along with the associated challenges and potential solutions to them.

4.1 *The EXTREMA Simulation Hub*

As said, the outcomes from each one of the three pillars will be validated with a tailored experiment featuring the model of the associated CubeSat subsystems. However, this does not guarantee the functionality of the interactions between the latter. For this reason, an integrated experiment involving all the components of a CubeSat GNC system is required. This experiment will be carried on in the EXTREMA Simulation Hub, an integrated facility that will simulate an interplanetary transfer with a hardware-in-the-loop setup.

The ESH

The EXTREMA Simulation Hub will represent the validation and success of the EXTREMA project.

Figure 8 represents a functional scheme for the integrated simulation. The subsystems already presented in the previous sections are here fully integrated.

4.1.1 On-board Computer

The aim of the ESH is to test autonomous GNC systems for CubeSats. Therefore, the core of the facility will be represented by the GNC computing unit, carefully selected to mimic the computational performance of a typical CubeSat OBC; this will host the algorithms developed in Pillars 1, 2, and 3 (Fig. 9):

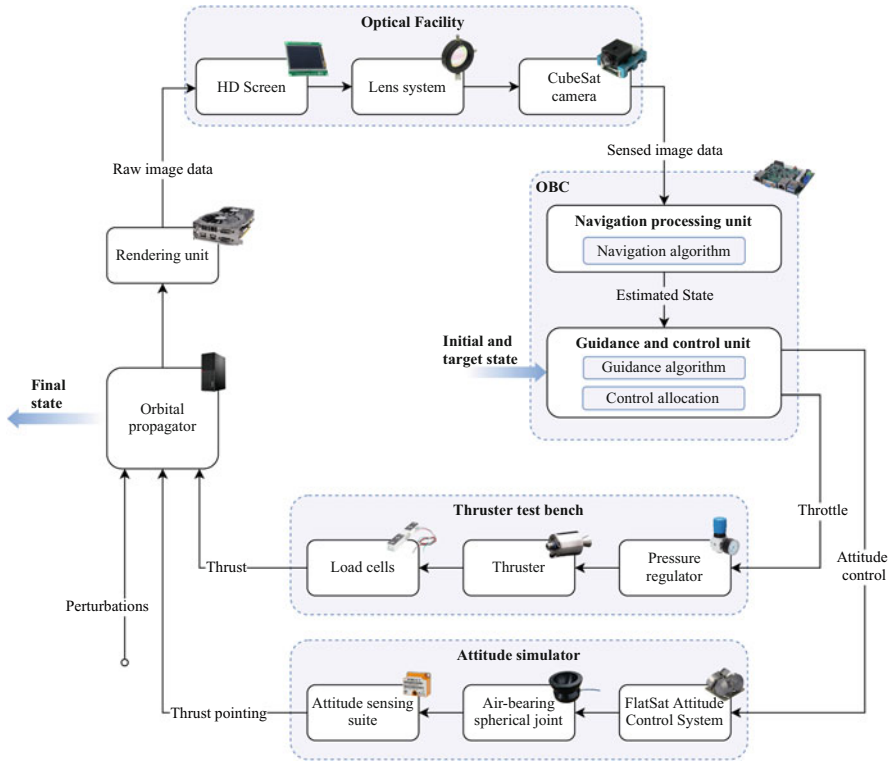


Fig. 8 Functional logic of the EXTREMA Simulation Hub

- (a) The navigation algorithm, which will extract information from the raw sensor outputs and reconstruct the spacecraft state
- (b) The numerical approximation and offline database of ballistic capture corridors, in order to achieve ballistic capture
- (c) The guidance algorithm, which will use the previous information as initial and target conditions, respectively, and will compute a feasible and optimal trajectory

In order to tailor the specifics of the OBC to be representative of the ones of a typical CubeSat, different approaches can be followed. In general, bare-metal measures as the number of computing cores, clock frequency, or instructions per second (IPS) cannot be trusted, not only because actual performances of computers are application-dependent [87] but also because spacecraft computers are also subjected to power constraints that can make actual specifications deviate from datasheet ones. Alternative measures, like Dhrystone MIPS or Whetstone MIPS [88, 89], can offer more reliable measures; still, a generic and reliable benchmark measure for deep-space applications does not exist at the moment.

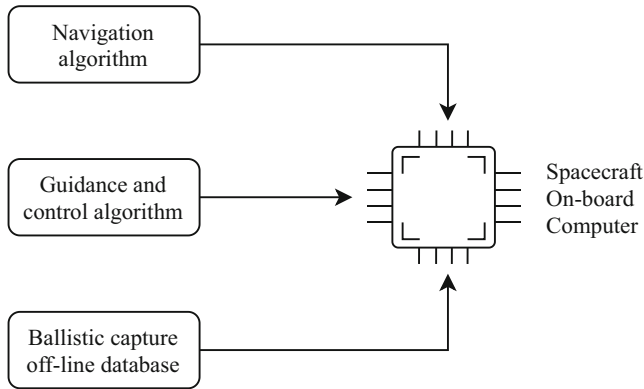


Fig. 9 Overview of software to embed on the OBC

4.1.2 Attitude

Multiple approaches to simulate the attitude evolution of a space system exist in the literature, including robotic arms [90] and frictionless anti-gravitational platforms [91]. In EXTREMA, an air-bearing spherical joint is employed: these systems exploit a thin film of air to guarantee rotational freedom around three axes. With proper care, the motion of the overlying platform can be considered frictionless.

The platform to be mounted on top of the joint is characterized by the following sub-assemblies:

- (a) A mass balancing system, which will guarantee the absence of gravitational torques on the platform by moving the center of mass of the system toward the center of rotation of the joint
- (b) The systems and units of the CubeSat, typically referred to as *flatsat*. This will include the OBC and the CubeSat's attitude determination and control system (ADCS).
- (c) A wireless power generation and distribution system, since no cabling is allowed to avoid perturbations affecting the attitude evolution of the platform. This will include a set of high-efficiency solar cells and a lamp that will emit radiation with the spectrum that will guarantee maximum power output from the system.

The information on the platform attitude is to be used to reconstruct the actual pointing of the spacecraft thruster. This information will then be fed to the numerical integrator to propagate the position of the spacecraft in the interstellar space. Despite air-bearing platforms being renowned for their frictionless capabilities, a proper estimation of the perturbations arising from aerodynamic forces acting on the platform must be considered. Indeed, despite being accelerated, the simulations to be performed in EXTREMA will span multiple days, leading to accumulation of errors and the actual behavior of the platform departing from the expected one.

A proper modelization of the perturbing effects is needed, in order to compensate them and ensure higher fidelity over longer timespans.

4.1.3 Orbital Control System

The GC unit will also command the thruster, mounted on a setup similar to the one described in Sect. 3.2 and employed in the experiment associated with Pillar 2. This will make sure that unmodeled perturbations arising from the physicality of the engine will be considered when evaluating the robustness of the algorithms.

The approach described in Sect. 3 for what concerns the acceleration of the simulation allows employing different kinds of thrusters instead of electric ones. The thrust output, after being measured, must or must not be scaled according to whether the system represented in the numerical integrator is subjected to the accelerating framework.

4.1.4 Navigation System

The experimental setup described in Sect. 3.1 for what concerns the EXTREMA Optical Facility can be easily adapted to be integrated in the ESH. However, there is a set of additional issues to consider:

- (a) The generation of the deep-space scene must take into account the actual attitude of the platform; subtle errors in the reading of the platform orientation could lead to images not representative of the actual environment surrounding the probe.
- (b) The deep-space scene must be triggered immediately after the computing of the spacecraft state by the numerical integrator; moreover, it must happen before the time interval associated with the single timestep has passed.
- (c) The raw image data must be relayed to the OBC wirelessly; a proper communication framework, including state-of-the-art interfaces and protocols, must be set up to avoid large communication lags.

4.1.5 Numerical Integrator

While deep-space phenomena have long characteristic times, the spacecraft rotational dynamics, together with sensors and actuators, works at higher frequencies. This leads to stiff ordinary differential equations for the dynamics, which require special attention in the integration scheme choice. Moreover, the integrator must have real-time capabilities, i.e., the equations of motion have to be generated and numerically solved fast enough and in a fixed time-frame, and it cannot evaluate the right-hand side in future time steps. For this reason, semi-implicit fixed step size and fixed order methods are the most suitable choice [92]. Inside this group,

the so-called singly diagonally implicit Runge-Kutta (SDIRK) algorithms [93] are advisable for real-time applications, since they are computationally efficient, while providing good stability and accuracy, even at lower order.

4.1.6 Additional Systems and Components

Apart from the ones already described, the faithfulness of the simulation and the functionality of the facility must be guaranteed with additional systems. Debugging units, schedulers, and fault generation units allow to monitor the progress of the simulation, ensure that all the internal clocks of the different sub-components are initially synchronized, and provide a framework to test the robustness of the algorithms and techniques to be tested against unexpected faults, respectively.

Moreover, the interaction between additional CubeSats subsystems (e.g., the thermal control one) must be properly analyzed and weighed against the drawbacks of a more complex, less flexible setup that envisions their implementation in the facility.

4.2 Remarks

While the determination and implementation of the different elements and subsystems for an integrated facility are not trivial, it is not sufficient to reach the objectives of the simulation. Indeed, particular attention must be given to how these components interface between themselves.

The choice of the simulation sampling rate is critical by itself. Indeed, any HIL facility mixes physical and virtual systems and both analog and digital signals, requiring setting a certain sampling frequency for handling data. Interplanetary transfers happen on large time scales; however, the presence of an accelerating framework, the long duration of the simulations, and the requirement of wireless connections to interface with the FlatSat subsystems call for strict requirements on the accuracy of time sampling, ultimately requiring soft real-time systems to guarantee the fidelity of the simulation.

5 Expected Outcomes

As said, the success of the EXTREMA project is represented by the realization and validation of the EXTREMA Simulation Hub. Currently, there are no analogs that simulate entire deep-space missions. It will be a valuable asset to conduct research and experiments in the field of deep-space astrodynamics and will act as a research cluster in which interested researchers could test systems for small probes, opening new ways to perform complementary research and test alternative scenarios.

5.1 Case Studies

The project itself will exploit the ESH to analyze two case studies, easily relatable to existing concepts for interplanetary missions:

- (a) **Mission to an asteroid.** An interplanetary transfer toward an asteroid in the inner solar system is simulated. The target object will be placed at around 1.2 AU from the Sun. At the initial time, the spacecraft will be assigned position and velocity corresponding to the Sun–Earth Lagrange point L_2 . A thrust level of 2 mN will be selected. The case study will mimic the M-ARGO mission concept, which successfully completed Phase A [94].
- (b) **Mission to Mars.** A stand-alone CubeSat mission to Mars will be simulated, moving the target to 1.5 AU from the Sun. The spacecraft will depart from an Earth orbit and has to achieve ballistic capture. The level of thrust will vary according to the distance from the Sun. This case study will reproduce the MARIO mission concept proposed in [95].

5.2 Potential Impact

EXTREMA is an ambitious project located at the fringe of current research in astrodynamics. It addresses an emerging problem in space engineering: to let future generations of spacecraft be independent of human interaction. In particular, it focuses on deep-space CubeSats. Until now, the approach to deep-space missions has been overly cautious due to high costs to sustain to carry on a space mission. Despite the tremendous benefits brought by CubeSat technology, operations still represent an obstacle to the flourishing growth of deep space. The success of EXTREMA would facilitate access to deep space for a multitude of small institutions not backed by big budgets. An increased number of small interplanetary missions will improve our knowledge of the physics of the Solar System and will favor a comprehensive exploration of diverse, yet unknown, minor bodies.

Moreover, another consideration is to be made. By focusing on CubeSats, characterized by skeletal budgets and subsystems with mediocre performances, the success of EXTREMA would allow a seamless technological transfer to bigger, better-performing spacecraft. This means that the project will impact also large interplanetary probes. By definition, the latter have more generous budgets and can therefore retain a much better orbit control compared to CubeSats.

EXTREMA aims to fill the gap between interplanetary CubeSats and autonomous interplanetary CubeSats, as shown in Fig. 10. Moreover, as bigger spacecraft have also access to better, more diverse payloads, it could be the key to paving the way to a new era of space exploitation, enabling applications not feasible under the current paradigm.

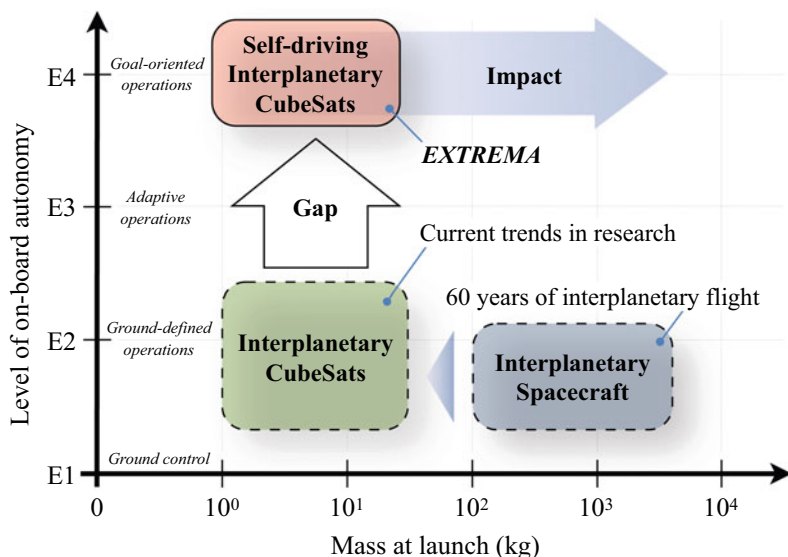


Fig. 10 Qualitative overview of the potential impact of EXTREMA

6 Conclusions

The challenge set in the EXTREMA project is ambitious. The objective to free interplanetary spacecraft from ground supervision emerges from the realization that the current deep-space GNC paradigm will be unsustainable in the near future.

The tasks the project must face are multiple and stem from different sub-fields of space engineering. By targeting CubeSats, the project will make sure that the autonomous capabilities developed for navigation and guidance will be attainable by any kind of spacecraft. Given the complexity of its objectives, EXTREMA should be seen as a high-risk/high-gain project, which outcomes can potentially be of major prominence for the future of space exploration and exploitation.

Acknowledgments This project has received funding from the European Research Council (ERC) under the European Union's Horizon 2020 research and innovation programme (grant agreement No. 864697).

References

1. Walker, R., Binns, D., Bramanti, C., Casasco, M., Concari, P., Izzo, D., Feili, D., Fernandez, P., Fernandez, J.G., Hager, P., Koschny, D., Pesquita, V., Wallace, N., Carnelli, I., Khan, M., Scoubeau, M., Taubert, D.: Deep-space CubeSats: thinking inside the box. *Astronomy & Geophysics* **59**(5), 5.24–5.30 (2018). <https://doi.org/10.1093/astrogeo/aty232>

2. Asmar, S.W., Matousek, S.: Mars Cube One (MarCO) shifting the paradigm in relay deep space operation. In: 14th International Conference on Space Operations, p. 2483 (2016). <https://doi.org/10.2514/6.2016-2483>
3. Boutonnet, A., Varga, G.: JUICE equinox Jupiter tour: The challenge of long eclipses. *Advances in the Astronautical Sciences* **168** (2019)
4. Conway, B.A.: A Survey of Methods Available for the Numerical Optimization of Continuous Dynamic Systems. *Journal of Optimization Theory and Applications* **152**(2), 271–306 (2012). <https://doi.org/10.1007/s10957-011-9918-z>
5. Renk, F., Hechler, M., Messerschmid, E.: Exploration missions in the Sun–Earth–Moon system: A detailed view on selected transfer problems. *Acta Astronautica* **67**(1), 82–96 (2010). <https://doi.org/10.1016/j.actaastro.2009.10.023>
6. Ozimek, M.T., Howell, K.C.: Low-Thrust Transfers in the Earth-Moon System, Including Applications to Libration Point Orbits. *Journal of Guidance, Control, and Dynamics* **33**(2), 533–549 (2010). <https://doi.org/10.2514/1.43179>
7. Epenoy, R.: Fuel Optimization for Continuous-Thrust Orbital Rendezvous with Collision Avoidance Constraint. *Journal of Guidance, Control, and Dynamics* **34**(2), 493–503 (2011). <https://doi.org/10.2514/1.50996>
8. Shan, J., Ren, Y.: Low-thrust trajectory design with constrained particle swarm optimization. *Aerospace Science and Technology* **36**, 114–124 (2014). <https://doi.org/10.1016/j.ast.2014.04.004>
9. Olds, A.D., Kluever, C.A., Cupples, M.L.: Interplanetary Mission Design Using Differential Evolution. *Journal of Spacecraft and Rockets* **44**(5), 1060–1070 (2007). <https://doi.org/10.2514/1.27242>
10. Haberkorn, T., Martinon, P., Gergaud, J.: Low Thrust Minimum-Fuel Orbital Transfer: A Homotopic Approach. *Journal of Guidance, Control, and Dynamics* **27**(6), 1046–1060 (2004). <https://doi.org/10.2514/1.4022>
11. Liu, H., Tongue, B.H.: Indirect Spacecraft Trajectory Optimization Using Modified Equinoctial Elements. *Journal of Guidance, Control, and Dynamics* **33**(2), 619–623 (2010). <https://doi.org/10.2514/1.45498>
12. Guo, C., Zhang, J., Luo, Y., Yang, L.: Phase-matching homotopic method for indirect optimization of long-duration low-thrust trajectories. *Advances in Space Research* **62**(3), 568–579 (2018). <https://doi.org/10.1016/j.asr.2018.05.007>
13. Taheri, E., Kolmanovsky, I., Atkins, E.: Enhanced Smoothing Technique for Indirect Optimization of Minimum-Fuel Low-Thrust Trajectories. *Journal of Guidance, Control, and Dynamics* **39**(11), 2500–2511 (2016). <https://doi.org/10.2514/1.G000379>
14. Guo, T., Jiang, F., Li, J.: Homotopic approach and pseudospectral method applied jointly to low thrust trajectory optimization. *Acta Astronautica* **71**, 38–50 (2012). <https://doi.org/10.1016/j.actaastro.2011.08.008>
15. Taheri, E., Li, N.I., Kolmanovsky, I.: Co-state initialization for the minimum-time low-thrust trajectory optimization. *Advances in Space Research* **59**(9), 2360–2373 (2017). <https://doi.org/10.1016/j.asr.2017.02.010>
16. Märten, M., Izzo, D.: The Asynchronous Island Model and NSGA-II: Study of a New Migration Operator and Its Performance. In: Proceedings of the 15th Annual Conference on Genetic and Evolutionary Computation, GECCO '13, p. 1173–1180. Association for Computing Machinery, New York, NY, USA (2013). <https://doi.org/10.1145/2463372.2463516>
17. Yao, W., Luo, J., Macdonald, M., Wang, M., Ma, W.: Improved Differential Evolution Algorithm and Its Applications to Orbit Design. *Journal of Guidance, Control, and Dynamics* **41**(4), 936–943 (2018). <https://doi.org/10.2514/1.G003214>
18. Toppo, F., Zhang, C.: Survey of Direct Transcription for Low-Thrust Space Trajectory Optimization with Applications. *Abstract and Applied Analysis* pp. 1–15 (2014). <https://doi.org/10.1155/2014/851720>
19. Biegler, L., Zavala, V.: Large-scale nonlinear programming using IPOPT: An integrating framework for enterprise-wide dynamic optimization. *Computers & Chemical Engineering* **33**(3), 575–582 (2009). <https://doi.org/10.1016/j.compchemeng.2008.08.006>. Selected Papers

- from the 17th European Symposium on Computer Aided Process Engineering held in Bucharest, Romania, May 2007
20. Darby, C.L., Hager, W.W., Rao, A.V.: An hp-adaptive pseudospectral method for solving optimal control problems. *Optimal Control Applications and Methods* **32**(4), 476–502 (2011). <https://doi.org/10.1002/oca.957>
 21. Patterson, M.A., Hager, W.W., Rao, A.V.: A ph mesh refinement method for optimal control. *Optimal Control Applications and Methods* **36**(4), 398–421 (2015). <https://doi.org/10.1002/oca.2114>
 22. Wang, Z., Grant, M.J.: Minimum-Fuel Low-Thrust Transfers for Spacecraft: A Convex Approach. *IEEE Transactions on Aerospace and Electronic Systems* **54**(5), 2274–2290 (2018). <https://doi.org/10.1109/TAES.2018.2812558>
 23. Cheng, X., Li, H., Zhang, R.: Autonomous trajectory planning for space vehicles with a Newton–Kantorovich/convex programming approach. *Nonlinear Dynamics* **89**(5), 2795–2814 (2017). <https://doi.org/10.1007/s11071-017-3626-7>
 24. Lantoine, G., Russell, R.P.: A Hybrid Differential Dynamic Programming Algorithm for Constrained Optimal Control Problems. Part 1: Theory. *Journal of Optimization Theory and Applications* **154**, 382–417 (2012). <https://doi.org/10.1007/s10957-012-0039-0>
 25. Aziz, J.D., Parker, J.S., Scheeres, D.J., Englander, J.A.: Low-Thrust Many-Revolution Trajectory Optimization via Differential Dynamic Programming and a Sundman Transformation. *The Journal of the Astronautical Sciences* **65**, 205–228 (2018). <https://doi.org/10.1007/s40295-017-0122-8>
 26. Varga, G.I., Pérez, J.M.S.: Many-revolution low-thrust orbit transfer computation using equinoctial Q-law including J2 and eclipse effects. *Advances in the Astronautical Sciences* **156**, 2463–2481 (2016)
 27. Dalin, Y., Bo, X., Youtao, G.: Optimal strategy for low-thrust spiral trajectories using Lyapunov-based guidance. *Advances in Space Research* **56**(5), 865–878 (2015). <https://doi.org/10.1016/j.asr.2015.05.030>
 28. Lee, S., von Ailmen, P., Fink, W., Petropoulos, A., Terrile, R.: Design and optimization of low-thrust orbit transfers. In: 2005 IEEE Aerospace Conference, pp. 855–869 (2005). <https://doi.org/10.1109/AERO.2005.1559377>
 29. Izzo, D., Sprague, C.I., Taylor, D.V.: Machine Learning and Evolutionary Techniques in Interplanetary Trajectory Design. In: G. Fasano, J.D. Pintér (eds.) *Modeling and Optimization in Space Engineering : State of the Art and New Challenges*, pp. 191–210. Springer International Publishing, Cham (2019). https://doi.org/10.1007/978-3-030-10501-3_8
 30. Izzo, D., Taylor, D., Vasileiou, T.: On the stability analysis of optimal state feedbacks as represented by deep neural models. *CoRR* **abs/1812.02532** (2018)
 31. Furfaro, R., Bloise, I., Orlandelli, M., Di Lizia, P., Topputo, F., Linares, R.: A recurrent deep architecture for quasi-optimal feedback guidance in planetary landing. *Advances in the Astronautical Sciences* **170**, 151–174 (2020)
 32. Thornton, C.L., Border, J.S.: *Radiometric tracking techniques for deep-space navigation*. John Wiley & Sons (2003). <https://doi.org/10.1002/0471728454.fmatter>
 33. Cheng, Y., Miller, J.: Autonomous landmark based spacecraft navigation system. In: 2003 AAS/AIAA Astrodynamics Specialist Conference, vol. 114, pp. 1769–1783 (2003)
 34. Canny, J.: A Computational Approach to Edge Detection. *IEEE Transactions on Pattern Analysis and Machine Intelligence* **PAMI-8**(6), 679–698 (1986). <https://doi.org/10.1109/TPAMI.1986.4767851>
 35. Prewitt, J.M.: Object enhancement and extraction. In: B. Lipkin, A. Rosenfeld (eds.) *Picture processing and Psychopictorics*, pp. 75–149. Academic Press New York (1970)
 36. Cheng, Y., Johnson, A.E., Matthies, L.H., Olson, C.F.: Optical landmark detection for spacecraft navigation. *Advances in the Astronautical Sciences* **114**, 1785–1803 (2003)
 37. Mourikis, A.I., Trawny, N., Roumeliotis, S.I., Johnson, A.E., Ansar, A., Matthies, L.: Vision-Aided Inertial Navigation for Spacecraft Entry, Descent, and Landing. *IEEE Transactions on Robotics* **25**(2), 264–280 (2009). <https://doi.org/10.1109/TRO.2009.2012342>

38. Christian, J.A.: Accurate Planetary Limb Localization for Image-Based Spacecraft Navigation. *Journal of Spacecraft and Rockets* **54**(3), 708–730 (2017). <https://doi.org/10.2514/1.A33692>
39. Mortari, D., D’Souza, C.N., Zanetti, R.: Image Processing of Illuminated Ellipsoid. *Journal of Spacecraft and Rockets* **53**(3), 448–456 (2016). <https://doi.org/10.2514/1.A33342>
40. Christian, J.A.: Optical Navigation Using Planet’s Centroid and Apparent Diameter in Image. *Journal of Guidance, Control, and Dynamics* **38**(2), 192–204 (2015). <https://doi.org/10.2514/1.G000872>
41. Christian, J.A., Robinson, S.B.: Noniterative Horizon-Based Optical Navigation by Cholesky Factorization. *Journal of Guidance, Control, and Dynamics* **39**(12), 2757–2765 (2016). <https://doi.org/10.2514/1.G000539>
42. Rufino, G., Accardo, D.: Enhancement of the centroiding algorithm for star tracker measure refinement. *Acta Astronautica* **53**(2), 135–147 (2003). [https://doi.org/10.1016/S0094-5765\(02\)00199-6](https://doi.org/10.1016/S0094-5765(02)00199-6)
43. Mortari, D., Conway, D.: Single-point position estimation in interplanetary trajectories using star trackers. *Celestial Mechanics and Dynamical Astronomy* **128**, 115–130 (2017). <https://doi.org/10.1007/s10569-016-9738-4>
44. Raymond Karimi, R., Mortari, D.: Interplanetary Autonomous Navigation Using Visible Planets. *Journal of Guidance, Control, and Dynamics* **38**(6), 1151–1156 (2015). <https://doi.org/10.2514/1.G000575>
45. Kalman, R.E.: A New Approach to Linear Filtering and Prediction Problems. *Journal of Basic Engineering* **82**(1), 35–45 (1960). <https://doi.org/10.1115/1.3662552>
46. Bryson, A.E., Ho, Y.C.: *Applied Optimal Control*. Taylor & Francis (1975). <https://doi.org/10.1080/00401706.1979.10489803>
47. Kugelmann, B., Pesch, H.J.: New general guidance method in constrained optimal control, part I: Numerical method. *Journal of Optimization Theory and Applications* **67**, 421–435 (1990). <https://doi.org/10.1007/BF00939642>
48. Chen, Z., Tang, S.: Neighboring optimal control for open-time multiburn orbital transfers. *Aerospace Science and Technology* **74**, 37–45 (2018). <https://doi.org/10.1016/j.ast.2018.01.003>
49. Eren, U., Prach, A., Koçer, B.B., Raković, S.V., Kayacan, E., Açıkmüşe, B.: Model Predictive Control in Aerospace Systems: Current State and Opportunities. *Journal of Guidance, Control, and Dynamics* **40**(7), 1541–1566 (2017). <https://doi.org/10.2514/1.G002507>
50. Wang, Y., Boyd, S.: Fast Model Predictive Control Using Online Optimization. *IEEE Transactions on Control Systems Technology* **18**(2), 267–278 (2010). <https://doi.org/10.1109/TCST.2009.2017934>
51. Würth, L., Hannemann, R., Marquardt, W.: Neighboring-extremal updates for nonlinear model-predictive control and dynamic real-time optimization. *Journal of Process Control* **19**(8), 1277–1288 (2009). <https://doi.org/10.1016/j.jprocont.2009.02.001>. Special Section on Hybrid Systems: Modeling, Simulation and Optimization
52. Sánchez-Sánchez, C., Izzo, D., Hennes, D.: Learning the optimal state-feedback using deep networks. In: 2016 IEEE Symposium Series on Computational Intelligence (SSCI), pp. 1–8 (2016). <https://doi.org/10.1109/SSCI.2016.7850105>
53. Heydari, A., Balakrishnan, S.N.: Adaptive Critic-Based Solution to an Orbital Rendezvous Problem. *Journal of Guidance, Control, and Dynamics* **37**(1), 344–350 (2014). <https://doi.org/10.2514/1.60553>
54. Gaudet, B., Linares, R., Furfaro, R.: Deep reinforcement learning for six degree-of-freedom planetary powered descent and landing. arXiv preprint arXiv:1810.08719 (2018). <https://doi.org/10.1016/j.asr.2019.12.030>
55. Belbruno, E.: Lunar capture orbits, a method of constructing Earth Moon trajectories and the lunar GAS mission. In: 19th International Electric Propulsion Conference. American Institute of Aeronautics and Astronautics (1987). <https://doi.org/10.2514/6.1987-1054>
56. Belbruno, E.A., Miller, J.K.: Sun-perturbed Earth-to-moon transfers with ballistic capture. *Journal of Guidance, Control, and Dynamics* **16**(4), 770–775 (1993). <https://doi.org/10.2514/3.21079>

57. Topputo, F., Belbruno, E.: Computation of weak stability boundaries: Sun–Jupiter system. *Celestial Mechanics and Dynamical Astronomy* **105**(1–3), 3 (2009). <https://doi.org/10.1007/s10569-009-9222-5>
58. Hyeraci, N., Topputo, F.: Method to design ballistic capture in the elliptic restricted three-body problem. *Journal of guidance, control, and dynamics* **33**(6), 1814–1823 (2010). <https://doi.org/10.2514/1.49263>
59. Luo, Z.F., Topputo, F.: Analysis of ballistic capture in Sun–planet models. *Advances in Space Research* **56**(6), 1030–1041 (2015). <https://doi.org/10.1016/j.asr.2015.05.042>
60. Topputo, F., Belbruno, E.: Earth–Mars transfers with ballistic capture. *Celestial Mechanics and Dynamical Astronomy* **121**(4), 329–346 (2015). <https://doi.org/10.1007/s10569-015-9605-8>
61. Brunini, A.: On the satellite capture problem. *Celestial Mechanics and Dynamical Astronomy* **64**(1), 79–92 (1996). https://doi.org/10.1007/978-94-009-0307-4_7
62. Neto, E., Winter, O.C.: Time analysis for temporary gravitational capture: satellites of Uranus. *The Astronomical Journal* **122**(1), 440 (2001). <https://doi.org/10.1086/321101>
63. Granvik, M., Vaubailon, J., Jedicke, R.: The population of natural Earth satellites. *Icarus* **218**(1), 262–277 (2012). <https://doi.org/10.1016/j.icarus.2011.12.003>
64. Sharma, S., Ventura, J., D’Amico, S.: Robust Model-Based Monocular Pose Initialization for Noncooperative Spacecraft Rendezvous. *Journal of Spacecraft and Rockets* **55**(6), 1414–1429 (2018). <https://doi.org/10.2514/1.a34124>
65. Comellini, A., Mavé, F., Dubanchet, V., Casu, D., Zenou, E., Espinosa, C.: Robust Navigation Solution for Vision-Based Autonomous Rendezvous. In: 2021 IEEE Aerospace Conference (50100), pp. 1–14. IEEE (2021). <https://doi.org/10.1109/aero50100.2021.9438241>
66. Panicucci, P.: Autonomous Vision-Based Navigation and Shape Reconstruction of an Unknown Asteroid during Approach Phase. Ph.D. thesis, Aeronautics–Astronautics Doctoral School (ED AA) (2021)
67. Bercovici, B., McMahan, J.W.: Robust autonomous small-body shape reconstruction and relative navigation using range images. *Journal of Guidance, Control, and Dynamics* **42**(7), 1473–1488 (2019). <https://doi.org/10.2514/1.g003898>
68. Mortari, D.: Second Estimator of the Optimal Quaternion. *Journal of Guidance, Control, and Dynamics* **23**(5), 885–888 (2000). <https://doi.org/10.2514/2.4618>
69. Andreis, E., Panicucci, P., Franzese, V., Topputo, F.: A Robust Image Processing Pipeline for Planets Line-of-Sight Extraction for Deep-Space Autonomous CubeSats Navigation. In: 44th Annual AAS Guidance, Navigation and Control (GN&C) Conference (2022)
70. Franzese, V., Topputo, F.: Optimal Beacons Selection for Deep-Space Optical Navigation. *The Journal of the Astronautical Sciences* **67**(4), 1775–1792 (2020). <https://doi.org/10.1007/s40295-020-00242-z>
71. Franzese, V., Topputo, F., Ankersen, F., Walker, R.: Deep-Space Optical Navigation for M-ARGO Mission. *The Journal of the Astronautical Sciences* **68**, 1034–1055 (2021). <https://doi.org/10.1007/s40295-021-00286-9>
72. Bella, S., Andreis, E., Franzese, V., Panicucci, P., Topputo, F.: Line-of-sight extraction algorithm for deep-space autonomous navigation. In: 2021 AAS/AIAA Astrodynamics Specialist Conference, pp. 1–18 (2021)
73. Andreis, E., Franzese, V., Topputo, F.: An Overview of Autonomous Optical Navigation for Deep-Space CubeSats. In: 72nd International Astronautical Congress (2021)
74. Hofmann, C., Topputo, F.: Rapid Low-Thrust Trajectory Optimization in Deep Space Based On Convex Programming. *Journal of Guidance, Control, and Dynamics* **44**(7), 1379–1388 (2021). <https://doi.org/10.2514/1.G005839>
75. Boyd, S., Vandenberghe, L.: *Convex Optimization*. Cambridge University Press (2004). <https://doi.org/10.1017/cbo9780511804441.005>
76. Liu, X., Lu, P., Pan, B.: Survey of convex optimization for aerospace applications. *Astrodynamics* **1**(1), 23–40 (2017). <https://doi.org/10.1007/s42064-017-0003-8>
77. Mao, Y., Szmuk, M., Xu, X., Açıkmeşe, B.: Successive Convexification: A Superlinearly Convergent Algorithm for Non-convex Optimal Control Problems (Preprint, submitted Feb. 2019). <https://arxiv.org/abs/1804.06539>

78. Merisio, G., Topputo, F.: Characterization of ballistic capture corridors aiming at autonomous ballistic capture at Mars. In: 2021 AIAA/AAS Astrodynamics Specialist Conference, pp. 1–21 (2021)
79. Aguiar, G., Topputo, F.: A Technique for Designing Earth-Mars Low-Thrust Transfers Culminating in Ballistic Capture. In: 7th International Conference on Astrodynamics Tools and Techniques (ICATT), pp. 1–8 (2018)
80. Topputo, F.: Fast numerical approximation of invariant manifolds in the circular restricted three-body problem. *Communications in Nonlinear Science and Numerical Simulation* **32**, 89–98 (2016). <https://doi.org/10.1016/j.cnsns.2015.08.004>
81. Bayındırlı, C., Akansu, Y.E., Salman, M.S.: The determination of aerodynamic drag coefficient of truck and trailer model by wind tunnel tests. *International Journal of Automotive Engineering and Technologies* **5**(2), 53–60 (2016). <https://doi.org/10.18245/ijaet.11754>
82. Glicksman, L., Hyre, M., Farrell, P.: Dynamic similarity in fluidization. *International Journal of Multiphase Flow* **20**, 331–386 (1994). [https://doi.org/10.1016/0301-9322\(94\)90077-9](https://doi.org/10.1016/0301-9322(94)90077-9)
83. Meliopoulos, A.S., Cokkinides, G.J., Mohagheghi, S., Dam, Q.B., Alaileh, R.H., Stefopoulos, G.K.: A laboratory setup of a power system scaled model for testing and validation of EMS applications. In: 2009 IEEE Bucharest PowerTech, pp. 1–8. IEEE (2009). <https://doi.org/10.1109/ptc.2009.5282224>
84. Heller, V.: Scale effects in physical hydraulic engineering models. *Journal of Hydraulic Research* **49**(3), 293–306 (2011). <https://doi.org/10.1080/00221686.2011.578914>
85. Polk, J.E., Pancotti, A., Haag, T., King, S., Walker, M., Blakely, J., Ziemer, J.: Recommended Practice for Thrust Measurement in Electric Propulsion Testing. *Journal of Propulsion and Power* **33**(3), 539–555 (2017). <https://doi.org/10.2514/1.B35564>
86. Polzin, K.A., Markusic, T.E., Stanojev, B.J., Dehoyos, A., Spaun, B.: Thrust stand for electric propulsion performance evaluation. *Review of Scientific Instruments* **77**(10), 105108 (2006). <https://doi.org/10.2514/6.2004-3441>
87. York, R.: Benchmarking in context: Dhrystone. ARM, March (2002)
88. Weicker, R.P.: Dhrystone: a synthetic systems programming benchmark. *Communications of the ACM* **27**(10), 1013–1030 (1984)
89. Randell, B.: Whetstone ALGOL Revisited, or Confessions of a Compiler Writer. *APIC Bulletin* (1964)
90. Benninghoff, H., Rems, F., Risse, E.A., Mietner, C.: European proximity operations simulator 2.0 (EPOS)-a robotic-based rendezvous and docking simulator. *Journal of large-scale research facilities JLSRF* (2017)
91. Schwartz, J.L., Peck, M.A., Hall, C.D.: Historical review of air-bearing spacecraft simulators. *Journal of Guidance, Control, and Dynamics* **26**(4), 513–522 (2003). <https://doi.org/10.2514/1.1035>
92. Arnold, M., Burgermeister, B., Eichberger, A.: Linearly implicit time integration methods in real-time applications: DAEs and stiff ODEs. *Multibody System Dynamics* **17**(2), 99–117 (2007). <https://doi.org/10.1007/s11044-007-9036-8>
93. Kennedy, C.A., Carpenter, M.H.: Diagonally Implicit Runge-Kutta methods for ordinary differential equations. A review. Tech. rep., NASA (2016)
94. Walker, R., Koschny, D., Bramanti, C., Carnelli, I., Team, E.: Miniaturised Asteroid Remote Geophysical Observer (M-ARGO): a stand-alone deep space CubeSat system for low-cost science and exploration missions. In: 6th Interplanetary CubeSat Workshop, Cambridge, UK, vol. 30 (2017)
95. Mani, K.V., Casado, A.S., Franzese, V., Cervone, A., Topputo, F.: Systems Design of MARIO: Stand-alone 16U CubeSat from Earth to Mars. In: 70th International Astronautical Congress, Washington DC, pp. 1–17 (2019)

Data Reduction for Optimizing the Attitude Control Dispatch in a Spacecraft



Christophe Durand, Giorgio Fasano, and Andrea Forestieri

1 Introduction

This work originates from the challenging problem of optimizing the attitude control dispatch of a spacecraft during its whole lifetime by an ad hoc layout of the thrusters (as well as their appropriate utilization on-board). The ultimate scope consists in minimizing the total propellant consumption (and/or different objective functions, if necessary). Actually, the positions and orientations of the attitude thrusters on-board a spacecraft can significantly affect the way the requested overall force and torque are exerted by means of propulsion. Although this issue does not always represent a major design concern in space engineering, it can be of utmost importance when in the presence of extremely demanding attitude control requirements. This occurs, for instance, in the upcoming Next Generation Gravity Mission (NGGM, see [4]), funded by the European Space Agency (ESA), and it is expected to characterize an increasing number of advanced missions in the near future.

While an efficient solution to the aforementioned attitude dispatch optimization problem should take into account the presence of redundant thrusters, aimed at replacing the nominal ones in case of failure (see [1]), this aspect is not considered here. The following simplified formulation (see [1]), sufficient for the task of this chapter, is outlined hereinafter to illustrate the reference context of the work

C. Durand (✉)
Eolen AS+, Malakoff, France

G. Fasano
Thales Alenia Space, Turin, Italy
e-mail: giorgio.fasano@thalesalieniaspace.com

A. Forestieri
Politecnico di Torino, Turin, Italy
e-mail: andrea.forestieri@polito.it

discussed (an extended version of the problem and a dedicated approach is discussed in depth in [6]).

To this purpose, the interval $[0, T]$, representing the timespan of interest for the relevant attitude control problem, is introduced, in addition to a spacecraft-based orthogonal reference frame (O, x, y, z) . Since the corrective actions exerted by the thrusters are executed at separate time steps, the interval $[0, T]$ may be considered as discretized, i.e., equipartitioned into a set of sub-intervals of duration Δ each, delimited by $N_I + 1$ instants $i \in \{0, 1, \dots, N_I\} = I$. At each time instant i (during the whole time sub-interval Δ), the force $F_i = F_{xi}, F_{yi}, F_{zi}$ and torque $T_i = T_{xi}, T_{yi}, T_{zi}$ represent the overall control request to be dispatched to the set A of available N_A thrusters (indexed as $r \in \{1, \dots, N_A\} = A$). The (major) constraints of the problem are thus expressed (in a compact formalism and allowing a slight abuse of notation) as follows:

$$\forall i \in I, \begin{pmatrix} v \\ p \times v_r \end{pmatrix} \begin{pmatrix} u_{1i} \\ \dots \\ u_{ri} \\ \dots \\ u_{N_A i} \end{pmatrix} = \begin{pmatrix} F_i \\ T_i \end{pmatrix} \quad (1)$$

$$\forall r \in A, \|v_r\| = 1$$

$$\forall r \in A, \forall i \in I, u_{ri} \in [\underline{U}_r, \overline{U}_r]$$

$$\forall r \in A, p_r \in D_{pr}, v \in D_{vr}$$

Here, $v = ((v_{1x}, v_{1y}, v_{1z})^T, \dots, (v_{rx}, v_{ry}, v_{rz})^T, \dots, (v_{N_A x}, v_{N_A y}, v_{N_A z})^T)$ is the sub-matrix whose columns are the column vectors associated with each $v_r = (v_{rx}, v_{ry}, v_{rz})$, the unit vector representing the orientation of thruster r .

$p \times v = ((q_{1x}, q_{1y}, q_{1z})^T, \dots, (q_{rx}, q_{ry}, q_{rz})^T, \dots, (q_{N_A x}, q_{N_A y}, q_{N_A z})^T)$ is the sub-matrix whose columns are the column vectors associated with each cross product $p_r \times v_r$, where $p_r = (p_{rx}, p_{ry}, p_{rz})$ is, for each thruster r , the application-point vector of the exerted force:

- u_{ri} is, for each thruster r , the (Euclidean) norm of the force exerted at instant i .
- \underline{U}_r and \overline{U}_r are, for each thruster, the lower and upper bounds imposed on, respectively.
- $D_{pr} \subset \mathbb{R}^3$ is the domain delimiting the admissible positions of thruster r .
- $D_{vr} \subset \mathbb{R}^3$ is the domain delimiting the admissible orientations of thruster r .

The matrix equations above are the dispatch constraints, while those involving the unit orientation vectors express normalization conditions (w.r.t. the Euclidean norm). Here, it is understood that the position and orientation of each thruster have to be kept fixed during the whole period $[0, T]$ envisaged. The following objective optimization criterion can be considered:

$$\min \sum_{\substack{r \in A \\ i \in I}} f_r(u_{ri}) \quad (2)$$

where $f_r(u_{ri})$ indicates the propellant consumption associated with each u_{ri} . As is gathered, any realistic time discretization of the whole interval (also taking into account potential reductions in virtue of occurring orbit periodicities) would inevitably make the above optimization problem intractable in practice. The basic idea of the approach proposed in this chapter consists in reducing the original set of instants to a selection of representative elements that enable a satisfactory (although not necessarily optimal) design of the thruster layout in terms of positions and orientations (see [1, 5]).

In this perspective and without any loss of generality, we can consider the (original) set of $N_I + 1$ instants (corresponding to the time discretization adopted) as associated with $N_I + 1$ “observations,” each consisting of a six-dimensional object. As a matter of fact, these observations represent the $N_I + 1$ demands (at each discretization instant) from the controller, in terms of overall forces and torques to keep the attitude of the spacecraft (constantly) in compliance with the mission requirements. More precisely, each instant i is associated with the three spatial components of force and torque, i.e., $F_i = (F_{xi}, F_{yi}, F_{zi})$ and $T_i = (T_{xi}, T_{yi}, T_{zi})$. Therefore, the $N_I + 1 \times 6$ matrix $D_{ext} = (F_x, F_y, F_z, T_x, T_y, T_z)$ represents the extended data set to be reduced.

Cluster analysis is a powerful tool that comes in handy when addressing data reduction problems, the objective of this work. The basic idea is to split matrix D_{ext} into K collections of observations, which are similar to one another. Then, one selected observation for each cluster is adopted as its representative. The resulting set of these K representatives defines the reduced mission scenario in terms of force and torque requests. This method is based on a suitable proximity measure and clustering criterion. The former can be expressed as a distance function determining the closeness between observations. The latter is a cost function (to be minimized), which is properly defined to evaluate the within-cluster cohesion and separation between clusters.

The remainder of this chapter is structured as follows. Section 2 introduces the overall clustering approach (referring the reader to the topical literature for a more in-depth discussion on the subject). Section 3 looks into the application of clustering techniques to the control dispatch optimization problem in question. Section 4 considers a case study inspired by the real-world NCGM exercise (not reported for confidentiality reasons). Section 5 concludes this chapter with some remarks and suggestions for future research activity.

2 Clustering Approach

The choice of the proximity measure and clustering criterion is strongly related to the specific problem under study, and there is no general rule to choose one over another. In the present work, *k-means* clustering (see [7]) represents the basic method and *K-medoids* (see [7]) that is actually a variant of *k-means* with its different versions has been considered as the reference framework for a comparative analysis.

2.1 Algorithmic Framework

Although *k-means* and *k-medoids* are actually quite similar clustering methods, they are overviewed separately hereinafter to pinpoint the relevant specificities.

2.1.1 K-means

K-means is arguably one of the most popular partitional clustering methods. The objective of *k-means* is to identify K clusters that minimize the sum-of-squared-error objective function. If the set of K clusters is $C = C_1, \dots, C_{K_0}$, the task of *k-means* consists in determining:

$$\underset{C}{\operatorname{argmin}} \sum_{i=1}^K \sum_{x \in C_i} \|x - \mu_i\|^2 \quad (3)$$

where x is the generic observation and μ_i is the mean (centroid) of cluster C_i . Although this problem is NP-hard (see [7]), there exists a vast variety of heuristic algorithms that converge rapidly to a local optimum. The best known is Lloyd's algorithm (see [7]), which operates as follows:

1. Select K initial-guess cluster centers (centroids). This can be done randomly or based on some initialization strategies.
2. Assign each observation to the nearest centroid.
3. Compute the averages of the observations in each cluster, which become the K new centroids.
4. Repeat Steps 2 and 3 until the objective function is no longer improved. The way it is formulated, *k-means* attempts to minimize the sum of within-cluster variances. Intuitively, the most appropriate choice as a proximity measure for Step 2 is the Euclidean distance because the sum of squared errors is the sum of squared Euclidean distances.

Initial Partition

The result of Lloyd's algorithm is highly dependent on the K initial clusters, and different initial partitions can converge to different local minima. Usually, the algorithm is run a number of times with different initial centroids in order to improve the solution. Among the possible initialization algorithms, *K-means++* (see, e.g., [2]) improves both the quality of the solution and the overall running time. *K-means++* (see, e.g., [2]) starts by randomly selecting an observation from the data matrix D_{ext} . The observation selected becomes the first centroid c_1 .

Let, at any given time, $d(x)$ be the distance from the observation x to the closest centroid we have already chosen. The next centroids, until we have a total of k , are chosen randomly from D_{ext} with probability:

$$\frac{d^2(x)}{\sum_{x \in D_{ext}} d^2(x)} \quad (4)$$

At every step, each point has a probability of being chosen as a centroid that is proportional to its squared distance from the closest centroid. The idea behind this algorithm is to choose initial centroids as far as possible from one another and to use a weighted probability to avoid picking outliers.

Convergence and Time Complexity

Lloyd's algorithm converges in a finite number of iterations. The time complexity of the algorithm and its variations is $O(nKdi)$, where n is the number of observations, d is the dimension of the observations, K is the number of clusters, and i is the number of iterations required for convergence. Most changes to the cluster partitioning typically occur during the first iterations. Because of this, i is often a small number and the algorithm can be considered to be linear in n .

2.1.2 K-medoids

The centroids of the clusters computed with the *k-means* algorithm are not necessarily observations, as the centroids are the mean of the observations within the clusters. As opposed to *k-means*, *k-medoids* methods choose actual observations as centers of the clusters (medoids). The objective of *k-medoids* is the minimization of the sum of the distances between the points belonging to the clusters and the corresponding medoids. Since the clustering criterion is based on a distance metric, any arbitrary dissimilarity measure can be used.

Partitioning Around Medoids (PAMs)

Among the *k-medoids* algorithms, Partitioning Around Medoids (see [7]) is the best known. The procedure of the PAM algorithm is summarized as follows:

A first “build” phase selects k initial medoids. This is done randomly or by using some initialization method. Then, each observation is assigned to its closest medoid. During a second “swap” phase, within each cluster, the medoids are swapped with each member of the cluster, and the algorithm checks if the corresponding sum of distances decreases. If this is the case, the point becomes the new medoid. Every point is then assigned to the closest medoid. The PAM algorithm iterates these two steps until the medoids stop changing. Alternatively, other termination criteria such as maximum iteration number can be adopted. The time complexity of the PAM algorithm per iteration is $O(K(nK)^2)$. Although this complexity can be reduced to $O(n^2)$ with some variations, for a non-exiguous number of observations, the needed computational time to converge becomes prohibitive.

Clustering LARge Applications (CLARA) is a variation of the PAM algorithm that aims to shorten the running time for clustering large data sets by using samples of the set. First, CLARA draws a number of samples from the set of observations and clusters them with the PAM algorithm. Subsequently, it assigns the observations from the full set to the closest medoid. The algorithm iterates the sampling and clustering until the medoids change. Typically, the sampling is performed a limited number of times in order to limit the computational effort. In practice, CLARA trades optimality for speed.

2.2 Cluster Evaluation

Different methods/algorithms will create different clusters and yield different representatives. In order to evaluate how well the representatives fit the initial data and what is the effect of a particular method/algorithm on the final partition, some sort of quantitative index is needed. The evaluation criteria are typically classified as external, internal, or relative depending on the kind of information used to evaluate the clusters (see [9]).

External criteria evaluate clusters according to pre-classified data that were not used for clustering. On the other hand, internal criteria evaluate clustering based on solely the observations contained in the initial data set. Finally, relative criteria compare the clusters with other clusters yielded by other algorithms or the same algorithm but with different parameters. That is, a relative criterion can be used to evaluate how the same algorithm performs with different values for K . A family of simple internal criteria that can be adopted to evaluate the results of clustering methods/algorithms in comparison with others is based on the sum of errors.

Another internal criterion for evaluating the goodness of the representatives is the Davies–Bouldin index (DBI, see [3]). It is defined as follows. Let us introduce, for each cluster, the quantity

$$S_i = \sqrt{\frac{1}{N_i} \sum_{x \in C_i} \|x - x_{rep_i}\|^2} \quad (5)$$

where N_i is the number of elements in cluster C_i . As defined, S_i is a measure of the within-cluster scattering. On the other hand, let us estimate the separation between clusters i and j with the quantity

$$M_{ij} = \|x_{rep_i} - x_{rep_j}\|$$

Let us now define

$$R_{ij} = \frac{S_i + S_j}{M_{ij}}$$

and

$$D_i = \max_{j \neq i} R_{ij}$$

The Davies–Bouldin index is defined as

$$DB = \frac{1}{K} \sum_{i=1}^K D_i \quad (6)$$

In accordance with Dunn’s and Silhouette criteria (see, e.g., [8]), a good clustering algorithm is expected to yield compact and well-separated clusters. This means that each of these clusters features a small variance and the means of the different clusters are sufficiently distant if compared to the within-cluster variance. Concerning, in particular, the DBI (which is a specific case of Dunn’s matrix), the lower its value is, the better the clustering scheme results.

3 A Clustering Approach Tailored to the Problem

Clustering methods find extended applications in a significant number of scientific and industrial areas, including big data analysis, computer graphics, pattern recognition, machine learning, and bioinformatics. Cluster analysis is expected to be adopted ever more frequently in space engineering as well. The overall approach outlined in Sect. 2 is applied hereinafter to the attitude control dispatch optimization problem, as stated in Sect. 1.

3.1 Data Normalization

The problem in question displays different data typologies. Actually, different dimensional units are involved, i.e., those associated with the given forces and torques, respectively. Additionally, also when the same physical quantities are concerned, different orders of magnitude may occur. For instance, the magnitudes of the longitudinal forces (along the motion direction) could prevail with respect to the others. This is the operational framework considered in this chapter. Since *k-means* minimizes the sum of squared deviations (respectively, multiplied by the cluster cardinality), clusters with the same cardinality and variance but different mean values yield the same deviation (i.e., error) contribution. Although they have the same cost with respect to the minimization criterion, they are not equivalent in terms of the relative errors (which are higher for the lower mean values). This means that in the overall partition, clusters with lower mean values may be poorly represented. As is gathered, the larger the oscillation range and the closer to zero the mean value, the more critical the corresponding quantity becomes. To overcome the abovementioned difficulties, the forces and torques can be normalized as follows:

$$\begin{aligned} F_{xi}^* &= \frac{F_{xi}}{\|F_x\|} & F_{yi}^* &= \frac{F_{yi}}{\|F_y\|} & F_{zi}^* &= \frac{F_{zi}}{\|F_z\|} & T_{xi}^* &= \frac{T_{xi}}{\|T_x\|} \\ T_{yi}^* &= \frac{T_{yi}}{\|T_y\|} & T_{zi}^* &= \frac{T_{zi}}{\|T_z\|} \end{aligned} \quad (7)$$

Here, F_{xi}^*, \dots , and T_{xi}^*, \dots are the normalized force and torque components, respectively. $\| \cdot \|$ is the Euclidean norm (in \mathbb{R}^{N_l+1}). The following observations offer an intuitive justification for the choice of the Euclidean norm. If x is the generic variable and x^* is the normalized one, the variance of x^* is $\sigma_{x^*}^2 = \sigma_x^2 / \|x\|^2$. The expression below holds

$$\sigma_x^2 = \frac{\|x\|^2}{N} - \bar{x}^2 \quad (8)$$

where \bar{x} is the mean value of x and σ^2 and N are the variance of x and the number of observations, respectively. Namely, Eq. (8) can be derived as follows:

$$\begin{aligned} \sigma_x^2 &= \frac{\sum_{i=1}^N (x_i - \bar{x})^2}{N} \\ &= \frac{\sum_{i=1}^N (x_i^2 - 2x_i\bar{x} + \bar{x}^2)}{N} \\ &= \frac{\sum_{i=1}^N x_i^2 - 2\bar{x} \sum_{i=1}^N x_i + N\bar{x}^2}{N} \end{aligned}$$

$$\begin{aligned}
&= \frac{\sum_{i=1}^N x_i^2 - 2N\bar{x}^2 + N\bar{x}^2}{N} \\
&= \frac{\sum_{i=1}^N x_i^2 - N\bar{x}^2}{N} \\
&= \frac{\|x\|^2}{N} - \bar{x}^2
\end{aligned}$$

Therefore, $\|x\|^2 = N(\sigma_x^2 + \bar{x}^2)$ and consequently $\sigma_x^2 = \sigma_x^2 / (N(\sigma_x^2 + \bar{x}^2))$, or equivalently

$$\sigma_x^2 = \frac{1}{N} \left(1 - \frac{\bar{x}^2}{\sigma_x^2 + \bar{x}^2} \right) \quad (9)$$

From Eq. (9), it can be observed that $\sigma_{x^*}^2$ varies in the range $[0, 1/N]$ (i.e., $\sigma_{x^*}^2 = 0$ when $\sigma_x^2 = 0$ and $x_2 \neq 0$, whereas $\sigma_{x^*}^2 = 1/N$ when $\bar{x}^2 = 0$ and $\sigma_x^2 \neq 0$). Additionally, for any σ_x fixed and different from zero, $\sigma_{x^*} \neq 0$. It can further be seen from the same expression that if x and y are two variables, the inequality $\sigma_{x^*}^2 > \sigma_{y^*}^2$ holds if and only if $\frac{\sigma_x^2}{\sigma_x^2} > \frac{x_2}{y_2}$. This is true, in particular, when $\sigma_x^2 = \sigma_y^2$ and $|x| < |y|$. In this case, in the minimization process carried out by *k-means* (for the same cardinality of the sets S_x and S_y), the cost associated with S_x (corresponding to the variable that has the smaller absolute mean value) is higher than that relevant to S_y (corresponding to the variable that has the larger absolute mean value). On the contrary, if no variable normalization were adopted, S_x and S_y would have exactly the same cost (and therefore the representation of S_x could be significantly biased). On the other hand, if $|x| = |y|$ (with $x, y \neq 0$) and $\sigma_x^2 > \sigma_y^2$, then again $\sigma_{x^*}^2 > \sigma_{y^*}^2$. That is, in the optimization process operated by *k-means*, given two variables with equal absolute mean values (for the same cardinality of S_x and S_y), the one with larger variance is dominant also when adopting the Euclidean normalization.

Therefore, the proposed normalization rescales the variances of the variables according to how critical they are to the attitude control dispatch problem.

3.2 Adopted Clustering Methodology

Since the *k-means* method yields a set of K centroids that generally do not belong to the set of observations, its implementation requires some adjustments to suitably define the representatives after clustering the set of observations. One way to proceed is described here below.

3.2.1 Adjusted *k*-means

The overall *k*-means method has been reshaped on the basis of the following steps:

1. Start *k*-means with *k*-means++ as an initialization method.
2. Compute the Euclidean distances from the first centroid to the whole set of observations.
3. Select the nearest observation as the first representative.
4. To choose (the general) representative *j*:
 - Compute the Euclidean distances from the centroid to the whole set of observations.
 - If the closest observation has not been already chosen as representative, select it as a representative. If it is already a representative, do not assign any other representative.

Although the above algorithm may end up with fewer representatives than the number *K* chosen initially, this outcome is deemed to occur very rarely. The approach however avoids having representatives too similar to one another. One of the major drawbacks of *k*-means is its sensitivity to outliers. Since centroids are mean values of clusters, the selected representatives are likely to be affected by observations that differ significantly from the others within the clusters. In light of this observation, the PAM algorithm would theoretically yield better representatives for the set (medoids). However, the effectiveness of its implementation will depend on the scale of the observation set. On the other hand, the implementation of the CLARA algorithm is likely to yield worse solutions than those related to *k*-means. One other solution to the outlier problem consists in applying a variant of Lloyd's algorithm to the *k*-medoids clustering, as described in Sect. 3.2.2, where the procedure is adapted to the problem object of this work.

3.2.2 Lloyd-Like Algorithm for *K*-medoid

The basic Lloyd algorithm is redefined by the following steps:

1. Select *K* initial medoids with *k*-means++.
2. Assign each observation to the closest medoid.
3. For each observation in each cluster, compute the sum of distances from the observation to every other observation in the cluster.
4. Select, for each cluster, the observation that minimizes the sum as the new medoid.
5. Assign each observation of the whole set to the closest medoid.
6. Repeat Steps 2 through 4 until no further updates occur.

The complexity of this algorithm is $O(nK)$, equivalent to that of *k*-means. The quality of the algorithm can also be improved by a PAM-like update. After Lloyd's iterations, the algorithm can select, for each cluster, the observations furthest from

and the closest to the corresponding medoid. Then, it checks if the sum of distances improves by using the selected observations as medoids. Namely, it performs a swap step limited to a small subset of observations. This variant aims to escape local minima and enhance the quality of the solution. Although the Lloyd-like *k-medoids* algorithm yields better results than CLARA, it has to be compared with the adapted *k-means* algorithm in order to draw valid conclusions.

3.2.3 Hybrid k-means–k-medoids

A further alternative consists in a hybrid algorithm, based on a joint use of *k-means* and *k-medoids*. The procedure is defined by the following steps:

1. Run the adapted *k-means* algorithm.
2. Run the Lloyd-like algorithm, using the output of the adapted *k-means* algorithm as the initial medoid instead of using *k-means++*.

Heuristically, this hybrid algorithm will refine the representatives chosen by *k-means* and locally improve the representation of the initial set.

3.3 Approach Evaluation and Practical Implementation

In accordance with the normalization for forces and torques introduced in Sect. 3.1, the clustering evaluation approach concerning the dispatch problem under study can be carried out on the basis of the specific error definition reported here below. Letting i denote the i -th row of matrix D_{ext} and j denote its j -th column, the generic normalized i -th observation is

$$o_i^* = (F_{x^*}, F_{y^*}, F_{z^*}, T_{x^*}, T_{y^*}, T_{z^*}) \quad (10)$$

Its normalized representative is

$$o_i^* = (F_{x_{rep}^*}, F_{y_{rep}^*}, F_{z_{rep}^*}, T_{x_{rep}^*}, T_{y_{rep}^*}, T_{z_{rep}^*}) \quad (11)$$

We can define the error of representation of the observation as the vector:

$$e_i = (F_{x^*} - F_{x_{rep}^*}, F_{y^*} - F_{y_{rep}^*}, F_{z^*} - F_{z_{rep}^*}, T_{x^*} - T_{x_{rep}^*}, T_{y^*} - T_{y_{rep}^*}, T_{z^*} - T_{z_{rep}^*}) \quad (12)$$

Using this notation, we can build a matrix E with the same size as D_{ext} where each row is the error of representation e_i of the i -th observation of matrix D_{ext} . The element e_{ij} is therefore the error of representation of the j -th component of the i -th observation. That is, for example, e_{45} is the error of representation of T_y of the fourth observation of matrix D_{ext} . We can now define some useful internal indexes. The *mean error* is given by

$$ME = \frac{1}{N} \sum_{i=1}^N \|e_i\|_2 \quad (13)$$

and it represents the average distance between each observation and its representative. The *mean squared error* is instead given by

$$MSE = \frac{1}{N} \sum_{i=1}^N \|e_i\|_2^2 \quad (14)$$

Since this index takes into account the sum of squared distances, the cost is shifted on observations with bigger errors of representation. Algorithms incrementing significantly the value of this index are therefore expected to provide subsets of observations that are poorly represented. When performing clustering evaluation, it may happen that an algorithm performs better than the others in terms of ME, yet worse in terms of MSE. This is an indication that although this algorithm is on average better than the others in representing the whole set, it performs poorly when comparing the worst represented observations. Analogous conclusions can be drawn using the *maximum error* index, which is useful to compare the worst represented observation:

$$MAX = \max_i \|e_i\|_2 \quad (15)$$

In any case, cluster evaluation should be carried out by comparing each one of the indexes. It is also strongly recommended to evaluate the DBI. By plotting *DBI* against *K*, the index is supposed to decrease monotonically until the correct number of clusters is achieved. However, the value of *K* for which this happens may not be appropriate for the problem under study, as the resulting complexity of the problem could become unacceptable. If possible, in practice, it is recommended to choose a value for *K* according to the elbow criterion. Namely, by plotting *DBI* against *K*, a good compromise between the representation error and the computational complexity is attained when the value of *K* corresponds to a sharp elbow (see Fig. 1). Assuming this happens, exceeding that number of clusters corresponds to a drop of added quality to the representation. If this does not happen, the number of *K* should be chosen according to an acceptable running time of the whole solution process.

Once *K* is assigned with a value, it is recommended to run each one of the three algorithms described above several times and choose the best representation according to the evaluation indexes. Moreover, extreme values, in terms of forces and torques, are expected to be included as representatives. That is, the observations that correspond to the maximum and minimum values of each one of the variables are considered. This way, twelve time instants are forcedly added to the representatives. Furthermore, the observations corresponding to the maximum and minimum values of F_k and T_k should be included as representatives. Thus, the total number of new representatives is sixteen. The corresponding adjustment

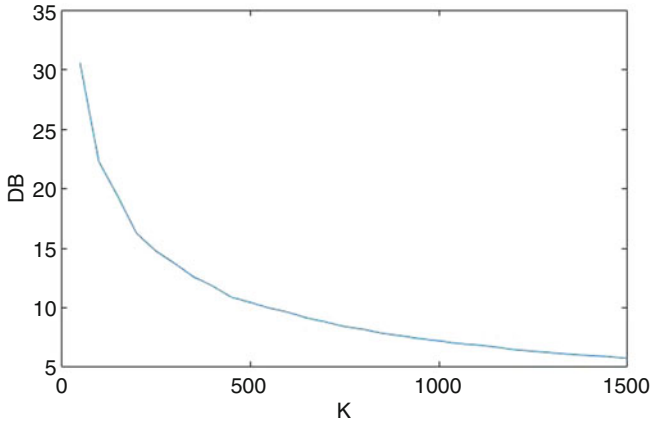


Fig. 1 *DB* index versus *K*

(involving the aforementioned sixteen elements) is recommended in order to be certain of finding solutions to the optimal control dispatch problem that can satisfy the maximum and minimum requests. The forced addition of new representatives modifies the clustering schemes. Therefore, prior to the evaluation of the internal indexes, clusters have to be redefined at the end of the procedure. This can be done by simply assigning each observation to its closest representative.

4 Case Study

4.1 Instance Reduction

The work discussed here has been prompted by the NGGM project. NGGM aims at providing an accurate description of the Earth gravitational field by utilizing two pairs of satellites in low orbit. A very precise measurement of the gravitational field is carried out by means of a laser interferometer that detects the distance variations between the satellites of each pair. To satisfy the extremely demanding measurement requirements, a very efficient attitude control must be exerted on each spacecraft. For the work here discussed, a time discretization of 150,000 samples (time intervals) is considered. A three-dimensional force and a three-dimensional torque are associated with each time interval.

The clustering approach proposed in this chapter is adopted to select a number of representative forces and torques, thus making the thruster layout optimization problem treatable. The results of the clustering approach relevant to the NGGM study are however not reported here for confidentiality reasons. A similar case study (a constructed example, still involving 150,000 samples) is considered instead to illustrate the methodology discussed.

The relevant clustering analysis consists of three steps. For each step, the algorithms Adjusted *k-means*, Lloyd-like *k-medoids*, and Hybrid are executed twenty times. The DBI is adopted to identify the best result for each algorithm. A subsequent comparative analysis is carried out to select the best algorithm. The evaluation is based on the average error, the average squared error, the vector maximum difference, and the DBI.

4.2 Applied Methodology

In the following, the results obtained are reported separately for each of the abovementioned steps.

4.2.1 First Step

The first step is based on the most complex optimization model, involving a large number of variables (including binary variables). This model is computationally very hard to solve and empirically allows a maximum value for K around 50. A quick evaluation of the DBI for increasing values of K (using all three algorithms) shows that the elbow mentioned in Sect. 3.3 corresponds to a much bigger value than 50. Therefore, the quality of the representation of this step is constrained by the computational burden of the model. The resulting representation given by the best run of each model is quite coarse (see Table 1). Figures 2 and 3 display the results given by the best performing algorithm, namely the hybrid one. Even though Lloyd-like *k-medoids* gives better results in terms of ME, the difference is not substantial and the hybrid performs better according to all other internal indexes.

4.2.2 Second Step

The second step refines the result of the first. The relevant model is simpler than that adopted in the first step since it does not include binary variables. The corresponding degrees of freedom are in fact set on the basis of the first step. In this case, the limit for K can be higher. Using the elbow method (Sect. 3.3), $K = 250$ is chosen as a reasonable compromise to significantly increase the precision of the representation

Table 1 Algorithm comparison for $K = 50$

Algorithm	ME	MSE	MAX	DBI
Adjusted <i>k-means</i>	0.0035997	$0.154313e - 04$	0.017872	28.660082
Lloyd-like <i>k-medoids</i>	0.0035569	$0.157626e - 04$	0.020397	30.591099
Hybrid	0.003579	$0.153366e - 04$	0.017043	28.576472

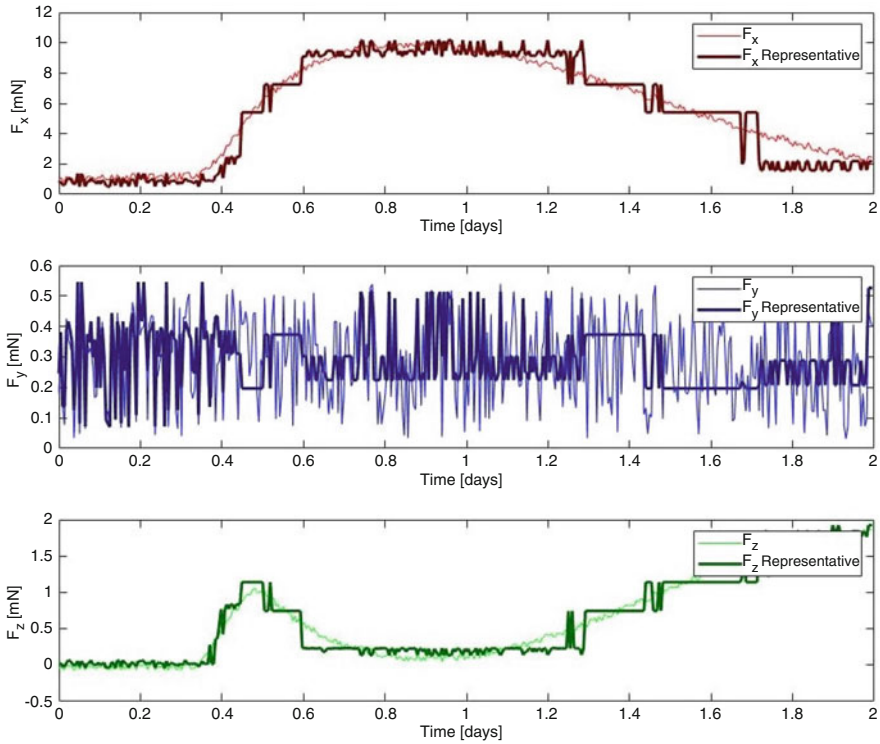


Fig. 2 Force samples and their representation for $K = 50$ (first 2 days)

(see Table 2, Figs. 4 and 5). Once again, the figures refer to the best run of the hybrid algorithm, which clearly performs better than the other two. In a real-case scenario, this algorithm would therefore be the obvious choice.

4.2.3 Third Step

The third step is aimed at assessing the previous results (Steps 1 and 2). K is allowed to reach 1000 since, according to the elbow criterion for the DBI, the actual benefits of a higher value for K would be limited. This choice is made as an acceptable compromise taking into account both the computational effort and the given memory limitations. The final results are reported in Table 3, Figs. 6 and 7. The hybrid algorithm was chosen for this final step. However, it is interesting to note that the best run of the adjusted *k-means* algorithm performs better than the best run of the hybrid in terms of maximum error. This is a clear sign that the local refinement provided by the second step of the hybrid algorithm (Sect. 3.2.3) improves the representation of the initial set in terms of ME and MSE.

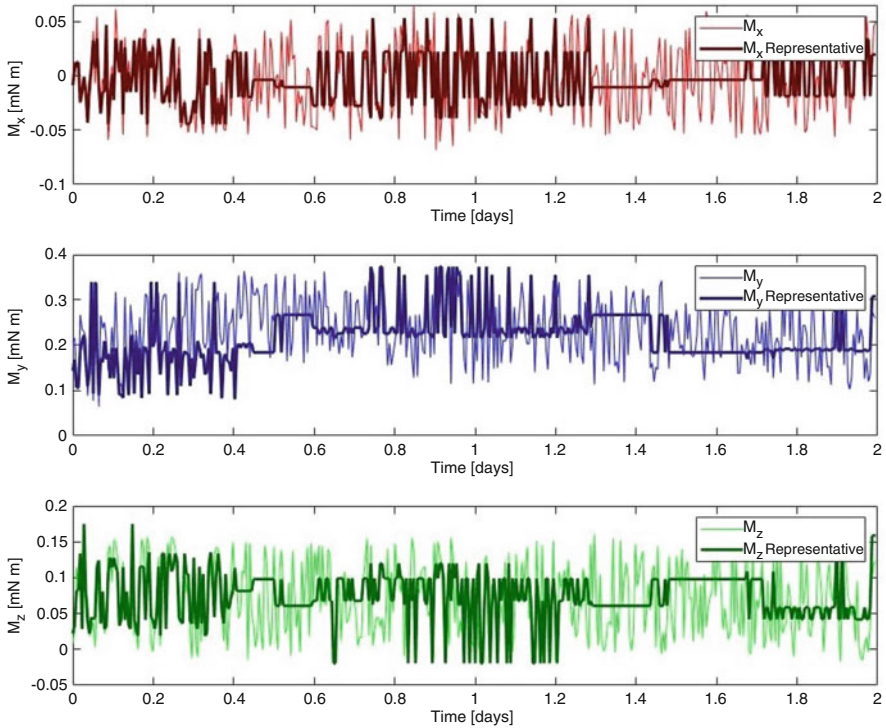


Fig. 3 Torque samples and their representation for $K = 50$ (first 2 days)

Table 2 Algorithm comparison for $K = 250$

Algorithm	ME	MSE	MAX	DBI
Adjusted <i>k-means</i>	0.0023661	$0.659904e - 05$	0.012811	13.818361
Lloyd-like <i>k-medoids</i>	0.002378	$0.709510e - 05$	0.014988	14.790639
Hybrid	0.002332	$0.641512e - 05$	0.011494	13.548339

5 Conclusive Remarks

This work originates from a very challenging optimization problem in the context of the NGGM ESA study.

This problem involves finding an appropriate layout for the attitude thrusters on board the spacecraft to minimize the propellant mass consumption. The relevant mathematical model is based on a time discretization yielding a huge set of time intervals. This chapter considers a dedicated clustering approach aimed at reducing the scale of the original problem by identifying a subset of time intervals representative of the whole discretization set.

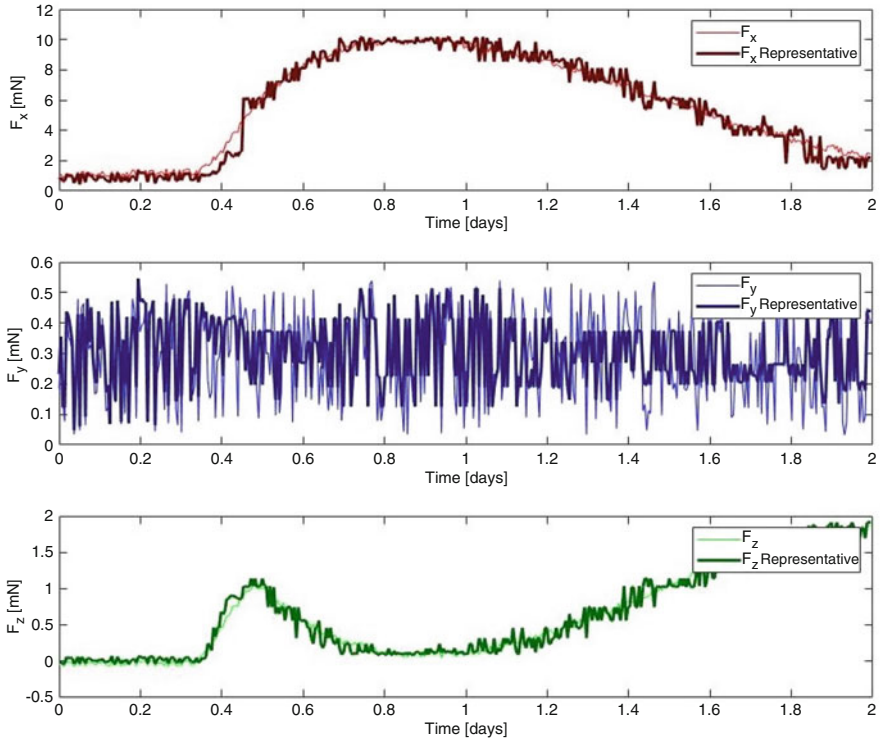


Fig. 4 Force samples and their representation for $K = 250$ (first 2 days)

The general thruster layout problem is briefly introduced first and the clustering issue, i.e., the subject of this chapter, stated. An overview of clustering algorithms is provided, focusing on the well-known *k-means* and *k-medoids* basic algorithms. The mean error, mean squared error, maximum error, and the DBI index are examined as the reference evaluation criteria.

The specific clustering problem associated with the thruster layout optimization issue is further discussed, and an ad hoc normalization is introduced for the vectors involved (forces and torques). A clustering case study similar to that relevant to NGGM (not reported here for confidentiality reasons) is investigated, providing the satisfactory results obtained simply by utilizing industry-standard computing equipment and available clustering software. The analysis carried out is tailored to the specific problem in question, with careful consideration of the efficiency of the representativeness attained.

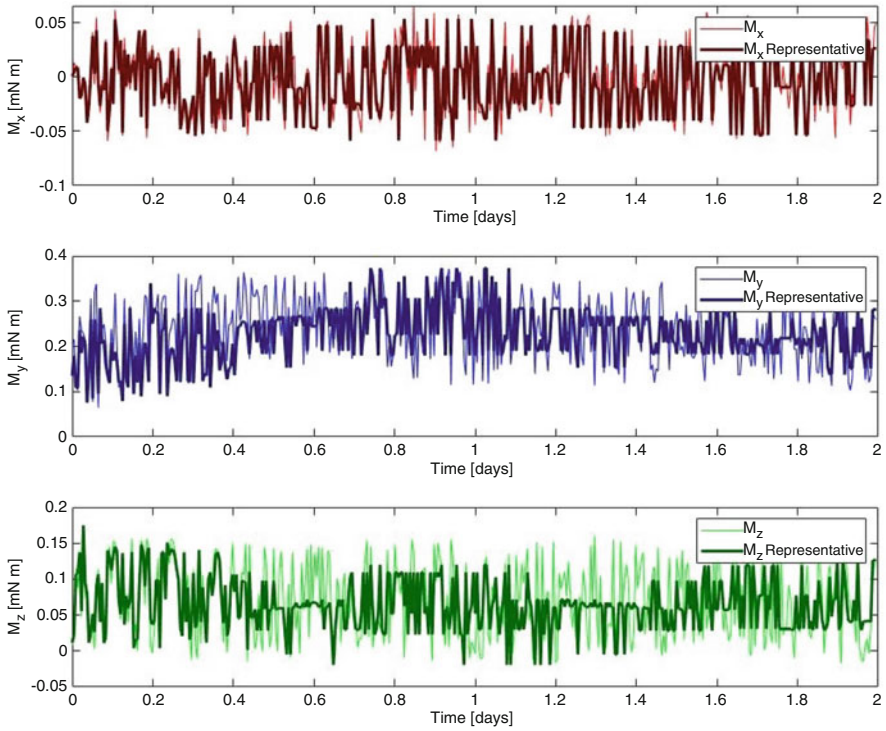


Fig. 5 Torque samples and their representation for $K = 250$ (first 2 days)

Table 3 Algorithm comparison for $K = 1000$

Algorithm	ME	MSE	MAX	DBI
Adjusted <i>k-means</i>	0.001691	$0.341172e - 05$	0.008483	7.233099
Lloyd-like <i>k-medoids</i>	0.001672	$0.351313e - 05$	0.010104	7.224523
Hybrid	0.001642	$0.321973e - 05$	0.008897	6.797483

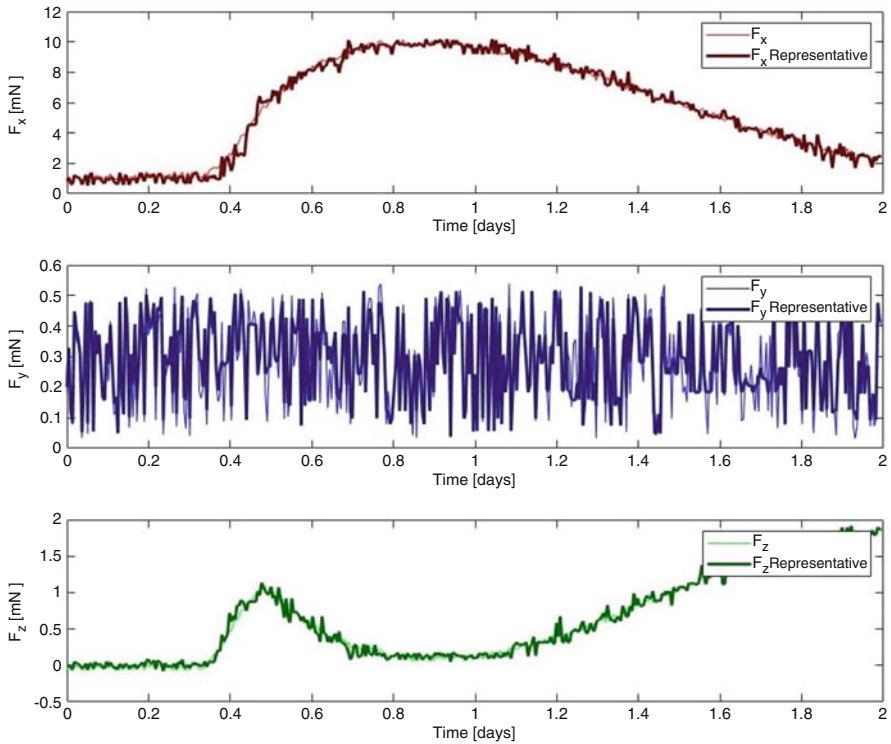


Fig. 6 Force samples and their representation for $K = 1000$ (first 2 days)

The results obtained in this work appear to confirm that the presented hybrid algorithm performs better than *k-means* and *k-medoids*. However, the results obtained refer to a specific case, and further investigation is needed to corroborate this result. Future research should therefore focus on different case studies and provide evidence for the intuitive explanation given in Sect. 3.2.3.

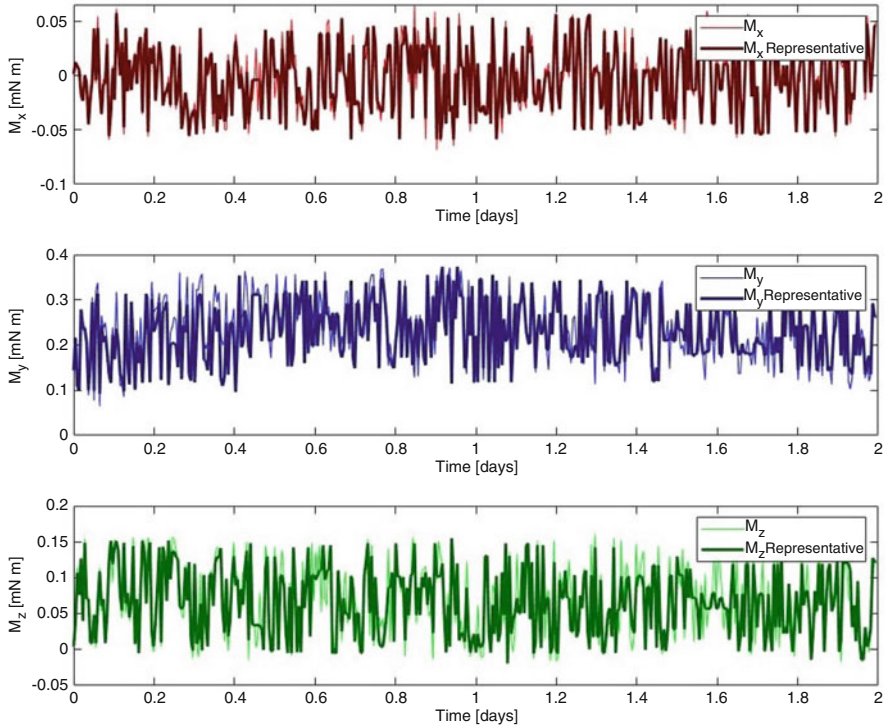


Fig. 7 Torque samples and their representation for $K = 1000$ (first 2 days)

References

1. Anselmi, A., Cesare, S., Dionisio, S., Fasano, G., Massotti, L.: Control Propellant Minimization for the Next Generation Gravity Mission pp. 1–32 (2019)
2. Arthur, D., Vassilvitskii, S.: K-Means++: The Advantages of Careful Seeding. Society for Industrial and Applied Mathematics, USA (2007)
3. Davies David L.; Bouldin, D.W.: A cluster separation measure. IEEE Transactions on Pattern Analysis and Machine Intelligence (1979)
4. Dionisio, S., Anselmi, A., Bonino, L., Cesare, S., Massotti, L., Silvestrin, P.: The next generation gravity mission challenges, consolidation of the system concepts and technological innovations (2018)
5. Durand, C.: Optimization of thrusters positions and orientations to minimize fuel consumption. Master Thesis at Politecnico di Torino (2020)
6. Fasano, G.: Dynamic System Control Dispatch: A Global Optimization Approach. Springer International Publishing, Cham (2019)
7. Lloyd, S.: Least squares quantization in PCM. IEEE Transactions on Information Theory **28**(2), 129–137 (1982)
8. Rousseeuw, P.J.: Silhouettes: a graphical aid to the interpretation and validation of cluster analysis. Computational and Applied Mathematics (1987)
9. Tan, P.N., Steinbach, M., Kumar, V.: Introduction to Data Mining, US ed edn. Addison Wesley (2005)

Second-order Sufficient Conditions of Strong Minimality with applications to Orbital Transfers



Leonardo Mazzini

1 Introduction

In optimal control problems, the first-order necessary conditions (NC) allow to identify extremals which are candidate to be optimal solutions. Then, second-order sufficient conditions should be checked to confirm the optimality. We present in this chapter the results demonstrated by the author in Ref. [1] concerning Extended Sufficiency Conditions (SC) which are applicable without Strict Legendre Conditions (SLC), without local controllability assumptions also in the frame of saturated and bang–bang control.

These conditions can be found in orbital transfers applications, where SLC are normally not verified and the thrust acceleration of the engine is bounded.

Extended Jacobi SC, using the method of the Verification Functions (VF), were introduced, to our knowledge, by V. Zeiden in a series of papers [2–4]. Our objective is to bring this approach to deal with a class of Irregular Hamiltonians that are typical in Space Trajectory optimization when the SLC are not verified. To reach this objective, we have used a class of discontinuous VFs which are presented in Ref. [1] and are solvable using a generalization of the classic Riccati Equations. It is possible to show that the extremal is always a minimum if t_0 is sufficiently close to t_f . The use of Riccati comparison theorems allows to determine the maximal interval where the extremal verifies the SC for the given class of VFs. When the SC are not verified, the extremal could still be a minimum not possessing a VF which can be resolved in terms of a solution of a Riccati Equation.

L. Mazzini (✉)

Thales alenia space Italy, Rome, Italy

e-mail: leonardo.mazzini@thalesaleniaspace.com

The classic approach to demonstrate SC is based on the non-existence of the conjugate point and rest on a wide literature whose examples are Ref. [5–7] which discuss the weak minimum problem with fixed and free time conditions. We show in this chapter that the conjugate point condition is weaker than our Extended SC. A more detailed study of the literature is presented in Ref. [1] where some modern contributions in Ref. [8, 9, 11] are evaluated with respect to the present work.

At the end of the chapter, we present applications of Theorem 1 to space trajectory optimization with numerical cases of practical interest in finite and infinite thrust optimization. The first example is based on the minimization of a low-thrust transfer with quadratic cost. It is a case taken from the literature, and we demonstrate that when the firing is too long, we lose the minimality of the extremal. The second case is a low-thrust problem with linear cost which is not tractable by classical methods, and we demonstrate that when the firing is too long we lose the Extended SC. The third case also, an impulsive transfer problem with three pulses, is not tractable by classical methods. In this case, we use a sequence of Riccati problems to extend the interval where SC can be verified.

2 The Bolza Problem and the First-order NC

The Bolza problem consists in finding an admissible pair (x, u) that minimizes the cost function:

$$J(x, u) = l(x_{t_f}, t_f) + \int_{t_0}^{t_f} \Lambda(x_t, u_t) dt$$

where t_f can be fixed or variable and (x, u) satisfies the constraints:

$$\begin{aligned} x &\in AC([t_0, t_f], \mathbb{R}^n), u \in L^\infty([t_0, t_f], U), U \subset \mathbb{R}^m \\ \dot{x}_t &= f(x_t, u_t) \\ x_{t_0} &= x_0, x_{t_f} \in E \subseteq \mathbb{R}^n, \dim(E) = d \end{aligned} \quad (1)$$

Any pair (x, u) satisfying Eq. (1) is called an admissible pair.

An admissible pair (\hat{x}, \hat{u}) realizes a strong minimum of the cost if $\exists \epsilon > 0 \mid J(\hat{x}, \hat{u}) \leq J(x, u), \forall (x, u) \mid \max_{[t_0, t_f]} |x_t - \hat{x}_t| \leq \epsilon$.¹

An admissible pair (\hat{x}, \hat{u}) realizes a weak minimum of the cost if $\exists \epsilon > 0 \mid J(\hat{x}, \hat{u}) \leq J(x, u), \forall (x, u) \mid (\max_{[t_0, t_f]} |x_t - \hat{x}_t| \leq \epsilon, \text{ess sup}_{[t_0, t_f]} |u_t - \hat{u}_t| \leq \epsilon)$.

Let us define the pre-Hamiltonian $H_P(x, p, u) = (p^T f(x, u) - \Lambda(x, u))$ and the associated Hamiltonian $H(x, p) = \sup_{u \in U} (p^T f(x, u) - \Lambda(x, u))$.

¹ The symbol $||$ will be used to mean the Euclidean Norm.

Typically, the target variety E is represented implicitly with a system of equations. Thus, $x \in E$ if and only if $\theta_i(x) = 0, i = 1, \dots, n - d$ a set of functions with linearly independent gradients. We introduce the following hypotheses **H0**.²

1. $f, \Lambda, l, \theta_i, i = 1, \dots, n - d$, are globally C^1 in all their arguments.
2. U is compact and constant in time.

With **H0**, $H_P(x, p, u) = (p^T f(x, u) - \Lambda(x, u))$ is C^1 in all its arguments.

Calling $z = (x, p)$, $F_b(z)$ the multi-valued feedback law derived from the Maximum Principle, we have (see [10])³

$$F_b(z) = \{u | H_P(z, u) = H(z)\}, \quad \partial_z H(z) = co_{u \in F_b(z)} \partial_z H_P(z, u)$$

$H(z)$ is a Lipschitz Continuous (in short *Lip*) function differentiable in z , where $F_b(z)$ is a singleton. $\partial_z H$ is the generalized gradient which extends the concept of derivative. The first-order Necessary Conditions for a minimum weak or strong—excluding the abnormal case—require the existence of a pair (\hat{x}, \hat{p}) , which we call extremal, that satisfies the following conditions:

$$\begin{aligned} \exists \hat{p} \in AC([t_0, t_f], \mathbb{R}^n), \exists v_i \in \mathbb{R}, i = 1, \dots, n - d : \\ \hat{\dot{x}} \in \partial_p H|_{(\hat{x}, \hat{p})}, \quad \hat{\dot{p}} \in -\partial_x H|_{(\hat{x}, \hat{p})} \\ \hat{x}_{t_0} = x_0, \quad \hat{x}_{t_f} \in E \subseteq \mathbb{R}^n, \quad \hat{p}_{t_f} + \partial_x g|_{\hat{x}_{t_f}} = 0 \end{aligned} \tag{2}$$

where $g(x) = l(x) + \sum_{i=1, \dots, n-d} v_i \theta_i(x)$. In the Open Time problems where t_f is not defined, we have the additional condition: $H|_{(\hat{x}_{t_f}, \hat{p}_{t_f}, t_f)} = 0$. The state and co-state dynamics are here represented as differential inclusions. When $\partial_z H$ is a singleton, the NC are written in the more usual form: $\hat{\dot{x}} = \partial_p H|_{(\hat{x}, \hat{p})}$ and $\hat{\dot{p}} = -\partial_x H|_{(\hat{x}, \hat{p})}$.

3 The Basic Assumptions on the Hamiltonian and the Extremal

We assume that the Hamiltonian is smooth in a neighborhood of the extremal, outside a finite number of surfaces where $H(z)$ is not differentiable. The feedback is piecewise continuous with jumps when the extremal crosses these surfaces of discontinuity that play the same role of the switching functions often used in the literature.

Given the extremal $\hat{z}_t = (\hat{x}_t, \hat{p}_t)$, consider a finite set of smooth hypersurfaces $S_k(z) = 0, k = 1, \dots, M$. Let $G = \cup_{k=1 \dots M} z | S_k(z) = 0$ be the union of all these hypersurfaces. The Hamiltonian $H(z) \in C^0(\mathbb{R}^{2n})$ and $H(z) \in C^3(\mathbb{R}^{2n}/G)$. Under

² Both hypotheses can be relaxed, and we introduce them in this form for simplicity.

³ We refer to the Clarke generalized gradient, see [10], which is a non-empty closed convex set; we use the same symbol to mean the generalized gradient set and the partial derivative, the ambiguity being resolved by the logical statement.

these conditions, the Hamiltonian can be represented in a neighborhood of a generic surface $S(z) = 0$ as

$$H(z) = H_0(z) + k(S(z)) S(z) \tag{3}$$

where $k(S)|_{S<0} = 0, k(S)|_{S\geq 0} = 1$, and $H_0(z)$ and $S(z)$ are two smooth functions in \mathbb{R}^{2n} whose properties will be specified hereunder.

In addition, the extremal crosses these surfaces transversally and never crosses them at the intersection of different hypersurfaces. The crossing times are finite in number.

This kind of Hamiltonians is very general for problems with saturated or bang-bang control.

Let us formalize all the hypotheses. Let $B_\rho(x)$ be the closed ball of radius ρ and center x , we will study Hamiltonians verifying, for a given extremal $\hat{z}_t = (\hat{x}_t, \hat{p}_t)$ and for some $\rho > 0$, the following hypotheses **H0/I**:

1. $(l, \theta_i, i = 1, \dots, n - d) \in C^2(\Gamma)$ where $\Gamma \in \mathbb{R}^n$ is open and $B_\rho(\hat{x}_{t_f}) \subset \Gamma$.
2. Let $N_\rho = \{(x, p, t) | t \in [t_0, t_f], (x, p) \in B_\rho(\hat{x}_t, \hat{p}_t)\}$ be a tubular neighborhood of radius ρ around the candidate extremal.
3. There is a sequence of strictly increasing times $t_{c_k}, k = 1, \dots, N_c$, with $t_0 < t_{c_1}$ and $t_{c_{N_c}} < t_f$ where the extremal makes a jump in the first derivative. Let us call $\Theta = \cup_{1, \dots, N_c} t_{c_k}$ and $\hat{z}_{t_{c_k}}$ cross points.
4. There is a finite set of connected compact smooth hypersurfaces

$$S_\rho^k = \left\{ z \in B_\rho(\hat{z}_{t_{c_k}}) \mid S_k(z) = 0 \right\}, k = 1, \dots, N_c,$$
 with $S_k \in C^3(\mathbb{R}^{2n})$, that intersects the extremal transversally only at the corresponding cross point $\hat{z}_{t_{c_k}}$; $S_k(\hat{z}_t)$ is strictly monotonic in a neighborhood of t_{c_k} and $S_k(\hat{z}_{t_{c_k}}) = 0$.
5. Each hypersurface S_ρ^k separates the tube N_ρ into two subsets $N_{\rho-}^k$, which contains the extremal arc in $[t_0, t_{c_k})$, and $N_{\rho+}^k$, which contains the extremal arc in $(t_{c_k}, t_f]$. All together the hypersurfaces decompose the tube N_ρ in $N_c + 1$ tube sections: $N_\rho^1 = N_{\rho-}^1, N_\rho^k = N_{\rho+}^{k-1} \cap N_{\rho-}^k, k = 2..N_c, N_\rho^{N_c+1} = N_{\rho+}^{N_c}$ not intersecting each other $N_{\rho-}^k \cap N_{\rho+}^{k+1} = \emptyset, k = 1, \dots, N_c$.
6. $H \in C^0(N_\rho)$, each restriction H_k in $N_{\rho-}^k$, can be smoothly continued, i.e., $H_k \in C^3(\Omega_k)$, where $\Omega_k \supset Cl(N_{\rho-}^k)$ are open subsets.
7. The Hamiltonian can be represented as $H(z) = H_0(z) + k(S)S(z)$, if $z \in \Omega_k \cap \Omega_{k+1}$, where $k(S)|_{S<0} = 0, k(S)|_{S\geq 0} = 1$. Two cases are possible: or $H_0 = H_k, S = H_{k+1} - H_k, \dot{S}_{t_c} > 0$, either $H_0 = H_{k+1}, S = H_k - H_{k+1}, \dot{S}_{t_c} < 0$.⁴
8. $F_b(z)$ is a singleton in each $N_{\rho-}^k$ and $u = F_b \in C^1(N_{\rho-}^k, U)$.

The assumptions chosen do not allow to treat some problems, like singular arcs where the extremals lay on the hypersurface for a finite interval of time or chattering

⁴ This representation structurally satisfies the Maximum Principle and is a general presentation of the **H0/I** Hamiltonians close to cross points. It is easy to verify that $H(z) = H_0(z) - k(S)S(z)$ does not agree with the Maximum Principle.

arcs, where we have an infinite number of crossings in a finite interval of time. However, they are applicable to all problems treated by the author in space trajectory optimization where a finite number of transversal crossings of these hypersurfaces are typical. In addition, they work without the controllability or the Legendre–Clebsch conditions, generating relatively easy procedures which we believe useful in many applications.

From the hypotheses **H0/I**, it follows that the second derivatives of $H(z)$ calculated along the candidate extremal are continuous functions of t in the intervals $[t_0, t_{c_1}), (t_{c_1}, t_{c_2}), \dots, (t_{c_{N_c}}, t_f]$. When the hypersurfaces of discontinuity are not present and $H \in C^2(\Omega)$, with Ω open set and $\Omega \supset Cl(N_\rho)$ and $F_b \in Lip(N_\rho, U)$, we will call the Hamiltonian Regular and the hypotheses **H0/R**.

Finally, we will call **H0/IOR** those Hamiltonians and extremals that fulfill hypotheses **H0/R** or **H0/I**.

3.1 An Example of Irregular Hamiltonian

We consider an optimization problem with a multidimensional control implementing a Hamiltonian model covering many applications and also providing a good insight on the discontinuity surfaces in the phase space.

$$\begin{aligned} \dot{x} &= f_0(x) + f_k(x)u_k \\ x &\in \mathbb{R}^n, u_k \in [-1, 1], k = 1, \dots, n_1, \dots, n_2, \\ \Lambda &= l_0(x) + \sum_{k=1, n_2} l_k(x)u_k + (1/2) \sum_{k=n_1+1, n_2} L_k u_k^2 \\ L_k &\in \mathbb{R}_+ \end{aligned} \tag{4}$$

We can easily find the Hamiltonian and the controls using the Maximum Principle, and the controls will be

$$\begin{aligned} u_k &= \text{sign}(p^T f_k(x) - l_k(x)), k = 1 \dots n_1 \\ u_k &= \text{sat}((p^T f_k(x) - l_k(x))/L_k), k = n_1 + 1 \dots n_2 \\ \text{sat}(y)|_{|y|>1} &= \text{sign}(y), \text{sat}(y)|_{|y|\leq 1} = y \\ \text{sign}(y)|_{y>0} &= 1, \text{sign}(y)|_{y\leq 0} = -1 \end{aligned} \tag{5}$$

Consequently, the Hamiltonian is

$$\begin{aligned} H(x, p) &= y_0 + \sum_{k=1, n_1} |y_k| + \sum_{k=n_1+1, n_2} (L_k y_k \text{sat}(y_k) - (L_k/2) \text{sat}(y_k)^2) \\ y_0 &= p^T f_0(x) - l_0(x) \\ y_k &= p^T f_k(x) - l_k(x), k = 1..n_1 \\ y_k &= (p^T f_k(x) - l_k(x))/L_k, k = n_1 + 1..n_2 \end{aligned} \tag{6}$$

From this expression, we see that we have two kinds of singular hypersurfaces.

On the surfaces $y_k = 0$, $k = 1..n_1$, we have a discontinuity of the first derivatives of the Hamiltonian, and we can put it in the standard representation form using the following equality: $|y_k| = -y_k + k(2y_k)(2y_k)$, $k = 1..n_1$.

On the surfaces $y_k - 1 = 0$, $y_k + 1 = 0$, $k = n_1 + 1..n_2$, we have a discontinuity of the second derivatives of the Hamiltonian. This can be checked using the following equality:

$$y \operatorname{sat}(y) - 0.5 \operatorname{sat}(y)^2 = y^2/2 - 1/2(k(y-1)(1-y) + k(-1-y)(-1-y))^2$$

which is a parabola that outside the saturation points is continued linearly with the tangent. We assume that these hypersurfaces do not intersect inside the N_ρ tube around the candidate optimal trajectory.

4 The Extended Sufficient Conditions

We synthesize here all the results obtained in Ref. [1] for the Sufficient Conditions of a strong minimum of the Bolza Problem. We will assume the Hamiltonian and the target as time independent. A transformation of the problem that allows to deal with the time dependent case is given in Ref. [1]. For a given Hamiltonian $H(x, p)$ and extremal \hat{x}_t, \hat{p}_t verifying the **H0IOR** conditions, we consider

$$\begin{aligned} A_{ij}(t) &= \frac{\partial^2 H}{\partial p_i \partial x_j} \Big|_{\hat{x}_t, \hat{p}_t} \quad i = 1, \dots, n, \quad j = 1, \dots, n, \\ B_{ij}(t) &= \frac{\partial^2 H}{\partial p_i \partial p_j} \Big|_{\hat{x}_t, \hat{p}_t} \quad i = 1, \dots, n, \quad j = 1, \dots, n, \\ C_{ij}(t) &= \frac{\partial^2 H}{\partial x_i \partial x_j} \Big|_{\hat{x}_t, \hat{p}_t} \quad i = 1, \dots, n, \quad j = 1, \dots, n \end{aligned} \quad (7)$$

These matrices will be time continuous in the **H0R** case, and for the general **H0I** case they are not defined in a finite set of cross points $t_c \in \Theta$. In both cases, we can define a solution of the following Riccati differential equation:

$$\dot{Q} + QA + A^T Q - Q^T B Q - C = 0 \quad (8)$$

In the **H0R** case, the solution is classic. When the Hamiltonian and the extremal verify **H0I**, the solution of Eq. (8) is classic between the cross points and, following Ref. [1], the matrix Q_t has jumps at each cross point t_c :

$$Q_+ - Q_- = \Delta Q = \frac{q - q_-^T}{(|\dot{S}_{t_c}| + q_-^T \partial_p S(\hat{x}_{t_c}, \hat{p}_{t_c}))} \quad (9)$$

where the function $S(x, p)$ is taken from the local representation of the Hamiltonian at the cross point and

$$\begin{aligned}
 Q_{\pm} &= \lim_{\epsilon \rightarrow 0^+} Q_{t_c \pm \epsilon} \\
 q_- &= \partial_x S(\hat{x}_{t_c}, \hat{p}_{t_c}) - Q_- \partial_p S(\hat{x}_{t_c}, \hat{p}_{t_c}) \\
 |\dot{S}|_{t_c} &= |\partial_x S_{t_c}^T \hat{x}_{t_c-} + \partial_p S_{t_c}^T \hat{p}_{t_c-}| = |\partial_x S_{t_c}^T \hat{x}_{t_c+} + \partial_p S_{t_c}^T \hat{p}_{t_c+}|
 \end{aligned}
 \tag{10}$$

In order to express the final conditions at the final time, we use the coordinates defined by the $[\Sigma, \Pi]$ transformation, whose columns represent the tangent and the normal vectors of the target variety E at the final point \hat{x}_{t_f} . We label the components after such transformation with subscripts (σ, π) .⁵

Let us define $\hat{x}_{\pi} = \Pi^T \dot{\hat{x}}$, the vector listing the $n - d$ components of the state velocity in the space normal to the target variety E at \hat{x}_{t_f} .

Let us define the unit vector $N = \Pi \Pi^T \hat{x} / |\hat{x}_{\pi}|$. Introduce ν as subscript to mean the component of a matrix or vector along the direction N . Taking the first column of the Π matrix the unit vector N , and calling the space of Π columns orthogonal to N as M , with component index μ , we can pose $\Pi = [N, M]$. Thus, Q_{t_f} is decomposed as

$$Q_{t_f} = \begin{pmatrix} Q_{\sigma,\sigma} & Q_{\sigma,\nu} & Q_{\sigma,\mu} \\ Q_{\nu,\sigma} & Q_{\nu,\nu} & Q_{\nu,\mu} \\ Q_{\mu,\sigma} & Q_{\mu,\nu} & Q_{\mu,\mu} \end{pmatrix}
 \tag{11}$$

We also define $\zeta = \dot{\hat{x}} / |\dot{\hat{x}}_{\pi}|$, $\lambda = \dot{\hat{p}} / |\dot{\hat{x}}_{\pi}|$.

In Ref. [1], we have derived the following propositions:

Proposition 1 *Given a Hamiltonian and an extremal \hat{x}_t, \hat{p}_t verifying the **H0/IOR** conditions and the Fixed Time NC, the existence of a symmetric matrix Q_t solution of the differential equation Eq. (8), having at each cross point the ΔQ jump determined by Eq. (9) strictly positive definite, with the boundary conditions*

$$\partial_{\sigma,\sigma} g(\hat{x}_{t_f}) \geq Q_{\sigma,\sigma}(t_f)
 \tag{12}$$

is an SC that this extremal is a strong minimum of the Fixed Time problem.

Proposition 2 *Given a Hamiltonian and an extremal \hat{x}_t, \hat{p}_t verifying the **H0/IOR** conditions and the Open Time problem NC and $|\dot{\hat{x}}_{\pi}| \neq 0$, the existence of a symmetric matrix Q_t solution of the differential equation Eq. (8), having at each cross point the ΔQ jump determined by Eq. (9) strictly positive definite, with the boundary conditions:*

⁵ To clarify the notation used, $\partial_{\sigma,\sigma} g = \Sigma^T \partial_{x,x} g \Sigma$. $x_{\sigma} = \Sigma^T x$, so σ, π, ν , and μ are multi-indices that indicate the components of a matrix after a transformation by Σ, Π, N, M ; $0_{1,\pi} = 0_{\nu,\pi} = 0_{1,dim(\pi)}$, and $I_{\sigma,\sigma}$ is the identity matrix of dimension $dim(\sigma)$.

$$\begin{pmatrix} \partial_{\sigma,\sigma} g & -\partial_{\sigma,\sigma} g \zeta_{\sigma} - \lambda_{\sigma} \\ (-\partial_{\sigma,\sigma} g \zeta_{\sigma} - \lambda_{\sigma})^T & \zeta_{\sigma}^T \partial_{\sigma,\sigma} g \zeta_{\sigma} + \zeta_{\sigma}^T \lambda_{\sigma} - \zeta_{\pi}^T \lambda_{\pi} \end{pmatrix} \geq \begin{pmatrix} Q_{\sigma,\sigma} & Q_{\sigma,\nu} \\ Q_{\nu,\sigma} & Q_{\nu,\nu} \end{pmatrix} (t_f) \quad (13)$$

is an SC that this extremal is a strong minimum of the Open Time problem.

If the extremal is such that $|\dot{\hat{x}}_{\pi}| = 0$ and

$$\dot{\hat{x}}_{\sigma}^T \partial_{\sigma,\sigma} g \dot{\hat{x}}_{\sigma} + \dot{\hat{p}}_{\sigma}^T \dot{\hat{x}}_{\sigma} > 0 \quad (14)$$

the same proposition applies with the following boundary conditions in place of IEq. (13):

$$\left(\partial_{\sigma,\sigma} g - \frac{(\partial_{\sigma,\sigma} g \dot{\hat{x}}_{\sigma} + \dot{\hat{p}}_{\sigma})(\partial_{\sigma,\sigma} g \dot{\hat{x}}_{\sigma} + \dot{\hat{p}}_{\sigma})^T}{\dot{\hat{x}}_{\sigma}^T \partial_{\sigma,\sigma} g \dot{\hat{x}}_{\sigma} + \dot{\hat{p}}_{\sigma}^T \dot{\hat{x}}_{\sigma}} \right) \geq Q_{\sigma,\sigma}(t_f) \quad (15)$$

4.1 The Jacobi Field

The ‘‘Jacobi Field’’ is the system of equations of variations of the Hamiltonian Flow. Given $H(x, p)$ and its extremal that satisfy **H0/IOR**, the solutions of the Hamiltonian Flow verify in the sense of Filippov (see [13] Ch2) a system of ordinary differential equations with discontinuous second members. The solutions close to the extremal (\hat{x}_t, \hat{p}_t) satisfy (see [13] Ch2.11)

$$x_t - \hat{x}_t = \bar{x}_t + o(|\bar{x}_{t_0}| + |\bar{p}_{t_0}|), \quad p_t - \hat{p}_t = \bar{p}_t + o(|\bar{x}_{t_0}| + |\bar{p}_{t_0}|) \quad (16)$$

where (\bar{x}_t, \bar{p}_t) are the solutions of the following system of equations of variations:⁶

$$\dot{\bar{x}}_t = \partial_{xp} \hat{H}_t \bar{x}_t + \partial_{pp} \hat{H}_t \bar{p}_t, \quad \dot{\bar{p}}_t = -\partial_{xx} \hat{H}_t \bar{x}_t - \partial_{px} \hat{H}_t \bar{p}_t \quad (17)$$

The solution (\bar{x}_t, \bar{p}_t) is called the variation of the Hamiltonian Flow.

In the case **H0/I**, the solution jumps across the discontinuity surfaces following the rules defined in Ref. [1]. Using Filippov theory, we derive the jump in state and co-state variations:⁷

$$\begin{aligned} \Delta \bar{x}|_{t_c} &= \left(\frac{\partial_p S \partial_x S^T}{|\dot{S}|} \right) |_{t_c} \bar{x}_{t_c-} + \left(\frac{\partial_p S \partial_p S^T}{|\dot{S}|} \right) |_{t_c} \bar{p}_{t_c-} \\ \Delta \bar{p}|_{t_c} &= - \left(\frac{\partial_x S \partial_x S^T}{|\dot{S}|} \right) |_{t_c} \bar{x}_{t_c-} - \left(\frac{\partial_x S \partial_p S^T}{|\dot{S}|} \right) |_{t_c} \bar{p}_{t_c-} \\ |\dot{S}|_{t_c} &= |\partial_x S_{t_c}^T \hat{x}_{t_c-} + \partial_p S_{t_c}^T \hat{p}_{t_c-}| = |\partial_x S_{t_c}^T \hat{x}_{t_c+} + \partial_p S_{t_c}^T \hat{p}_{t_c+}| \end{aligned} \quad (18)$$

⁶ $\partial_{\alpha,\beta} \hat{H}_t$ are the second derivatives of the Hamiltonian on the candidate extremal arc.

⁷ Δ gives the jump of the variable in the time positive direction, i.e., $\bar{x}|_t = \bar{x}|_{t+} - \bar{x}|_{t-}$

$|\dot{S}|_{t_c} \neq 0$ at all the cross points guarantees the existence and uniqueness of the Jacobi Field Dynamics. Equations (18) are valid also substituting $(\bar{x}_{t_c-}, \bar{p}_{t_c-})$ with $(\bar{x}_{t_c+}, \bar{p}_{t_c+})$. The solution (\bar{x}_t, \bar{p}_t) is called the variation of the Hamiltonian Flow and represents the variation between neighboring extremals and our candidate extremal. We introduce an n -dimensional family of variations of the Hamiltonian Flow through the following positions: $\bar{x}_t = U_t k$, $\bar{p}_t = V_t k$, $\forall k \in \mathbb{R}^n$, in such family, if $\det(U_t) \neq 0$, $\bar{p}_t = V_t U_t^{-1} \bar{x}_t$. The pair of matrices (U_t, V_t) verifies the following matricial version of the Jacobi Field:⁸

$$\begin{aligned} \dot{U} &= A_t U + B_t V \\ \dot{V} &= -C_t U - A_t^T V \\ B_t &= B_t^T \geq 0, C_t = C_t^T. \end{aligned} \quad (19)$$

For Irregular Hamiltonians, these equations are not defined at the cross points where the solution (U_t, V_t) undergoes a discontinuity jump. In Ref. [1] we developed expressions for the jumps of the (U_t, V_t) solution at the cross points, which are useful for the numerical integration of the Jacobi Field along an extremal of a **H0/I** Hamiltonian. At a generic cross point placed in $t_c = 0$ to give an example \hat{p}_t and \hat{x}_t have a jump in the state and co-state derivative:

$$\begin{aligned} \Delta \hat{x} &= \hat{x}_{0+} - \hat{x}_{0-} = \text{sign}(dS/dt) \partial_p S|_{(\hat{x}_0, \hat{p}_0)} \\ \Delta \hat{p} &= \hat{p}_{0+} - \hat{p}_{0-} = -\text{sign}(dS/dt) \partial_x S|_{(\hat{x}_0, \hat{p}_0)} \end{aligned} \quad (20)$$

and a jump in the (U_t, V_t) matrices, coherent with Eq. (9):

$$\begin{aligned} U_+ - U_- &= (-\Delta \hat{x} \Delta \hat{p}^T U_- + \Delta \hat{x} \Delta \hat{x}^T V_-) / |\dot{S}|, \\ V_+ - V_- &= (-\Delta \hat{p} \Delta \hat{p}^T U_- + \Delta \hat{p} \Delta \hat{x}^T V_-) / |\dot{S}| \end{aligned} \quad (21)$$

For the backward integration, we use the equivalent formulae:

$$\begin{aligned} U_- - U_+ &= (\Delta \hat{x} \Delta \hat{p}^T U_+ - \Delta \hat{x} \Delta \hat{x}^T V_+) / |\dot{S}|, \\ V_- - V_+ &= (\Delta \hat{p} \Delta \hat{p}^T U_+ - \Delta \hat{p} \Delta \hat{x}^T V_+) / |\dot{S}| \end{aligned} \quad (22)$$

These last expressions are the more convenient for the applications considering that we have to perform normally a backward integration.

Equations (19) are strictly linked to Eq. (8) as discussed in many references (e.g., [4]), and consequently the pair (U_t, V_t) allows to reformulate the SC by checking $\det(U_t)$ in the given interval. We have the following proposition from Ref. [1]:

⁸ Calling as before in Eqs. (7) $A_t = \partial_{xp} \hat{H}_t$, $B_t = \partial_{pp} \hat{H}_t$, $C_t = \partial_{xx} \hat{H}_t$.

Proposition 3 Let U_{t_f} and V_{t_f} satisfy the so-called self-conjugate initial conditions, $K_{t_f} = U_{t_f}^T V_{t_f} - V_{t_f}^T U_{t_f} = 0$, then the backward integrated solution U_t, V_t of Eqs. (19), with jumps defined by Eqs. (22) at the cross points remains self-conjugate $\forall t \in \mathbb{R} - \Theta$, and in a time interval where $\det(U_t) \neq 0$ the matrix $Q_t = -V_t U_t^{-1}$ is symmetric and solves Eq. (8) with jumps defined by Eq. (9) at the cross points.

Proposition 4 In Propositions 1 and 2, under hypotheses **H0/I**, the SC for an extremal verifying the NC to be a minimum are defined by the existence of a matrix Q_t in $t \in [t_0, t_f]$ that verifies:

1. Equation (8) in the intervals between the cross points $t_c \in \Theta$.
2. Boundary Conditions (BC) on Q_{t_f} verifying the conditions of Proposition 1 for the Fixed Time case and Proposition 2 for the Open Time case.
3. Jump discontinuities $\Delta Q = \frac{q - q^T}{(|\dot{S}_{t_c}| + q^T \partial_p S)}$ at the cross points.
4. Q_t is bounded in $t \in [t_0, t_f]$
5. $|\dot{S}_{t_c}| + q^T \partial_p S > 0$ at the cross points $t_c \in \Theta$.

The above conditions 1, 2, 3, 4, 5 can be expressed in terms of the pair U_t, V_t in $t \in [t_0, t_f]$ as follows:

1. Equation (19) in the intervals between the cross points $t_c \in \Theta$
2. Self-conjugate BC in t_f with $\det(U_{t_f}) \neq 0$ and $Q_{t_f} = -V_{t_f} U_{t_f}^{-1}$. For example, $U_{t_f} = I_{n,n}, V_{t_f} = -Q_{t_f}$. Q_{t_f} verifies the conditions of Proposition 1 for the Fixed Time case and Proposition 2 for the Open Time case.
3. Jump discontinuities as per Eqs. (21) or (22) at the cross points $t_c \in \Theta$.
4. $\det(U_t) \neq 0$, in $t \in [t_0, t_f] - \Theta$.
5. $\det(U_{t_c+}) \det(U_{t_c-}) > 0$ at the cross points $t_c \in \Theta$.

With the choice $U_{t_f} = I_{n,n}, V_{t_f} = -Q_{t_f}$, the last two items are equivalent to ask that $\det(U_t) > 0$ in $t \in [t_0, t_f] - \Theta$

5 Maximal Interval for the Extended Sufficient Conditions

Propositions 1 and 2 can be improved in order to maximize the existence interval for the Extended SC by pushing back as much as possible the interval of existence of the Riccati solution using the BC To better clarify this pushing back, we introduce the following definition:

Definition 5.1 Take a matrix Q_t that verifies Eq. (8) in some interval including t_f for some final condition Q_{t_f} . Consider the pair (U_t, V_t) self-conjugate that satisfy Eqs. (19), with jumps defined by Eqs. (22) at the cross points, such that $Q_t = -V_t U_t^{-1}$ and $U_{t_f} = I_{n,n}, V_{t_f} = -Q_{t_f}$. Let us associate with this matrix a time a_Q defined as follows:

Given the two sets:

$$\begin{aligned} \mathcal{L} &= [t \mid t < t_f, t \notin \Theta, \det(U_t) = 0] \\ \mathcal{D} &= [t \mid t < t_f, t \in \Theta, \det(U_{t+})\det(U_{t-}) < 0] \end{aligned} \tag{23}$$

If $\mathcal{L} \cup \mathcal{D} = \emptyset$, $a_Q = -\infty$, else $a_Q = \sup(\mathcal{L} \cup \mathcal{D})$.

Thus, a_Q is the first time at the left of t_f when Q_t diverges or a cross point does not satisfy the positivity condition. Note that a_Q is well defined even if $\det(U_{t_f}) = 0$, in such a case if U_t is singular in a neighborhood of t_f , then $a_Q = t_f$, if instead t_f is an isolated zero of the determinant then $a_Q < t_f$.

5.1 Maximal Interval for the Extended Sufficient Conditions

Using a Riccati comparison theorem, we provide in Ref. [1] a theorem that allows to maximize the interval where the Extended Sufficient Conditions can be applied. In particular we can define a point a_{Q^∞} that is the infimum among all matrices verifying the Boundary conditions, to do that we use this proposition from Ref. [1] (Proposition 5.2):

Proposition 5 Consider a \hat{Q}_t that verifies conditions 1, 2, 3, 4, and 5 in $t \in [a, t_f]$ of Proposition 4. Any Q_t that verifies conditions 1, 2, and 3 in $t \in [a, t_f]$, such that $Q_{t_f} > \hat{Q}_{t_f}$ verifies also conditions 4 and 5 of Proposition 4. In addition, $Q_t > \hat{Q}_t$ in $t \in [a, t_f]$ and $a_Q \leq a_{\hat{Q}}$. Given $\hat{W}_t = \int_{t_f}^t \hat{U}_s^{-1} B_s \hat{U}_s^{-T} ds \leq 0$, the following representation formula applies $\hat{U}_t^T (Q_t - \hat{Q}_t) \hat{U}_t = ((Q_{t_f} - \hat{Q}_{t_f})^{-1} - \hat{W}_t)^{-1}$ to any Q_t that verifies conditions 1,2, and 3 in an interval $t \in [s, t_f]$, $s \geq a$, where the second member is not singular.

We use this proposition to implement a sequence of Riccati problems that can be used to find the minimum possible a_Q among all the matrices that fulfill the boundary constraints for the SC

Definition 5.2 In the Fixed Time problem, take an integer $\mathcal{N} > 0$ and define a $Q_t^{\mathcal{N}}$ that verifies Eq. 8 whose terminal value $Q_{t_f}^{\mathcal{N}}$ is represented in the target variety E basis (see Eq. (11)), as follows:

1. $Q_{\sigma,\sigma}^{\mathcal{N}}$ is formed using IEqs. (12) with the equal sign.
2. $Q_{\sigma,\pi}^{\mathcal{N}} = 0$.
3. $Q_{\pi,\pi}^{\mathcal{N}} = I_{n-d,n-d}$, \mathcal{N} .

$$Q_{t_f}^{\mathcal{N}} = \begin{pmatrix} \partial_{\sigma,\sigma} g(\hat{x}_{t_f}) & 0_{\sigma,\pi} \\ 0_{\pi,\sigma} & I_{n-d,n-d}, \mathcal{N} \end{pmatrix} \tag{24}$$

In the Open Time problem, take an integer $\mathcal{N} > 0$ and define a $Q_{t_f}^{\mathcal{N}}$ that verifies Eq. 8 whose terminal value $Q_{t_f}^{\mathcal{N}}$ is represented in the target variety E basis (see Eq. (11)), as follows:

if $|\hat{x}_\pi| \neq 0$:

1. $Q_{\sigma,\sigma}^{\mathcal{N}}$, $Q_{\sigma,v}^{\mathcal{N}}$, and $Q_{v,v}^{\mathcal{N}}$ follow from IEq. (13) with equal sign.
2. $Q_{\sigma,\mu}^{\mathcal{N}} = 0$, $Q_{v,\mu}^{\mathcal{N}} = 0$.
3. $Q_{\mu,\mu}^{\mathcal{N}} = I_{n-d-1,n-d-1} \mathcal{N}$.

$$Q_{t_f}^{\mathcal{N}} = \begin{pmatrix} \partial_{\sigma,\sigma} g & -\partial_{\sigma,\sigma} g \zeta_\sigma - \lambda_\sigma & 0_{\sigma,\mu} \\ (-\partial_{\sigma,\sigma} g \zeta_\sigma - \lambda_\sigma)^T & \zeta_\sigma^T \partial_{\sigma,\sigma} g \zeta_\sigma + \zeta_\sigma^T \lambda_\sigma - \zeta_\pi^T \lambda_\pi & 0_{v,\mu} \\ 0_{\mu,\sigma} & 0_{\mu,v} & I_{n-d-1,n-d-1} \mathcal{N} \end{pmatrix} \quad (25)$$

if $|\hat{x}_\pi| = 0$ and IEq. (14) is verified:

1. $Q_{\sigma,\sigma}^{\mathcal{N}}$ is formed using IEqs. (15) with the equal sign.
2. $Q_{\sigma,\pi}^{\mathcal{N}} = 0$.
3. $Q_{\pi,\pi}^{\mathcal{N}} = I_{n-d,n-d} \mathcal{N}$.

$$Q_{t_f}^{\mathcal{N}} = \begin{pmatrix} \partial_{\sigma,\sigma} g - \frac{(\partial_{\sigma,\sigma} g \hat{x}_\sigma + \hat{p}_\sigma)(\partial_{\sigma,\sigma} g \hat{x}_\sigma + \hat{p}_\sigma)^T}{\hat{x}_\sigma^T \partial_{\sigma,\sigma} g \hat{x}_\sigma + \hat{p}_\sigma^T \hat{x}_\sigma} & 0_{\sigma,\pi} \\ 0_{\pi,\sigma} & I_{n-d,n-d} \mathcal{N} \end{pmatrix} \quad (26)$$

In all above cases, any $Q^{\mathcal{M}}$ with $\mathcal{M} > \mathcal{N}$ will be such that $a_{Q^{\mathcal{M}}} \leq a_{Q^{\mathcal{N}}}$.

The monotonic sequence $a_{Q^1}, a_{Q^2} \dots a_{Q^{\mathcal{N}}}$ converges to a_{Q^∞} , for $\mathcal{N} \rightarrow \infty$, where $-\infty \leq a_{Q^\infty} < t_f$.

Then, using the above propositions, we can proceed to demonstrate the following theorem.

Theorem 1 *The condition $t_0 > a_{Q^\infty}$ is a Sufficient Condition for the strong minimality of the extremal (we call it Extended SC). There is no matrix \bar{Q} that verifies the Riccati Equation and the Boundary conditions for the Fixed Time or the Open Time problem such that $a_{\bar{Q}} < a_{Q^\infty}$. If a matrix \bar{Q} verifies the SC given by Propositions 1 or 2, then $t_0 > a_{\bar{Q}} \geq a_{Q^\infty}$ and there is an \mathcal{N} such that $Q^{\mathcal{N}}$ as by definition 5.2 verifies the Sufficient Conditions.*

Proof The first part of the theorem comes easily from the application of Propositions 1 and 5. We assume first that the Hamiltonian is regular.

If $\bar{Q}_{\pi\sigma} = 0$, the demonstration is trivial. So let us assume $\|\bar{Q}_{\pi\sigma} \bar{Q}_{\sigma\pi}\| > 0$. Consider a generic \bar{Q} that verifies the Riccati Equation and the Boundary conditions for the Fixed Time problem. Define $J_{\mathcal{N}} = \max_{x^T x=1} x^T (\bar{Q}_{t_f} - Q_{t_f}^{\mathcal{N}}) x$, and then

$$J_{\mathcal{N}} = \max_{(\sigma^T \sigma + \pi^T \pi = 1)} 2\pi^T \bar{Q}_{\pi\sigma} \sigma + (\pi^T \bar{Q}_{\pi\pi} \pi - \mathcal{N} \pi^T \pi) \quad (27)$$

When $\bar{Q}_{\pi\sigma} \neq 0$, the maximum is obtained with $\sigma = \lambda \bar{Q}_{\sigma\pi} \pi$ for some $\lambda > 0$.

From $\sigma^T \sigma + \pi^T \pi = 1$, we get $\lambda = \sqrt{\frac{1 - \pi^T \pi}{\pi^T \bar{Q}_{\pi\sigma} Q_{\sigma\pi} \pi}}$.

Thus, $J_{\mathcal{N}} = \max_{(\pi^T \pi \leq 1)} 2\sqrt{1 - \pi^T \pi} \sqrt{\pi^T \bar{Q}_{\pi\sigma} \bar{Q}_{\sigma\pi} \pi + \pi^T \bar{Q}_{\pi\pi} \pi - \mathcal{N} \pi^T \pi}$.
 $J_{\mathcal{N}} \geq 0$ because this is the value obtained in the previous formula at $\pi = 0$.

Let us introduce $q_1 = \|\bar{Q}_{\pi\sigma} \bar{Q}_{\sigma\pi}\|$, $q_2 = \|\bar{Q}_{\pi\pi}\|$, $y = \sqrt{\pi^T \pi}$.

Clearly, $0 \leq J_{\mathcal{N}} \leq \max_{(0 \leq y \leq 1)} 2q_1 y \sqrt{1 - y^2} - (\mathcal{N} - q_2) y^2$.

If we derive the second member in y to look for the maximum, we find that it is obtained in $y = q_1/\mathcal{N} + O(1/\mathcal{N}^2)$ and by substitution $0 \leq J_{\mathcal{N}} \leq q_1^2/\mathcal{N} + O(1/\mathcal{N}^2)$. Consequently, $\lim_{\mathcal{N} \rightarrow \infty} J_{\mathcal{N}} = 0$.

Now, we prove by contradiction that $a_{\bar{Q}} \geq a_{Q^\infty}$, and we assume that $a_{\bar{Q}} < a_{Q^\infty}$. We consider a matrix solution of the Riccati equation $\tilde{Q}_i^{\delta, \mathcal{N}}$ so that $\tilde{Q}_{t_f}^{\delta, \mathcal{N}} = \bar{Q}_{t_f} - \delta_{\mathcal{N}}$ for a small positive parameter $\delta_{\mathcal{N}} = 2q_1^2/\mathcal{N}$ so that $(\tilde{Q}_{t_f}^{\delta, \mathcal{N}} - Q_{t_f}^{\mathcal{N}}) = (\bar{Q}_{t_f} - Q_{t_f}^{\mathcal{N}}) - \delta_{\mathcal{N}}$ is negative for $+\infty > \mathcal{N} > \mathcal{N}_q$. From Proposition 5, $a_{Q^\infty} \leq a_{Q^{\mathcal{N}}} \leq a_{\tilde{Q}^{\delta, \mathcal{N}}}$. At the same time, for construction and continuity of the Riccati solutions with the data, $a_{\tilde{Q}^{\delta, \mathcal{N}}} \rightarrow a_{\bar{Q}}$, which is not compatible with $a_{\bar{Q}} < a_{Q^\infty}$. It follows that the assumption is false and $a_{\bar{Q}} \geq a_{Q^\infty}$. From this last property, an \mathcal{N} such that $t_0 > a_{\mathcal{N}}$ surely exists because by assumption $t_0 > a_{\bar{Q}}$.

In the case of Irregular Hamiltonians, we can apply the same proof given here on the Regularized Hamiltonian H^δ introduced in Ref. [1] for the proof of Propositions 5.2 and 5.3 arriving to the same conclusions by sending δ to zero. □

This theorem shows that a_{Q^∞} is uniquely defined for any given problem and that there are no Sufficient Conditions that can be obtained using the solution of a Riccati Equations better than $t_0 > a_{Q^\infty}$. This justifies the name of Extended SC The classic Jacobi conditions are weaker than the Extended SC as will be demonstrated in the next chapter.

6 The Conjugate Point Condition

The Jacobi condition (JC) refers to the existence of a non-degenerate “Neighboring Extremals Field” or “Jacobi Field” close to the extremal candidate to be a minimum. This is the classic approach to study the sufficiency. The point where the field becomes degenerate is called conjugate point, and we will label it a_J to underline its link with the Jacobi Field. Studying the Classic Auxiliary Problem for Regular Hamiltonians under Legendre–Clebsch strict conditions and controllability, the JC provides Sufficiency and Necessity results based on the position of the conjugate point with respect to t_0 .

By definition, the Jacobi Field must satisfy the linearized BC of the problem at t_f and the system of equations of the variations of the Hamiltonian Flow Eqs. (19).⁹ We will investigate on the connections between the JC and the Extended SC provided with Theorem 1 in the frame of our **H0/IO** assumptions. As already shown, Eqs. (19) provide the dynamics of the state and co-state variation through the following positions:

$$\bar{x}_t = U_t k, \quad \bar{p}_t = V_t k, \quad \forall k \in \mathbb{R}^n \tag{28}$$

We define as Jacobi matrices (U_t^J, V_t^J) a solution of Eqs. (19), which satisfies at the terminal t_f the BC obtained taking the linearized form of the Boundary Condition of the NC

We introduce the suffix $(\cdot)_f$ to indicate the value of any extremal at its final time $t_f + \bar{t}_f$ in the general Open Time case, while the Fixed Time relationships are derived setting $\bar{t}_f = 0$. From the NC given by Eq. (2) (see also Ref.[6]), we have

$$\begin{aligned} g(x) &= l(x) + \sum_{i=1..n-d} v_i \theta_i(x) \\ \hat{p}_f &= -\partial_x g|_{\hat{x}_f}, \Rightarrow \\ \bar{p}_f &= -\partial_{xx} g|_{\hat{x}_f} \bar{x}_f - \sum_{i=1..n-d} \bar{v}_i \partial_x \theta_i|_{\hat{x}_f} \end{aligned} \tag{29}$$

The \bar{v}_i can be solved introducing the orthonormal basis $[\Sigma, \Pi]$ which defines the tangent and the normal space of the variety E in \hat{x}_{t_f} . The following relationships hold:

$$\bar{x}_f \in Range(\Sigma), \quad [\partial_x \theta_1, \partial_x \theta_2, \dots, \partial_x \theta_{n-d}]|_{\hat{x}_f} \in Range(\Pi) \tag{30}$$

Clearly, $rank(\Pi) = n - d$, and we can write

$$\bar{p}_f = -\partial_{xx} g|_{\hat{x}_f} \Sigma k_1 - \Pi k_2, \quad k_1 \in \mathbb{R}^d, \quad k_2 \in \mathbb{R}^{n-d} \tag{31}$$

In the Time Open problem, the difference in state and co-state at their final time of two close extremals is

$$\bar{x}_f = \bar{x}_{t_f} + \partial_p H|_{t_f} \bar{t}_f, \quad \bar{p}_f = \bar{p}_{t_f} - \partial_x H|_{t_f} \bar{t}_f \tag{32}$$

From Eqs. (29), (30), (31), and (32), we have all the ingredients to determine the BC in matricial form $(U_{t_f}^J, V_{t_f}^J)$ for the Fixed and the Open Time cases.

⁹ $A_t, B_t,$ and C_t are defined by Eqs. (7).

6.1 The Jacobi Sufficiency Conditions in the Fixed Time Case

In this section, we will see how the Jacobi SC is related to the Extended SC exposed in the previous chapters.

From Eqs. (29), (30), (31), and (32) and setting $\bar{t}_f = 0$ (see also [6]), we get

$$\bar{x}_{t_f} = \Sigma k_1, \quad \bar{p}_{t_f} = -\partial_{xx}g \bar{x}_{t_f} + \Pi k_2, \quad \forall k_1 \in \mathbb{R}^d, \quad k_2 \in \mathbb{R}^{n-d} \tag{33}$$

These conditions are equivalent to the following BC for the system Eqs. (19):

$$U_{t_f}^J = [\Sigma, 0_{n,n-d}], \quad V_{t_f}^J = [-\partial_{xx}g \Sigma, \Pi], \quad \partial_{xx}g = \partial_{xx}(l(x) + v_i\theta_i(x)). \tag{34}$$

$(U_{t_f}^J, V_{t_f}^J)$ are self-conjugate as per Proposition 3, integrating them backward using Eqs. (19) and using the jumps Eqs. (22) at the cross points, they provide a self-conjugate pair (U_t^J, V_t^J) and from Proposition 3 in an interval where $\det(U_t^J) \neq 0$ the matrix

$$Q_t^J = -V_t^J U_t^{J-1} \tag{35}$$

is a symmetric solution of Eq. (8) and $Q_t^J \bar{x}_t = -\bar{p}_t$.

The existence of a bijective local mapping between \bar{x}_t and $k = [k_1, k_2]^T$ depends on the invertibility of the linear mapping U_t^J . To provide such invertibility, we must have not only $\det(U_t) \neq 0$ in any open interval between two adjacent cross points but also the determinant must not change sign at the cross points; in fact in Ref.[1], it is shown that this condition guarantees that passing through the discontinuity surface the flow does not lose the bijective mapping property. With this premise, we state the JC¹⁰ for an extremal of a Fixed Time problem as follows:

Definition 6.1 The JC for a Fixed Time extremal and Hamiltonian verifying **H0/IOR** is $a_{Q^J} < t_0$, and this is equivalent to say that an invertible relationship between $k = [k_1, k_2]^T \in \mathbb{R}^n$ and $\bar{x}_t \forall t \in [t_0, t_f) - \Theta$ exists.

In all the problems where $\dim(\Sigma) < n$, Q_t^J diverges in t_f because $\det(U_{t_f}^J) = 0$, so we cannot use Proposition 4 to demonstrate SC However, from the Jacobi matrix, Q^J is possible to derive easily with a small perturbation of the matrix $U_{t_f}^J$ another matrix with the characteristics requested by Proposition 4, and the following result applies:

Theorem 2 *If a Hamiltonian and its Fixed Time extremal verify **H0/IOR** and the JC, that extremal is a local strong minimum. In addition, $a_{Q^J} \geq a_{Q^\infty}$.*

¹⁰ This is an extension of the classic ones which do not take into account the jumps at the cross points.

Proof The method of proof is simple. We construct a pair of matrices (U_t, V_t) close to the Jacobi ones that verify the SC from Theorem 1. Let us use coordinates where the $[\Sigma, \Pi]$ frame is the identity matrix. We label

$$g_{\sigma,\sigma} = \Sigma^T \partial_{x,x} g \Sigma, \quad g_{\pi,\sigma} = \Pi^T \partial_{x,x} g \Sigma, \quad g_{\pi,\pi} = \Pi^T \partial_{x,x} g \Pi \tag{36}$$

Pre-multiplying Eqs. (34) by $[\Sigma, \Pi]^T$, we get

$$U_{t_f}^J = \begin{pmatrix} I_{\sigma,\sigma} & 0_{\sigma,\pi} \\ 0_{\pi,\sigma} & 0_{\pi,\pi} \end{pmatrix} V_{t_f}^J = \begin{pmatrix} -g_{\sigma,\sigma} & 0_{\sigma,\pi} \\ -g_{\pi,\sigma} & I_{\pi,\pi} \end{pmatrix} \tag{37}$$

Let us define for $\beta > 0$:

$$U_{t_f}^\beta = \begin{pmatrix} I_{\sigma,\sigma} & 0_{\sigma,\pi} \\ \beta g_{\pi,\sigma} & -\beta I_{\pi,\pi} \end{pmatrix} V_{t_f}^\beta = V_{t_f}^J \tag{38}$$

It follows

$$U_{t_f}^{\beta^{-1}} = \begin{pmatrix} I_{\sigma,\sigma} & 0_{\sigma,\pi} \\ g_{\pi,\sigma} & -I_{\pi,\pi}/\beta \end{pmatrix} \tag{39}$$

From which we derive $Q_{t_f}^\beta$:

$$Q_{t_f}^\beta = -V_{t_f}^\beta U_{t_f}^{\beta^{-1}} = \begin{pmatrix} g_{\sigma,\sigma} & 0_{\sigma,\pi} \\ 0_{\pi,\sigma} & I_{\pi,\pi}/\beta \end{pmatrix} \tag{40}$$

By setting $\mathcal{N} = \beta^{-1}$, it follows that $Q_{t_f}^\beta = Q_{t_f}^\mathcal{N}$, the same defined in Theorem 1, so $a_{Q^{\beta=0^+}} = a_{Q^\infty}$. The following sentences hold:

- Q_t^β verifies Proposition 1 in $(a_{Q^\beta}, t_f]$ and provides SC if $t_0 > a_{Q^\beta}$.
- From the Riccati Comparison Theorem (see Ref.[1]), we have that $Q_t^\beta > Q_t^{\beta+\epsilon}$ and $a_{Q^{\beta+\epsilon}} \geq a_{Q^\beta}$, $\forall \epsilon \in \mathbb{R}^+$, $t \in (a_{Q^{\beta+\epsilon}}, t_f]$.
- The pair (U_t^β, V_t^β) backward propagated from $(U_{t_f}^\beta, V_{t_f}^\beta)$ with Eq. (8) and the jumps, Eqs. (22), at the cross points converge uniformly to $(U_t^J, V_t^J) \forall t \in [t_0, t_f] - \Theta$.¹¹ Consequently, $\lim_{\beta \rightarrow 0^+} U_t^\beta \rightarrow U_t^J$, $\forall t \in [t_0, t_f] - \Theta$ and $\forall \epsilon > 0, \exists \hat{\beta} : |\det(U_t^\beta) - \det(U_t^J)| < \epsilon, \forall \beta < \hat{\beta}$.

¹¹ The solution at a given time $t \in [t_0, t_f] - \Theta$ can be seen as a finite chain of continuous functions. From the terminal point to the first crossing point, (U_t^β, V_t^β) are locally continuous with respect to β due to the classic ODE theorems and the continuity of A_t, B_t , and C_t , at the crossing point the left limit of the solution is continuous with respect to the right limit (see Eqs. (22)), and then we sequentially continue this process in a finite number of steps until we reach the point t .

- By assumption, $a_{Q^J} < t_0$, and consequently there is a $\hat{\beta}$ enough small so that $a_{Q^{\hat{\beta}}} < t_0$.
- If in the previous bullet we substitute t_0 with a decreasing sequence $t_k \rightarrow a_{Q^J}$ and $\hat{\beta}$ with a decreasing sequence $\hat{\beta}_k > 0$ such that $|\det(U_t^{\hat{\beta}_k})| > 0, t \in [t_k, t_f]$, we get $a_{Q^{\hat{\beta}_k}} < t_k$ and at the limit $a_{Q^\infty} \leq a_{Q^J}$.

The last two sentences contain the proposition we wanted to demonstrate. □

7 Applications to Space Orbital Transfers

We will consider three study cases. The first example is based on the minimization of a low-thrust transfer with quadratic cost. It is a case taken by the literature, and we demonstrate that when the firing is too long we lose the Extended SC of the extremal. The second case is a low thrust problem with linear cost, we have studied the NC for this class of problems in Ref. [17]. Here to study the Sufficient Conditions we use Theorem 1, and also in this case, which is not tractable by classical methods, we demonstrate that when the firing is too long we lose the Extended SC The third study case is based on the minimization of Impulsive firing transfers that lead to an Irregular Hamiltonian. We use the Extended SC and Theorem 1 on Irregular Hamiltonians to establish SC of minimality.

7.1 Low-thrust Planar Orbital Transfer with Quadratic Integral Cost and Regular Hamiltonian

We consider a planar transfer problem with low thrust using polar coordinates already presented in Ref. [14] who elaborates SC from Ref. [15]. The context is that of SLC with a Regular Hamiltonian. The coordinates are $x_1 = \rho$, the orbit radius, $x_2 = \vartheta$, the polar anomaly, $x_3 = v_\rho = \dot{\rho}$, and $x_4 = v_\vartheta = \rho \dot{\vartheta}$.

Calling $\mu = GM_{Earth}$, where G is the Universal Gravitational Constant, $\Gamma = T/m$, where T is the thruster force and m is the satellite mass, the equation of the orbital dynamics is

$$\begin{aligned}
 \dot{\rho} &= v_\rho \\
 \dot{\vartheta} &= v_\vartheta / \rho \\
 \dot{v}_\rho &= v_\vartheta^2 / \rho - \mu / \rho^2 + \Gamma \sin(\beta) \\
 \dot{v}_\vartheta &= -v_\rho v_\vartheta / \rho + \Gamma \cos(\beta)
 \end{aligned}
 \tag{41}$$

We introduce also the energy per unit mass $E = (v_\vartheta^2 + v_\rho^2) / 2 - \mu / \rho$ and the cost $J = -E(x_{t_f}) + \chi \int_{t_0}^{t_f} \Gamma^2 / 2 dt$, where χ is a weighting factor.

The optimal transfer that is obtained minimizing the cost J tends to realize a compromise between maximizing the energy of the final orbit and minimizing the propellant consumed to reach this orbit.

When the integral cost is quadratic, it represents the minimum propellant consumption cost for a Plasmic Thruster working at constant power. This model of integral cost is often used outside its domain of applicability because it simplifies the optimization task.

If we consider a Plasmic Thruster as propulsor (see Ref. [18], Ch.8), the consumed mass rate is $\dot{m} = -m^2\Gamma^2/(2\eta P)$, where P is the power of the motor and η is its efficiency.

If the motor works at constant power—which is not the case in the majority of the applications—then we get that the mass evolves as

$$m_t^{-1} - m_0^{-1} = (\eta P)^{-1} \int_{t_0}^{t_f} \Gamma^2/2dt.$$

This formula justifies the selection we have done for the integral cost; minimizing it equals minimizing the mass consumption for this type of motor.

By scaling space and time coordinates, we can set $\mu = 1$.

With the given cost and dynamics, we obtain a pre-Hamiltonian:

$$H_P = p_1x_3 + \frac{p_2x_4}{x_1} + \left(-\frac{1}{x_1^2} + \frac{x_4^2}{x_1} + \Gamma \sin \beta\right) p_3 - \frac{\chi \Gamma^2}{2} - \frac{p_4x_3x_4}{x_1} + p_4\Gamma \cos \beta \tag{42}$$

We introduce the control $u_s = \Gamma \sin \beta$, $u_c = \Gamma \cos \beta$. The problem control set U is still undefined. Because the Hamiltonian verifies the SLC everywhere, an optimal control exists in $U = \mathbb{R}^2$, and to make applicable our theorem, we choose $U = B(2 \max_{t \in [t_0, t_f]} \sqrt{\hat{u}_s(t)^2 + \hat{u}_c(t)^2})$. By taking the *sup* of H_P , we get the feedback law:

$$\Gamma = \sqrt{p_3^2 + p_4^2}/\chi, \quad u_s = p_3/\chi, \quad u_c = p_4/\chi \tag{43}$$

and consequently the Hamiltonian:

$$H(x, p) = p_1x_3 - \left(\frac{1}{x_1^2} - \frac{x_4^2}{x_1}\right) p_3 + \frac{p_3^2 + p_4^2}{2\chi} + \frac{p_2x_4}{x_1} - \frac{p_4x_3x_4}{x_1} \tag{44}$$

The first derivatives of the Hamiltonian that allow to calculate the extremal flow are

$$\partial_x H = \left(\frac{2p_3 - p_3x_1x_4^2 - p_2x_1x_4 + p_4x_1x_3x_4}{x_1^3} \quad 0 \quad p_1 - \frac{p_4x_4}{x_1} \quad \frac{2p_3x_4 - p_4x_3 + p_2}{x_1} \right) \tag{45}$$

$$\partial_p H = \left(x_3 \frac{x_4}{x_1} \frac{x_4^2}{x_1} - \frac{1}{x_1^2} + \frac{p_3}{\chi} \frac{p_4}{\chi} - \frac{x_3x_4}{x_1} \right) \tag{46}$$

From which we can derive the second derivatives that allow to calculate the A_t , B_t , and C_t matrices necessary to propagate the Riccati solution and assess the SC given by Theorem 1.

$$\partial_{xx}H = \begin{pmatrix} -\frac{2(3p_3 - p_3x_1x_4^2 - p_2x_1x_4 + p_4x_1x_3x_4)}{x_1^4} & 0 & \frac{p_4x_4}{x_1^2} & -\frac{2p_3x_4 - p_4x_3 + p_2}{x_1^2} \\ 0 & 0 & 0 & 0 \\ \frac{p_4x_4}{x_1^2} & 0 & 0 & -\frac{p_4}{x_1} \\ -\frac{2p_3x_4 - p_4x_3 + p_2}{x_1^2} & 0 & -\frac{p_4}{x_1} & \frac{2p_3}{x_1} \end{pmatrix} \tag{47}$$

$$\partial_{px}H = \begin{pmatrix} 0 & 0 & 1 & 0 \\ -\frac{x_4}{x_1^2} & 0 & 0 & \frac{1}{x_1} \\ -\frac{x_1x_4^2 - 2}{x_1^3} & 0 & 0 & \frac{2x_4}{x_1} \\ \frac{x_3x_4}{x_1^2} & 0 & -\frac{x_4}{x_1} & -\frac{x_3}{x_1} \end{pmatrix} \tag{48}$$

$$\partial_{pp}H = \begin{pmatrix} 0 & 0 & 0 & 0 \\ 0 & 0 & 0 & 0 \\ 0 & 0 & \frac{1}{\chi} & 0 \\ 0 & 0 & 0 & \frac{1}{\chi} \end{pmatrix} \tag{49}$$

With the selected Hamiltonian, we consider a Bolza Problem with Fixed Time and Free Final state, and we set $\chi = 100$ as in Ref.[14]. In this case, the first-order NC provide the co-state as a function of the final state. To avoid solving the Two-Boundary-Value Problem, we fix arbitrarily the final state and study the extremal strong minimality for the given Bolza Problem varying the initial time t_0 . We choose as final state

$$x_{t_f} = [10, 0, 0, 1/\sqrt{(10)}]^T$$

Being the final cost $l(x) = -E(x)$, it follows that $p_{t_f} = -Dl(x) = DE(x)$:

$$p_{t_f} = [1/100, 0, 0, 1/\sqrt{(10)}]^T.$$

The resulting extremal is plotted in the following Figs. 1, 2, 3, 4, and 5.

In this problem, the target variety is the complete state space \mathbb{R}^4 , so $\Sigma = I_{4,4}$ and $\Pi = \emptyset$.

Theorem 1 gives the conditions for the SC To establish the SC, we need to verify that $\det(U(t)) \neq 0$ in $[t_0, t_f)$. The terminal conditions for the Jacobi Field Eqs. 19 are $U_{t_f} = I_{4,4}$, $V_{t_f} = -Q_{t_f}$, and $Q_{t_f} = \partial_{xx}l(x_{t_f}) = -\partial_{xx}E(x_{t_f})$. The determinant of U_t is plotted in Fig. 6, it shows that the extremal satisfies the sufficiency conditions for strong minimality when $t_0 \in [-56.4, 0]$, and outside this interval the SC are not verified. In this example, we can also use some NC of the second-order which we find in Ref.[12] because the quadratic problem verifies

the SLC and the additional Normality conditions requested.¹² We conclude that the extremal is a strong minimum for $t_0 > -56.4$ and is not a strong minimum $t_0 < -56.4$.

7.2 Low-thrust Planar Orbital Transfer with Linear Integral Cost and Irregular Hamiltonian

We consider the planar transfer problem of the previous chapter with a linear different integral cost and the controls limited to be in a circular domain.

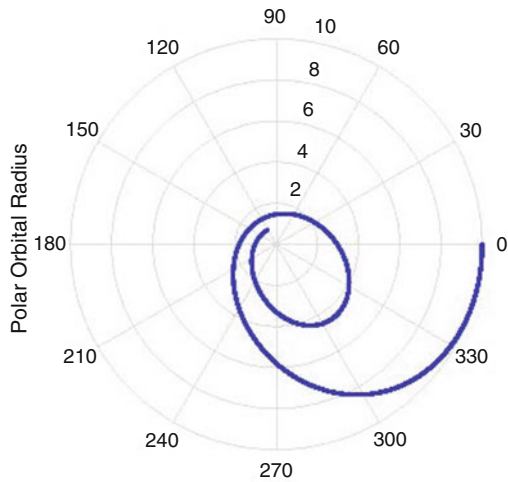
$$\begin{aligned}
 \dot{\rho} &= v_\rho \\
 \dot{\vartheta} &= v_\vartheta / \rho \\
 \dot{v}_\rho &= v_\vartheta^2 / \rho - \mu / \rho^2 + \Gamma \sin(\beta) \\
 \dot{v}_\vartheta &= -v_\rho v_\vartheta / \rho + \Gamma \cos(\beta) \\
 \Gamma &\leq \bar{\Gamma}
 \end{aligned}
 \tag{50}$$

The cost will be $J = -E(t_f) + \chi \int_{t_0}^{t_f} \Gamma dt$, where χ is a weighting factor.

By scaling space and time coordinates, we can set $\mu = 1$.

With the given cost and dynamics, we obtain a pre-Hamiltonian:

Fig. 1 Plane extremal: $\rho(\vartheta)$



¹² The additional Normality condition requested in Ref.[12] is the Strong Normality of both terminals. The condition for the right terminal is obviously satisfied because $\Pi = \emptyset$. The condition for the left terminal can be easily proved because $p^T f(\hat{x}, \hat{u}) - p^T f(\hat{x}, u) = p_3(\hat{p}_3/\chi - u_s) + p_4(\hat{p}_4/\chi - u_c) \geq 0, \forall (u_s, u_c) \in U$ admits as only solution $p = 0$ (it suffices to choose $u_s = 2p_3/\chi, u_c = 2p_4/\chi$ to make this expression strictly negative for any $p \neq 0$).

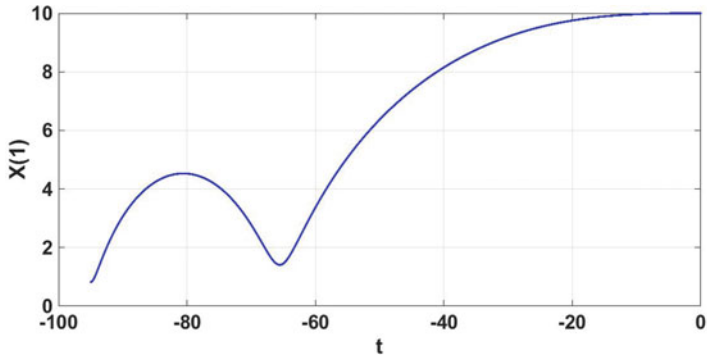


Fig. 2 Plane extremal: orbital radius

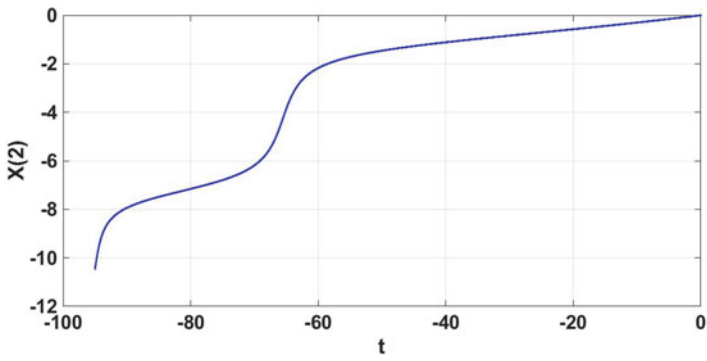


Fig. 3 Plane extremal: orbital anomaly

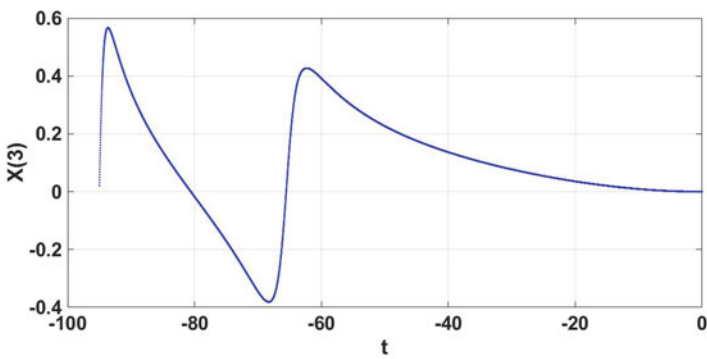


Fig. 4 Plane extremal: orbital radial velocity

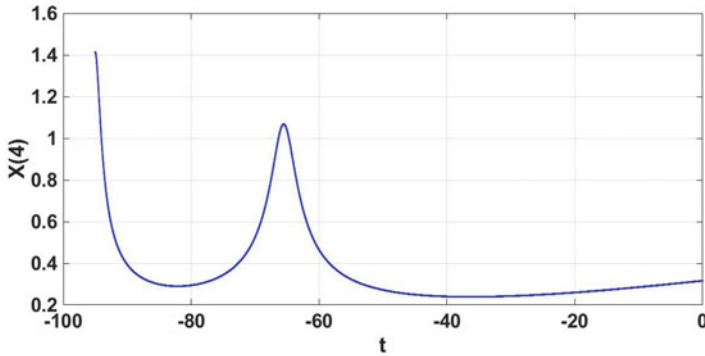


Fig. 5 Plane extremal: orbital tangential velocity

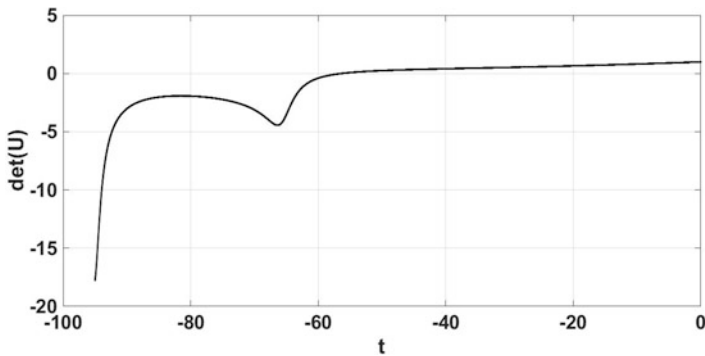


Fig. 6 Plane extremal: $\det(U^J(t))$

$$H_P = p_1 x_3 + \frac{p_2 x_4}{x_1} + \left(-\frac{1}{x_1^2} + \frac{x_4^2}{x_1} + \Gamma \sin \beta \right) p_3 - \chi \Gamma - \frac{p_4 x_3 x_4}{x_1} + p_4 \Gamma \cos \beta \tag{51}$$

We introduce the control $u_s = \Gamma \sin \beta$, $u_c = \Gamma \cos \beta$, $U = [(u_s, u_c) | \sqrt{u_s^2 + u_c^2} \leq \bar{\Gamma}]$. By taking the *sup* of H_P , we get the feedback law:

$$\begin{aligned} \sqrt{p_3^2 + p_4^2} \geq \chi, \quad u_s = \bar{\Gamma} p_3 / \sqrt{p_3^2 + p_4^2}, \quad u_c = \bar{\Gamma} p_4 / \sqrt{p_3^2 + p_4^2}, \\ \sqrt{p_3^2 + p_4^2} < \chi, \quad u_s = 0, \quad u_c = 0 \end{aligned} \tag{52}$$

and consequently the Hamiltonian:

$$\begin{aligned} H(x, p) = p_1 x_3 - \left(\frac{1}{x_1^2} - \frac{x_4^2}{x_1} \right) p_3 + \frac{p_2 x_4}{x_1} - \frac{p_4 x_3 x_4}{x_1} + \\ \bar{\Gamma} k(\sqrt{p_3^2 + p_4^2} - \chi)(\sqrt{p_3^2 + p_4^2} - \chi) \end{aligned} \tag{53}$$

We see that the Irregular Hamiltonian is set in the standard form. We report the first and second derivatives for the case $k(S) = 1$, and to recover those of the case $k(S) = 0$, it suffices to set $\bar{\Gamma} = 0$.

$$\partial_p H = \left(x_3, \frac{x_4}{x_1}, \frac{x_4^2}{x_1} - \frac{1}{x_1^2} + \frac{\bar{\Gamma} p_3}{\sqrt{p_3^2 + p_4^2}}, \frac{\bar{\Gamma} p_4}{\sqrt{p_3^2 + p_4^2}} - \frac{x_3 x_4}{x_1} \right) \quad (54)$$

$$\partial_x H = \left(\left(\frac{2}{x_1^3} - \frac{x_4^2}{x_1^2} \right) p_3 - \frac{p_2 x_4}{x_1^2} + \frac{p_4 x_3 x_4}{x_1^2}, 0, p_1 - \frac{p_4 x_4}{x_1}, \frac{p_2}{x_1} + \frac{2 p_3 x_4}{x_1} - \frac{p_4 x_3}{x_1} \right) \quad (55)$$

$$\partial_{xx} H = \begin{pmatrix} \frac{2 p_2 x_4}{x_1^3} - \left(\frac{6}{x_1^4} - \frac{2 x_4^2}{x_1^3} \right) p_3 - \frac{2 p_4 x_3 x_4}{x_1^3}, 0, \frac{p_4 x_4}{x_1^2}, \frac{p_4 x_3}{x_1^2} - \frac{2 p_3 x_4}{x_1^2} - \frac{p_2}{x_1^2} \\ 0, 0, 0, 0 \\ \frac{p_4 x_4}{x_1^2}, 0, 0, -\frac{p_4}{x_1} \\ \frac{p_4 x_3}{x_1^2} - \frac{2 p_3 x_4}{x_1^2} - \frac{p_2}{x_1^2}, 0, -\frac{p_4}{x_1}, \frac{2 p_3}{x_1} \end{pmatrix} \quad (56)$$

$$\partial_{px} H = \begin{pmatrix} 0, 0, 1, 0 \\ -\frac{x_4}{x_1^2}, 0, 0, \frac{1}{x_1} \\ \frac{2}{x_1^3} - \frac{x_4^2}{x_1^2}, 0, 0, \frac{2 x_4}{x_1} \\ \frac{x_3 x_4}{x_1^2}, 0, -\frac{x_4}{x_1}, -\frac{x_3}{x_1} \end{pmatrix} \quad (57)$$

$$\partial_{pp} H = \begin{pmatrix} 0, 0, 0, 0 \\ 0, 0, 0, 0 \\ 0, 0, \frac{\bar{\Gamma}}{\sqrt{p_3^2 + p_4^2}} - \frac{\bar{\Gamma} p_3^2}{(p_3^2 + p_4^2)^{3/2}}, -\frac{\bar{\Gamma} p_3 p_4}{(p_3^2 + p_4^2)^{3/2}} \\ 0, 0, -\frac{\bar{\Gamma} p_3 p_4}{(p_3^2 + p_4^2)^{3/2}}, \frac{\bar{\Gamma}}{\sqrt{p_3^2 + p_4^2}} - \frac{\bar{\Gamma} p_4^2}{(p_3^2 + p_4^2)^{3/2}} \end{pmatrix} \quad (58)$$

As before, we consider a Bolza Problem with Fixed Time and Free Final state. In this problem, the target variety is the complete state space \mathbb{R}^4 , so $\Sigma = I_{4,4}$ and $\Pi = \emptyset$. We can produce a spiral similar to the one obtained for the quadratic cost case and test the sufficiency (see Figs. 7 and 8). We select $\bar{\Gamma} = 0,004$ and $\chi = 0,31$. The switching function is always positive. We integrate Riccati using the BC $U_{t_f} = I_{4,4}$, $V_{t_f} = -Q_{t_f}$, $Q_{t_f} = \partial_{xx} l(x_{t_f}) = -\partial_{xx} E(x_{t_f})$. The zero of the $\det(U_t)$ appears at $t = -156.65$, as we can verify by Figs. 9 and 10. This conjugate point can be used only to demonstrate sufficiency, that is, we cannot demonstrate, as was done in the case of quadratic cost, that, for $t_0 < -156.65 \text{sec}$ the extremal is not a minimum. This is due to the fact that the Strong Normality property can be demonstrated at the right terminal but not at the left terminal.

Fig. 7 Plane extremal: $\rho(\vartheta)$

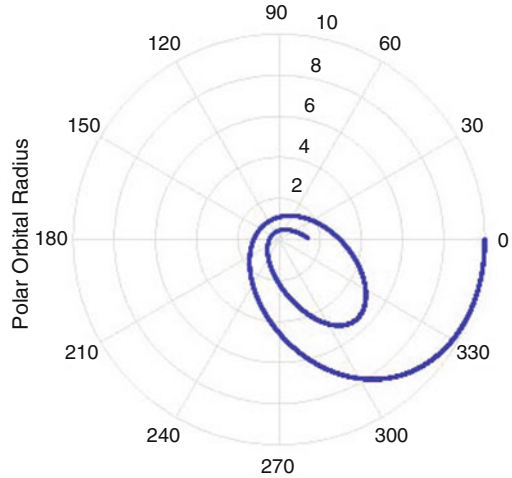
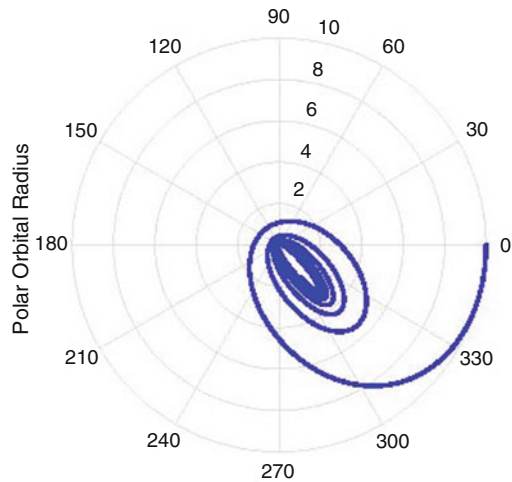


Fig. 8 Plane extremal: $\rho(\vartheta)$



7.3 Three Impulse Orbital Transfer

We verify in this example the SC for a general three impulse transfer moving all the orbital coordinates but the semimajor axis a_0 . The extremal under study is the same extremal given in Ref. [16] Ch. IX, with $45deg.$ rotations of g, I, h . Specifically, $e_0 = 0.5, e_f = 0.5, a_0/a_f = 1, g_0 = 0, g_f = 45deg, I_0 = 90deg, I_f = 45deg, h_0 = 0, h_f = 45deg, x_0 = [0.6666, 0, 1.3333, 0, 0, 0]^T$

$$x_f = [0.4714, 0.4714, 1.3333, 0.7071, 0.7853, 5.9015]^T$$

The final co-state is $p_f = [-0.2083, 0.0812, 0.2177, -0.1604, 0.2289, 0]^T$. The extremal is the result of a Two-Boundary-Value Problem where we have fixed

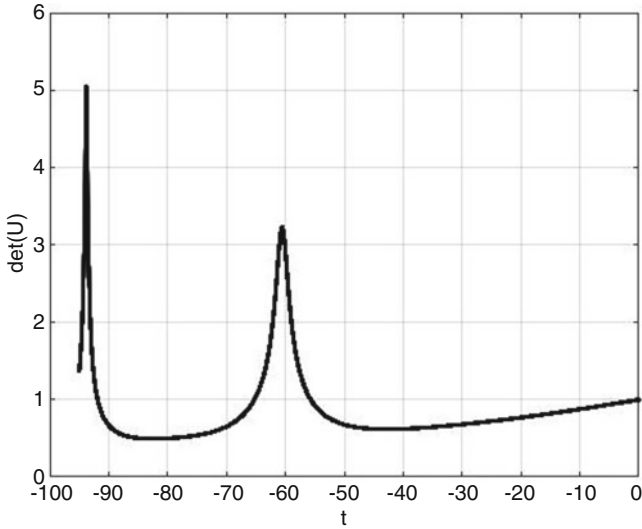


Fig. 9 Plane extremal: $\det(U)$

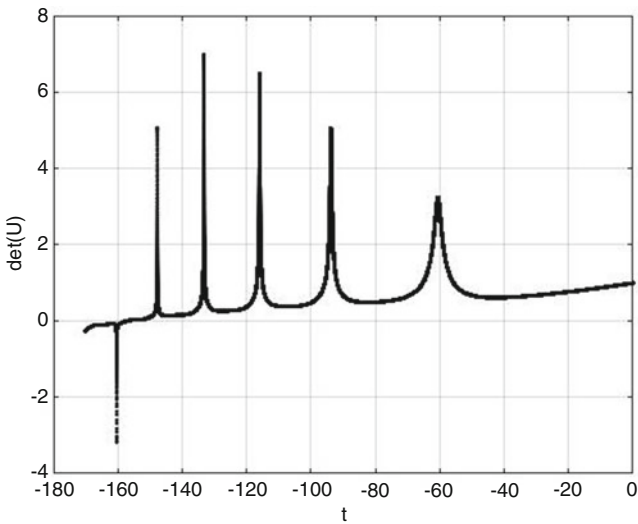


Fig. 10 Plane extremal: $\det(U)$

the values of $x(0)$ and $x_1(s_f), x_2(s_f), x_3(s_f), x_4(s_f), x_5(s_f), p_6(s_f), H(x_{s_f}, p_{s_f})$. The values of $x_6(s_f)$ and s_f are free. The target is reached at $s_f = 0.7799$.

The overall trajectory in the Cartesian space is shown in Fig. 11. The large rotations maneuvers are obtained by raising the transfer orbit apogee. The dynamics of the extremal in the invariant coordinates is shown in Figs. 12 and 13. The tangent space of the target variety at the final terminal is $\Sigma = (0, 0, 0, 0, 0, 1)^T$. The orthogonal complement can be written as

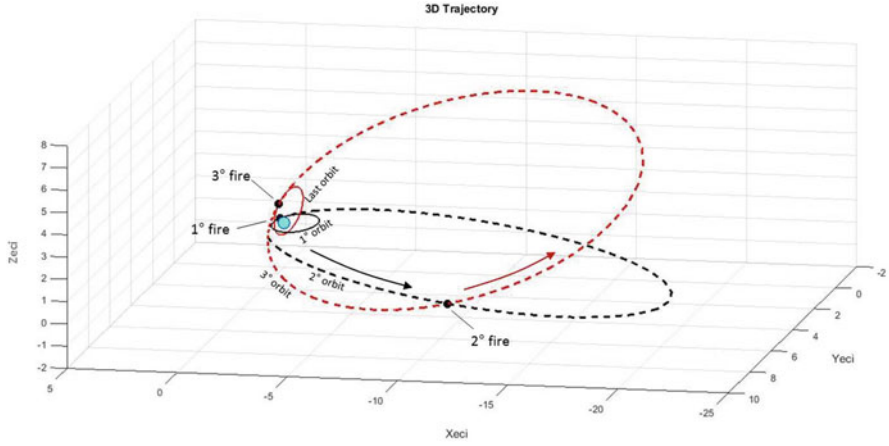


Fig. 11 Transfer trajectories

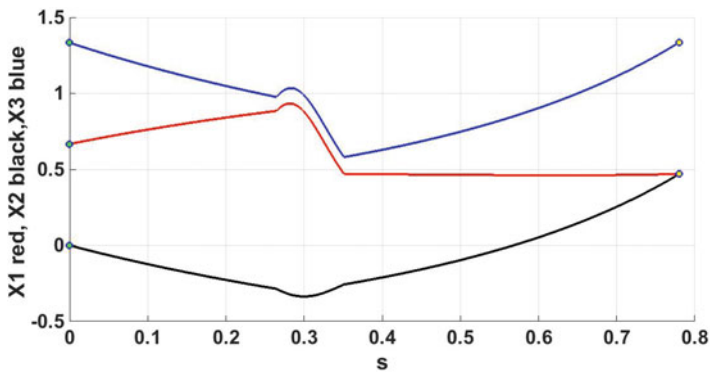


Fig. 12 x_1, x_2, x_3 vs s

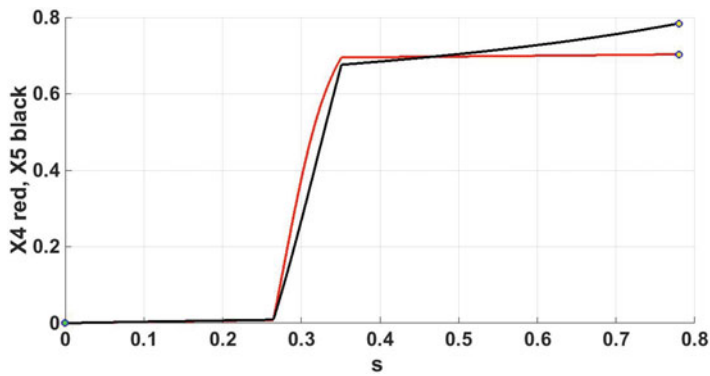


Fig. 13 x_4, x_5 vs s

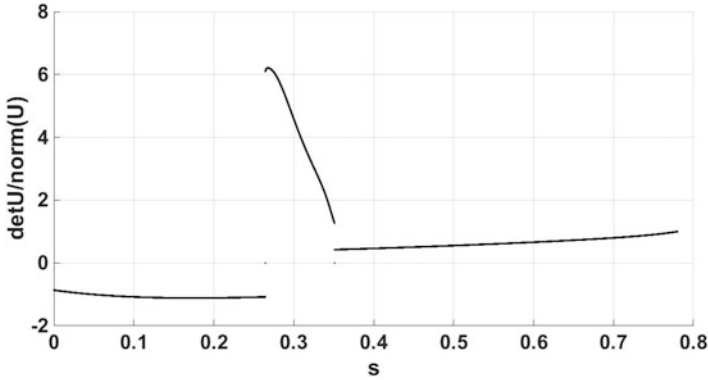


Fig. 14 $\det(U)/|U|$, $N = 1$

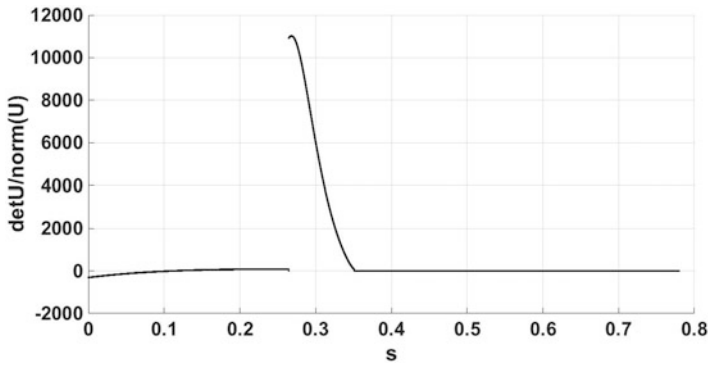


Fig. 15 $\det(U)/|U|$, $N = 10$

$\Pi = (I_{5,5}, 0_{5,1})^T$
 $N = \Pi \Pi^T \dot{\hat{x}}_{s_f} / |\Pi \Pi^T \dot{\hat{x}}_{s_f}|$, $M = [\Sigma, N]^\perp$, $\zeta = \dot{\hat{x}}_{s_f} / |\Pi \Pi^T \dot{\hat{x}}_{s_f}|$, $\lambda = \dot{\hat{p}}_{s_f} / |\Pi \Pi^T \dot{\hat{x}}_{s_f}|$
 Q_{s_f} is written following Theorem 1 with $\partial_{\sigma,\sigma} g = 0$ in the target coordinates:

$$\begin{pmatrix} 0 & -\lambda_\sigma & 0_{1,4} \\ -\lambda_\sigma^T & \zeta_\sigma^T \lambda_\sigma - \zeta_\pi^T \lambda_\pi & 0_{1,4} \\ 0_{4,1} & 0_{4,1} & \mathcal{N} I_{4,4} \end{pmatrix} = \begin{pmatrix} Q_{\sigma,\sigma} & Q_{\sigma,v} & Q_{\sigma,\mu} \\ Q_{v,\sigma} & Q_{v,v} & Q_{v,\mu} \\ Q_{\mu,\sigma} & Q_{\mu,v} & Q_{\mu,\mu} \end{pmatrix} \quad (59)$$

We then transform the Q_{s_f} from the local target coordinates to the natural coordinates using the transformation $[\Sigma, v, M]$ and then backward integrate Q_s for $\mathcal{N} = 1, 10, 20$.

With $\mathcal{N} = 1$, we get $\det(U_s)/|U_s|$ as in Fig. 14. With $\mathcal{N} = 10$, we get $\det(U_s)/|U_s|$ as in Fig. 15. With $\mathcal{N} = 20$, we get $\det(U_s)/|U_s|$ as in Figs. 16, 17. This last Q_s confirms the minimality of the extremal.

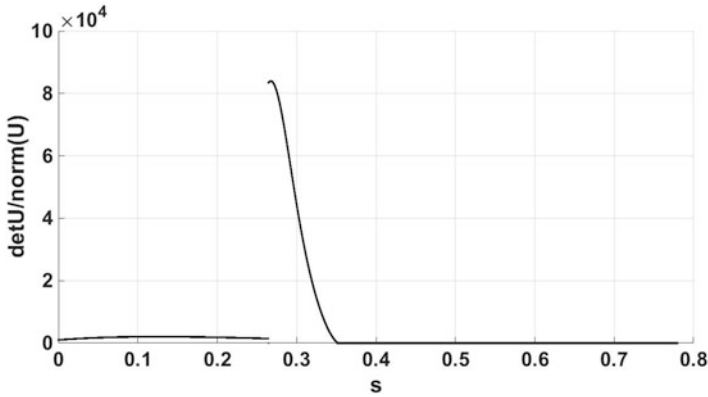


Fig. 16 $det(U)/|U|$, $N = 20$

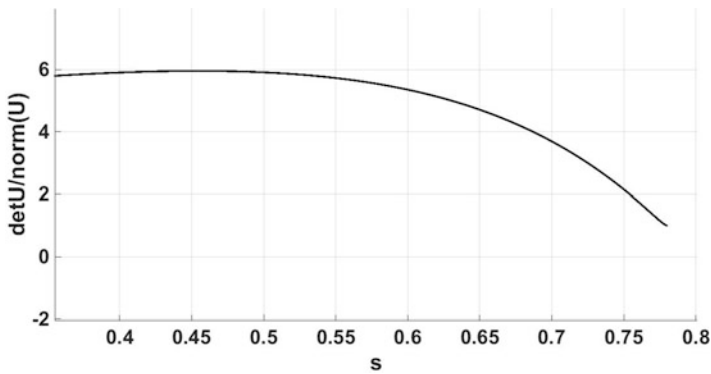


Fig. 17 $det(U)/|U|$, $N = 20$ zoom on the final part

References

1. L.Mazzini, *Extended Sufficient Conditions for Strong Minimality in the Bolza Problem. Applications to Space trajectory Optimization*, JOTA, Journal 10957, Article No. 1798, 2021/1/2
2. V. Zeidan, *Extended Jacobi Sufficiency Criterion for Optimal Control*, SIAM, Journal of Control and Optimization, Vol.22, No 2, Mar. 1984.
3. V. Zeidan, *Sufficiency Conditions with Minimal Regularity Assumptions*, Applied Mathematics and Optimization 20:19–31 (1989), Springer Verlag New York.
4. V. Zeidan, *Sufficient Conditions for the generalized problem of Bolza*, Transactions of the American Mathematical Society, Vol.275, Number 2, February 1983.
5. D.G. Hull, *Sufficient Conditions for a Minimum of the Free-Final-Time Optimal Control Problem*, JOTA, Vol. 68, No. 2, Feb. 1991.
6. D.G. Hull, *Optimal Control Theory for Applications*, 2003 Springer-Verlag New York.
7. L.J. Wood, A.E. Bryson, *Second-order optimality conditions for variable end time optimal control problems*, AIAA Journal, VOL. 11, No 9, Sept. 1973

8. H. Schattler, U. Ledzewicz , *Geometric Optimal Control: Theory, Methods and Examples*, Interdisciplinary Applied Mathematics 38, Springer (2012)
9. A.A.Agrachev, G. Stefani, P.Zezza , *Strong Optimality for a Bang-Bang Trajectory*, SIAM J. Control and Optimization (2002), Vol. 41, No. 4, pp. 991–1014
10. F.H. Clarke, *Generalized Gradients and Applications*, Transactions of the American Mathematical Society, Vol. 197, 1975
11. N.P.Osmolovskji, H.Maurer, *Applications to Regular and Bang-Bang Control: Second-Order Necessary and Sufficient Optimality Conditions in Calculus of Variations and Optimal Control*, SIAM, 2012
12. V. Zeidan, P. Zezza , *The Conjugate point condition for smooth control sets*, Journal of Mathematical Analysis and Applications, 572–589 (1988)
13. A.F. Filippov, *Differential Equations with Discontinuous Right Hand Sides*, Springer, 1988
14. J.W. Jo, J. E. Prussing, *Procedure for Applying Second-Order Conditions in Optimal Control Problems*, Journal of Guidance, Control and Dynamics, Vol. 23, No.2, March-April 2000
15. L.J. Wood, *Sufficient conditions for a local minimum of the Bolza Problem with multiple terminal point constraints*, AAS/AIAA Astrodynamics Specialists Conference, Durango, Colorado August 19–22, 1991, AAS Publication Office, P.O. Box 28130, San Diego CA 92128
16. L.Mazzini, *Time Open Orbital Transfer in a Transformed Hamiltonian Setting*, Journal of Guidance, Control and Dynamics, Vol. 36, No. 5, September-October 2013
17. L. Mazzini, *Finite Thrust Orbital Transfers*, Acta Astronautica, AA-D-13-00699, 2014
18. L. Mazzini, *Flexible Spacecraft Dynamics, Control and Guidance*, Springer, 2016

Evolutionary Optimisation of a Flexible-Launcher Simple Adaptive Control System



Erwin Mooij

1 Introduction

From the early days in aeronautical engineering, where aircraft design problems have ranged from wing divergence and control reversal to dynamic flutter calculations for avoiding wing failure, static, and dynamic aeroelasticity issues have caused many control challenges and even loss of (fighter) aircraft during high-speed manoeuvring (Schwanz and Cerra 1984). Not only can aircraft suffer from aeroelastic effects, but also (small) conventional launch systems, which have long and slender bodies, may suffer from an unwanted coupling between the rigid body and its flexible modes. Even more so than for aircraft, this is not an isolated problem. During the launcher's flight, it uses a large amount of oxidiser and fuel, giving rise to large changes in mass properties and thus the flexible response. Because also the operational and atmospheric environment varies significantly, the entire flight profile should be examined rather than a single worst-case point, to identify the stability and controllability characteristics of the launch vehicle.

To control such a (very) non-linear system, robust non-linear control systems are required to stabilise the system and respond to both modelled and unmodelled disturbances. Two (non-linear) controllers that can potentially handle the aforementioned perturbations are an Incremental Non-linear Dynamic Inversion (INDI) controller and a system based on Simple Adaptive Control (SAC). Amongst others, INDI controllers have shown robust performance when applied to quadrotors (Smeur et al. 2016), both in a simulation environment and during flight tests, as well as hydraulic robot motion control (Huang et al. 2019). The alternative candidate, SAC, has shown good performance for a variety of applications in the fields of

E. Mooij (✉)

Delft University of Technology, Faculty of Aerospace Engineering, Delft, The Netherlands
e-mail: e.mooij@tudelft.nl

autopilot design (Barkana 2004), space-telescope control (Mehiel and Balas 2004), flexible structures (Barkana 2016), entry systems (Mooij 2018) and satellites with flexible appendages (Gransden and Mooij 2018).

The focus of this chapter is, however, not to design the best possible control system, but to develop a methodology to improve the performance of a controller with multiple design parameters. The design of linear control systems, such as the traditional proportional, integral, and derivative (PID) controllers, can be easily done, using, for instance, Bode plots, Nyquist criteria, etc. For non-linear controllers, the design criteria are much harder to formulate. Having concrete performance indices, though, would facilitate the use of optimisation algorithms that can then be used to improve the controller performance. To show the benefit of such a methodology, we will centre it around the design of a SAC system, as it has many more design parameters and would show the benefit of the proposed methodology.

Due to the nature of the control system design, performance optimisation is relatively difficult for the following reasons: (i) a large number of design parameters, (ii) a complex system, (iii) no analytical gradient information, (iv) a large parameter search space, (v) non-linear constraints and (vi) multiple objectives that may be conflicting. One (global) optimisation technique that may prove useful for this particular problem is the one based on evolutionary strategies. These have arisen from the desire to model the biological processes of natural selection and population genetics, with the original aim of designing autonomous learning and decision-making systems (Holland 1975). Evolutionary algorithms, and their binary counterparts genetic algorithms, have found widespread use in engineering systems (Zalzala and Fleming 1997), *e.g.*, aerodynamic plan-form design, optimal motion of industrial robot arms, and the design of VLSI layouts. Also, in the field of control engineering, many applications can be found: Tanaka and Chuang (1995) applied a genetic algorithm in combination with a neural network to the scheduling of linear controllers for the X-29, whereas Menon et al. (1995) used genetic programming for the synthesis of a non-linear flight control system of a high-performance aircraft. Fleming and Purshouse (2001) have given an extensive overview of genetic algorithms in control systems engineering: applications include controller design and system identification, as well as fault diagnosis, stability analysis and sensor-actuator placement.

It is stressed that the proposed design methodology could well be connected to other (multi-objective) optimisation algorithms, such as particle swarm optimisation, differential evolution or ant-colony optimisation, to name but just a few. The evolutionary algorithm has been selected as a showcase, mainly for its ease of implementation, not claiming that it is the best method to use. For similar reasons as the selection of the simple adaptive control system, we want to present a design approach for control systems with multiple design parameters and potentially conflicting performance objectives, thereby highlighting several steps in the design process.

As a reference, the two-stage PacAstro launcher for small payloads up to 225 kg has been selected for its availability of some geometrical and structural data.¹ The launcher is treated as a flexible beam with lumped masses to account for the subsystems and the fuel. Its design and modelling has been extensively discussed in earlier work, see, for instance, the work by Mooij and Gransden (2016), and will only be summarised here to have some insight in the system that we will be working with.

The layout of the rest of this chapter is as follows. In Sect. 2, the simulation model is introduced, *i.e.*, the pitch-plane state-space model of a flexible launcher. In Sect. 3, the control system design is covered, starting with the definition of performance metrics to be used in the (numerical) optimisation procedure, then followed by the theory on simple adaptive control systems, and concluded by a summary of the implementation and application of this control system to the flexible launcher. The optimisation problem is formulated in Sect. 4, including a top-level description of the evolutionary algorithm. Section 5 presents the results, divided into those obtained with a single-objective and multi-objective approach. Section 6 concludes this chapter with some final remarks.

2 Pitch-plane State-space Model of Flexible Launcher

For a first analysis towards investigating the stability and control characteristics of flexible launchers, it suffices to consider the (linearised) pitch-plane motion only. Mooij and Gransden (2016) describe a state-space model, derived for the error dynamics of a flexible launcher, and the configuration for which is shown in Fig. 1. For that error dynamics model, input is a modal description as a function of current mass, the normal-load and pitch-moment distribution, and, of course, the flight conditions. The mass matrix is created using a consistent formulation for a linearised beam element. Furthermore, the launcher is assumed to move with a steady-state velocity u_0 , and the local deformation is determined by the combination of thrust, T , gravity, mg_d , aerodynamic normal force, N , and aerodynamic pitch moment, M .

In its general form, the system equation of this state-space model is given by

$$\dot{\mathbf{x}} = \mathbf{A}\mathbf{x} + \mathbf{B}\mathbf{u} \quad (1)$$

with \mathbf{A} and \mathbf{B} being the system and control matrix, respectively. Due to the different nature of groups of state variables, it makes sense to partition \mathbf{A} and \mathbf{B} into sub-

¹ PacAstro was a US transportation service company, formed in 1990, to provide low-cost transportation of small satellites to Low Earth Orbit for approximately \$5 million per launch using proven technology (Fleeter et al. 1992). Unfortunately, the launcher never came to operation despite several engine tests and three launch contracts, due to the lack of development funding. The company ceased to be in 1997. In Appendix A, some geometrical and mass properties have been provided.

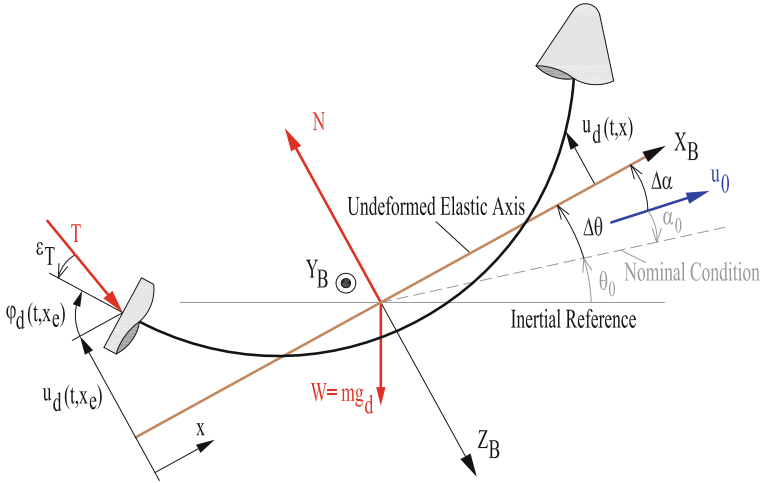


Fig. 1 Flexible vehicle definitions

matrices representing the rigid-body motion, the engine dynamics, and the flexible-body motion, thereby identifying the coupling terms between the different sets. The corresponding state-space matrices are then written as

$$\mathbf{A} = \begin{bmatrix} \mathbf{A}_{RR} & \mathbf{A}_{RE} & \mathbf{A}_{RF} \\ \mathbf{A}_{ER} & \mathbf{A}_{EE} & \mathbf{A}_{EF} \\ \mathbf{A}_{FR} & \mathbf{A}_{FE} & \mathbf{A}_{FF} \end{bmatrix} \quad \text{and} \quad \mathbf{B} = \begin{pmatrix} \mathbf{B}_R \\ \mathbf{B}_E \\ \mathbf{B}_F \end{pmatrix} \quad (2)$$

with

1. R for the rigid-body states angle of attack,² α , pitch angle, θ , and pitch rate, q
2. E for the engine states $\ddot{\varepsilon}_T$ (angular acceleration), $\dot{\varepsilon}_T$ (angular velocity), and ε_T (the angular position or swivel angle). These states originate from the assumption that the engine is modelled as an electro-hydraulic servo system, represented by a third-order transfer function.
3. F for the flexible-body states $\dot{\eta}_i$ and η_i for mode i . The total number of states in this group depends on how many bending modes n_f are taken into account.

² Pitch-plane translational motion is defined by u_0 and the vertical velocity, w . However, to study the rotational motion for a single point in the trajectory, it makes more sense to use the angle of attack, α , which can be derived from the (small) w through the relation

$$\Delta\alpha = \frac{\Delta w}{u_0} \quad \Rightarrow \quad \Delta\dot{\alpha} = \frac{\Delta\dot{w}}{u_0} \quad (3)$$

The state vector, \mathbf{x} , is thus given by $\mathbf{x}^T = (\alpha \theta q \ddot{\varepsilon}_T \dot{\varepsilon}_T \varepsilon_T \dot{\eta}_1 \eta_1 \dots \dot{\eta}_{n_f} \eta_{n_f})^T$. The only control is the commanded swivel angle, so $u = \varepsilon_{T,c}$. The corresponding sub-matrices, derived by Mooij and Gransden (2016), are given in Appendix B.

The engine is considered to be an electro-hydraulic servo system, approximated by a third-order system (Rolland Collette 1967),

$$(s^3 + 2\zeta_e \omega_e s^2 + \omega_e^2 s + K_e \omega_e^2) \varepsilon_T = K_e \omega_e^2 \varepsilon_{T,c} \tag{4}$$

with defining parameters ω_e and ζ_e , the natural frequency and damping of the engine dynamics, and a gain, K_e , an amplification factor that improves the response (time). The values used in this study are $\omega_e = 50 \text{ rad/s}$, $\zeta_e = 0.7$, and $K_e = 15$. Given the above transfer function means that the acceleration derivative ($\ddot{\varepsilon}_T$) is excited by $K_e \omega_e^2 \varepsilon_{T,c}$, with the latter parameter being the commanded swivel angle. In case of a significant attitude correction, $\varepsilon_{T,c}$ may be deflected at its limit value (of $\pm 6^\circ$), which means that $\ddot{\varepsilon}_T = 3927 \text{ rad/s}^3$. Consequently, even after a mere 0.01 s, the acceleration $\ddot{\varepsilon}_T$ will be about 40 rad/s^2 . It is clear that therefore some (mechanical) limits should be imposed on the engine states. As mentioned, $\varepsilon_{T,max} = 6^\circ$, but the values for the maximum acceleration are not known for the PacAstro. Sutton and Biblarz (2017) mention a value of $\ddot{\varepsilon}_T = 30 \text{ rad/s}^2$ and $\dot{\varepsilon}_T = 20 \text{ rad/s}$ for the Space Shuttle main engines. Even though these engines may be heavier than the one of the current study, they give a good indication. Considering smaller (and lighter) nozzles, the acceleration limit is put to $\ddot{\varepsilon}_{T,max} = 50 \text{ rad/s}^2$.

In Fig. 2, the reference trajectory of the PacAstro until first-stage burnout ($t_f = 126 \text{ s}$, $h_f = 67.7 \text{ km}$) is plotted. The figure shows an almost linear increase in velocity with altitude and, similarly, also in Mach number up to a maximum value of $M = 8.8$. The dynamic pressure peaks at $\bar{q} = 43.5 \text{ kPa}$ at around $h = 11.1 \text{ km}$ (time of maximum dynamic pressure (TMDP), $t = 63 \text{ s}$, $M = 1.83$). With an initial

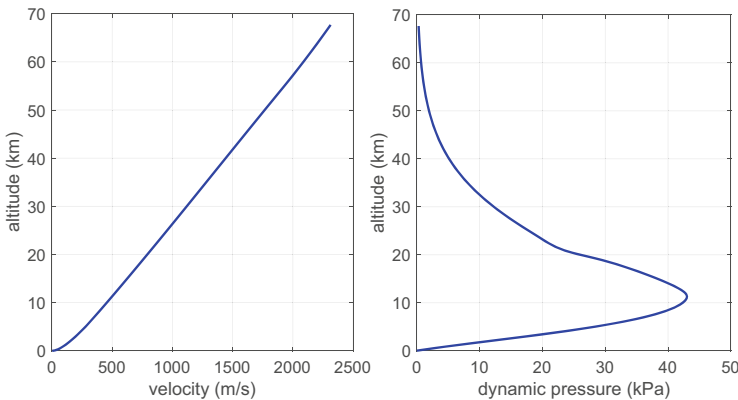


Fig. 2 PacAstro reference trajectory until first-stage burnout

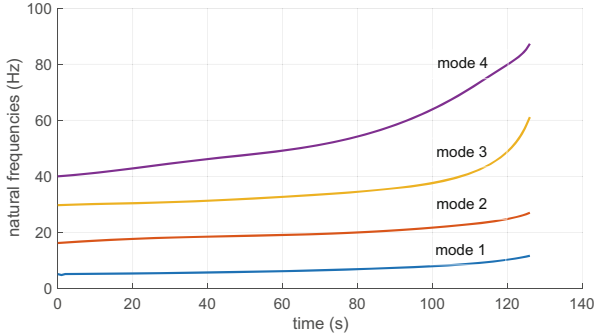


Fig. 3 Natural frequencies of the launch vehicle during flight

mass of $m_0 = 32,475$ kg and a constant mass flow of $\dot{m} = -186.6$ kg/s, the final mass is $m_f = 8963.4$ kg.

The normalised bending modes, necessary to find the in-flight bending deformations of the longitudinal axis, were calculated in Matlab[®] using an in-house finite-element mesher and solver. At $t = 0$ s, the four lowest initial natural frequencies are 5.2, 16.2, 29.7, and 40.0 Hz, respectively, whereas their variation as a function of the flight time is shown in Fig. 3.

To generate an N -degree-of-freedom approximate differential equation model for a continuous system, the displacement of the continuous system is expanded as a linear combination of N prescribed shape functions. In other words, the deformation $u(x, t)$ is approximated by

$$u_d(x, t) = \sum_{i=1}^N \phi_i(x) \eta_i(t) \quad (5)$$

where x is the spatial coordinate, t is the time, $\phi_i(x)$ is the i th assumed mode shape, $\eta_i(t)$ is the i th generalised coordinate, and N is the number of terms or modes that are included in the approximation. The rotation $\varphi_d(x, t)$ of (an element of) the structure is given by

$$\varphi_d(x, t) = - \sum_{i=0}^N \sigma_i(x) \eta_i(t) \quad (6)$$

with $\sigma_i(x) = -\frac{d\phi_i(x)}{dx}$. In the current research, for the mode shapes, ϕ_i , the eigenvectors, derived from the finite-element model's mass and stiffness matrices, will be used.

3 Control System Design

3.1 Introduction

As benchmark, we assume a feedback law with proportional and derivative gains of $K_p = 2.8$ (on θ) and $K_d = 0.9$ s (on q) (Mooij and Gransden 2016). This design is based on a closed-loop rigid-body requirement of $3 \text{ rad/s} \leq \omega_r \leq 8 \text{ rad/s}$, with a damping factor of $\zeta \approx 0.7$, and designed for the point of maximum dynamic pressure ($t = 63$ s).³

The Bode plot for the elastic system is given in Fig. 4 for the moment of maximum dynamic pressure. It shows that the elastic mode may pose a problem while controlling high-frequency oscillations due to, for instance, turbulence. It is clear that perturbations will be amplified while controlling an error in the pitch angle (by using the engine swivel angle). However, in case the deformations remain small, the problems will most likely remain limited. At its natural frequency of 37.3 rad/s, the bending mode spikes. The second bending mode spikes at a frequency around 105 rad/s and will probably have marginal to no effect on the control.

Section 3.2 will summarise the design elements of the selected robust control system that should be able to counter the (non-linear) effects of engine dynamics and flexible modes.

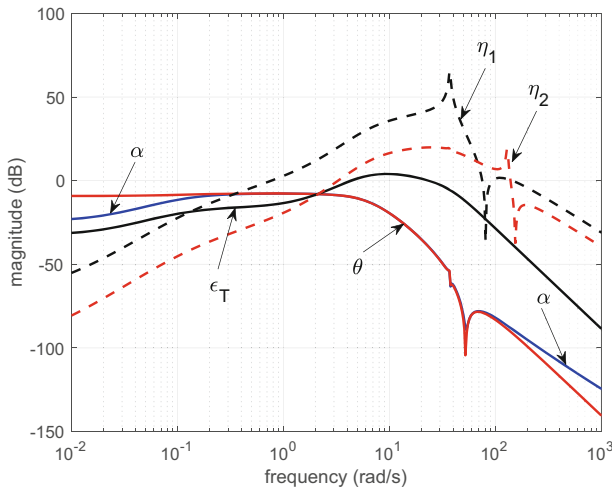


Fig. 4 Bode plots for the time of maximum dynamic pressure ($t = 63$ s)

³ The achieved closed-loop natural frequencies for rigid body and engine were $\omega_{r,cl} = 4.9 \text{ rad/s}$ (rigid body) and $\omega_{e,cl} 37.1 \text{ rad/s}$ (engine), with damping factors $\zeta_{cl} = 0.75$ and $\zeta_e = 0.64$.

To allow for comparison of the different control system designs, the performance of a controller can be judged by several metrics. For the current control system design, we may look at the minimum state deviation of the plant with respect to the guidance commands. Another objective in the design could be to minimise the control effort that is required to influence the launcher's behaviour. For instance, in the case of launcher control system design, these two objectives can be expressed as the integrated pitch-angle deviation and the integrated swivel angle (equivalent to, for instance, the total hydraulic power required), and are given by

$$\sum_{\theta_{err}} = \int_0^t |\theta_c(t) - \theta_p(t)| dt \quad \sum_{\varepsilon_T} = \int_0^t |\varepsilon_T(t)| dt \quad (7)$$

A graphic representation of the above metrics is shown in Fig. 5a, represented by the grey areas enclosed by the curves. It may be obvious that both individual areas should be as small as possible for optimal controller performance, which means that their numerical equivalent can be used to evaluate different controller designs. In the given example, $\sum_{\theta_{err}} = 6.55^\circ\text{s}$ and $\sum_{\varepsilon_T} = 17.21^\circ\text{s}$.

Another metric could be the oscillatory behaviour of either the state or control variables. Oscillations in the control may not only be energy expensive and a burden on the hardware, and it could also lead to instabilities. To detect oscillations or otherwise discrete changes in the controls, the cumulative moving standard deviation can be used. For a subset j of n_s out of a total of N samples of an arbitrary control signal u , the moving mean is defined as $\bar{y}_j = \frac{1}{n_s} \sum_{i=j}^{j+n_s-1} u_i$. Here, j will run from $j = 1+n_s/2$ to $N-n_s/2$, so each subsequent subset will shift by only one sample. Let the squared deviation from this mean be defined as $s_{u,j} = (u_{j+n_s/2} - \bar{y}_j)^2$, which represents the value at the midpoint of subset j . The cumulative standard deviation, F_u , for subset j is then

$$F_{u_j} = \sqrt{\frac{1}{N - n_s - 1} \sum_{k=1}^j s_k} \quad (8)$$

Figure 5b shows the oscillation pattern of the swivel angle for two (poor) controller performances. The cumulative standard deviation increases more rapidly when a discrete jump occurs or when there is an interval with persistent oscillations. As a metric, the grey area under the curve can be used, which, while minimised, would lead to a smoother behaviour. For the two cases shown, the numerical values are $F_{\varepsilon_T} = 36.2^\circ$ and 116.9° , respectively.

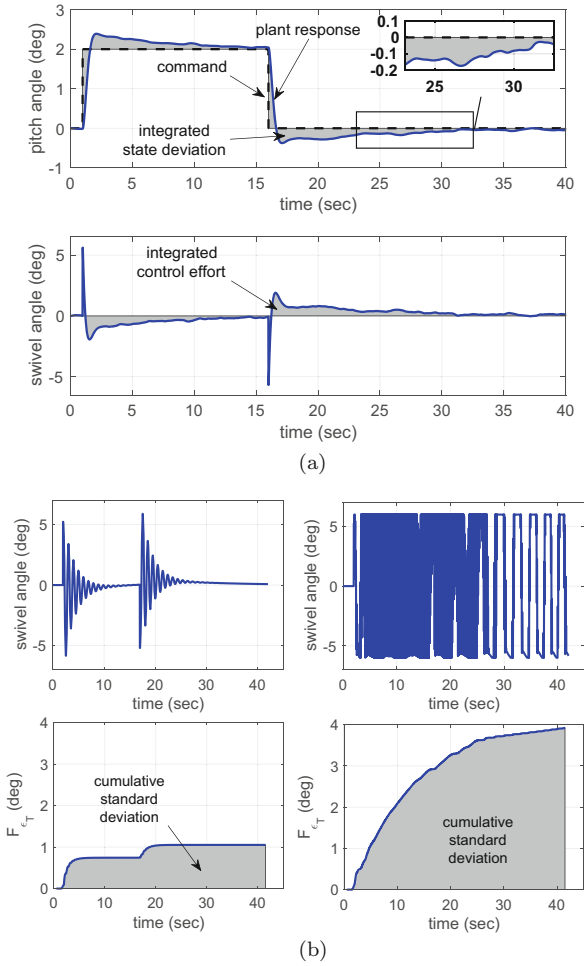


Fig. 5 Controller performance indices. **(a)** Integrated state deviation and control effort: $\sum_{\theta_{err}} = 6.55^\circ\text{s}$ and $\sum_{\epsilon_T} = 17.21^\circ\text{s}$. **(b)** Oscillation metrics: $F_{\epsilon_T} = 36.2^\circ$ (left) and 116.9° (right)

3.2 Simple Adaptive Control

The concept of so-called simple adaptive control (SAC) is based on the principle of tracking the output of a reference model (Kaufman et al. 1998). Therefore, this system could also be classified as a model reference adaptive control (MRAC) system, although a principal difference from the original MRAC is that full state knowledge of the plant to be controlled is not required. A schematic overview of

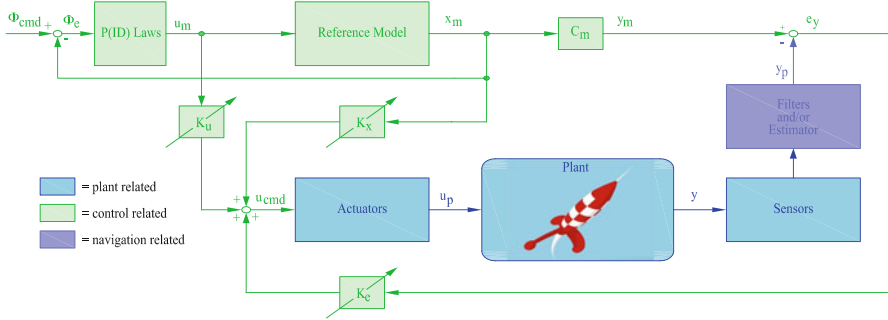


Fig. 6 Basic architecture of a simple adaptive control algorithm

a simple adaptive controller is shown in Fig. 6. The (single-actuator) control law is given by

$$u_p(t) = \mathbf{K}_r(t)\mathbf{r}(t) \tag{9}$$

where $\mathbf{r}(t) = (e_y(t) \mathbf{x}_m^T(t) u_m^T(t))^T$ and $\mathbf{K}_r(t) = (K_e(t) \mathbf{K}_x^T(t) K_u(t))$. It can be seen that the model input \mathbf{u}_m and model state \mathbf{x}_m are required to form part of the input signal \mathbf{u}_p to the plant. Moreover, the so-called output error e_y serves as a feedback quantity to form the third element that composes u_p . The three gains, *i.e.*, K_e , \mathbf{K}_x , and K_u , are adaptive.

To compute the adaptive gains, \mathbf{K}_r is defined to be the sum of a proportional and an integral component:

$$\mathbf{K}_r(t) = \mathbf{K}_p(t) + \mathbf{K}_i(t) \tag{10}$$

with

$$\mathbf{K}_p(t) = e_y(t)\mathbf{r}^T(t)\mathbf{T}_p \tag{11}$$

$$\mathbf{K}_i(t) = \mathbf{K}_{i,0} + \int_0^t e_y\mathbf{r}^T(t)\mathbf{T}_i dt \tag{12}$$

In Eqs. (11) and (12), the weighting matrices \mathbf{T}_p and \mathbf{T}_i are positive semi-definite and positive definite, respectively. Note that the proportional gain component has a direct influence on the transient tracking behaviour but is strictly speaking not required to enforce asymptotic tracking, as \mathbf{T}_p can be zero; tracking is guaranteed by the integral gain. To improve the transient response by only using an integral gain, a constant gain value has been added to \mathbf{K}_i . An advantage over the use of the proportional gain is that this constant value is independent of e_y and is therefore non-zero even if e_y is zero.

One way to improve the damping of the system is to include the error derivatives in the output error vector and apply a form of PD error scaling. The attitude controller aims at simultaneously reducing both the pitch angle, θ , and the pitch rate, q (which equals $\dot{\theta}$). This means that if errors in both are added together (with a proper scaling), the combined error would be similar to the output of a PD controller. And we know of such controller that the D term improves stability and damping of the control. Thus, the generic formulation of the output error becomes in that case

$$e_y = \mathbf{K} (\mathbf{y}_m - \mathbf{y}_p) = \mathbf{K} (\mathbf{C}_m \mathbf{x}_m(t) - \mathbf{C}_p(\mathbf{x}_p, t) \mathbf{x}_p(t)) \quad (13)$$

where \mathbf{K} includes the appropriate ratio of adding the proportional and derivative signals together.

So far, an ideal environment has been considered. To cope with environmental disturbances, such as wind gust and turbulence, that lead to a persistent non-zero error and therefore to a continuous change in the integral gain \mathbf{K}_i , a robust design can be applied to adjust the integral gain and preventing it from reaching very high values. The integral term of Eq. (11) is adjusted as follows:

$$\dot{\mathbf{K}}_i = e_y(t) \mathbf{r}^T \mathbf{T}_i - \sigma_i \mathbf{K}_i(t) \quad (14)$$

Without the σ_i -term, $\mathbf{K}_i(t)$ is a perfect integrator and may steadily increase (and even diverge) whenever perfect output-following is not possible. Including the σ_i -term, $\mathbf{K}_i(t)$ is obtained from a first-order filtering of $e_y(t) \mathbf{r}^T \mathbf{T}_i$ and, therefore, cannot diverge, unless the output error diverges.

3.3 Implementation

The current application of SAC focuses on a flexible launch vehicle with third-order engine dynamics. As a reference model, a simplified model is chosen: a rigid representation of the same launcher, stabilised by a PD controller and ideal engine dynamics. The reference model includes pitch angle and pitch rate only, contrary to the rigid-body model given by Eq. (B.1). In this way, the model is insensitive to angle-of-attack perturbations and will provide a more stable model that is easier to follow. The reference model is excited by the output error, *i.e.*, the current difference between model output and plant output, and transformed to equivalent model state errors. If at every control sample the difference between the current state error and the one of the previous sample is added to the model state vector, the model controller will bring this error back to zero. In that way, the signals u_m and \mathbf{x}_m are created. Together with e_y , Eq. (13), the vector \mathbf{r} is composed, and the plant input u_p can be calculated according to Eq. (9), after having calculated \mathbf{K}_p and \mathbf{K}_i , Eqs. (11) and (12).

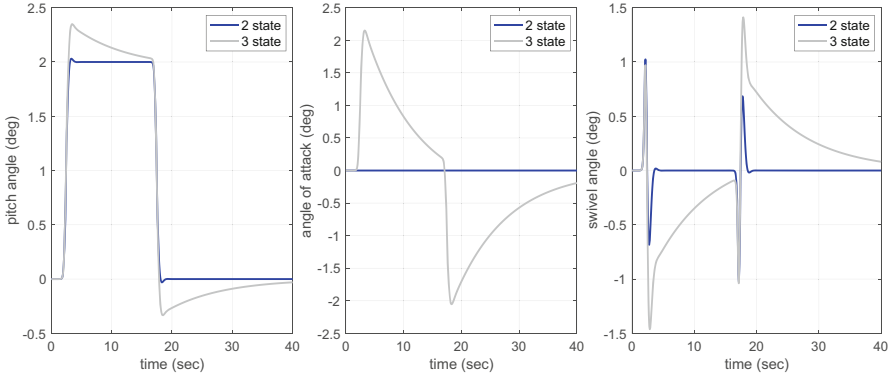


Fig. 7 Reference-model response to a 2° step command in pitch angle: difference between the two-state and three-state models (includes angle of attack)

So, the reference model is given by the reduced rigid-body model, and the full form of which is given in Appendix B:

$$\begin{pmatrix} \dot{\theta}_m \\ \dot{q}_m \end{pmatrix} = \begin{bmatrix} 0 & 1 \\ 0 & \frac{C_{mq} \bar{q} S_{ref} d_{ref}}{I_{yy}} \end{bmatrix} \begin{pmatrix} \theta_m \\ q_m \end{pmatrix} + \begin{bmatrix} 0 \\ \frac{L_e T}{I_{yy}} \end{bmatrix} \varepsilon_{T,m} \quad (15)$$

so $\mathbf{x}_m = (\theta_m \ q_m)^T$ and $u_m = \varepsilon_{T,m}$. The reference model is controlled by the benchmark PD controller, with $K_p = 2.8$ on the pitch-angle error and $K_d = 0.9$ on the pitch-rate error. The attitude command that the launcher has to follow is now enforced on the reference model, which will provide a smooth transient response that the plant will try to follow. The output error, e_y , will be formed as $e_y = K_p(\theta_m - \theta_p) + K_d(q_m - q_p)$, with the initial setting for the gains to be the same as for the reference-model controller. It is noted that both the model-controller gains and the output-error gains could be part of the optimisation process and do not necessarily have to be the same. However, initial runs showed that using the selected gains gives a good model performance. To avoid having an excessive number of design variables, we will keep these values for now. Finally, the nominal controller frequency is set to 100 Hz. This may seem like a rather large value, but it is, unfortunately, one of the characteristics of SAC (Messer et al. 1994).

Figure 7 shows the transient response of the reference model, while being subjected to a pitch-angle command of $\theta_c = 2^\circ$ for the time of maximum dynamic pressure ($t = 63$ s). For each plot, two curves are shown, *i.e.*, one for the model with two states, given by Eq. (15), and one for a three-state model. The latter model also includes the angle of attack, see Eq. (B.1) for the corresponding state matrix. The difference in response is immediately clear. Due to the strong coupling between angle of attack and pitch motion, a large angle of attack is induced. Because the launcher is unstable ($C_{m_\alpha} > 0$), it takes a lot longer and more control effort to stabilise the system. The two-state model settles almost immediately, and this is

exactly the kind of behaviour that we want the plant to have, thus confirming the choice of reference model.

The design parameters of the adaptive controller are the weighting matrices, \mathbf{T}_p and \mathbf{T}_i , the initial values of the integral gain, $\mathbf{K}_{i,0}$, and, as a safeguard against diverging output errors, the filter parameter, σ_i . The full form of either \mathbf{T}_p or \mathbf{T}_i is given by

$$\mathbf{T} = \begin{bmatrix} T_{e_y e_y} & T_{e_y \theta_m} & T_{e_y q_m} & T_{e_y \varepsilon_{T,m}} \\ T_{\theta_m e_y} & T_{\theta_m \theta_m} & T_{\theta_m q_m} & T_{\theta_m \varepsilon_{T,m}} \\ T_{q_m e_y} & T_{q_m \theta_m} & T_{q_m q_m} & T_{q_m \varepsilon_{T,m}} \\ T_{\varepsilon_{T,m} e_y} & T_{\varepsilon_{T,m} \theta_m} & T_{\varepsilon_{T,m} q_m} & T_{\varepsilon_{T,m} \varepsilon_{T,m}} \end{bmatrix} \tag{16}$$

which represents 16 design parameters per matrix. However, it is common practise to restrict to diagonal matrices, and thus only four parameters per matrix remain. With four initial gain values, $\mathbf{K}_{i,0}$, and a single filter parameter σ_i associated with e_y , the total number of design parameters can vary between 13 and 37.⁴

4 Optimisation Problem

Ever since its conception in the 1970s, there has been a non-wavering interest in problem-solving systems based on the principles of evolution: such systems maintain a population of potential solutions and include some selection process, which is based on the fitness of individuals, and some “genetic” operators that allow for the creation of new individuals. Almost each genetic (operating on binary strings) or evolutionary (operating on “real-life” parameters, *e.g.*, floating-point variables) algorithm has the following structure (Goldberg 1989, Michalewicz 1996):

```
begin
  initialise population P(0) with N individuals;
  evaluate P(0) and assign fitness to individuals;
  t := 1;
  repeat
    select P(t) from P(t - 1);
    recombine P(t) through crossover and mutation;
    evaluate P(t) and assign fitness to individuals;
    t := t + 1;
  until (termination condition)
end
```

⁴ The minimum number could actually be four, as the principal requirement that \mathbf{T}_i is positive definite dictates four diagonal elements larger than zero. The positive semi-definite condition of \mathbf{T}_p could in principle lead to $\mathbf{T}_p = \mathbf{0}$. All other parameters can be non-zero to improve the performance but can be zero in the baseline algorithm.

The above pseudo-code represents a probabilistic algorithm, which maintains a population of individuals, $P(t) = \{\mathbf{x}_1^t \cdots \mathbf{x}_N^t\}$ for iteration t . Each individual \mathbf{x}_i^t , which represents a potential solution to the problem at hand, is evaluated to give some measure of its “fitness.” A new population is formed by selecting the more fit individuals. Some members of the new population undergo transformations by means of genetic operators: unary transformations (mutation), which create new individuals by a small change in a single individual, and higher order transformations (crossover), which create new individuals by combining parts from two or more individuals. The termination condition can be a predefined number of iterations (also called generations) or a convergence criterion.

The applied operators in this study are a combination of simple, arithmetic and heuristic crossover, and multi non-uniform mutation. A detailed description of these (and other) operators can be found in the book by Michalewicz (1996). Here, we will restrict to a brief description. In simple crossover, two parents p_1 and p_2 are selected, and a simple single-point crossover is applied. This means that an independent parameter in p_1 is selected at random and one child is formed by taking the first part of p_1 (up to the selected parameter) and the second part of p_2 (onwards from the selected parameter). A second child is formed by the two remaining parts. Arithmetic crossover takes two parents p_1 and p_2 and performs an interpolation over a random distance along the line formed by the two parents. Heuristic crossover, finally, takes two parents p_1 and p_2 and performs an extrapolation along the line formed by the two parents outward in the direction of the better parent.

Non-uniform mutation randomly selects one variable x_j of an individual p_i and sets it equal to a non-uniform random number, with a (random) dependency on the generation number. This latter Gaussian distribution starts wide and narrows to a point distribution as the current generation approaches the maximum generation. In multi-non-uniform mutation, this operator is applied to each independent variable of the chosen individual.

For the selection method, we use stochastic universal sampling (SUS) (Baker 1987), which is some variation of roulette wheel selection (RWS) in the sense that the fitness determines the probability that the individual is selected. However, contrary to RWS where only one individual is selected, in SUS up to N individuals can be selected with multiple equally spaced pointers. By applying SUS, clustering of individuals in subsequent generations (genetic drift) will be reduced.

The fitness Φ_i of an individual i can either be directly or indirectly derived from its objective function(s). In single-objective optimisation, any one of the above defined performance metrics can be used directly. In case two or more objective functions are used, a trade-off has to be made if improving one objective will result in the simultaneous degradation of the other. From the available methods to derive a single fitness value from multiple objectives, the concept of Pareto ranking is used (Cvetković 2000, Fonseca 1995).

Pareto-based fitness assignment was first proposed by Goldberg (1989), who suggested the use of non-domination ranking and selection to move a population towards the Pareto front in a multi-objective optimisation problem. Fonseca (1995)

discusses a variation of this ranking method, which will be used in this study and is summarised below.

The problem under consideration is to simultaneously minimise the k components of a vector function $\mathbf{f} = (f_1, f_2, \dots, f_k)$, each of which is a function of the design variables $\mathbf{x} = (x_1, x_2, \dots, x_n)$. The problem has usually no unique solution, but a set of equally efficient (or non-inferior) alternative solutions, which together form the so-called Pareto-optimal set or Pareto front when they are plotted in relation to the inferior solutions. For a minimisation problem, a vector $\mathbf{f} = (f_1, f_2, \dots, f_k)$ is said to be inferior to $\mathbf{g} = (g_1, g_2, \dots, g_k)$ if \mathbf{g} is partially less than \mathbf{f} , *i.e.*,

$$\forall \mathbf{i} \in \{1, 2, \dots, k\}, g_i \leq f_i \wedge \exists \mathbf{i} \in \{1, 2, \dots, k\}, g_i < f_i \tag{17}$$

Consider now an individual \mathbf{x}_f at generation t with corresponding objective vector \mathbf{f} , and let $r_f^{(t)}$ be the number of individuals in the current population which are preferable (or superior) to it. The current position of \mathbf{x}_f in the individuals' rank is then given by

$$\text{rank}(\mathbf{x}_f, t) = r_f^{(t)} \tag{18}$$

Note that by definition the individuals that form the Pareto front all have rank zero. The rank-based fitness assignment is further developed as follows:

1. Sort population according to rank.
2. Assign fitness Φ by interpolating from the best individual to the worst according to some function. In the current study, an exponential function of the form

$$\Phi \left(r_f^{(t)} \right) = s \rho^{r_f^{(t)}} \tag{19}$$

is used, where s is the relative fitness ($s > 1$), whereas the parameter ρ should fulfil

$$\sum_{i=0}^{N-1} = \frac{N}{s} \tag{20}$$

with N being the population size. In the limit case of N approaching infinity, the above power series equals $\frac{1}{1-N}$, which yields $\rho = 1 - \frac{s}{N}$.

3. Average the fitness assigned to individuals with the same rank, to sample them at the same rate while keeping the global population fitness constant.

5 Results

In this section, we present the results of the optimisation study, where different combinations of design variables will be explored. Note that the results are in support to present (and discuss) the design methodology for control systems with more than just a few design parameters. All simulations are run for a single point in the trajectory, *i.e.*, the point of maximum dynamic pressure ($t = 63$ s). We will not try to get the best possible design and establish its robustness by doing an extensive sensitivity analysis. To do so would require quite some more space than we have available in this chapter.

To begin with, in Sect. 5.1, the parameter ranges will be established by doing a simple Monte Carlo simulation. Inspecting the results and varying the ranges will quickly lead to a design space that is not too large (and non-linear) and will allow the optimisation algorithm to find an optimal design. In case the design space is too large, convergence may become an issue for some evolutionary algorithms.

Section 5.2 will present the results for a single-objective optimisation. There, the focus is on minimising the integrated pitch-angle deviation, without looking at the associated control effort and possible oscillations in either state or control. Finally, in Sect. 5.3, the exercise is repeated by optimising multiple objectives simultaneously.

5.1 Design Space Exploration

The design space exploration will be done for the rigid launcher, as the optimisation later will be carried out for a so-called nominal (= ideal) system. The effect of engine dynamics and flexible modes will be studied later, after an optimal control system design has been established.

Assuming diagonal \mathbf{T}_p and \mathbf{T}_i , four initial integral gains, and one filter parameter, the 13 parameters are varied according to a uniform distribution. After some trial and error, the final ranges that were determined are the following:

1. \mathbf{T}_p : $T_{e_y e_y} \in [0, 400]$, $T_{\theta_m \theta_m} \in [0, 800]$, $T_{q_m q_m} \in [0, 1600]$, and $T_{\varepsilon_{T,m} \varepsilon_{T,m}} \in [0, 1600]$.
2. \mathbf{T}_i : $T_{e_y e_y} \in [0.15, 60]$, $T_{\theta_m \theta_m} \in [25, 10000]$, $T_{q_m q_m} \in [1.5, 600]$, and $T_{\varepsilon_{T,m} \varepsilon_{T,m}} \in [1, 400]$.
3. $\mathbf{K}_{i,0}$: each gain is sampled from the interval $[0, 5]$.
4. σ_i is sampled from $[0, 2]$.

A total of $N = 2500$ runs were executed, using the Mersenne Twister random generator, initialised with random seed 0.

In Fig. 8, the four objectives, integrated state deviation, $\sum_{\theta_{err}}$, integrated control effort, \sum_{ε_T} , and the two corresponding oscillatory indices, F_θ and F_{ε_T} , have been plotted. It is obvious that there is a large variation in performance, but it appears

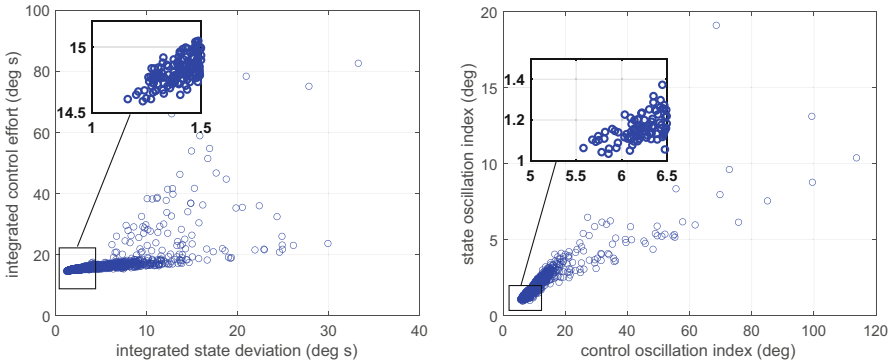


Fig. 8 Design space exploration: four objectives, $N = 2500$ Monte Carlo runs ($t = 63$ s)

that for each of the objectives there are quite small values. Just looking at the two plots indicates a dense band of points that seem to converge in the direction of some minimum value. Obviously, the integrated control effort can never reach zero because that would mean that the launcher is not controlled, immediately leading to a large integrated pitch-angle error. However, the two oscillation indices could converge to values close to zero, as that would imply a very smooth control. Note, though, that even a relatively smooth change of the control or state would already increase these objectives, so they could never be exactly zero.

It should also be noted that a small value in one objective does not necessarily mean a small value for all other objectives as well. In other words, the Pareto front in a four-dimensional objective space does not necessarily lie close to the bottom-left corner (the *origin*). In Sect. 5.3, the Pareto concept will be discussed in more detail.

Now that we have established the ranges of the independent parameters, we can move on to the next step, *i.e.*, the single-objective optimisation.

5.2 Single-objective Optimisation

Before any optimisation process can start, it is important to *tune* the algorithm, *i.e.*, to determine the (optimal) values of algorithm-specific settings, *in relation to the problem at hand*. The optimisation of the integrated state deviation by means of the evolutionary algorithm is done for 30 generations, with an initial population size of 50 individuals. The settings (and operators) we found to work well for the problem at hand were:

- Stochastic universal sampling as selection method, with the number of spins being 1

- Arithmetic crossover, with the total number of crossovers⁵ being 40 and the number of retries to obtain a valid design with respect to the constraints being 10 (if no valid design is obtained, the objective value is penalised with a large value of 10^5).
- Multi-non-uniform mutation, with the number of mutations being 10, the maximum number of generations, $G_{max} = 30$, and the shape parameter, $b = 3$

To eliminate the random effect, the runs were repeated with different random seeds. We found that the solutions converged to (almost) the same value; nonetheless, re-running the optimisation multiple times should be standard practise.

For the first batch, the objective is the integrated state deviation, with the reference-model pitch angle being the target value. Figure 9a shows the average objective value, \bar{y} , as a function of generation number. Also included are the $\bar{y} \pm 1\text{-}\sigma$ lines, to show the spread of individuals in objective space as a function of the successive generations.⁶ The results show a quick convergence, with reaching the best value after about eight generations. The response curves for the best individual are shown in Fig. 9b. The plant responds a bit faster than the reference model, which is most likely due to the perturbing angle of attack. As we mentioned, this perturbation is absent in the reference model. However, it induces a deviation between reference-model and plant pitch angle, which leads to larger gains to anticipate on the induced error. The global response of the plant becomes thus a bit more “aggressive.” As the plant is faster, it will also slow down a bit quicker, thus becoming slower than the reference model close to the set point. Finally, the swivel angle remains non-zero for a much longer time than would be suggested by the practically zero error in the pitch angle. This is easily explained by the fact that the angle of attack needs quite a long time to be “pushed back” to zero.

In case we change the objective to be minimised to the integrated state deviation with respect to the guidance command,⁷ *i.e.*, the step command, the results shown in Fig. 10a, b are obtained. At first sight, the results seem to be similar, but some small differences can be seen. In the first place, the converged minimum value is a bit smaller and convergence is slightly faster. In the second place, because the response is even faster than before, there is a slight overshoot of the plant pitch angle.

To compare the two final designs, in Table 1, the design parameters are listed. It is clear that both designs are not the same, although with some imagination one

⁵ A crossover involves two parents and will produce two children. This means that given a number of crossovers and depending on their fitness (and selection), the population size is not constant and could be even double of the one with what we started.

⁶ This figure shows that there is a significant spread in the initial (= first) generation, implying a good coverage of the design space. However, it is important to realise that a large standard deviation can also be caused by just a few outliers, not necessarily in the direction of the optimum.

⁷ Note that the adaptive algorithm still aims at tracking the reference model. However, since the optimiser is forced to follow the guidance command, the resulting response is somewhat of a compromise: the optimiser pushes forward to the guidance command, whereas the controller pulls back towards the reference model.

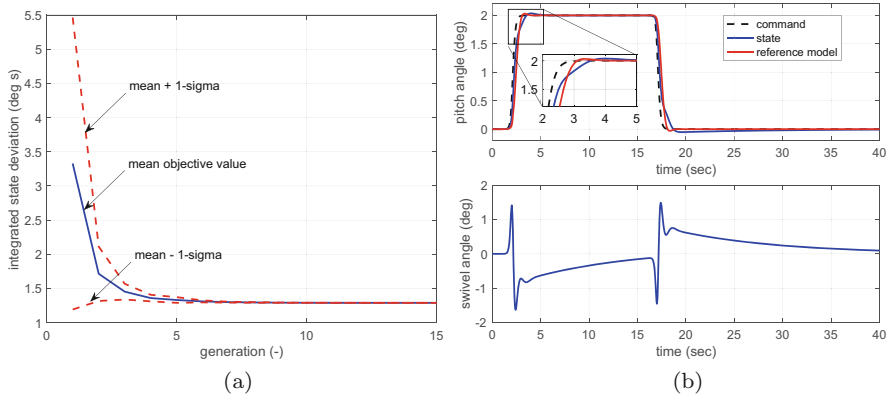


Fig. 9 Single-objective optimisation (reference-model tracking): mean fitness as a function of generation number and best individual’s response. (a) Average fitness. (b) Best individual

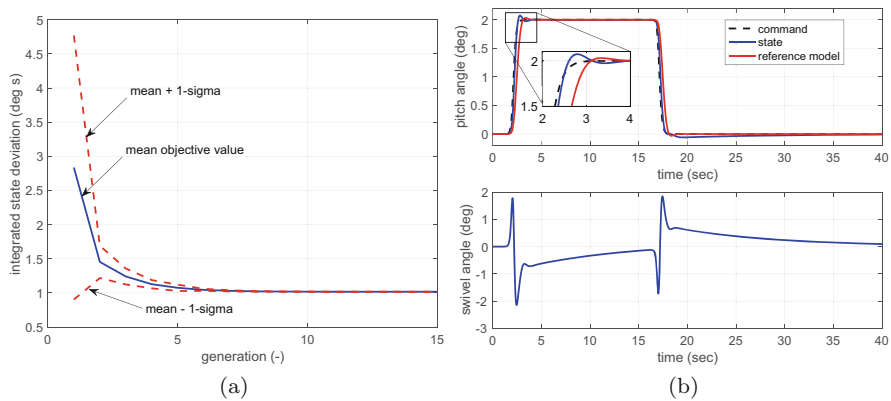


Fig. 10 Single-objective optimisation (command-value tracking): mean fitness as a function of generation number and best individual’s response. (a) Average fitness. (b) Best individual

could say that the order of magnitude is the same. Conclusion from this is that there will be multiple solutions possible, leading to more or less the same performance, *i.e.*, there are possibly many local optima. That means that it is not always easy for the optimiser to find *the* optimal solution. Concerning the adaptive algorithm, it may be possible that minute changes in the design parameters have no effect on the performance; only relatively large variations will show in a change in performance.

Until now we have kept both the reference-model-controller gains, K_p and K_d , and the output-error gains, Eq. (13), constant and in both cases the same. However, as they are directly related to both the reference model and the plant response, it may be interesting to see whether the optimiser will also keep the gains constant (and the same). We will therefore add four more independent parameters: $\mathbf{K}_m =$

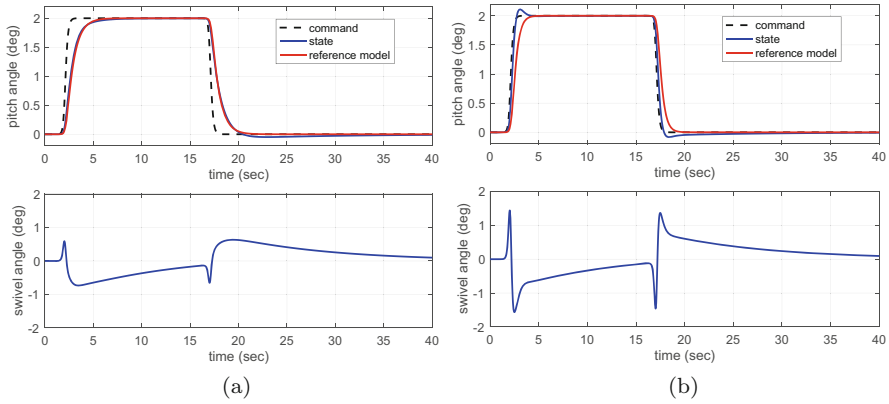


Fig. 11 Single-objective optimisation including with reference-model gains and output gains: response plots. **(a)** Reference-model tracking. **(b)** Guidance-command tracking

Table 1 Optimal design parameters simple adaptive controller (single-objective optimisation)

	Reference-model tracking				Guidance-command tracking			
	T_p	T_i	$K_{i,0}$	σ_i	T_p	T_i	$K_{i,0}$	σ_i
e_y	290	45	1.37	4.43	317	33	1.31	3.96
θ_m	670	5952	0.0	1.43	698	4248	0.0	1.48
q_m	737	279	0.0	0.63	419	151	0.0	3.20
$\varepsilon_{T,m}$	1238	246	0.0	1.02	803	125	0.0	1.59

$(K_{m,p} \ K_{m,d})^T$, with each gain varied over the range $[0.5,5]$, and the output-error gains, $\mathbf{K}_e = (K_{e,p} \ K_{e,d})^T$, varied over the range $[0.5,4]$.

With otherwise the same settings, the optimiser is run twice, once for reference-model tracking and once for guidance-command tracking. The response curves for the optimal designs are shown in Fig. 11, with corresponding gain values $\mathbf{K}_m = (3.50, 2.79)^T$ and $\mathbf{K}_e = (2.84, 2.58)^T$ for the former and $\mathbf{K}_m = (3.06, 1.53)^T$ and $\mathbf{K}_e = (3.31, 1.20)^T$ for the latter. Tracking the reference model leads to a more relaxed response and a much lower control effort. However, one should not forget that the reference-model response should meet with the requirements set to the attitude controller design. Thus, it might be that the response is too slow. A separate optimisation of the reference model is thus always required. In case of guidance-command tracking, one can also see that the reference model is quicker to act, with a steeper transient response. Comparing the results with those of Figs. 9b and 10b does show a smoother response, so it would be a good idea to keep the gains as design variables.

Comparing \mathbf{K}_m and \mathbf{K}_e , they are obviously not the same, as we had assumed in our initial runs. Also, if we compare the gain sets between the two designs, they are not the same. Inspecting the other design parameters, they differ as well from the values listed in Table 1. All in all, we can conclude that the design space and its relation with the objective space is a complex one, which should be kept in mind.

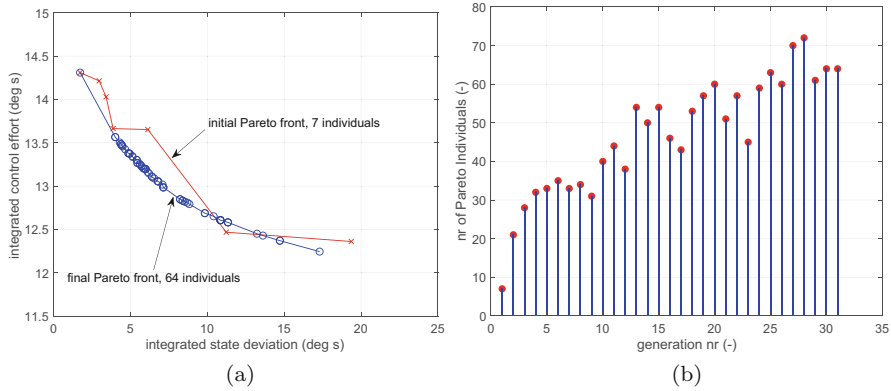


Fig. 12 Multi-objective optimisation (command-value tracking), rigid launcher. Initial population size 50 individuals. (a) Pareto front, initial and final. (b) Number of Pareto individuals

What we saw from the above results is that a smaller integrated state deviation means that the plant is closer in following the reference model or the guidance command. However, as found by Messer et al. (1994), this may indicate that the control effort is ever increasing. Comparing the two profiles of the swivel angle, we see that while tracking the command the swivel angle is indeed slightly larger. Therefore, it would be wise to include minimisation of the integrated control effort in the optimisation process. This will be addressed in the next section.

5.3 Multi-objective Optimisation

From the single-objective optimisation results, we found that a closer model or command-following would require more control effort, which was not taken into account in the optimisation process. Furthermore, we established that the design parameters to be included are \mathbf{T}_p , \mathbf{T}_i , $\mathbf{K}_{i,0}$, σ_i , \mathbf{K}_m , and \mathbf{K}_e , representing a total of 17 design parameters.

For our first batch of simulations, we will include the integrated control effort, \sum_{ϵ_T} , besides the integrated state deviation, $\sum_{\theta_{err}}$. With otherwise the same algorithm settings, the results shown in Figs. 12 and 13 are obtained. Two initial population sizes have been used, *i.e.*, 50 and 200, to try and find out which minimum population size we can use. Figure 12a shows the progression of the Pareto front for the 50-individual initial population. The progression of the front is clear, *i.e.*, in the midrange an improvement in $\sum_{\theta_{err}}$ of more than 10% is achieved. Also, the initial front was quite sparse, whereas the final front is much denser and seems to have converged quite well.

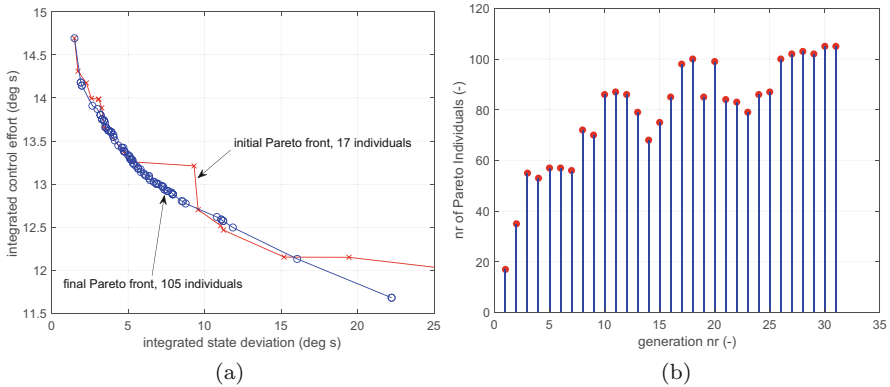


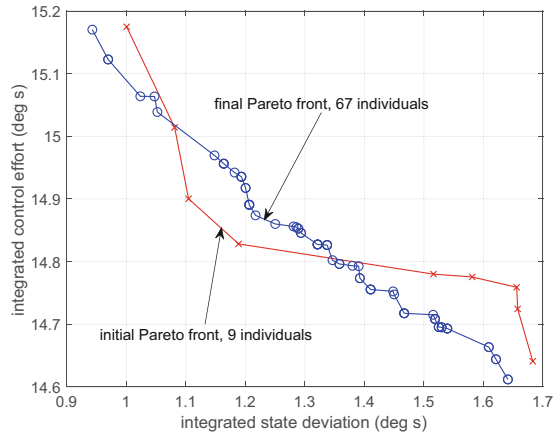
Fig. 13 Multi-objective optimisation (command-value tracking), rigid launcher. Initial population size 50 individuals. **(a)** Pareto front, initial and final. **(b)** Number of Pareto individuals

The total range of variation for either objective is 2° s for the control effort and 17° s for the state deviation. Each of the Pareto individuals represents a(n)(sub-) optimal control system design: selecting a better control effort has obviously an adverse effect on the state deviation, and *vice versa*, as was already established from the single-objective optimisation runs. In case either or both have a minimum/maximum requirement, a plot like this will allow for the selection of the right design.

One should not forget, however, that for any of these so-called heuristic methods it cannot be proven that the Pareto front has indeed converged to its “theoretical” value and that the global optimum has been found. It could be, after all, that the algorithm got stuck in a local minimum. A way to check this is to let the algorithm run for more generations, but looking at the “clustered” condition of the final front—as well as the total number of individuals in the front, see Fig. 12b—it does not seem likely that more progress can be made. A second check could be to do a localised small-scale Monte Carlo run around each Pareto individual, with, for instance, a 5% variation of the original range of the design parameters. Having done this, only showed a marginal shift of the front, so with this method it is as far as we can go. It is curious to note, though, that one individual of the initial front is ahead of the final front, so the conclusions are not black and white. It would be good to keep track of all fronts and compose a final Pareto front from all individual fronts. In that respect, we will include *elitism* for the remainder of the runs, *i.e.*, the best individual for each objective is carried over to the next generation, to avoid losing out on potentially good individuals.

Figure 13 shows the same plots, but now for an initial population size of 200. Apart from the much larger number of individuals in the Pareto fronts, the final front is more stretched out, and at the lower right corner, it is also more rotated towards the origin. In the mid-region, the values seem to be more or less the same, but at the edges a better performance in the individual objectives is found. In conclusion, for the number of design parameters, a population size of 50 seems on the low side.

Fig. 14 Multi-objective optimisation, including off-diagonal elements in T_p , rigid launcher. Initial population size 200 individuals



However, for mid-level performance individuals, it is sufficient. The advantage is, of course, that with a smaller initial population (and correspondingly a smaller number of crossovers and mutations), the CPU load of the algorithm is far less.

One additional test is done, to verify whether off-diagonal elements in one (or both) of the weighting matrices has an advantage. Since there are 10 more design parameters per matrix, we decided to extend only T_p , as the integral gains already have a (constant) initial value. The range of the off-diagonal elements is taken as $\pm 10\%$ of the corresponding diagonal element in that row. Any T_p that is not positive semi-definite, taken as a constraint, is penalised with a very large objective value and effectively “killed off.” Doing the run, with an initial population of 200 to account for the 25 design parameters, resulted in the plot of Fig. 14a. Some interesting aspects came forward. Despite the large variation in performance in the initial population, the converged Pareto front only occupies a small region in the objective space. The integrated state deviation has decreased to quite low values, albeit at the expense of a slightly larger control effort. The final Pareto front could have progressed more, as is evident from the initial Pareto front, that intersects with the final one.⁸ The conclusion is that including off-diagonal elements may be beneficial and should be studied in more detail. Because of the different focus of this chapter, unfortunately we have to leave it at that.

⁸ These results show that the *elitism* operator should not be limited to keeping only the best values for each objective, as has been implemented here, but should potentially include the complete Pareto front. A good algorithm to do so has been proposed by Tan et al. (2003), involving Tabu search. This method keeps an archive of the latest Pareto individuals, and in each successive generation the current Pareto front is removed from the population to maintain search diversity and added to the archive. From this archive, the newly dominated individuals are removed such that the absolute best Pareto front is maintained. It is possible to insert a few Pareto individuals back into the population, e.g., every fifth generation, as it may help convergence to the (global) optimum.

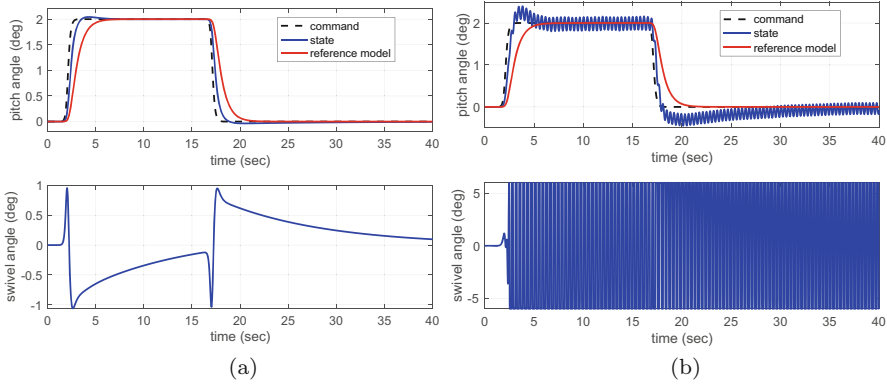
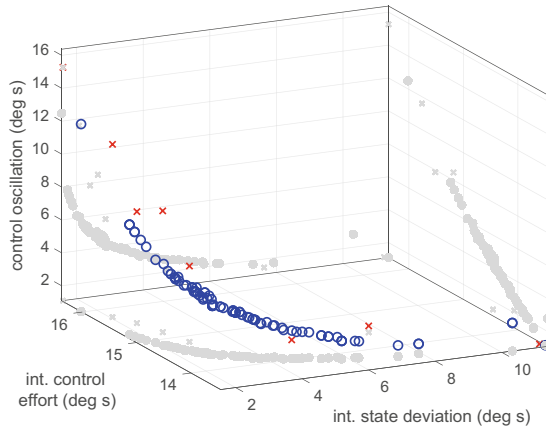


Fig. 15 Controller designed for a rigid body applied to one with engine dynamics. Controller frequency 100 Hz. **(a)** Rigid-body response. **(b)** Rigid body with engine dynamics

So far, we have been studying the response of the rigid launcher. Let us now include engine dynamics and see how this changes the picture. In principle, we would expect that if the engine dynamics is sufficiently fast—which should be the case with $\omega_e = 50 \text{ rad/s}$ —adding the dynamics will not change the response. However, upon inspection, selecting a Pareto individual from the final front with small state deviation and slightly larger control effort (such that engine dynamics will be excited a bit more), this is not the case. For the rigid system, the response is smooth (Fig. 15a), with performance indices given by $\sum_{\theta_{err}} = 1.73^\circ\text{s}$, $\sum_{\varepsilon_T} = 14.31^\circ\text{s}$, $F_\theta = 1.28^\circ\text{s}$, and $F_{\varepsilon_T} = 3.50^\circ$. The value of the oscillation indices is mainly driven by the discrete changes in the system. Changing to a rigid launcher with engine dynamics, the response deteriorates significantly, with performance indices of $\sum_{\theta_{err}} = 6.09^\circ\text{s}$, $\sum_{\varepsilon_T} = 211.86^\circ\text{s}$, $F_\theta = 2.78^\circ\text{s}$, and $F_{\varepsilon_T} = 126.37^\circ$. Looking at the corresponding response in Fig. 15b, the high oscillation index means that the system is in a high-frequency bang–bang state.

The SAC system is in principle a high-gain system, which will amplify the noise that enters the system. From the theoretical model of a rigid launcher with engine dynamics (Eq. (B.2)), we find there is a (strong) coupling between the engine and the angle of attack and, through the aerodynamics, the pitch rate and thus pitch angle. Having fast dynamics in the system requires a high controller frequency, as was also confirmed by Messer et al. (1994). They found, for their experimental setup of a suspended mass system, that for successful realisation of the controller a sampling frequency 40–80 times the Nyquist frequency is required. Going back to the results we got, it could lead to two changes in the approach: the control system

Fig. 16 Pareto front for three-objective optimisation, rigid launcher with engine dynamics. Initial population size 100 individuals



has to be re-optimised, but now with engine dynamics included, or the frequency of the controller is significantly increased, and then the system is re-optimised. Being able to find a good design with controller frequency set to 100 Hz would be the best, of course, in terms of on-board computer load. Unfortunately, a proper design could not be found. Thus, we will increase the frequency to 500 Hz and add the swivel oscillation index to the objectives.

The results of the three-objective optimisation are shown in Fig. 16. What is immediately clear is that there is an almost linear relationship between the integrated control effort and the control oscillation. That means that in principle we can do with one of the two, most notably the control oscillation, because lowering the oscillation seems to lower the control effort as well. This was indeed confirmed by doing a two-objective optimisation with $\sum_{\theta_{err}}$ and F_{ϵ_T} , which gave almost the same final Pareto front.⁹

From the obtained results, we will now select a design with a low oscillation index, which, unfortunately, will give us a large pitch-angle deviation. In a way this makes sense because a slower control response would induce smaller oscillations that are then less amplified. But a slower response would also yield a larger state deviation. Running the design does indeed show that the oscillations have almost disappeared. The optimisation process has thus led to a conceptual design of the control system that forms a good basis for further refinement. To show the final result, we will run the simulation once more, with the same settings for the controller, but now also including the first and second flexible modes. The result can be seen in Fig. 17.

Figure 17a shows the pitch-angle response, which is on the slow side, as expected. Even though the reference model tracks the command very well (in part

⁹ The alternative of keeping the integrated control effort as objective was not as effective to reduce the oscillation index, though.

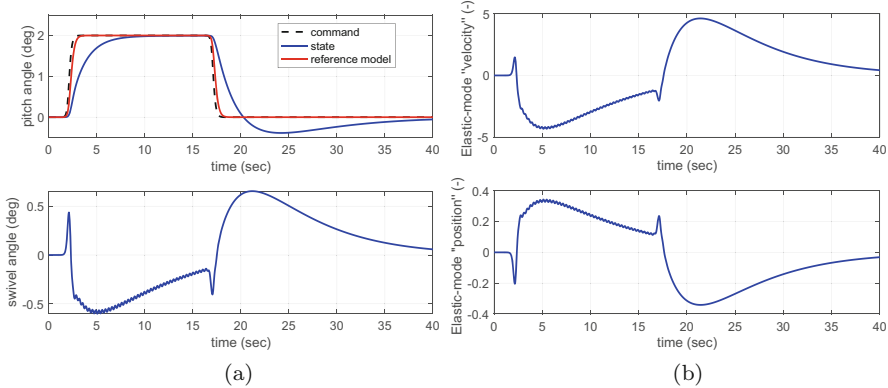


Fig. 17 Final controller design applied to flexible launcher with engine dynamics. **(a)** Rigid-body response. **(b)** First flexible mode

due to the high frequency), the plant response lags behind due to the lower swivel command. Because the swivel oscillations are virtually absent, also the flexible modes are not more excited than what is due to the rigid-body coupling (Fig. 17b). The corresponding performance indices are $\sum \dot{\eta}_{f,1} = 94.7 \text{ s}$, $\sum \eta_{f,1} = 7.4 \text{ s}$, $F_{\dot{\eta}_{f,1}} = 5.1 \text{ s}$, and $F_{\eta_{f,1}} = 0.6 \text{ s}$.¹⁰

6 Concluding Remarks

In this chapter, a methodology has been presented to design and analyse control systems with multiple design parameters and possibly conflicting objectives. These objectives have been formulated in a numerical way, *i.e.*, the integrated state deviation, integrated control effort, and an oscillation index using a moving-average technique. Because of such a formulation, numerical optimisation can be applied to go through a large number of designs and converge towards an optimum. As an example of the methodology, an evolutionary algorithm has been applied to the design of a simple adaptive control system.

Design space exploration helps to establish the bounds on the independent variables. Too large bounds can lead to a random behaviour of the optimisation algorithm, and with too narrow bounds the algorithm may miss the global optimum

¹⁰ For comparison, if the simulation with results shown in Fig. 15b would be repeated for a flexible launcher, the indices would be $\sum \dot{\eta}_{f,1} = 774.5 \text{ s}$, $\sum \eta_{f,1} = 75.2 \text{ s}$, $F_{\dot{\eta}_{f,1}} = 650.1 \text{ s}$, and $F_{\eta_{f,1}} = 53.5 \text{ s}$. These very high values indicate severe deflections/vibrations, which could lead to hardware damage or even a complete breakup of the launcher.

and get stuck in a local one. The first step in the design process was to use single-objective optimisation. This led to a small integrated state deviation, but without guarantee that the control effort would be low. Adding this objective and executing the next step in the design process gave a Pareto front with converged close-to-optimal solutions. Finally, by adding also a control oscillation index as third objective, an attempt was made to lower the oscillatory behaviour of the control. It was observed that the same could be achieved by using only the integrated state deviation and the oscillation index.

In terms of controller performance, the results worked well enough for the rigid launcher. However, when engine dynamics was added, the same controller could not stabilise the system, and a strong oscillatory behaviour was the result. This could be solved by increasing the controller frequency and redoing the optimisation by including the aforementioned oscillation index. The final design was practically oscillation free and worked also well on the flexible launcher.

The introduced control system design methodology was shown to work well in a conceptual design environment, where baseline controllers (with multiple design parameters and thus quite a number of design degrees of freedom) can be quickly analysed, and their performance improved. Depending on the complexity of the design space, convergence will sometimes quickly come to a stop. Local refinement by using a limited Monte Carlo analysis around the Pareto solutions could serve as a confirmation for convergence. To account for the random effect, it is advised to always redo the optimisation with multiple seeds to initialise the random generator.

As recommendations for future work, one could think of confirming the versatility of this methodology by designing different control systems, possibly using different (and more complex) design criteria. Because the evolutionary algorithm was applied without a proper trade-off, other (global) optimisation techniques could be tried to improve the efficiency of the methodology.

Zooming in on the application at hand, it should be verified what the computational load means for an on-board implementation. Requiring a controller frequency of 100 or even 500 Hz is perhaps not a trivial requirement. For the flexible launcher, it would be interesting to study whether the same controller compared to one for the rigid launcher comes out of the optimisation process and whether the use of a different reference model may lead to an improved performance. Finally, the controlled flight from launch to payload separation should be verified to ensure that the controller always meets the performance requirements, taking transient effects due to the rapidly changing flight conditions, aerodynamic properties, and depletion of the fuel and oxidiser tanks into account. In principle, the adaptive controller should be able to adapt to those changes, but re-optimising the controller parameters for different conditions and using some form of interpolation in between design points may ultimately yield the best possible performance.

Appendix A: Pac Astro Mass Properties and Geometry

Tables A.1 and A.2 show the mechanical properties and additional masses of the launch vehicle model.

Table A.1 Mechanical properties of the launch vehicle structural model

Section	End coordinate [m]	Area [m ²]	Thickness [mm]	Moment of inertia [m ⁴]	Mass [kg]	Young's Modulus [GPa]	Density [kg/m ³]
Aft stage 1	3.07	3.93e-3	0.69	1.63e-3	30.46	72.4	2740
Fuel 1	6.03	1.51e-2	2.64	6.28e-3	230.91	73.8	2710
Intertank 1	8.63	1.78e-2	3.10	7.37e-3	102.69	72.4	2740
LOX 1	14.36	1.98e-2	3.46	8.23e-3	546.42	73.8	2710
Forward stage 1	16.79	1.48e-2	2.59	6.16e-3	67.30	72.4	2740
Aft stage 2	17.91	1.48e-2	2.59	6.16e-3	67.30	72.4	2740
Fuel 2	18.30	9.45e-3	1.65	3.92e-3	16.29	73.8	2710
Intertank 2	19.87	1.28e-2	2.24	5.33e-3	55.21	72.4	2740
LOX 2	20.96	1.03e-2	1.79	4.27e-3	49.62	73.8	2710
Forward stage 2	21.97	9.16e-3	1.60	3.81e-3	25.37	72.4	2740
Fairing	22.97	8.36e-3	1.46	3.47e-3	22.70	113	4430
Frustrum	25.58	7.04e-3	1.23	2.93e-3	53.54	113	4430
Nose	25.77						

Table A.2 Additional masses of the launch vehicle model (excluding fuel masses)

Subsystem	Stage 1		Stage 2	
	Mass [kg]	Location [m]	Mass [kg]	Location [m]
Engine	225	1.54	60	16.79
Thrust structures	55	2.20	20	21.46
Gimbal system	80	2.20	20	17.35
Pressurant	130	7.50	30	19.87
Valves and lines	130	7.50	50	19.00
GNC electronics			40	21.97
Payload adapter			20	22.47
Payload			225	22.97

Appendix B: State-space Matrices

The rigid-body sub-matrices (including coupling terms), \mathbf{A}_{RR} , \mathbf{A}_{RE} , and \mathbf{A}_{RF} are given by

$$\mathbf{A}_{RR} = \begin{bmatrix} -\frac{C_{N\alpha}\bar{q}S_{ref}}{mu_0} & -\frac{g_d \sin \theta_0}{u_0} & \frac{C_{Nq}\bar{q}S_{ref}}{mu_0} + 1 \\ 0 & 0 & 1 \\ \frac{C_{m\alpha}\bar{q}S_{ref}d_{ref}}{I_{yy}} & 0 & \frac{C_{mq}\bar{q}S_{ref}d_{ref}}{I_{yy}} \end{bmatrix} \quad (\text{B.1})$$

$$\mathbf{A}_{RE} = \begin{bmatrix} \frac{m_e \Delta L_e}{mu_0} & 0 & \frac{T}{mu_0} \\ 0 & 0 & 0 \\ \frac{m_e L_e \Delta L_e + I_e}{I_{yy}} & 0 & \frac{L_e T}{I_{yy}} \end{bmatrix} \quad (\text{B.2})$$

$$\mathbf{A}_{RF} = \begin{bmatrix} a_{\alpha, \dot{\eta}_1} & a_{\alpha, \eta_1} & \dots & a_{\alpha, \dot{\eta}_N} & a_{\alpha, \eta_N} \\ 0 & 0 & \dots & 0 & 0 \\ a_{q, \dot{\eta}_1} & a_{q, \eta_1} & \dots & a_{q, \dot{\eta}_N} & a_{q, \eta_N} \end{bmatrix} \quad (\text{B.3})$$

with, for $i = 1, \dots, n_f$:

$$a_{\alpha, \dot{\eta}_i} = -C_{N\dot{\eta}_i} \bar{q} S_{ref} \quad a_{\alpha, \eta_i} = -\frac{C_{N\eta_i} \bar{q} S_{ref} - T \sigma_i(x_e)}{mu_0}$$

$$a_{q, \dot{\eta}_i} = \frac{C_{q, \eta_i} \bar{q} S_{ref} d_{ref}}{I_{yy}} \quad a_{q, \eta_i} = \frac{C_{m\eta_i} \bar{q} S_{ref} d_{ref} - L_e T \sigma_i(x_e) - T \phi_i(x_e)}{I_{yy}}$$

In the above equations, m and I_{yy} are the (current) mass and moment of inertia of the launcher, m_e and I_e are the mass and moment of inertia of the engine, and $\Delta L_{cm,e}$ is the distance from gimbal point to centre of mass of the engine. $C_{N\alpha}$ and C_{Nq} are the normal force gradients with respect to α and q , and $C_{m\alpha}$ and C_{mq} are the corresponding pitch-moment gradients. Due to the bending of the launcher frame, local aerodynamic force and moment effects are introduced through the gradients $C_{N\dot{\eta}_i}$, $C_{N\eta_i}$, C_{q, η_i} , and $C_{m\eta_i}$, and the details of which are provided by Mooij and Gransden (2016). Finally, $\phi_i(x)$ and $\sigma_i(x)$ are the modal-mass normalised i^{th} bending shape and slope at location x , in this case the engine location x_e .

The engine is modelled as third-order transfer function, with input parameters ω_e , ζ_e , and K_e , which are the natural frequency and damping of the engine dynamics and an amplification gain, respectively. The 3×3 engine sub-matrix, \mathbf{A}_{EE} , is defined to be

$$\mathbf{A}_{EE} = \begin{bmatrix} -2\zeta_e\omega_e & -\omega_e^2 & -K_e\omega_e^2 \\ 1 & 0 & 0 \\ 0 & 1 & 0 \end{bmatrix} \quad (\text{B.4})$$

where the corresponding coupling matrices are zero, *i.e.*, $\mathbf{A}_{ER} = \mathbf{A}_{EF} = \mathbf{0}$.

Each bending motion depends on the generalised force for that specific motion. This generalised force is found by multiplying all the external loads with the eigenvector of that mode. As before, the external loads are a function of the bending motion and the position along the vehicle. Note that the subscripts i and j below both indicate a flexible mode, up to the maximum of n_f . So, for \mathbf{A}_{FR} , \mathbf{A}_{FE} and \mathbf{A}_{FF} , we have

$$\mathbf{A}_{FR} = \begin{bmatrix} a_{\dot{\eta}_{1,\alpha}} & a_{\dot{\eta}_{1,\theta}} & a_{\dot{\eta}_{1,q}} \\ 0 & 0 & 0 \\ \vdots & \vdots & \vdots \\ a_{\dot{\eta}_{n_f,\alpha}} & a_{\dot{\eta}_{n_f,\theta}} & a_{\dot{\eta}_{n_f,q}} \\ 0 & 0 & 0 \end{bmatrix} \quad (\text{B.5})$$

with

$$a_{\dot{\eta}_{i,\alpha}} = -\bar{q} S_{ref} \int_0^{L_{tot}} C'_{N_\alpha} \phi_i(x) dx \quad a_{\dot{\eta}_{i,\theta}} = -g_d \sin \theta_0 \int_0^{L_{tot}} \phi_i(x) m(x) dx$$

$$a_{\dot{\eta}_{i,q}} = -\frac{\bar{q} S_{ref}}{u_0} \int_0^{L_{tot}} (x - x_{cm}) C'_{N_\alpha} \phi_i(x) dx$$

$$\mathbf{A}_{FE} = \begin{bmatrix} a_{\dot{\eta}_{1,\ddot{\varepsilon}_T}} & 0 & a_{\dot{\eta}_{1,\varepsilon_T}} \\ 0 & 0 & 0 \\ \vdots & \vdots & \vdots \\ a_{\dot{\eta}_{n_f,\ddot{\varepsilon}_T}} & 0 & a_{\dot{\eta}_{n_f,\varepsilon_T}} \\ 0 & 0 & 0 \end{bmatrix} \quad (\text{B.6})$$

with

$$a_{\dot{\eta}_{i,\ddot{\varepsilon}_T}} = m_e \Delta L_{cm,e} \phi_i(x_e) + I_e \sigma_i(x_e) \quad a_{\dot{\eta}_{i,\varepsilon_T}} = T \phi_i(x_e)$$

$$\mathbf{A}_{FF} = \begin{bmatrix} a_{\dot{\eta}_1, \dot{\eta}_1} & a_{\dot{\eta}_1, \eta_1} & \dots & a_{\dot{\eta}_1, \dot{\eta}_{n_f}} & a_{\dot{\eta}_1, \eta_{n_f}} \\ a_{\eta_1, \dot{\eta}_1} & a_{\eta_1, \eta_1} & \dots & a_{\eta_1, \dot{\eta}_{n_f}} & a_{\eta_1, \eta_{n_f}} \\ \vdots & \vdots & \vdots & \vdots & \vdots \\ a_{\dot{\eta}_{n_f}, \dot{\eta}_1} & a_{\dot{\eta}_{n_f}, \eta_1} & \dots & a_{\dot{\eta}_{n_f}, \dot{\eta}_{n_f}} & a_{\dot{\eta}_{n_f}, \eta_N} \\ a_{\eta_{n_f}, \dot{\eta}_1} & a_{\eta_{n_f}, \eta_1} & \dots & a_{\eta_{n_f}, \dot{\eta}_{n_f}} & a_{\eta_{n_f}, \eta_{n_f}} \end{bmatrix} \tag{B.7}$$

with, for $i \neq j$:

$$a_{\dot{\eta}_i, \dot{\eta}_j} = -\frac{\bar{q} S_{ref}}{u_0} \int_0^{L_{tot}} \phi_i(x) C'_{N\alpha} \phi_j(x) dx$$

$$a_{\dot{\eta}_i, \eta_j} = -\bar{q} S_{ref} \int_0^{L_{tot}} \phi_i(x) C'_{N\alpha} \sigma_j(x) dx - T \phi_i(x_e) \sigma_j(x_e)$$

$$a_{\eta_i, \dot{\eta}_j} = a_{\eta_i, \eta_j} = 0$$

and for $i = j$

$$a_{\dot{\eta}_i, \dot{\eta}_i} = a_{\dot{\eta}_i, \dot{\eta}_i} - 2\zeta_{f,i} \omega_{f,i}^2 \qquad a_{\dot{\eta}_i, \eta_i} = a_{\dot{\eta}_i, \eta_i} - \omega_{f,i}^2$$

$$a_{\eta_i, \dot{\eta}_i} = 1 \qquad a_{\eta_i, \eta_i} = 0$$

Lastly, to complete the model description, the components of \mathbf{B} are stated:

$$\mathbf{B}_R = \mathbf{B}_F = \mathbf{0} \tag{B.8}$$

and

$$\mathbf{B}_E = \begin{pmatrix} K_e \omega_e^2 \\ 0 \\ 0 \end{pmatrix} \tag{B.9}$$

References

Baker, J.E., "Reducing Bias and Inefficiency in the Selection Algorithm", *Proceedings of the Second International Conference on Genetic Algorithms and their Application*, pp. 14–21, Hillsdale, New Jersey, 1987.

- Barkana, I., "Classical and Simple Adaptive Control for Non-Minimum Phase Autopilot Design", *Journal of Guidance, Control, and Dynamics*, Vol. 24, No. 4, pp. 631–638, July-August 2004.
- Barkana, I., "Parallel Feedforward and Simple Adaptive Control of Flexible Structures: First-Order Pole Instead of Collocated Velocity Sensors?", *Journal of Aerospace Engineering*, Vol. 29, Issue 2, March 2016.
- Cvetković, D., "Evolutionary multi-objective decision support systems for conceptual design", PhD thesis, University of Plymouth, 2000.
- Fleeter, R., McLoughlin, F. and Mills, R., "A Low-Cost Expendable Launch Vehicle for 500-Pound Class Satellites", Marketing brochure, PacAstro, Herndon, VA, 26 May 1992.
- Fleming, P.J. and Purshouse, R.C., "Genetic algorithms in control system engineering", Research Report no. 789, Department of Automatic Control and Systems Engineering, University of Sheffield, May 2001.
- Fonseca, C.M.M. de, "Multiobjective Genetic Algorithms with Applications to Control Engineering Problems", PhD thesis, Department of Automatic Control and Systems Engineering, University of Sheffield, UK, 1995.
- Goldberg, D.E. *Genetic Algorithms in Search, Optimization and Machine Learning*, Addison-Wesley Longman Publishing Co., Inc., 1989.
- Gransden, D.I. and Mooij, E., "Control Recovery of a Satellite with Flexible Appendages after Space Debris Impact", AIAA-2018-2099, *AIAA SciTech Forum, Guidance, Navigation, and Control Conference*, Kissimmee, FL, 8–12 January 2018.
- Holland, J.H., *Adaptation in natural and artificial systems*, The University of Michigan Press, Ann Arbor, MI, 1975.
- Huang, Y., Pool, D.M., Stroosma, O. and Chu, Q., "Long-Stroke Hydraulic Robot Motion Control with Incremental Nonlinear Dynamic Inversion", *IEEE/ASME Transactions on Mechatronics*, Vol. 24, No. 1, February 2019, pp. 3044–314.
- Kaufman, H., Barkana, I. and Sobel, K., *Direct adaptive control algorithms: Theory and applications*, Second edition, Springer-Verlag, New York, 1998.
- Mehiel, E.A. and Balas, M.J., "Adaptive Control for a Deployable Optical Telescope", AIAA-2004-5222, From: *AIAA Guidance, Navigation, and Control Conference*, Providence, RI, August 16–19, 2004.
- Menon, P.K., Yousefpor, M., Lam, T. and Steinberg, M.L., "Nonlinear flight control system synthesis using genetic programming", AIAA-1995-3224, *AIAA Guidance, Navigation, and Control Conference*, Baltimore, MD, August 7–10, 1995.
- Messer, R.S., Haftka, R.T. and Cudney, H.H., "Cost of Model Reference Adaptive Control: analysis, experiments, and optimization", *Journal of Guidance, Control and Dynamics*, vol. 17, no. 5, pp. 975–982, Sep.–Oct. 1994.
- Michalewicz, Z., *Genetic Algorithms + Data Structures = Evolution Programs*, Springer-Verlag, third edition, 1996.
- Mooij, E., "Simple Adaptive Bank-Reversal Control for Non-linear Winged Re-entry Vehicles", *Mathematics In Engineering, Science And Aerospace*, MESA, Vol. 9, No. 1, 2018, pp. 85–110.
- Mooij, E., and Gransden, D. I., "The Impact of Aeroelastic Effects on the controllability of Conventional Launch Vehicles", *Proceedings of the 67th IAC Conference*, Guadalajara, Mexico, September, 2016.
- Rolland Collette, J.G., "Analysis and Design of Space Vehicle Flight Control Systems, Volume XI, Component Dynamics", NASA CR-830, 1967.
- Schwanz, R.C. and Cerra, J.J., "Dynamic modeling uncertainty affecting control system design", AIAA-1984-1057, From: *AIAA Dynamics Specialists Conference*, Palm Springs, CA, May 17–18, 1984.
- Smear, E.J.J., Chu, Q. and De Croon, G.C.H.E., "Adaptive Incremental Nonlinear Dynamic Inversion for Attitude Control of Micro Air Vehicles", *Journal of Guidance, Control, and Dynamics*, Vol. 39, No. 3, March 2016, pp. 450–460.
- Sutton, G.P. and Biblarz, O., *Rocket Propulsion Elements*, 9th edition, John Wiley & Sons, Inc., 2017.

- Tan, K.C., Khor, E.F., Lee, T.H., and Yang, Y.J., "A Tabu-based Exploratory Evolutionary Algorithm for Multiobjective Optimisation", *Artificial Intelligence Review*, Vol. 19, pp. 231–260, 2003.
- Tanaka, T. and Chuang, C.-H., "Scheduling of linear controllers for X-29 by neural network and genetic algorithm", AIAA-1995-3270, *AIAA Guidance, Navigation, and Control*, Baltimore, MD, August 7–10, 1995.
- Zalzala, A.M.S. and Fleming, P.J. (Eds.), *Genetic algorithms in engineering systems*, IEE Control Engineering Series 55, London, 1997.

Optimization and Solution Approaches in Utilizing Wireless Sensor Networks for Exploring Moon, Planets, and Space



Omer Ozkan

1 Introduction

The trends and studies in micro-electro-mechanical systems and wireless communications have led to the invention of small-sized, low-cost, low-power, and multifunctional sensor nodes (SNs) that are deployed to the environment to sense the following [1]:

- Temperature
- Humidity
- Gas
- Vehicular movement
- Color
- Lightning condition
- Pressure
- Soil composition
- Noise levels
- Light
- Smoke
- The presence or absence of certain objects
- Mechanical stress levels on attached objects and
- Current characteristics such as speed, direction, acceleration, and object size, etc.

The large number of these seismic, low-sampling-rate mechanical, magnetic, thermal, visual, infrared, chemical, biological, optical, acoustic, or radar wireless

O. Ozkan (✉)

Industrial Engineering Department, Turkish Air Force Academy, National Defence University, Istanbul, Turkey

e-mail: o.ozkan@hho.msu.edu.tr

Table 1 WSN types [2, 3]

Types	Cost	Deployment	Challenges
Terrestrial WSN	Low	Structured, unstructured	Energy
Underground WSN	High	Structured, unstructured	Energy, signal loss, attenuation
Underwater WSN	High	Structured, unstructured	Energy, bandwidth, signal fading
Multimedia WSN	Low	Structured, unstructured	Energy, high data rate, high bandwidth
Mobile WSN	High	Initial spreading	Energy, localization, placement

sensors, which make up the wireless sensor network (WSN), aim to sense, process data, and communicate collaboratively about the physical characteristics of the located field [1, 2]. The deployment positions of the sensors across the field should be determined carefully and should be located to increase data-collection efforts while minimizing costs. Coverage, energy consumption, reliability, security, communication range, memory, and network lifetime are other properties that can be included in the problem definition. Possible WSN applications include monitoring or tracking health, military, environment, agriculture, building (home, office, etc.), security, energy, traffic, infrastructure, and space fields [1–4].

WSN types can be classified into five categories, as presented in Table 1. According to the sensor type, a WSN can also be categorized as static, mobile, hybrid, or mobile robot [5]. The WSN protocol consists of the application, transport, network, data links, and physical layers with power management, mobility management, and task management planes. ZigBee and Bluetooth are the two standard communication tools utilized in WSNs [6], and the network design topologies in WSNs can be defined as point-to-point, star, tree, or mesh [7].

In this study, WSN applications for exploring the Moon, planets, and space are analyzed, and the literature is summarized. The optimization and solution methodologies in these applications are presented, and the opportunities and challenges of using WSNs in space-based missions are revealed. The remainder of this paper is organized as follows: Sect. 2 gives an overview of studies exploring the Moon using WSNs. Section 3 includes papers about exploring planets, and Sect. 4 discusses several WSN applications in space. Section 5 concludes this chapter.

2 Exploring the Moon by Using WSNs

Throughout the entire existence of humanity, the Moon has consistently affected the musings and beliefs of numerous societies, and it has been used as a source to comprehend and measure time. Beginning after the 1950s, technology has allowed people to reach the Moon physically and discover it more profoundly. Up to today, hundreds of missions have been devoted to exploring the Moon, and in addition to the USA and Russia, new countries have joined the competition in recent years. Since the Apollo 11 landing on the Moon in 1969, governments and private

companies still aim to explore the entirety of and create settlements for humans on the Moon.

WSNs can be a highly efficient and effective alternative to explore the Moon as the closest target to Earth in space (Fig. 1). In the literature, [8] intend to reveal the theoretical aspects of the deployment problem of WSNs on the Moon. The deployment methodology of water ice sensors on the Moon differs from those deployed at a site on Earth. The sensor deployment, area coverage, wireless connectivity, and sensor deployment cost are considered by using placement topologies via MATLAB and the number of sensors are minimized.

Pabari et al. [9] study radio frequency modeling of WSNs on the Moon and propose a model using fundamental physical phenomena resulting from wave propagation on the Moon. Digital Elevation Model of four sites of the Moon are used by the proposed model and the models of sites are obtained by Terrain Mapping Camera on Chandrayan-1 which is an Indian probe to the Moon. The results in the paper provide information about the area coverages of sensors, potential sensor deployment sites and usage of sensors in path planning of rovers on the Moon.

Prasad and Murty [10] present several scenarios in single and multi-tier WSN architectures for searching for water or ice on the Moon. The study reveals positive opinions about the feasibility for the sensor node hardware based on current progresses while [11] also discusses the chance of the in-situ exploration of lunar

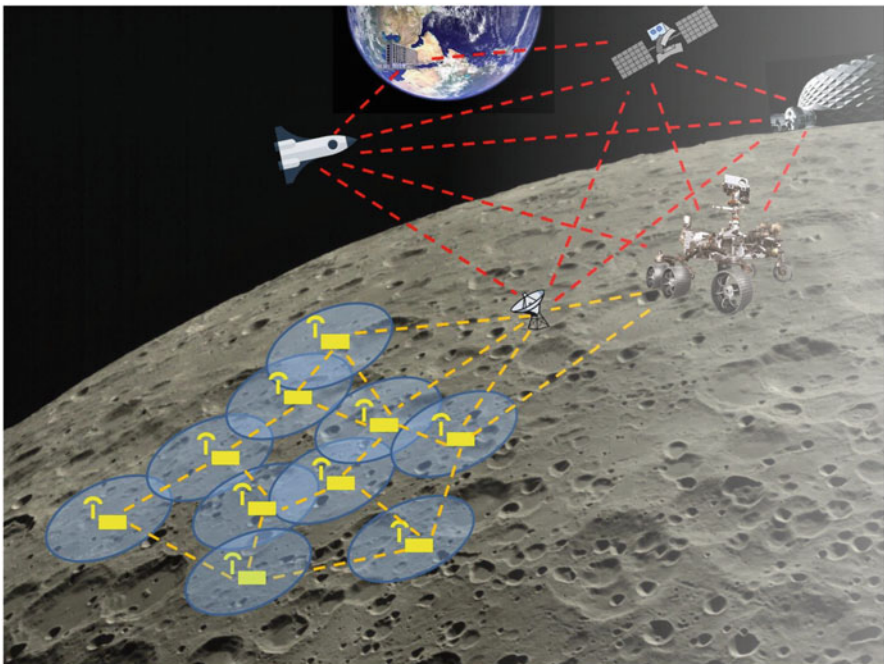


Fig. 1 A possible network on the Moon

ice via WSNs. In recent works, lunar ice has been detected via using remote sensing techniques by lunar programs and it is expected that the ice has been formed in permanently dark areas of the Moon at very low temperatures. The study proposes to use WSNs for in-situ measurement of the potential ice.

Meanwhile, [12] study the design and implementation of data aggregation algorithms for lunar missions via WSNs. The size of the data packet is optimized for better energy consumption in WSNs, and the effectiveness of the data aggregation scheme is maximized. The presented data aggregation algorithms are also applied successfully on a system-on-a-chip embedded platform utilizing a Xilinx Zynq FPGA tool. The life time of the WSN is increased via the saved energy and the original data accuracy is protected by using data aggregation. It is assumed that this research can be helpful for security and safety related studies about the Earth by using the Moon, such as monitoring the space or preventing military bases on the lunar surface.

Lopez-Matencio [13] develops an ant colony optimization-based metaheuristic algorithm for deploying SNs and compares the results with the four-directional placement heuristic. The multi-objective optimization problem in the study aims to select optimal observation sites and to maximize the WSN lifetime. The methodology aims to solve a multi-objective WSN placement problem by focusing on node placement, sensing capacities, network connectivity and network lifetime. In the study, a network is designed to explain the distribution of helium-3, a potential enabling element for fusion reactors, on the Moon.

In addition, [14] define a comprehensive mass-constrained deployment model for missions exploring the Moon's surface. The problem includes heterogeneous relevance on the map, detailed lifetime, node airborne launch, or propellant calculations. Since the defined problem is too complex, a simulated annealing algorithm is also proposed to solve it. The placement positions of sensors are optimized to describe water distribution in the Bullialdus Crater on the Moon.

Further, [15] studies the WSN deployment problem on the Moon to maximize coverage and develop a hybrid memetic algorithm. Sixty-four scenarios are created based on the real 3-D digital elevation model of the surface of the Moon for two different terrains near the South Pole. The results of the hybrid memetic algorithm are compared with local search and simulated annealing algorithms. It is presented that the hybrid memetic algorithm has better coverage values in reasonable CPU times.

In summary, the deployment, coverage, energy consumption, and communication characteristics of WSNs are the most studied properties for optimizing the utilization of WSNs on the Moon's surface. In the literature, different scenarios are solved with exact or approximate optimization approaches specific to the characteristics of the Moon.

3 Exploring the Planets by Using WSNs

In the literature, WSNs are also proposed to be used in exploring planets. However, the planet environments are harsh, with some example values listed below [16, 17]:

- Temperature range: -133 to $+22$ °C on the surface of Mars, -173 to $+427$ °C on the surface of Mercury
- Pressure range: up to 90 bar on the surface of Venus
- Irradiation: krad to several mrad depending on orbit, solar activity, and mission duration
- Atmospheric constituents: hydrogen, helium, and methane in Uranus and Neptune
- Vibrations: up to 20 G from 5 to 2000 Hz at launch
- Shocks: up to 10,000 G at separation of stages and heat shield

The detailed information about the atmospheres, surfaces, and tectonic behaviors of the planets and Titan (the largest moon of Saturn and the second-largest natural satellite in the Solar System) can be found in [18–24], and because of these compelling physical conditions, the deployed WSN nodes on the planets should be resistant to these conditions. Dubois et al. [16] consider physical and chemical sensing of the atmosphere, surface, and soil on a Solar System object by utilizing WSNs, including two scenarios with static or moving SNs. The SNs can be located on the ground or in the atmosphere of a Solar System object. Self-organization and localization are the main challenges to design a reliable network in such environments. The study explains the diversity of environmental and operational constraints and also covers the specific requirements of WSNs when using them to explore the space. Trebi-Ollennu et al. [25] conduct an extensive analysis, simulations, and experiments concerning a sun sensor to be used in Field Integrated, Design and Operations (FIDO) rover to explore planets. The study aims to develop a sun sensor that fills the current cost/performance gap, utilizes the power of subpixel interpolation, makes use of available hardware on the rover, and needs very little computational overhead. The sensor is used to estimate the heading of planetary rovers including integration of noisy rotational-speed evaluations.

Because the planet environments can be dangerous, [26] study a reliable WSN design for planet exploration. The WSNs can serve remote monitoring of not easily reachable regions in preparation of human or robotic missions. Therefore, the study presents a method named “confidence weighted voting” that can increase the reliability of the data and the fault tolerance in WSNs. The method is compared with the traditional approaches, such as majority voting and distance weighted voting. The results present the confidence weighted voting has as much as 49% more resilient and better performance values than the traditional approaches.

In addition, [27] work on a hardware design for sensors to be used in planetary exploration missions. The seismic, chemical, temperature, and visual properties in a sensor payload are proposed, and the power and communication features needed

to achieve these kinds of planetary exploration missions are also included. The experiment offers a positive assertion of feasibility for the sensor node hardware, provided current levels of MEMS and VLSI technologies. The study also points out the necessity about the works in the wireless ad-hoc networking sides of the proposed deployment approach.

Further, [28] propose to utilize WSNs to explore planets (for instance, on the surface, on rover platforms, etc.) and summarize the objectives of using WSNs in exploring planets as follows:

- Decide whether life ever arose on a specific celestial object
- Define the geology and topology of the land surface
- Describe the climate
- Make ready for human discovery

Medina et al. [28] propose that the WSNs have more scientific and economic benefits than the traditional devices while exploring space and planets, such as:

- Increased spatial and temporal sampling capabilities
- Increased reliability
- Decreased payload weight
- Decreased overall costs
- Decreased mission programmatic

Medina et al. [28] also outline the deployment strategies of sensors in exploring scenarios as follows:

- Dropped by an orbiter and with individual propulsion
- Dropped by the Lander
- Dropped while using small parachutes, balloons, or rotors (that depends on the target body)
- Dropped by a rover
- Fired by the Lander

Pabari et al. [29] design and develop an extremely compact impedance-based WSN node to infer the existence of water/ice in a soil sample to be used in planetary explorations. The proposed sensor aims to evaluate the permittivity of lunar regolith and make out the presence of water ice and it runs in the frequency domain with a provided range by sweeping the frequency. This wireless sensor requires only electrical contact with the ground surface that helps to save energy. The sensor data are transmitted at 2.4 GHz to the aggregator. Sand-type terrestrial soil, lunar soil simulant JSC-1A, and Milli-Q water are tested to present the performance of the sensor.

Prasad et al. [30] design a sensitive ambient light-sensing module with a wide dynamic range to be used in WSNs for planetary exploration missions. The performance of the sensor is tested under different circumstances. The variance in light intensities differentiates from <1 to 1.2×10^5 lx that could be noticed from dawn to dusk. Meanwhile, the European Space Agency (ESA) funded a project named RF Wireless for Planetary Exploration (RF-WIPE) to research the deployment of

several self-organizing WSNs for exploring a planetary body [31]. This real project aims to simulate and prototype a WSN to be used in planetary exploration and to present the potential and limitations of the proposed methodology. In the work, a distributed sensor network-based instrument and networked planetary surface exploration are studied as case scenarios with different network configurations. Energy models, node deployment, and communication protocols are advanced, simulated, and validated with laboratory and outdoor tests.

Rodrigues et al. [32] study the design of nodes and the WSN architecture with data fusion for planetary discovery. The paper summarizes the difficulties, principles, and solutions to design issues. In addition, the study presents supporting data fusion architecture in terms of node and network structures that affects the performance of WSNs. Meanwhile, [33] illustrate the issues and challenges of using WSNs on planet surfaces, especially with the Mars example. The application includes node placement, coverage, communication, and data transfer issues.

Space Wireless Sensor Networks for Planetary Exploration (SWIPE) is another real project funded by the European Commission, and it aims to transfer WSN technology to space [34]. Radiation, temperature, illumination, and dust deposition sensor types are used with clustered network topology to generate a WSN in SWIPE. Planetary surface environment monitoring scenario in SWIPE is presented in Fig. 2

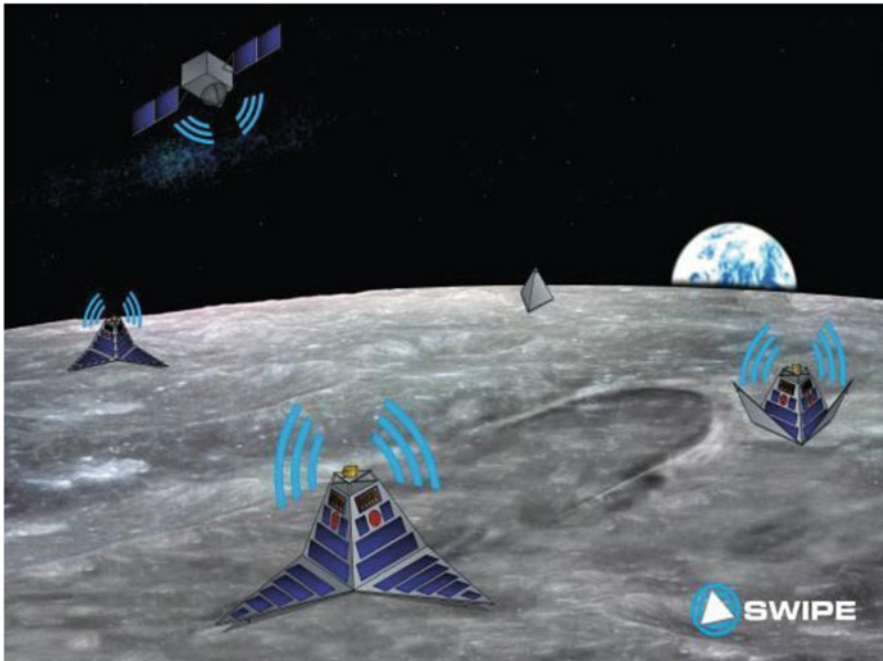


Fig. 2 Planetary surface environment monitoring scenario [34]

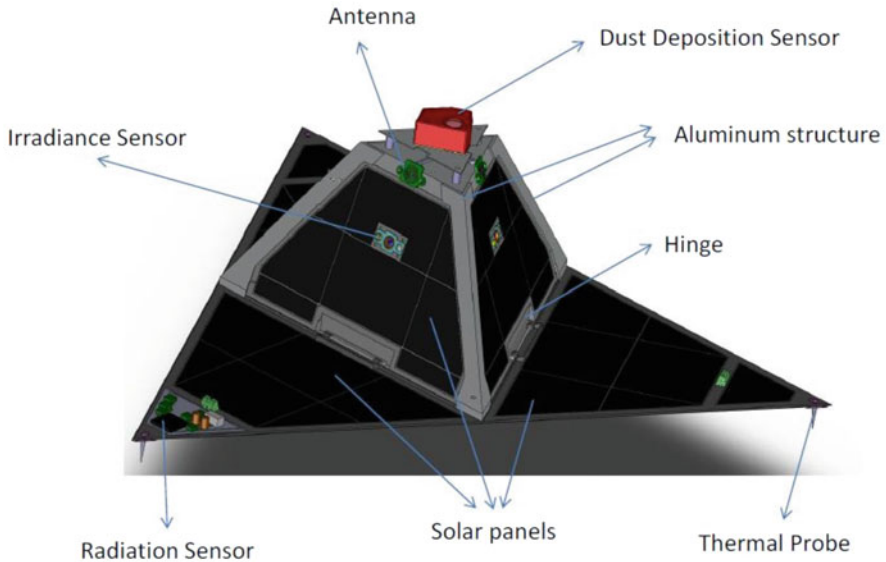


Fig. 3 SWIPE node configuration [34]

and SWIPE node configuration is illustrated in Fig. 3. The project ended in 2015 after achieving several scientific and technical objectives, such as:

- Defining complexities and needs
- Improving hybrid satellite–mobile ad-hoc network routing algorithms
- Applying multi-sensor data-processing and fusion
- Designing seven node prototypes
- Conducting detailed tests in high-fidelity environments

Zhai and Vladimirova [35], as a part of SWIPE, propose data-processing/fusion algorithms for WSNs on planets and aim to integrate the sensor data and to reduce data volume using satisfying energy constraints. Extensive simulations are done and the performance of the proposed data-processing/fusion algorithms are tested. The results reveal that the algorithms can decrease the node energy necessity significantly, and the data transmission energy up to 91% while preserving the original data up to 99% accuracy.

Meanwhile, [36] develop an ad-hoc routing algorithm and with several simulations to achieve five objectives as:

- Making sure of any-cast communications with multiple data sinks
- Decreasing the control overhead for routing maintenance
- Being light in terms of memory/computational necessities, to be deployed into low-power and low-memory/processing devices
- Acting rapidly to restructure in the occurrence of node failures
- Making optimal choices about the routes to balance and save energy

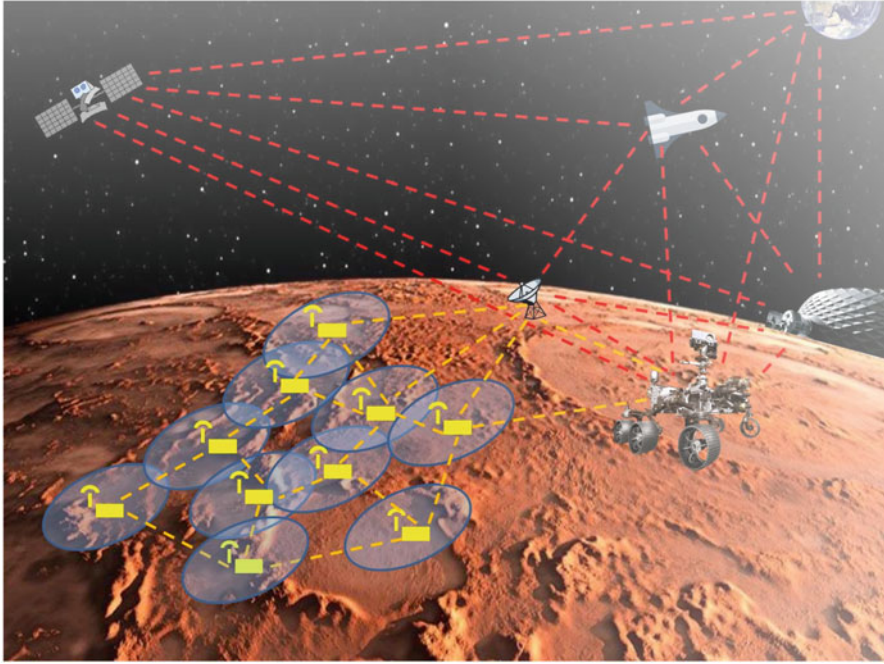


Fig. 4 A possible network on the Mars

Mars is the most studied planet on which to deploy WSNs, and they could be effective in the network that is aiming to prepare the first human settlements (Fig. 4). Ulmer et al. [37] propose a distributed WSN model performing measurements and data transfers in the Mars environment, while [38] present a poll-reply scheme for gathering sensor data on Mars while considering energy conservation and network lifetime. The study proposes a clustering assisted, energy aware polling model. The methodology uses passive clustering protocol and maintains an efficient forwarding mesh with more equally distributed energy consumption. By this way, the lifetime of the network is increased while satisfying connectivity and latency constraints.

Again, [39] develop an efficient routing scheme for Mars WSNs using sensors, rovers, and packet radio network connections that considers energy conservation and network lifetime. A multi-path routing scheme is developed with a mesh structure that decreases the congestion and increases the energy efficiency and reliability. The energy aware path selection helped the network to increase its lifetime. Del Re et al. [40] and Pucci et al. [41] investigate the performance of an IEEE 802.15.4 standard-based WSN working at 2.4 GHz in the Mars environment with several simulations on Simulink and OMNET++. A characterization of the most preferred five frequency channels is considered with Martian geomorphologic, atmospheric, and eolian features to test the performance of the IEEE 802.15.4 standard. Bit Error

Rate (BER), Symbol Error Rate (SER), and Throughput are evaluated to present the network performance.

Further, [42] studies CubeSats-aided WSNs in discovering Mars and Venus, and details about the design, development, testing, and possible mission architectures of the proposed instruments are revealed. The results present that these devices can operate in such extreme environments. Despite the average surface temperature being $+462\text{ }^{\circ}\text{C}$ on Venus, it is the second-most studied planet in the literature in terms of discovery via WSNs. Ponchak et al. [43] also describe and prove the possible utilization of a high-temperature wireless seismometer sensor to be deployed on Venus.

In the NASA Venus Technology Plan published in 2014 [44], one of the technological improvements needed for operation in the Venus ambient is the development of high-temperature electronics, sensors, and thermoelectric power sources for future missions. In the plan, it is emphasized that sensors should operate at temperature levels from $100\text{ }^{\circ}\text{C}$ to above $460\text{ }^{\circ}\text{C}$ on Venus. Geophysical, chemical, imaging, infrared, and other types of sensors can be used in missions, and the WSNs must work for long durations (i.e., months). Glaze et al. [45] also state that the sensors developed for exploring Venus must be temperature-resistant and should have long-term surface survival.

In many of the studies, Mars and Venus are the most studied planets that can be discovered by deploying WSNs on their surfaces. The requirements for the WSNs to be operable on the planet surface are mostly described and studied in the papers. Titan can also be added to the exploration list soon.

4 Using WSNs in Space Missions

Clare et al. [46] propose a communications architecture for space-based SNs and a method that reveals the link activation schedule (transmit/receive mode and communications neighbor choosing) and routes utilized for efficient traffic relay. Since the inter-spacecraft distances are long, directional antennas are utilized with a single half-duplex transceiver per spacecraft to decrease the cost. An illustrative example by evaluating throughput and latency performance is covered in the study. An extension to the networking approach is also defined which is traffic adaptive.

Then, [47] study integrated vehicle health monitoring (IVHM) sensor technology to be used in future spacecraft for keeping the crew and the vehicle safe. This technology has high costs and its weight, size, and other specifications can be obstacles for them to be integrated onto a spacecraft. The study presents a few new wireless sensing technologies such as IVHM for future spacecraft and it also emphasizes the challenges about utilizing WSNs for aerospace vehicles.

Vladimirova et al. [48] introduce a picosatellite SN. The research is carried out at the Surrey Space Centre and aims at space weather missions in low Earth orbit (LEO). The satellite SN demonstrates improvements in the modified IEEE 802.11 wireless standard for inter-satellite links, the distributed computing for inten-

sive onboard signal processing, and the reconfigurable system-on-a-chip design. Meanwhile, [49] deal with the design issues of the satellite SNs, and a distributed computing platform is presented. Distributed satellite system scenarios considering the flower constellation set are presented. Communication subjects of a space based-WSN (SB-WSN) in reference to the Open Systems Interconnection (OSI) networking scheme are covered. A new configurable inter-satellite communications module for picosatellites is summarized.

Sun et al. [50] express some application scenarios for space-based WSNs as very-small-satellite cluster/swarms, autonomous formation flying, onboard sensor networks, fractionated spacecrafts, and surface vehicles on the Moon, planets, and asteroids. Network scale, link range, degree of dynamics, data rate, power consumption, time intensive requirement, and degree of cooperation criteria are presented to categorize applications and to select the most potentially feasible technologies. The difficulties about implementing the application are also divided into levels and compared. Wagner [51] surveys two WSN protocols as Wireless HART (from the HART Communication Foundation) and ISA100.11a (from the International Society of Automation) for both spaceflight and terrestrial implementations and illustrates a new standards-based SN architecture. The research also illustrates the structure for a new standards-based SN for networking and applications.

Meanwhile, [52] and [53] conduct an overview of the chances for partnerships to develop new wireless sensors to be used in space applications. The studies emphasize the benefits of utilizing small, passive, wireless sensors in space environments from ground tests to operations on orbit. The sensors can decrease the launch and fabrication costs because of their wireless structure. The studies also mention that using VHMSs can increase safety, provide examples from NASA applications, and suggest that to the universities, industry, and other governmental agencies work together about new wireless sensors.

Wagner and Barton [54] perform a comparison of the relative performance of the ZigBee Pro and ISA100.11a WSN protocols in a crewed aerospace scenario and the WSN protocols in an aerospace analog environment are analyzed. The study compares message delivery rates succeeded by both under different levels of 802.11g Wi-Fi traffic while [55] focus on the design issues of space-based WSNs and study the network architecture. An algorithm is also proposed to schedule communications while satisfying the SN traffic with the least latency. Further, [56] present the design and measurement of an ultrasonic WSN in the on-earth Columbus Module that is a replication of the main module connected to the International Space Station (ISS). The module is testing new hardware before deployment to the ISS.

In brief, utilizing WSNs in spacecraft and space stations or sometimes using satellites as SNs is the most studied topic under this subject. Besides the Moon and planets, asteroids can also be targets of WSN utilization. According to NASA findings, there are currently 1,064,044 known asteroids and 3,714 known comets awaiting exploration [57].

5 Conclusion

In this chapter, studies of the utilization of WSNs in space missions are investigated and summarized. In conclusion, the technological developments in wireless communication technologies allow WSNs to be utilized in space applications and to discover the Moon, planets, natural moons of the planets, or asteroids. Humankind sent humans and vehicles to the Moon, rovers to explore the surface of Mars, and vehicles to investigate Venus and an asteroid named Eros. Thus, WSNs can be good alternatives to gather critical physical data including temperature, seismic, visual, infrared, light, pressure, radiation, and gas data, among others about target objects. Nevertheless, the environments on the planets or on other space bodies can be highly difficult for such instruments. Therefore, there are still many areas to be studied by researchers and scientists so the capabilities of sensors and their communication skills can be adapted to space applications.

References

1. Akyildiz IF, Su W, Sankarasubramaniam Y et al (2002) Wireless sensor networks: A survey. *Computer Networks* 38:393–422
2. Yick J, Mukherjee B, Ghosal D (2008) Wireless sensor network survey. *Computer Networks* 52:2292–2330
3. Solaiman B, Sheta A (2013) Computational intelligence for wireless sensor networks: Applications and clustering algorithms. *International Journal of Computer Applications* 73(15):1–8
4. Virmani D, Soni A, Chandel S et al (2014) Routing attacks in wireless sensor networks: A survey. *International Journal of Computer Science and Information Technologies* 5(2):2665–2671
5. Mohamed SM, Hamza HS, Saroit IA (2017) Coverage in mobile wireless sensor networks (M-WSN): A survey. *Computer Communications* 110:133–150
6. Prasad P (2015) Recent trend in wireless sensor network and its applications: A survey. *Sensor Review* 35(2):229–236
7. Singh MK, Amin SI, Imam SA et al (2018) A survey of wireless sensor network and its types. In: *International Conference on Advances in Computing, Communication Control and Networking*, Greater Noida, India, 12–13 October 2018
8. Pabari JP, Acharya YB, Desai UB (2009) Investigation of wireless sensor deployment schemes for in-situ measurement of water ice near lunar south pole. *Sensors & Transducers Journal* 111(12):86–105
9. Pabari JP, Acharya YB, Desai UB et al (2010) Radio frequency modelling for future wireless sensor network on surface of the moon. *International Journal of Communications, Network and System Sciences* 3:395–401
10. Prasad KD, Murty SVS (2011) Wireless sensor networks – A potential tool to probe for water on moon. *Advances in Space Research* 48:601–612
11. Pabari JP, Acharya YB, Desai UB et al (2013) Concept of wireless sensor network for future in-situ exploration of lunar ice using wireless impedance sensor. *Advances in Space Research* 52:321–331
12. Zhai X, Vladimirova T (2015) Data aggregation in wireless sensor networks for lunar exploration. In: *Sixth International Conference on Emerging Security Technologies*, Braunschweig, Germany, 03–05 September 2015

13. Lopez-Matencio P (2016) An ACOR-based multi-objective WSN deployment example for lunar surveying. *Sensors* 16(209):1–20
14. Parrado-García FJ, Vales-Alonso J, Alcaraz JJ (2017) Optimal planning of WSN deployments for in situ lunar surveys. *IEEE Transactions on Aerospace and Electronic Systems* 53(4):1866–1879
15. Ozkan O (2020) Wireless sensor deployment on 3-D surface of moon to maximize coverage by using a hybrid memetic algorithm. *Uludağ University Journal of the Faculty of Engineering* 25(1):303–324
16. Dubois A, Botteron C, Mitev V et al (2009) Ad hoc wireless sensor networks for exploration of solar-system bodies. *Acta Astronautica* 64:626–643
17. NASA (2021a) Planet compare. <https://solarsystem.nasa.gov/planet-compare/> Accessed 24 February 2021
18. Coustenis A, Lunine J, Lebreton J-P et al (2009) Earth-based support for the Titan Saturn system mission. *Earth Moon Planet* 105:135–142
19. Mocquet A, Rosenblatt P, Dehant V et al (2011) The deep interior of Venus, Mars, and the Earth: A brief review and the need for planetary surface-based measurements. *Planetary and Space Science* 59:1048–1061
20. Launius RD (2012) Venus-Earth-Mars: Comparative climatology and the search for life in the solar system. *Life* 2:255–273
21. Lorenz RD (2012) Planetary seismology—expectations for lander and wind noise with application to Venus. *Planetary and Space Science* 62:86–96
22. Edberg NJT, Andrews DJ, Agren K et al (2013) Space weather at Venus, Mars and Titan. In: European Planetary Science Congress, London, United Kingdom, 08–13 September 2013
23. Greenwood JP, Karato S-i, Kaaden KEV et al (2018) Water and volatile inventories of Mercury, Venus, the Moon, and Mars. *Space Science Reviews* 214(92):1–39
24. Garg K, Kuhn T (2020) Balloon design for Mars, Venus, and Titan atmospheres. *Applied Sciences* 10(3204):1–25
25. Trebi-Ollennu A, Huntsberger T, Cheng Y et al (2001) Design and analysis of a sun sensor for planetary rover absolute heading detection. *IEEE Transactions on Robotics and Automation* 17(6):939:947
26. Sun T, Chen L-J, Han C-C et al (2005) Reliable sensor networks for planet exploration. In: 4th International Conference on Networking, Reunion Island, France, 17–21 April 2005
27. Gaura E, Newman RM (2006) Wireless sensor networks: The quest for planetary field sensing. In: 31st IEEE Conference on Local Computer Networks, Tampa, FL, USA, 14–16 November 2006
28. Medina A, de Nequeruela C, Mollinedo L et al (2010) Wireless sensor web for rover planetary exploration. In: 10th International Symposium on Artificial Intelligence, Robotics and Automation in Space, Sapporo, Japan, 29 August – 01 September 2010
29. Pabari JP, Acharya YB, Desai UB (2012) Development of impedance-based miniaturized wireless water ice sensor for future planetary applications. *IEEE Transactions on Instruments and Measurement* 61(2):521–529
30. Prasad KD, Bhattacharya A, Murty SVS (2012) An ambient light sensing module for wireless sensor networks for planetary exploration. *Planetary and Space Science* 70:10–19
31. Sanz D, Barrientos A, Garzon M et al (2013) Wireless sensor networks for planetary exploration: Experimental assessment of communication and deployment. *Advances in Space Research* 52:1029–1046
32. Rodrigues P, Oliveira A, Alvarez F et al (2014) Space wireless sensor networks for planetary exploration: Node and network architectures. In: NASA/ESA Conference on Adaptive Hardware and Systems, Leicester, United Kingdom, 14–17 July 2014
33. Sergiou C, Paphitis A, Panagiotou C et al (2014) Wireless sensor networks for planetary exploration: Issues and challenges through a specific application. In: SpaceOps 2014 Conference, Pasadena, CA, JSA, 05–09 May 2014

34. Oliveira MA (2016) Space wireless sensor networks for planetary exploration (SWIPE) project final report. <https://cordis.europa.eu/project/id/312826/en?format=pdf> Accessed 24 February 2021
35. Zhai X, Vladimirova T (2016) Efficient data-processing algorithms for wireless-sensor-networks-based planetary exploration. *Journal of Aerospace Information Systems*, 13(1):46–66
36. Oddi G, Pietrabissa A, Liberati F et al (2017) An any-sink energy-efficient routing protocol in multi-hop wireless sensor networks for planetary exploration. *International Journal of Communication Systems* 30(e3020):1–25
37. Ulmer C, Yalamanchili S, Alkalai L (2000) Wireless distributed sensor networks for in-situ exploration of Mars. NASA Technical Report <http://citeseerx.ist.psu.edu/viewdoc/download?doi=10.1.1.116.324&rep=rep1&type=pdf> Accessed 24 February 2021
38. Hong X, Gerla M, Bagrodia R et al (2001) The Mars sensor network: Efficient, energy aware communications. In: MILCOM Proceedings Communications for Network-Centric Operations, McLean, VA, USA, 28–31 October 2001
39. Hong X, Gerla M, Wang H et al (2002) Load balanced, energy-aware communications for Mars sensor networks. In: IEEE Aerospace Conference, Big Sky, MT, USA, 09–16 March 2002
40. Del Re E, Pucci R, Ronga LS (2009) IEEE802.15.4 wireless sensor network in Mars exploration scenario. In: International Workshop on Satellite and Space Communications, Siena, Italy, 09–11 September 2009
41. Pucci R, Ronga LS, Del Re E et al (2009) Performance evaluation of an IEEE802.15.4 standard based wireless sensor network in Mars exploration scenario. In: 1st International Conference on Wireless Communication, Vehicular Technology, Information Theory and Aerospace & Electronic Systems Technology, Aalborg, Denmark, 17–20 May 2009
42. Prasad KD (2019) CubeSats aided wireless sensor networks for exploration of Mars and Venus. In: URSI Asia-Pacific Radio Science Conference, New Delhi, India, 09–15 March 2019
43. Ponchak GE, Scardelletti MC, Taylor B et al (2012) High temperature, wireless seismometer sensor for Venus. In: IEEE Topical Conference on Wireless Sensors and Sensor Networks, Santa Clara, CA, USA, 15–18 January 2012
44. NASA (2014) Venus Technology Plan. <https://www.lpi.usra.edu/vexag/reports/Venus-Technology-Plan-140617.pdf> Accessed 24 February 2021
45. Glaze LS, Wilson CF, Zasova LV et al (2018) Future of Venus research and exploration. *Space Science Reviews* 214(89):1–37
46. Clare LP, Gao JL, Jennings EH et al (2004) Communications architecture for space-based sensor networks. In: IEEE Aerospace Conference Proceedings, Big Sky, MT, USA, 06–13 March 2004
47. Wilson W, Atkinson G (2008) Wireless sensing opportunities for aerospace applications. *Sensors & Transducers Journal* 94(7):83–90
48. Vladimirova T, Wu X, Bridges CP (2008) Development of a satellite sensor network for future space missions. In: IEEE Aerospace Conference, Big Sky, MT, USA, 01–08 March 2008
49. Vladimirova T, Bridges CP, Paul JR et al (2010) Space-based wireless sensor networks: Design issues. In: IEEE Aerospace Conference, Big Sky, MT, USA, 06–13 March 2010
50. Sun R, Guo J, Gill EKA (2010) Opportunities and challenges of wireless sensor networks in space. In: 61st International Astronautical Congress, Prague, CZ, 27 September – 01 October 2010
51. Wagner RS (2010) Standards-based wireless sensor networking protocols for spaceflight applications. In: IEEE Aerospace Conference, Big Sky, MT, USA, 06–13 March 2010
52. Wilson W, Atkinson G (2011a) Wireless sensors for space applications. *Sensors & Transducers Journal* 13:1–9
53. Wilson WC, Atkinson GM (2011a) Space applications for wireless sensors. In: NSTI Nanotechnology Conference & Expo, Boston, MA, USA, 13–16 June 2011
54. Wagner RS, Barton RJ (2012) Performance comparison of wireless sensor network standard protocols in an aerospace environment: ISA100.11a and ZigBee Pro. In: IEEE Aerospace Conference, Big Sky, MT, USA, 03–10 March 2012

55. Gowda CH, Prakruthi MK (2014) Wireless sensor networks for space and solar-system missions. *International Journal of Engineering Research & Technology* 2(13):395–400
56. Kesuma H, Ahmadi-Pour S, Zimmerman H-J et al (2019) Ultrasonic wireless sensor network for human habitation in deep space mission. In: *IEEE International Conference on Wireless for Space and Extreme Environments*, Ottawa, ON, Canada, 16–18 October 2019
57. NASA (2021b) Asteroids, Comets & Meteors. <https://solarsystem.nasa.gov/asteroids-comets-and-meteors/overview/> Accessed 24 February 2021

Near-Optimal Guidance and Pulse-Modulated Reduced-Attitude Control for Orbit Injection



Mauro Pontani, Andrea Pianalto, Stefano Carletta, and Paolo Teofilatto

1 Introduction

Multistage launch vehicles are employed to place satellites in their operational orbits. Ascent path optimization plays a crucial role in the preliminary analysis of the performance of a launch vehicle, with prescribed aerodynamics and propulsion characteristics. The scientific literature includes a number of relevant contributions on trajectory optimization of multistage launch vehicles. Calise et al. [1] and Gath and Calise [2] proposed a hybrid analytic/numerical approach, based on homotopy. Lu and Pan [3] and Lu et al. [4] applied a multiple-shooting method to optimize exoatmospheric trajectories composed of two powered phases and a coast arc, whereas Weigel and Well [5] focused on the ascent trajectories of two launch vehicles with splash-down constraints. Miele [6] introduced and applied the multiple-subarc gradient restoration algorithm for the purpose of optimizing the ascent path of a three-stage vehicle, in the presence of constraints. These represent a common issue, especially for the first two stages, which encounter significant atmospheric density and thus are subject to relevant dynamical stress. Pontani [7] considered the constraint related to the dynamical pressure, and proposed a geometrical method to enforce it, based on the Pontryagin minimum principle.

M. Pontani (✉)

Department of Astronautical, Electrical, and Energy Engineering, Sapienza Università di Roma, Rome, Italy

e-mail: mauro.pontani@uniroma1.it

A. Pianalto

Faculty of Civil and Industrial Engineering, Sapienza Università di Roma, Rome, Italy

S. Carletta · P. Teofilatto

School of Aerospace Engineering, Sapienza Università di Roma, Rome, Italy

Palaia et al. [8] included the same constraint, while adopting a very accurate modeling for aerodynamics and propulsion. These works [7, 8] employed the indirect heuristic method for ascent path optimization, based on the joint use of the necessary conditions for optimality and a heuristic technique. While the preceding publications focused on methodologies that are essentially indirect in nature, other scientific contributions [9–11] dealt with direct approaches applied to multistage rocket trajectory optimization.

In the early phases of the ascent path, the existence of constraints greatly affects the performance of a launch vehicle. Along the powered arcs of the first two stages, the feedback compensation of nonnominal flight conditions must avoid violating these constraints. In fact, at low and moderate altitudes, where the atmospheric density is relevant, the dynamical constraints are usually enforced by maintaining a modest angular displacement between the relative velocity and the longitudinal axis of the ascent vehicle.

Ignition of the upper stage occurs at altitudes where the previously mentioned constraints are no longer effective. This circumstance allows the use of efficient real-time guidance and control approaches, tailored to driving the upper stage toward the desired injection conditions. Precision of orbit insertion, which occurs at burnout of the upper stage, represents a crucial issue, and potentially affects the subsequent phases of spaceflight, because corrective maneuvers may be needed if orbit injection is completed with unsatisfactory accuracy. Traditionally, two different approaches to guidance exist. Explicit algorithms stem from the idea of re-defining the flight trajectory at the beginning of each guidance interval, at which an updated trajectory (leading to the target final condition) is computed [12, 13]. Implicit algorithms consider the perturbations from a specified nominal trajectory, and define the feedback control corrections aimed at maintaining the vehicle in the proximity of the nominal path [14–16]. Neighboring optimal guidance (NOG) can be regarded as an implicit guidance technique that relies on the analytical second-order optimality conditions, in order to find the corrective control actions in the neighborhood of the reference (optimal) path. Most recently, Variable-Time-Domain NOG [17–19] emerged as an effective algorithm, capable of circumventing the major difficulties of former contributions focused on NOG. However, only a limited number of works dealt with the joint application of guidance and control (G&C) algorithms to aerospace vehicles. In Ref. [20] proportional-derivative (PD) control is employed for both G&C algorithms. Guidance and control based on Nonlinear Dynamic Inversion is studied by Marcos et al. [21] and a comparison between Dynamic Inversion and State Dependent Riccati Equation approaches is presented in Ref. [22]. An integrated G&C method is proposed by Tian et al. [23], while the use of G&C based on sliding-mode is investigated in Ref. [24]. Most recently, Pontani and Celani [25–27] proposed two distinct guidance and attitude control architectures based on VTD-NOG. In particular, Ref. [27] addresses the problem of orbit injection of ascent vehicles using VTD-NOG & CPD (“Constrained Proportional-Derivative Control”).

It is apparent that NOG schemes represent a very attractive solution for guidance of aerospace vehicles, because perturbed paths are strictly related to the nominal (optimal) solution. This means that in most cases the vehicle performance, in terms of propellant consumption or time of flight, is subject to modest degradation with respect to the optimal solution. However, the major shortcoming of implicit-type guidance algorithms is in the need of a precomputed nominal trajectory. Furthermore, all NOG schemes assume that the reference path is optimal, and this requires the availability of all the state and co-state variables that appear in the necessary conditions for optimality. Although NOG schemes outperform all the explicit guidance algorithms, the latter have the great advantage of not requiring any nominal trajectory. Moreover, usually explicit guidance techniques are more robust than implicit algorithms.

The work that follows is aimed at (i) introducing a new explicit near-optimal guidance, based on the local projection of the position and velocity variables, (ii) formulating and addressing the reduced-attitude-control problem, which consists in driving the actual longitudinal axis of the upper stage toward the commanded thrust direction, and (iii) providing an accurate modeling of the actuation dynamics, based on thrust vectoring and modulated side jets for roll control. Near-optimal guidance (i), reduced-attitude control (ii), and actuation (iii) are integrated in a unified architecture. The explicit guidance, control, and actuation approach proposed in this study does not require the offline preliminary computation of any reference trajectory or quantity. Monte Carlo simulations are run, for the purpose of ascertaining the effectiveness and accuracy of the G&C architecture at hand, in the presence of significant displacements from the nominal initial conditions.

2 Dynamics of the Upper Stage of a Launch Vehicle

This work is concerned with the accurate orbit insertion of the upper stage of a launch vehicle, tailored to injecting the payload into its operational orbit. The spacecraft of interest is assumed to be subject to the gravitational attraction of a single body (i.e., the Earth). This section describes the equations that govern both trajectory and attitude.

2.1 Trajectory

The spacecraft motion takes place about the Earth, and the dynamics of its mass center is investigated under the following assumptions:

- (a) The Earth has spherical mass distribution.
- (b) The propulsive thrust is continuous and has constant magnitude T .

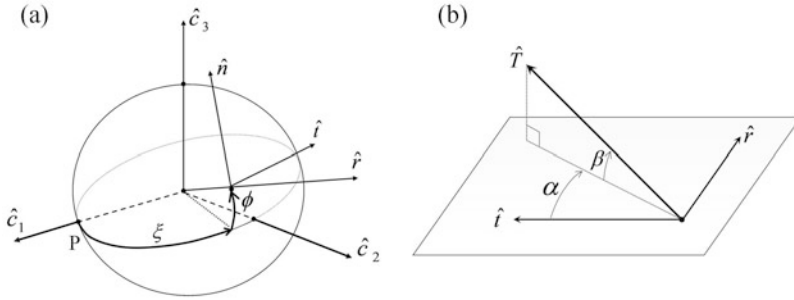


Fig. 1 Reference frames for trajectory (a) and thrust angles (b)

Assumption (a) implies that the gravitational attraction is directed radially. Due to (b), the thrust acceleration a_T is

$$a_T = \frac{T}{m} = \frac{n_0}{\eta} \quad \text{where} \quad \eta := \frac{m}{m_0} \quad \text{and} \quad n_0 := \frac{T}{m_0} \quad (1)$$

where m is the spacecraft instantaneous mass and m_0 denotes the respective initial value.

The spacecraft motion can be described in a convenient inertial reference frame, associated with the right-hand sequence of unit vectors $(\hat{c}_1, \hat{c}_2, \hat{c}_3)$. Its origin is located at the center of the attracting body, and the target orbit lies on the (\hat{c}_1, \hat{c}_2) -plane (cf. Fig. 1a). The time-varying position can be identified by the following three variables: radius r , right ascension ξ , and declination ϕ , portrayed in Fig. 1a. The spacecraft velocity can be projected into the rotating frame $(\hat{r}, \hat{t}, \hat{n})$, where \hat{r} is aligned with the position vector \mathbf{r} and \hat{t} is parallel to the (\hat{c}_1, \hat{c}_2) -plane (and in the direction of the spacecraft motion, cf. Fig. 1a). The related components are denoted with (v_r, v_t, v_n) and termed, respectively radial, transverse, and normal velocity component. The upper stage is controlled through the thrust direction, defined by the in-plane angle α and the out-of-plane angle β , both illustrated in Fig. 1b (in which \hat{T} is aligned with the thrust direction).

The trajectory equations involve $(r, \xi, \phi, v_r, v_t, v_n, \eta)$,

$$\dot{r} = v_r \quad (2)$$

$$\dot{\xi} = \frac{v_t}{r \cos \phi} \quad (3)$$

$$\dot{\phi} = \frac{v_n}{r} \quad (4)$$

$$\dot{v}_r = -\frac{\mu}{r^2} + \frac{v_t^2 + v_n^2}{r} + a_T \sin \alpha \cos \beta \quad (5)$$

$$\dot{v}_t = \frac{v_t}{r} (v_n \tan \phi - v_r) + a_T \cos \alpha \cos \beta \quad (6)$$

$$\dot{v}_n = -\frac{v_t^2}{r} \tan \phi - \frac{v_r v_n}{r} + a_T \sin \beta \quad (7)$$

$$\dot{\eta} = -\frac{n_0}{c} \quad (8)$$

where c is the effective exhaust velocity of the propulsion system, a_T is given by Eq. (1), and $\mu (=398600.4 \text{ km}^3/\text{s}^2)$ is the Earth gravitational parameter.

2.2 Attitude

The spacecraft instantaneous orientation is associated with the body frame. Its origin is in the center of mass of the vehicle, while its axes are aligned with the right-hand sequence of unit vectors $(\hat{i}, \hat{j}, \hat{k})$, with \hat{i} pointing toward the longitudinal axis of the upper stage. Vectrix $\underline{\underline{B}}$ is composed of $(\hat{i}, \hat{j}, \hat{k})$, i.e., $\underline{\underline{B}} := [\hat{i} \ \hat{j} \ \hat{k}]$; similarly, the right-hand sequence $(\hat{c}_1, \hat{c}_2, \hat{c}_3)$, corresponding to the inertial frame, forms vectrix $\underline{\underline{N}} := [\hat{c}_1 \ \hat{c}_2 \ \hat{c}_3]$.

In this research, the instantaneous attitude is referred to $\underline{\underline{N}}$ and is described through Euler parameters (quaternions), denoted with $\{q_0, \mathbf{q}\}$, where q_0 is the scalar part, whereas \mathbf{q} is the (3×1) -vector part. If ${}^N \underline{\underline{\omega}}^B$ denotes the vector angular rate of $\underline{\underline{B}}$ with respect to $\underline{\underline{N}}$, the attitude kinematics equations are [28]

$$\dot{q}_0 = -\frac{1}{2} \mathbf{q}^T \underline{\underline{\omega}} \quad (9)$$

$$\dot{\mathbf{q}} = \frac{1}{2} [q_0 \mathbf{I}_{3 \times 3} + \tilde{\mathbf{q}}] \underline{\underline{\omega}} \quad (10)$$

where $\underline{\underline{\omega}}$ denotes the (3×1) -vector that contains the three components of ${}^N \underline{\underline{\omega}}^B$ in $\underline{\underline{B}}$, i.e., ${}^N \underline{\underline{\omega}}^B = \underline{\underline{B}} \underline{\underline{\omega}}$, $\tilde{\mathbf{q}}$ is the skew-symmetric matrix associated with \mathbf{q} , and $\mathbf{I}_{3 \times 3}$ is the (3×3) identity matrix.

Under the (approximating) assumption that the mass center C does not move during the entire time of flight, the attitude dynamics equations are decoupled from the trajectory equations, and involve the spacecraft angular momentum with respect to C , $\underline{\underline{H}}_C$. If \mathbf{H}_C denotes the (3×1) -vector that includes the three components of $\underline{\underline{H}}_C$ in $\underline{\underline{B}}$, then [28]

$$\dot{\mathbf{H}}_C = -\tilde{\underline{\underline{\omega}}} \mathbf{H}_C + \mathbf{M}_C \quad (11)$$

where $\tilde{\omega}$ denotes the skew-symmetric matrix associated with ω , whereas \mathbf{M}_C is a (3×1) -vector that includes the components of the external torque in $\underline{\mathbf{B}}$. Let $\mathbf{J}_C^{(B)}$ denote the spacecraft inertia matrix with respect to C, resolved in $\underline{\mathbf{B}}$. Because $\mathbf{H}_C = \mathbf{J}_C^{(B)} \omega$, and taking into account the torque $\underline{\mathbf{T}}_C$ due to thrust misalignment (related to thrust vectoring or side jets), Eq. (11) becomes

$$\dot{\omega} = \left[\mathbf{J}_C^{(B)} \right]^{-1} \left(-\tilde{\omega} \mathbf{J}_C^{(B)} \omega - \dot{\mathbf{J}}_C^{(B)} \omega + \mathbf{M}_C + \underline{\mathbf{T}}_C \right), \quad \text{with } \underline{\mathbf{T}}_C = \underline{\mathbf{B}} \mathbf{T}_C \quad (12)$$

In Eq. (12), $\dot{\mathbf{J}}_C^{(B)}$ is the time derivative of the inertia matrix, which is nonzero due to propellant consumption. In this research, external torques are considered negligible, thus $\mathbf{M}_C = \mathbf{0}$ hence forward.

The nonlinear differential system composed of Eqs. (9), (10), and (12) govern the instantaneous attitude and angular rate of the spacecraft. The torque components of \mathbf{T}_C represent the control input.

3 Near-Optimal Guidance

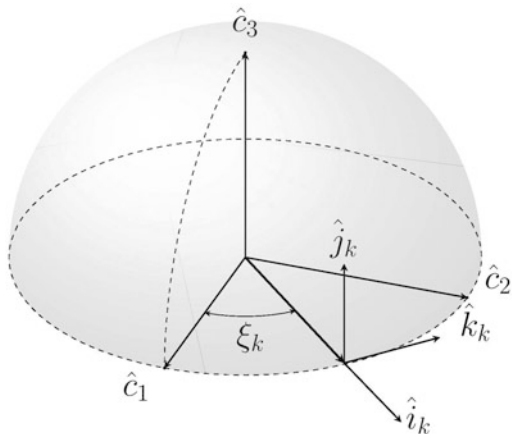
In the great majority of spacecraft guidance scenarios, explicit real-time guidance algorithms are aimed at identifying the optimal thrust direction capable of driving the space vehicle toward the final desired conditions. This study proposes a near-optimal guidance scheme based on local projection of the spacecraft position and velocity, under the assumption that the instantaneous trajectory is sufficiently close to the (\hat{c}_1, \hat{c}_2) -plane, which contains the target orbit. This is assumed to be a circular orbit, with radius R_f .

3.1 Local Projection of Position and Velocity

The guidance algorithm is run repeatedly and starts at equally spaced discrete times $\{t_k\}_{k=0, \dots, N-1}$. The symbol Δt_S denotes the sampling time interval, i.e., $\Delta t_S = t_{k+1} - t_k$ ($k = 1, \dots, N-2$); the last interval is shorter, because the guidance and control algorithm stops when the desired conditions are reached with satisfactory accuracy. At time t_k , the spacecraft position and velocity are denoted with $\underline{\mathbf{r}}_k$ and $\underline{\mathbf{v}}_k$, and are associated with $(r_k, \xi_k, \phi_k, v_{t,k}, v_{n,k}, v_{n,k})$ and $(\hat{r}_k, \hat{t}_k, \hat{n}_k)$ (i.e., $(\hat{r}, \hat{t}, \hat{n})$ at t_k , cf. Fig. 1b). Let $(\hat{x}_k, \hat{y}_k, \hat{z}_k)$ denote three unit vectors obtained from $(\hat{r}_k, \hat{t}_k, \hat{n}_k)$ through a counterclockwise rotation about axis 2 by angle ϕ_k (cf. Fig. 2). Vectors $\underline{\mathbf{r}}_k$ and $\underline{\mathbf{v}}_k$ are projected along $(\hat{x}_k, \hat{y}_k, \hat{z}_k)$,

$$\underline{\mathbf{r}}_k = r_k \begin{bmatrix} \cos \phi_k & 0 & \sin \phi_k \end{bmatrix} \begin{bmatrix} \hat{x}_k & \hat{y}_k & \hat{z}_k \end{bmatrix}^T \quad (13)$$

Fig. 2 Reference frame for the near-optimal guidance



$$\underline{v}_k = [v_{r,k} \ v_{t,k} \ v_{n,k}] \mathbf{R}_2(-\phi_k) \begin{bmatrix} \hat{x}_k \\ \hat{y}_k \\ \hat{z}_k \end{bmatrix} = \begin{bmatrix} v_{r,k} \cos \phi_k - v_{n,k} \sin \phi_k \\ v_{t,k} \\ v_{r,k} \sin \phi_k + v_{n,k} \cos \phi_k \end{bmatrix}^T \begin{bmatrix} \hat{x}_k \\ \hat{y}_k \\ \hat{z}_k \end{bmatrix} \quad (14)$$

Then, the locally flat variables (x, y, z, v_x, v_y, v_z) are introduced, with values at t_k corresponding to the components of \underline{r}_k and \underline{v}_k along $(\hat{x}_k, \hat{y}_k, \hat{z}_k)$, i.e.,

$$x_k = r_k \cos \phi_k \quad y_k = 0 \quad z_k = r_k \sin \phi_k \quad (15)$$

$$v_{x,k} = v_{r,k} \cos \phi_k - v_{n,k} \sin \phi_k \quad v_{y,k} = v_{t,k} \quad v_{z,k} = v_{r,k} \sin \phi_k + v_{n,k} \cos \phi_k \quad (16)$$

The locally flat variables are governed by the following equations of motion [19]:

$$\dot{x} = v_x \quad \dot{y} = v_y \quad \dot{z} = v_z \quad (17)$$

$$\dot{v}_x = \tilde{a}_T \sin \theta_1 \cos \theta_2 - g \quad \dot{v}_y = \tilde{a}_T \cos \theta_1 \cos \theta_2 \quad \dot{v}_z = \tilde{a}_T \sin \theta_2 \quad (18)$$

where angles (θ_1, θ_2) identify the thrust direction in $(\hat{x}_k, \hat{y}_k, \hat{z}_k)$, g denotes the (local) gravitational acceleration, and \tilde{a}_T is the thrust acceleration. Because the final orbit is circular, using (x, y, z, v_x, v_y, v_z) , the desired conditions at orbit injection are rewritten as

$$x_f = R_f \quad z_f = 0 \quad v_{x,f} = 0 \quad v_{y,f} = \sqrt{\frac{\mu}{R_f}} \quad v_{z,f} = 0 \quad (19)$$

It is worth remarking that these projected variables are used only in the context of the guidance algorithm, and allow a sufficiently accurate approximate description of the spacecraft trajectory, provided that the injection arc is sufficiently short.

3.2 Optimal Control

In general, the numerical solution of spacecraft trajectory optimization problems is an offline task, which cannot be demanded to onboard guidance algorithms. In this study, the projected variables, in conjunction with the related governing Eqs. (17), (18) and boundary conditions (19), are employed for the purpose of identifying the optimal thrust direction that minimizes the time of flight. Let $\mathbf{x} = [x \ y \ z \ v_x \ v_y \ v_z]^T$ and $\mathbf{u} = [\theta_1 \ \theta_2]^T$ represent, respectively, the state and control vector. The following optimal control problem is introduced:

$$\mathbf{u}^*(t) = \arg \min_{\mathbf{u}} t_f \quad \text{subject to} \quad \text{Eqs. (17) – (19)}$$

where the star denotes the optimal value of the related vector.

The problem at hand admits an analytical solution that depends on the initial values of the adjoint vector conjugate to the state Eqs. (17) and (18), if \tilde{a}_T and g are assumed constant in Eq. (18). To prove this, a Hamiltonian H and the auxiliary function Φ are introduced,

$$H = \lambda_1 v_x + \lambda_2 v_y + \lambda_3 v_z + \lambda_4 (\tilde{a}_T \cos \theta_2 \sin \theta_1 - g) + \lambda_5 \tilde{a}_T \cos \theta_2 \sin \theta_1 + \lambda_6 \tilde{a}_T \sin \theta_2 \quad (20)$$

$$\Phi = t_f + v_1 (x_f - R_f) + v_2 z_f + v_3 v_{x,f} + v_4 \left[v_{y,f} - \sqrt{\frac{\mu}{R_f}} \right] + v_5 v_{z,f} \quad (21)$$

where $\{\lambda_j\}_{j=1, \dots, 6}$ are the adjoint variables conjugate to the state Eqs. (17) and (18). The necessary conditions for optimality include the boundary conditions for the adjoint variables [14],

$$\lambda_{1,f} = v_1 \quad \lambda_{2,f} = 0 \quad \lambda_{3,f} = v_2 \quad \lambda_{4,f} = v_3 \quad \lambda_{5,f} = v_4 \quad \lambda_{6,f} = v_5 \quad (22)$$

accompanied by the adjoint equations

$$\dot{\lambda}_1 = -\frac{\partial H}{\partial x} = 0 \quad \Rightarrow \quad \lambda_1 = \lambda_{1,0} \quad (23)$$

$$\dot{\lambda}_2 = -\frac{\partial H}{\partial y} = 0 \Rightarrow \lambda_2 = \lambda_{2,0} = \lambda_{2,f} = 0 \quad (24)$$

$$\dot{\lambda}_3 = -\frac{\partial H}{\partial z} = 0 \Rightarrow \lambda_3 = \lambda_{3,0} \quad (25)$$

$$\dot{\lambda}_4 = -\frac{\partial H}{\partial v_x} = -\lambda_1 \Rightarrow \lambda_4 = \lambda_{4,0} - \lambda_{1,0}t \quad (26)$$

$$\dot{\lambda}_5 = -\frac{\partial H}{\partial v_y} = -\lambda_2 \Rightarrow \lambda_5 = \lambda_{5,0} - \lambda_{2,0}t = \lambda_{5,0} \quad (27)$$

$$\dot{\lambda}_6 = -\frac{\partial H}{\partial v_z} = -\lambda_3 \Rightarrow \lambda_6 = \lambda_{6,0} - \lambda_{3,0}t \quad (28)$$

where subscript 0 denotes the value of the corresponding variable at the initial time t_0 . The Pontryagin minimum principle leads to expressing the control angles in terms of the adjoint variables,

$$\mathbf{u}^* = \arg \min_{\mathbf{u}} H \Rightarrow \begin{cases} \sin \theta_1 = -\frac{\lambda_4}{\sqrt{\lambda_4^2 + \lambda_5^2}} & \cos \theta_1 = -\frac{\lambda_5}{\sqrt{\lambda_4^2 + \lambda_5^2}} \\ \theta_2 = -\arcsin \frac{\lambda_6}{\sqrt{\lambda_4^2 + \lambda_5^2 + \lambda_6^2}} \end{cases} \quad (29)$$

The condition $\lambda_{5,0} = 0$ leads to $\theta_1 = \pm \pi/2$, which implies the violation of the final conditions, therefore $\lambda_{5,0} \neq 0$. Hence, the closed-form expressions of $\{\lambda_1, \lambda_3, \lambda_4, \lambda_5, \lambda_6\}$ can be scaled by $\lambda_{5,0}$, to yield

$$\sin \theta_1 = -\frac{\tilde{\lambda}_{4,0} - \tilde{\lambda}_{1,0}t}{\sqrt{[\tilde{\lambda}_{4,0} - \tilde{\lambda}_{1,0}t]^2 + 1}} \quad \cos \theta_1 = \mp \frac{1}{\sqrt{[\tilde{\lambda}_{4,0} - \tilde{\lambda}_{1,0}t]^2 + 1}} \quad (30)$$

$$\theta_2 = -\arcsin \frac{\tilde{\lambda}_{6,0} - \tilde{\lambda}_{3,0}t}{\sqrt{[\tilde{\lambda}_{4,0} - \tilde{\lambda}_{1,0}t]^2 + 1 + [\tilde{\lambda}_{6,0} - \tilde{\lambda}_{3,0}t]^2}} \quad (31)$$

where $\tilde{\lambda}_{j,0} = \lambda_{j,0}/\lambda_{5,0}$ ($j = 1, 3, 4, 6$). These quantities are collected in $\boldsymbol{\lambda}_0 := [\tilde{\lambda}_{1,0} \tilde{\lambda}_{3,0} \tilde{\lambda}_{4,0} \tilde{\lambda}_{6,0}]^T$. The analytical expressions (30) and (31) are used in Eqs. (17) and (18), and lead to obtaining closed-form solutions for all of the state variables,

$$\begin{aligned} x &= f_1(\boldsymbol{\lambda}_0, t) & y &= f_2(\boldsymbol{\lambda}_0, t) & z &= f_3(\boldsymbol{\lambda}_0, t) \\ v_x &= f_4(\boldsymbol{\lambda}_0, t) & v_y &= f_5(\boldsymbol{\lambda}_0, t) & v_z &= f_6(\boldsymbol{\lambda}_0, t) \end{aligned} \quad (32)$$

where $\{f_j\}_{j=1, \dots, 6}$ are nonlinear functions of (λ_0, t) . The explicit expressions for $\{f_j\}_{j=1, \dots, 6}$, written in terms of elementary functions, are omitted for the sake of conciseness. The preceding solutions for $\{x, z, v_x, v_y, v_z\}$ are evaluated at t_f and inserted in the boundary conditions (19),

$$\begin{aligned} f_1(\lambda_0, t_f) - R_f &= 0 & f_3(\lambda_0, t_f) &= 0 & f_4(\lambda_0, t_f) &= 0 \\ f_5(\lambda_0, t) - \sqrt{\frac{\mu}{R_f}} &= 0 & f_6(\lambda_0, t_f) &= 0 \end{aligned} \quad (33)$$

Equation (33) contains a system of 5 nonlinear equations in 5 unknowns, i.e., t_f and the 4 components of λ_0 . Numerical solvers (such as the embedded routine *fsolve* in Matlab) can be employed to find the numerical solution of this system in extremely short times (of order of 0.01 s), provided that a proper guess is supplied. To do this, the analysis described in Ref. [19] can be used. In fact, for planar trajectories, corresponding to $z = 0$ and $v_z = 0$, a suitable first-attempt solution is proven to be [19]

$$\begin{aligned} t_f &= -\frac{v_{y,f} - v_{y,0}}{\tilde{a}_T} \frac{\tan \theta_{1,0}^{(G)} - \tan \theta_{1,f}^{(G)}}{\operatorname{asinh}(\tan \theta_{1,f}^{(G)}) - \operatorname{asinh}(\tan \theta_{1,0}^{(G)})} \\ \tilde{\lambda}_{1,0}^{(G)} &= -\frac{\tan \theta_{1,0}^{(G)} - \tan \theta_{1,f}^{(G)}}{t_f} & \tilde{\lambda}_{4,0}^{(G)} &= -\tan \theta_{1,0}^{(G)} \end{aligned} \quad (34)$$

where $\theta_{1,0}^{(G)}$ and $\theta_{1,f}^{(G)}$ are two guess values for the thrust angle θ_1 at t_0 and t_f , respectively; in this work, $\theta_{1,0}^{(G)}$ is set to $\arctan(v_{y,0}/v_{x,0})$, whereas $\theta_{1,f}^{(G)} = 0$. These two values correspond to a thrust direction pointing toward the instantaneous velocity (at t_0) and the desired velocity (at t_f). The remaining two guess values, for $\tilde{\lambda}_{3,0}^{(G)}$ and $\tilde{\lambda}_{6,0}^{(G)}$, are both set to 0. Moreover, in the second relation of Eq. (31) the sign + is chosen [19].

The guidance algorithm repeats the preceding solution process at each sampling time t_k , which becomes the initial time t_0 of the optimal control problem. The final time t_f can be regarded as the time-to-go, and will be denoted with t_{go} hence forward. However, constant values of g and \tilde{a}_T are needed in each guidance interval, which has duration Δt_S . For the gravitational acceleration, the initial value is chosen, i.e., $g = \mu/r_k^2$. Instead, for the thrust acceleration, the average value of \tilde{a}_T in $[t_k, t_{k+1}]$ is employed. Letting $n_k := (T/m(t_k))$, in $[t_k, t_{k+1}]$ the thrust acceleration equals $n_k c / [c - n_k(t - t_k)]$. Hence, \tilde{a}_T is set to

$$\tilde{a}_T = \frac{1}{\Delta t_S} \int_{t_k}^{t_{k+1}} \frac{n_k c}{c - n_k(t - t_k)} dt = -\frac{c}{\Delta t_S} \ln \left(1 - \frac{n_k}{c} \Delta t_S \right) \quad (35)$$

It is worth noticing that Eq. (30) resembles the linear tangent steering law [29, 30]. However, preceding formulations of this well-consolidated guidance technique introduce approximate assumptions [29] or employ complicated geometric analyses [31] to solve the problem. Instead, the three-dimensional guidance

approach proposed in this work is based on the real-time numerical solution of the minimum-time problem formulated in flat coordinates, through enforcement of all the necessary conditions of optimality and without any further approximation or arbitrary assumption on the initial thrust angles θ_1 and θ_2 .

3.3 Commanded Attitude

The real-time numerical solution of the preceding optimal control problem provides the thrust angles (θ_1, θ_2) , which identify the desired thrust direction in $(\hat{x}_k, \hat{y}_k, \hat{z}_k)$. The latter sequence is obtained from $(\hat{c}_1, \hat{c}_2, \hat{c}_3)$ through a single counterclockwise elementary rotation about axis 3 by angle ξ_k . Therefore, the commanded thrust direction $\hat{T}^{(C)}$ is

$$\begin{aligned} \hat{T}^{(C)} &= [\cos \theta_2 \sin \theta_1 \cos \theta_2 \cos \theta_1 \sin \theta_2] [\hat{x}_k \hat{y}_k \hat{z}_k]^T \\ &= [\cos \theta_2 \sin \theta_1 \cos \theta_2 \cos \theta_1 \sin \theta_2] \mathbf{R}_3(\xi_k) [\hat{c}_1 \hat{c}_2 \hat{c}_3]^T \end{aligned} \quad (36)$$

Under the assumption that the thrust is aligned with the longitudinal axis of the upper stage, unit vector $\hat{T}^{(C)}$ identifies the commanded direction $\hat{l}^{(C)}$. The actual body axis \hat{l} must be driven toward $\hat{l}^{(C)}$ by the attitude control system. The remaining two commanded body axes, $\hat{j}^{(C)}$ and $\hat{k}^{(C)}$, are defined as

$$\hat{k}^{(C)} := \frac{\hat{c}_3 \times \hat{l}^{(C)}}{|\hat{c}_3 \times \hat{l}^{(C)}|} \quad \text{and} \quad \hat{j}^{(C)} := \hat{k}^{(C)} \times \hat{l}^{(C)} \quad (37)$$

These three unit vectors form vectrix $\underline{\underline{C}}$, i.e., $\underline{\underline{C}} := [\hat{l}^{(C)} \hat{j}^{(C)} \hat{k}^{(C)}]$. Because closed-form expressions are available for (θ_1, θ_2) , the components of $\hat{l}^{(C)}$ (cf. Eq. (36)), $\hat{j}^{(C)}$, and $\hat{k}^{(C)}$ can be written in closed form, as well as the rotation matrix that relates $(\hat{l}^{(C)}, \hat{j}^{(C)}, \hat{k}^{(C)})$ to $(\hat{c}_1, \hat{c}_2, \hat{c}_3)$, i.e., $\mathbf{R}_{C \leftarrow N}$. Using the kinematics equation that governs the time evolution of rotation matrices, it is straightforward to obtain the commanded angular velocity. In fact,

$$\dot{\mathbf{R}}_{C \leftarrow N} = -\tilde{\omega}_C \mathbf{R}_{C \leftarrow N} \quad \Rightarrow \quad \tilde{\omega}_C = -\dot{\mathbf{R}}_{C \leftarrow N} \mathbf{R}_{C \leftarrow N}^T \quad (38)$$

Because analytical expressions are available for both $\mathbf{R}_{C \leftarrow N}$ and $\dot{\mathbf{R}}_{C \leftarrow N}$, matrix $\tilde{\omega}_C$ contains the closed-form expressions of the three components of the commanded angular rate ${}^N \underline{\underline{\omega}}^C$ ($= \underline{\underline{C}} \omega_C$) along $(\hat{l}^{(C)}, \hat{j}^{(C)}, \hat{k}^{(C)})$. The time derivative of ω_C supplies $\dot{\omega}_C$, which is necessary for nonlinear attitude control (cf. Sect. 4).

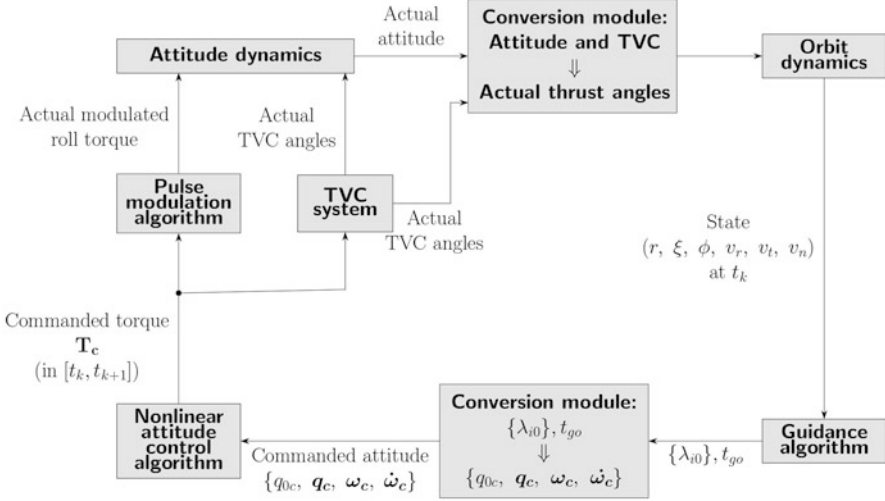


Fig. 3 Block diagram of the guidance, control, and actuation architecture

3.4 Guidance Algorithm

The guidance algorithm is intended to provide the commanded orientation and angular rate to the attitude control system. Therefore, the guidance algorithm has

Input : $r_k, \xi_k, \phi_k, v_{r,k}, v_{t,k}, v_{n,k}, n_k$ (at t_k) \rightarrow Output : t_{go} and $\mathbf{R}_{C \leftarrow N}, \boldsymbol{\omega}_C, \dot{\boldsymbol{\omega}}_C$ (in $[t_k, t_{k+1}]$)

In summary, the following steps are completed at each sampling time t_k :

1. The spherical coordinates of position and velocity are converted into locally flat variables (cf. Eqs. (15) and (16)).
2. The guess solution for the optimal control problem is identified (cf. Eq. (34)).
3. The equation system (33) is solved numerically.
4. t_{go} and the closed-form expressions for $\theta_1, \theta_2, \mathbf{R}_{C \leftarrow N}, \boldsymbol{\omega}_C,$ and $\dot{\boldsymbol{\omega}}_C$ in $[t_k, t_{k+1}]$ are obtained.

The last guidance interval occurs when $t_{go} \leq \Delta t_S$.

It is worth stressing that the guidance approach at hand requires no interpolation or finite-difference method for finding $\mathbf{R}_{C \leftarrow N}$ and $\dot{\boldsymbol{\omega}}_C$, thanks to the availability of analytical expressions for the previously mentioned variables.

Figure 3 depicts the block diagram of the guidance, control, and actuation architecture for the upper stage. The nonlinear attitude control algorithm and the actuation systems, corresponding to the blocks named ‘‘Pulse modulation algorithm’’ and ‘‘TVC system’’ (where TVC is the acronym for thrust vector control), are being described in Sects. 4 and 5, respectively.

4 Nonlinear Quaternion-Based Reduced-Attitude Control

The guidance algorithm provides the desired orientation and angular rates, which must be pursued by the attitude control system. However, only the alignment of the longitudinal axis \hat{l} with $\hat{l}^{(C)}$ is crucial for the purpose of pointing the thrust toward the correct direction. A reduced-attitude-tracking algorithm, which aims at pursuing the desired alignment for a single axis, represents a suitable solution to the problem of interest. This section addresses a new feedback quaternion-based reduced-attitude-tracking algorithm.

4.1 Relative Attitude Kinematics

As a preliminary step, the commanded Euler parameters (quaternions) are obtained from $\mathbf{R}_{C \leftarrow N}$ and denoted with $\{q_0^{(C)}, \mathbf{q}^{(C)}\}$. The actual body axes are aligned with the unit vectors that form $\underline{\mathbf{B}}$. The rotation matrix that relates $\underline{\mathbf{B}}$ and $\underline{\mathbf{C}}$, associated with the commanded body axes, can be written in terms of the error quaternion $\{q_0^{(E)}, \mathbf{q}^{(E)}\}$ [28],

$$\mathbf{R}_{B \leftarrow C} = \mathbf{R}_{B \leftarrow NC \leftarrow N} \mathbf{R}^T = \left\{ \left[q_0^{(E)} \right]^2 - \left[\mathbf{q}^{(E)} \right]^T \mathbf{q}^{(E)} \right\} \mathbf{I}_{3 \times 3} + 2\mathbf{q}^{(E)} \left[\mathbf{q}^{(E)} \right]^T - 2q_0^{(E)} \tilde{\mathbf{q}}^{(E)} \quad (39)$$

From inspection of the first row of $\mathbf{R}_{B \leftarrow C}$, it is apparent that correct alignment of \hat{l} and $\hat{l}^{(C)}$, i.e., $\hat{l} \equiv \hat{l}^{(C)}$, corresponds to

$$\left[q_2^{(E)} \right]^2 + \left[q_3^{(E)} \right]^2 = 0 \quad (40)$$

where subscripts 2 and 3 refer to the components of $\mathbf{q}^{(E)}$. Moreover, the kinematics equations for $\{q_0^{(C)}, \mathbf{q}^{(C)}\}$ are [32]

$$\dot{q}_0^{(E)} = -\frac{1}{2} \left[\mathbf{q}^{(E)} \right]^T \boldsymbol{\omega}_E \quad (41)$$

$$\dot{\mathbf{q}}^{(E)} = \frac{1}{2} \left[q_0^{(E)} \mathbf{I}_{3 \times 3} + \tilde{\mathbf{q}}^{(E)} \right] \boldsymbol{\omega}_E \quad (42)$$

where $\boldsymbol{\omega}_E := \boldsymbol{\omega} - \mathbf{R}_{B \leftarrow C} \boldsymbol{\omega}_C$. The time evolution of the rotation matrix $\mathbf{R}_{B \leftarrow C}$ is governed by the following Eq. (32):

$$\dot{\mathbf{R}}_{B \leftarrow C} = -\tilde{\boldsymbol{\omega}}_E \mathbf{R}_{B \leftarrow C} \quad (43)$$

4.2 Feedback Control Law and Stability Analysis

The target set for the attitude tracking problem is

$$\left[q_2^{(E)} \right]^2 + \left[q_3^{(E)} \right]^2 = 0 \quad \text{and} \quad \boldsymbol{\omega}_E = \mathbf{0} \quad (44)$$

and corresponds to achieving $\boldsymbol{\omega}_E = \mathbf{0}$ and the correct alignment of axis 1, while the commanded orientation of the remaining two axes is not tracked.

Proposition 1 For the torque vector T_C , the following feedback control law is introduced:

$$T_C = \tilde{\boldsymbol{\omega}}_C^{(B)} \boldsymbol{\omega} + \mathbf{j}_C^{(B)} \boldsymbol{\omega} + \mathbf{J}_C^{(B)} \left[\begin{array}{c} \mathbf{R} \\ B \leftarrow C \end{array} \dot{\boldsymbol{\omega}}_C - \tilde{\boldsymbol{\omega}}_{E \leftarrow C} \mathbf{R} \boldsymbol{\omega}_C \right] - \mathbf{J}_C^{(B)} \mathbf{A}^{-1} \left[\mathbf{B} \boldsymbol{\omega}_E + f \left(q_0^{(E)}, \mathbf{q}^{(E)} \right) \right] \quad (45)$$

where

$$f \left(q_0^{(E)}, \mathbf{q}^{(E)} \right) := \left[0 \ q_0^{(E)} q_2^{(E)} + q_1^{(E)} q_3^{(E)} \ q_0^{(E)} q_3^{(E)} - q_1^{(E)} q_2^{(E)} \right]^T \quad (46)$$

and \mathbf{A} and \mathbf{B} are two constant positive definite matrices; \mathbf{A} is also symmetric. The control law (45) drives the dynamical system described by Eqs. (12), (41) and (42) toward the attracting set associated with $\boldsymbol{\omega}_E = \mathbf{0}$.

Proof As a first step, the following candidate Lyapunov function is introduced:

$$V = \frac{1}{2} \boldsymbol{\omega}_E^T \mathbf{A} \boldsymbol{\omega}_E + \left[q_2^{(E)} \right]^2 + \left[q_3^{(E)} \right]^2 \quad (47)$$

It is apparent that this function is always positive definite and vanishes only in the target set. Second, V has continuous partial derivatives. Using Eqs. (12), (42), and (43), the time derivative of V equals

$$\begin{aligned} \dot{V} = \boldsymbol{\omega}_E^T \mathbf{A} \left\{ \left[\mathbf{J}_C^{(B)} \right]^{-1} \left(-\tilde{\boldsymbol{\omega}}_C^{(B)} \boldsymbol{\omega} - \mathbf{j}_C^{(B)} \boldsymbol{\omega} + T_C \right) - \begin{array}{c} \mathbf{R} \\ B \leftarrow C \end{array} \dot{\boldsymbol{\omega}}_C + \tilde{\boldsymbol{\omega}}_{E \leftarrow C} \mathbf{R} \boldsymbol{\omega}_C \right\} \\ + \left[q_0^{(E)} q_2^{(E)} + q_1^{(E)} q_3^{(E)} \right] \omega_{E,2} + \left[q_0^{(E)} q_3^{(E)} - q_1^{(E)} q_2^{(E)} \right] \omega_{E,3} \end{aligned} \quad (48)$$

where $\omega_{E,j}$ denotes component j of $\boldsymbol{\omega}_E$. Insertion of the feedback law (45) leads to

$$\dot{V} = -\boldsymbol{\omega}_E^T \mathbf{B} \boldsymbol{\omega}_E \quad (49)$$

which is negative (because \mathbf{B} is positive definite), except at $\boldsymbol{\omega}_E = \mathbf{0}$, where \dot{V} vanishes. Definitely, V is a positive definite function, with continuous partial

derivatives and such that $\dot{V} < 0$ (unless $\boldsymbol{\omega}_E = \mathbf{0}$), therefore V is a Lyapunov function [33]. \square

Because the attracting set, denoted with A , does not coincide with the target set (44), Proposition 1 does not ensure asymptotic convergence toward the desired final conditions (44). However, the LaSalle's invariance principle can be used to identify the invariant set.

Proposition 2 The control law (45) drives the dynamical system described by Eqs. (12), (41) and (42) toward the invariant set composed of the following two subsets:

1. $\boldsymbol{\omega}_E = \mathbf{0}$ and $\left[q_2^{(E)} \right]^2 + \left[q_3^{(E)} \right]^2 = 0$
2. $\boldsymbol{\omega}_E = \mathbf{0}$ and $\left[q_1^{(E)} \right]^2 + \left[q_0^{(E)} \right]^2 = 0$

Proof Because \dot{V} is continuous and negative (except at $\boldsymbol{\omega}_E = \mathbf{0}$), the condition $V\left(q_0^{(E)}(t), \mathbf{q}^{(E)}(t), \boldsymbol{\omega}_E(t)\right) \leq V\left(q_0^{(E)}(t_0), \mathbf{q}^{(E)}(t_0), \boldsymbol{\omega}_E(t_0)\right)$ defines a compact set C . The invariant set, which plays a crucial role in the LaSalle's principle, is to be sought in $A \cap C$, i.e., in the portion of the attracting set A contained in C . By definition, the invariant set collects all the dynamical states (in the attracting set) that remain unaltered. This means that once the invariant set is reached, $\boldsymbol{\omega}_E = \mathbf{0}$ at future times, which implies $\dot{\boldsymbol{\omega}}_E = \mathbf{0}$, i.e.,

$$\dot{\boldsymbol{\omega}}_E = \dot{\boldsymbol{\omega}} - \underset{B \leftarrow C}{\mathbf{R}} \dot{\boldsymbol{\omega}}_C + \tilde{\boldsymbol{\omega}}_E \underset{B \leftarrow C}{\mathbf{R}} \boldsymbol{\omega}_C = \dot{\boldsymbol{\omega}} - \underset{B \leftarrow C}{\mathbf{R}} \dot{\boldsymbol{\omega}}_C = \mathbf{0} \quad (50)$$

Using Eqs. (12) and (45), the preceding relation simplifies to

$$\mathbf{A}^{-1} \mathbf{f}\left(q_0^{(E)}, \mathbf{q}^{(E)}\right) = \mathbf{0} \quad \Rightarrow \quad \mathbf{f}\left(q_0^{(E)}, \mathbf{q}^{(E)}\right) = \mathbf{0} \quad (51)$$

i.e.,

$$q_0^{(E)} q_2^{(E)} + q_1^{(E)} q_3^{(E)} = 0 \quad \text{and} \quad q_0^{(E)} q_3^{(E)} - q_1^{(E)} q_2^{(E)} = 0 \quad (52)$$

Let $\left\{ \underset{B \leftarrow C}{\mathbf{R}} \right\}_{jk}$ denote element (j, k) of $\underset{B \leftarrow C}{\mathbf{R}}$. Insertion of the two conditions (52) in $\underset{B \leftarrow C}{\mathbf{R}}$, written in terms of the error quaternion (cf. Eq. (39)), leads to obtaining

$\left\{ \underset{B \leftarrow C}{\mathbf{R}} \right\}_{11} = \pm 1$. Thus, the invariant set includes two subsets:

1. $\boldsymbol{\omega}_E = \mathbf{0}$ and $\left\{ \underset{B \leftarrow C}{\mathbf{R}} \right\}_{11} = 1$ or, equivalently, $\boldsymbol{\omega}_E = \mathbf{0}$ and $\left[q_2^{(E)} \right]^2 + \left[q_3^{(E)} \right]^2 = 0$
 2. $\boldsymbol{\omega}_E = \mathbf{0}$ and $\left\{ \underset{B \leftarrow C}{\mathbf{R}} \right\}_{11} = -1$ or, equivalently, $\boldsymbol{\omega}_E = \mathbf{0}$ and $\left[q_1^{(E)} \right]^2 + \left[q_0^{(E)} \right]^2 = 0$
- \square

Hence, the invariant set includes two subsets, denoted with (1) and (2). It is apparent that subset (1) is the target set, whereas subset (2) corresponds to the alignment of body axis 1 toward a direction opposite to the desired one. However, convergence toward subset (2) is only theoretical. In fact $\left[q_1^{(E)}\right]^2 + \left[q_0^{(E)}\right]^2 = 0 \iff \left[q_2^{(E)}\right]^2 + \left[q_3^{(E)}\right]^2 = 1$, and this implies that V has a maximum in subset (2). Although $\dot{V} = 0$ in subset (2), if $\left[q_2^{(E)}\right]^2 + \left[q_3^{(E)}\right]^2 = 1 - \varepsilon$ (where ε is a positive and arbitrarily small constant), then $\dot{V} < 0$, and the reduction of V leads the dynamical system to converge toward the target set, i.e., subset (1) of the invariant set. In other words, subset (2) represents an unstable equilibrium, whereas the target set corresponds to a stable equilibrium. This circumstance has the very interesting practical consequence that – from the numerical point of view – the dynamical system of interest enjoys global convergence toward the desired alignment conditions, provided that the feedback control law (45) is adopted.

4.3 Gain Selection

The feedback control law (45) is defined in terms of two constant, positive definite matrices, i.e., \mathbf{A} and \mathbf{B} . Selection of these matrices affects the transient behavior and the convergence time of the actual attitude toward the commanded one. In this research, these two matrices are selected by assuming that both of them are diagonal and written as

$$\mathbf{A}^{-1} = k_1 \mathbf{I}_{3 \times 3} \quad \text{and} \quad \mathbf{B} = k_2 \mathbf{I}_{3 \times 3} \quad (53)$$

where k_1 and k_2 are two positive constants.

For the purpose of a preliminary selection of the control gains, in three-axial (full-attitude) maneuvers, the rotation is assumed to occur about the eigenaxis, and the gains of the quaternion-based nonlinear feedback law are found using the second-order Eq. (32)

$$\ddot{\varphi}_E + k_1 k_2 \dot{\varphi}_E + k_1 \sin \frac{\varphi_E}{2} = 0 \quad (54)$$

where φ_E is the principal angle. If φ_E is sufficiently small, then $\sin(\varphi_E/2) \approx \varphi_E/2$, and Eq. (54) assumes the form of a second-order linear differential equation:

$$\ddot{\varphi}_E + 2\zeta\omega_n\dot{\varphi}_E + \omega_n^2\varphi_E = 0 \quad \text{with} \quad k_1 = 2\omega_n^2 \quad \text{and} \quad k_2 = \frac{\zeta}{\omega_n} \quad (55)$$

The associated second-order system has damping coefficient ζ and natural frequency ω_n . Selection of these two parameters, which have a straightforward

interpretation in relation to the transient behavior, leads to selecting two proper values of k_1 and k_2 . Although the reduced-attitude control algorithm differs to some extent from the full-attitude control scheme, this methodology for preliminary selection of \mathbf{A} and \mathbf{B} is adopted and implemented.

5 Actuation

Upper stages of launch vehicles employ two distinct actuation strategies for roll motion and pitch/yaw motion. In fact, thrust vectoring, based on modest deviations of the direction of exhausted gases from the longitudinal axis of the spacecraft, provides a torque action with components along body axes 2 and 3 (cf. Fig. 4a). The reaction control system (RCS) based on side jets supplies the required roll torque about axis 1 (cf. Fig. 4b) [34, 35]. This section describes the dynamical modeling of thrust vectoring, using the Kane's method for multibody spacecraft dynamics, and pulse modulation applied to side jets.

5.1 Pulse Modulation for Side Jets

The RCS consists of 4 thrusters ignited in couples, to generate the clockwise (2, 3) or counterclockwise (1, 4) roll torque. Because each actuator can only provide a constant thrust (with magnitude T_{SJ}), the instantaneous value of the roll torque $\underline{T}_C^{(RCS)}$ is constant and given by

$$\underline{T}_C^{(RCS)} = DT_{SJ}\hat{i} \quad (56)$$

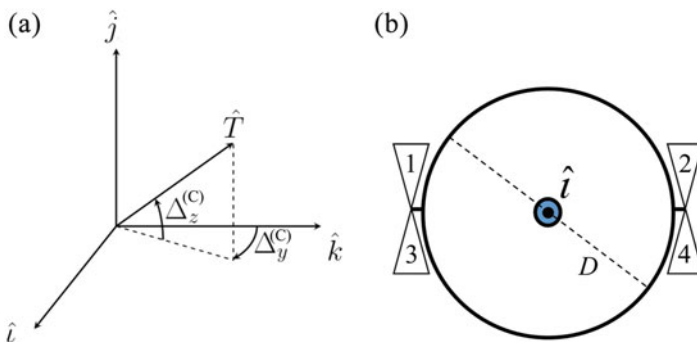


Fig. 4 Thrust deflection angles and thrust direction \hat{T} (a) and illustrative sketch of the RCS (b)

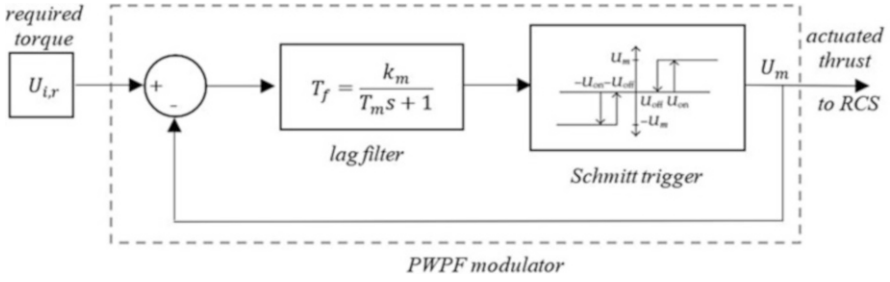


Fig. 5 Scheme of the PWWF modulator

When a lower torque magnitude εDT_{SJ} ($\varepsilon < 1$) is required, the RCS is activated in pulse mode, consisting in a sequence of ON-OFF cycles of relatively short length T_i . For any given i -th cycle, one couple of thrusters is ignited only for a fraction of time $D_i = (t_{i,ON}/T_i)$, named the duty cycle, and is off for the remaining time $t_{i,OFF} = T_i(1 - D_i)$, such that the average torque produced over T_i equals εDT_{SJ} [36]. It is worth outlining that the minimum nonzero duty cycle strictly depends on the specifics of the RCS [37, 38], in particular on the minimum actuation frequency of the thrusters when used in pulse-mode. Actuation of the RCS in pulse-mode generates a nonlinear control action. Therefore, the continuous time history of the required roll torque, yielded by the attitude control algorithm and denoted with $U_{i,r}$ in Fig. 5, is processed through pulse-width pulse-frequency (PWWF) modulation, aimed at determining the appropriate values of D_i and T_i .

The PWWF modulator, illustrated in Fig. 5, includes a Schmitt trigger, whose ON and OFF trigger values are indicated as U_{ON} and U_{OFF} , and a linear lag filter characterized by a gain k_m , a lag time constant T_m , and the following transfer function T_f [39, 40] in the Laplace domain:

$$T_f = \frac{k_m}{T_m s + 1} \quad (57)$$

For each cycle of duration T_i , the input to the filter is the error signal e_i , i.e., the difference between the required control torque component ($U_{i,r}$), computed by the attitude control algorithm at the beginning of the duty cycle, and the output of the Schmitt trigger (U_m), representing the actual control torque demanded to the RCS. The filtered signal (F_i) is processed by the Schmitt trigger, which provides one of the following outputs:

$$\begin{cases} U_m \text{ sign}(F_i) & \text{if } |F_i| > U_{ON} \\ 0 & \text{if } |F_i| < U_{OFF} \end{cases} \quad (58)$$

The values of D_i and T_i can be easily determined based on the parameters of the PWWF modulator (k_m , T_m , U_m , U_{ON} , U_{OFF}). First, the ON and OFF time can be computed through the following Eq. (41):

$$t_{i,\text{ON}} = -T_m \ln \left[1 + \frac{U_{\text{ON}} - U_{\text{OFF}}}{k_m (U_{i,r} - U_m) - U_{\text{ON}}} \right] \quad \text{and} \quad t_{i,\text{OFF}} = -T_m \ln \left(1 - \frac{U_{\text{ON}} - U_{\text{OFF}}}{k_m U_{i,r} + U_{\text{OFF}}} \right) \quad (59)$$

Then, the total duration for the i -th modulation is given by the sum of the two relations in Eq. (59), i.e., $T_i = t_{i,\text{ON}} + t_{i,\text{OFF}}$. Finally, the duty cycle is the ratio $D_i = (t_{i,\text{ON}}/T_i)$. The parameters of the PWPF modulator must be accurately selected through a quasi-static analysis, to obtain the desired performance for the RCS. Typically, this is an iterative process, which can require long time and could benefit from dedicated techniques available in the literature [41, 42]. A compact expression relating the PWPF modulator parameters with the maximum pulse frequency of the thruster, δ , is [43]

$$\delta = \frac{1}{T_m} \left[1 - \frac{U_{\text{ON}} - U_{\text{OFF}}}{k_m U_m} \right] \quad (60)$$

Once the actuators are selected, Eq. (60) helps reducing by one the number of PWPF parameters to select.

5.2 Thrust Vectoring

Thrust vectoring is assumed to be implemented through deflection of the nozzle. As a preliminary step, the desired deflection angles, depicted in Fig. 4a, must be obtained from the required torque $\mathbf{T}_C^{(C)}$, yielded by the nonlinear control algorithm. From inspection of Fig. 4a, it is straightforward to obtain the torque due to thrust vectoring:

$$\mathbf{T}_C^{(C)} = \hat{j} T l \cos \Delta_z^{(C)} \sin \Delta_y^{(C)} - \hat{k} T l \sin \Delta_z^{(C)} \quad (61)$$

where T is the thrust magnitude, l is the distance of the nozzle from the center of mass of the entire spacecraft, and superscript (C) denotes the commanded value of the respective variable. Inversion of the preceding relations yields the two commanded values of the thrust deflection angles, denoted with $\Delta_y^{(C)}$ and $\Delta_z^{(C)}$. These represent the input variables for the thrust vector control mechanism.

Because the nozzle is deflected, the spacecraft can be modeled as a system of two rigid bodies, i.e., the nozzle (body 2) and the remaining portion of the upper stage (body 1), termed also main body henceforth. They are connected through a two-degree-of-freedom joint, and the two-body system has 8 degrees of freedom (6 degrees for the main body and 2 additional degrees related to the type of joint). Two vectrices are associated with the axes of these two bodies, i.e., $\underline{\underline{\mathbf{B}}}_1$ and $\underline{\underline{\mathbf{B}}}_2$. They are related through a sequence of two elementary rotations:

$$\underline{\underline{\mathbf{B}}}_1 = \underline{\underline{\mathbf{B}}}_2 \mathbf{R}_3(\Delta_z) \mathbf{R}_2(-\Delta_z) \quad (62)$$

5.3 Kane's Description of the Spacecraft Dynamics

Kane's method [44, 45] has recently emerged as a general and effective technique tailored to modeling the overall dynamics of multibody spacecraft. It is based on introducing a number of generalized velocities, which equal the number of degrees of freedom of the system. The angular rate and the velocity of the center of mass of each rigid body can be expressed in terms of generalized velocities by introducing the partial velocities. These may be regarded as operators that project the trajectory and attitude dynamics equations onto the subspace of allowed motion, identified by the existing constraints.

This research adopts the formalism introduced by Stoneking [46] for multibody spacecraft. First, each partial velocity is projected along a specific reference frame. Then, the components of the partial velocities are collected in two fundamental matrices, i.e., $\mathbf{\Omega}$ and \mathbf{V} . Let \underline{r}_{21} and $\underline{r}_{2,G1}$ denote the vectors that connect the center of mass of body 2 to the center of mass of body 1 and to the joint, respectively. For the problem at hand, the two matrices $\mathbf{\Omega}$ and \mathbf{V} are

$$\mathbf{\Omega} = \begin{bmatrix} \mathbf{I}_{3 \times 3} & \mathbf{0}_{3 \times 2} & \mathbf{0}_{3 \times 3} \\ \mathbf{R}_{2 \leftarrow 1} & \mathbf{\Gamma}_{G1} & \mathbf{0}_{3 \times 3} \end{bmatrix} \quad (63)$$

$$\mathbf{V} = \begin{bmatrix} \mathbf{0}_{3 \times 3} & \mathbf{0}_{3 \times 2} & \mathbf{I}_{3 \times 3} \\ \underline{r}_{21} \mathbf{R}_{N \leftarrow 1} & \underline{r}_{2,G1} \mathbf{R}_{N \leftarrow 2} & \mathbf{\Gamma}_{G1} \mathbf{I}_{3 \times 3} \end{bmatrix} \quad (64)$$

where $\underline{r}_{21} = \underline{\underline{B}}_2 \underline{r}_{21}$, $\underline{r}_{2,G1} = \underline{\underline{B}}_2 \underline{r}_{2,G1}$; $\mathbf{R}_{N \leftarrow j}$ ($j = 1, 2$) is the rotation matrix from body j to the inertial frame, whereas $\mathbf{R}_{2 \leftarrow 1}$ ($= \mathbf{R}_3(\Delta_z) \mathbf{R}_2(-\Delta_z)$) relates body 1 to body 2. Because the joint has two degrees of freedom, the joint partial is

$$\mathbf{\Gamma}_{G1} = \begin{bmatrix} -\sin \Delta_y & 0 \\ 0 & 1 \\ \cos \Delta_y & 0 \end{bmatrix} \quad (65)$$

The number of columns of $\mathbf{\Omega}$ and \mathbf{V} equals the number of degrees of freedom of the system, i.e., 8. Using $\mathbf{\Omega}$ and \mathbf{V} the angular rates, ${}^N \underline{\omega}^1$ and ${}^N \underline{\omega}^2$, and the velocities of the mass centers, \underline{v}_{C1} and \underline{v}_{C2} , can be retrieved for both bodies:

$$[\underline{\omega}_1^T \ \underline{\omega}_2^T] = \mathbf{\Omega} \mathbf{u}_G \quad \text{and} \quad [\underline{v}_{C1}^T \ \underline{v}_{C2}^T] = \mathbf{V} \mathbf{u}_G \quad (66)$$

where ${}^N \underline{\omega}^1 = \underline{\underline{B}}_1 \underline{\omega}_1$, ${}^N \underline{\omega}^2 = \underline{\underline{B}}_2 \underline{\omega}_2$, $\underline{v}_{C1} = \underline{\underline{N}} \underline{v}_{C1}$, and $\underline{v}_{C2} = \underline{\underline{N}} \underline{v}_{C2}$ (with \underline{v}_{Cj} denoting the velocity of the center of mass of body j). The symbol \mathbf{u}_G denotes the (8×1) generalized velocity vector, given by

$$\mathbf{u}_G = [\boldsymbol{\omega}^T \dot{\Delta}_z \dot{\Delta}_y \mathbf{v}_{C1}^T]^T \quad (67)$$

Kane's equations provide the time derivatives of \mathbf{u}_G and can be written in terms of $\boldsymbol{\Omega}$ and \mathbf{V} as [46]

$$\dot{\mathbf{u}}_G = \left(\boldsymbol{\Omega}^T \mathbf{J} \boldsymbol{\Omega} + \mathbf{V}^T \mathbf{M} \mathbf{V} \right)^{-1} \left[\boldsymbol{\Omega}^T (\mathbf{T}_I - \boldsymbol{\alpha}_R - \boldsymbol{\omega}_J - \mathbf{J} \boldsymbol{\omega}) + \mathbf{V}^T (\mathbf{F} - \mathbf{M} \mathbf{a}_R) \right] \quad (68)$$

where $\boldsymbol{\alpha}_R$ and \mathbf{a}_R denote the (6×1) remainder acceleration vectors [46], whose expressions are omitted for the sake of brevity, whereas

$$\mathbf{J} := \begin{bmatrix} \mathbf{J}_{C1}^{(B1)} & \mathbf{0}_{3 \times 3} \\ \mathbf{0}_{3 \times 3} & \mathbf{J}_{C2}^{(B2)} \end{bmatrix}, \quad \mathbf{M} := \begin{bmatrix} m_1 \mathbf{I}_{3 \times 3} & \mathbf{0}_{3 \times 3} \\ \mathbf{0}_{3 \times 3} & m_2 \mathbf{I}_{3 \times 3} \end{bmatrix}, \quad \boldsymbol{\omega}_J := \begin{bmatrix} \tilde{\boldsymbol{\omega}}_1 \mathbf{J}_{C1}^{(B1)} \boldsymbol{\omega}_1 \\ \tilde{\boldsymbol{\omega}}_2 \mathbf{J}_{C2}^{(B2)} \boldsymbol{\omega}_2 \end{bmatrix} \quad (69)$$

In the preceding relations superscripts and subscripts 1 and 2 refer to body 1 and 2, m_j is the instantaneous mass of body j , and

$$\dot{\mathbf{J}} := \begin{bmatrix} \dot{\mathbf{J}}_{C1}^{(B1)} & \mathbf{0}_{3 \times 3} \\ \mathbf{0}_{3 \times 3} & \mathbf{0}_{3 \times 3} \end{bmatrix}, \quad \text{with } \dot{\mathbf{J}}_{C1}^{(B1)} = -\frac{n_0}{c} \mathbf{J}_{C1}^{(B1)}(t_0) \quad (70)$$

Moreover, the term \mathbf{F} includes the components of the propulsive forces (\mathbf{T} and $DT_{Sj}\hat{i}$) and the external forces $\mathbf{F}_{\text{ext},j}$ on each body (projected in $\underline{\mathbf{N}}$), whereas \mathbf{T}_I collects the components of the contributing interaction torque due to the electric motor,

$$\mathbf{F} = \begin{bmatrix} \mathbf{F}_{\text{ext},1} + DT_{Sj}\hat{i} \\ \mathbf{F}_{\text{ext},2} + \mathbf{T} \end{bmatrix} \quad \text{and} \quad \mathbf{T}_I = \begin{bmatrix} \mathbf{T}_{I,1} \\ \mathbf{T}_{I,2} \end{bmatrix}, \quad \text{with } \underline{\mathbf{T}}_{I,1} = \underline{\mathbf{B}}_1 \mathbf{T}_{I,1} \quad \text{and} \quad \underline{\mathbf{T}}_{I,2} = \underline{\mathbf{B}}_2 \mathbf{T}_{I,2} \quad (71)$$

Because $\underline{\mathbf{T}}_{I,1}$ and $\underline{\mathbf{T}}_{I,2}$ are two interacting torques, respectively, on body 1 and body 2, $\underline{\mathbf{T}}_{I,1} = -\underline{\mathbf{T}}_{I,2}$. The motor torque on the nozzle represents a control input and is chosen in order to drive the instantaneous deflection angles, Δ_y and Δ_z , toward the desired values, $\Delta_y^{(C)}$ and $\Delta_z^{(C)}$:

$$\underline{\mathbf{T}}_{I,2} = \underline{\underline{\mathbf{B}}}_1 \begin{bmatrix} \left[k_P (\Delta_z - \Delta_z^{(C)}) + k_D \dot{\Delta}_z \right] \sin \Delta_y \\ k_P (\Delta_y - \Delta_y^{(C)}) + k_D \dot{\Delta}_y \\ - \left[k_P (\Delta_z - \Delta_z^{(C)}) + k_D \dot{\Delta}_z \right] \cos \Delta_y \end{bmatrix} = \underline{\underline{\mathbf{B}}}_2 \begin{bmatrix} \left[k_P (\Delta_y - \Delta_y^{(C)}) + k_D \dot{\Delta}_y \right] \sin \Delta_z \\ \left[k_P (\Delta_y - \Delta_y^{(C)}) + k_D \dot{\Delta}_y \right] \cos \Delta_z \\ - \left[k_P (\Delta_z - \Delta_z^{(C)}) + k_D \dot{\Delta}_z \right] \end{bmatrix} \quad (72)$$

In the last relation, Eq. (62) was used. Once the constant, positive gains k_P and k_D have been selected, Eq. (72) allows identifying the net motor torque (both in magnitude and direction) needed to drive (Δ_y, Δ_z) toward $(\Delta_y^{(C)}, \Delta_z^{(C)})$.

6 Orbit Injection at GEO

This section considers the orbit injection of an upper stage with initial mass of 1515 kg and inertia matrix (at t_0) $\mathbf{J}_C^{(B1)}(t_0) = \text{diag}\{751.5, 814.4, 814.4\}$ kg m². The thrust magnitude T , which is assumed constant, equals 24.4 kN, whereas the effective exhaust velocity is 3 km/s. The thrust yielded by the side jet thrusters is 350 N, and their effective exhaust velocity equals 2.080 km/s. The main thruster and each side jet have distance from the center of mass C equal to 1.19 m and 1.09 m, respectively (i.e., $l = 1.19$ m and $D = 1.09$ m). Moreover, the commanded deflection angles are constrained to $|\Delta_{y/z}^{(C)}| \leq 3$ deg. Using the methodology described in Sect. 4.3, the following gains were selected for the attitude control system: $c_1 = 4.1 \cdot 10^{-3}$ s⁻² and $c_2 = 6.4 \cdot 10^{-2}$ s. Instead, using a trial-and-error approach, for the thrust vector mechanism the following gains were chosen: $k_P = 320$ Nm and $k_D = 3.03$ N m sec. These values lead to net motor torques not exceeding 25 Nm in magnitude. The sampling time is $\Delta t_S = 1$ s, whereas the following parameters were chosen for implementing the PWPF:

$$k_m = 100.2 \quad T_m = 1.5 \text{ s} \quad U_{ON} = 0.2 \text{ Nm} \quad U_{OFF} = 0.067 \text{ Nm} \quad U_m = 770 \text{ Nm} \quad (73)$$

The target orbit is geostationary, and the (nominal) conditions for position and velocity at t_0 are

$$r(t_0) = 42163.9 \text{ km} \quad \xi(t_0) = 0 \quad \phi(t_0) = 0 \quad (74)$$

$$v_r(t_0) = 8.3 \text{ m/s} \quad v_t(t_0) = 1.618 \text{ km/s} \quad v_n(t_0) = 0 \quad (75)$$

The nominal attitude at t_0 corresponds to the alignment of the longitudinal axis with the spacecraft velocity vector at t_0 , whereas nominally the remaining two body axes are aligned with the respective commanded values (cf. Eq. (37)). The nominal angular rate $\omega(t_0)$ is zero.

A Monte Carlo (MC) campaign, composed of 100 simulations, was performed, assuming initial errors on trajectory and attitude. More specifically, for position and velocity stochastic displacements from the nominal initial conditions (74)–(75) were assumed, with zero mean and standard deviations (denoted with superscript (σ)):

Table 1 Orbit injection at GEO: statistics obtained from the MC campaign

$\overline{\Delta r_f}$ (m)	$\overline{\Delta \phi_f}$ (deg)	$\overline{\Delta v_{rf}}$ (m/s)	$\overline{\Delta v_{tf}}$ (m/s)	$\overline{\Delta v_{nf}}$ (m/s)	\bar{t}_f (s)
1.41	1.3e-6	0.37	-0.84	0.60	75.9
$r_f^{(\sigma)}$ (m)	$\phi_f^{(\sigma)}$ (deg)	$v_{rf}^{(\sigma)}$ (m/s)	$v_{tf}^{(\sigma)}$ (m/s)	$v_{nf}^{(\sigma)}$ (m/s)	$t_f^{(\sigma)}$ (s)
4.02	5.5e-6	3.88	3.22	3.60	2.9

$$r^{(\sigma)} = 10 \text{ km} \quad \xi^{(\sigma)} = 0.0136 \text{ deg} \quad \phi^{(\sigma)} = 0.0136 \text{ deg} \quad (76)$$

$$v_r^{(\sigma)} = 50 \text{ m/s} \quad v_t^{(\sigma)} = 50 \text{ m/s} \quad v_n^{(\sigma)} = 50 \text{ m/s} \quad (77)$$

The two standard deviations $\xi^{(\sigma)}$ and $\phi^{(\sigma)}$ correspond to spatial displacements equal to 10 km. Each component of $\omega(t_0)$ is associated with a stochastic value, with zero mean and standard deviation of 1 deg/s. The initial attitude misalignment is defined in terms of a sequence 3-2-1 of displacement angles. This means that the displaced initial attitude, identified by $\underline{\underline{B_D}}$, is obtained from the nominal attitude $\underline{\underline{B_N}}$ through

$$\underline{\underline{B_D}}^T = \mathbf{R}_1 (\Delta\psi) \mathbf{R}_2 (\Delta\Theta) \mathbf{R}_3 (\Delta\phi) \underline{\underline{B_N}}^T \quad (78)$$

The three displacement angles $(\Delta\psi, \Delta\Theta, \Delta\phi)$ are stochastic variables with zero mean and standard deviation equal to 10 deg.

Table 1 reports the statistics for all the quantities of interest, i.e., radius, declination, velocity components, and time of flight. Figures 6, 7, 8, 9 and 10 depict the time histories of the position and velocity variables. Figure 11 illustrates Φ_E , which is the angle between the instantaneous (actual) longitudinal axis and the commanded one. Moreover, Fig. 12 portrays the time history of the commanded and actual thrust deflection angles in a single Monte Carlo simulation. Figure 13 depicts the modulated torque provided by the RCS. In particular, Fig. 14 shows a zoom that illustrates the time histories of some characteristic functions that are used for the implementation of pulse modulation. Both the figures and the statistics collected in Table 1 point out the satisfactory convergence toward the desired final conditions, even in the presence of large initial displacements from the nominal flight conditions. Starting from nominal initial conditions and under the assumption of modeling the ascent vehicle as a point mass, the minimum time required for orbit injection is 72.2 s, i.e., 4.8% less than the average value obtained from MC simulations (75.9 s), performed by modeling guidance, control, and actuation. In light of the numerical results and the preceding considerations, the guidance, control, and actuation architecture at hand turns out to be a valuable and efficient option for successful precise orbit injection.

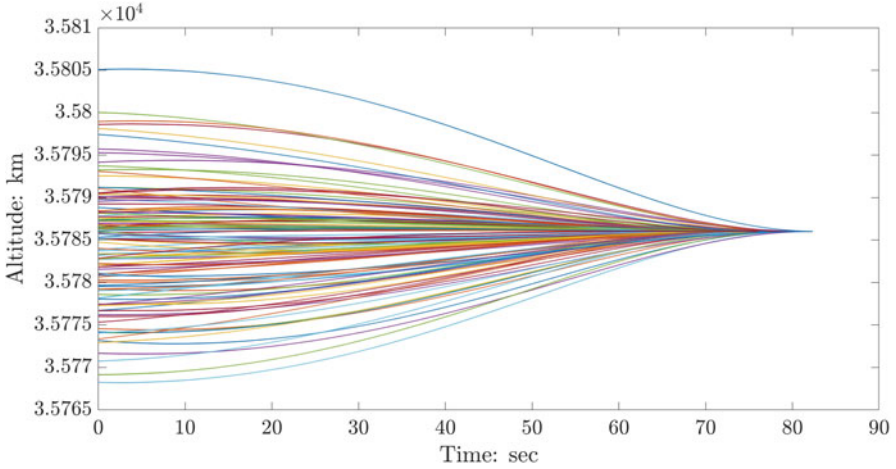


Fig. 6 Altitude time histories obtained in the MC campaign

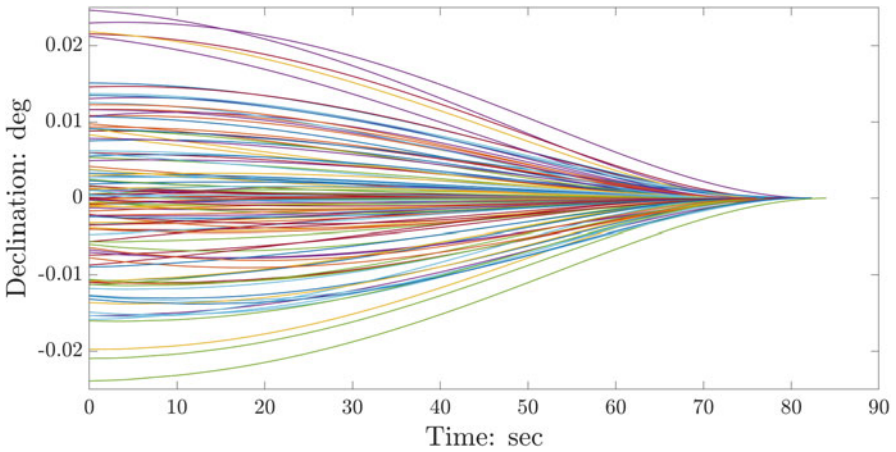


Fig. 7 Declination time histories obtained in the MC campaign

7 Concluding Remarks

This research proposes a new guidance and control architecture for upper stage orbit injection maneuvers. A novel, semi-analytic explicit near-optimal guidance algorithm is introduced that is based on the local projection of the position and velocity variables. A minimum-time problem is defined using the locally flat coordinates of position and velocity, and consists in finding the optimal thrust direction that minimizes the time of flight for achieving the desired orbit insertion conditions. The optimal control problem at hand is proven to be amenable to an analytical solution. This circumstance allows translating the minimum-time

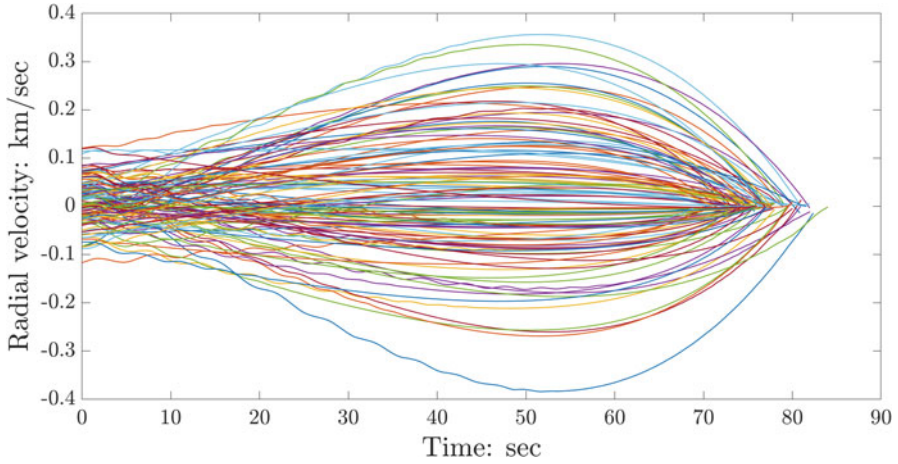


Fig. 8 Time histories of the radial velocity, obtained in the MC campaign

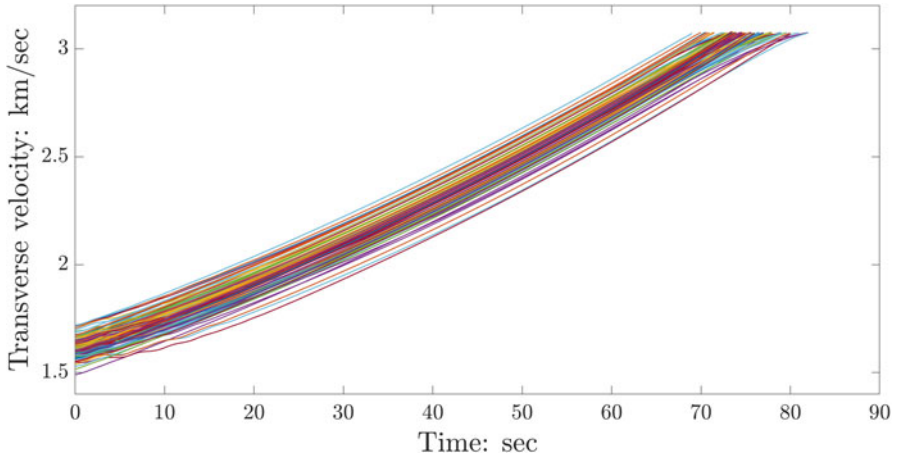


Fig. 9 Time histories of the transverse velocity, obtained in the MC campaign

problem of interest into five nonlinear equations in five unknowns. Their numerical solution can be performed as a real-time process, because a suitable guess, related to intuitive dynamical variables, is available. The guidance scheme at hand yields the commanded thrust direction, which must be pursued by the attitude control system. Unlike three-axial control, reduced-attitude-control has the purpose of aligning a single axis of the vehicle with a desired direction. This work introduces and applies a new quaternion-based nonlinear reduced-attitude control algorithm. This leads to defining an effective feedback law, which supplies the required torque. The Lyapunov theorem and the LaSalle's invariance principle provide the theoretical background needed to prove that the feedback law at hand enjoys quasi-global

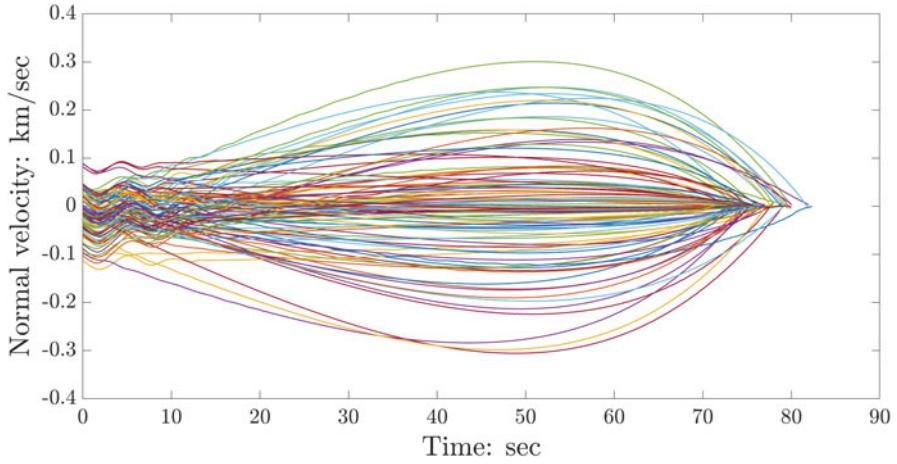


Fig. 10 Time histories of the normal velocity, obtained in the MC campaign

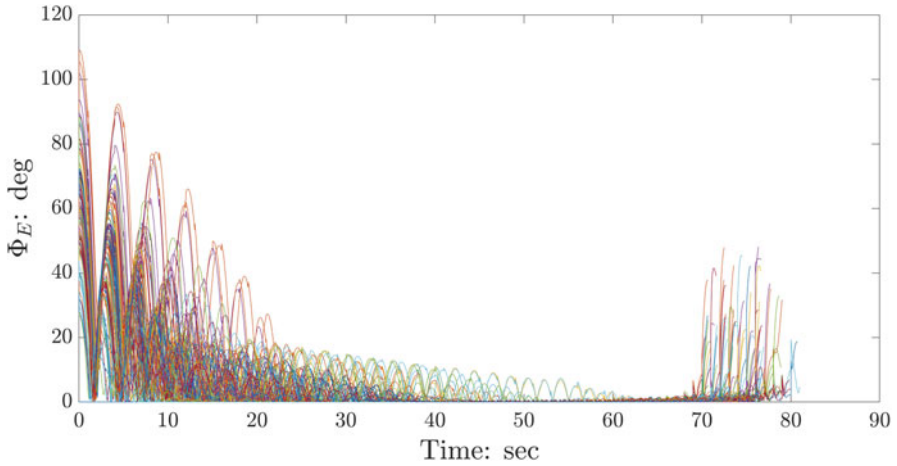


Fig. 11 Time histories of the displacement angle Φ_E , obtained in the MC campaign

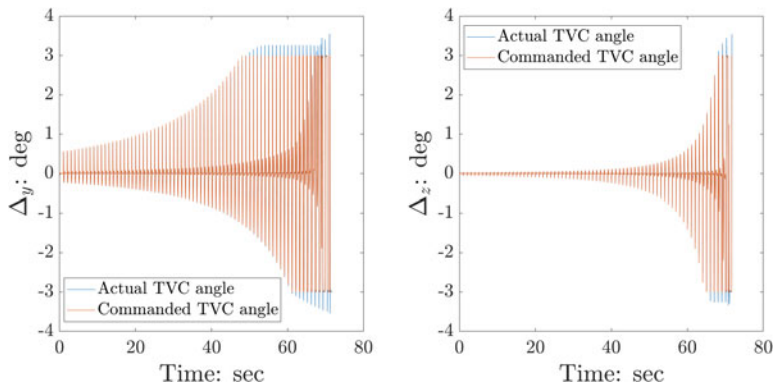


Fig. 12 Time histories of the thrust deflection angles, in a single MC simulation

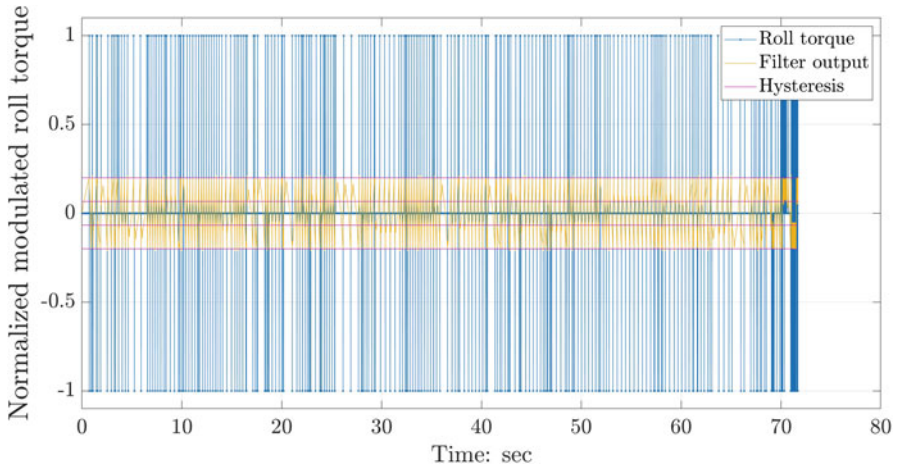


Fig. 13 Time history of the modulated thrust (with y-axis normalized to the maximum torque magnitude), in a single MC simulation

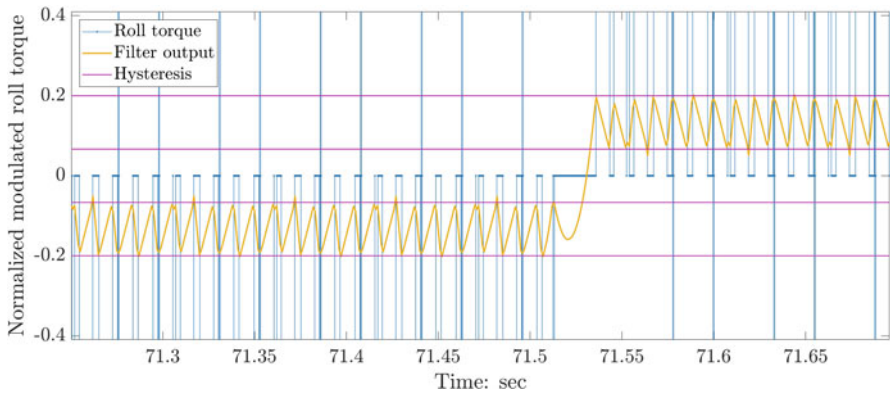


Fig. 14 Zoom on the time history of the modulated thrust (with y-axis normalized to the maximum torque magnitude), in a single MC simulation

convergence properties. Actuation is demanded to thrust vectoring, in conjunction with PWPF-modulated side jets for roll control. The overall dynamics of the upper stage, regarded as a system of two connected bodies, is modeled using the Kane's method, for accurate prediction of the system behavior. To test the guidance, control, and actuation architecture at hand, a Monte Carlo campaign is run, assuming significant displacements from the nominal initial conditions. The numerical results unequivocally demonstrate that the joint use of the locally flat near-optimal guidance and pulse-modulated reduced-attitude control introduced in this research represents an effective approach for upper stage precise orbit injection.

References

1. Calise, A.J., Tandon, S., Young, D.H., Kim, S.: Further Improvements to a Hybrid Method for launch Vehicle Ascent Trajectory Optimization. AIAA Guidance, Navigation and Control Conference and Exhibit, Denver (2000)
2. Gath, P.F., Calise, A.J.: Optimization of launch vehicle ascent trajectories with path constraints and coast arcs. *J. Guid. Control Dynam.* **24**(2), 296–304 (2001)
3. Lu, P., Pan, B.: Trajectory optimization and guidance for an advanced launch system. 30th Aerospace Sciences Meeting and Exhibit, Reno (1992)
4. Lu, P., Griffin, B.J., Dukeman, G.A., Chavez, F.R.: Rapid optimal multiburn ascent planning and guidance. *J. Guid. Control Dynam.* **31**(6), 45–52 (2008)
5. Weigel, N., Well, K.H.: Dual payload ascent trajectory optimization with a splash-down constraint. *J. Guid. Control Dynam.* **23**(1), 45–52 (2000)
6. Miele, A., Multiple-subarc gradient-restoration algorithm, part 2: application to a multistage launch vehicle design. *J. Optim. Theory Appl.* **116**(1), 19–19 (2003)
7. Pontani, M.: Particle swarm optimization of ascent trajectories of multistage launch vehicles. *Acta Astronaut.* **94**(2), 852–864 (2014)
8. Palaia, G., Pallone, M., Pontani, M., Teofilatto, P.: Ascent Trajectory Optimization and Neighboring Optimal Guidance of Multistage Launch Vehicles. In Fasano G., Pintér J. (eds) *Modeling and Optimization in Space Engineering*. Springer Optimization and Its Applications, **144**, 343–371 (2019)
9. Roh, W., Kim, Y.: Trajectory optimization for a multi-stage launch vehicle using time finite element and direct collocation methods. *Eng. Optim.* **34**(1), 15–32 (2002)
10. Jamilnia, R., Naghash, A.: Simultaneous optimization of staging and trajectory of launch vehicles using two different approaches. *Aerosol Sci. Technol.* **23**, 65–92 (2012)
11. Martinon, P., Bonnans, F., Laurent-Varin, J., Trélat, E.: Numerical study of optimal trajectories with singular arcs for an Ariane 5 launcher. *J. Guid. Control Dynam.* **32**(1), 51–55 (2009)
12. Calise, A.J., Melamed, N., Lee, S.: Design and evaluation of a three-dimensional optimal ascent guidance algorithm. *J. Guid. Control Dynam.* **21**(6), 867–875 (1998)
13. Teofilatto, P., De Pasquale, E.: A non-linear adaptive guidance algorithm for last-stage launcher control. *J. Aerosp. Eng.* **213**, 45–55 (1999)
14. Hull, D.G.: *Optimal Control Theory for Applications*. Springer, New York, pp. 199–254 (2003)
15. Lu, P.: Optimal feedback control laws using nonlinear programming. *J. Optim. Theory Appl.* **71**(3), 599–611 (1991)
16. Townsend, G.E., Abbott, A.S., Palmer, R.R.: *Guidance, Flight Mechanics and Trajectory Optimization, Volume VIII, Boost Guidance Equations*. NASA Contractor Report, Washington (1968)
17. Pontani, M., Cecchetti, G., Teofilatto, P.: Variable-time-domain neighboring optimal guidance, part 1: algorithm structure. *J. Optim. Theory Appl.* **166**(1), 76–92 (2015)
18. Pontani, M., Cecchetti, G., Teofilatto, P.: Variable-time-domain neighboring optimal guidance, part 2 application to lunar descent and soft landing. *J. Optim. Theory Appl.* **166**(1), 93–114 (2015)
19. Pontani, M., Cecchetti, G., Teofilatto, P.: Variable-time-domain neighboring optimal guidance applied to space trajectories. *Acta Astronaut.* **115**, 102–120 (2015)
20. Geller, D.K.: Linear Covariance Techniques for Orbital Rendezvous Analysis and Autonomous Onboard Mission Planning. *J. Guid. Control Dynam.* **29**(6), 1404–1414 (2006)
21. Marcos, A., Peñín, L.F., Sommer, J., Borschlegl, E.: Guidance and Control Design for the Ascent Phase of the Hopper RLV. AIAA Guidance, Navigation and Control Conference and Exhibit, Honolulu (2008)
22. Lam, Q.M., McFarland, M.B., Ruth, M., Drake, D., Ridgely, D.B., Oppenheimer, M.W.: Adaptive Guidance and Control for Space Access Vehicle Subject to Control Surface Failures. AIAA Guidance, Navigation and Control Conference and Exhibit, Honolulu (2008)

23. Tian, B., Fan, W., Zong, Q.: Integrated guidance and control for reusable launch vehicle in reentry phase. *Nonlin. Dyn.* **80**(1–2), 397–412 (2015)
24. Yeh, F.-K.: Sliding-mode-based contour-following controller for guidance and autopilot systems of launch vehicles. *Proc. Instit. Mech. Eng. Part G: J. Aerosp. Eng.* **227**(2), 285–302 (2015)
25. Pontani, M., Celani, F.: Neighboring optimal guidance and constrained attitude control applied to three-dimensional lunar ascent and orbit injection. *Acta Astronaut.* **156**, 78–91 (2019)
26. Pontani, M., Celani, F.: Variable-time-domain neighboring optimal guidance and attitude control of low-thrust lunar orbit transfers. *Acta Astronaut.* **175**, 616–626 (2020)
27. Pontani, M., Celani, F.: Neighboring Optimal Guidance and Constrained Attitude Control for Accurate Orbit Injection. *Aerotech. Miss. & Spazio*, online 12 May 2021
28. Hughes, P.C.: *Spacecraft Attitude Dynamics*. Dover Publications, Inc., Mineola, 55–61 (2004)
29. Perkins, F.M.: Explicit Tangent-Steering guidance for Multi-Stage Boosters. *Astronaut. Acta* **12**, 212–223 (1966)
30. Smith, I.E.: General Formulation of the Iterative Guidance Mode. NASA TM X-53414 (1966)
31. Brusch, R.G.: Bilinear Tangent Yaw Guidance. *Guidance and Control Conference*, Boulder (1979)
32. Weiss, H.: Quaternion-based rate/attitude tracking system with application to gimbal attitude control. *J. Guid. Control Dynam.* **16**(4), 609–616 (1993)
33. Sastry, S.: *Nonlinear Systems. Analysis, Stability, and Control*. Springer, New York, 182–234 (1999)
34. Wertz, J.R.: *Spacecraft Attitude Determination and Control*. Springer, Dordrecht, 487–509; 206–209, 649–654 (1978)
35. Knauber, R.N.: Roll Torques Produced by Fixed-Nozzle Solid Rocket Motors. *J. Spacecr. Rock.* **33**(6), 789–485 (1996)
36. Holmes, D.G., Lipo, T.A.: *Pulse Width Modulation for Power Converters*. Wiley-Interscience, 183–199 (2003)
37. Tourne, C., Shtessel, Y.B., Wells, E.: Upper stage rocket guidance and control using discontinuous reaction control thrusters via sliding modes. *American Control Conference*, Albuquerque (1997)
38. Kienitz, K.H., J. Bals, J.: Pulse modulation for attitude control with thrusters subject to switching restrictions. *Aerosol Sci. Technol.* **9**, 635–640 (2005)
39. Anthony, T., Wei, B., Carroll, S.: Pulse Modulated Control Synthesis for a Spacecraft. *J. Guid. Control Dynam.* **13**(6), 1014–1015 (1990)
40. Navabi, M., Rangraz, H.: Comparing Optimum Operation of Pulse Width Pulse Frequency and Pseudo-Rate Modulators in Spacecraft Attitude Control Subsystem Employing Thruster. *Recent Advances in Space technologies (RAST)*, 625–630 (2013)
41. Chegeni, E., Hoseini, S.M., Madadpour Inallou, M.: Attitude Control of Satellite with PWPF Modulator Using Generalized Incremental Predictive Control. *J. Knowl.-Based Eng. Innov.* **1**(2), 131–141 (2015)
42. Jalali-Naini, S.H., Darani, S.: Preliminary Design of Spacecraft Attitude Control with Pulse-Width Pulse-Frequency Modulator for Rest-to-Rest Maneuvers. *J. Aerosol Sci. Technol.* **11**(1), 1–8 (2017)
43. Arantes, G. Jr., Martins-Filho, L.S., Santana, A.C.: Optimal On-Off Control for the Brazilian Multimission Platform. *Mathem. Probl. Eng.* (2009)
44. Kane, T.R., Levinson, D.A.: *Dynamics, theory and applications*. McGraw-Hill, New York (1985)
45. Roithmayr, C.M., Hodges, D.H.: *Dynamics: Theory and Application of Kane’s Method*. Cambridge University Press, 39–51, 100–117, 191–199 (2016)
46. Stoneking, E. T.: Implementation of Kane’s Method for a Spacecraft Composed of Multiple Rigid Bodies. *AIAA Guidance, Navigation, and Control (GNC) Conference*, Boston (2013)

A Pareto Front Numerical Reconstruction Strategy Applied to a Satellite System Conceptual Design



Gustavo J. Santos, Sebastián M. Giusti, and Roberto Alonso

1 Introduction

The most important and crucial decisions in the life-cycle of a space mission are made during the conceptual design phase. The satellite architecture has to: (i) fulfill the mission's requirements (the objective) and (ii) reduce the resources applied to materialize the selected solution (the implementation).

Later project stages are focused on the detailed implementation, checking, verification, and testing of the selected architecture during that conceptual design phase.

In the process of designing complex systems the concurrence of multidisciplinary teams is required. Specialists in structures, thermal, power, navigation, communications, software, and control systems, among others are needed. Each of these team-work carries out their design based on requirements imposed by the system engineering office, leaving room on each subsystem to obtain a locally optimal design. It is important to remark that each specialist group receives the set of

G. J. Santos

Unidad de Formación Superior CONAE – Universidad Tecnológica Nacional, Falda del Cañete, Córdoba, Argentina

e-mail: gsantos@conae.gov.ar

S. M. Giusti (✉)

Universidad Tecnológica Nacional, Facultad Regional Córdoba UTN-FRC/CONICET, Maestro M. López esq. Cruz Roja Argentina, Córdoba, Argentina

e-mail: sgiusti@frc.utn.edu.ar

R. Alonso

Comisión Nacional de Actividades Espaciales (CONAE), Falda del Cañete, Córdoba, Argentina

e-mail: roberto.alonso@conae.gov.ar

requirements addressed to their subsystem and the connection between subsystems is managed by the system engineering group.

The usual procedure to close the satellite conceptual design phase is based on the overlapping of these optimal subsystems to obtain a system that is not optimal (in almost all cases). Note that each individual solution (at subsystem level) is optimal in its search region, that is related to the others (in the overlapping process) until completing the region that covers all the satellite subsystems.

Each particular solution is located on the border of the solution set generated at the subsystem level, because of its optimal condition. The superposition of all the subsystems moves each solution towards the interior of this new larger space defined by the union of the smaller set. See [1–3] for a detailed understanding.

The process to design a satellite is characterized by having conflicting requirements that cannot be directly satisfied by a maximization or a minimization. As a quick example, the instrument room needs to be as large as possible, but the launching cost should be as low as possible. These two variables are not directly correlated. But, since the launching cost is proportional to the mass of the satellite, a detailed analysis of the influence of the instrument room must be performed during the modeling of the whole problem.

Complex systems are characterized by mixing, in the search space, discrete sequences and/or continuous functions. In these cases, the usual concept of the derivative or gradient takes a different meaning. In mono-objective problems, usually a procedure to follow the direction indicated by the gradient path to find the minimum objective value (optimization solution) is defined.

According to the theory of Pareto, in the multi-objective optimization problems, there is not a unique optimal solution. In fact, a family of possible optimal configurations can be obtained. This means that any other solution can not improve at least one of the design variables without worsening at least one of the others (Pareto definition). To use the steepest descent method in a multi-objective optimization problem, the set of objective functions must be reformulated in a mono-objective function. However, the obtained solution strongly depends on how the objective functions are combined. Therefore, the solution is sub-optimal for the multi-objective problem. Optimization of a complex system by considering simultaneously several disciplines and engineering constraint can be made by Multidisciplinary design optimization (MDO) frameworks. Developments of these techniques in spacecraft and satellite conceptual design can be found, among others, in [24–26].

To deal with the optimization problem at hand, it is essential to define the mathematical model for the satellite, involving both systems and subsystems as a whole. See, for example, [5–10] for the description of each satellite component.

The set of algebraic, differential equations (continuous) and difference equations (discrete) represent as close as possible the set of objective variables and the constraints imposed on the system and on each component.

The output obtained from the optimization algorithm presents several admissible configurations. Each one of them represents a suitable architecture according to the set of high-level requirements. The selection of the best one among the possible solutions involves technical and non-technical reasons, as it is discussed later.

In this chapter, a new strategy to accomplish the conceptual design of a satellite system is addressed. The Pareto theory supplies the theoretical background needed to select the optimal solutions from a cloud of possible configurations. Our strategy is based on the Direct Numerical Simulation (DNS) of the optimization problem, which computes all possible admissible configurations. Clearly, the global minimum belongs to the set composed by all combinations.

The Pareto front allows us distinguishing the optimal solution from the other admissible configurations. The DNS techniques have increased their popularity in the scientific community because of the increasing capability of computers. Some applications of this numerical method in space engineering can be found in [11–14].

Other approaches dealing with multi-objective schema involving continuous and discrete variables are the ones based on heuristics and/or meta-heuristics methods, where the genetic algorithms (GA) are the most well-known. These ones find a subset of local minimum solutions, some of them are discarded during the selection process based on the values of some parameters, previously established with heuristic reasoning. Later, this concept is demonstrated with a study case. Examples of application in engineering problems of these optimization approaches are found in [15–23]

The content of the chapter covers most of the subjects needed to understand the proposed strategy and to point out the importance of having a global optimizer for a complex system. Section 2 deals with a description of the satellite subsystems and the components and equipment which are inside of each one. The multi-objective optimization problem is presented in Sect. 3 by indicating the role of each variable in the problem. The proposed methodology to solve this particular problem is presented in Sect. 4. In order to obtain a comparison framework, a complete study case is analyzed by using numerical algorithms of DNS and GA in Sect. 5. The work ends in Sect. 6 where some concluding remarks are presented.

2 Satellite System

The satellites are usually divided into two sections, the payload, and the service module. The payload basically contains the instruments and their support equipment, calibrators, etc. which are in charge of fulfilling the mission objectives. The service module contains the equipment and components to guarantee the proper functioning of the payload. Basically, it has actuators, sensors, mass memories, transmitters and receivers in different bands, GPS, computers, solar arrays, batteries, antennas, etc.

The proposed approach is focused to design the service module, while other characteristics related to the payload and the orbit are taken into account for the elaboration of the system constraints. However, the method is not restricted to a particular module, it can be used for the complete system at once. To mathematically model the system and/or subsystems of the service module, see the works [5–10]

The service module is divided into different subsystems each one specialized in a particular function:

- **Attitude Determination and Control (ADC):** controls the satellite orientation. Its design variables are the sensors and actuators. The typical space sensors are star trackers, Earth and Sun sensors, GPS, and magnetometers. The common set of actuators are momentum wheels, reaction wheels, torque rods, and thrusters (propulsion subsystem). The constraints associated with this subsystem are the accuracy of the control pointing, the attitude determination knowledge, and the agility for satellite maneuvering.
- **Structure (STR):** provides mechanical support and its design variables usually are the shape and materials of the structure. The size is considered a constraint, obviously as smaller its diameter, the greater the number of launchers where it can fit in.
- **Communications (COM):** is the interface with the ground segment, allowing to download science data and housekeeping telemetry, also allows receiving commands and software patches from the ground station. The design variables are the type of transmitter/receiver, the RF amplifier, and the antenna, while its main restriction is the maximum bit rate and the tolerable bit error rate.
- **Electrical Power Subsystem (EPS):** provides electrical energy to the rest of the satellite. The design variables are the kind of technology and size of batteries and solar arrays. The constraints associated with this subsystem are the bus voltage, demanded power consumption, and satellite autonomy (without Sun exposure).
- **Thermal Control Subsystem (TCS):** maintains the temperature inside the allowable range according to the thermal requirements on each component or equipment. Its design variables are the radiator's material and the characteristics of the heater (number, power, etc.), while the constraints are the maximum and minimum temperatures required and the power used to warm the system.

3 Multi-Objective Optimization Problem

In general terms, the multi-objective problem can be written as:

$$\text{Minimize } F(\mathbf{X}) = [f_1(\mathbf{X}), f_2(\mathbf{X}), \dots, f_k(\mathbf{X})]^T$$

$$\text{Subject to } g_i(\mathbf{X}) = 0, \quad i = 1, 2, \dots, m$$

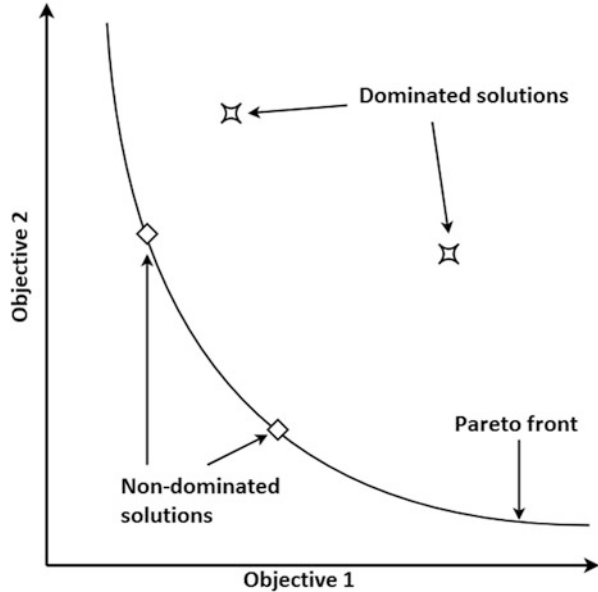
$$\text{Subject to } h_i(\mathbf{X}) \leq 0, \quad i = 1, 2, \dots, n$$

$$\text{Where } \mathbf{X}_{\text{inf}} \leq \mathbf{X} \leq \mathbf{X}_{\text{sup}},$$

where $F(\mathbf{X})$ is the set of the complete objective functions of the system, $g_i(\mathbf{X})$ and $h_j(\mathbf{X})$ are the equality and inequality constraints, respectively, and \mathbf{X} is the input vector for the optimization or decision variables, see [1, 2].

Usually, there is not a single optimal solution to the exposed problem, but there are several potential solutions, each one having different strengths and weaknesses, called *optimal Pareto solutions* or *Pareto front*. These solutions are also called *non-*

Fig. 1 Pareto front of a two-objectives minimization problem. The non-dominated solutions are on the border of the Pareto region. It is observed, from this sketch, that each solution cannot be improved in one variable without leaving the border, that it is quitting the optimal condition. This is the definition of optimally according to the Pareto theory. The solutions located inside the Pareto region are not optimal, because each one can move to the border without worsening any one of the variables



dominated solutions since no variable can be improved without damaging another in its optimally. Figure 1 shows an optimization problem based on two objective functions in order to show both types of solutions.

The above optimization problem can be solved using many methods, most of them are heuristic algorithms, on the other side there is the direct numerical simulation method, later explained. See [3] for further details.

Heuristic methods have been successfully used to find solutions in many applications in a large number of areas. In the aerospace industry, the most frequently used are those of evolutionary approaches, such as genetic algorithms, simulated annealing, tabu search, or hybrid algorithms.

These techniques are of the utmost importance in optimization problems that contain wide search spaces with sets of design variables of different nature. Generally, the main objectives are: minimizing mass and cost, maximizing system performance and reliability [4, 23].

The direct numerical simulation (DNS) is a tool that finds a solution on a constrained set of equations that describe the behavior of the true physical model, by computing on the entire mathematical model, without any approximation or tuning which may reduce the number of admissible solutions.

This technique intends to reconstruct the objective function through a direct evaluation of all possible values and/or combinations of variables (in brief: *all against all*). Once the objective function is obtained numerically, the minimum is identified as well as the values of each variable that contribute to this minimum. For continuous optimization variables, the DNS technique is not completely appropriated. Due to the computational times required to obtain the optimal solution

or Pareto front grows exponentially with the number of variables (the continuous set of design variables must be numerically discretized). Then in a continuous optimization framework, a standard optimization procedure could be recommended.

In summary, the genetic algorithms require lower computational capacity, but they need to be configured properly and their result may not contain the overall minimum, because the natural selection may leave some solutions out of the admissible set. On the other hand, the numerical simulation (DNS) gets the global minimum, but it demands a much greater computing capacity, time, and effort to obtain the solution set.

Selecting the appropriate method depends on the resources and available time to deal with the problem at hand. For example, in the feasibility phase, the genetic algorithms are more attractive because require a shorter time to reach some solution even if it is not exactly the best one. In the design phase, the DNS is more useful because generates the complete map of solutions to obtain the global optimum.

4 Proposed Methodology

The diagram in Fig. 2 describes the steps related to the proposed methodology for designing. The process begins with the acceptance of the requirements of the highest level, which define the objectives of the mission, the characteristics of the payload, the orbit parameters, and the main characteristics of the service module needed to accomplish the mission. This data is strictly necessary to feed the process. The requirement document also contains programmatic issues, which cannot be translated into a mathematical language, but the decision-maker after the admissible solutions map is set has to include these elements to adopt the best system concept. The best configuration is the conjunction between technical and programmatic results.

Initially, a possible architecture is proposed as the first guess that can qualitatively fulfill the mission objectives. This design skeleton allows the design variables of the optimization model to be defined. The decision taken during this step is simple and to some extent *binary*, for example, the system needs (yes/no) a propulsion system on-board if orbit maintenance is required. For a deeper understanding of the design variables which define the space project, see, [5, 6].

The next step is to adopt a first approximation to the architecture, once the requirements have been deeply interpreted. After that, an analytical description of the system, by means of the mathematical equation set on which the optimization process works, must be obtained. The mathematical modeling represents the relationship between the system input and output, including the objective functions and the constraints imposed by the requirements and some by the selected architecture.

The algorithm operates on the model in order to obtain the admissible outputs. The region, where the solutions *live*, is obtained by the direct application of the optimization algorithm to solve multi-objective schemes.

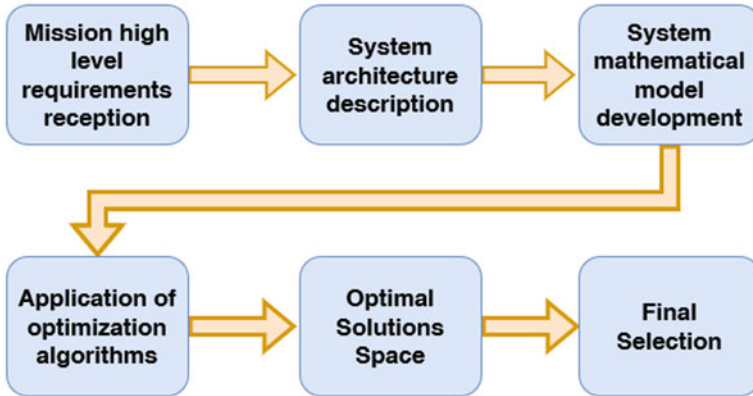


Fig. 2 Steps necessary to complete the proposed method to design the complex system. It is noted that all the activities are in series

The admissible solutions have to be on the Pareto front, later one of these choices is selected by the decision-maker taking into account not only the mathematical solution but also the programmatic requirements. For example, the need to have some percentage of in-house development may leave some solutions out of consideration.

5 Application to a Study Case

The proposed methodology is applied to a study case, which is the design of the service module of an Earth Observation Satellite at low altitude orbit, similar to those manufactured by many satellite suppliers.

5.1 High-Level Mission Requirements

As it was pointed out in the previous section, the high-level requirement's document is mandatory to start the satellite design, by using the proposed methodology or by applying the nominal procedure (non-optimal) of partitioning the satellite in subsystems and then integrate the parts to recompose the system.

The set of requirements imposes hard constraints to the design of the service module, most of them are listed in Table 1. Most of these values were taken from past satellite missions of the Argentinean Space Agency -CONAE- (designed for remote sensing) in order to create a feasible set of requirements.

Table 1 Study case mission requirements

Requirement	Variable	Value	Unit
Mission lifetime	m_{years}	5	years
Orbit altitude	h_{orb}	702	km
Orbital period	t_{orb}	98.8	min
Eclipse time	t_{ecl}	30	min
Payload mass	$mass_{PL}$	20	Kg
Payload cost	$cost_{PL}$	1×10^6	USD
Payload power	P_{PL}	50	W
Launcher diameter	$D_{launcher}$	2	m
Launcher height	$h_{launcher}$	2.2	m
Minimum structure fundamental frequency	$f_{Olauncher}$	2	Hz
S Band Tx frequency	f_{BS}	2.03	GHz
X Band Tx frequency	f_{BX}	8.20	GHz
Minimum antenna elevation	El_{min}	10	°
S Band bit rate	BR_{BS}	32,768	bit/s
X Band bit rate	BR_{BX}	1.20×10^8	bit/s
S Band max. bit error rate	BER_{BS-req}	100×10^{-5}	1/bit
X Band max. bit error rate	BER_{BX-req}	1.00×10^{-6}	1/bit
S Band Eb/No margin	$Eb/No_{Marg-BS}$	3	dB
X Band Eb/No margin	$Eb/No_{Marg-BX}$	3	dB
Maximum pointing error (control)	$\sigma_{pointing}$	180	arc-sec
Maximum attitude determination error	σ_{θ}	3.6	arc-sec
Maximum single maneuver angle	$\Theta_{man-req}$	90	°
Maximum maneuver time	$t_{man-req}$	240	sec
Bus voltage	$V_{BUS-req}$	28	V
Maximum battery DOD	DOD_{req}	25	%
Minimum OBC processing capacity	$OBC_{MIPS-req}$	5	MIPS
OBC flight heritage	$OBC_{FHer-req}$	Yes	–
Minimum operation temp.	$T_{min-req}$	0	°C
Maximum operation temp.	$T_{max-req}$	30	°C

5.2 System Architecture

Initially, a feasible architecture must be selected. This topology can be considered as the first guess and it is based on the designer group's knowledge and heritage from previous projects.

The reason for having this preliminary configuration is to size and reduce the search region to speed up the process by shrinking the number of admissible solutions.

A simple example for easy understanding: let us consider that the download data rate can be satisfied with the type of solid-state transmitter. Therefore, other candidates using high power, cost, volume, temperature control constraints, etc., based

on higher technology, can be deleted from our database. The proposed strategy can exclude solutions with this high-tech transmitter, to reduce the processing time. For this reason, some rules on the design to size the design variables according to the selected architecture must be imposed.

Since the case under analysis is focused on the service module, the design variables are the representative characteristics of each subsystem. In fact, the concept of the subsystem is introduced here just for easy understanding, because the proposed methodology is not based on rigid subsystem or parts, the method adopts the concept of integrity which is clear in the formulation of the mathematical model. Figure 3 represents the selected architecture with each characteristic elements. The main components of each one are shown.

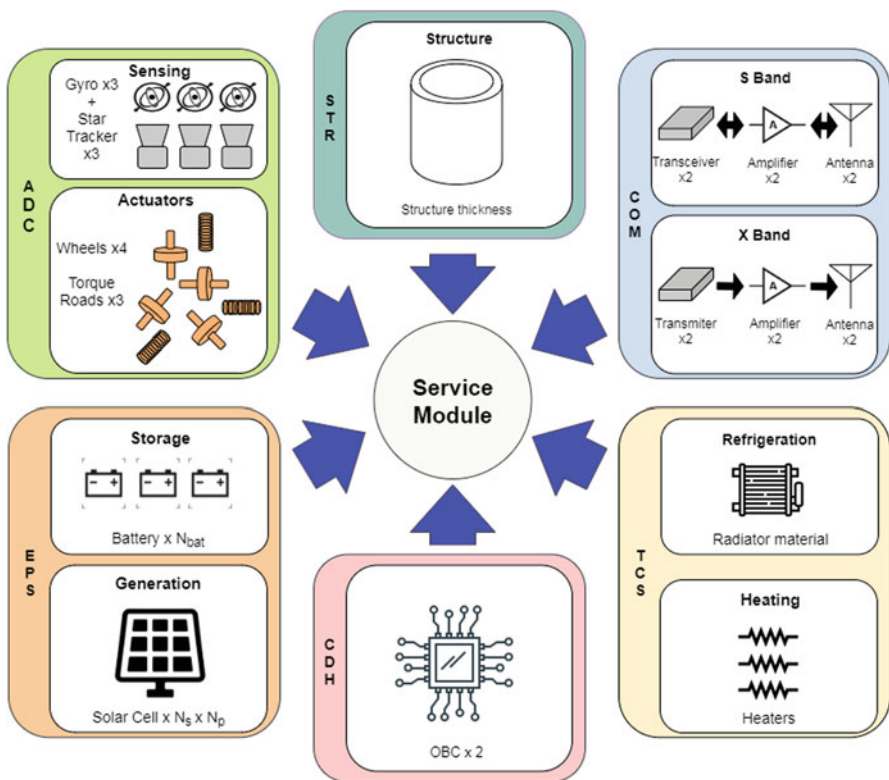


Fig. 3 Conceptual design of the satellite’s service module. The system is divided into subsystems, where the main components are shown

5.3 Optimization Problem

The mathematical model for the optimization problem includes the objective functions (representing the parameters subject to minimize/maximize), the constraints (that limit the design options), and the design variables (depicting the components of the system to be analyzed, such as inertia wheels, batteries, etc.).

Design Variables For the present study case, the selected design variables are shown in Table 2. For example, in the EPS subsystem, each combination of solar cell and battery technologies, the size of the solar panel, and the battery array are determined to fulfill the power requirement of the mission. A cylinder structure made of Aluminum 7075 (Al 7075) is taken into account for the satellite. In this case, as a structural design variable, the commercial thickness of the cylinder is considered and must fulfill the requirement on the natural frequency of the launcher vehicle. Four materials were considered for the design of the radiators: Aluminum 6061-T6 (Al 6061-T6), Aluminum 6061-T6 (finishing: polished) (Al 6061-T6), Silverized Teflon (Ag/FEP), and Aluminized-Teflon (Al/FEP). For each one, the heater system and radiator size are obtained to fulfill the TCS requirements.

Objective Functions In this study case, the cost and mass of the system were chosen to be optimized simultaneously in the multi-objective framework. Although other characteristics of the system such as reliability or volume were not considered as objective functions, some of them are taken into account as constraints to set a more realistic solution.

Table 2 Study case design variables

Variable	Description	Subsystem
x_1	S-band transceiver	COM
x_2	S-band antenna	COM
x_3	S-band amplified	COM
x_4	X-band transceiver	COM
x_5	X-band antenna	COM
x_6	X-band amplified	COM
x_7	Star-Tracker	ADC
x_8	Gyro	ADC
x_9	Momentum wheel	ADC
x_{10}	Magnetorquer	ADC
x_{11}	Battery (technology and size)	EPS
x_{12}	Solar cell technology	EPS
x_{13}	OBS	CDH
x_{14}	Radiator material	TCS
x_{15}	Heaters	TCS
x_{16}	Thickness of structure	STR

Constraints The constraints are introduced to distinguish between viable options from the non-admissible solutions, see [7, 8]. Table 1 shows the considered mission requirements.

Table 3 compiles the parts of the model that characterize the optimization problem proposed for this study case.

5.4 Optimization Schemes. Application

The design variables define the architecture of the system associated with its mathematical model, used to find the (optimal) selection of space components that generate the (optimal) system. To this end, both genetic algorithms and direct numerical simulation are applied to the same study case to check differences in their respective performance.

Table 3 Study case mathematical model summary

Objective functions		
Equation	Description	System/subsystem
$f_1 : Mass_{sat} = Mass_{PL} + \sum Mass_{SS}$	Satellite mass	Satellite
$f_2 : Cost_{sat} = Cost_{PL} + \sum Cost_{SS}$	Satellite cost	Satellite
Restrictions		
$g_1 : BER_{BS-req} - f_{BER} \left(\frac{E_b}{N_o} - Marg_{BS} \right) \leq 0$	S band link	Communication
$g_2 : BER_{BX-req} - f_{BER} \left(\frac{E_b}{N_o} - Marg_{BX} \right) \leq 0$	X band link	Communication
$g_3 : \sigma_{\theta-req} - \sigma_n \sqrt{1 - (frac{x_{su}})^2} \leq 0$	Maximum attitude determination error	Attitude control
$g_4 : \sigma_{pointing-req} - (\sigma_{\theta} + \sigma_{act}) \leq 0$	Maximum pointing error	Attitude control
$g_5 : 4 * \Theta_{man-req} \frac{I_{sat}}{I_{man-req}} - \tau_{ADC} \leq 0$	Torque required	Attitude control
$g_6 : 100 \frac{P_{Sat}^{lecl}}{V_{bus} \eta_d C_{bat}} - DOD_{req} \leq 0$	Battery capacity	Electrical power
$g_7 : Area_{SA} - 4 * D_{launcher} * h_{launcher} \leq 0$	Solar panels area	Electrical power
$g_8 : OBC_{MIPS-req} - OBC_{MIPS} \leq 0$	OBC processing velocity	Command and data handling
$g_9 : OBC_{FHer-req} - OBC_{FHer} \leq 0$	OBC flight heritage	Command and data handling
$g_{10} : T_{max} - T_{max-req} \leq 0$	Maximum temperature	Thermal control
$g_{11} : T_{min-req} - T_{min} \leq 0$	Minimum temperature	Thermal control
$g_{12} : f_{\theta lanzador} - f_{\theta Sat} \leq 0$	Structure natural frequency	Structure

5.4.1 Direct Numerical Simulation

The optimization problem is solved by using a direct numerical simulation to build up the Pareto front. The Pareto map contains all possible combinations among the design variables (all against all). Each possible solution is computed and placed in the Pareto chart according to its final values.

The system under analysis has 16 design variables each one with its database, which implies a search space of 764,411,904 elements. To determine the feasibility of each of these cases, a cluster of eight computers was used. The technical characteristics of this cluster are shown in Table 4.

The feasibility analysis has determined that 86,190,912 combinations fulfill the restrictions and constraints. The following step is to build up the Pareto front from this solution subset. Figure 4 shows this result.

The Pareto front shown in Fig. 4 consists of 105 solutions grouped into 31 different points which are all optimal. The determination process to find the solutions took approximately six hours using the hardware described in Table 4.

Table 4 Technical specifications of the computer cluster used to resolve this study case

Computer quantity	8
Processor	Intel Core I7-4790 @ 3.60GHz x 8
RAM memory	32 GiB
Hard disk	512 GB
Operative system	Ubuntu 16.04 LTS

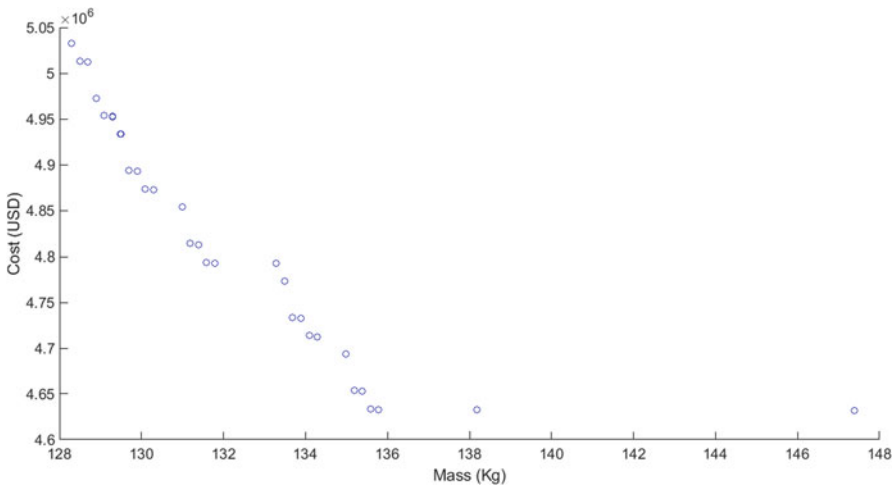


Fig. 4 Pareto front obtained by applying DNS to the case under analysis

5.4.2 Genetic Algorithm

To solve the same problem using genetic algorithms, a modified version of MATLAB `gamultiobj` function is applied. The modification of this routine consists of changing the type of design variables from continuous to discrete.

The `gamultiobj` function enables the setting of the parameters which have a direct relation to the solution of the optimization problem. In this case, the parameters are the population size, the total number of generations, and the global tolerance of the algorithm. Table 5 shows the different configurations used to run the case under analysis and the obtained results are presented in Fig. 5. Note that the variation of the parameters does not significantly affect the results obtained, the only factor that changes considerably is the time used.

Table 5 Genetic algorithm configurations and its results

Characteristics	Config. 1	Config. 2	Config. 3	Config. 4
Population	1000	1000	2500	2500
Generations	200	500	200	500
Global tolerance	1×10^{-5}	1×10^{-5}	1×10^{-5}	1×10^{-5}
Solutions obtained	12	11	12	12
Processing time	3 [min]	4 [min]	5 [min]	9 [min]

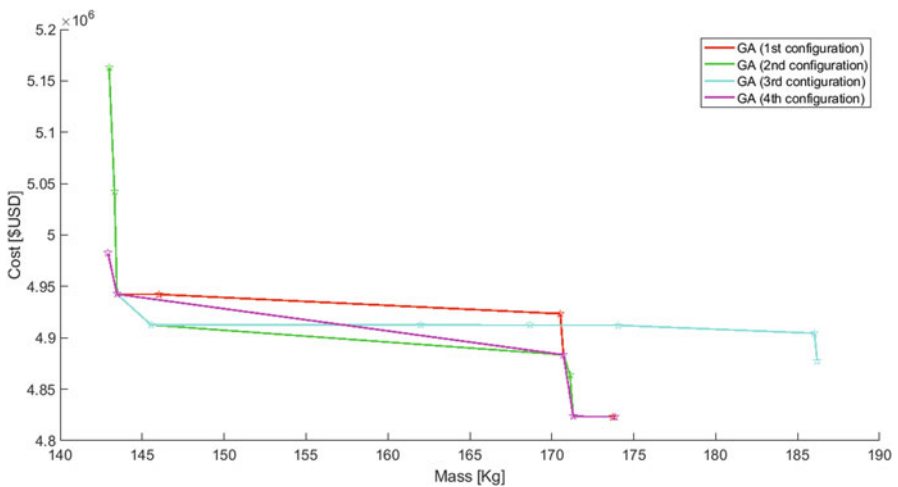


Fig. 5 Pareto fronts obtained using genetic algorithms

5.5 Comparison between DNS and GA

The results obtained using both algorithm strategies are evaluated by comparing each individual Pareto fronts in Fig. 6.

As is expected, the solution set delivered from the DNS is better than that obtained using the genetic algorithm. This difference appears because in the direct numerical simulation the objective functions are reconstructed, so all of them are considered without any loss. It takes longer processing time, but all of the possible solutions are firmly evaluated. On the other hand, the genetic algorithm only studies a subset of the entire search space; therefore, some admissible solutions can be left out from our consideration.

Although this seems to be a clear disadvantage for the genetic algorithms compared to direct numerical simulation, if we compare it with other non-optimal solutions, it is notable that all the fronts obtained comprise quite good solutions. This can be seen in Fig. 7.

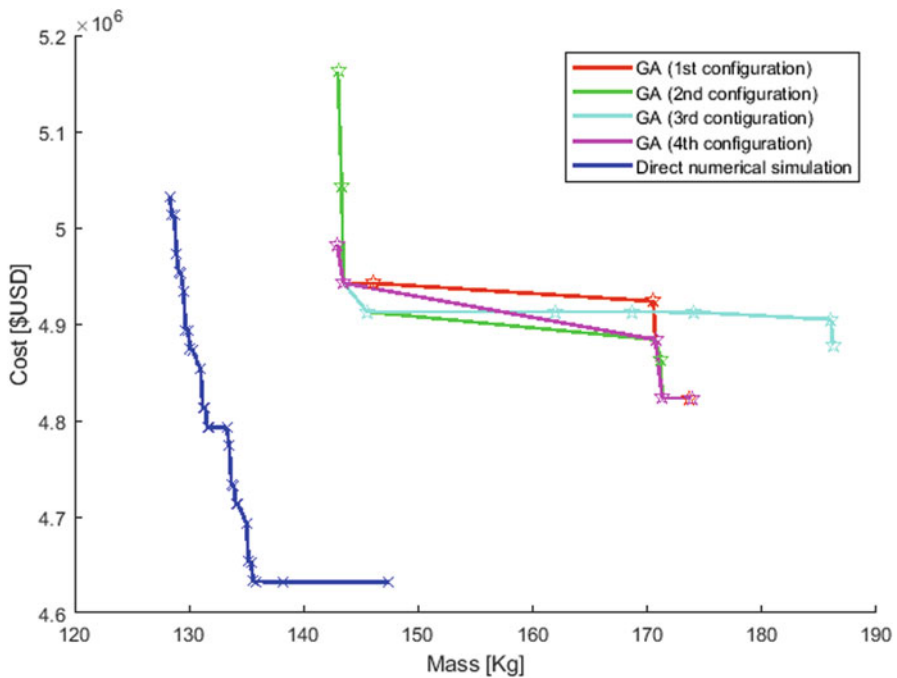


Fig. 6 Pareto fronts obtained with genetic algorithms and direct numerical simulation

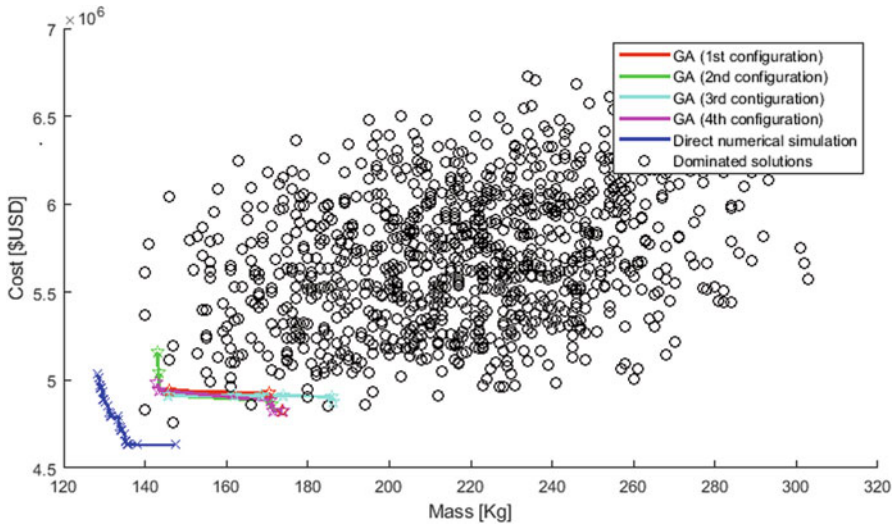


Fig. 7 Pareto fronts obtained with genetic algorithms and direct numerical simulation together with some random dominated solutions

5.6 Final Selection Process

The last step of the methodology is the final selection of the solution given by the Pareto front. Three different criteria are proposed for decision-makers to determine which of the solutions fit best the requirements. Each of the criteria will be analyzed based on the global optimum given by the Pareto front constructed by the DNS.

The approaches are written below:

1. **Minimum distance to the origin:** If the stated objectives are equally important, the best solution will be the one that is closest to the origin (as long as it is necessary to minimize the objective functions). Figure 8 shows the solution selected under this criterion on the Pareto front of the study case.
2. **Weighting selection:** This selection criterion is based on giving different priority levels to each proposed objective, taking the multi-objective problem to a single dimension. In this case, it will be necessary to normalize the objective functions and then perform the following operation:

$$F(x) = \sum_{i=1}^n K_i f_i(x), \quad \text{for } 0 \leq K_i \leq 1, \tag{1}$$

where $F(x)$ is the new objective function composed of the original objective functions $f_i(x)$ and K_i a weighting factor that will be determined by the designer and whose value is lower as the importance of this requirement is lower.

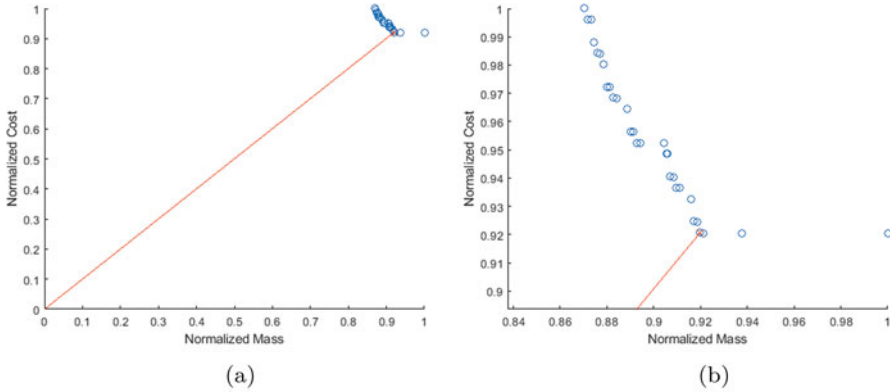


Fig. 8 Determination of the closest to the origin solution. **(a)** Referred to origin. **(b)** Zoom to the selected solution

3. **Reducing the problem to a single objective:** As with the criterion presented above, it is possible to reduce a multi-objective problem to one of a single objective by translating the rest of the functions in terms of the first one. For example, it is common to transfer all targets to a monetary value or to working hours. In this case, the total cost of the satellite can be calculated with Eq. 2.

$$\mathcal{F}(x) = f_1(x) + \sum_{i=2}^n C_i f_i(x), \quad (2)$$

where C_i are the different constants that relate the units of the objective function f_1 with the other objective functions. In the proposed study case, for example, it is easy to relate the cost of the satellite to its mass knowing the price of the launch service, which depends directly on the weight of the object to be put into orbit.

6 Final Remarks

A comprehensive design strategy is presented in this chapter in order to reduce the subjectivity of the designer group by defining a satellite as a system. A multi-objective optimization problem is formulated, based on the high-level requirements and exploring a set of admissible solutions. The proposed procedure is based on the numerical reconstruction of the Pareto front. After that, some criteria are exposed to select the best solution according to technical issues. The programmatic items are not taken into account in this presentation of the methodology. A comparison with a genetic algorithm, a common tool to solve this class of optimization problem, was performed. These two strategies are compared in terms of computational time spent

and the quality of the obtained results, instead of function evaluations. Both the genetic algorithms and the numerical simulations offer the possibility of finding the optimal solutions through their application in dedicated software, taking the design problem to a modeling problem. In the case of DNS, an expensive computational time is required to obtain the solution. In fact, from our numerical test DNS takes 6 h to obtain the solution and GA only 9 min. However, only the direct numerical simulation can guarantee the global minimum (optimal solution). To decide the best technique to solve the multi-objective optimization problem applied to a large-scale satellite model, an equilibrium between computational cost and processing time must be found.

Acknowledgments This research was partially supported by PID-UTN (Research and Development Program of the National Technological University, Argentina), CONICET (National Council for Scientific and Technical Research, Argentina), and CONAE (National Space Activities Commission, Argentina). The supports of these agencies are gratefully acknowledged.

References

1. Papalambros, P. Y., Wilde, D. J. (2000) Principles of Optimal Design. Cambridge University Press, Cambridge, UK
2. Rao, S. S. (2009) Engineering Optimization - Theory and Practice. Wiley, NJ, USA
3. Belegundu, A. D., Chandrupatla, T. R. (2011) Optimization Concepts and Applications in Engineering. Cambridge University Press, New York, USA
4. Deb, K. (2001) Multi-Objective Optimization Using Evolutionary Algorithms. Wiley, New York, USA
5. Space Flight Program and Project Management Handbook (2014) National Aeronautics and Space Administration, USA
6. System Engineering Handbook (2017) National Aeronautics and Space Administration, USA
7. Larson, W. J., Wertz, J. R. (2005) Space Mission Analysis and Design. Microcosm Press, El Segundo, California, USA
8. Ley, W., Wittmann, K., Hallmann, W. (2009) Handbook of Space Technology. Wiley, Chichester, UK
9. W. J. Larson and J. R. Wertz (2005) Space Mission Analysis and Design. Space Technology Library - Vol 8. Microcosm.
10. M. Macdonald and V. Badescu (2014) The International Handbook of Space Technology. Springer
11. M. M. Rai (2015) Utilizing Direct Numerical Simulations of Transition and Turbulence in Design Optimization. National Aeronautics and Space Administration, Report ID 2015-218932
12. R. Monti and P. Gasbarri (2017) Dynamic load synthesis for shock numerical simulation in space structure design. *Acta Astronautica*, 137:222–231
13. C. Li and Z. Zheng and J. Yuan (2020) A trajectory optimization method with frictional contacts for on-orbit capture. *Acta Astronautica*, 175:90–98
14. C. Wang and T. Huan and A. Li and H. Lu (2020) Mission analysis and optimal control for cislunar mission with spinning tether system in hyperbolic orbits. *Acta Astronautica*, 177:862–870
15. H. Yano and I. Nishizaki (2020) Multiobjective two-level simple recourse programming problems with discrete random variables. *Optimization and Engineering*, In Press

16. S. Kravanja and A. Sorsak and Z. Kravanja (2003) Efficient Multilevel MINLP Strategies for Solving Large Combinatorial Problems in Engineering. *Optimization and Engineering*, 4:97–151
17. P.K. Lewis and M.W.P. Tackett and C.A. Mattson (2014) Considering dynamic Pareto frontiers in decision making. *Optimization and Engineering*, 15:837–854
18. A.P. Curty Cuco and F.L. de Sousa and A.J. Silva Neto (2015) A multi-objective methodology for spacecraft equipment layouts. *Optimization and Engineering*, 16:165–181
19. A. Weber and S. Fasoulas and K Wolf (2011) Conceptual interplanetary space mission design using multi-objective evolutionary optimization and design grammars. *Proceedings of the Institution of Mechanical Engineers, Part G: Journal of Aerospace Engineering*, 225(11):1253–1261
20. B. Saboori and A. M. Bidgoli and B. Saboori (2014) Multiobjective Optimization in Repeating Sun-Synchronous Orbits Design for Remote-Sensing Satellites. *Journal of Aerospace Engineering*, 27(5)
21. I. Meziane-Tani and G. Métris and G. Lion and A. Deschamps and F. T. Bendimerad and M. Bekhti (2016) Optimization of small satellite constellation design for continuous mutual regional coverage with multi-objective genetic algorithm. *International Journal of Computational Intelligence Systems*, 9(4):627–637
22. Y. Jia and X. Yang (2015) Optimization of control parameters based on genetic algorithms for spacecraft attitude tracking with input constraints. *Neurocomputing*, 177:334–341
23. A. Ravanbakhsh and S. Franchini (2012) Multiobjective optimization applied to structural sizing of low cost university-class microsatellite projects. *Acta Astronautica* 79:212–220
24. H.R. Fazeley, H. Taei, H. Naseh and M. Mirshams (2016) A multi-objective, multidisciplinary design optimization methodology for the conceptual design of a spacecraft bi-propellant propulsion system. *Structural and Multidisciplinary Optimization*, 53:145–160
25. X.H. Wang, R.J. Li and R.W. Xia (2013) Comparison of MDO Methods for an Earth Observation Satellite. *Procedia Engineering*, 67:166–177
26. Zheng You (2017) *Space Microsystems and Micro/Nano Satellites*. Butterworth-Heinemann and Elsevier Inc.

Indirect Optimization of Robust Orbit Transfer Considering Thruster Underperformance



Francesco Simeoni, Lorenzo Casalino, and Antonio Amelio

1 Introduction

Space is an unforgiving environment: if there is an error, a ten-year multibillion-dollar project may be lost. To avoid this undesirable situation, the space industry puts a lot of efforts in improving the design of the spacecraft. An intensive testing campaign is put in place in the spacecraft validation and verification phase before the launch. Testing is done at equipment level, subsystem level, and system levels. Some of the functionalities of the integrated system cannot be fully tested on ground, before the nominal operation phase. In this respect, the in-flight commissioning phase is meant to be used as preliminary phase where the functionalities can be verified under flight conditions and the spacecraft performance can be characterized. Calibration of the sensors and actuators and eventually fine tuning of software parameters is also part of this phase. One of the most critical spacecraft subsystems is the propulsion one, in particular, if toxic propellants (such as hydrazine) are used. The thrusters can be tested and characterized at equipment level but they cannot be tested once they are integrated in the spacecraft platform. The actuation of the thrusters is safety hazardous on ground and, even if the tank is loaded with nitrogen, the electrical-mechanical test is constrained by a limited number of actuation when not used in vacuum, in order to not damage the catalytic heaters. After launch the attitude control thrusters are used without being initially commissioned. The same limitation applies to the main thruster used for delta-V maneuvers that have

F. Simeoni (✉) · A. Amelio
Thales Alenia Space, Torino, Italy
e-mail: francesco.simeoni@thalesaleniaspace.com; antonio.amelio@thalesaleniaspace.com

L. Casalino
Politecnico Torino, Torino, Italy
e-mail: lorenzo.casalino@polito.it

an obvious impact on the orbit itself. Considering this, the first S/C maneuver is generally a critical moment both because there is a time-criticality and in terms of the knowledge of the real performance of the thruster. Postponing the maneuver may require a significantly larger amount of ΔV , i.e., propellant, that in turn could cause to shorten the operational lifetime of the spacecraft or even make the mission impossible to be concluded.

During a trajectory design process, there are multiple local minima with very close values of the performance index that can be found. The global optimum represents the best solution for nominal conditions. However, uncertainties may be present during the realization of the trajectory (actuators performances, pointing errors, initial state); also, the possible requirement of changing the final boundary conditions (after the initial maneuver) may be considered. In these cases, the control variables of the first part of the trajectory should be computed in order to be robust in all possible realizations. The design of a trajectory is a process which starts from the early phase of a mission design, with preliminary assumptions about the spacecraft properties and performances. Then it is continuously updated with the design consolidation and assembly until the launch. During the operational phase, the trajectory must be observed continuously and the future maneuvers updated based on the current trajectory realization, the observed states and the actuators estimated performances. The maneuvers that modify the trajectory can be carefully planned on ground and executed by the spacecraft under operator supervision or can autonomously be computed by the on-board software. In both cases the maneuvers are traditionally computed and optimized considering specific nominal values for the spacecraft performance (nominal case), while the robustness of the designed trajectory is tested against one or more identified worst-case scenarios or Monte Carlo simulations.

The baseline configuration is used for the optimization of the control variables in contrast to compute them for the identified worst-case scenario, because in the latter case there is the risk to have an over-sizing of the spacecraft. Monte Carlo simulations assume a stochastic probability distribution of the uncertainties, the correlation among the uncertainties and the probability density function of the trajectory realization. The confidence level increases with the number of test runs. However, in the Monte Carlo approach, the most “dangerous” trajectory realizations are often at the tails of the distributions (typically Gaussian), so they are very rare. Besides, Monte Carlo simulations are expensive in terms of CPU time and resources (disk memory). The approach is clearly not suited for on-board applications.

The need to find a nominal trajectory which is, at the same time, sufficiently optimal and robust is an active research field (robust optimization). Different approaches have been proposed and hereafter summarized. The main practical approach is to check and improve the trajectory robustness to uncertainties a posteriori, by means of time-consuming iterative procedures, which often bring to suboptimal solutions and over-conservative margins. This design methodology is particularly unsuitable for micro-spacecraft missions, where the possibility to have large propellant margins and hardware redundancy is not a viable option.

Stochastic robustness is typically defined using chance constraints, which require that the probability of state constraints being violated is below a prescribed value (inequality constraints on the state). Prior work showed that in the case of linear system dynamics, Gaussian noise and convex state constraints, optimal chance-constrained finite-horizon control results in a convex optimization problem. Solving this problem in practice, however, requires the evaluation of multivariate Gaussian densities through sampling, which is time-consuming and inaccurate. An approach was proposed [1] to chance-constrained finite-horizon control that does not require the evaluation of multivariate densities. It introduces a conservative bounding approach to ensure that chance constraints are satisfied, while showing empirically that the conservatism introduced is small.

Space trajectories are subject to state uncertainty due to imperfect state knowledge, random disturbances, and partially known dynamical environments. Ideally, such uncertainty and associated risks must be properly quantified and taken into account in the process of trajectory design, ensuring a sufficiently low risk of causing hazardous events. An approach based on the indirect method by incorporating uncertainty and probabilistic path constraints into the primer vector framework [2], called stochastic primer vector, provides an analytical open-loop optimal control law that respects a probabilistic path constraint with a user-specified confidence level.

Differential dynamic programming [3, 4] was applied to trajectory optimization with an expected value formulation for Gaussian-modeled uncertainties. In particular, the nonlinear constrained stochastic optimal control problem is transformed into a problem through approximations (the stochastic process is reduced to Gaussian process). Then the deterministic problem is solved using a trajectory optimization method such as modified version of the Differential Dynamic Programming. The method gains robustness against duty cycle, thrust direction changes and thrusting time shifts.

An approach based on evidence theory to model uncertainty was developed [5] for the robust optimization of transfers under system and dynamical uncertainties. Optimal Control problems under specific epistemic uncertainty in system parameters (thrust, specific impulse, magnitude of the excess velocity vector) can be solved using Evidence Theory to model the uncertainties, Belief functions, and then transform the exact but discontinuous Belief problem to an inexact but continuous Statistical problem. The optimization stage is carried on the uncertainty space rather than the control space so to minimize the computational time. The target problem is low-thrust transfer from Earth to an asteroid.

A Belief-based procedure for stochastic optimal control problems has been used [6] for the robust design of a space trajectory under stochastic and epistemic uncertainties that incorporates navigation analysis to update of the knowledge of the spacecraft state in presence of observations. The target problem is one part of the Europa Clipper flyby tour.

The use of a deep neural network as machine learning tool has been proposed [7]. The training strategy is based on a Reinforcement Learning (RL) approach. The RL approach is used for the robust design of a low-thrust interplanetary trajectory in presence of various sources of uncertainty, which are (1) dynamic uncertainty, due

to possible un-modeled forces acting on the spacecraft; (2) navigation errors, which bring to an inaccurate knowledge of the spacecraft state; (3) control errors, due to erroneous actuation of the commanded control; and (4) a Missed Thrust Event (MTE), related to the unexpected occurrence of a safe mode during a thrusting period. The target problem is time-fixed low-thrust Earth–Mars rendezvous mission.

The authors used an indirect method for the deterministic optimization of the deployment of two satellites into a highly elliptical orbit [8]. In this chapter, they look for a relatively simple method to be introduced in their already available code to provide a robust solution to tackle underperformance during the first maneuver of the ΔV thruster. In order to make comparisons with their past works, the authors took in consideration the problem of the transfer orbit of a satellite into a highly elliptical orbit in presence of luni-solar perturbation and a J8x8 Earth gravitational model. The optimal solution found in the past for this specific problem was a perigee maneuver followed by one or more apogee maneuvers [8].

The novelty of the approach, based on the knowledge of the authors, is to use an indirect optimization method for a robust optimization that does not include any stochastic information of the uncertainties but rather selects a limited number of possible realizations of spacecraft trajectories and optimizes the chosen performance index, e.g., sum of the final mass, considering all the selected scenarios. The resulting optimal control, if exists, allows to reach the final boundary values for each scenario, modifying the control strategy to include all realizations. The selected scenario can be extreme, such as thrust level reduced before a long maneuver, but the switching times can be adjusted to mitigate the impact of such negative event on the final performance.

2 Indirect Method Optimization

The application of an indirect method to robust optimization is described in this chapter. Indirect methods are based on the theory of optimal control [16] and the basic concepts are here summarized.

Time t is here the independent variable, the n -component vector \mathbf{x} contains the state variables, and \mathbf{u} is the control vector (m components). Differential equations in the form $\dot{\mathbf{x}}(t) = \mathbf{f}(\mathbf{x}, \mathbf{u}, t)$ rule the state variables. A q -component vector of constraints on the state variables $\boldsymbol{\psi} = \mathbf{0} \in \mathbb{R}^q$ is considered.

The Bolza problem looks to find the extremal path $\mathbf{x}(t)$ and the corresponding optimal control law $\mathbf{u}(t)$ that satisfy the differential equation $\dot{\mathbf{x}}(t) = \mathbf{f}(\mathbf{x}, \mathbf{u}, t)$ and the boundary equations, maximizing (or minimizing) the performance index J .

$$J = \phi(\mathbf{x}_0, \mathbf{x}_{1\pm}, \dots, \mathbf{x}_f, t_0, t_{1\pm}, \dots, t_f) + \sum_{j=i}^f \int_{t_{(j-1)+}}^{t_{(j)-}} \Phi(\mathbf{x}, \dot{\mathbf{x}}, t) dt \quad (1)$$

In this chapter Meyer's formulation will be used and $\Phi = 0$.

The trajectory is split into j phases. The variables can have different values before and after the points at phase junctions, so that discontinuity can be handled.

The j -th interval goes from $t_{(j-1)+}$ to $t_{(j)-}$ and the variable values at the extremities are indicated as $\mathbf{x}_{(j-1)+}$ to $\mathbf{x}_{(j)-}$.

The boundary conditions are written as

$$\boldsymbol{\psi}(\mathbf{x}_{(j-1)+}, \mathbf{x}_{j-}, t_{(j-1)+}, t_{j-}) = 0 \quad j = 1, \dots, f \quad (2)$$

An augmented index can be introduced to consider differential equations and boundary conditions:

$$J^* = \phi + \boldsymbol{\mu}\boldsymbol{\psi} + \sum_{j=i}^f \int_{t_{(j-1)+}}^{t_{(j)-}} [\Phi + \boldsymbol{\lambda}^T(\mathbf{f} - \dot{\mathbf{x}})] dt \quad (3)$$

Adjoint variables $\boldsymbol{\lambda}$ (n -component vector) and constants $\boldsymbol{\mu}$ are introduced. When boundary conditions and differential equation are satisfied (the solution is feasible), $J = J^*$ for any choice of $\boldsymbol{\lambda}$ and $\boldsymbol{\mu}$, which can be selected to nullify the first variation of J^* (necessary condition for optimality).

Introducing the Hamiltonian defined as $H = \Phi + \boldsymbol{\lambda}^T \mathbf{f}$, the differential equation for the adjoint variables, i.e., the Euler–Lagrange equations, is obtained

$$\frac{d\boldsymbol{\lambda}}{dt} = - \left(\frac{\partial H}{\partial \mathbf{x}} \right)^T \quad (4)$$

In addition, m algebraic equations for the control variables

$$\left(\frac{\partial H}{\partial \mathbf{u}} \right)^T = 0 \quad (5)$$

and optimality conditions

$$-\boldsymbol{\lambda}_{j-}^T + \frac{\partial \phi}{\partial \mathbf{x}_{j-}} + \boldsymbol{\mu}^T \left[\frac{\partial \boldsymbol{\psi}}{\partial \mathbf{x}_{j-}} \right] = 0 \quad j = 1, \dots, f \quad (6)$$

$$\boldsymbol{\lambda}_{j+}^T + \frac{\partial \phi}{\partial \mathbf{x}_{j+}} + \boldsymbol{\mu}^T \left[\frac{\partial \boldsymbol{\psi}}{\partial \mathbf{x}_{j+}} \right] = 0 \quad j = 0, \dots, f - 1 \quad (7)$$

$$H_{j-} + \frac{\partial \phi}{\partial t_{j-}} + \boldsymbol{\mu}^T \frac{\partial \boldsymbol{\psi}}{\partial t_{j-}} = 0 \quad j = 1, \dots, f \quad (8)$$

$$-H_{j+} + \frac{\partial \phi}{\partial t_{j+}} + \boldsymbol{\mu}^T \frac{\partial \boldsymbol{\psi}}{\partial t_{j+}} = 0 \quad j = 0, \dots, f - 1 \quad (9)$$

complete the boundary value problem.

Without bounds on state and control variables, the maximization of H implies $H_u = 0$ and H_{uu} negative definite (local conditions), where the subscript indicates derivative with respect to the variable. This means that if H is linear with respect to a control variable u_j , $\frac{\partial H}{\partial u_j} = 0$ does not contain u_j , that is, it is indeterminate. The problem has a solution only if u_j is bounded. In this case the optimal control value is the one that maximizes H according to Pontryagin's maximum principle (PMP). This is called a Bang-Bang control.

The Optimal Control Theory exposed here formulates a multi-point boundary value problem (BVP), where initial values of some state values and adjoint variables and some constants (e.g., discontinuities at internal boundaries) are unknowns. An iterative procedure [17] based on Newton's method is used to obtain a converged solution.

3 Transfer between Highly Elliptic Orbits with Luni-Solar Perturbations

The problem of satellite deployment in highly elliptic orbit considering luni-solar perturbation is presented as example of application of the robust approach. The example is taken by Simeoni [8]. The initial orbit is an elliptic orbit with a perigee of 6728 km and an apogee above 191,116 km, while the final orbit has the same apogee with a perigee of 21,378 km (see also Sect. 3.3). In space trajectory design, the simplest gravitational model used is the two-body problem. The only way to modify the satellite trajectory is by using the thrust (generally the only available control). This model is well suited for some conceptual design (i. e. interplanetary trajectories) but it has strong limitations in some scenarios, such as missions around the Earth. In low Earth orbit a big issue is certainly the drag of the highest layers of the atmosphere. If the spacecraft is close to the Earth, it is also influenced by the perturbations due to the non-spherical shape of our planet. When the altitude of the orbit grows, other two actors come on the stage: the Moon and the Sun.

The perturbations included in this problem are:

- perturbations due to the asphericity of the Earth
- the presence of Sun and Moon
- the effects of solar radiation pressure

The perturbations are relative small in comparison to Earth's gravity so the effects can be seen and appreciated only in a mid-long period [9–15]. Aerodynamic can be neglected due to the relatively high altitudes involved.

3.1 Differential Equation

The relevant perturbations are added to the two-body problem equations to write the state differential system in vectorial form. All quantities have been made dimensionless using as reference length the Earth radius ($R_{conv} = 6378.1363$ km), as reference velocity $V_{conv} = \sqrt{\mu/R_{conv}}$, as mass $m = 1000$ kg. After that, the other dimensionless quantities (time, acceleration) have been derived. The gravitational parameter in adimensional form is $\mu = 1$.

$$d\mathbf{r}/dt = \mathbf{V} \quad (10)$$

$$d\mathbf{V}/dt = -\mu\mathbf{r}/r^3 + \mathbf{T}/m + \mathbf{a}_p \quad (11)$$

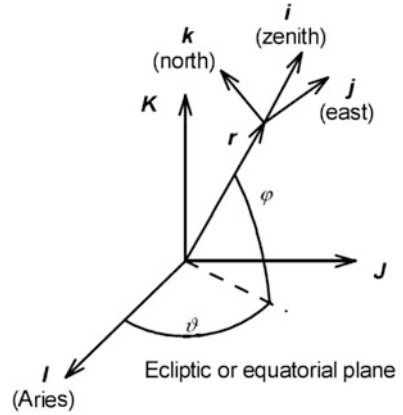
$$dm/dt = -T/c \quad (12)$$

where $-\mu\mathbf{r}/r^3$ is the central body spherical gravitational acceleration, while \mathbf{a}_p collects the perturbing accelerations. For further details about the derivation of perturbations components in the differential equations and for the derivation of adjoint variables equations see [8]. In the mass differential equation c is the effective exhaust velocity and T/c is the mass flow rate. The thrust vector is the only control of the trajectory and can vary its magnitude between maximum and minimum values. The specific impulse, and so c , is considered constant in this problem. In the specific problem of orbital transfer between elliptic orbits, the central body is the Earth and the perturbations, which are considered in this work are:

$$\mathbf{a}_p = \mathbf{a}_J + \mathbf{a}_{lsg} + \mathbf{a}_{srp} \quad (13)$$

where \mathbf{a}_J are the perturbations due to Earth asphericity, \mathbf{a}_{lsg} are the gravitational forces of “third bodies,” in particular, the subscript l indicates the lunar perturbation, while s indicates solar ones. \mathbf{a}_{srp} represents the perturbations due to solar radiation pressure, that is the pressure of the photons coming from the Sun. Different frames are used: The Earth Mean Equator and Equinox of Epoch J2000 (i.e., EME2000) reference frame is adopted to write the equations in a compact form. In this reference frame the unit vectors are indicated as \mathbf{I} , \mathbf{J} , \mathbf{K} . The first vector points towards the Vernal Equinox, the third is perpendicular to the equatorial plane and points towards the celestial North Pole, and the second one is chosen in order to have a right hand frame. Precession and nutation are neglected. For integration, a proper set of scalar variables must be used, and spherical coordinates are selected for position, which is described by radius r , right ascension ϑ , and declination φ . Velocity is defined by components in the radial eastward and northward directions, u , v , w , respectively, in a topocentric frame centered at the spacecraft and defined by unit vectors \mathbf{i} (radial or zenith), \mathbf{j} (eastward), and \mathbf{k} (northward) (see Fig. 1). The position of the Moon and the Sun is computed in EME2000 reference frame from JPL ephemeris [18, 19]. The thrust vector direction is defined also in the inertial reference frame EME2000. Once the positions of the celestial bodies have been retrieved, the accelerations acting on

Fig. 1 Spherical Reference frame



the S/C are projected in the topocentric reference frame (see also Eq. (36)) and the differential equations are integrated in this rotating reference frame.

The Hamiltonian in the vectorial form is quite simple

$$H = \lambda^T \dot{\mathbf{x}} = H_{2B} + H_T + H_p \tag{14}$$

$$H_{2B} = \lambda_r^T \mathbf{V} + \lambda_V^T \mathbf{g} \tag{15}$$

$$H_T = \lambda_V^T \mathbf{T}/m - \lambda_m(T/c) \tag{16}$$

$$H_p = \lambda_V^T \mathbf{a}_p = H_J + H_{lsg} + H_{srp} \tag{17}$$

$$H_J = \lambda_V^T \mathbf{a}_J \tag{18}$$

$$H_{lsg} = \lambda_V^T \mathbf{a}_{lsg} \tag{19}$$

$$H_{srp} = \lambda_V^T \mathbf{a}_{srp} \tag{20}$$

and Euler–Lagrange equations are written (when the thrust direction is free and thrust is independent of the state variables) as

$$d\lambda_r/dt = (\partial \mathbf{g}/\partial \mathbf{r} + \partial \mathbf{a}_p/\partial \mathbf{r})^T \lambda_V \tag{21}$$

$$d\lambda_V/dt = -\lambda_r \tag{22}$$

$$d\lambda_m/dt = \lambda_V \mathbf{T}/m^2 \tag{23}$$

The subscripts stand: J for geopotential perturbation, lsg for luni-solar gravity, and srp stands for solar radiation pressure.

3.2 Optimal Controls

The control is the vector \mathbf{T} that can vary in magnitude and direction. The thrust magnitude will be either maximum or minimum in order to fulfill optimality condition. For the sake of clearness here the Hamiltonian of Eq. (14) is re-written in a compact form, emphasizing the dependence on thrust and where H' collects all the terms that do not contain the control:

$$H = \boldsymbol{\lambda}^T \mathbf{x} = H' + \boldsymbol{\lambda}_V^T \mathbf{T}/m - \lambda_m(T/c) \quad (24)$$

$\boldsymbol{\lambda}_V$ is the adjoint vector to velocity and in literature is called primer vector [20]; its magnitude is λ_V . The expression of the primer vector is:

$$\boldsymbol{\lambda}_V = \lambda_u \mathbf{i} + \lambda_v \mathbf{j} + \lambda_w \mathbf{k} \quad (25)$$

The projection of the thrust vector direction on the primer vector is indicated as

$$\Delta_T = \lambda_u T_u/T + \lambda_v T_v/T + \lambda_w T_w/T \quad (26)$$

The Hamiltonian can be written as

$$H = \boldsymbol{\lambda}^T \mathbf{x} = H' + T(\Delta_T/m - \lambda_m/c) = H' + T \cdot S_F \quad (27)$$

where

$$S_F = (\Delta_T/m - \lambda_m/c) \quad (28)$$

is the Switching function and it is called in this way because its sign determines if the thruster is switched ON or OFF. From optimal control theory, the optimal thrust magnitude should be derived from $\partial H/\partial T = 0$, but the Hamiltonian is linear with the thrust magnitude. However, PMP states that the optimal control is the value that maximizes the Hamiltonian. So if the switching function is positive, the optimal value of thrust is T_{max} , otherwise is null. In equation is

$$T = \begin{cases} T_{max} & \text{for } S_F > 0 \\ 0 & \text{for } S_F < 0 \end{cases} \quad (29)$$

The control is bang-bang.

The optimal thrust elevation angle γ_T and thrust heading angle ψ_T are found by posing $\partial H/\partial \gamma_T = 0$ and $\partial H/\partial \psi_T = 0$. These equations provide

$$\sin \gamma_T = \lambda_u/\lambda_V \quad (30)$$

$$\cos \gamma_T \cos \psi_T = \lambda_v/\lambda_V \quad (31)$$

$$\cos \gamma_T \sin \psi_T = \lambda_w / \lambda_V \quad (32)$$

These are the cosine director of the primer vector. In other words the optimal direction of the thrust is parallel to the primer vector. If the optimal strategy is adopted $\Lambda_T = \lambda_V$. For this chapter, optimal thrust direction is not used but the thrust direction of each burn is instead fixed in the inertial reference frame. In fact, for this type of transfer, the thrust direction is mainly perpendicular to the line of apsides, with little components out of plane or along apsides, and little penalty occurs with the simplified control law and obtained thrust arcs.

The simplest solution is to keep an inertial fixed attitude during the ΔV maneuver, so the optimization problem takes into account the thrust angles α_j and β_j for each single burn. A different approach could optimize the thrust vector direction taking into account also the maximum angular rate of the Spacecraft. During the j -th burn, thrust components in the geocentric inertial reference frame (**I**, **J**, **K**) are written as

$$T_x = T \cos \alpha_j \cos \beta_j \quad (33)$$

$$T_y = T \sin \alpha_j \cos \beta_j \quad (34)$$

$$T_z = T \sin \beta_j \quad (35)$$

where α_j and β_j are the thrust angles. A simple change of reference frame provides the component in the topocentric frame **i**, **J**, **k**,

$$\begin{Bmatrix} T_u \\ T_v \\ T_w \end{Bmatrix} = \begin{bmatrix} \cos \vartheta \cos \varphi & \sin \vartheta \cos \varphi & \sin \varphi \\ -\sin \vartheta & \cos \vartheta & 0 \\ -\cos \vartheta \sin \varphi & -\sin \vartheta \sin \varphi & \cos \varphi \end{bmatrix} \begin{Bmatrix} T_x \\ T_y \\ T_z \end{Bmatrix} \quad (36)$$

So the thrust components in local frame T_u , T_v , and T_w now depend also on the state variables ϑ and φ . The Euler–Lagrange equations for the corresponding adjoint variables must take this dependence into account and a further component is added to Eq. (21):

$$d\lambda_r/dt = (\partial \mathbf{g}/\partial \mathbf{r} + \partial \mathbf{a}_p/\partial \mathbf{r} + \partial \mathbf{T}/(m \partial \mathbf{r}))^T \lambda_V \quad (37)$$

Further details have been presented in [8]. In this case $\Lambda_T \neq \lambda_V$ (see 26) and the general expression of the Switching function has to be taken in account.

First fixed values are considered for the thrust angles of the reference satellite mission. A tentative solution is needed: in this case, the target orbit has the line of the apsides along y axis and is coincident with the line of the nodes, $\alpha = 0$ and $\beta = -i_0$ (where i_0 is the inclination of the initial orbit) are adopted during the perigee burn, whereas $\alpha = \pi$ and $\beta = i_0$ are used during the apogee burns. This thrust vector lays on the orbital plane and it is always accelerating. Convergence to

optimal solutions is easily achieved using as tentative guess an orbit transfer with J2 perturbations only and a continuation technique as described in the following.

The two thrust angles α and β remain fixed in the inertial frame during the burn arc, but they change from one arc to another. Optimal control theory is applied to determine the optimal thrust angles. Each thrust angle for each burn arc is a standalone variable, i.e., there are $j \times 2$ variables, but they are independent between them (they are not “active” at the same time) so they can be stored in the same array in the implementation. There will be the optimal thrust angles α_j and β_j and their adjoint variables λ_{α_j} and λ_{β_j} . For each pair of angles with subscript j there are the correspondent Euler–Lagrange equations $d\lambda_{\alpha_j}/dt = -\partial H/\partial\alpha_j$, that is and $d\lambda_{\beta_j}/dt = -\partial H/\partial\beta_j$

$$\dot{\lambda}_{\alpha} = -\frac{T}{m} \left(\lambda_u \frac{\partial(T_u/T)}{\partial\alpha} + \lambda_v \frac{\partial(T_v/T)}{\partial\alpha} + \lambda_w \frac{\partial(T_w/T)}{\partial\alpha} \right) \tag{38}$$

$$\dot{\lambda}_{\beta} = -\frac{T}{m} \left(\lambda_u \frac{\partial(T_u/T)}{\partial\beta} + \lambda_v \frac{\partial(T_v/T)}{\partial\beta} + \lambda_w \frac{\partial(T_w/T)}{\partial\beta} \right) \tag{39}$$

The partial derivative of the cosines director of the with respect to α and β are:

$$\left\{ \begin{array}{l} \frac{\partial(T_u/T)}{\partial\alpha} \\ \frac{\partial(T_v/T)}{\partial\alpha} \\ \frac{\partial(T_w/T)}{\partial\alpha} \end{array} \right\} = \begin{bmatrix} \cos\vartheta \cos\varphi & \sin\vartheta \cos\varphi & \sin\varphi \\ -\sin\vartheta & \cos\vartheta & 0 \\ -\cos\vartheta \sin\varphi & -\sin\vartheta \sin\varphi & \cos\varphi \end{bmatrix} \left\{ \begin{array}{l} -\sin\alpha \cos\beta \\ \cos\alpha \cos\beta \\ 0 \end{array} \right\} \tag{40}$$

$$\left\{ \begin{array}{l} \frac{\partial(T_u/T)}{\partial\beta} \\ \frac{\partial(T_v/T)}{\partial\beta} \\ \frac{\partial(T_w/T)}{\partial\beta} \end{array} \right\} = \begin{bmatrix} \cos\vartheta \cos\varphi & \sin\vartheta \cos\varphi & \sin\varphi \\ -\sin\vartheta & \cos\vartheta & 0 \\ -\cos\vartheta \sin\varphi & -\sin\vartheta \sin\varphi & \cos\varphi \end{bmatrix} \left\{ \begin{array}{l} -\cos\alpha \sin\beta \\ -\sin\alpha \sin\beta \\ \cos\beta \end{array} \right\} \tag{41}$$

According to these equations the λ_{α_j} and λ_{β_j} are always null except in the $j - th$ arc and so the optimal boundary conditions are

$$\lambda_{\alpha_j} = 0 \quad j = 1, \dots, f - 1 \tag{42}$$

$$\lambda_{\beta_j} = 0 \quad j = 1, \dots, f - 1 \tag{43}$$

at the beginning and at the end of the arc. The thrust components

$$T_u = T \sin\gamma_T \tag{44}$$

$$T_v = T \cos\gamma_T \cos\psi_T \tag{45}$$

$$T_w = T \cos\gamma_T \sin\psi_T \tag{46}$$

are obtained with Eq. (36), the angles are shown in Fig. 2

Fig. 2 Thrust direction

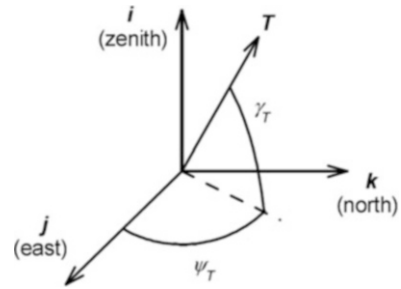


Table 1 Initial and final orbit characteristics

	a , km	e	i , deg	Ω , deg	ω , deg	ν	r_p , km	r_a , km
Initial	98,922	0.931985	5.2	90.0	270.0	0.0	6728	191,116
Final	106,247	0.798788	–	–	–	180.0	21,378	191,116

Table 2 Satellites properties

	Data
Launch	1250
mass (kg)	
Propellant	200
mass (kg)	
Mean	4.2
surface (m ²)	
Initial S/m	$3.36 \cdot 10^{-3} \text{ m}^2/\text{kg}$
Isp [s]	220
Nominal T [N]	4N
Failure scenario T [N]	2N

3.3 Boundary Conditions

In the following Table 1 it is possible to see the initial and final orbit parameters considered in the problem. The final orbit is defined only in semi-major axis and eccentricity, so the other final orbital parameters are free. Satellites properties are defined in Table 2.

The thruster exploits hydrazine as propellant. The satellite is injected by the launcher directly at the perigee of the initial orbit and has to perform, with its own propellant, the orbit transfer to the final orbit. For operational reason no burns are permitted in the first revolution, so the first phase is pure coasting and only at the following apogee or perigee passage the satellite can fire its engine.

The initial and final orbit are both HEOs, but the initial reference orbit has a low perigee, so the influence of the non-sphericity of the Earth is relevant. Since the first simulation runs it was also clear that J2 perturbations were very important in the first revolution and also in the overall strategy of the burns times. The J2 effects on semi-major axis are null in average in a complete revolution, but if the satellite is

injected at the perigee, the results are an instant drop of the semi-major axis that will change the optimal strategy. The high apogee makes Moon and Sun perturbations very important. Satellites perigee shows significant variations even considering only the ballistic flight.

Lunar perturbation brakes or accelerates the spacecraft when it is at the apogee, changing its semi-major axis, perigee, and orbital period. The period changes the next apogee passage (when compared with the 2 body solution) and so it is difficult to forecast the position of the Moon and its influence at the next revolution. The effect of these perturbations on the switching structures for the optimal fuel save deployment is hard to predict.

The perturbation of the Moon in the first revolution of the spacecraft, that is ballistic, can lower the perigee and makes the spacecraft plunge into the atmosphere. The impossibility of controlling the spacecraft orbit in the first phase of the mission makes important the analysis of moon influence and the choice of the departure date. For this chapter this constraint is not considered because it depends only on the launch window, it does not affect the control law.

4 Reference Satellite Transfer and Boundary Conditions

Most of the considerations and the procedure developed for the optimization of the reference (or baseline) satellite optimization are valid even for robust approach.

The statement of the problem is described in Sect. 1. From the statement the mathematical formulation of the boundary conditions has to be derived. The dynamical equations, the differential equations for adjoint variables, optimality and transversality conditions define the problem.

The dynamical equations and differential equations are defined in Sect. 3

At the initial point $j = 0$ all state variables are assigned. In the optimal procedure the initial time t_0 is considered to be given. A parametric analysis to evaluate the influence of the departure date on the mission has been performed. At the final point $j = f$ apogee radius r_A and orbit semilatus rectum $p = a(1 - e^2)$ are given. The final point is the apogee. The conditions of the state variables at the terminal point are:

$$r_f - r_A = 0 \quad (47)$$

$$u_f = 0 \quad (48)$$

$$v_f^2 + w_f^2 - \mu p / r_A^2 = 0 \quad (49)$$

The performance index to be maximized is the final mass, implying $\phi = m_f$ and $\Phi = 0$ in Eq. (1). The optimality conditions (6–7), eliminating the adjoint constants, are:

$$\lambda_{\vartheta f} = 0 \quad (50)$$

$$\lambda_{\varphi f} = 0 \quad (51)$$

$$\lambda_{vf} w_f - \lambda_{wf} v_f = 0 \quad (52)$$

$$\lambda_{mf} = 1 \quad (53)$$

The final time is free, so the transversality condition (9) gives Hamiltonian null at the end.

$$H_f = 0 \quad (54)$$

Application of Eqs.(6) and (7) at every switching point gives Hamiltonian continuity. State and adjoints variables are also continuous and so the switching function has to be null at the switch points (Points where engines turns OFF-ON or vice versa)

$$S_{Fj} = 0 \quad j = 1, \dots, f - 1 \quad (55)$$

The numerical problem consists of 14 differential equations represented by Eqs. (10–12) and (21–23). The state variables initial values are given, but the initial values of the adjoint state variables are unknown. The lengths of the coast and burn arcs are also unknown; an equal number of boundary conditions, given by Eqs. (47)–(55), completes the MPBVP. The problem is homogeneous in the adjoint variables and Eq. (53) can be replaced by assigning the initial value $\lambda_{m0} = 1$ in order to reduce the number of unknowns.

The optimal deployment strategy consists in a perigee (P) burn followed by a series of burns at the following apogee (A) passages. In this chapter the 3.5-revolution transfer is considered and the burn sequence is P-A-A. Indirect methods need a tentative solution. Since it is easier to estimate the burn angular positions (i.e., it is at the apes) than the corresponding time, a change of independent variables is adopted. The right ascension ϑ is introduced as new independent variable, and the differential equations are obtained by multiplying the time derivatives by $dt/d\vartheta$. The independent variable is further normalized as:

$$\varepsilon = j - 1 + \frac{\vartheta - \vartheta_{j-1}}{\vartheta_j - \vartheta_{j-1}} \quad (56)$$

A continuation technique using the perturbation fraction as parameter is introduced to improve solution convergence. Moon's influence may cause the vanishing of an apogee burn and one cannot know the switching structure in advance. The solution for the problem that only considers J2 has always burns at each apogee passage and is easily found. Then, the additional perturbations are gradually introduced with a multiplying factor that grows from 0 to 1. Failed convergence occurs when the switching structure changes and a burn arc must be removed, but

the switching function behavior of the previous converged solution suggests how it should be modified [8]. The perturbation fraction is increased with step 0.2. This procedure failed to obtain convergence in only 2% of the treated cases. The use of a reduced perturbation step solves the problem when convergence is not immediately obtained.

5 Robust Approach

The single satellite optimization helps to understand the influence of the perturbation and it is also a good testbed to build a robust procedure for seeking the optimal solution and optimal structure. The first perigee burn is critical. Thruster failure during this maneuver would dramatically change the trajectory and a dedicated recovery maneuver would be needed. In this chapter, thruster failure during the apogee burns is considered, as a robust trajectory may be capable of easily compensate for this anomaly, as shown in the following.

Three different optimization procedures are developed to test the solution robustness. The same variables and differential equations characterize the three scenarios. Two trajectories are integrated simultaneously with 28 state variables. One satellite represents the nominal case, while the other corresponds to the failure scenario. Thrust is 4 N in the nominal case. A reduced 2 N thrust is adopted for apogee burns A1 and A2 in case of failure.

Ideal Failure Recovery

In the ideal case the thruster failure is known in advance, before A1 is performed. The trajectory can, therefore, be optimized with the new thrust value, obtaining the maximum theoretical performance in case of failure. This case is equivalent to the solution of two separate single satellite scenarios as the equations of the two trajectories are uncoupled. These solutions represent the global optimum for the maneuvers with nominal and reduced thrust.

Failure Recovery for the Nominal Solution

In a real scenario, the failure is discovered after the A1 burn. The first apogee burn is, therefore, performed with commanded values (start and final time, thrust angles) of the nominal solution. After A1 the reached state of the satellite is not the desired one and the optimization procedure re-computes the A2 apogee burn. The solution will be suboptimal with respect to the failed scenario trajectory of the ideal case.

The nominal solution is found first. At the switching points, H continuity requires the switching function to be null:

$$S_{Fj} = 0 \quad j = 1, \dots, f - 1 \quad (57)$$

and the optimal thrust angles are found in each burn. In the failed scenario, start and end of the A1 burn are constrained and must be the same as the nominal ones. At $j = 4, 5$ Eq. (57) does not hold for the trajectory with reduced thrust, but these

conditions are replaced by

$$t_{4fail} = t_{4nom} \quad (58)$$

$$t_{5fail} = t_{5nom} \quad (59)$$

On top of that also the thrust angles are fixed in the inertial reference frame of the failed scenario in the A1 burn and shall be equal to the angles of the nominal scenario.

$$\alpha_{2fail} = \alpha_{2nom} \quad (60)$$

$$\beta_{2fail} = \beta_{2nom} \quad (61)$$

The second apogee burn is instead re-optimized, with the same boundary conditions as in the nominal solution.

In the re-optimization procedure the solution imposed to the satellite representing the failed scenario is far the optimal one, so the convergence to the suboptimal solution is generally slower than the ideal procedure. The nominal solution is independent of the failed scenario and equal to the ideal case (maximum m_{fS1}); the other trajectory separately maximizes m_{fS2} with the constraints on A1 determined by the nominal solution.

Robust Case

With the robust approach, the nominal trajectory is replaced by a robust trajectory. Nominal and off-nominal trajectories are now coupled and optimized simultaneously. The Hamiltonian is the sum of the contributions of the two satellites $H_{SYS} = H_{nom} + H_{fail}$ and the sum of the nominal and off-nominal final masses is maximized

$$\varphi = m_{fS1} + m_{fS2} \quad (62)$$

In the robust solution t_{4nom} , t_{5nom} , α_{2nom} , β_{2nom} assume different values with respect to the nominal optimal solution in order to maximize the sum of nominal and off-nominal final masses. At $j = 4, 5$:

$$t_{4fail} = t_{4nom} \quad (63)$$

$$t_{5fail} = t_{5nom} \quad (64)$$

and during the burn

$$\alpha_{2fail} = \alpha_{2nom} \quad (65)$$

$$\beta_{2fail} = \beta_{2nom} \quad (66)$$

At the A1 switching points the Hamiltonian of the coupled system shall still be continuous. For example, at the beginning of the arc, with $j = 4$

$$\begin{aligned} (H_{dyn,nom})_{j-} + (H_{dyn,fail})_{j-} &= (H_{dyn,nom})_{j+} + (H_{dyn,fail})_{j+} \\ &+ \lambda_{\alpha nom,j} \alpha_{nom,j+} + \lambda_{\alpha fail,j} \alpha_{fail,j+} + \lambda_{\beta nom,j} \beta_{nom,j+} \\ &+ \lambda_{\beta fail,j} \beta_{fail,j+} + SF_{nom,j} T_{nom} + SF_{fail,j} T_{fail} \end{aligned} \quad (67)$$

For $j = 4, 5$, considering Eqs. (65) and (66), one has:

$$\lambda_{\alpha nom,j} + \lambda_{\alpha fail,j} = 0 \quad (68)$$

$$\lambda_{\beta nom,j} + \lambda_{\beta fail,j} = 0 \quad (69)$$

$$SF_{nom,j} T_{nom} + SF_{fail,j} T_{fail} = 0 \quad (70)$$

The problem stated in this way has $(\lambda_m)_f = 1$ as final condition and λ_{m_0} as unknown parameter to be determined (for each satellite). But adjoint differential equations are homogeneous ($\mathbf{g}_\lambda(\lambda) = 0$), so it is possible to scale all λ in order to have an easier BVP problem to solve. So the final boundary conditions are:

$$\lambda'_{\alpha nom,j} / \lambda'_{mnom,f} + \lambda'_{\alpha fail,j} / \lambda'_{mfail,f} = 0 \quad (71)$$

$$\lambda'_{\beta nom,j} / \lambda'_{mnom,f} + \lambda'_{\beta fail,j} / \lambda'_{mfail,f} = 0 \quad (72)$$

$$SF'_{nom,j} / \lambda'_{mnom,f} T_{nom} + SF'_{fail,j} / \lambda'_{mfail,f} T_{fail} = 0 \quad (73)$$

$$\lambda'_{m_0 nom} = 1$$

$$\lambda'_{m_0 fail} = 1$$

6 Results

The indirect approach to robust optimization is here applied for the deployment of a satellite in a highly elliptic orbit. The deployment is accomplished in 3.5 revolutions. The satellite is assumed to be injected by a launcher in an already elliptic orbit. The satellite has then to perform in sequence:

- An initial perigee burn to achieve the required apogee.
- Two apogee burns to adjust the perigee.

A sketch of the nominal trajectory is shown in Fig. 3.

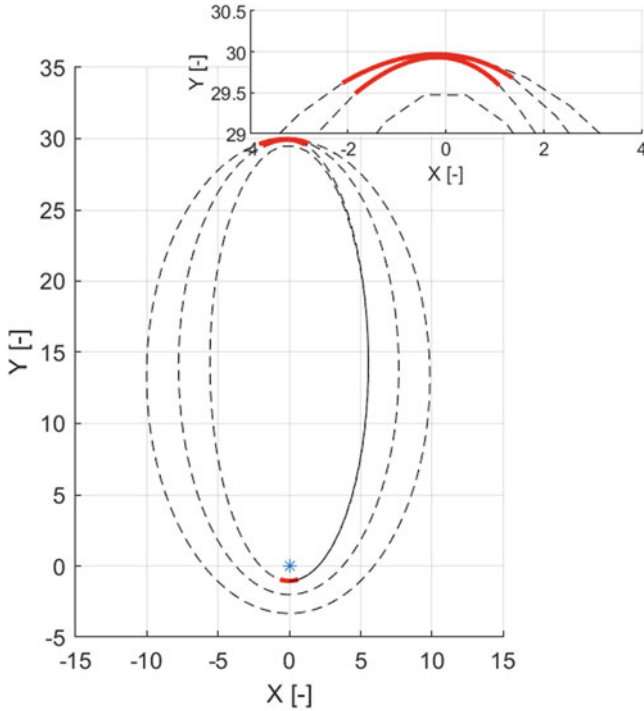


Fig. 3 Deployment trajectory

6.1 Ideal Failure Recovery

In the ideal case the trajectory of the baseline scenario ($4N$, thrust for each burn) and the failed scenario ($4N$ at perigee burn and $2N$ at the two apogee burns) are considered separately. It is assumed the perfect knowledge of the system, i.e., the best performance of the baseline scenario and the maximum achievable performance of the failed one. This translates to six switching points (initial and final for each burn) where the Switching Function is 0 for each satellite (optimality condition). Figure 4 shows the final mass of the SC in the baseline scenario ($4N$, optimal solution) and the failed scenario ($2N$). The horizontal axis shows the departing date in Modified Julian Date (MJD) while the vertical axis has the evolution of the final mass. For both cases the influence of the Sun/Moon perturbations can be appreciated.

The difference in the final mass between optimal baseline scenario and failed scenario is between 1.8 and 2 kg based on 1 year data. Figure 5 shows the peak to peak mass difference in a shorter range of time to improve the readability of the picture. The differences are mainly due to the higher gravitational losses. The apogee burn is not an impulsive maneuver, so the ΔV is not perpendicular to the

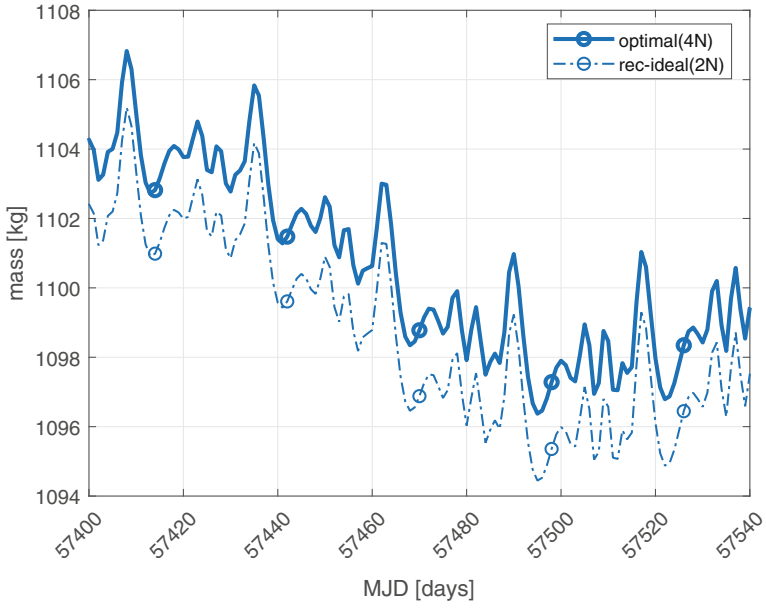


Fig. 4 Ideal recovery final mass

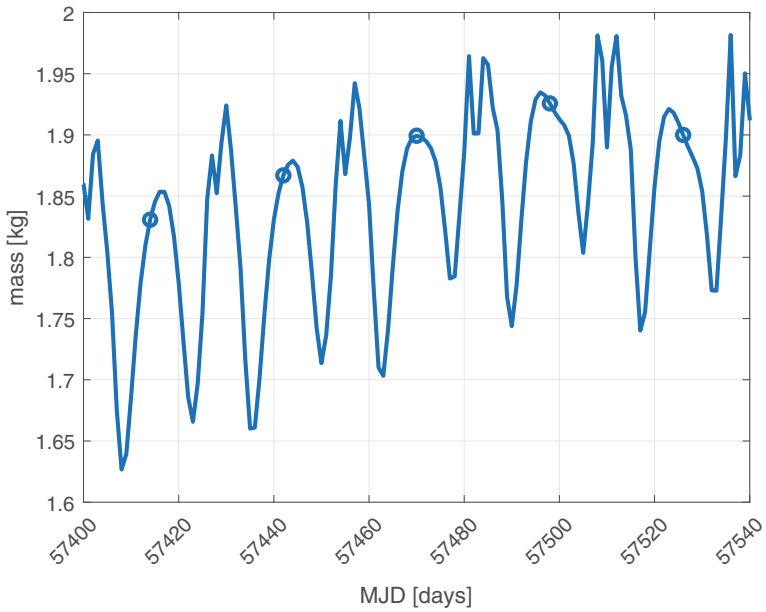


Fig. 5 Ideal recovery—difference in final mass

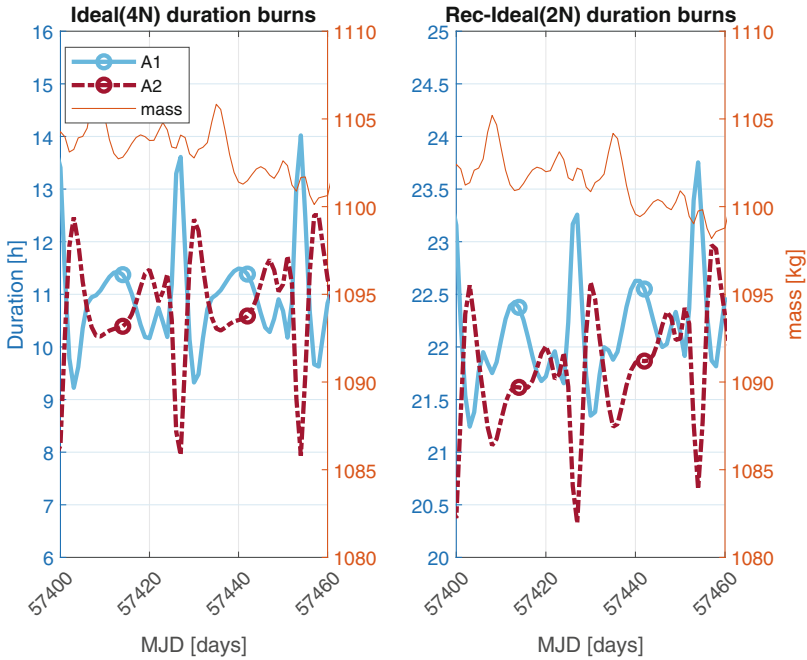


Fig. 6 Duration of the burns

radius of the orbit and to the gravitational acceleration. The failed scenario, with a lower thrust, needs a large time to perform its own ΔV and so the gravitational losses increase. This effect can be reduced if a larger number of revolutions is foreseen, e.g., 4.5 or 5.5 revolutions instead of 3.5 revolutions. In this way the apogee burn arcs are smaller and so the maneuver is closer to the ideal one.

For each departure date the duration of the burns has been computed. Figure 6 (left) shows the duration of the three burns for the optimal trajectory of the 4N thrust nominal scenario. The perigee burn is very small compared to the apogee ones. The two apogee burns (for a fixed MJD) are similar in duration (about 10 h). It is worth noting that large durations of A1 indicate that there is a benefit in reducing the satellite angular rate, in order to have a more favorable influence from the Moon at the following apogee passage. Short durations happen when faster rotation is needed. Figure 6 (right) shows the optimal trajectory for the 2N failed case, with larger duration of the burns (up to 1 day), but a similar trend along the MJD axis.

6.2 Failure Recovery of Optimal Solution

This case assumes the discovery of the failure after the A1 burn (no perfect knowledge). The commanded ΔV times are the same as planned for the baseline

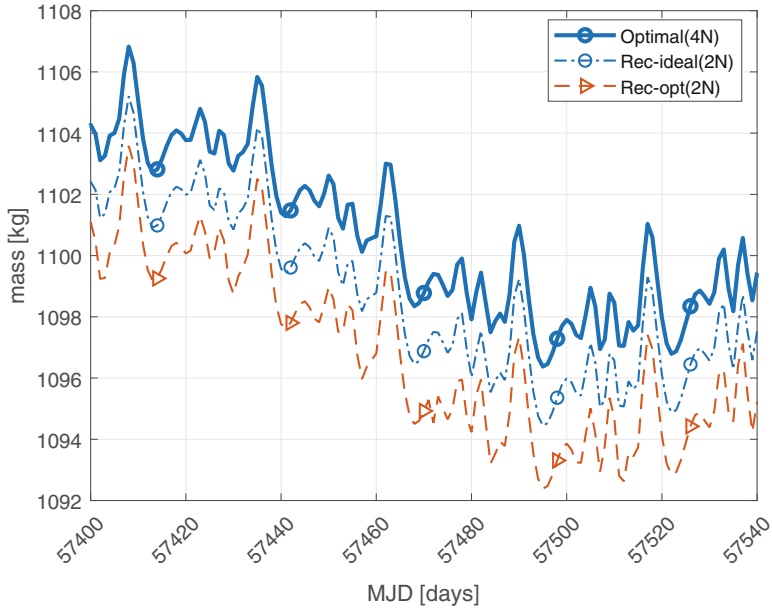


Fig. 7 Final mass comparison: Ideal vs. optimal solution recovery

optimal scenario. After the discovery of the failure, the trajectory is re-optimized from the conditions after the A1 burn. Ground can re-compute the optimal duration of the A2 apogee burn to meet the final orbit.

The re-optimized case assumes the first arc to be in common (perigee burn) but with the optimality conditions of the optimal solution de-coupled from the failed scenario. This is equivalent to a re-optimization after a state determination. From mathematical point of view the re-optimized case is obtained imposing a constraint on the first apogee burn so that the initial and final instant of the maneuver are coincident with those of the baseline scenario.

Figure 7 shows the comparison of the final mass between the ideal recovery and the recovery of the optimal solution (Rec-opt 2N, dashed line) in the failed scenario. This case is the closest to the reality. In fact the command to start the maneuver is sent by ground at a planned time or released by the on-board software considering a reference mission timeline. Even if the most recent generation missions use on-board accelerometers to estimate the executed ΔV , a timeout duration is, however, imposed for safety. Future application of inertial position navigation based on pulsar can improve ΔV estimation and orbit control.

Figure 8 shows the burn duration of the baseline case (left) and the duration of the burns in case of the re-optimization (right). The duration of the first apogee burn for the re-optimized case is the same of the baseline one, as it is imposed by the boundary conditions. The second apogee burn of the failed scenario has to recover all the difference in energy lost during the first apogee burn with increased gravitational losses.

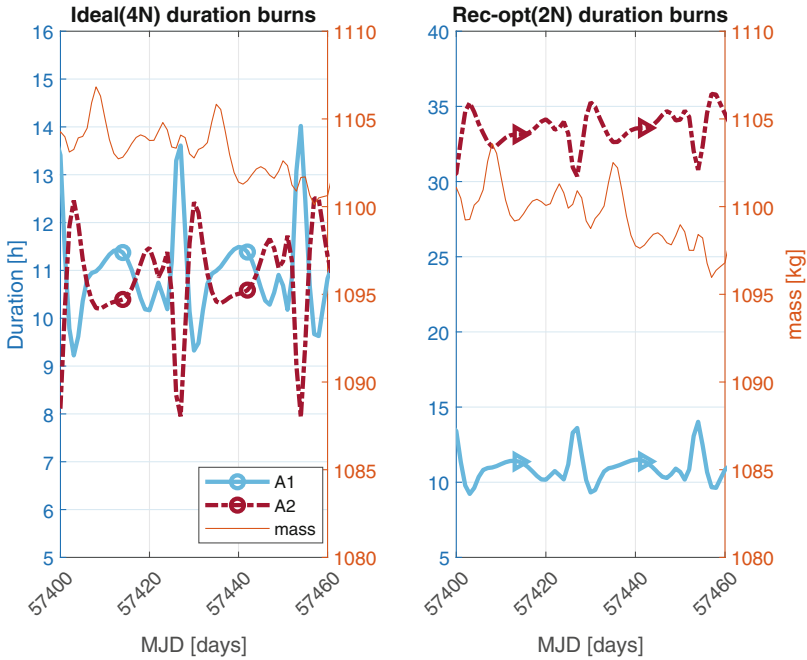


Fig. 8 Duration of the burns for the re-optimized case

Figure 9 shows the difference between the nominal scenario and failed scenario. In case of re-optimization the difference between the failed scenario and the baseline (rec-opt, dashed line) is larger, as expected. It is possible to note that in the ideal case optimization the difference between the two scenarios ($m_{fS1} - m_{fS2}$) varies from 1.67 to 1.82 kg, while in the re-optimized scenario the difference is larger between 3.22 and 4.08 kg and the trend is not regular. The hypothesis is that the suboptimal solution for the failed case prevents the possibility to exploit the Moon gravitational pull or to avoid its interference.

6.3 Robust Case

The robust solution takes into account the event of failure when the nominal solution is selected; the nominal solution and the failed solution are optimized simultaneously with coupled boundary conditions. The sum of the final masses for the two cases is maximized. The failed case has again the same A1 burn times of the nominal solution, but these values are now determined also considering the performance of the failed trajectory. The boundary conditions for optimality state that at the A1 switching times the sum of the switching function of the two cases (weighted with the with the thrust magnitude) must be equal to zero.

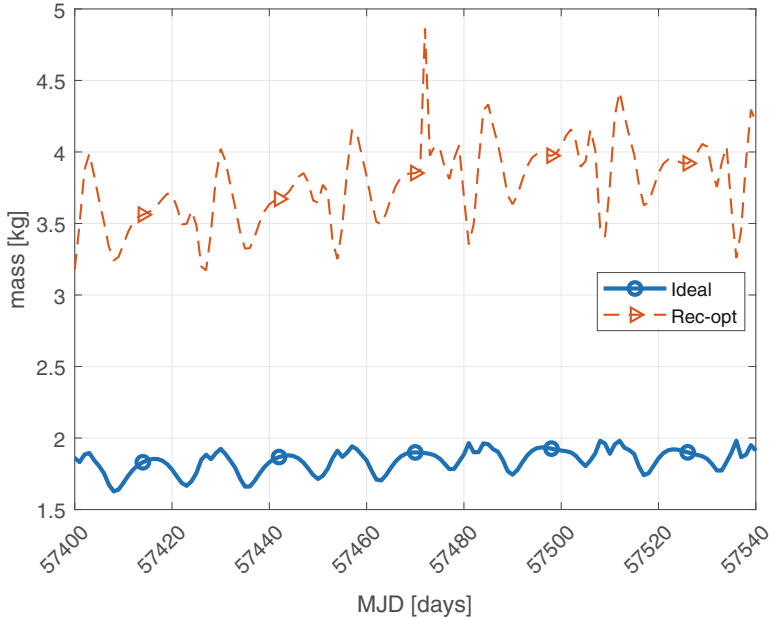


Fig. 9 Separated and Re-optimized difference in final mass

After the new (“robust”) first apogee burn, thruster magnitude underperformance is discovered and a re-optimized solution is found for the trajectory with failure. The continuous lines (Fig. 10) represent the nominal scenario while the dashed ones are the failed ones. The lines with circle markers refer to the two scenario optimized separately (optimal, rec-ideal), the dashed line with triangle markers refers to the recovery of the optimal solution (Rec-opt), which shows a large penalty in case of the failed scenario. The lines with square markers are the robust approach that, despite the small penalty in the nominal scenario (Rob, dashed), allows a recovery of performance in the failed one (rec-Rob, dash-dotted).

The robust nominal solution is close to the baseline optimal one with only a small penalty in terms of final mass (less than 1 kg). However, when thruster failure is considered, the mass decrease of the robust solution is much lower compared to the re-optimization of the nominal trajectory and the final mass is instead almost coincident with the ideal recovery.

The starting and ending instant of the maneuvers depend on the departing date. The first apogee burn (A1) is shorter for the nominal scenario (Fig. 11, left) in case of ideal optimization (Ideal) with respect to the robust one (Rob). This is expected because in the robust approach the first apogee burn is longer in order to take into account the possible thruster failure. Conversely, the duration of the second apogee burn for the nominal robust scenario (Rob) is shorter than the ideal one. In fact the most of the perigee raise has already been performed in the apogee burn

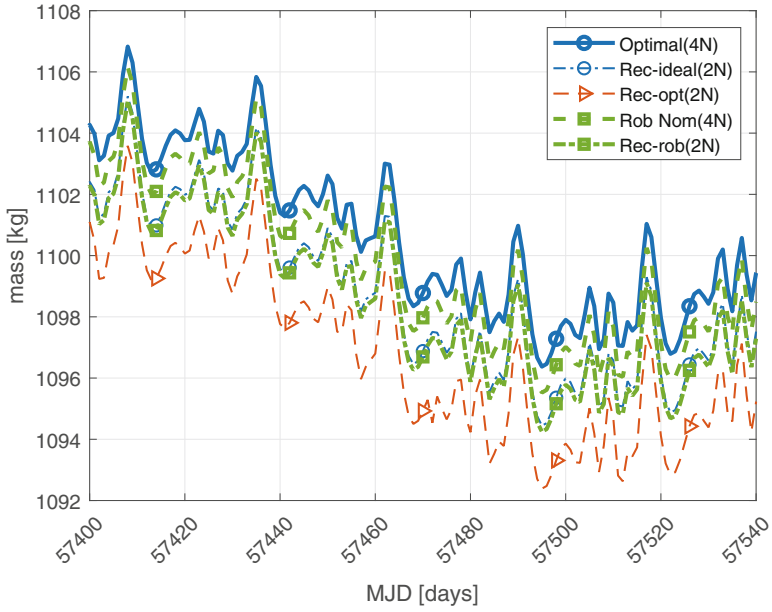


Fig. 10 Final mass for all cases

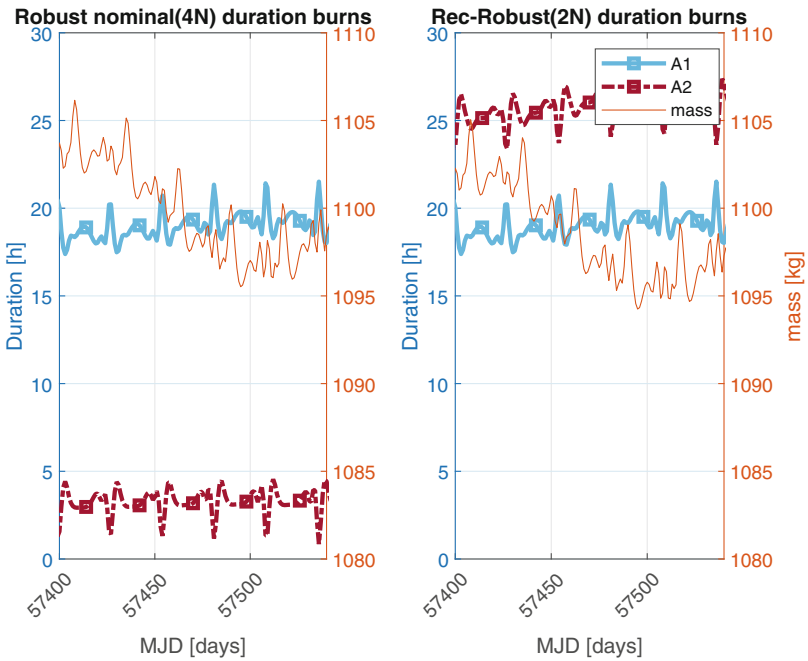


Fig. 11 Duration of the burns for the robust case

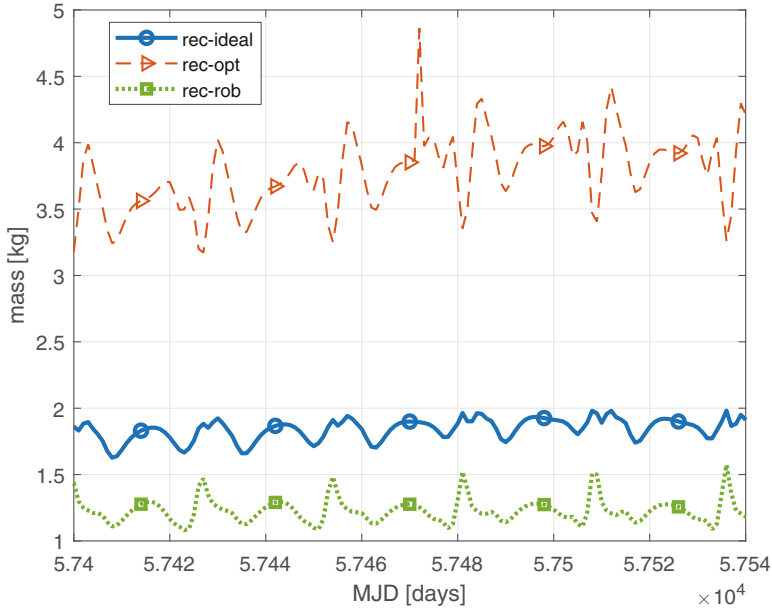


Fig. 12 Difference in final mass for all cases

A1. The thruster switch-off instant is similar to the nominal scenario in the ideal optimization, signaling that the thruster switch-on has been delayed.

The difference in final mass between each nominal solution and the corresponding failed solution is shown in Fig. 12. The nominal mass of the robust solution is lower than the optimal one, but failure recovery requires a very small penalty, as it is even less demanding than the ideal recovery of the optimal solution, notwithstanding the advanced knowledge of the failure in the latter case.

7 Conclusions

This chapter presents a robust approach to the design of optimal trajectories and its application to the deployment of a satellite in highly elliptic orbit. Thruster partial failure at apogee burns (thrust 50% of the nominal value) is considered. The use of an indirect optimization procedure allows for a robust approach, which is easy to be implemented and can be used in the preliminary phase of a trajectory design. The robust solution is obtained with a continuation technique that varies the perturbations, and less than ten minutes are typically required with a PC based on a Intel® Core™ i5-6198DU CPU @ 2.30GHz 2.40 GHz (a single core was used in this analysis). RAM usage is negligible.

When the nominal optimal trajectory is adopted, severe performance degradation is obtained in the case of thruster failure, even after re-optimization of the second burn. On the contrary, the robust solution is only slightly worse than the optimal one for nominal behavior, but greatly mitigates the mass reduction in the case of failure. If the failed-thrust scenario performance is a requirement for the mission, the robust solution may be preferable to the optimal solution.

This robust optimization method can be readily extended to different scenarios. Future possible works can concern the application of the same approach to multiple-failure scenarios (e.g., intermediate thrust levels and different points where the failure can occur). The use of different weights for the final masses in the definition of the performance index can provide alternative solutions with different degrees of “optimality” and “robustness.” Extension to multiple-failure scenarios (e.g., thrust magnitude and direction errors) is straightforward, by increasing the number of trajectories that are simultaneously optimized.

References

1. Blackmore L. and Ono M.: Convex Chance Constrained Predictive Control without Sampling. AIAA Guidance Navigation and Control Conference 10–13 August 2009, Chicago, Illinois
2. Oguri K. and McMahon J. W.: Stochastic Primer Vector for Robust Low-Thrust Trajectory Design Under Uncertainty. *JOURNAL OF GUIDANCE, CONTROL, AND DYNAMICS*. Vol. 45, No. 1, January 2022
3. Ozaki N., Campagnola S., Funase R. and Hong Yam C.: Stochastic Differential Dynamic Programming with Unscented Transform for Low-Thrust Trajectory Design. *JOURNAL OF GUIDANCE, CONTROL, AND DYNAMICS*, Vol. 41, No 2. February 2018
4. Ozaki N., Campagnola S. and Funase R.: Tube Stochastic Optimal Control for Nonlinear Constrained Trajectory Optimization Problems. *JOURNAL OF GUIDANCE, CONTROL, AND DYNAMICS*, Vol. 43, No. 4, April 2020
5. Di Carlo M., Vasile M., Greco C. and Epenoy R.: Robust Optimization of Low-Thrust Interplanetary Transfers using Evidence Theory. 29th AAS/AIAA Space Flight Mechanics Meeting, Vol. 168, Pages 339–358
6. Greco C., Campagnola S. and Vasile M.: Robust Space Trajectory Design using Belief Stochastic Optimal Control. AIAA 2020-147 Session: Space Trajectory Design and Optimization III, January 2020
7. Zavoli A. and Federici L.: Reinforcement Learning for Robust Trajectory Design of Interplanetary Missions. *JOURNAL OF GUIDANCE, CONTROL, AND DYNAMICS*. Vol. 44, No. 8, August 2021
8. Simeoni F.: Cooperative Deployment of satellite formation into Highly Elliptic Orbit. PhD Thesis
9. J. Fontdecaba, G. Métris, P. Gamet, P. Exertier, “Solar radiation pressure effects on very high-eccentric formation flying”, Proceedings of the 3rd International Symposium on Formation Flying, Missions and Technologies, 23–25/04/2008, Noordwijk, Pays-Bas
10. E. Wnuk, Accuracy of predicted earth’s artificial satellite orbits, *Advances in Space Research*, Volume 16, Issue 12, 1995, Pages 101–104, ISSN 0273-1177, [https://doi.org/10.1016/0273-1177\(95\)98790-U](https://doi.org/10.1016/0273-1177(95)98790-U). (<http://www.sciencedirect.com/science/article/pii/027311779598790U>)
11. Edwin Wnuk, Recent progress in analytical orbit theories, *Advances in Space Research*, Volume 23, Issue 4, 1999, Pages 677–687, ISSN 0273-1177, [https://doi.org/10.1016/S0273-1177\(99\)00148-9](https://doi.org/10.1016/S0273-1177(99)00148-9). (<http://www.sciencedirect.com/science/article/pii/S0273117799001489>)

12. Siebold, K. H. and Reynolds, R., C., "Lifetime Reduction of a Geosynchronous Transfer Orbit with the Help of Lunar-Solar Perturbations", *Advances in Space Research*, vol. 16, No. 11, (11)155-(11)161, 1995
13. Martynenko, B. K., *Lunar-solar gravitational perturbations for artificial satellite with twenty-four hour sidereal*, Marshall Space Flight Center, 1967
14. Fisher, D., "Lunisolar perturbations of the motion of artificial satellites", Goddard Space Flight Center, NASA-TM-X-65476, X-552-71-60, 1971
15. Fisher, D., "Analytic short period lunar and solar perturbations of artificial satellites", Goddard Space Flight Center, NASA-TM-X-65869, X-552-72-83, 1972
16. Bryson, A. E., and Ho, Y.-C., *Applied Optimal Control*, rev. ed., Hemisphere, Washington, DC, 1975, pp. 42–89.
17. Colasurdo, G., Pastrone, D., "Indirect Optimization Method for Impulsive Transfer," AIAA/AAS Astrodynamics Conference, Scottsdale, AZ August 1–3, 1994, page. 558–563, ISBN: 156347090X. Paper AIAA 94-3762.
18. http://ssd.jpl.nasa.gov/?planet_eph_export [retrieved October 27, 2011].
19. E. M. Standish, "JPL planetary and lunar ephemerides, DE405/LE405." JPL IOM 312F 98 048, 1998.
20. Lawden, D.F., *Optimal Trajectories for Space Navigation*, Butterworths, London, 1963, pp. 54–68.

Time-Varying Lyapunov Control Laws with Enhanced Estimation of Distribution Algorithm for Low-Thrust Trajectory Design



Abolfazl Shirazi, Harry Holt, Roberto Armellin, and Nicola Baresi

List of Acronyms

EA	Evolutionary Algorithm
EDA	Estimation of Distribution Algorithm
EEDA	Enhanced Estimation of Distribution Algorithm
GA	Genetic Algorithm
PSO	Particle Swarm Optimization
Q-law	Proximity Quotient Control Law

1 Introduction

Low-thrust many-revolution trajectory design and orbit transfer are becoming increasingly important with the development of high specific impulse, low-thrust engines such as electric propulsion (EP) systems. Finding an optimal transfer trajectory is a challenging task due to the nonlinearity of the system's dynamics and the problem complexity. Many approaches have been developed so far to overcome

A. Shirazi

Basque Center for Applied Mathematics - BCAM, Bilbao, Spain
e-mail: ashirazi@bcamath.org

H. Holt · N. Baresi

Surrey Space Centre, University of Surrey, Guildford, UK
e-mail: h.holt@surrey.ac.uk; n.baresi@surrey.ac.uk

R. Armellin (✉)

Te Pūnaha Ātea - Space Institute, University of Auckland, Auckland, New Zealand
e-mail: roberto.armellin@auckland.ac.nz

the difficulty of finding optimal transfer trajectories of the space systems. In general, these can be divided into one of the two categories: indirect and direct methods. Direct methods convert a continuous optimal control problem into a parameter optimization problem, often via discretization and subsequent transcription, to find an approximate solution to the original problem. Indirect methods, on the other hand, use calculus of variation to reduce the optimal control problem to the solution of a two-point boundary value problem [1–3]. Both techniques can be used to solve low-thrust trajectory design problems, and however, they are computationally intensive and still present many challenges. Direct methods generate a large optimization problem and result in approximate solutions. Indirect methods can produce rigorously optimal solutions, but they need a good initial guess and have difficulties in handling discontinuous controls. Both methods provide point solutions, i.e., for the assumed initial condition, and cannot be used as guidance laws due to time limitations and difficulties in ensuring convergence [3].

In recent years, advances in artificial intelligence and evolutionary computations have shifted the attention of the aerospace community toward the employment of evolutionary algorithms (EAs) in spacecraft trajectory optimization [3]. The motivation for utilizing EAs is based on their ability in dealing with local optimal region of the solution domain and handling nonlinear constraints that naturally appear in nonlinear optimal control problems. The development of novel EAs in these applications covers the vast types of space missions. Such developments are mainly within the framework of well-known EAs. For instance, in [4], a fuzzy goal programming-based Genetic Algorithm. The proposed algorithm is a hybrid technique based on the combination of a gradient-based method and Genetic Algorithm (GA). This algorithm is used to solve an optimal flight path design for a constrained multi-objective aero-assisted vehicle trajectory optimization problem. An improved NSGA-II algorithm is developed in [5] for solving non-coplanar orbit transfers in multi-impulse Lambert rendezvous problems. The proposed algorithm benefits from a self-adaptive differential evolution technique to increase the efficiency of the algorithm. In another recent research by Pontani [6], Particle Swarm Optimization (PSO) is utilized in an indirect approach based on Pontryagin principle. This approach is used to solve low-thrust Earth to Mars trajectory optimization problem. Englander and Conway [7] presented a modified GA and incorporated it in low-thrust interplanetary trajectory optimization problem. Algorithm modification in this research is toward the elitism operator within GA which preserves the best members of the population and encourages diversity at the same time. Many other algorithm enhancements have been proposed for various types of space applications including, satellite formation [8], mission planning [9], asteroid exploration [10], and orbit determination [11].

Following the progress in evolutionary methods with application in astrodynamics, it can be observed that the algorithm improvements are mostly based on the traditional evolutionary algorithms. One of the frameworks that did not receive much attention in spacecraft trajectory optimization is Estimation of Distribution Algorithms (EDAs) [12]. EDAs are a class of EAs. EDAs are a class of EAs that work based on probabilistic models. In an EDA, a probabilistic model is learned

at each iteration, and new solutions are sampled from that model. The obtained solutions have similar characteristics as those used for learning the model. One of the characteristics of EDAs is to have an explicit description of the promising solutions in terms of probabilistic models. Due to this feature, they have a great potential for enhancement toward further improvements. This characteristic is the main motivation in this research, and the effort here is to enhance the mechanisms of EDAs for obtaining higher quality solutions in spacecraft trajectory optimization.

The emergence of closed-loop feedback-driven (CLFD) controllers, particularly those based on Lyapunov control theory, has allowed the computation of sub-optimal trajectories with minimal computational cost [13–15]. The control profile is readily available as they only require knowledge of the current and target spacecraft states to compute it, making them suitable as initial guesses for indirect and direct methods [16, 17]. However, as they treat the problem from a targeting perspective, Lyapunov controllers are inherently sub-optimal and often have many user-defined parameters which significantly affect their performance [18–20]. One method for improving their performance involves EA. Both Lee et al. 2005 [18] and Varga et al. 2016 [19] used a multi-objective genetic algorithm to optimize Petropoulos’s Lyapunov-based Q-law design parameters for a variety of Earth orbit transfers, with the design parameters remaining fixed throughout the transfer. Yang et al. [21] used an artificial neural network and improved cooperative evolutionary algorithm optimizer to make the design parameters of a Lyapunov-based Q-law state-dependent.

In this research, both a simple Lyapunov function and a Q-law are formulated in Classical Orbital Elements (COEs) to provide a closed-loop low-thrust trajectory profile. Both control formulations are considered in order to assess whether the EEDA is capable of recovering the finer nuances embedded within the analytical expressions in the Q-law when using a simple Lyapunov controller. The optimal variations of weighting coefficients are interpolated via Hermite interpolation. The time series of weighting coefficients are turned into decision variables, and a black-box optimization problem is formed. Having the transfer time and the fuel mass as the objective functions, an enhanced EDA (EEDA) is proposed to find the unknown weighting coefficients. The proposed optimizer benefits from a new learning mechanism based on a mixture of Gaussian distribution. The mechanism prevents diversity loss of the population during the optimization process of EDA. The approach is tested in some time-optimal and fuel-optimal cases, and the optimality of the obtained solutions is analyzed.

The outline of the chapter is as follows. In Sect. 2, the two-body dynamical model is given and the proposed simple Lyapunov Controller is presented alongside the Petropoulos Q-law. Section 3 is dedicated to the optimization process in finding the optimal weighting coefficients for minimum-time and minimum-fuel transfer trajectories. Numerical simulations are provided in Sect. 4, where several cases of the orbit transfer missions are considered as the benchmark problems. The problems are solved using the proposed approach with a variety of settings as algorithm parameters. Finally, Sect. 5 contains the conclusions remarks and future works.

2 Low-Thrust Trajectory Design

2.1 Two-Body Dynamics

The spacecraft's motion about a central body is described in terms of the classical orbit element (COEs) semi-major axis a , eccentricity e , inclination i , right ascension of the ascending node (RAAN) Ω , and argument of periapsis ω . If the perturbing acceleration \mathbf{a}_d is described in the radial, transverse, and normal (RTN) frame, then the set of variational equations in a, e, i, Ω, ω and the true anomaly ν take Gauss's form of the Lagrange Planetary Equations [22]. These can be expressed as

$$\begin{bmatrix} \dot{\mathbf{X}} \\ \dot{\nu} \end{bmatrix} = \begin{bmatrix} \mathbf{B} \\ 0 \end{bmatrix} \mathbf{a}_d + \begin{bmatrix} \mathbf{0} \\ \frac{h}{r^2} \end{bmatrix}, \quad (1)$$

where $\dot{\mathbf{X}}$ represents the dynamics of the COE state, $p = a(1 - e^2)$ is the semi-latus rectum, μ is the gravitational parameter, and $h = \sqrt{\mu p}$. The matrix \mathbf{B} represents the Gauss Variational Equations (GVEs) for the slow variables and is required later to compute the control.

$$\mathbf{B} = \begin{bmatrix} \frac{2a^2}{h} e \sin(\nu) & \frac{2a^2}{h} \frac{p}{r} & 0 \\ \frac{1}{h} p \sin(\nu) & \frac{1}{h} ((p+r) \cos(\nu) + re) & 0 \\ 0 & 0 & \frac{r \cos(\omega+\nu)}{h} \\ 0 & 0 & \frac{r \sin(\omega+\nu)}{h \sin(i)} \\ -\frac{1}{he} p \cos(\nu) & \frac{1}{he} (p+r) \sin(\nu) & -\frac{r \sin(\omega+\nu) \cos(i)}{h \sin(i)} \end{bmatrix} \quad (2)$$

When examining Eq. (2), it is clear that singularities occur when $i = 0$ or $e = 0$. The modified equinoctial elements (MEEs) p, f, g, h, k and fast variable L are used in the dynamical integrator instead of COEs to avoid these issues[23]. However, the control remains in COEs in order to preserve the physical interpretation of the variables and extract insights from the observed behavior.

2.2 Lyapunov Control

Lyapunov functions offer a method for computing continuous-thrust trajectories with minimal computational cost. Obtaining an estimate of the low-thrust profile required for the acquisition of the different target orbits is straightforward thanks to the computation ease and closed-loop nature. The most well known and widely used is perhaps the Petropoulos Q-law [14, 15]. We provide an outline of this control law here, although the interested reader should refer [15] for full details. We also propose a very simple Lyapunov feedback control law, formulated in Classical Orbital Elements (COEs). Although the Q-law is a more optimal Lyapunov feedback

control laws exist, the simplicity gives the subsequent enhanced EDA more freedom and avoids potential singularity issues. As such, it is interesting to compare the performance of these two controllers.

2.2.1 Simple Lyapunov Controller

The proposed simple Lyapunov control function can be written as

$$V = \sum_X W_X \delta(X, X_T)^2, \tag{3}$$

where $\delta(X, X_T) = X - X_T$ for $X = a, e, i$, while $\delta(X, X_T) = \arccos(\cos(X - X_T))$ for $X = \Omega, \omega$. The weights W_X can be used to prioritize which elements to target. As written above, the control law is a proportional function and as such W are normalized.

2.2.2 Proximity Quotient Controller (Q-law)

The Q-law is best thought of as a weighted squared summation of the time required to change the current state $\mathbf{X} = [a, e, i, \Omega, \omega]^T$ to the target state $\mathbf{X}_T = [a_T, e_T, i_T, \Omega_T, \omega_T]^T$. It can be written as

$$V = Q = (1 + W_P P) \sum_X S_X W_X \left(\frac{\delta(X, X_T)}{\max_v(\dot{X})} \right)^2, \tag{4}$$

where Q and V can be used interchangeable in the following formulas. Here, W_P and P form a penalty function and S_X are scaling functions. These are functions of the state and can be found in Ref [15]. Again, $\delta(X, X_T) = X - X_T$ for $X = a, e, i$, while $\delta(X, X_T) = \arccos(\cos(X - X_T))$ for $X = \Omega, \omega$. The expressions $\max_v(\dot{X})$ are the maximum rate of change of each COE over the current osculating orbit and can be calculated analytically for all elements except ω . For a more detailed breakdown of the components of the Q-law, the reader is encouraged to look at Refs. [15], [24], and [25]. All user-defined parameters aside from the weights W_X (for instance, those in W_P, P , and S_X) are assumed constant, as these terms are only activated to prevent particular behavior that we also want to prevent. The values are given in Table 1.

Table 1 Table of standard Q-law parameters from Ref. [15]

Parameter	Value	Parameter	Value	Parameter	Value
r	2	k	100	b	0.01
$r^{p-\min}$	6578 km	m	3	n	4

2.2.3 Control Direction

Lyapunov's second theorem states that for a system $\dot{\mathbf{Z}} = \mathbf{f}(\mathbf{Z})$, $\mathbf{Z} = \mathbf{X} - \mathbf{X}_T$, the equilibrium point \mathbf{X}_T is asymptotically stable if there exists a scalar Lyapunov function $V(\mathbf{Z})$ such that $V(\mathbf{0}) = 0$, it is positive-definite ($V(\mathbf{Z}) > 0, \forall \mathbf{Z} \neq \mathbf{0}$), the derivative is negative-definite ($\dot{V}(\mathbf{Z}) < 0, \forall \mathbf{Z} \neq \mathbf{0}$), and $\lim_{|\mathbf{Z}| \rightarrow \infty} V(\mathbf{Z}) = \infty$ [26]. A very thorough discussion on the implications of this for trajectory design using nonlinear control can be found in Ref. [27].

A stable control is therefore one that ensures $\dot{V} < 0$ throughout the transfer. One way of doing this is to select a controller that minimizes the rate of change of the Lyapunov function (in this case, the most negative value).

$$\dot{V} = \frac{\partial V}{\partial \mathbf{X}} \dot{\mathbf{X}} = \frac{\partial V}{\partial \mathbf{X}} \mathbf{B} \mathbf{u}. \quad (5)$$

Given an engine thrust T and a spacecraft mass m , the control vector is computed as (using $f = T/m$)

$$\mathbf{u} = -f \frac{\mathbf{B}^T \left(\frac{\partial V}{\partial \mathbf{X}} \right)^T}{\left\| \left(\frac{\partial V}{\partial \mathbf{X}} \right) \mathbf{B} \right\|}. \quad (6)$$

Coasting can be introduced using effectivity thresholds η^{thresh} . These attempt to quantify the effectivity of changing an orbital parameter at a given point in an orbit compared to the optimum point for changing the same orbital parameter. Definitions for both the absolute and relative effectivity parameters exist. Studies [18] have also shown that when varying other control law parameters in addition to the effectivity, there is a little difference in performance between relative and absolute effectivity, and, instead, the specific transfer will determine which is more applicable. Hence, in this work, the absolute effectivity

$$\eta_a = \frac{\min_{\alpha, \beta} \dot{V}}{\min_{\nu} (\min_{\alpha, \beta} \dot{V})} \quad (7)$$

is used. α and β are the in-plane and out-of-plane angles of the thrust vector, while $\min_{\nu} (\min_{\alpha, \beta} \dot{V})$ is computed numerically by scanning through the possible true anomaly ν values to find the maximum and minimum \dot{V} for the particular osculating orbit. The authors note that an alternative approach first found in Ref. [19] can be used, which now avoids any numerical derivations thanks to recent work in Ref. [25].

3 Optimization Approach

Following the proposed approaches including the Q-law and the Lyapunov methods, achieving optimal transfer trajectory lies upon finding a suitable set of values for unknown weighting coefficients of the proposed techniques. In this research, the unknown weighting coefficients are defined as

$$\vec{x} = [\eta_a \quad W_a \quad W_e \quad W_i \quad W_\Omega \quad W_\omega] \tag{8}$$

which include the normalized state weights $W_X = [W_a \quad W_e \quad W_i \quad W_\Omega \quad W_\omega]$ and the absolute effectivity threshold η_a . Tuning these parameters for a given orbit design problem yields time-optimal or mass-optimal transfer trajectories. Basically, constant values are the primary choice for these parameters. However, in this research, these parameters are considered as functions of transfer time. Therefore, the problem turns into finding proper time series for the weighting coefficient to achieve optimal transfer trajectories.

3.1 Direct Interpolation

Parameterizing the unknown weighting coefficients has a significant impact on the convergence of the optimization algorithm, and consequently, obtaining optimal transfer trajectories. In this research, the time series of decision variables \vec{x} is approximated by considering N_p number of interpolation points in the desired time of flight interval $0 < t < t_f$. Noting the fact that all weighting coefficients are normalized, the weights' variation are in the limits of $0 < \vec{x} < 1$. Having N_p number of uniformly discretized points, the overall time span is divided into $N_p - 1$ sub-intervals. The interpolating polynomial for the time interval can be represented by:

$$\hat{x}(t) = \sum_{k=1}^N \left(\prod_{j \neq k} \frac{t - t_j}{t_k - t_j} \right) p_k \tag{9}$$

where $\hat{x}(t)$ denotes any of the unknown weighting coefficients in \vec{x} , t_k are the discretized times, and p_k are the discrete points within the time interval. Given the number of discrete points N_p for each decision variable, the time series of the corresponding weighting coefficient may be interpolated with different shapes. One of the most popular methods is using piecewise cubic Hermite interpolating polynomials [28]. Various types of splines can be obtained depending on the choice of tangents in each node. One type of spline from the family of Hermite splines, which is frequently used in many applications, is illustrated in Fig. 1 for approximating the weighting coefficients.

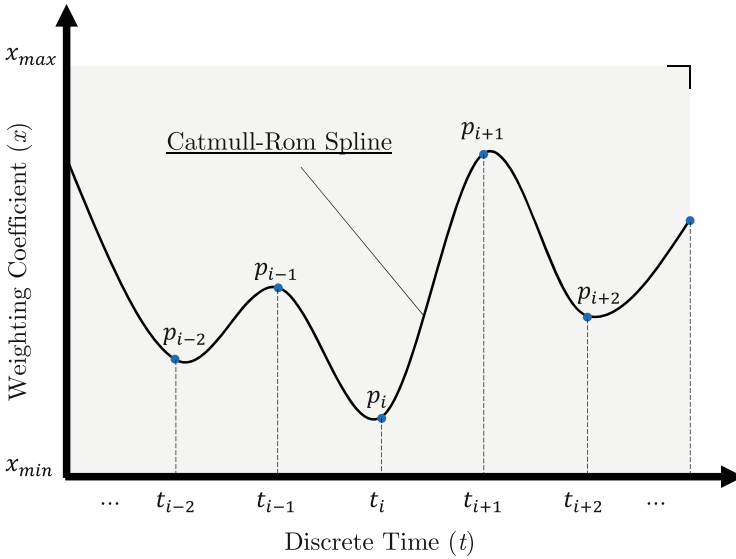


Fig. 1 Weighting coefficient interpolating with piecewise cubic Hermite splines

This interpolation represents Catmull Rom spline [29], which has a continuous first derivative. The difference between this polynomial and other types of Hermite interpolation schemes is the choice of tangents in the internal and end nodes. This spline has a balanced smoothness, and the slope of the spline at data points depends directly on the points before and after. The resulting piecewise cubic does not have a continuous second derivative, and it does not always preserve shape. However, it can be evaluated quickly by a convolution operation. More details regarding the derivation of this spline and its difference from the other types of interpolations are beyond the scope of this research, and the reader is urged to refer to the provided references for details [29–31].

Regarding this explanation, the low-thrust trajectory design can be defined as an unconstrained optimization problem. The general form of such an optimization problem is

$$\begin{aligned}
 & \text{Minimize} && F(x) \quad x = (x_1, x_2, \dots, x_n) \\
 & \text{Subject to} && x_{min} < x_i < x_{max},
 \end{aligned}
 \tag{10}$$

where n is the number of decision variables, and $F(x)$ represents the objective function, which is the actual transfer time for time-optimal transfers and fuel mass of the spacecraft for mass-optimal transfers. Based on the proposed formulation of the low-thrust space orbit transfer problem, the decision variables $x = (x_1, x_2, \dots, x_n)$ are the interpolation points for unknown weighting coefficients of the proposed controller:

$$x = p_i \quad (i = 1, \dots, N_v \times N_p), \tag{11}$$

where N_v is the number of unknown weighting coefficients (i.e., $N_v = size(\vec{x})$). As can be seen, an equal number of interpolation points are dedicated to every unknown variable in this research. However, in a more general concept, one may consider different interpolation points for each of the weighting coefficients. To deal with this unconstrained continuous optimization problem, an EDA-based algorithm is proposed in the following section.

3.2 Enhanced Estimation of Distribution Algorithm

EDAs are a type of population-based optimization algorithms, designed for solving numerical optimization problems. Based on machine learning techniques, at each iteration, EDAs learn a probabilistic model from a subset of the most promising solutions, trying to explicitly express the interrelations between the different variables of the problem. Then, by sampling the probabilistic model learned in the previous iteration, a new population of solutions is created. In other words, EDAs work based on two major key methods: learning and sampling, where a probabilistic model that estimates the probability distribution of the selected solutions is learned and then utilized for sampling new individuals [32]. In this work, an improved learning mechanism is presented and applied to an EDA based on multivariate Gaussian distribution. It will be shown that the new enhanced algorithm outperforms traditional EAs within the proposed optimization problem.

The overall pseudo code of the proposed algorithm is presented in Algorithm 1. Following the pseudo code, the optimization process begins with N as the population size and M as the maximum number of iterations. Initially, the **SEEDING** mechanism is utilized to generate an initial population. Having the initial feasible solutions, with corresponding objective values f obtained from **EVALUATION**, the main optimization loop starts. At each iteration, the algorithm begins by selecting the top promising individuals in the current population according to the **SELECTION** method. The truncation selection method [32] is used in this research, with γ as the truncation factor. In this method, the γ fraction $\gamma \in (0, 1]$ of the best individuals is selected. All the individuals have the same selection probability defined as

$$P_j = \begin{cases} \frac{1}{N_s} & 1 < j < N_s \\ 0 & N_n < j < N, \end{cases} \tag{12}$$

where N_s is the number of selected individuals as $N_s = \gamma N$. Having the selected population x_{sel} and the corresponding objective values f_{sel} , a probability model is learned via the **LEARNING** mechanism. In the proposed learning mechanism, the selected population is divided into two types of clusters. These clusters include

Algorithm 1: Overall pseudo code of EDA

Input: $F(x), x_{min}, x_{max}$
Parameters: $N, M, \gamma, \alpha, \lambda, N_c$

- 1 $x \leftarrow \text{SEEDING}(x_{min}, x_{max}, N)$
- 2 $f \leftarrow \text{EVALUATION}(x, F(x))$
- 3 **if** $i < M$ **then**
- 4 **for** $iter \leftarrow i$ **to** M **do**
- 5 $[x_{sel}, f_{sel}] \leftarrow \text{SELECTION}(x, f, \gamma)$
- 6 $[\Phi, \phi] \leftarrow \text{LEARNING}(x_{sel}, f_{sel}, \alpha, \lambda, N_c)$
- 7 $x_{sam} \leftarrow \text{SAMPLING}(\Phi, \phi, N)$
- 8 $x_{rep} \leftarrow \text{REPAIRING}(x_{sam}, x_{min}, x_{max})$
- 9 $f_{rep} \leftarrow \text{EVALUATION}(x_{rep}, F(x))$
- 10 $[x, f] \leftarrow \text{REPLACEMENT}(x_{rep}, f_{rep}, x, f)$
- 11 EXTRACT $[x_{best}, f_{best}]$ FROM $[x, f]$;
- 12 **if** *stopping criteria are met* **then**
- 13 BREAK;
- 14 **end if**
- 15 **end for**
- 16 **else**
- 17 EXTRACT $[x_{best}, f_{best}]$ FROM $[x, f]$;
- 18 **end if**

Output: x_{best}, f_{best}

Algorithm 2: Pseudo code of the learning mechanism

Input: $x_{sel}, f_{sel}, \alpha, \lambda, N_c$

- 1 $[t, \mu] \leftarrow \text{k-means}(x_{sel}, i)$;
- 2 CONSTRUCT Φ FROM $[\mu, x_{sel}(t)]$
- 3 **for** $i \leftarrow 1$ **to** N_c **do**
- 4 EXTRACT $[\hat{x}, \hat{f}, \hat{\mu}, \hat{\sigma}]$ FROM $\Phi(i)$
- 5 $[\hat{x}_{sel}, \hat{f}_{sel}] \leftarrow \text{SELECTION}(\hat{x}, \hat{f}, \alpha)$
- 6 $d \leftarrow ||\hat{x}_{sel} - \hat{\mu}||$
- 7 $j \leftarrow 0$
- 8 **if** $d > \lambda \times \hat{\sigma}$ **then**
- 9 $j \leftarrow j + 1$
- 10 CONSTRUCT $\hat{\phi}$ FROM $[\hat{\mu}, \hat{x}_{sel}]$
- 11 $\phi(j) \leftarrow \hat{\phi}$
- 12 **end for**

Output: Φ, ϕ

parent clusters, denoted by Φ , and smart clusters denoted by ϕ . The pseudo code of the learning mechanism is shown in Algorithm 2.

The main idea of the learning process is based on utilizing a mixture of Gaussian distributions as a probabilistic model whose density function is formalized as

$$P(x) = \sum_{k=1}^{N_c} \pi_k f_k(x | \mu_k, \Sigma_k), \quad (13)$$

where each $f_k(x|\mu_k, \Sigma_k)$ component of the mixture is a multivariate Gaussian distribution, and μ_k and Σ_k are the mean value (the centroid) and the covariance matrix of the k model for $k = 1, \dots, N_c$, respectively, with π_k as the mixing coefficient for the k th component.

In the proposed learning stage, the Gaussian mixture model is constructed in two steps. The first step consists of clustering the selected population according to N_c number of parent clusters. In this research, *k-means++* is chosen as the clustering method [33]. However, other methods could also be considered. Following the clustering process, the mixture of Gaussian distributions model is learned by calculating the maximum likelihood estimators of the parameters of the components in this mixture, using the solutions in the respective clusters. This process is the first step of the learning process. Finalizing the process, the components Φ , referred to as the parent clusters, are extracted, which contain corresponding solutions \hat{x} , objective values \hat{f} , centroids $\hat{\mu}$, and covariances $\hat{\sigma}$. In the next step of the learning process, more components are added to the model. This step is to compensate the covariance loss during the optimization process after the sampling stage. In this step, for each component Φ_i , first, the top α percentage of the best solutions (\hat{x}_{sel} and \hat{f}_{sel}) are selected. Then, the selected set of solutions is analyzed to see if they have outliers using the Z-score outlier detection method [34]. This method is represented as

$$\frac{\|\hat{x}_{sel} - \hat{\mu}\|}{\hat{\sigma}} > \lambda, \quad (14)$$

where λ is the distance threshold from the centroids $\hat{\mu}$. According to this mechanism, if an outlier solution is at the top α percentage of the best solutions, it will be considered as the centroid of a new component in the mixture $\hat{\phi}$, referred to as an *outlier-based cluster*. For the newly formed components, we assume an independent multivariate Gaussian distribution, where the variance of each dimension is calculated as half of the distance from the initial centroid in each component.

By the end of the learning mechanism, a mixture of models is learned, one component on top of each cluster, in such a way that the probability of sampling top quality solutions becomes high. Having the mixture of models, new solutions are sampled via the **SAMPLING** method as x_{sam} . Then, the **REPAIRING** method simply refines the newly sampled solutions based on the boundaries of the solution domain x_{min} and x_{max} . Following the repairing process, new individuals will be obtained as x_{rep} . After evaluating the objective value of the obtained solutions, f_{rep} , via the **EVALUATION** process, the new individuals are combined with the individuals from the previous population, and the **REPLACEMENT** mechanism is invoked to form the new population and the corresponding objective values f in the current iteration. Population aggregation method is used for this mechanism in this research. The process mentioned continues until at least one stopping criteria is met.

4 Numerical Simulations

The presented algorithm is incorporated with two aforementioned low-thrust trajectory optimization schemes including Lyapunov and Q-law feedback control methods. In this section, the presented optimization approach is tested in two experiments, with respect to the orbit transfer missions from the literature. Both time-optimal and mass-optimal trajectories are considered in each experiment and the results are analyzed accordingly.

In the first experiment, a low-thrust orbital maneuver from a Geostationary Transfer Orbit to Geostationary Orbit (GTO to GEO) is considered [21, 35]. Owing to the almost circular nature of the target orbit in this case, Ω and ω are free variables, and the algorithm needs to target only a , e , and i . In this experiment, EEDA is incorporated in both Lyapunov and Q-law control methods in order to compare their performances. Results indicate that the proposed approach outperforms the other method based on averaging technique and another Q-law-based method from the literature. Furthermore, we observe a similar performance between the EEDA+Lyapunov and EEDA+Q-law approaches in some circumstances. This shows the potential of the EEDA to extract nuances in the behavior that allows the simple Lyapunov controller to match the much more advance Q-law controller performance.

The second experiment is a transfer from a Geostationary Transfer Orbit to a retrograde Molniya-type orbit (GTO to Molniya) [18, 20, 36]. In this case, the weighting coefficients corresponding to all slowly varying orbital elements are considered to be optimized. The Lyapunov feedback control method incorporated with the proposed EEDA is implemented in this experiment. It will be shown that the obtained solutions have higher quality in terms of fuel consumption and transfer time in comparison to the results from other references based on nominal Q-law methods. Also, the quality of the obtained solutions and the convergence of the algorithm are compared with other EAs. However, when compared to other Genetic Algorithm Q-law solutions, there is a gap in performance that can arise due to the use of a simple Lyapunov controller instead of the Q-law.

In the case of time-optimal transfers, the cost function provided to the optimizer is simply the final time of flight. A penalty term is added for not converging to the target orbit, along with a residual on the orbit elements. The mass-optimal transfers are more complex. It is unclear if truly mass-optimal low-thrust transfers will converge to the target orbit within a practical time frame, and thus it is necessarily to impose a time restriction. This can be done by fixing the arrival time and incorporating this as a constraint in the optimization process. However, relaxing this to a maximum time constraint is easier to solve whilst ensuring the same mass-optimal solution as long as the dynamics remain Keplerian. Hence, the cost function includes the propellant mass used and a penalty term when the time of flight exceeds the desired maximum arrival time. Again a penalty term on the residual is provided to encourage trajectories to converge.

Table 2 EEDA parameter settings

Parameter	Value
Number of parent clusters	$3 \leq N_c \leq 8$
Truncation factor	$0 \leq \gamma \leq 1$
Outlier detection parameter	$0.01 \leq \alpha \leq 0.1$
Distance threshold	$\lambda = 1$
Number of iterations	$N = 100$
Population size	$M = 100$

Table 3 Initial and final orbital parameters for GTO to GEO transfer

	a (km)	e	i (deg)	Ω (deg)	ω (deg)	ν (deg)
Initial orbit	24505.9	0.725	7	0	0	0
Final orbit	42,165	0	0	<i>free</i>	<i>free</i>	<i>free</i>
Convergence	36.0	8.5e-4	0.1	-	-	-

In order to realize the best choice for the interpolation spline, several numbers of interpolation points have been considered. It is possible to consider a very high number of interpolation points. However, increasing the number of interpolation points results in having more number of decision variables to be optimized and an increase in the optimization problem complexity. Having this insight, the number of interpolation points is considered as $N_p = 1$ to $N_p = 5$. The optimization has been run 10 times for each case. Therefore, a total number of 50 optimization runs have been processed, including 10 runs for each $N_p = 1, \dots, 5$. Some of the EEDA parameters are randomly selected for each individual run, while some other settings have been set to constant values. The algorithm settings are provided in Table 2.

According to the provided settings, the total number of decision variables \vec{x} varies with the number of interpolation points and the number of weights that are considered for the problem. In GTO to GEO mission, we have $4 \times N_p$ decision variables to consider in the optimization since two orbital elements are considered free, along with the absolute effectivity threshold. However, in GTO to Molniya mission, the number of decision variables is $6 \times N_p$ since all orbital elements are considered in optimization. Also, the boundaries of the decision variables are $x_{min} = 0$ and $x_{max} = 1$ since the weights are normalized as mentioned previously.

4.1 GTO to GEO

First, a GTO to GEO transfer with an inclination change is considered in Keplerian dynamics, and the details for which are provided in Table 3.

The parameters are chosen to compare with [21] and [35]. The modeled spacecraft has the mass of 2000 kg, the thrust level of $0.35N$, and the specific impulse (Isp) of 2000s, giving an initial thrust-to-mass ratio of 0.000175 ms^{-2} . In the mass-optimal case, the upper bound on the time of flight is 150 days. Following

the insights from the previous experiment, the incorporation of EEDA with Lyapunov method is competitive to Q-law methods. Therefore, in this experiment, the proposed algorithm is implemented in both Lyapunov and Q-law control methods in this space mission, and time-optimal and fuel-optimal transfers are solved. The best obtained transfer trajectories for the Q-law method are shown in Fig. 2a and b for fuel-optimal and time-optimal transfers, respectively. Also, Fig. 3a and b show the best obtained solutions for the Lyapunov method, similarly for fuel-optimal and time-optimal transfers, respectively.

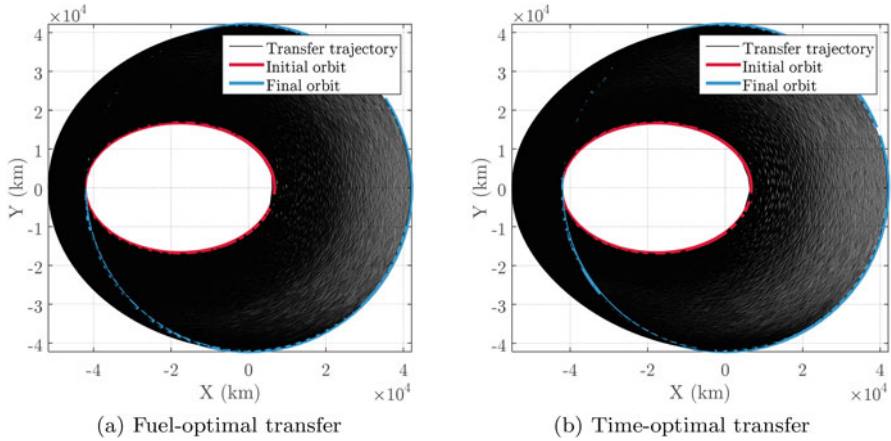


Fig. 2 3D visualization of trajectories for GTO to GEO transfer based on Q-law method

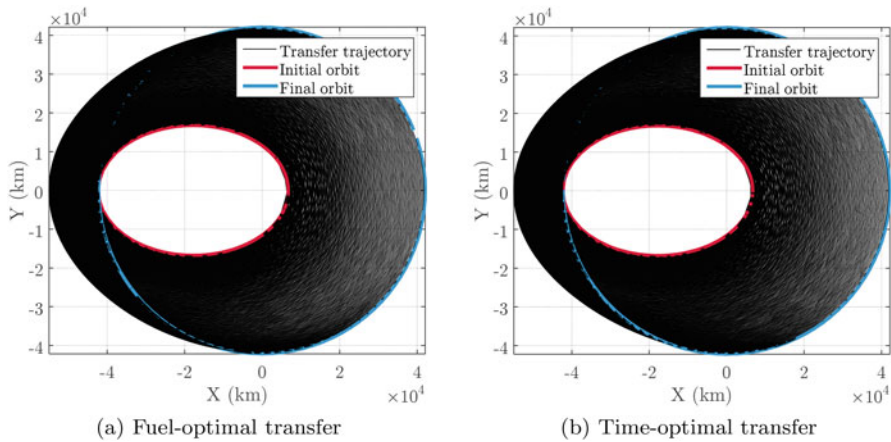


Fig. 3 3D visualization of trajectories for GTO to GEO transfer based on simple Lyapunov method

As the figures indicate, the transfer trajectories have small difference, mainly due to the very low amount of thrust level. In order to realize the differences within the transfer trajectories, the time variation of state variables is depicted in Figs. 4 and 5 for the Q-law method and simple Lyapunov method, respectively.

The exact values of the transfer time and the actual fuel mass consumption for this problem are provided in Table 4.

Several observations can be made from Table 4. First, the implementation of the proposed algorithm with Lyapunov method ends up in the solutions with almost the same quality of the averaging method in [35]. However, the implementation of the proposed algorithm with Q-law method results in a slightly better solutions in both time-optimal and fuel-optimal transfers. Comparing the obtained results from the Q-law implementation with the results from [21] shows that the proposed approach is able to find a solution close to the one presented in the literature in the time-optimal problem. However, in fuel-optimal problem, the amount of fuel mass is a bit higher than the solution from [21]. Overall, the proposed approach is shown to be competitive to the recently developed methods for obtaining low-thrust transfer trajectory design and optimization.

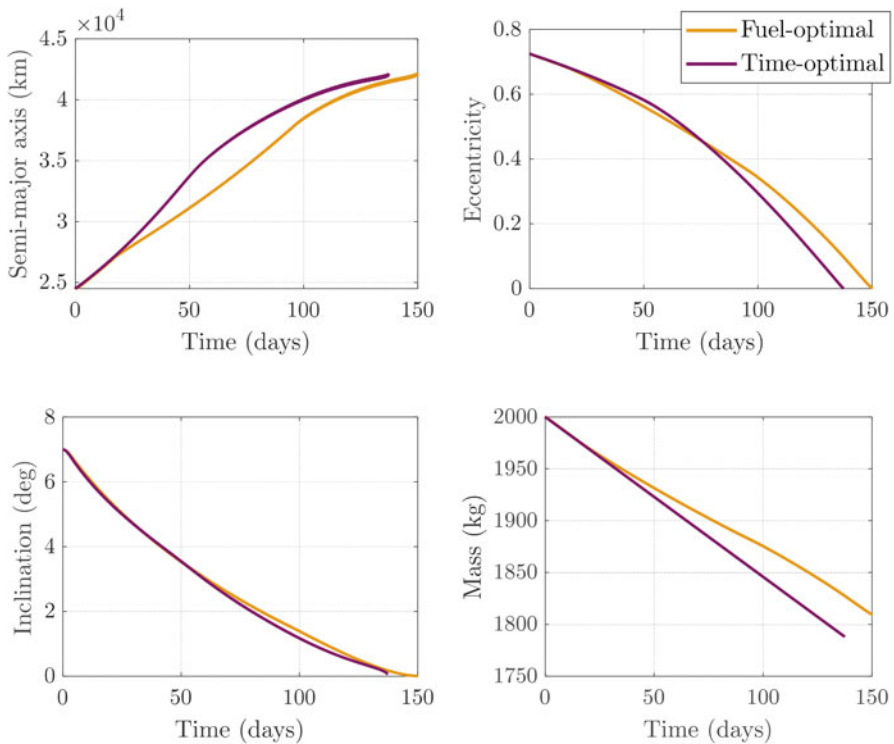


Fig. 4 State variables for fuel-optimal and time-optimal transfers based on Q-law method in GTO to GEO transfer

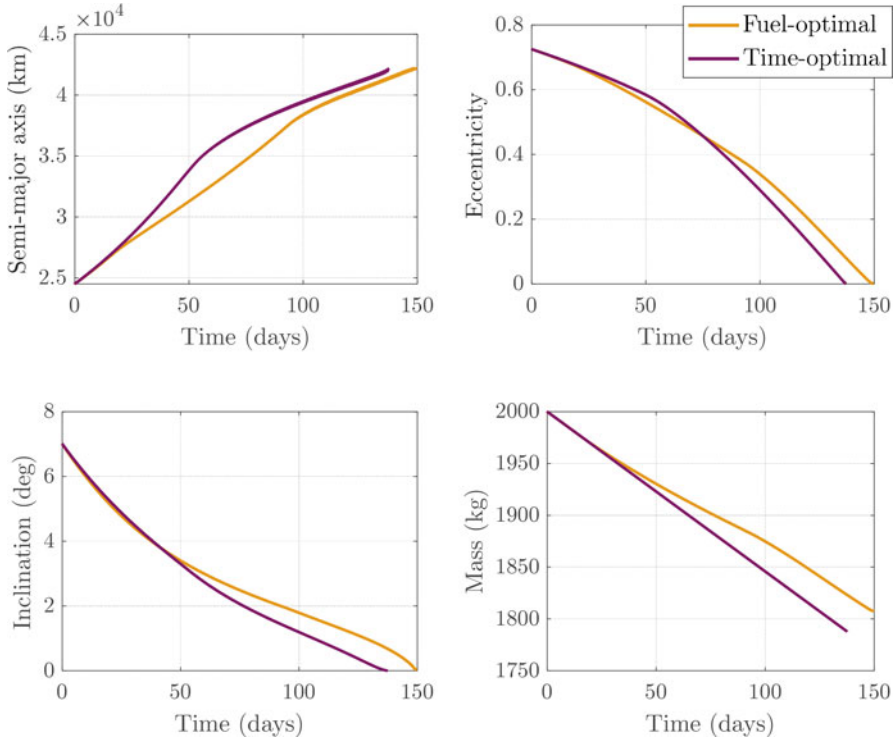


Fig. 5 State variables for fuel-optimal and time-optimal transfers based on simple Lyapunov method in GTO to GEO transfer

Table 4 Comparison of the obtained solutions for GTO to GEO transfer

	Min-time	Fuel mass (kg)	Min-fuel	Fuel mass (kg)
	Time (day)		Time (day)	
Q-law+EEDA method	137.34	211.76	149.99	190.40
Lyapunov+EEDA method	137.5	212.01	149.70	192.34
Averaging method [35]	137.5	212	150	192
Q-law method [21]	137.3	211.72	150	187.97

The corresponding variation of the optimized weights for Q-law method is depicted in Fig. 6a and b for fuel-optimal and time-optimal transfers, respectively.

As shown in the figures, the variations of weights for semi-major axis, eccentricity, and inclination start with the values which are close in fuel-optimal and time-optimal transfers. The significant difference between the two is the mean value of the absolute threshold, which is higher in fuel-optimal transfer in comparison to time-optimal transfer. Similarly, the optimized variation of weights for Lyapunov method is illustrated in Fig. 7a and b

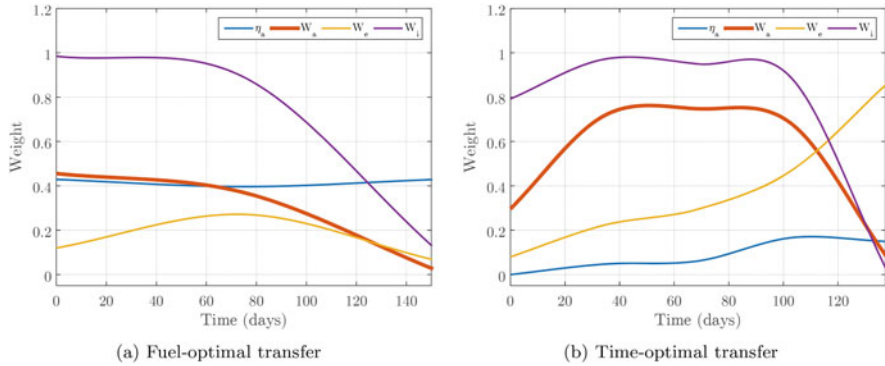


Fig. 6 Weighting coefficient profiles for GTO to GEO transfer based on Q-law method

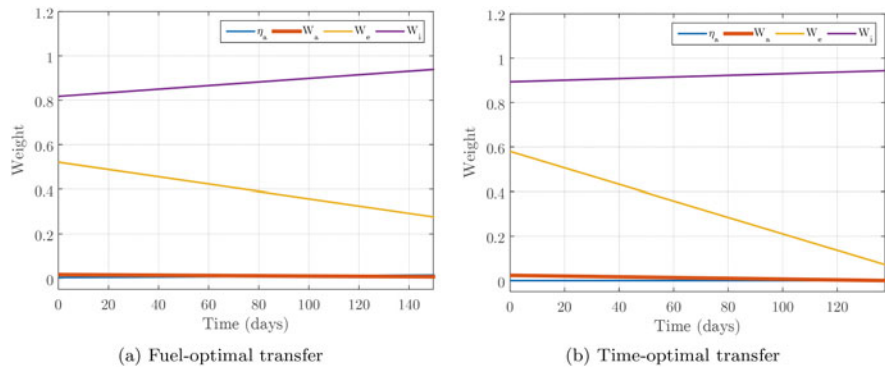


Fig. 7 Weighting coefficient profiles for GTO to GEO transfer based on simple Lyapunov method

Analyzing the weighting coefficients in Lyapunov method reveals a noticeable difference. According to the time variation of the weighting coefficients for Lyapunov method, the low-point interpolation seems to be more beneficial for the optimizer to find high-quality solutions in both fuel-optimal and time-optimal transfers. In this regard, the best obtained solution for time-optimal and fuel-optimal transfers for Lyapunov method is associated with $N_p = 2$, leading to conclude that the Lyapunov method requires less variation of weights for achieving optimal solutions, while Q-law method is more sensitive to time-variation of weights.

4.2 GTO to Molniya

In the second experiment, a GTO to Molniya transfer is considered, and the orbital elements of the initial and final orbits are provided in Table 5.

Table 5 Initial and final orbital parameters for GTO to Molniya transfer

	a (km)	e	i (deg)	Ω (deg)	ω (deg)	ν (deg)
Initial orbit	24505.9	0.725	0.06	0	0	0
Final orbit	26,500	0.7	116	270	180	<i>free</i>
Convergence	10.0	0.005	1.0	1.0	1.0	–

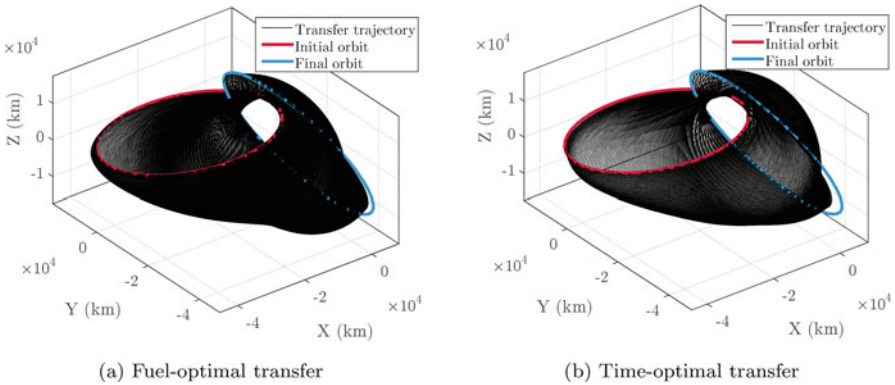


Fig. 8 3D visualization of trajectories for GTO to Molniya transfer based on simple Lyapunov method

As is evident from the table, this case involves large changes. The required plane change is about 116° . The modeled spacecraft has the mass of $= 2000$ kg, the thrust level of $T = 0.35N$, and the specific impulse of $I_{sp} = 2000s$, giving an initial thrust-to-mass ratio of 0.000175 ms^{-2} . In the mass-optimal case, the upper bound on the time of flight is 150 days.

For this case, the proposed algorithm is implemented in Lyapunov control method, and time-optimal and fuel-optimal transfers are solved. Figure 8a and b show the initial and final orbits along with the transfer trajectory, corresponding to the best obtained solution in min-fuel and min-time problems, respectively.

As can be seen, the time-optimal transfer trajectory significantly has more revolutions to reach the final orbit relative to fuel-optimal transfer. The time variation of state variables for this example is shown in Fig. 9.

The details of the transfer time and the actual fuel mass consumption for this problem are provided in Table 6.

Table 6 also includes the corresponding transfer time and fuel mass of the obtained solutions from other methods in the literature. As can be seen, the obtained solutions by the proposed method in this research significantly have higher quality than the Lyapunov method in [36] and even the Q-law method in [20]. This comparison shows that the incorporation of the proposed optimizer within the Lyapunov control method is competitive to the Q-law method, which is a more complicated control technique. The variation of the weighting coefficients for the obtained transfers is illustrated in Fig. 10a and b.

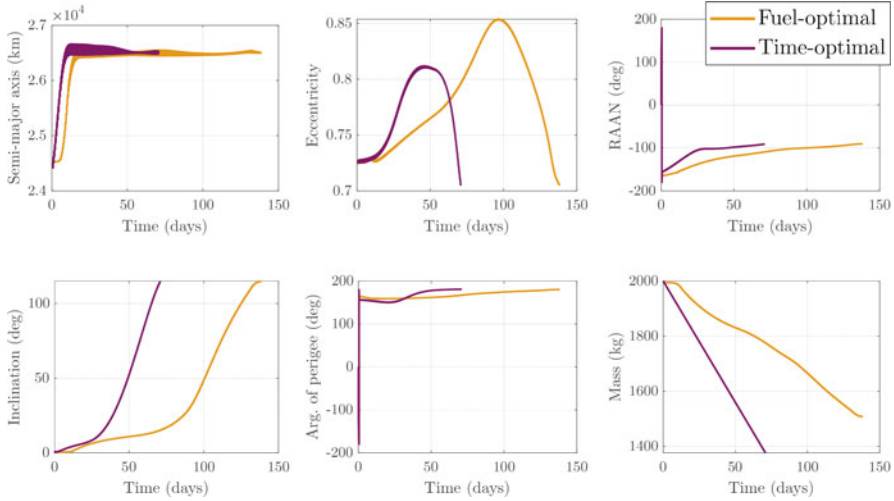


Fig. 9 State variables for fuel-optimal and time-optimal transfers based on simple Lyapunov method in GTO to Molniya transfer

Table 6 Comparison of the obtained solutions for GTO to Molniya transfer

	Min-time		Min-fuel	
	Time (day)	Fuel mass (kg)	Time (day)	Fuel mass (kg)
Lyapunov+EEDA method	70.83	624.01	138.34	492.89
Lyapunov method [36]	96.6	677.2	N. A.	N. A.
Q-law method [20]	84	734	150	580

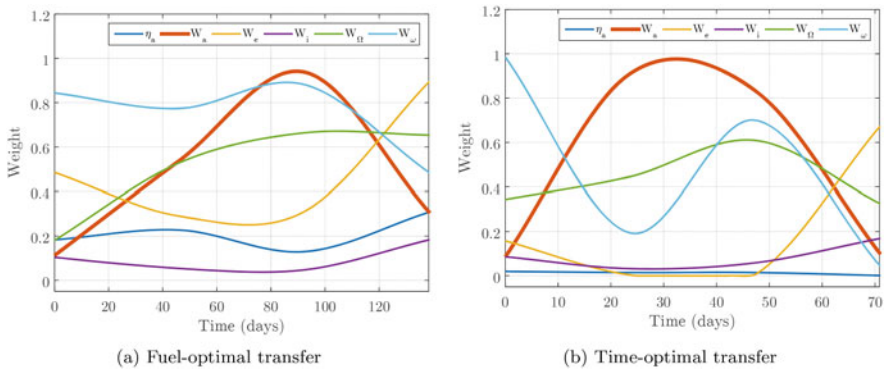


Fig. 10 Weighting coefficient profiles for GTO to Molniya transfer based on simple Lyapunov method

Following the variation of the optimized weighting coefficients, some remarks can be highlighted. It can be observed that there are some small similarities between time-optimal and fuel-optimal transfers. For instance, the absolute threshold η_a

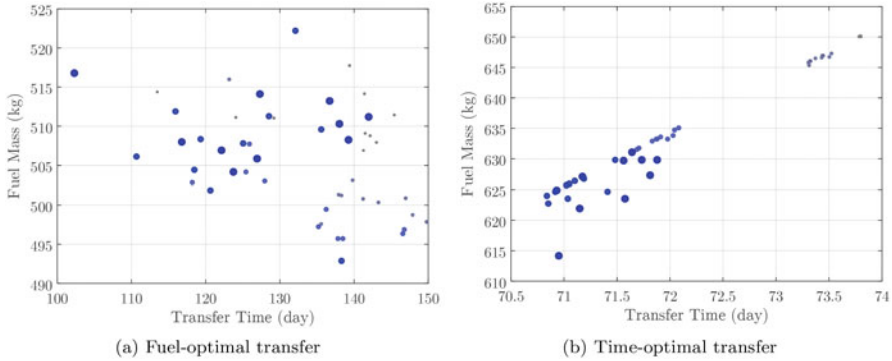


Fig. 11 Obtained solutions after optimization for GTO to Molniya transfer based on simple Lyapunov method

begins with a high value in both transfers. However, it slightly changes based on the desired objective. The semi-major axis weight has similar variation, and the weights of inclination are low in both problems.

It is noteworthy that the best obtained solution in both time-optimal and fuel-optimal cases corresponds to $N_p = 4$ in this scenario. Other solutions have been obtained as well out of 50 optimization runs, and they have more or less similar objective values. However, the absolute best solutions (min-time and min-fuel) indicate that 4-point interpolation can interpret the optimal variation of weights better than other number of interpolation points. In other words, a simple increase in the number of interpolation points does not necessarily lead us to high-quality solutions. The spread of the obtained solutions, depicted in Fig. 11a and b, confirms this fact.

Figure 11a and b show the relative position of the obtained solution in each optimization run. In these figures, solutions that correspond to a higher number of interpolation points are plotted with bigger markers. As can be observed, it can be highlighted that in fuel-optimal transfer (Fig. 11a), the optimizer did not find any high-quality solutions with 5-point interpolation, and the majority of the points with lower fuel mass correspond to 3-point and 4-point interpolation. The existence of some of the points near the transfer time of 150 days (the maximum allowable simulation time) with fuel mass less than 500 kg indicates that this region has the potential for finding better solutions. Interesting remarks can be highlighted from the distribution of the obtained solutions in time-optimal transfer (Fig. 11b) as well. Unlike the previous case, the distribution of the 5-point interpolation shows that increasing the number of interpolation points leads the optimizer to find solutions with better quality. As can be seen, the solution with the lowest fuel mass in time-optimal solution belongs to $N_p = 5$ with a transfer time of 70.95 days and the fuel mass of 614.1 kg. This solution can also be selected as a substitute for the absolute best solution provided in Table 6. Other remark in this figure is the stock of the solutions for $N_p = 1$ in a specific region far from the desired region. This is another

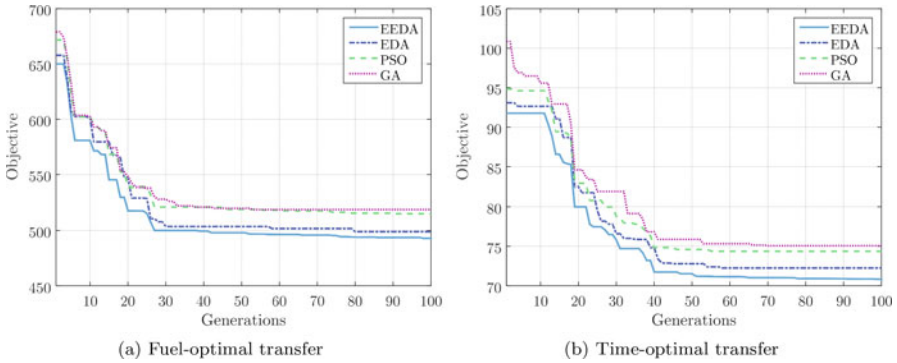


Fig. 12 Convergence of the algorithms for GTO to Molniya transfer based on simple Lyapunov method

observation which confirms the fact that increasing the number of interpolation points eventually leads the optimizer to find high-quality solutions.

The other analysis in this space mission is the comparison of the performance of EEDA with other well-known EAs. Such a comparison is shown in Fig. 12a and b.

In Fig. 12a and b, the convergence of the proposed algorithm EEDA is compared with normal EDA, PSO, and GA for fuel-optimal and time-optimal transfers. Comparing EEDA and EDA confirms the effectiveness of the proposed learning mechanism in enhancing the optimization process. Also, it is evident that EDA-based algorithms outperform traditional EAs such as PSO and GA in finding optimal transfer trajectories in this research.

5 Conclusion

In this chapter, the problem of optimal design of low-thrust Earth-orbiting trajectories for space missions is considered. When considering complex trajectory optimization problems with non-convexity and strong nonlinearity, it has been demonstrated that intelligent optimization algorithms are effective in optimal trajectory design. To tackle the extreme complexity of the search space, an enhanced evolutionary algorithm within the framework of EDAs, named EEDA, is proposed and applied to an approach based on Lyapunov and Q-law methods. In both methods, the unknown weighting coefficients are interpolated with Hermite polynomials, and the optimizer is implemented to optimize the variation of weights for minimizing the transfer time and the fuel consumption. Simulation results are carried out to demonstrate the effectiveness of the proposed approach. It has been realized that the implementation of EEDA with simple Lyapunov function is competitive to the Q-law method. The comparison shows the potential of the EEDA in enabling the simple Lyapunov controller to recover the finer nuances explicitly

given within the analytical expressions in the Q-law. Also, it has been discovered that increasing the number of interpolation points does not necessarily increase the chance of achieving the optimal solution. In other words, the choice of the proper number of interpolation points is problem-dependence and needs to be adjusted according to the type of the orbit transfer mission.

Current research can be extended in various aspects. Regarding the algorithm enhancement, various further improvements can be the aim for the future research. As for the seeding mechanism, the improvement can be toward obtaining initial feasible population in a more efficient method. For instance, the current mechanism does not use any information from the gradient of the solution domain. Therefore, future works can be conducted in considering gradient-based methods within the seeding mechanism to improve the process. Incorporation of such techniques, more specifically, gradient-based stochastic operators, in minimization of the objective function is also a new area for further research.

References

1. J. T. Betts, *Practical Methods for Optimal Control and Estimation Using Nonlinear Programming*. Society for Industrial and Applied Mathematics, 2010.
2. B. A. Conway, *Spacecraft trajectory optimization*. Cambridge University Press, 2010.
3. A. Shirazi, J. Ceberio, and J. A. Lozano, "Spacecraft trajectory optimization: A review of models, objectives, approaches and solutions," *Progress in Aerospace Sciences*, vol. 102, pp. 76–98, oct 2018.
4. R. Chai, A. Savvaris, A. Tsourdos, S. Chai, and Y. Xia, "Unified multiobjective optimization scheme for aeroassisted vehicle trajectory planning," *Journal of Guidance, Control, and Dynamics*, vol. 41, no. 7, pp. 1521–1530, Jul. 2018. [Online]. Available: <https://doi.org/10.2514/1.g003189>
5. G. qun Wu, L.-G. Tan, X. Li, and S.-M. Song, "Multi-objective optimization for time-open lambert rendezvous between non-coplanar orbits," *International Journal of Aeronautical and Space Sciences*, vol. 21, no. 2, pp. 560–575, Nov. 2019. [Online]. Available: <https://doi.org/10.1007/s42405-019-00231-z>
6. M. Pontani, "Optimal low-thrust hyperbolic rendezvous for earth-mars missions," *Acta Astronautica*, vol. 162, pp. 608–619, 2019.
7. J. A. Englander and B. A. Conway, "Automated solution of the low-thrust interplanetary trajectory problem," *Journal of Guidance, Control, and Dynamics*, vol. 40, no. 1, pp. 15–27, 2017.
8. S. Sarno, J. Guo, M. D'Errico, and E. Gill, "A guidance approach to satellite formation reconfiguration based on convex optimization and genetic algorithms," *Advances in Space Research*, vol. 65, no. 8, pp. 2003–2017, Apr. 2020. [Online]. Available: <https://doi.org/10.1016/j.asr.2020.01.033>
9. Z. Zheng, J. Guo, and E. Gill, "Distributed onboard mission planning for multi-satellite systems," *Aerospace Science and Technology*, vol. 89, pp. 111–122, Jun. 2019. [Online]. Available: <https://doi.org/10.1016/j.ast.2019.03.054>
10. Z. Fan, M. Huo, N. Qi, Y. Xu, and Z. Song, "Fast preliminary design of low-thrust trajectories for multi-asteroid exploration," *Aerospace Science and Technology*, vol. 93, p. 105295, Oct. 2019. [Online]. Available: <https://doi.org/10.1016/j.ast.2019.07.028>
11. X. Li, X. Wang, and Y. Xiong, "A combination method using evolutionary algorithms in initial orbit determination for too short arc," *Advances in Space Research*, vol. 63, no. 2, pp. 999–1006, Jan. 2019. [Online]. Available: <https://doi.org/10.1016/j.asr.2018.08.036>

12. J. A. Lozano, P. Larrañaga, I. Inza, and E. Bengoetxea, *Towards a new evolutionary computation: advances on estimation of distribution algorithms*. Springer, 2006, vol. 192.
13. C. A. Kluever, "Simple guidance scheme for low-thrust orbit transfers," *Journal of Guidance, Control, and Dynamics*, vol. 21, no. 6, pp. 1015–1017, 1998.
14. A. E. Petropoulos, "Simple control laws for low-thrust orbit transfers," *AAS/AIAA Astrodynamics Specialists Conference*, 2003.
15. A. Petropoulos, "Refinements to the Q-law for low-thrust orbit transfers," in *Advances in the Astronautical Sciences*, vol. 120, 2005, pp. 963–982.
16. Y. Gao and X. Li, "Optimization of low-thrust many-revolution transfers and Lyapunov-based guidance," *Acta Astronautica*, vol. 66, no. 1–2, pp. 117–129, 2010.
17. J. L. Shannon, M. T. Ozimek, J. A. Atchison, and M. Christine, "Q-law aided Direct Trajectory Optimization for the High-fidelity, Many-revolution Low-thrust Orbit Transfer Problem," in *AAS*, no. 19, 2019, p. 448.
18. S. Lee, A. Petropoulos, and P. von Allmen, "Low-thrust Orbit Transfer Optimization with Refined Q-law and Multi-objective Genetic Algorithm," *Advances In The Astronautical Sciences*, 2005.
19. G. Varga and J. M. Sánchez Pérez, "Many-Revolution Low-Thrust Orbit Transfer Computation Using Equinoctial Q-Law Including J2 and Eclipse Effects," *Icatt 2016*, pp. 2463–2481, 2016.
20. A. E. Petropoulos, Z. B. Tarzi, G. Lantoine, T. Dargent, and R. Epenoy, "Techniques for designing many-revolution electric-propulsion trajectories," *Advances in the Astronautical Sciences*, vol. 152, no. 3, pp. 2367–2386, 2014.
21. D. L. Yang, B. Xu, and L. Zhang, "Optimal low-thrust spiral trajectories using Lyapunov-based guidance," *Acta Astronautica*, vol. 126, pp. 275–285, 2016.
22. K. F. Wakker, *Fundamentals of Astrodynamics*. TU Delft Library, 2015.
23. R. H. Battin, *An Introduction to the Mathematics and Methods of Astrodynamics*. New York: AIAA Education Series, 1987.
24. H. Holt, R. Armellini, N. Baresi, Y. Hashida, A. Turconi, A. Scorsoglio, and R. Furfaro, "Optimal q-laws via reinforcement learning with guaranteed stability," *Acta Astronautica*, vol. 187, pp. 511–528, 2021.
25. J. L. Shannon, D. Ellison, and C. Hartzell, "Analytical Partial Derivatives of the Q-Law Guidance Algorithm," in *AAS*, 2021, pp. 1–15.
26. H. Schaub and J. L. Junkins, *Analytical Mechanics of Space Systems, Fourth Edition*. American Institute of Aeronautics and Astronautics, Inc., 2018.
27. M. Pontani and M. Pustorino, "Nonlinear earth orbit control using low-thrust propulsion," *Acta Astronautica*, vol. 179, pp. 296–310, 2021.
28. J. R. Rice, *Numerical Methods in Software and Analysis*. Elsevier, 2014.
29. E. Catmull and R. Rom, "A class of local interpolating splines," in *Computer Aided Geometric Design*. Elsevier, 1974, pp. 317–326.
30. F. N. Fritsch and R. E. Carlson, "Monotone piecewise cubic interpolation," *SIAM Journal on Numerical Analysis*, vol. 17, no. 2, pp. 238–246, 1980.
31. C. De Boor, C. De Boor, E.-U. Mathématicien, C. De Boor, and C. De Boor, *A practical guide to splines*. Springer-Verlag New York, 1978, vol. 27.
32. P. Larrañaga and J. A. Lozano, *Estimation of distribution algorithms: A new tool for evolutionary computation*. Springer Science & Business Media, 2001, vol. 2.
33. D. Arthur and S. Vassilvitskii, "k-means++: The advantages of careful seeding," Stanford, Tech. Rep., 2006.
34. V. Hodge and J. Austin, "A survey of outlier detection methodologies," *Artificial intelligence review*, vol. 22, no. 2, pp. 85–126, 2004.
35. S. Geffroy and R. Epenoy, "Optimal low-thrust transfers with constraints - Generalization of averaging techniques," *Acta Astronautica*, vol. 41, no. 3, pp. 133–149, 1997.
36. A. Petropoulos, "Low-thrust orbit transfers using candidate Lyapunov functions with a mechanism for coasting," in *AIAA/AAS Astrodynamics Specialist Conference and Exhibit*, 2004, p. 5089.